Surface Science of Catalysis

Surface Science of Catalysis
In Situ Probes and Reaction Kinetics

Daniel J. Dwyer, EDITOR
University of Maine at Orono

Friedrich M. Hoffmann, EDITOR
Exxon Research and Engineering

The paper used in this publication meets the minimum requirements of American National
Standard for Information Sciences—Permanence of Paper for Printed Library Materials, ANSI
Z39.48–1984.

American Chemical Society
Library
1155 16th St., N.W.
Washington, D.C. 20036

ACS Symposium Series

M. Joan Comstock, *Series Editor*

1992 ACS Books Advisory Board

Foreword

THE ACS SYMPOSIUM SERIES was founded in 1974 to provide a medium for publishing symposia quickly in book form. The format of the Series parallels that of the continuing ADVANCES IN CHEMISTRY SERIES except that, in order to save time, the papers are not typeset, but are reproduced as they are submitted by the authors in camera-ready form. Papers are reviewed under the supervision of the editors with the assistance of the Advisory Board and are selected to maintain the integrity of the symposia. Both reviews and reports of research are acceptable, because symposia may embrace both types of presentation. However, verbatim reproductions of previously published papers are not accepted.

Preface

RESEARCHERS IN THE FIELDS OF SURFACE SCIENCE AND CATALYSIS share the desire to understand and control molecular processes at the gas–solid interface. In spite of this mutual interest, these fields have evolved from quite opposite perspectives. Catalysis that deals with complex reactions on supported metals at high pressures has been increasingly concerned with identifying fundamental steps that control reaction kinetics and selectivities. To characterize the structural and electronic factors that control these elementary reaction steps, it is necessary to obtain a better understanding of the gas–solid interaction. Surface science, on the other hand, has evolved from the study of gas–solid interaction at well-characterized single-crystal surfaces at low pressure. The knowledge gained from these simple model systems has made it clear that surface science must move to study reactions on more complex surfaces under more realistic conditions.

These developments have led to a condition in which catalysis and surface science are integrally linked and often difficult to distinguish. This book presents an overview of programs that are bridging the gap between these two communities and reflects the exciting developments and new discoveries in these merging fields.

The symposium on which this book is based brought together approximately 25 speakers from North America and Europe and represented a broad spectrum of chemists, physicists, and chemical engineers. Because of this high concentration of expertise in the fields of catalysis and surface science, it seemed appropriate that a permanent record of the proceedings be made.

The organization of this book follows that of the symposium under three broad topics: fundamental concepts of surface reactions, catalytic reactions at high pressure and in situ probes, and reactions induced by photons and electrostatic fields. We believe that this book will serve as

an important reference not only for experts in the field but also for those interested in gaining an overview of how the synergism between surface science and catalysis is advancing this important area.

DANIEL J. DWYER
University of Maine
Orono, ME 04469–0107

FRIEDRICH M. HOFFMANN
Exxon Research and Engineering Company
Annandale, NJ 08801

August 1991

Chapter 1

The Promise of Surface Science in Catalysis
Success or Failure?

Friedrich M. Hoffmann[1] and Daniel J. Dwyer[2]

[1]**Exxon Research and Engineering Company, Annandale, NJ 08801**
[2]**Laboratory for Surface Science and Technology, University of Maine, Orono, ME 04469-0107**

Heterogeneous catalysis is an important part of the technology that supports industrially developed societies. Production of transportation fuels, pollution control, production of low-cost and high-quality raw materials are just some of the areas in which heterogeneous catalysis impacts. The Council on Competitiveness, a non-profit and non-partisan organization of chief executives from business, higher education and organized labor, has identified catalysis as one of the technologies critical to international competitiveness [1]. Over the past two decades, the importance of heterogeneous catalysis resulted in considerable research and development activity, especially in such areas as synthetic fuels and pollution control. These efforts have significantly advanced the field and have lead to a new generation of catalysts ranging from the three-way automotive exhaust catalyst to new selective Fischer-Tropsch catalysts. Heterogeneous catalysis, however, is an interesting mixture of engineering, science and "art". In fact, much of the catalyst development since the beginning of this century has used a catalyst screening process, where literally thousands of catalysts were evaluated for their activity and selectivity. This has had some remarkable success, for example with the ammonia synthesis catalysts, which were developed 75 years ago at BASF or with the Fischer Tropsch catalysts developed during World War II in Germany. Even to date new or improved catalysts are often discovered by apparent intuition or happenstance rather than by design and it is often difficult to evaluate the contribution of science to advancement of the field. This is especially true when one considers the contributions of surface science. In the early to mid seventies, the advent of UHV surface characterization and the emergence of modern surface science promised to revolutionize the field by unlocking the details of the surface processes that control heterogeneous catalysis. Optimistic proponents of this new thrust promised that studies of surface structure, adsorption, chemisorption and catalytic reactions over well characterized surfaces would reveal the all important surface structure-function relationships. That knowledge then would revolutionize the development of "tailored", highly product

specific catalysts. In spite of some remarkable successes in elucidating the structural factors of catalytic reactions, these predictions have proven too optimistic, at least in a short-term time frame. Indeed, to our knowledge, no new catalyst system has been developed solely on leads originating from surface science. Nevertheless, surface science has been very successful in a less obvious way by making major inroads in the understanding of the elementary steps of many catalytic reactions. Just a casual examination of the literature will reveal that surface science increasingly has an important impact on the way the catalysis community approaches the art of catalysis. Surface science has changed the way researchers in catalysis address their field, it has shaped the way they think and it has made immeasurable contributions to the knowledge base from which their intuitive leaps are made.

Many of these changes were brought about by a new approach of synthesizing model catalysts, whose surface composition and structure can be controlled and characterized with a variety of surface probes from UHV to atmospheric conditions. Some of the advances gained from this new approach have led to:

1. A new understanding of *the interaction of molecules with surfaces* giving new insights into the adsorption properties and dynamics of molecules. In many cases, surface studies provide *reference data from single crystals surfaces* such as vibrational or electronic fingerprint data, which are useful to characterize more complex supported catalysts. Thermodynamic and kinetic data can be used to predict more complex catalytic processes, as discussed further below. Many new concepts have emerged or were unequivocally established from this new understanding. Examples are the characterization of molecular precursors, e.g. molecular oxygen, or reactions intermediates such as ethylidine, methoxy, formate species. Many of those species have been characterized in great detail with respect to their structure and adsorption geometry by a variety of powerful surface probes.

2. Information on the mechanism of reactions from *characterization of the elementary steps and intermediates*. Examples are the investigation of the role of kinetic energy in the dissociation of molecules with molecular beams, which have contributed among others to the understanding of CH bond activation of methane [2], [3], or the CO oxidation reaction (discussed further below).

3. The application of new *surface spectroscopies* in catalysis, many of which have originated in surface science and which are now commonly used both in catalysis and surface science. In this respect *surface physics* has played an important role by providing a fundamental understanding of these new spectroscopies. Examples are electron spectroscopies (Photoemission, AES, X-Ray Absorption), synchrotron probes (NEXAFS, FYNES, X-Ray scattering, Microtomography), Thermal Desorption Mass Spectroscopy, SIMS, vibrational spectroscopies, Scanning Tunneling Microscope (STM, AFM) etc.

In this chapter we present examples which demonstrate the strong mutual interaction between catalysis and surface science and which one might tentatively term "success stories of surface science in catalysis". These examples are by no means a complete list nor are they presented in order of importance. Our choice of

examples was driven primarily by our own research interests and therefore represent only a small fraction of the total body of literature that has been published. For a more detailed discussion of catalytic reactions over single crystal surfaces we refer to reviews by Somorjai [4], Campbell [5] and Rodriguez and Goodman [6].

Hydrogenation of Carbon Monoxide over Single Crystals

The energy crises of the early seventies led to a reconsideration of various alternative energy sources including the production of transportable fuels manufactured by synthesis gas chemistry. In this technology, synthesis gas (CO/H_2) prepared by gasification of coal is converted to liquid hydrocarbons over iron or cobalt catalysts in the Fischer-Tropsch reaction ($CO + H_2 \rightarrow C_nH_{2n+2} + ...$) or to methane over nickel catalysts ($CO + 3H_2 \rightarrow CH_4 + H_2O$). These forms of synthetic fuel production had been extensively studied in the forties and early fifties but interest waned upon the discovery of oil in the middle east after World War II. The extensive studies of this era, expertly summarized by Storch et al. [7], raised a number of interesting mechanistic issues involving the surface reaction pathways. Two general classes of reaction mechanisms were considered as possibilities at that time, the carbide model of Craxford and Rideal [8] and the hydroxymethylene model of Storch et al. [7]. One important distinction between the two concerned whether the carbon-oxygen bond of CO broke prior to or after hydrogen attack. In the carbide model CO was thought to be dissociatively chemisorbed on the catalysts surface forming a metal carbide, i.e. $CO_g \rightarrow CO_a \rightarrow C_a + O_a$. The metal carbide was subsequently hydrogenated to form the hydrocarbon intermediates which polymerize to form hydrocarbon products. The hydroxymethylene model, on the other hand, involved direct reaction between chemisorbed atomic hydrogen and chemisorbed molecular CO to form a hydroxymethylene intermediate. The postulated hydroxymethylene intermediate then underwent a stepwise polymerization process which lead to products. Support for the carbide model of Rideal was severely undermined by the radiotracer studies performed by Kummer, DeWitt and Emmett [9] which indicated that only a small fraction of carbidic carbon could be incorporated into the products. This study was widely cited as evidence that the hydrogenation of carbidic carbon was not a dominant reaction channel in the overall process. This tracer study coupled with the ability of the hydroxymethylene model to explain the presence of oxygenated hydrocarbons in the products resulted in the carbide mechanism being shelved for more than twenty years. However, when the oil embargoes of the seventies motivated renewed interest in the catalytic production of fuels, the carbide mechanism reemerged with the help of surface science and is today the most widely accepted.

In the seventies a new and promising approach appeared, which combined traditional high pressure catalytic reaction studies with modern UHV surface analytical tools. In this approach the catalytic response of well characterized single crystal surfaces was used to investigate the role of surface structure and composition in determining the catalytic response of hydrocarbon synthesis catalysts. This approach was pioneered by Somorjai and coworkers [10-12] who evaluated methanation and Fischer-Tropsch kinetics over atomically clean metal surfaces. These studies showed that the low surface area metal catalysts displayed product selectivities

and catalytic rates that were directly comparable to those observed for high surface area supported metal catalysts. The studies also showed the importance of surface carbon deposits in determining the rates and selectivities of the reactions. Working hydrocarbon synthesis catalysts were found to be covered by a mixture of carbidic and hydrocarbon fragments, whereas deactivation of the catalyst was accompanied by deposition of graphitic type of carbon. Interest in the nature of this carbonaceous deposit and the role it played in the overall reaction mechanism became a topic of some interest. The work of Biloen et al. [13], Kellner, Bell [14] and Brady, Pettit [15] indicated that surface carbon deposits on a number of transition metals could be hydrogenated to form a slate of products virtually identical to those encountered in conventional Fischer-Tropsch catalysis. The outcome of this work was the rebirth of the surface carbide mechanism and the definition of the terms reactive surface carbon (carbidic) and inactive carbon (graphitic).

The surface science approach to CO/H_2 catalysis was substantiated by Goodman et al. [16] who showed that the rate of methane formation over a Ni(100) single crystal surface was identical to that observed over high surface area supported Ni catalysts. This study was an important milestone in the establishment of low surface area single crystals as valid models of high surface area catalysts. The reason that the Ni(100) surface successfully reflected, on a per surface atom basis, the more complex surface of the supported metal particles was clearly demonstrated by Kelly and Goodman [17] in a subsequent paper. In this study the authors investigated the role of surface structure in the methanation reaction by comparing reaction rates obtained over two different single crystal faces of Ni with those obtained over supported metals. The data of Kelley and Goodman are reproduced in Figure 1 where the methanation kinetics for the Ni(100), Ni(111) and two high surface area materials are compared in an Arrhenius format. It can be seen in this figure that all of the rates are virtually identical indicating that the reaction is surface structure insensitive, at least within the experimental error. This structure insensitivity of the methanation reaction was unanticipated and resulted in much discussion within the catalysis community. The results, however, have stood up to the test of time and represent one of the important contributions of surface science to catalysis. These studies also substantiated the surface carbide mechanism by correlating the methanation rate to the amount and type of surface carbon as shown in Fig. 2. The surface carbon level was determined by Auger electron spectroscopy. From a line shape analysis of the Auger spectra these authors also could distinguish different forms of carbon, reactive surface carbide and unreactive graphite, which deactivated the catalyst. These findings clearly supported the hypothesis that surface carbide formation was an intermediate step to methane formation.

Bonzel and coworkers [18-21], using a similar approach, investigated the reaction of CO and H_2 over iron single crystals. These surfaces produced the traditional Fischer-Tropsch products, straight chained alkanes. The iron surfaces were found to be quite susceptible to the deposition of carbon which had a substantial impact on the reaction rates. The investigators were able to identify with X-ray Photoelectron Spectroscopy (XPS) three types of carbon on the surface after reaction. The working catalytic surface was found to be covered by a mixture of hydrocarbon fragments as well as carbidic carbon. Once again, deactivation of the surface under reaction conditions was associated with excessive carbon deposition in the form of graphitic carbon.
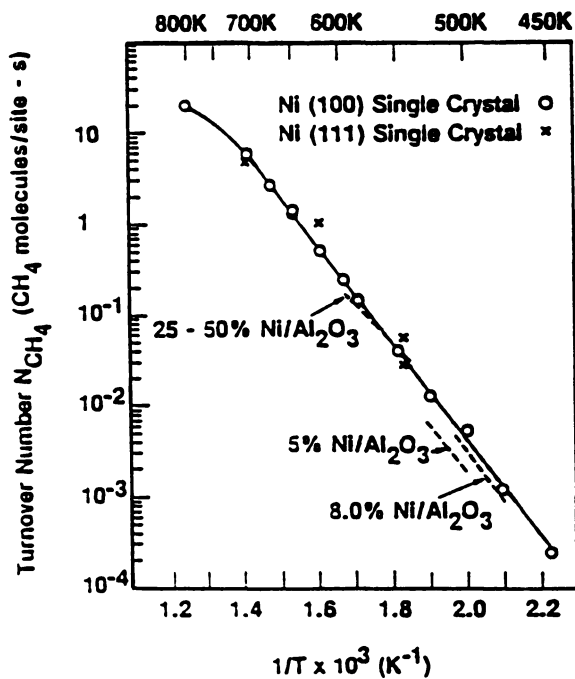
Figure 1: Comparison of methane synthesis rate over Ni(100) and Ni(111) single crystal catalysts and supported Ni catalysts for reaction at 120 Torr and a H_2:CO ratio of 4:1. (Reproduced with permission from ref. 17. Copyright 1982 Elsevier.)

Pt. No.	H_2/CO Ratio	Press. (Torr)
1	4.0	1
2	4.0	10
3	4.0	36
4	4.0	61
5	4.0	50
6	4.0	120
7	4.0	500
8	4.0	1000
9	1.0	10
10	1.0	50
11	1.0	200
12	1.0	500
13	0.1	110
14	0.4	34
15	2.7	89

Figure 2: Methanation rate versus surface carbon level for CO hydrogenation at 625 K over a Ni(100) catalyst. (Reproduced with permission from ref. 17. Copyright 1982 Elsevier.)

Clearly, surface science has had an impact on the CO/H_2 catalysis. The use of well characterized surfaces as models for high surface area materials has contributed extensively to our knowledge base in this area. The definition of reactive surface carbon, the role of alkali promoters, the structure insensitivity of methanation, surface reconstruction under reaction conditions are just a few of the concepts that surface science has introduced into the language of catalysis. These types of studies are continuing to uncover new and exciting leads in the area of CO/H_2 catalysis such as the creation of bimetallic model systems where ultrathin metal overlayers exhibit highly unusual chemisorptive and catalytic behavior [22].

Ammonia Synthesis

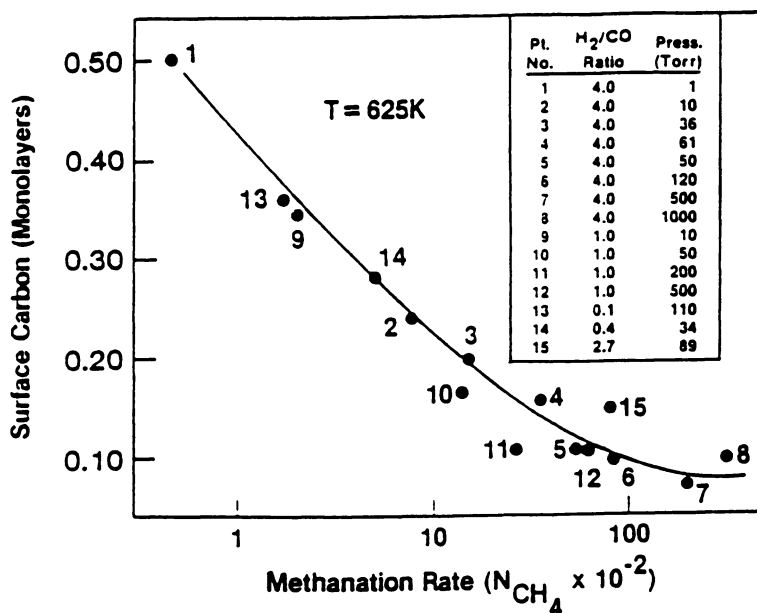The ammonia synthesis ($N_2 + 3H_2 \rightarrow 2NH_3$) is an example of a *structure sensitive reaction*. The development of a commercial catalyst for this process at the beginning of this century has been one of the early successes of catalysis. The catalyst, iron promoted with alumina and potassium, is still commercially used today. Its composition has been found by Mitasch, Haber and Bosch at BASF through extensive screening of about 2500 catalysts [23]. In spite of the early success in developing a working catalyst and the intensive research which followed, the mechanism of the reaction was not established unequivocally until the late seventies with pioneering work by the groups of Ertl [24], [25] and Somorjai [4]. The development of new surface science techniques permitted to establish the structural sensitivity of this reaction as a key factor controlling the activity. Detailed investigations of the adsorption of nitrogen on iron single crystal surfaces by Ertl and collaborators [26],[27] showed that the rate of dissociative nitrogen chemisorption depends strongly on the surface structure. Fig. 3 shows that the rates of dissociative adsorption of nitrogen on the three low-indexed iron surfaces are found to be in the sequence (111) > (100) > (110). From the initial rates it can be seen that the open (111) surface is about 60 times more active for nitrogen dissociation than the closed packed (110) surface (for bcc structure models see Fig. 4). Moreover, Boszo et al. found that the sticking coefficient of nitrogen was very low in the order of 10^{-6}. The latter indicates that the dissociation of nitrogen is the rate-limiting step in this reaction. The relevance of these findings to the synthesis of ammonia has been demonstrated by the Somorjai group [28],[29]. Studies of the ammonia synthesis reaction over single crystal surfaces at high pressure (20 bar) and temperature (500°C) revealed that the activity varied for iron by two orders of magnitude in the same order (111) > (100) > (110) as shown in Fig. 4. These results confirm that the Fe(111) surface is the most active of the basal orientations and hence suggest that this surface might be a good model catalyst. In fact, high resolution Transmission Electron Microscope images obtained together with the corresponding electron diffraction pattern of an activated catalyst particle show that the catalyst primarily consists of small crystallite particles of (111) orientation [30].

The knowledge of the parameters describing the kinetics of the elementary steps on the Fe(111) model catalyst has enabled Stoltze and Nørskov [31] to predict theoretically the ammonia yield of a commercial catalyst in high pressure industrial
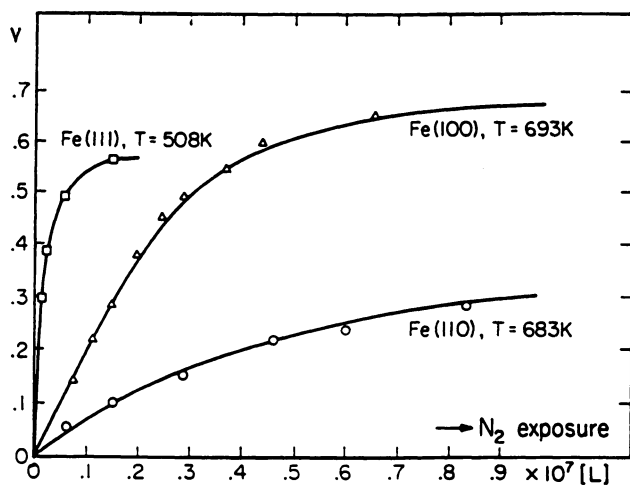
Figure 3: Adsorption of nitrogen on the Fe(111), (100), and (110) surfaces measured as a function of N_2 exposure. (Reproduced with permission from ref. 27. Copyright 1977 Academic.)
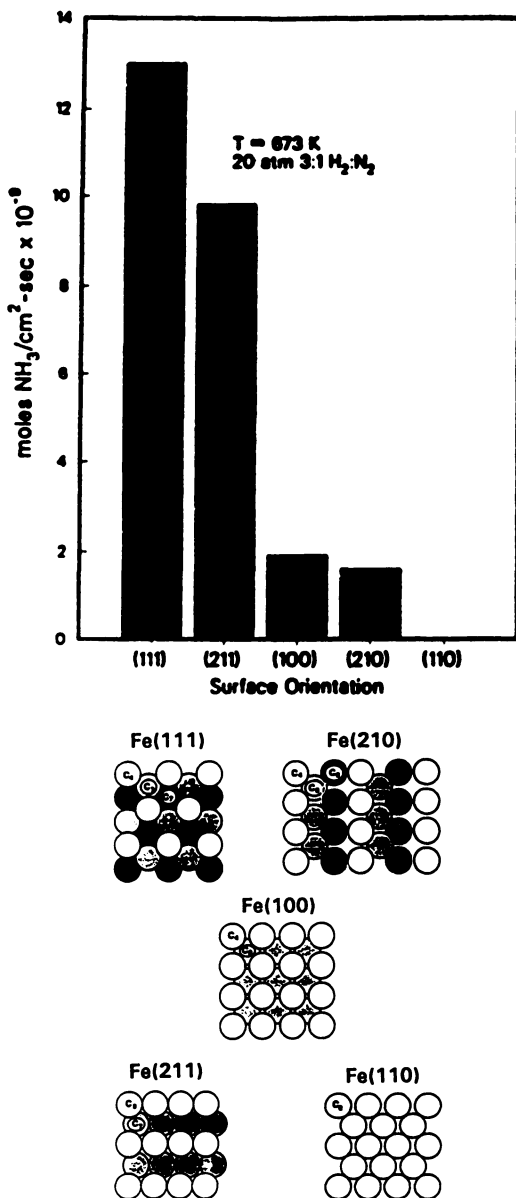
Figure 4: Structure sensitivity of the rate of ammonia synthesis studied over different iron single crystal surfaces at 673 K and 20 atm (H_2:N_2=3:1). The bottom shows structure models of the low index surfaces of bcc iron. (Reproduced with permission from ref. 29. Copyright 1987 Academic.)

reactors. As shown in Fig. 5, the theoretical predictions show excellent agreement with experimental values covering a pressure range from 1 atm to 150 atm. These calculations demonstrate that from the knowledge of the elementary reaction steps a quantitative description of a complex technical process can be obtained. Thus the ammonia synthesis reaction is a particularly good example demonstrating the successful interaction of surface science and catalysis, where studies on model catalysts preformed under UHV and atmospheric conditions allow to elucidate the elementary steps of a catalytic reaction.

CO Oxidation Reaction

The catalytic oxidation of CO is an economically important reaction due to its relevance for automotive emission control. Moreover, it is considered as a model for a "simple" surface reaction since the classic work of Langmuir [32]. The large number of studies following Langmuir's work, however, show that even "simple" surface reactions can be quite complex. At low pressure, the reaction mechanism on platinum group metals has been explored in detail [33] and proceeds via the following steps

$$
\begin{aligned}
CO &\rightarrow CO_{ad} \\
O_2 &\rightarrow 2O_{ad} \\
CO_{ad} + O_{ad} &\rightarrow CO_2
\end{aligned}
$$
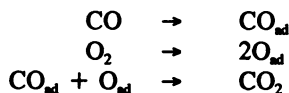
Pioneering molecular beam studies by Engel, Ertl and collaborators [34], [35] have unambiguously established the Langmuir-Hinshelwood mechanism as the only reaction path on platinum metals at low pressure, i.e. the reaction occurs at the surface with both reactants in the chemisorbed state. In detailed UHV studies, using a variety of surface probes, Ertl and collaborators also have characterized the adsorption energetics and kinetics of oxygen and carbon monoxide on various single crystal surfaces of Pd and Pt [33]. These and other studies have led to a detailed understanding of the CO oxidation on platinum metals at low pressure. This is illustrated in Fig. 6 with the energetics of the reaction on Pt(111) in the limit of low coverage [36,37]. The potential energy diagram shows that the transition state between the chemisorbed state of $CO_{ad} + O_{ad}$ and $CO_{2,ad}$ is about 30 kcal/mole above that of the adsorbed CO_2 molecule. This leaves the CO_2 molecule with considerable excess energy which can be either transferred to the substrate or leave a vibrationally and translationally "hot" molecule as demonstrated by Haller and collaborators [38] and discussed in detail in Chapter 4.

Models based on parameters from the adsorption energetics and kinetics determined in UHV studies have been successful in predicting most of the reaction behavior at high pressure as demonstrated for the reaction on rhodium by Oh et al. [39] and by Schwartz et al. [40]. Measurements of the steady-state kinetics of the CO oxidation reaction at high pressures by Peden, Goodman and collaborators [41-45] demonstrate the validity of single crystal models. The comparison of reaction rates over single crystal surfaces for Ru and Rh in Fig. 7 shows excellent agreement with reaction rates measured over supported metals. These high pressure experiments with
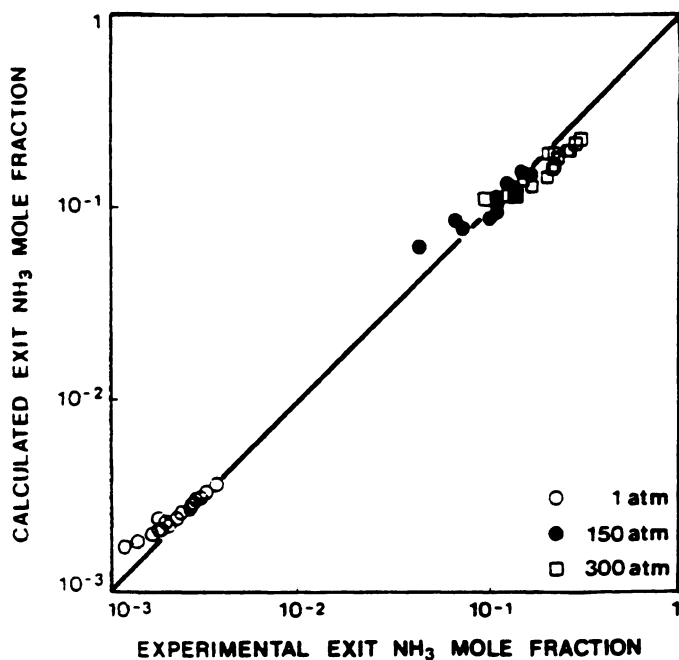
Figure 5: Comparison of calculated vs. experimentally determined ammonia yields from a commercial catalytic reactor. The data span a broad range of pressures from 1 atm to 300 atm. The calculation is based on values obtained from single crystal model studies. (Reproduced with permission from ref. 31. Copyright 1985 American Physical Society.)
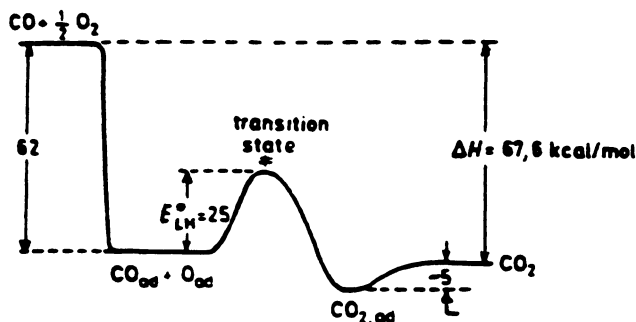
Figure 6: Potential energy diagram for the CO oxidation reaction on Pt(111) in the limit of low coverage. (Reproduced with permission from ref. 37. Copyright 1984 Elsevier.)
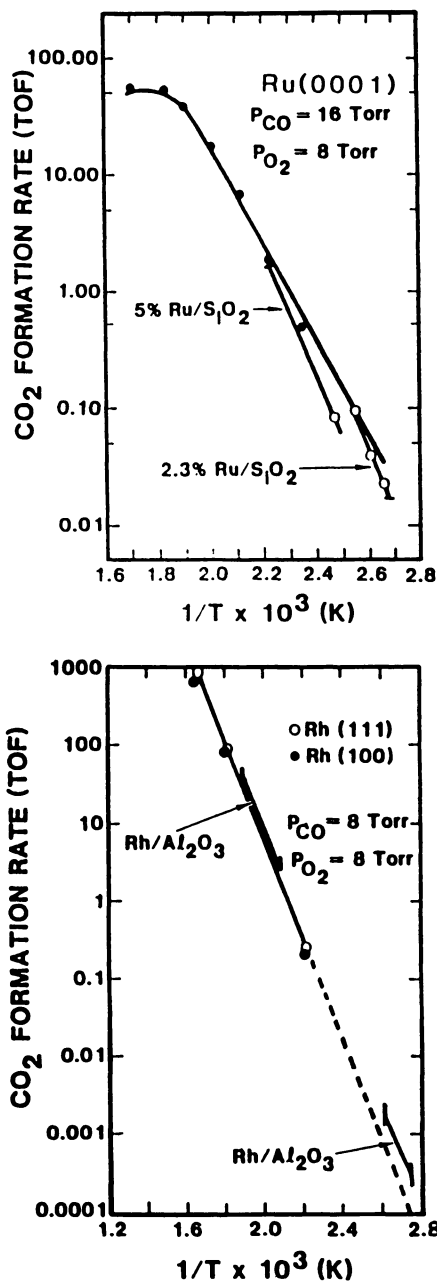
Figure 7: Comparison of CO oxidation rates obtained for single crystal model catalysts and supported metals for ruthenium (top panel) and rhodium (bottom panel). (Reproduced from ref. 42. Copyright 1986 American Chemical Society.)

single crystal surfaces also demonstrate some characteristic differences to the reaction at low pressure. Ruthenium, for example, is the least active of these metals in UHV. At high pressures, on the other hand, it is the most active metal [41]. This has been explained with the unique ability of ruthenium to maintain high oxygen coverages ($\approx 1$ ML) at high pressures [41] leading to unusually weak CO adsorption ($E_{CO} < 10$ kcal/mole) [46, 47], as discussed in detail in Chapter 9.

In spite of this rather detailed understanding of the energetics and kinetics on platinum metals, in particular at low pressure, the CO oxidation reaction is still the subject of very active research. Recently, Ertl and collaborators [48] have studied the oscillatory behavior of the CO oxidation reaction on Pt single crystal surfaces revealing on a microscopic level complex spatial and temporal patterns in this seemingly "simple" reaction.

Alkali Promotion - Surface Additives

Surface additives play an important role in the inhibition, promotion or selectivity of catalytic reactions. Alkali promoters are used in a large number of commercial catalytic processes, e.g. the Ammonia synthesis, CO hydrogenation, gasification, methanol synthesis and direct methane oxidation. Although alkali promoters have been in use for about eighty years, the mechanism of alkali promotion is still the subject of intense studies due to its complexity. One aspect of the promoter effect on the rate of a catalytic reaction is due to the modification of the adsorption properties of a metal surface promoted by an alkali metal. In the case of a coadsorbed molecule this can lead to molecular bond weakening and enhanced molecular dissociation. One model of the promoter mechanism has been proposed in the late sixties by Dry et al. [49], who suggested that adsorbed alkali atoms enhance the ability of the metal substrate to donate charge into antibonding orbitals of a coadsorbed molecule, e.g. CO. This enhanced backdonation of metal electrons then results in internal bond weakening of the adsorbed molecule and enhanced dissociation. Early systematic surface science studies with single crystal surfaces have confirmed that coadsorption of alkali metals leads to a considerable increase in the dissociative adsorption for NO [50], CO [51] and N_2 [52]. These early studies initiated an enormous number of surface science studies [53], [54]. The full extent of the alkali induced molecular bond weakening probably was not fully recognized until it had been dramatically demonstrated with high resolution Electron Energy Loss Spectroscopy. CO adsorbed in the presence of potassium on Pt(111) [55] and Ru(001) [56] exhibited dramatic frequency shifts for the C-O stretching vibration (2000 cm^{-1} to 1400 cm^{-1}). Overtone spectroscopy and isotopic scrambling in thermal desorption confirmed the existence of anomalously weak bonds [56]. Despite a large number of studies, a full quantitative understanding of the mechanism causing the frequency shifts and the bond weakening is still in dispute to date. It is clear that a through-metal interaction mechanism alone cannot give a full account of these observations. Direct interaction via molecular overlap and rehybridization between the CO molecule and the K-atom [57], [58] and electrostatic interactions [59] have been suggested to be important factors as well. Rehybridization and direct molecular overlap become more dominant at high alkali coverage, where the alkali atom exhibits "metallic" behavior. The latter

is due to the adsorption properties of alkali atoms on transition metal surfaces. At low coverage, K adsorbs strongly on Ru with high adsorption energy ($\approx$ 60-80 kcal/mole) and a large workfunction decrease (-4.3 eV) characteristic of a highly polarized ("ionic") K atom and significant K-Ru rehybridization. At high potassium coverage the adsorption behavior is dominated by strong K-K repulsion, the metal-substrate interaction is reduced and the K-atoms exhibit "metallic" behavior and a chemical behavior similar to that of bulk potassium. This different chemical behavior has been demonstrated with the interaction of methanol with potassium on Ru(001) [60]. At high submonolayer K-coverage, potassium compound formation to potassium methoxide was observed. In contrast, at low potassium coverage compound formation was absent, but potassium affected the decomposition behavior of methanol through electronic modification of the ruthenium substrate. The strong dependence of the alkali-substrate and alkali-coadsorbate interaction both on the alkali coverage and on the coverage of the coadsorbate accounts for the complex behavior of alkali promoters in surface reactions. Thus it is not surprising that even the "simplest" case CO/K is still a subject of controversy.

Studies of alkali promoter effects in catalytic reactions on single crystals have been carried out for the ammonia synthesis reaction and the CO hydrogenation reaction. These two reactions are typical examples of two different ways the alkali promoter affects catalytic reactions by either promoting activity or by product selectivity. In the former case of ammonia synthesis, alkali promotion results in a substantial increase in activity [61]. Ertl and coworkers [52] showed that on iron single crystal surfaces the rate of ammonia dissociation is increased by at least two orders of magnitudes. For N_2/Fe(111), the adsorption energy of the molecular 'precursor' was found to increase from 8 to 11 kcal/mole [62]. This stabilization of the molecular 'precursor' by the alkali metal also lowers the overall barrier for dissociation as shown schematically in Fig. 8.

In CO Hydrogenation studies, addition of potassium promoters did *not* result in an overall increase in activity. In contrast, even though the CO dissociation rates are markedly increased by the presence of potassium [19],[64], the methanation rate is generally decreased. However, kinetic measurements over Ni(100) [65] and iron [64], [66] showed a marked increase in the selectivity towards higher hydrocarbons. Figure 9 shows that alkali promotion shifts the product distribution from the light alkanes CH_4 and C_2H_6 to higher molecular weight alkenes and aldehydes. This increase in higher hydrocarbon production has been attributed by Campbell and Goodman [65] to the increase in the steady-state level of active carbon, which is seen as a factor leading to increased C-C bond formation. While this model is helpful in explaining the increased C-C bond formation, it is most likely *not* the sole mechanism responsible for the effect of alkalis on the selectivity in this reaction. For example, an important secondary reaction in F-T chemistry is the readsorption and incorporation of the primary products, alkenes. It is most likely that potassium may modify either the adsorption of these alkenes or their hydrogenability to alkanes [66]. Similarly, the improved selectivity towards oxygenates which is observed on Fe [66] most likely results from changes in surface chemistry of the alkali promoted surface. The importance of alkali compound formation has been demonstrated with recent CO/H_2 studies on K/Ru(001) surfaces which show the direct participation of potassium in the hydrogenation of CO to formate [67].
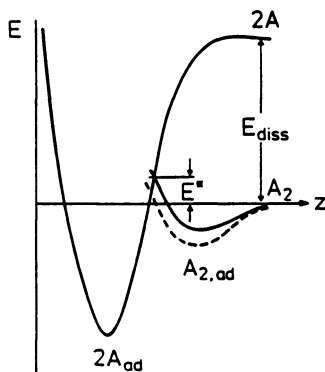
Figure 8: Potential diagram for adsorbed molecular and dissociated nitrogen. The presence of an alkali metal increases the adsorption energy for molecular nitrogen resulting in a lowering of the activation energy for dissociation E*. (Reproduced with permission from ref. 63. Copyright 1989 Elsevier.)

Figure 9: Product distributions from CO hydrogenation over potassium promoted and unpromoted iron powders (H_2:CO=3:1, 7 atm, 540 K). (Reproduced with permission from ref. 66. Copyright 1989 Elsevier.)

The examples presented here illustrate only some aspects of 'the' alkali promoter mechanism. We feel, that in spite of large number of surface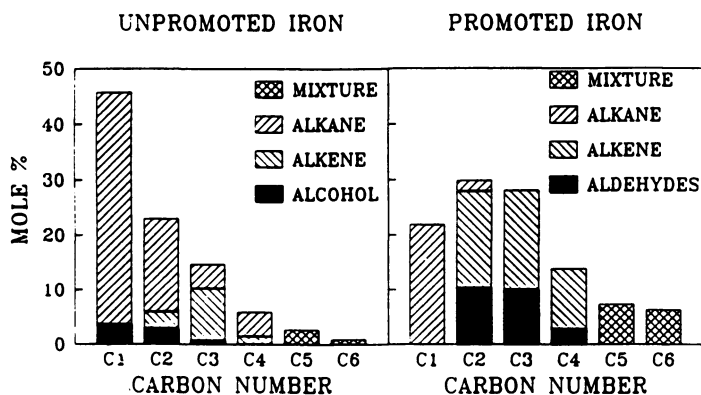 studies we are just at the beginning of understanding alkali promotion and much is yet to come. Alkali promotion is an example for the complexity which can govern catalytic reactions. It demonstrates at the same time, however, the power of the surface science synthesis approach which allows us to make model systems and study them in great detail in spite of their complexity.

Bimetallic Model Catalysts

Bimetallic catalysts are of great importance in reforming catalysis and their development has been an important factor in the emergence of modern (unleaded) gasolines. The study of bimetallic model catalysts and their effect on catalytic reactivity and selectivity has been pioneered by Schwab [68], Hall and Emmett [69] and others in the decades after World War II. These studies concentrated on exploring the effect of the "electronic" factor on the *catalytic activity* resulting from *alloy* formation of Group VIII and IB metals [70]. Pioneering work by Sinfelt and collaborators [71] resulted in the discovery that the addition of Group IB to a Group VIII metal also resulted in remarkable changes in *catalytic selectivity*, e.g. for the hydrogenolysis reaction, which was inhibited at the expense of improved selectivity to alkane isomerization. It was also recognized that miscibility and the ability to form alloys between the two metals were not a necessary prerequisite for this effect. This resulted in the establishment of immiscible *bimetallic* model catalysts such as the classical ruthenium-copper system introduced by Sinfelt [72]. Utilizing a surface science approach, Christmann, Ertl and collaborators [73-76] introduced a new method of synthesizing Cu-Ru model catalysts by evaporation of copper onto single crystal Ru(001) under UHV conditions. This approach permitted the use of a variety of surface sensitive probes in characterizing thin metallic overlayers, e.g. Electron Spectroscopies (Auger, LEED, UPS, XPS etc.), thermal desorption and workfunction probes. Using probe molecules such as carbon monoxide, whose adsorption properties on metals are well understood, the chemical properties of thin metallic overlayers can be characterized. This is demonstrated for the case Cu/Ru(001) with Fig. 10, which shows thermal desorption data for CO adsorbed on Cu-Ru(001) as a function of copper coverage [78]. CO adsorbed on a monolayer of Cu (α_4) desorbs at a temperature between that of a thick copper overlayer (α_1, α_2) and that of CO adsorbed on clean Ru(001) (β_2, β_3). This suggests that CO adsorbs on the copper monolayer with higher adsorption energy than on bulk copper indicating a chemical modification of copper by the underlying ruthenium substrate. The coexistence of thermal desorption features characteristic of pure ruthenium (β_2, β_3) at submonolayer coverages indicates the existence of domains of unmodified ruthenium substrate. The latter can be quite convincingly demonstrated with vibrational data obtained by Fourier Transform Infrared Reflection-Absorption Spectroscopy in Fig. 11, where CO adsorbed on Ru and Cu can be distinguished by their characteristic C-O stretch frequencies [79]. At submonolayer coverages both CO-Cu (2082 cm^{-1}) and CO-Ru (2054 cm^{-1}) bands are observed while at 1 ML coverage only a CO-Cu band is observed. The latter is characteristic of a pseudomorphic copper monolayer indicating
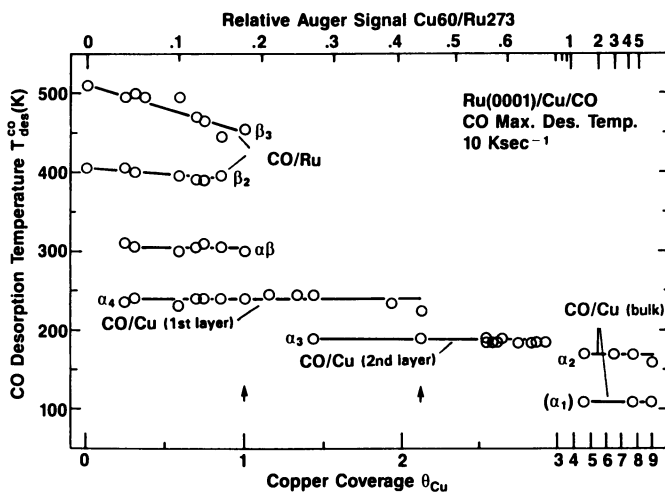
Figure 10: CO desorption temperatures for Cu/Ru(001) surfaces as a function of copper coverage. (Reproduced with permission from ref. 78. Copyright 1986 Elsevier.)

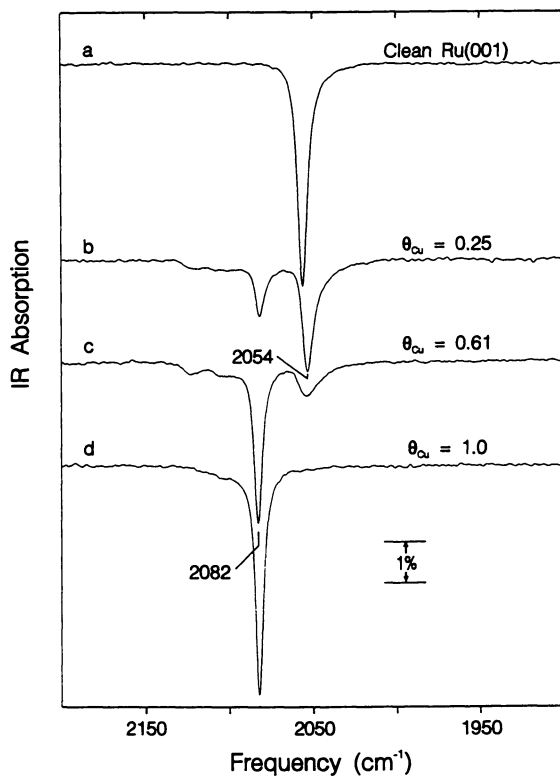Figure 11: Vibrational spectra of CO adsorbed on Cu-Ru(001) surfaces as a function of copper coverage. At submonolayer coverages, both CO-Ru and CO-Cu bands are observed. The disappearance of the CO-Ru band at $\theta_{CO} = 1.0$ is characteristic for the pseudomorphic Cu monolayer indicating layer-by-layer growth. (Reproduced with permission from ref. 79. Copyright 1986 American Institute of Physics.)

layer-by-layer growth of the copper film [75, 77]. At submonolayer coverages island formation of copper can be concluded from an analysis of the vibrational lineshapes, as discussed in detail in Chapter 13. An analysis of the frequency shifts for the CO stretch of CO-Cu and CO-Ru shows indeed a chemical modification of the copper overlayer as previously suggested by the TDMS data [79]. Frequency shifts of the CO-Cu band indicate a higher amount of backdonation for CO adsorbed on a copper monolayer in comparison to CO adsorbed on bulk copper. The sensitivity of the C-O stretch with respect to its chemical environment has also been used to characterize the changes in copper dispersion resulting from annealing of the overlayer [80]. The method of using FT-IRAS and CO as a molecular probe to characterize metallic overlayers has been recently used by Goodman and collaborators on a variety of bimetallic systems as described in detail in Chapter 5.

To date a large number of bimetallic model systems has been studied both at low and high pressure and the reader is referred to excellent recent reviews on this subject by Campbell [81] and Rodriguez, Goodmann [6]. High pressure studies on single crystal Au/Pt(111) surface alloys by Sachtler and Somorjai [82-84] have shown similar increases in the selectivity towards isomerization at the expense of hydrogenolysis as has been observed for the supported systems. The authors attributed this result to an ensemble effect, i.e. to the requirement of a large number of adjacent Pt sites for hydrogenolysis. Similarly, Peden and Goodman [85, 86] observe for the Cu/Ru(001) system a linear decrease in the ethane hydrogenolysis rate, which is ascribed to the role of Cu as an inactive site-blocker. For the same system, these authors also find that the addition of Cu causes a dramatic increase in the rate for the dehydrogenation of cyclohexane to benzene. This enhancement may be related to the altered geometric and electronic properties of the strained Cu overlayer or to a hydrogen spillover effect from Ru to Cu. Peden and Goodman [86] also point out that the hydrogen spillover from Ru to Cu which they observe may lead to an overestimate in the Ru surface atom density for supported metals since the latter is determined by H_2 chemisorption.

Conclusion

The examples which we have presented here, demonstrate the mutual interaction of surface science and catalysis in the study of fundamental aspects of catalytic reactions. This mutual interaction has had some remarkable successes in obtaining a rather detailed understanding of the fundamental processes controlling reactions. This success is based on a large span in activity ranging from studies on single crystal surfaces in UHV to catalytic studies on supported catalysts at high pressure. The development of in-situ and ex-situ techniques to study catalytic reactions at high pressures both on single crystal surfaces and supported catalysts has been a vital ingredient to this success.

Literature Cited

1.   *Gaining New Ground: Technology Priorities for America's Future*; Council of Competitiveness, Washington, D.C., 1991.

2.   Rettner, C.T.; Pfnür H.E.; Auerbach, D.J. *Phys. Rev. Lett.* **1985**, *54*, 2716.
3.   Lee, M.B.; Yang, Q.Y.; Tang S.L.; Ceyer, S.T. *J. Chem. Phys.* **1986**, *85*, 1693.
4.   Somorjai G.A. in *Chemistry in Two Dimensions*; Cornell University Press, Ithaca, 1981.
5.   Campbell, C.T. *Adv. Catalysis*, **1989**, *36*, 1.
6.   Rodriguez J.A.; Goodman, D.W. *Surface Sci. Rep.*, in press.
7.   Storch, H. H.; Golumbic, N.; Anderson, R.B. *The Fischer-Tropsch and Related Syntheses*, Wiley, New York, 1951.
8.   Craxford, S. R.; Rideal E.K. *J. Chem. Soc.* **1939**, *1*, 604.
9.   Kummer, J.T.; DeWitt, T.W.; Emmett, P.H. *J. Amer. Chem. Soc.* **1948**, *70*, 3632.
10. Sexton, B.A.; Somorjai, G.A. *J. Catal.* **1977**, *46*, 167.
11. Dwyer, D.J.; Somorjai, G. A. *J. Catal.* **1978**, *52*, 291.
12. Dwyer, D.J.; Somorjai, G. A. *J. Catal.* **1979**, *56*, 249.
13. Biloen, P.; Helle, H.N.; Sachtler W.M.H. *J. Catal.* **1979**, *58*, 95.
14. Kellner, C.S.; Bell, A.T. *J. Catal.* **1981**, *70*, 418.
15. Brady, R.C.; Pettit, R. *J. Am. Chem. Soc.* **1981**, *103*, 1287.
16. Goodman, D.W.; Kelley, R.D.; Madey T.E.; Yates J.T. *J. Catal.* **1980**, *63*, 226.
17. Kelley, R.D.; Goodman D.W. *Surface Sci.* **1982**, *123*, L743.
18. Bonzel H.P.; Krebs H.J. *Surface Sci.* **1981**, *109*, L527.
19. Bonzel H.P.; *Chem. Ing. Tech.* **1982**, *54*, 908.
20. Krebs H.J.; Bonzel H.P., *Surface Sci.* **1982**, *88*, 269.
21. Bonzel H.P.; Broden G.; Krebs H.J. *Appl. Surface Sci.* **1983**, *16*, 373.
22. Greenlief C.M.; Berlowitz P.J.; Goodman D.W.; White J.M. *J. Phys. Chem.*, **1987** *91*, 6669.
23. Mitasch, A. in *Geschichte der Ammoniaksynthese*, Verlag Chemie, Weinheim, 1951.
24. Ertl, G. in *Catalytic Ammonia Synthesis*, J.R. Jennings, Ed., Plenum, New York, 1983.
25. Ertl, G. *Angew. Int. Ed. Engl.* **1990**, *29*, 1219.
26. Boszo, F.; Ertl, G.; Grunze M.; Weiss M. *J. Catal.* **1977**, *49*, 18.
27. Boszo, F.; Ertl, G.; Weiss, M. *J. Catal.* **1977**, *50*, 519.
28. Spencer, N.D.; Schoonmaker, R.C.; Somorjai G.A. *J. Catal.* **1982**, *74*, 129.
29. Strongin, D.R.; Carrazza J.; Bare, S.R.; Somorjai G.A. *J. Catal.* **1987**, *103*, 213.
30. Schlögl, R. in *Catalytic Ammonia Synthesis*, J.R. Jennings (Ed.), Plenum, New York, 1983.
31. Stoltze, P.; Nørskov, J.K. *Phys. Rev. Letters* **1985**, *55*, 2502.
32. Langmuir, I. *Trans. Faraday Soc.* **1922**, *17*, 621.
33. Engel, T.; Ertl, G. *Adv. Catal.* **1979**, *28*, 1.
34. Engel, T.; Ertl, G. *Chem. Phys. Lett.* **1978**, *54*, 95.
35. Engel, T.; Ertl, G.J. *Chem. Phys.* **1978**, *69*, 1267.
36. Campbell, C.T.; Ertl, G.; Kuipers, H.; Segner, J. *J. Chem. Phys.* **1980**, *73*, 5862.

37. Segner, J.; Campbell, C.T.; Doyen, G.; Ertl, G. *Surface Sci.* **1984**, *138*, 505.
38. Mantell, D.A.; Ryali, S.B.; Halpern, B.L.; Haller, G.L.; Fenn, J.B. *Chem. Phys. Letters* **1981**, *81*, 185.
39. Oh, S.H.; Fisher, G.B.; Carpenter, J.E.; Goodman, D.W. *J. Catal.* **1986**, *100*, 360.
40. Schwartz, S.B.; Schmidt, L.D.; Fisher, G.B. *J. Phys. Chem.* **1984**, *90*, 6194.
41. Peden, C.H.F.; Goodman, D.W. *J. Phys. Chem.* **1986**, *90*, 1360.
42. Goodman, D.W.; Peden, C.H.F. *J. Phys. Chem.* **1986**, *90*, 4839.
43. Peden, C.H.F.; Goodman, D.W.; Blair, D.S.; Berlowitz, P.J.; Fisher, G.B.; Oh, S.H. *J. Phys. Chem.* **1988**, *92*, 1563.
44. Kellogg, G.L. *J. Catal.* **1985**, *92*, 162.
45. Berlowitz, P.J.; Peden, C.H.F.; Goodman, D.W. *J. Phys. Chem.* **1988**, *92*, 5213.
46. Peden, C.H.F.; Goodman, D.W.; Weisel, M.D.; Hoffmann, F.M. *Surface Sci.*, **1991**, *253*, 44.
47. Hoffmann, F.M.; Weisel, M.D.; Peden, C.H.F. *Surface Sci.*, **1991**, *253*, 59.
48. Ertl, G. *Adv. Catal.*, **1990**, *37*, 213.
49. Dry, M.E.; Shingles, T.; Boshoff, L.F.; Oosthuizen, G.F. *J. Catal.* **1969**, *15*, 190.
50. Goddard, P.J.; West, J.; Lambert, R.M. *Surface Sci.* **1978**, *71*, 447.
51. Broden, G.; Gafner, G.; Bonzel, H.P. *Surface Sci.* **1979**, *84*, 295.
52. Ertl, G.; Weiss, M.; Lee, S.B. *Chem. Phys. Lett.* **1979**, *60*, 391.
53. Bonzel, H.P. *Surface Sci. Reports*, **1987**, *8*, 866.
54. *Physics and Chemistry of Alkali Adsorption*, Bonzel, H.P.; Bradshaw, A.M.; Ertl, G., Eds.; Materials Science Monographs, Elsevier, 1989; Vol. 57, and references therein.
55. Crowell, J.E.; Garfunkel, E.L.; Somorjai, G.E. *Surface Sci.* **1982**, *121*, 303 and *J. Phys. Chem.* **1982**, *86*, 310.
56. Hoffmann, F.M.; de Paola, R.A. *Phys. Rev. Letters* **1984**, *52*, 1697.
57. Wimmer, E.; Fu, C.L.; Freeman, A.J. *Phys. Rev. Letters* **1985**, *55*, 2618.
58. Eberhardt, W.; Hoffmann, F.M., de Paola, R.A.; Heskett, D.; Strathy, I.; Plummer, E.W. *Phys. Rev. Letters* **1985**, **54**, 1856.
59. Lang, N.D.; Holloway, S.; Nørskov, J.K. *Surface Sci.* **1985**, *150*, 24.
60. Hrbek, J.; de Paola, R.A.; Hoffmann, F.M. *Surface Sci.* **1986**, *166*, 361.
61. Strongin, D.R.; Somorjai, G.A. *J. Catal.* **1988**, *109*, 51.
62. Ertl, G.; Lee, S.B.; Weiss, M. *Surface Sci.* **1982**, *114*, 515.
63. Ertl, G. in *Physics and Chemistry of Alkali Adsorption*, Bonzel, H.P.; Bradshaw, A.M.; Ertl, G., Eds.; Materials Science Monographs, Elsevier, 1989; Vol. 57, p. 1.
64. Bonzel, H.P.; Broden, G.; Krebs, H.J. *Appl. Surface Sci.* **1983**, *16*, 373.
65. Campbell, C.T.; Goodman, D.W. *Surface Sci.* **1982**, *123*, 413.
66. Dwyer, D.J. in *Physics and Chemistry of Alkali Adsorption*, Bonzel, H.P.; Bradshaw, A.M.; Ertl, G., Eds.; Materials Science Monographs, Elsevier, 1989; Vol. 57, p. 307.
67. Hoffmann, F.M.; Weisel, M.D. *Surface Sci.*, **1991**, *253*, L402.

68. Schwab, G.M. *Disc. Faraday Soc.* **1950**, *8*, 166.
69. Hall, W.K.; Emmett; P.H. *J. Phys. Chem.* **1959**, *63*, 1102.
70. Sachtler, W.M.H.; van der Plank, P. *Surface Sci.* **1969**, *18*, 62.
71. Sinfelt, J.H. in *Bimetallic Discoveries and Concepts and Applications*, Wiley, New York, 1983.
72. Sinfelt, J.H. *J. Catal.* **1973**, *29*, 308.
73. Christmann, K.; Ertl, G.; Shimizu, H. *J. Catal.* **1980**, *61*, 397.
74. Shimizu, H.; Christmann, K.; Ertl, G. *J. Catal.* **1980**, *61*, 412.
75. Vickerman, J.C.; Christmann, K.; Ertl, G. *J. Catal.* **1981**, *71*, 175.
76. Vickerman, J.C.; Christmann, K. *Surface Sci.* **1982**, *120*, 1.
77. Houston, J.E.; Peden, C.H.F.; Blair, D.S.; Goodman D.W. *Surface Sci.* **1986**, *167*, 427.
78. Paul, J.; Hoffmann, F.M. *Surface Sci.* **1986**, *172*, 151.
79. Hoffmann, F.M.; Paul, J. *J. Chem. Phys.* **1986**, *86*, 2990.
80. Hoffmann, F.M.; Paul, J. *J. Chem. Phys.* **1987**, *87*, 1857.
81. Campbell, C.T. *Annu. Rev. Phys. Chem.* **1990**, *41*, 775.
82. Sachtler, W.M.H.; Somorjai G.A. *J. Catal.* **1983**, *81*, 77.
83. Sachtler, W.M.H.; Somorjai G.A. *J. Catal.* **1984**, *89*, 35.
84. Sachtler, W.M.H.; Somorjai G.A. *J. Catal.* **1987**, *103*, 208.
85. Peden, C.H.F.; Goodmann, D.W. *J. Catal.* **1986**, *100*, 520.
86. Peden, C.H.F.; Goodmann, D.W. *J. Catal.* **1987**, *104*, 347.

Chapter 2

Molecular-Beam Studies of the Effect of Surface Temperature on the Probability of Dissociative Chemisorption

Charles T. Rettner

IBM Research Division, Almaden Research Center, K33/801, 650 Harry Road, San Jose, CA 95120–6099

Molecular beam techniques have been employed to study the dissociative chemisorption dynamics of a number of systems with particular regard to understanding the effect of surface temperature on the probability of this process. It is now apparent that this parameter can affect the outcome of potentially reactive gas-surface encounters in a number of different ways. These include effects on the trapping probability into weakly bound states, the fraction of adsorbed molecules that proceed to dissociate, and even the probability of direct dissociative chemisorption. We illustrate these findings with reference to studies of the dissociation of N_2 on W(100) (which proceeds via a precursor at low kinetic energies), of N_2 on Fe(111) and O_2 on Pt(111) (both of which involve dissociation via an intermediate state that is accessed only at high kinetic energies), and of CH_4 on Pt(111) (where we believe that direct dissociation occurs).

There have been many recent molecular beam studies of the dynamics and kinetics of dissociative chemisorption *(1-28)*. These have shown, for example, that the kinetic energy, E_i, of the incident molecule can both inhibit *(1-9)* and enhance *(10-28)* the probability of dissociation. By comparison, relatively little attention has been paid to the effect of surface temperature, T_s, on the dissociation process. This contrasts with non-beam studies, where surface temperature is one of the key variables *(29-32)*. The lack of emphasis on surface temperature effects in beam studies is not particularly surprising. We might naively expect such effects to be small compared to those associated with changes in the energy of the incident molecule, since E_i may be many times greater than kT_s. In fact, surface temperature can have a very significant effect on the dissociation probability. This article summarizes our current understanding of the different ways in which this may occur.

Surface temperature can influence the dissociation probability in at least three distinct ways. It can affect:

1. The trapping probability into precursor states
2. The fate of precursor states
3. The probability of overcoming potential barriers

These three effects are indicated schematically in Figure 1, which displays a one-dimensional interaction potential appropriate to dissociative chemisorption, as first described by Lennard-Jones in 1932 *(33)*. This indicates how a barrier to dissociation can arise at the crossing of the potential curves associated with bringing the molecule or the separated atoms up to the surface.

We will illustrate these different effects and indicate what can be learnt from their study by considering specific model systems. First we will examine the effect of changing T_s on the dissociative chemisorption of N_2 on W(100) for low incidence energies, where dissociation proceeds by a classical precursor mechanism. Next we will describe studies of the dissociation of N_2 on Fe(111) and of O_2 on Pt(111), where the T_s dependence of the dissociation probability provides a crucial clue to the surprising dissociation mechanism that these systems share. Finally, we will report on very recent work on the dynamics of the dissociative chemisorption of CH_4 on Pt(111), where it has been shown that T_s can have an important effect on the dissociation probability even when dissociation occurs more or less directly as the molecule passes over a barrier such as that indicated in Figure 1.

Experimental

Our approach to studying the dynamics and kinetics of dissociative chemisorption is to use molecular beam techniques to control the incidence energy and angle, θ_i, of molecules striking a surface. We then determine trapping and sticking probabilities as a function of these variables and of the surface temperature and coverage. In this paper we will be concerned exclusively with experiments appropriate to the low coverage limit, where the dissociation probability is termed the initial sticking probability, S_0. Important information is also obtained by measuring the angular and velocity distributions of the scattered molecules and by recording temperature programmed desorption spectra. Details of the apparatus and of our experimental procedure have been published previously *(13,20)*.

Briefly, supersonic molecular beams are directed at a chosen single crystalline sample contained in an ultra-high vacuum scattering chamber and mounted on a manipulator that provides accurate control of incidence angle. The surface temperature can be varied between 90 K and the crystal melting point. Samples are prepared with standard techniques and all display sharp LEED patterns and have contamination levels below the $\simeq 1\%$ limit of Auger spectroscopy. Beam energies are varied by changing the nozzle temperature between 100 K and 2100 K and by seeding in H_2, He, and Ar. These energies are directly determined by time-of-flight techniques. Time-of-flight distributions are obtained using a differentially-pumped rotatable mass spectrometer referenced to the opening of a high-speed chopper, as discussed
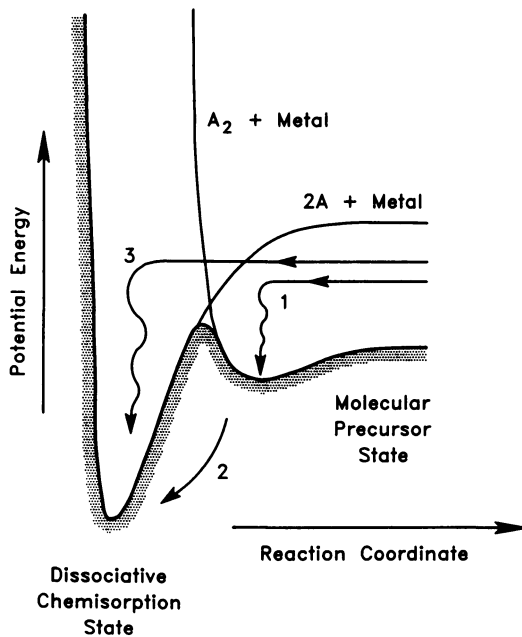
Figure 1. Schematic representation of potentials for dissociative chemisorption indicating how a barrier to dissociation can arise at the crossing of curves that correspond to bringing atoms and molecules up to the surface. The three numbers refer to three different ways in which surface temperature can affect dissociation: 1, by its effect on the trapping probability; 2, by affecting the fraction of intermediate states that go on to dissociate; and 3, by influencing the probability of direct dissociation.

previously *(20)*. Beams typically pass through a 1% chopper and have fluxes of about 10^{13} molecule/s. Adsorption probabilities greater than 0.05 are determined by a beam reflection technique *(20,34)*. Lower probabilities are estimated from the slope of sticking vs. coverage plots. In this case, coverages are determined from Auger or from TPD measurements.

Results and Discussion

N_2/W(100).   Figure 2 shows how the dissociation probability of N_2 on W(100) varies with E_i for $T_s = 300$ K and 800 K. It is apparent that this probability decreases with increasing E_i below about 0.5 eV, then rises slowly with increasing E_i above this energy. We have shown that this behavior is due to the fact that dissociation can occur by two dynamically distinct mechanisms in this system *(4,6,35)*. At low energies, dissociation proceeds by an intermediate or precursor state, while at high energies, E_i serves to directly overcome a barrier to dissociation. This latter process appears to be essentially independent of T_s in this system. However, the low-energy precursor-mediated process is seen to exhibit a substantial surface temperature dependence. In fact this sensitivity nicely illustrates the central theme of this paper. Cooling the surface from 800 K to 300 K has a bigger effect on the dissociation probability at the lowest energies than increasing E_i by over 5 eV!

Our assignment of a precursor mediated mechanism to this system at low energies is consistent with many previous studies *(31,34-37)*. It is generally accepted that the probability for dissociation by such a mechanism is the product of the trapping probability, $\alpha(E_i, \theta_i, T_s)$, and the probability that trapped species will proceed to dissociate rather than desorb. Thus we may write:

$$S_0 = \frac{\alpha k_c}{k_c + k_d} \qquad (1)$$

where k_c is the rate coefficient for the evolution of precursor species into the chemisorption state and k_d is the rate coefficient for desorption of these molecules. This can be rewritten as:

$$S_0 = \alpha(E_i, \theta_i, T_s)\left[1 + \frac{\nu_d}{\nu_c}\exp(-\Delta E/kT_s)\right]^{-1} \qquad (2)$$

where ν_d/ν_c is the ratio of pre-exponentials for the two processes. From this it follows that if α is assumed to be independent of surface temperature, a plot of $\text{Ln}[(\alpha/S_0)-1]$ vs. $1/T_s$ should be linear with a slope corresponding to $\Delta E = (E_d - E_c)$, where E_d and E_c are the activation energies for desorption and dissociation of the precursor species, respectively.

It is by no means obvious what the relative importance of the two temperature-dependent terms will be for a given system. Some workers have argued that variations in the trapping probability will dominate *(36,38)*, while others have assumed this to be negligible *(34,37)*; with the entire

dependence on T_s being attributed to the kinetic term. This may be particularly important if one wishes to determine kinetic parameters such as ν_d/ν_c or $E_d - E_c$ from measurements of the temperature dependence of S_0.

Using an approach similar to that of Janda et al.*(38)*, we have shown that it is possible to resolve this issue for the N_2/W(100) system by separately determining the surface temperature dependence of the trapping probability *(35,39)*. Measurements of the angular and velocity distributions of N_2 scattering from W(100) reveal two separate scattering components: a quasi-specular lobe associated with molecules that make essentially one collision with the surface, and a broad lobe centered along the surface normal, which is attributed to molecules that have become accommodated on the surface and then later desorbed. We will refer to these as the direct-inelastic and trapping-desorption scattering components, respectively, with associated fluxes of I_{di} and I_{td}. It then follows that $I_{di} = 1 - \alpha$ and $I_{td} = \alpha - S_0$. Measuring I_{di}, I_{td}, and S_0 as a function of surface temperature therefore yields α for that temperature, beam energy, and incidence angle. A series of measurements then gives the temperature dependence of α, which can be substituted into Equations 1 and 2 to obtain the kinetic terms. A detailed analysis presented elsewhere *(35,39)* indicates that these kinetic terms account for almost a factor of 5 decrease in S_0 when T_s is raised from 200 K to 1200 K. In contrast, α falls from about 0.58 to 0.50 over this range for $E_i = 0.088$ eV. For $E_i = 0.045$ eV and 0.025 eV, α falls from 0.70 to 0.55 and from 0.80 to 0.58, respectively, over this range. We conclude that the **primary effect of T_s is to change the fraction of trapped molecules that proceed to dissociate for these incidence energies.** Since we observe no significant dependence on incidence angle in this system *(9)*, and since ambient gas molecules at 300 K have a mean energy of about 0.05 eV, we believe that this conclusion may hold quite generally for the N_2/W(100) system.

Note, however, that the T_s dependence of the trapping probability is related to the efficiency of energy transfer between the incident gas molecules and the substrate. This will vary from system to system. In particular, energy transfer should be much more efficient for a heavy molecule striking a substrate with relatively light atoms (e.g., Cl_2 striking a Si surface). In these cases the effect of surface temperature on the trapping probability could be much greater and may even be greater than the variation in dissociation probability associated with the kinetic term. However, we stress that the methodology described here and presented in detail in our recent studies *(35,39)* indicates how these factors can be resolved for a given system.

N_2/Fe(111) and O_2/Pt(111). Now we consider two studies in which examination of the effect of surface temperature on the dissociative chemisorption probability led to new insight into the dissociation mechanism. In 1987, we observed that the dissociative chemisorption probability of N_2 on Fe(111) could be increased enormously (by five orders of magnitude) by increasing the kinetic energy of the incident N_2. While somewhat more dramatic, this observation was qualitatively similar to that seen in earlier studies *(11-20)*, such as that of the dissociation of N_2 on W(110) (11), where an increase in S_0 of over a factor of 100 had been reported. However, in all previous studies, results had been discussed in terms of a more or less direct dissociation mechanism, similar to that indicated in Figure 1. We were therefore surprised and

puzzled to observe that the dissociative chemisorption probability of N_2 on Fe(111) displayed a strong dependence on T_s, even at the highest incidence kinetic energy of about 5 eV. In fact the dependence on T_s was found to be similar over the whole range of E_i employed. Moreover, the observed dependence was seen to be close to that reported earlier for studies involving the adsorption of ambient N_2 gas *(40)*. In these cases, it had been established that dissociation occurs via sequential precursors: the so-called α-N_2 and γ-N_2 states *(41-45)*. The appropriate one-dimensional potential energy diagram then contains an additional molecular chemisorption well when compared to Figure 1. We were forced to consider that a similar mechanism might hold for this system at high kinetic energies, far above those where trapping into a classical precursor state would be possible. In fact, this turned out to be the case; the key point being that in this case access to the precursor state is blocked by a large potential barrier, which also serves to prevent prompt return to the gas phase once molecules have passed over it. We have been able to show that the relevant state is the α-N_2 species, which is not populated significantly upon exposure to low energy incident molecules. Looking at the desorption peak at about 160 K as a measure of the population of this state, we found that the probability of accessing it is proportional to the probability of dissociation, increasing rapidly with increasing E_i. The fate of these intermediates is then sensitive to T_s in an analogous manner to that for the N_2/W(100) case, although the kinetics are somewhat more complicated *(44,45)*.

About two years later, Luntz, Williams, and Bethune reported rather intriguing results for the dissociation of O_2 on Pt(111) *(5)*, which showed qualitative similarities to the N_2/Fe(111) study. The effect of E_i on S_0 reported by these workers is displayed in Figure 3. At first sight, their measurements appear qualitatively similar to those of Figure 2 for the N_2/W(100) system. The dissociation probability falls with increasing E_i at low energies, passes through a minimum and increases at high E_i. These authors thus proposed that dissociation is precursor-mediated at low E_i and proceeds through a direct mechanism at high E_i, the precursor state being the well-known molecular chemisorption, O_2^{n-}, species. However, unlike the N_2/W(100) system, it is seen that the dissociation probability depends on T_s even at high E_i. Luntz, Williams, and Bethune *(5)* accounted for this aspect of their measurements in terms of a quasi-direct dissociation model similar to that described by Gadzuk and Holloway *(46)*. While such a quasi-direct process could indeed lead to a temperature dependence, the fact that this dependence appears to be essentially independent of E_i above about 0.1 eV, argues against such a picture. Rather, we believed that the mechanism might be that described above for the N_2/Fe(111) case.

In a more recent study, Luntz, Grimblot, and Fowler *(47)* showed that O_2 can exist as a molecule on the Pt(111) surface in a molecular physisorption state, as well as in the molecular chemisorption state. Thus the one-dimensional potential diagram must indeed look qualitatively similar to that for the N_2/Fe(111) system, with at least two molecular states in addition to the dissociative state. We thus proposed that the rapid fall of S_0 with E_i at low E_i corresponds to a decrease in the trapping probability into the physisorption state, rather than the molecular chemisorption state, and that the rise at higher energies is associated with the overcoming of a barrier that
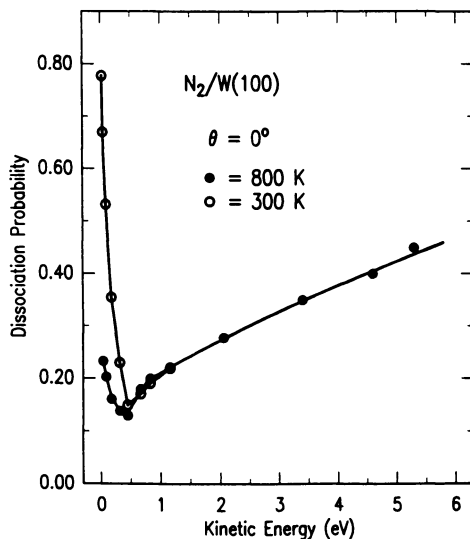
Figure 2. Effect of incidence energy on the dissociative chemisorption probability of N_2 on W(100) at normal incidence. Results are displayed for surface temperatures of 300 and 800 K. Lines are provided as a guide to the eye. Measurements for E_i > 1 eV are essentially indistinguishable for these two temperatures. (Reproduced with permission from ref. 35. Copyright 1990 American Institute of Physics.)
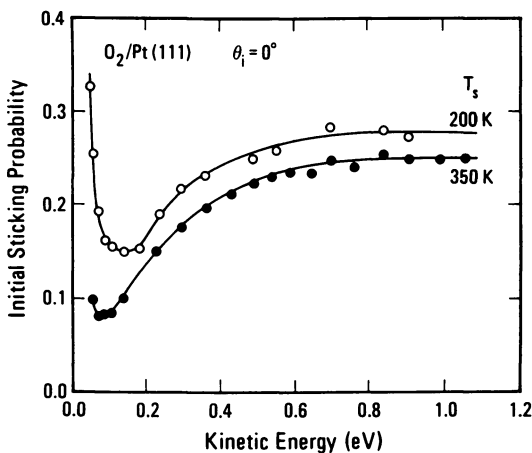

Figure 3. Initial sticking probability of O_2 on Pt(111) for normal incidence, measured as a function of kinetic energy as reported by Luntz et al. (*see* ref. 5). These results refer to surface temperatures of 200 and 350 K, as indicated. (Reproduced with permission from ref. 48. Copyright 1991 American Institute of Physics.)

blocks access to the molecular chemisorption state *(48)*. The first part of this revised mechanism had also been proposed by Luntz and co-workers, but the idea that direct dissociation does not occur for this system over the energy range investigated had not been considered previously.

In order to test this hypothesis, we needed to establish that no oxygen atoms are produced on the surface by direct dissociative chemisorption, even for high beam energies. Since molecularly chemisorbed O_2 dissociates thermally when the surface is heated above about 150 K, it is necessary to determine the molecularity of the adsorbed oxygen below this temperature. The method that we chose to distinguish O atoms from O_2 molecules on the Pt(111) surface is based on the temperature programmed desorption spectroscopy of the evolution of CO_2 from the oxidation of CO on this surface. Matsushima has shown that the resulting spectra differ markedly for $O + CO \rightarrow CO_2$ and $O_2 + CO \rightarrow CO_2$ systems *(49)*. Our experiment is thus as follows. A Pt(111) surface is held at 90 K and exposed to beams of O_2 having different incidence energies. A large dose of CO is then applied and the surface heated to produce CO_2. The resulting spectra are compared with each other and with spectra obtained when the oxygen is known to be dissociated prior to adsorption of CO . This latter condition is achieved either by thermal dissociation of adsorbed O_2 or by direct adsorption of atomic oxygen from a microwave discharge beam source. The essential result is displayed in Figure 4, which shows CO_2 TPD spectra from the oxygen + *CO* process for which the oxygen has been deposited using three different beam conditions. The upper curves correspond to a low energy beam incident at 60°, the middle curves are for $E_i = 0.088$ eV (room temperature beam) with $\theta_i = 35°$, and the lower curves were obtained with a 1.1 eV beam at normal incidence. Referring to Figure 2 and to Reference 5, it is seen that these beam conditions span the range from the lowest to highest energies employed to date to explore this system. It is clearly apparent from Figure 4 that the results are essentially indistinguishable. We note also that the oxygen coverages inferred from these TPD spectra and from separate O_2 TPD experiments are consistent in each case with the full amount of oxygen expected on the surface as estimated from the sticking probability and beam flux. We conclude that at $T_s = 90$ K **the same oxygen species is formed over the entire range of energies, and that direct dissociation can be only a relatively minor channel even at the highest energies.** More quantitatively, from a consideration of the uncertainties in these measurements, we estimate that less than 10% of the sticking probability at 1.1 eV involves a direct dissociation process for a 90 K surface. The overall kinetic mechanism appropriate to the O_2/Pt(111) system is summarized in Figure 5.
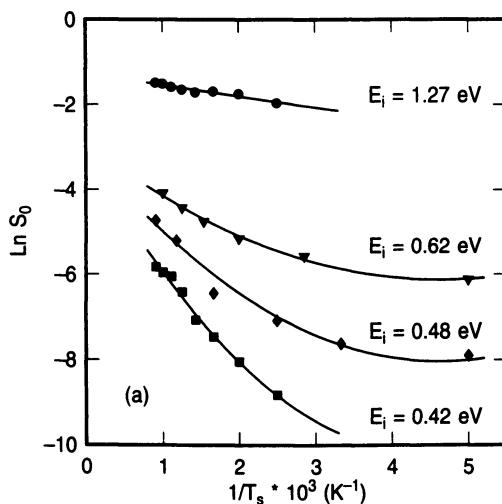
CH_4/Pt(111). So far the surface temperature dependencies have been associated with different aspects of precursor-mediated dissociation. In this section we will describe how a significant surface temperature dependence can arise even when dissociation occurs by an essentially direct process. This concerns very recent work on the dissociative chemisorption of methane by Harris *et al. (50)* which builds upon a theoretical study by Hand and Harris *(51)*, and on the measurements of Luntz and Bethune *(25)*. An extensive study of this issue has recently been completed *(52)*. A summary of the observed effects is shown in Figure 6, which displays the temperature dependence of the
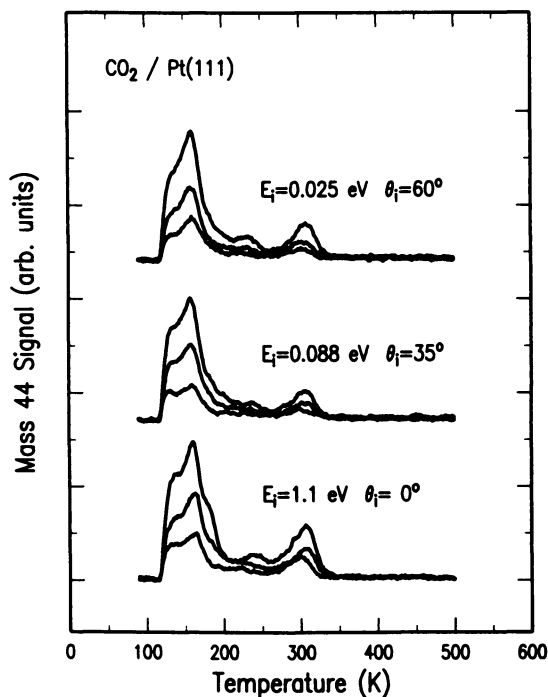
Figure 4. Temperature programmed desorption spectra recorded following the exposure of a 90 K Pt(111) surface to three different doses of O_2 for three different molecular beam energies. The doses were chosen to give coverages equivalent to 0.063 ML, 0.033 ML, and 0.015 ML, where 1 ML refers to one oxygen atom per Pt atom. These were recorded following post exposure to a saturation CO dose using the differentially pumped mass spectrometer tuned to mass 44 and aligned along the surface normal. The upper set of curves were obtained following exposure to a 0.025 eV beam incident at 60°, the middle set to a 0.088 eV beam with θ_i=35°, and the lower set with E_i=1.1 eV at normal incidence. (Reproduced with permission from ref. 48. Copyright 1991 American Institute of Physics.)
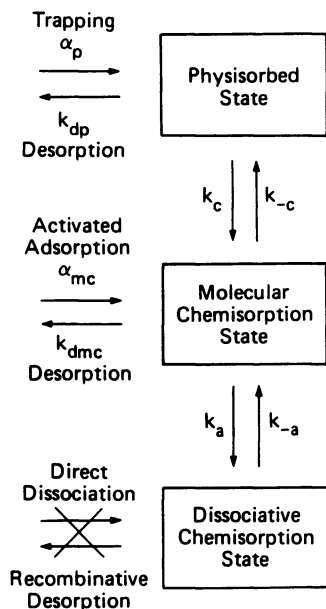
Figure 5. Schematic representation of the various kinetic paths relevant to the adsorption of O_2 on Pt(111) for incidence energies up to ~1.1 eV. Note that no direct path is indicated connecting the dissociative chemisorption state with the gas phase. We believe that a qualitatively similar diagram applies to the N_2/Fe(111) system. (Reproduced with permission from ref. 48. Copyright 1991 American Institute of Physics.)

Figure 6. Effect of surface temperature on the dissociative chemisorption of CH_4 on Pt(111) for various incidence energies at normal incidence. Note how the temperature dependence is different for each energy. (Reproduced with permission from ref. 50. Copyright 1991 American Physical Society.)

dissociative chemisorption of CH_4 on Pt(111) for a range of different inci-
dence energies.

Many groups have now shown that the dissociative chemisorption of CH_4
can be greatly enhanced by increasing kinetic energy *(12,18,23-25)*. This has
generally been interpreted in terms of a direct dissociation process similar to
that indicated schematically in Figure 1. Several groups have further pro-
posed that dissociation proceeds by a tunneling mechanism, consistent with
the exponential increase of S_0 with E_i *(12,18,52)*, and with the observed dif-
ferences between the behavior for CH_4 and CD_4. In fact a tunneling mech-
anism was first proposed by Winters *(53)* based entirely upon measurements
of the effect of T_s on the dissociation probability of methane in a "bulb"
experiment. In this case, it was proposed that dissociation occurred only after
adsorption of methane molecules on the surface; a requirement that seemed
necessary in order to allow sufficient time for the molecule to become accom-
modated to the surface temperature. In contrast, most of the molecular beam
studies have paid little attention to this variable, although Rettner, Pfnür,
and Auerbach *(12)* noted a modest enhancement of S_0 with increasing T_s.
The major exception is the study of Luntz and Bethune *(25)*, where large
variations of S_0 with T_s were noted. At the time, these observation were diffi-
cult to reconcile with any obvious model of the dissociation dynamics.

The essence of what we now believe is responsible for the observed
behavior can be found in the paper by Hand and Harris *(51)*, which con-
siders how lattice recoil may affect the effective barrier to dissociation. These
authors use a model potential energy surface suggested by electronic structure
calculations for the dissociation of H_2 on Cu, which they then couple to a
harmonic oscillator that can exchange energy with the incident molecule as it
ascends the dissociation barrier. Using masses appropriate to the dissociation
of N_2 on Fe, they show that energy loss to the oscillator (lattice recoil) can
suppress the dissociation probability as compared with the "stiff-barrier" (no
recoil) case. Here the oscillator becomes excited from its ground state during
the collision. Conversely, if the oscillator is "prepared" in an excited state
prior to the collision, the incident molecules can show energy gain as well as
energy loss during the collision. When the dissociation probability is less than
about 60%, the net effect is to increase this probability. Many subtle effects
are possible, depending on the manner in which the oscillator is coupled to
the barrier *(51)*.

The magnitude to the temperature dependence will be strongest for highly
activated systems, where S_0 increases very rapidly with E_i. We can gain
useful physical insight into such behavior by considering the energetics of a
simple one-dimensional collision. The hard-cube model *(54)* of gas-surface
energy transfer is a convenient starting point. This treats the surface as a
hard cube of mass m_s with a one-dimensional Maxwellian velocity distrib-
ution. The distribution function for the cube velocities v_s at which collisions
occur is then given approximately by:

$$F(v_s) = (m_s/2\pi kT_s u^2)^{1/2}(u - v_s) \exp(-v_s m_s/2kT_s) \qquad (3)$$

where u is the velocity of the incident molecule. Consider now a 0.4 eV CH_4
molecule. This will have a velocity of about u = 2200 m/s. Taking m_s equal

to that of one Pt atom and substituting $T_s = 800$ K yields a probability of about 0.01 of colliding with this oscillator when it is moving towards the incident molecule faster than 430 m/s. Adding 430 m/s in the center-of-mass reference frame will increase the available energy to that of a CH_4 molecule with over 0.57 eV. If the increase in S_0 with energy is sufficiently rapid, it is possible to more than compensate for the low probability of finding such a favorable oscillator phase. However, taking $T_s = 300$ K gives a probability of less than 10^{-4} for such a high "surface" velocity. Raising T_s from 300 K to 800 K could cause a substantial increase in S_0 in such a case. However, it will also be clear that the effect of T_s must become increasingly small as the magnitude of S_0 increases. This is consistent with detailed calculations *(50,52)*. While this one-dimensional picture is certainly oversimplified *(50,52)*, it is hoped that its transparency may help to communicate how relatively slow surface motions may complement much higher incidence velocities.

The detailed quantum calculations are in fact able to reproduce the trends in Figure 6 semi-quantitatively *(50,52)*. They are also able to account for the temperature dependence observed by Winters *(53)*, entirely within the framework of a direct dissociation model *(52)*. We thus believe that the basic mechanism whereby surface temperature complements the incidence energy in promoting direct dissociation may be quite general for the interaction of methane with metals. The term **thermally assisted tunneling** has been suggested to describe this process *(50,52)*. Although we expect this mechanism to apply equally to higher hydrocarbons, its importance in a given system will depend on the degree to which direct dissociation dominates over precursor-mediated reaction. For the precursor-mediated case, the effect of T_s on the kinetic branching (as discussed above) may be more important.

Acknowledgments

Literature Cited

1.   Auerbach, D. J.; Rettner, C. T. In *Kinetics of Interface Reactions*; Grunze, M.; Kreuzer, H. J., Eds.; Springer Series in Surface Science 8; Springer-Verlag: Berlin, 1987; p. 125.
2.   Hamza, A. V.; Steinrück; Madix, R. J. *J. Chem. Phys.* **1986** *85*, p. 7494.; **1987** *86*, p. 6506.
3.   Williams, M. D.; Bethune, D. S.; Luntz, A. C. *J. Chem. Phys.* **1988**, *88*, p. 2843.
4.   Rettner, C. T.; Stein, H.; Schweizer, E. K. *J. Chem. Phys.* **1988**, *89*, p. 3337.
5.   Luntz, A. C.; Williams, M. D.; Bethune, D. S. *J. Chem. Phys.* **1988**, *89*, p. 4381.

6. Rettner, C. T.; Stein, H.; Schweizer, E. K.; Auerbach, D. J. *J. Vac. Sci. Technol. A* **1989**, *7*, p. 1863.
7. Mullins, C. B.; Weinberg, W. H. *J. Chem. Phys.* **1990**, *92*, p. 4508; *J. Vac. Sci. Technol. A* **1990**, *8*, p. 2458.
8. Williams, M. D.; Bethune, D. S.; Luntz, A. C. *J. Vac. Sci. Technol. A* **1988**, *6*, p. 788.
9. Rettner, C. T.; Schweizer, E. K.; Stein, H. *J. Chem. Phys.* **1990**, *93*, p. 1442.
10. Balooch, M.; Cardillo, M.; Miller, D. R.; Stickney, R. E. *Surf. Sci.* **1974**, *46*, p. 358.
11. Auerbach, D. J.; Pfnür, H. E.; Rettner, C. T.; Schlaeger, J. E.; Lee, J.; Madix, R. J. *J. Chem. Phys.* **1984**, *81*, p. 2515.
12. Rettner, C. T.; Pfnür, H. E.; Auerbach, D. J. *Phys. Rev. Lett.* **1985**, *54*, p. 2716; Rettner, C. T.; Pfnür, H. E.; Auerbach, D. J. *J. Chem. Phys.* **1986**, *84*, p. 4163.
13. Pfnür, H. E.; Rettner, C. T.; Auerbach, D. J.; Madix, R. J.; Lee, J. *J. Chem. Phys.* **1986**, *85*, p. 7452; Lee, J.; Madix, R. J.; Schlaegel, J. E.; Auerbach, D. J. *Surf. Sci.* **1984**, *143*, p. 626.
14. Robota, H. J.; Vielhaber, W.; Liu, M. C.; Segner, J.; Ertl, G. *Surf. Sci.* **1985**, *155*, p. 101.
15. Hamza, A. V.; Madix, R. J. *J. Phys. Chem.* **1985**, *89*, p. 5381.
16. Hayward, D. O.; Taylor, A. O. *Chem. Phys. Lett.* **1986**, *124*, p. 264.
17. Steinrück, H.-P.; Hamza, A. V.; Madix, R. J. *Surf. Sci.* **1986**, *173*, p. L571.
18. Lee, M. B.; Yang, Q. Y.; Tang, S. L.; Ceyer, S. T. *J. Chem. Phys.* **1986**, *85*, p. 1693.
19. D'Evelyn, M. P.; Hamza, A. V.; Gdowski, G.E.; Madix, R. J. *Surf. Sci.* **1986**, *167*, p. 451.
20. Rettner, C. T.; DeLouise, L. A.; Auerbach, D. J. *J. Chem. Phys.* **1986**, *85*, p. 1131; Rettner, C. T.; DeLouise, L.A.; Auerbach, D. J. *J. Vac. Sci. Tech. A* **1986**, *4*, p. 1491.
21. Rettner, C. T.; Stein, H. *Phys. Rev. Lett.* **1987**, *59*, p. 2768.
22. Rettner, C. T.; Stein, H. *J. Chem. Phys.* **1987**, *87*, p. 770.
23. Lee, M. B.; Yang, Q. Y.; Ceyer, S. T. *J. Chem. Phys.* **1987**, *87*, p. 2724.
24. Hamza, A. V.; Madix, R. J. *Surf. Sci.* **1987**, *179*, p. 25.
25. Luntz, A. C.; Bethune, D. S. *J. Chem. Phys.* **1989**, *90*, p. 1274.
26. Rendulic, K. D.; Anger, G.; Winkler, A. *Surf. Sci.* **1989**, *208*, p. 404.
27. Anger, G.; Winkler, A.; Rendulic, K. D. *Surf. Sci.* **1989**, *220*, p. 1.
28. Hayden, B. E.; Lamont, C. L. A. *Phys. Rev. Lett.* **1989**, *1823*, p. 1823.
29. Langmuir, I. *Chem. Rev.* **1929**, *6*, p. 451; Taylor, J. B.; Langmuir, I. *Phys. Rev.* **1933**, *44*, p. 423.
30. Ehrlich, G. *J. Phys. Chem. Solids* **1956**, *1*, p. 3.
31. King, D. A. *CRC Critical Rev. Solid State Mater. Sci.* **1978**, *167*, p. 451.

32. Weinberg, W. H. In *Kinetics of Interface Reactions*; Grunze, M.; Kreuzer, H. J., Eds.; Springer Series in Surface Science 8; Springer-Verlag: Berlin, 1987, p. 94.
33. Lennard-Jones, J. E. *Trans. Faraday Soc.* **1932**, *28*, p. 333.
34. King, D. A.; Wells, M. G. *Proc.R. Soc. Lond. A* **1974**, *339*, p. 245.
35. Rettner, C. T.; Schweizer, E. K. Stein, H. *J. Chem. Phys.* **1990**, *93*, p. 1442.
36. Clavenna, R.; Schmidt, L. D. *Surf. Sci.* **1970**, *22*, p. 365.
37. Alnot, P.; King, D. A. *Surf. Sci.* **1983**, p. 359.
38. Janda, K. C.; Hurst, J. E.; Becker, C. A.; Cowin, J. P.; Wharton, L.; Auerbach, D. J. *Surf. Sci.* **1980**, *93*, p. 270.
39. Rettner, C. T.; Schweizer, E. K.; Stein, H.; Auerbach, D. J. *Phys. Rev. Lett.* **1988**, *61*, p. 986.
40. Ertl, G.; Lee, S. B.; Weiss, M. *Surf. Sci.* **1982**, *114*, p. 515.
41. Grunze, M.; Golze, M.; Hirschwald, W.; Freund, H.-J.; Pulm, H.; Seip, U.; Tsai, M. C.; Ertl, G.; Küppers, J. *Phys. Rev. Lett.* **1984**, *53*, p. 850.
42. Tsai, M. C.; Seip, U.; Bassignana, I. C.; Küppers, J.; Ertl, G. *Surf. Sci.* **1985**, *155*, p. 387.
43. Whitman, L. J.; Bartosch, C. E.; Ho, W.; Strasser, G.; Grunze, M. *Phys. Rev. Lett.* **1986**, *56*, p. 1984.
44. Grunze, M.; Golze, M.; Fuhler, J.; Neumann, M.; Schwarz, E. *Proc. 8th Intern. Congr. Catal.*, West-Berlin, Germany, p. IV-133.
45. Whitman, L. J.; Bartosch, C. E.; Ho, W. *J. Chem. Phys.* **1986**, *85*, p. 3688.
46. Gadzuk, J. W.; Holloway, S. *Chem. Phys. Lett.* **1985**, *114*, p. 314; Holloway, S.; Gadzuk, J. W. *J. Chem. Phys.* **1985**, *82*, p. 5203.
47. Grimblot, J.; Luntz, A. C.; Fowler, D. *J. Electron. Spec. Rel. Phenom.* **1990**, *52*, p. 161; Luntz, A. C.; Grimblot, J.; Fowler, D. *Phys. Rev. B* **1989**, *39*, p. 12903.
48. Rettner, C. T.; Mullins, C. B. *J. Chem. Phys.* **1991**, *94*, p. 1626.
49. Matsushima, T. *Surf. Sci.* **1983**, *127*, p. 403.
50. Harris, J.; Simon, J.; Luntz, A. C.; Mullins, C. B.; Rettner, C. T. *Phys. Rev. Lett.* **1991**, *67*, 652.
51. Hand, M.; Harris, J. *J. Chem. Phys.* **1990**, *92*, p. 7610.
52. Luntz, A. C.; Harris, J. *Surf. Sci.*, submitted.
53. Winters, H. F. *J. Chem. Phys.* **1975**, *62*, p. 2454; *J. Chem. Phys.* **1976**, *64*, p. 3495.
54. Grimmelmann, E. K.; Tully, J. C.; Cardillo, M. J. *J. Chem. Phys.* **1980**, *72*, p. 1039.

Chapter 3

New Molecular-Beam Methods for Coverage-Dependent Kinetic Measurements Using Time-Resolved Specular Helium Scattering

K. A. Peterlinz, T. J. Curtiss, and S. J. Sibener

**Department of Chemistry and James Franck Institute, University
of Chicago, 5640 South Ellis Avenue, Chicago, IL 60637**

New multiple molecular beam scattering techniques are introduced and applied to measure the coverage dependent kinetics of CO desorption from and CO oxidation on Rh(111). Kinetic measurements were performed by establishing the desired steady state reactant coverage with a continuous and relatively intense molecular beam, with concurrent specular helium scattering being used to quantify adsorbate coverage. A second, weak, modulated molecular beam was then used to induce small coverage perturbations around the selected steady state. Linearized kinetics under essentially isosteric conditions were then assessed with *time-resolved* specular helium scattering, which we show to be a remarkably sensitive in-situ kinetic probe. He diffraction was also used to monitor adsorbate overlayer structure under reaction conditions.

Most known heterogeneous catalytic reactions occur by the Langmuir-Hinshelwood mechanism in which reactants adsorb onto a surface and react to form new species which subsequently desorb. Catalytic reaction rates can thus be dominated by one of several steps, including the rate of adsorption of one of the reacting species, the rate of on-surface reactions, or the rate of desorption of a reactant or product species.

Modulated molecular beam methods have been successfully utilized in the past to study the kinetics and dynamics of these fundamental reaction steps (*1*). By independently controlling incident gas flux densities, angles, velocities, and internal states, researchers have been able to determine how the dynamical parameters of the incident gas affect molecular adsorption or dissociation on a surface (see reviews *2-13*). These experiments provide the basis for comparison with theoretical models of these reactions. Reactive scattering experiments, in which one incident reactant beam flux is held constant while the other is modulated, are one of the only ways of measuring unambiguous on-surface reaction rates (*14-17*).

Until recently, most molecular beam experiments were performed in the low coverage regime where interactions between adsorbed species were negligible (*18-20*). Practical catalytic systems, though, utilize high reactant gas pressures and can thus achieve high coverages during reactions. Furthermore, thin film and materials growth processes by their very nature occur across the entire range of adsorbate coverage. Chemisorption on surfaces is dominated energetically by adsorbate-surface interactions, measurable at low coverages. However, interadsorbate interactions can cause dramatic changes in adsorption-desorption rates, reaction kinetics (including mechanistic pathways), and dynamics as adsorbate coverages are increased (*21,22*). Reactive scattering experiments have been performed with at least one species at a known, near saturation coverage, but intermediate coverages were difficult to access and measure experimentally (*16*). Only by the arduous task of integrating the entire angular dependent distribution of desorbing product molecules could a researcher determine the specific coverage at which a given kinetic measurement was performed.

Only in the past few years have molecular beam experiments begun to achieve the routine ability to address high coverage systems where adsorbate interactions have significant effects on the kinetics and dynamics of the system (*23-31*). With multiple molecular beam scattering machines and in-situ surface coverage probes such as EELS or, as we shall discuss, specular He scattering, kinetics are linearized and coverages measured in-situ thus allowing unambiguous measurements of complex, coverage dependent kinetics.

In this paper we present studies involving CO adsorption-desorption (*27*) and CO oxidation (*26*) on Rh(111) which illustrate these recent advances. These linearized and coverage dependent measurements were performed with a novel triple molecular beam ultra-high vacuum scattering apparatus which, as we shall show, permits kinetic measurements to be performed under essentially isosteric conditions. Concurrent modulated He scattering was used during these studies as a non-destructive in-situ probe of overlayer structure and coverage. More importantly, the modulated He scattering was used in a time-resolved modality as a remarkably sensitive probe of surface kinetics. Coverage dependent sticking coefficients for CO adsorption, and structural studies of O and CO on Rh(111) as a function of temperature, will also be reported.

Apparatus

Our apparatus, described elsewhere (*24,32*), consists of a triple molecular beam source which is coupled to a UHV chamber which contains a rotatable quadrupole mass spectrometer. The molecular beam source has three quadruply differentially pumped molecular beams horizontally co-planar, aligned, and collimated to a single scattering center in the UHV chamber. All beams can be slowly modulated up to 2 Hz with independent beam shutters. The center beam can also be modulated from 10 to 200 Hz with a square wave chopper. The mass spectrometer, rotatable from 0° (i.e., the beam axis) to 135°, was doubly differentially pumped. The crystal mount can be cooled with liquid nitrogen and heated resistively.

Linearization of Kinetics

When kinetics are linear, they are easy to analyze from measured kinetic data. Kinetics are linear when the reaction rate can be expressed as the the first-order product of a coverage independent rate constant, $k(T_S)$ (where T_S is the surface temperature), and the instantaneous adsorbate coverage $\theta(t)$,
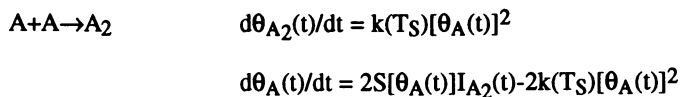
$$d\theta(t)/dt = SI(t) - k(T_S)\theta(t) \qquad\qquad\qquad (1)$$

Note that for a modulated beam experiment, we also include the coverage contribution from a time dependent incident gas flux, I(t), which is related to coverage changes via the sticking coefficient S. Equation 1, which represents desorption as a simple, stochastic depletion of isoenergetic surface sites, is always true for coverage independent desorption and, when applicable, reduces the problem of kinetic analysis to the minimum number of parameters.

However, many desorption systems, such as CO/Rh(111) (*33*), have been shown to be coverage dependent (*21, 22, 27-31, 34*) and to have coverage dependent sticking coefficients as well (*1*). The resulting coverage dependent kinetic equation for such a system cannot be expressed as a simple linear equation over all possible coverages, and thus the desorption rates cannot be extracted by a simple, first order analysis of a desorption experiment (*34*).

In addition, all reaction rates involving the combination of surface species are inherently either second or higher order in one species, or involve the product of coverages of two or more species, as illustrated below.

Recombination:

$$A+A \rightarrow A_2 \qquad d\theta_{A_2}(t)/dt = k(T_S)[\theta_A(t)]^2$$

$$d\theta_A(t)/dt = 2S[\theta_A(t)]I_{A_2}(t) - 2k(T_S)[\theta_A(t)]^2$$

Reaction between two species:

$$A+B \rightarrow AB \qquad d\theta_{AB}(t)/dt = k(T_S)\theta_A(t)\theta_B(t)$$

$$d\theta_A(t)/dt = S[\theta_A(t),\theta_B(t)]I_A(t) - k(T_S)\theta_A(t)\theta_B(t)$$

$$d\theta_B(t)/dt = S[\theta_A(t),\theta_B(t)]I_B(t) - k(T_S)\theta_A(t)\theta_B(t)$$
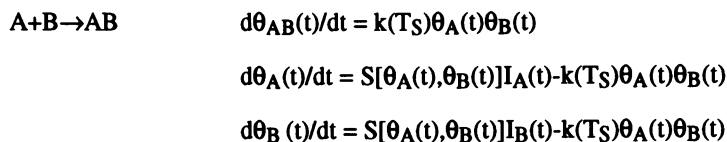
As with desorption, the rate constants themselves can be coverage dependent, thus further complicating the kinetic rate equations. As we will show, by using multiple molecular beams to minimize changes in coverage, we can reduce the kinetic rate expressions to a series of linear equations thus simplifying the kinetic analysis. In optimal situations, these linearized and coupled differential equations can be solved perturbatively, giving clear physical insight into the reaction mechanism under investigation.

Modulated molecular beam experiments, in general, determine reaction rates by modulating the surface concentration or coverage of one reactant via a modulated molecular beam and observing the resulting change in product flux or reactant coverage(*35,36*). Additional reactants may be introduced to the surface via continuous flux molecular beams. As will be discussed later, linear reaction rates are simple and straightforward to analyze via the application of Fourier analysis to the modulated beam data. Nonlinear systems, however, are not as easy to analyze, and rates at high coverages cannot always be determined from a simple, conventional modulated beam experiment. Figure 1a presents a schematized view of a conventional experimental arrangement. When a small modulated beam flux is used (scheme A,
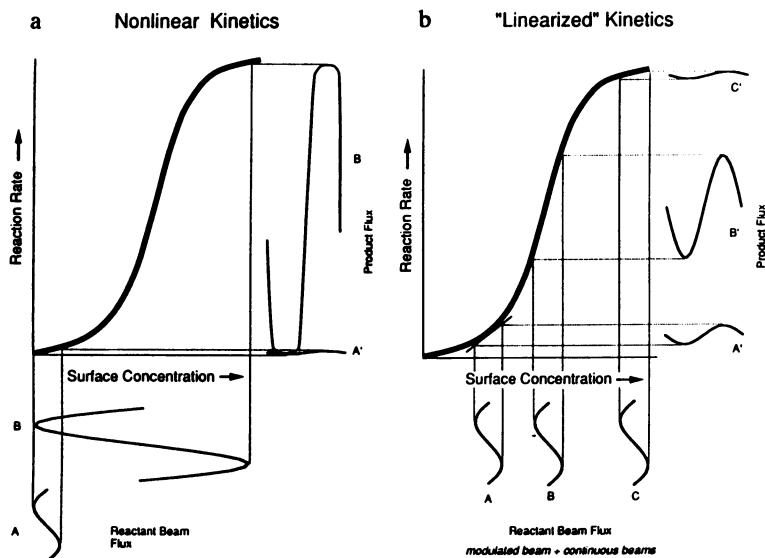
Figure 1. Different modulation schemes that can be used during surface reactive scattering experiments. Panel (a) is of the conventional type. Panel (b), after Foxon et al. (*35*), portrays a scheme which allows linearization of kinetics at all coverages. (Reproduced from ref. *26*. Copyright 1991 American Chemical Society).

Figure 1a) the response may be linear, but is restricted to a low coverage regime. When an intense modulated beam is used (scheme B, Fig. 1a) a wide coverage range is spanned during each modulation cycle, producing a nonlinear response that is difficult to analyze. This "strong modulation" scheme can further complicate matters by inducing time dependent behavior in other reactants and reaction intermediates.

Ideally, one would like to avoid these problems by sampling the kinetics under isosteric conditions. The straightforward solution is to establish a steady state reaction on the surface with arbitrarily chosen adsorbate coverages, and to then superimpose a small modulation about the selected steady state. Such a scenario is shown in Figure 1b. Modulation schemes A,B, and C here, i.e. for three different coverages, all involve sufficiently small reactant coverage modulations that the product flux response is linear with respect to the changes in reactant coverage. The linearized kinetic equation, then, describes the small coverage perturbation, $\Delta\theta(t)$, associated with the now weakly modulated beam intensity $I(t)$.

$$d\Delta\theta(t)/dt = SI(t) - k_m(T_S)\Delta\theta(t) \tag{2}$$

As will be shown, k_m, the measured first order rate constant, contains all the relevant kinetic contributions from the steady state coverages and incident gas fluxes that are held constant during the linearized kinetic experiment. By varying the molecular beam parameters and configurations, reaction mechanisms and coverage dependencies of the rate constants may be determined over the global range of conditions for the nonlinear reactions.

Fourier Analysis of Kinetics

Fourier analysis is a powerful tool for analyzing discrete data. The advantages of this method include the ability to easily deconvolute instrument and time-of-flight (TOF) contributions from our measurements, the ability to quickly and easily assess whether or not the kinetics have been linearized, and the ability to subsequently calculate the linearized first-order rate constants from the discrete Fourier components. The deconvolution process has been described in detail by Brown et. al.(17), and we only note here that our incident beam TOF distributions were measured directly, and that we assume thermal TOF distributions for desorbing molecules. The need for making this assumption in our laboratory will soon be eliminated due to the installation of a post-collision chopper.

Sawin (37,38) has shown that the mapping of the complex Fourier components of a waveform (i.e., the transfer function) to the complex plane can be used to characterize the underlying kinetics and kinetic mechanisms. For a linear system modulated at frequency τ, the discrete Fourier transform of equation 2 is expressed in terms of the discrete components for $\Delta\theta(t)$ and $I(t)$, $\Delta\theta_j$ and I_j respectively.

$$-i\sum_{j=0}^{2^n}\omega_j\Delta\theta_j\exp(-i\omega_j t) = S\sum_{j=0}^{2^n}I_j\exp(-i\omega_j t) - k_m\sum_{j=0}^{2^n}\Delta\theta_j\exp(-i\omega_j t) \tag{3}$$

where $\omega_j = 2\pi j/2\tau$. The transform for $I(t)$ contains no even components (j even), so the odd harmonics (j odd) are used to determine the rate constant. Solving equation 3 for the individual components:

$$-i\omega_j \Delta\theta_j = SI_j - k_m\Delta\theta_j \tag{4}$$

In practice we normalize I(t) and $\Delta\theta(t)$, so $S=I_0=\Delta\theta_0=1$. By solving equation 4 for $\Delta\theta_j$ and dividing $\Delta\theta_j$ by I_j, we solve for the kinetic response function P_j:

$$P_j = \frac{\Delta\theta_j}{I_j} = \frac{k_m + i\omega_j}{k_m^2 + \omega_j^2} = \mathrm{Re}(P_j) + i\,\mathrm{Im}(P_j) \tag{5}$$

We recover k_m by noting that $k_m=\omega_j\mathrm{Re}(P_j)/\mathrm{Im}(P_j)$. We use the $j=1$ components to evaluate k_m, since they are least sensitive to high frequency noise in the data.

We used the transform to characterize the linearization by first noting that a linearized rate should result in a single exponential in the response function P_j, which has a semicircular shape in the complex Fourier plane. We illustrate this with the simulated waveforms shown in Figure 2. As the modulation amplitude is increased for waveforms with an exponentially increasing rate constant with coverage in Figure 2a, the increasingly non-linear response is reflected in the shape of the transfer function in Figure 2b. If coverage changes due to adsorption of the modulated species are not small enough, then the coverage dependent terms incorporated into k_m will become significantly modulated resulting in an asymmetric response function as reflected by the increase in the amplitude of the $j=2$ harmonic in Figure 2c.

Problems can arise if the modulation period is too short for the measured rate constant. In practice, the transform is carried out by subtracting a baseline from each discrete point in the waveform and then applying a fast Fourier transform (FFT) routine to the normalized modulated part of the signal. An explicit solution and subsequent transform of the kinetic response function reveals that, if the modulation period is not long enough with respect to k_m, the odd components produced in this traditional way will not fall on the semicircle; however, the explicit solution also produces a correction factor $c=(1+\exp(-k_m\tau))/(1-\exp(-k_m\tau))$ that, when divided into each real and imaginary odd component, will put the truly first order components on the semicircle. With these corrections, the transform was used to calculate rate constants and assess whether or not those rate constants were truly first order rate constants for the reactions studied.

Helium Reflectivity As An In-Situ Probe of Surface Coverage and Kinetics

Linearized reaction conditions are achieved by holding all but one reactant or reactant intermediate at a constant coverage while changing the modulated species' coverage by an amount small enough to produce only a linear response in reaction rate. Linearization may be possible, at times, only by reducing coverage changes to amounts undetectable by traditional measurements of the resulting change in desorbing product flux. In order to take full advantage of the linearization scheme, our ability to linearize a reaction should not be limited by our ability to detect small changes in product flux. In addition, our ability to change steady state reactant coverages by changing beam parameters should be complimented by our ability to determine these steady state coverages quickly and easily.

Comsa and Poelsema (*39-41*) demonstrated that the large He scattering cross sections from disordered adsorbates on low index surfaces result in a sharp attenuation of the specular He signal with increasing adsorbate coverages. We make
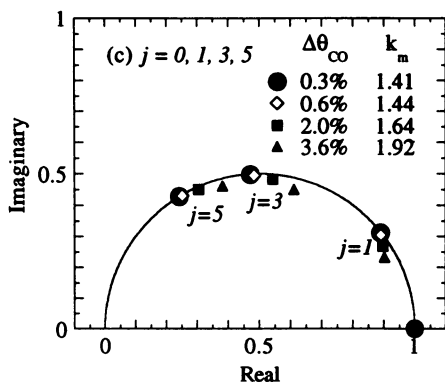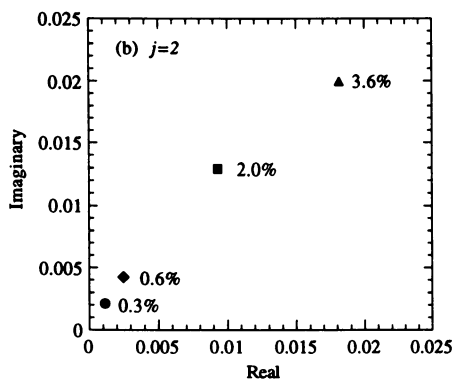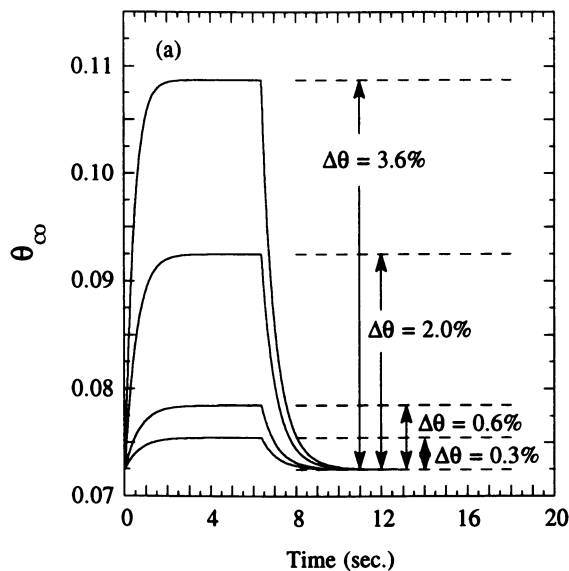
Figure 2.   Panel (a): Overmodulated waveforms and the observable effects on the even (panel (b)) and the odd (panel (c)) components of the transfer function.

use of these extremely large attenuation cross sections (i) to make in-situ measurements of steady state adsorbate coverage using He attenuation, and, most importantly, (ii) to conduct kinetic measurements with high sensitivity in the limit of small modulation depth using time-resolved He reflectivity. (Modulation depth here refers to the coverage change induced by the modulated molecular beam). We would like to emphasize that the specular He scattering served as a **"kinetic response amplifier"**. Changes in He reflectivity due to changes in coverage occur at a much higher signal level than changes in desorbing product flux. Specular He scattering was easily included in the reactive scattering scheme by either mixing it with the modulated reactant or setting up a neat He beam in addition to the modulated and continuous reactant beams as shown in Figure 3 for the CO oxidation and CO desorption experimental setups.

Coverage measurements made with specular He scattering require comparative He intensity measurements of the bare and adsorbate covered surface (*39-41*). A relatively simple model accounts for the attenuation by assuming that the cross section for diffusely scattered He can be associated with the (large) elastic scattering cross section which exists between the He atom and the adsorbate. Assuming a random distribution of adsorbates on surface sites, and the associated random overlap, a "lattice gas formula" is derived:

$$\frac{I_{\theta_A}}{I_{00}} = (1-\theta_A)^{\Sigma_A \eta} \tag{6}$$

where I_{00} is the specular He intensity from the bare surface, I_{θ_A} is the specular He intensity at coverage θ of species A, Σ_A is the cross section associated with that molecule for the selected incident angle and beam energy, and η is the surface atom density. The ratio I_{θ_A}/I_{00} is defined here as the He reflectivity for that adsorbate coverage. If repulsive interactions exist between adsorbates, then equation 6 is altered to account for the exclusion of possible adsorbates at neighboring lattice sites,

$$\frac{I_{\theta_A}}{I_{00}} = (1-m\theta_A)^{\frac{\Sigma_A \eta}{m}} \tag{7}$$

where m is the reciprocal of the saturation coverage for the adsorbate.

Oxygen dissociates and produces a well known (2x2) overlayer on Rh(111) which disorders upon heating to 320 K (Figure 4), while CO adsorbs molecularly, producing a well known ($\sqrt{3}$x$\sqrt{3}$) R30° overlayer which disorders upon heating to 325 K (Figure 5). He scattering intensities from ordered structures lead to complex relationships between specular He scattering intensities and coverages. However, all of our kinetic measurements were made with the surface above the disordering temperatures for CO and O on Rh(111). He reflectivity was calibrated against disordered adsorbate surface coverages utilizing titration for O, and thermal desorption for CO, to determine relative coverages.

For O, we dosed a Rh(111) surface with O_2 and monitored the He reflectivity for a room temperature, i.e. 63 meV, He beam at 45 degrees incident angle, then we determined the relative oxygen coverages at various dosing times by titrating the adsorbed oxygen with CO and measuring the resultant CO_2 signal. We can then plot He reflectivity against the relative O coverage, θ'_O, where $\theta'_O=1$ represents a saturated disordered O overlayer. Since the absolute O coverage (relative to the Rh atom density), θ_O, was unknown, we fit our data to equation 6 with $\theta_O=B\theta'_O$ where

(a) CO Desorption

Detector   He

Beams

INTENSE CO

He

Rh(111)

WEAK CO

(b) CO Oxidation

Detector   He

CO_2

Beams

O_2

CO+He
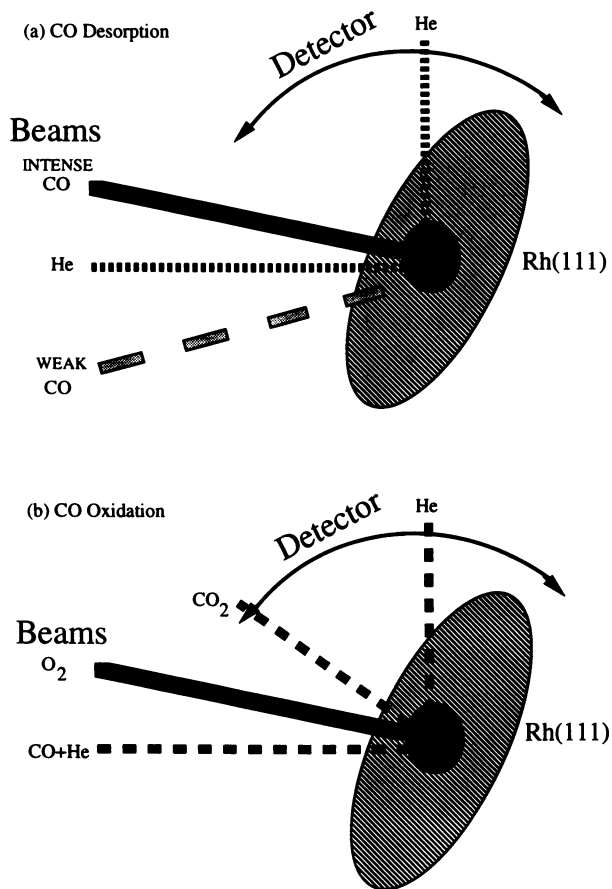
Rh(111)

Figure 3.   Beam arrangements for CO desorption (panel (a)) and CO oxidation experiments (panel (b)).
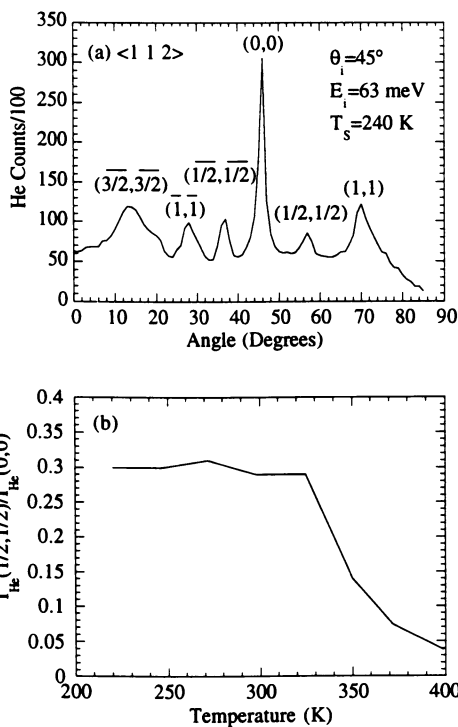
Figure 4.   Panel (a): He diffraction from (2x2) O/Rh(111) overlayer. Panel (b): Temperature dependence of a superlattice diffraction peak indicates order to disorder phase transition.
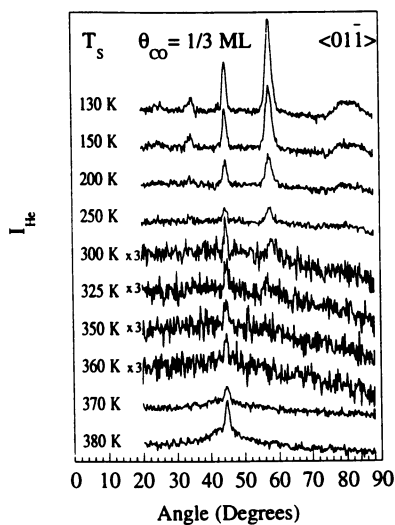
Figure 5.   Temperature dependence of He diffraction from $(\sqrt{3} \times \sqrt{3})$ R30° CO/Rh(111) overlayer indicates that the saturated $(\theta_{CO} = 0.33)$ CO overlayer becomes disordered above $T_S \approx 325$ K. (Reproduced with permission from ref. *27*. Copyright 1991 American Institute of Physics).

θ'_O is the measured coverage, and B is the absolute O coverage relative to the Rh atom density. Equation 6 fits our data (Figure 6a, circles) up to $\theta'_O = 0.65$, with $\Sigma_O = 44.2$ Å^2, $\eta = 0.13$ Å^{-2}, and B=0.826 (Figure 6a, solid line). Root et. al. (*42*) measured B=0.83 using XPS. A similar experiment for CO on Rh(111), in which we applied Equation 7, fits our data (Figure 6b, circles) with $\Sigma_{CO} = 148$ Å^2 and m=3.1 (Figure 6b, solid line).

CO Desorption from Rh(111)

Linearization of Coverage Dependent CO Desorption. Here we present the example of CO desorption from Rh(111). Desorption rates and sticking coefficients of CO on Rh(111) have been shown in the past to be coverage dependent (*33*). The coverage dependent rate expression is:

$$\frac{d\theta_{CO}}{dt} = S_{CO}(\theta_{CO}, T_S)I_{CO} - k(\theta_{CO}, T_S)\theta_{CO} \tag{8}$$

Experimentally, we use an intense, continuous CO beam to produce a desired steady state coverage while a weak, modulated beam induces small coverage perturbations. The kinetic response to the weak coverage modulation can then be analyzed to extract the change in desorption rate as a function of coverage. For the case of CO oxidation, the oxygen coverage changes are small enough to neglect in an overall analysis of the total rate. However, since in the CO desorption experiment both beams introduce the same species to the surface, there is a first-order rate change not only in the desorption rate for the modulated species but also for the rate constant and the sticking coefficient of the steady state species.

The rate expressions for this linearized modulated beam experiment are derived by expressing each coverage dependent term, *including the sticking coefficient and the desorption rate constant*, as a Taylor expansion in terms of CO coverage (*27, 28*). Here we include the contribution of the weak time dependent incident beam flux density, I(t), to the measured first-order desorption rate expression to extract steady state and time-dependent equations:

$$S(T_S, \theta_0)I = k(T_S, \theta_0)\theta_0 \tag{9}$$

$$\frac{d\Delta\theta(t)}{dt} = S(\theta_0)I(t) - k_m(T_S, \theta_0)\Delta\theta(t) \tag{10}$$

θ_0 (θ_S in reference *28*) and $\Delta\theta(t)$ are the steady state and weakly modulated surface coverages, respectively. $S(\theta_0)$ is the coverage dependent sticking coefficient at the steady state coverage, and $k_m(T, \theta_0)$ is the measured relaxation rate constant given by:

$$k_m(T_S, \theta_0) =$$

$$\begin{cases} k(T_S, \theta_0) + \theta_0 \left.\dfrac{dk(T_S, \theta)}{d\theta}\right|_{\theta_0} - (I_S + I_W)\left.\dfrac{dS(\theta)}{d\theta}\right|_{\theta_0} & 0 \le t \le \tau \\ k(T_S, \theta_0) + \theta_0 \left.\dfrac{dk(T_S, \theta)}{d\theta}\right|_{\theta_0} - I_S \left.\dfrac{dS(\theta)}{d\theta}\right|_{\theta_0} & \tau < t < 2\tau \end{cases} \tag{11}$$
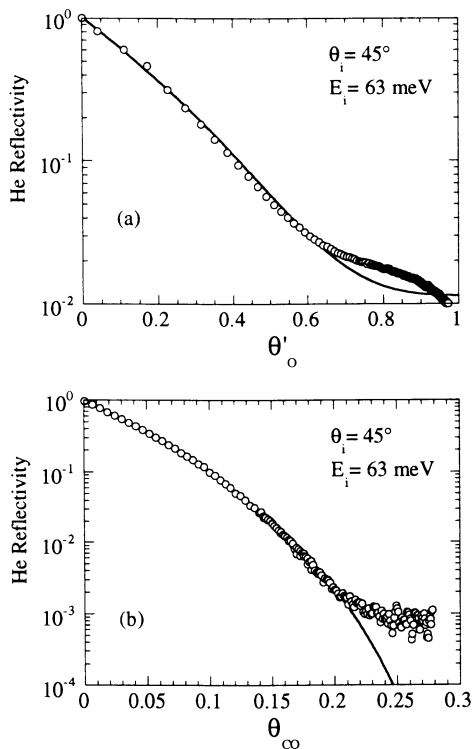
Figure 6.   He reflectivity calibration curves for O/Rh(111) (panel (a)) and CO/Rh(111) (panel (b)).

This approach requires that one either knows or makes assumptions about the sticking coefficient and coverage dependent form for the true rate constant. There are two ways to check these assumptions if relative beam intensities are known. One is to use equation 9 to predict the coverage based on the incident beam intensity, T_S, and the coverage dependent sticking coefficient and desorption rate. Another more reliable way is to allow the modulated coverage to reach a steady state and use a combination of the two steady state expressions, equations 9 and 13 (presented shortly), to derive a unique solution for the desorption rate constant.

In our experiment we use square wave modulation:

$$I(t) = \begin{cases} I_W & 0 \le t \le \tau \\ 0 & \tau < t < 2\tau \end{cases} \tag{12}$$

for which 2τ is the modulation period, and I_W and I_S (σ_S in reference *28*) are the weak and strong beam flux densities, respectively ($I_W \ll I_S$). In the steady state limit, equation 10 assumes the same form as equation 9:

$$S(\theta_0)I_W = k_m(T_S, \theta_0)\Delta\theta(\tau) \qquad (\lim \ \tau \to 4 / k_m(T_S, \theta_0)) \tag{13}$$

The desorption rate can be expressed independently of the sticking coefficient by dividing equation 13 by equation 9 and solving for $k(T_S, \theta_0)$:

$$k(T_S, \theta_0) = k_m(T_S, \theta_0) \frac{\Delta\theta(\tau)}{\theta_0} \frac{I_S}{I_W} \qquad (\lim \ \tau \to 4 / k_m(T_S, \theta_0)) \tag{14}$$

As an aside, we note that if the coverage probe is isotopically selective (such as EELS detection of an isotopically labeled species) but the adsorption-desorption rates are not, then isotopic substitution of one of the beams will reduce the rate expression to the form shown for CO oxidation and $k_m = k$.

Specular He Scattering Measurements of Coverage Dependent CO Desorption. Linearized CO desorption measurements cannot be made in the high CO coverage limit by monitoring the desorbing CO because of the high background due to desorbing and diffusely scattered CO from the continuous beam. As shown in Figure 7, time resolved specular He scattering allows measurements of desorption rates down to coverage modulations of hundredths of a monolayer. He reflectivity time response can be converted quickly to a coverage response by realizing that He reflectivity changes have a logarithmic dependence on coverage for small coverage changes.

The desorption rate constants, $k(T_S, \theta_0)$, are calculated from the measured rate constants $k_m(T_S, \theta_0)$ with equation 11 using the measured $S(\theta_0) = 1 - 3\theta_0$ and assuming that either the pre-exponential ν_0 or the activation energy E_a is coverage dependent. The two expressions derived from this analysis are:

$$k(\theta, T_S) = 1.33 \times 10^{14} \exp(0.344 \ \theta + 48.8 \ \theta^2 - (32.3 \ \text{kcal/mol})/(k_b T_S)) \ \text{sec}^{-1} \tag{15}$$

or:

$$k(\theta, T_S) = 1.33 \times 10^{14} \exp(-(32.3 - 1.62 \ \theta - 38.3 \ \theta^2 \ \text{kcal/mol})/(k_b T_S)) \ \text{sec}^{-1} \tag{16}$$
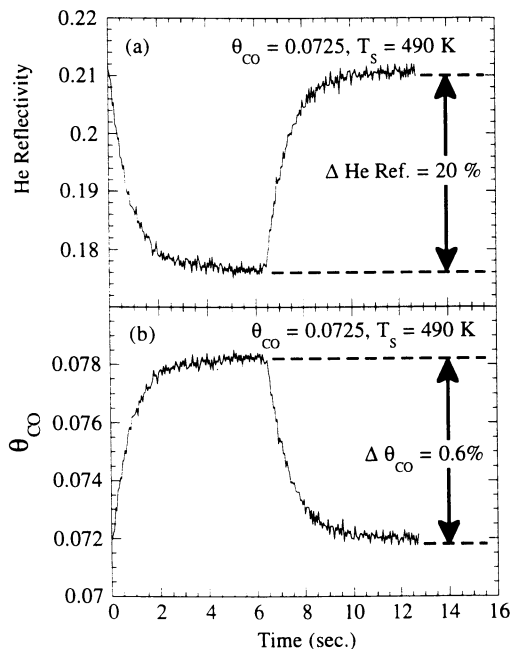
Figure 7. CO desorption measured with He reflectivity demonstrates the extraordinary sensitivity of He reflectivity to small coverage changes and thus its utility as a **"kinetic response amplifier"**. Panel (a) shows time resolved He reflectivity response to modulated CO. Panel (b) shows actual CO coverage calculated from data in panel (a). (Reproduced with permission from ref. *27*. Copyright 1991 American Institute of Physics).

As shown in Figure 8a, these equations reflect nearly equivalent rate constants. Figure 8b confirms the rate constants for $\theta_{CO}=0.16$ by making the measurements in a different and complimentary way. Using accurately quantified incident beam fluxes, we measure steady state CO coverages at a given surface temperature as well as the relaxation rate between these two coverages. We extract the true desorption rate constant using equation 14. Excellent agreement can be seen between data taken in this way and data obtained using assumptions about the coverage dependence of the rate constant (equations 15 and 16, Figure 8a) for $\theta_{CO}=0.16$. The solid line in Figure 8b is from a linear fit to $\theta_{CO}=0.16$ data in Figure 8a. The dashed lines are from linear fits for the other coverages in Figure 8a and are for comparison.

CO Oxidation on Rh(111)

Linearization of the CO oxidation reaction. Here we present the example of CO oxidation on Rh(111). Brown and Sibener (*17*) determined the reaction kinetics for CO oxidation in the low CO coverage regime by using a continuous O_2 beam and a modulated CO beam. The rate expression for this reaction is:

$$\frac{d\theta_{CO}}{dt} = S_{CO}(\theta_O,\theta_{CO},T_S)I_{CO} - k(\theta_O,\theta_{CO},T_S)\theta_O\theta_{CO} \tag{17}$$

$$I_{CO_2} = k(\theta_O,\theta_{CO},T_S)\theta_O\theta_{CO} \tag{18}$$

I_{CO_2} is the time-dependent flux of CO_2 leaving the surface; θ_{CO} and θ_O are the time-dependent CO and O coverages, respectively; $S_{CO}(\theta_O,\theta_{CO},T_S)$ is the coverage and temperature dependent sticking coefficient for CO; I_{CO} is the incident CO flux; and $k(\theta_O,\theta_{CO},T_S)$ is the coverage and temperature dependent rate constant. For sufficiently low CO intensity, θ_O is constant and the kinetics follow a pseudo-first-order behavior:

$$\frac{d\theta_{CO}}{dt} = S_{CO}(\theta_O,T_S)I_{CO} - k_m(\theta_O,T_S)\theta_{CO} \tag{19}$$

$$I_{CO_2} = k_m(\theta_O,T_S)\theta_{CO} \tag{20}$$

where $k_m(\theta_O,T_S)=k(\theta_O,\theta_{CO},T)\theta_O$.

Specular He Scattering Measurements of CO Oxidation. In order to determine the steady state oxygen coverage as well as the coverage dependent sticking probability, a CO-He mixture was used for the incident modulated beam. I_0 was determined for this beam by extrapolating from high temperature (>650 K) measurements where CO has an insignificant residence time and thus no effect on the scattering intensity. During the modulated beam experiment, the rotatable mass spectrometer was changed to look at either the product CO_2 intensity at the surface normal or the He intensity at specular. Here a dual chopper wheel, with a square wave and time-of-flight pattern, was used to modulate the mixed CO-He beam. The He signal, shown in Figure 9 as a dashed line, therefore disappears at the midpoint of the CO_2 wave, shown as a solid line, since the chopper blocked the incident beam.

Since both CO and O were adsorbed on the surface during the modulated beam experiment, there were two surface species to attenuate the He signal. The contribution from O was determined from the reflectivity at low θ_{CO} or low I_{CO_2},
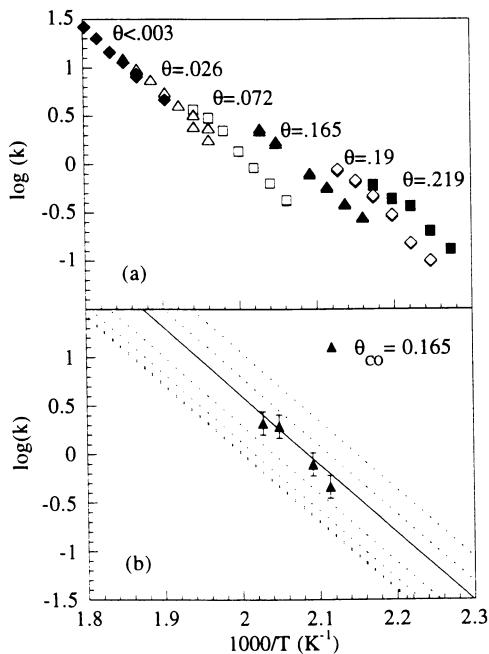
Figure 8.   Arrhenius plots of CO desorption rate constants derived from time-resolved He reflectivity measurements. Panel (a): Rate constants derived using equation 11. Panel (b): Rate constants derived using equation 14. Rate constants derived these two ways are in excellent agreement.
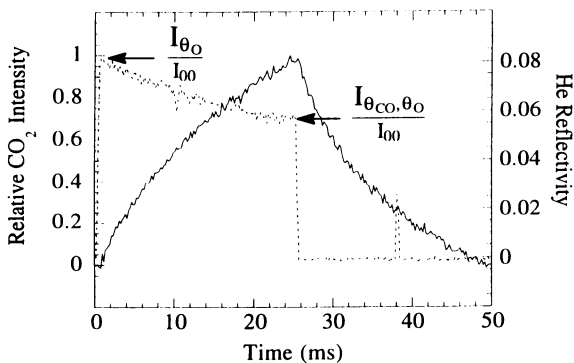
Figure 9.   Product CO_2 intensity (solid line) and He reflectivity (dashed line) waveforms for CO oxidation on 525 K Rh(111). From the He reflectivity at t=0, we find $\theta_O = 0.350$, and at $t=\tau$, the midpoint, we find $\Delta\theta_{CO}$(max.) = 0.012. From both waveforms, we find $k_m = 55$ sec^{-1}.

where there was an insignificant contribution from adsorbed CO and thus the He reflectivity was largest. Here $I_{\theta_O}/I_{00} = 0.0825$, which corresponds to $\theta_O = 0.350$. The exponential decay in He signal after 0.5 ms in Figure 9 is due to the rise in θ_{CO} during the open chopper part of the modulation period. Solving explicitly for this part of the waveform:

$$\theta_{CO}(t) = \frac{S(\theta_O)I_{CO}}{k_m(\theta_O,T_S)}\left(1 - \exp(-k_m(\theta_O,T_S)t)\right) \tag{21}$$

I_{CO} can be measured from the direct beam flux and k_m, the pseudo-first-order rate constant, can also be determined as explained above. If $\theta_{CO}(t)$ can be determined from He reflectivity, as will be shown, and I_{CO} is known, then $S_{CO}(\theta_O)$ is readily calculable from equation 21.

Assuming that CO occupies random surface sites unoccupied by O and thus the area associated with the CO cross section overlaps randomly with O covered sites in the mixed overlayer, the cross section for small CO coverages can be expressed:

$$\frac{I_{\theta_{CO},\theta_O}}{I_{\theta_O}} = \exp\left(\frac{-\eta\Sigma_{CO}\theta_{CO}}{1-\theta_O}\right) \tag{22}$$

or

$$\theta_{CO} = -\frac{1-\theta_O}{\eta\Sigma_{CO}}\ln\left(\frac{I_{\theta_{CO},\theta_O}}{I_{\theta_O}}\right) \tag{23}$$

where I_{θ_O} is the He signal from the O covered surface and $I_{\theta_O,\theta_{CO}}$ is the He signal from the CO and O covered surface. The maximum CO coverage for the waveform in Figure 9, calculated from equation 23, is 0.012 monolayers, and the rate constant calculated from the θ_{CO} waveform is identical, within experimental error, to the rate constant from the CO_2 waveform.

Conclusion

We have described here a complete approach to studying coverage dependent kinetics for surface reactions and have illustrated applications to two fundamentally different surface processes, desorption and oxidation. Utilizing two reactant beams, one intense and continuous, the other weak and modulated, we linearize kinetics for CO oxidation on and CO desorption from Rh(111) by reducing the modulation depth of the weak beam to force the kinetics to a linear response limit. With modulated specular He scattering measurements, we were able to assess steady state adsorbate coverages in-situ. Using time-resolved specular He scattering, we were able to measure coverage changes directly. For many measurements, He reflectivity acted as a **"kinetic response amplifier"**, compensating for the loss of signal due to the reduction of modulation depth by producing large changes of He reflectivity in response to small changes in surface coverage. With transfer function analysis to distinguish the linearized kinetics from any other distinct kinetic processes, the measured rate constants were shown to be for a single step process, either CO desorption or the $CO_a + O_a \rightarrow CO_2$ reaction.

This approach has also been applied previously to water formation on Rh(111) (23-25) and Pt(111) (43) as well as hydrogen recombination (23,24) on Rh(111). As these techniques are extended to more complex surface reactions, the dependence of the rates of all reaction steps on coverage can now be used to develop better theories of what types of interadsorbate interactions exist, and how they affect the dynamics of these reactions. Recent analysis of the CO desorption kinetics indicate that weak attractive interadsorbate interactions from as many as three lattice spacings away can be determined in the presence of much larger nearest and next-nearest neighbor repulsive terms from the high coverage desorption rates (44).

Now that we understand how to control and measure adsorbate coverages, structures, and configurations with the multiple molecular beam techniques described above, the door has been opened for more direct dynamical probes of the dissociative adsorption process as a function of coverage. As with bare surface measurements, the incident scattering conditions can be varied to probe how these interadsorbate interactions change potential energy surfaces for adsorption. The translational energy and internal state distributions for desorbing species can also be probed as coverage increases. The exothermic CO oxidation reaction on Rh(111) is known to deposit much of the excess energy in the translational motion of the CO_2 as it leaves the surface (45). We are installing a post-collision chopper to measure the CO_2 time-of-flight distributions as we vary the coverage. By combining the on-surface kinetic information with information derived from dynamical measurements, we are developing a better picture of how catalytic systems and other surface processes such as thin film growth occur at higher coverages.

Acknowledgments

Literature Cited

1.   For a review see D'Evelyn M. P.; Madix R. J. *Surf. Sci. Reports* **1984**, *3*, p. 413.
2.   *Interactions of Atoms and Molecules with Solid Surfaces*; Bortolani V.; March N. H.; Tosi M. P., Eds.; Plenum Press: New York, NY, 1990.
3.   Zacharias H. *Int. J. Mod. Phys. B* **1990**, *4*, p. 45.
4.   Depristo A. E.; Kara A. *Advances in Chem. Phys.* **1990**, *77*, p. 163.
5.   Ceyer S. T. *Ann. Rev. Phys. Chem.* **1988**, *39*, p. 479.
6.   Gerber R. B. *Chemical Reviews* **1987**, *87*, p. 29.
7.   Lin. M. C.; Ertl G. *Ann. Rev. Phys. Chem.* **1986**, *37*, p. 587.
8.   Barker J. A.; Auerbach D. J. *Surf. Sci. Rep.* **1985**, *4*, p. 1.
9.   Comsa G.; David R. *Surf. Sci. Rep.* **1985**, *5*, p. 145.
10.   Cardillo M. J. *Ann. Rev. Phys. Chem.* **1981**, *32*, p. 331.
11.   Tully J. C.; *Ann. Rev. Phys. Chem.* **1980**, *31*, p. 319.
12.   Goodman F. O.; Wachman H. Y. *Dynamics of Gas Surface Scattering*; Academic Press: New York, NY, 1976.
13.   Schwarz J. A.; Madix R. J. *Surf. Sci.* **1974**, *46*, p. 317.

14. Engel T.; Ertl G. *J. Chem Phys* **1978**, *69*, p. 1267.
15. Fair J. A..; Madix R. J. *J. Chem.Phys.* **1980**, *73*, 3486.
16. Campbell C. T.; Ertl G.; Kuipers H.; Segner J. *J. Chem Phys.* **1980**, *73*, p. 5862.
17. Brown L. S.; Sibener S. J. *J. Chem Phys.* **1988**, *89*, p. 1163.
18. Olander D. R.; Ullman A. *Int. J. Chem. Kinetics* **1976**, *8* , p. 625.
19. Schwarz J. A.; Madix R. J. *Surf. Sci.* **1974**, *46*, p. 317.
20. Jones R. H.; Olander D. R.; Siekhaus W. J.; Schwarz J. A. *J. Vacuum Sci. Technol.* **1972**, *9* , p. 1429.
21. Pfnür H.; Menzel D. *J. Chem. Phys.* **1983**, *79*, p. 2400.
22. Pfnür H.; Menzel D. *J. Chem. Phys.* **1983**, *79*, p. 4613.
23. Padowitz D. F. *Ph. D. Dissertation*, University of Chicago, Chicago, IL, December 1989.
24. Padowitz D. F.; Sibener S. J. *J. Vac. Sci. Tech. A* **1991**, *9*, p.2289.
25. Padowitz D. F.; Sibener S. J., *Surf. Sci.* **1991**, *254*, p. 125.
26. Padowitz D. F.; Peterlinz K. A.; Sibener S. J. *Langmuir*, in press
27. Peterlinz K. A.; Curtiss T. J.; Sibener S. J. *J. Chem. Phys.*, in press.
28. Hinch B. J.; Dubois L. H. *Chem. Phys. Let.* **1990**, *171*, p. 131.
29. Rettner C. T.; Bethune D. S.; Scweizer E. K. *J. Chem. Phys.* **1990**, *92*, p. 1442.
30. Peterson L. D.; Kevan S. D. *Surf. Sci. Let.* **1990**, *235*, L285.
31. Scharpf E. W.; Benziger J. B., submitted to *Langmuir*.
32. Gibson K. D.; Sibener S. J. *J. Chem. Phys.* **1988**, *88*, p. 791.
33. Thiel P. A.; Williams E. D.; Yates J. T. Jr.; Weinberg W. H. *Surf. Sci.* **1979**, *84*, p. 54.
34. For a review of TPD studies see Seebauer E. G.; Kong A. C. F.; Schmidt L. D. *Surf. Sci.* **1988**, *193*, p. 417.
35. Foxon C. T.; Boudry M. R.; Joyce B. A. *Surf. Sci.* **1974**, *44* , p. 69.
36. Chang H. -C.; Weinberg W. H. *J. Chem. Phys.* **1977**, *66*, p. 4176.
37. Sawin H. H.; Merrill R. P. *J. Vac. Sci. Tech.* **1981**, *19*, p. 40.
38. Sawin H. H. *Ph. D. Dissertation*, University of California, Berkeley, CA, May, 1980.
39. Poelsema B.; Palmer R. L.; Comsa G. *Surf. Sci.* **1984**, *136*, p. 1.
40. Poelsema B.; Comsa G. *Faraday Discuss. Chem. Soc.* **1985**, *80*, p. 247.
41. Poelsema B.; Comsa G. *Scattering of Thermal Energy Atoms from Disordered Surfaces*; Springer Tracts in Modern Physics 115; Springer-Verlag: Berlin, 1989.
42. Root T. W.; Schmidt L. D.; Fisher G. B. *Surf. Sci.* **1983**, *134*, p. 30.
43. Verheij L. K.; Hugenchmidt M. B.; Cölln L.; Poelsema B.; Comsa G. *Chem. Phys. Lett.* **1990**, *166*, p. 523.
44. Kreuzer H. J.; Payne S. H.; Peterlinz K. A.; Sibener S. J., work in progress.
45. Brown L. S.; Sibener S. J. *J. Chem Phys.* **1989**, *90*, p. 2807.

Chapter 4

Kinetics and Mechanism of Carbon Monoxide Oxidation on Platinum, Palladium, and Rhodium Foils

George W. Coulston[1] and Gary L. Haller

Department of Chemical Engineering, Yale University,
New Haven, CT 06520

The kinetics of CO oxidation have been measured on Pt, Pd and Rh, as well as the heat of adsorption of CO, ΔH_{CO}, under reaction conditions. It is observed that a linear correlation exists between the activation energy for the surface reaction, E_{SR}, and ΔH_{CO} (a Polanyi relation). It is proposed that ΔH_{CO} is an indirect measure of the ability of chemisorbed CO to extract strongly bound O atoms from the surface.

We have been interested in the dynamics of CO oxidation on Pt and have investigated this system in some detail via the analysis of the infrared emission from the desorbed product CO_2 (1). Very recently we have extended our study of CO oxidation to Pd (2,3,4) and Rh (3,4) and improved our CO oxidation on Pt analysis as a result of increased spectral resolution (3,4). As a necessary preliminary set of experiments, we also investigated the kinetics of CO oxidation on Pd, Rh and Pt. As a result of signal to noise constraints, our primary objective was to determine conditions of CO/O_2 ratio and surface temperature that would provide the maximum rate and therefore the optimum CO_2 density for the dynamics experiments.

From our previous work on Pt foil we knew that CO/O_2 ratios of about one and a surface temperature just above that of the maximum rate were likely to be near optimum. It is well known that on all of the metals of group VIII in the second and third transition (5), the reaction

[1]Current address: E. I. du Pont de Nemours & Company, Experimental Station, Wilmington, DE 19880–0262

rate passes through a maximum as a function of CO/O_2 ratio at a fixed surface temperature (at a ratio of around one) and as a function of surface temperature (at a fixed CO/O_2 ratio). The origin of the maximum is similar in both cases, i.e., at high CO/O_2 ratios or low surface temperatures, the surface is covered with CO which inhibits the adsorption of O_2 and thus the rate. As the surface temperature is raised, CO is desorbed and the rate increases but passes through a maximum at some temperature where the rate of desorption of CO begins to compete with the rate at which CO finds an adsorbed oxygen with which to react. There is an analogous optimum when the ratio of CO/O_2 is varied at constant temperature. Both the reactant ratio (at fixed surface temperature) and the optimum surface temperature (at fixed reactant ratio) will, of course, depend on the particular metal under consideration. At 373K and a stoichiometric reactant ratio, the three metals have rates in the order Pt>Rh>Pd (5). At this temperature all three metals are significantly CO inhibited, first order in oxygen, zero order in CO and the activation energy is essentially equal to the heat of adsorption of CO; the absolute pressure is a less important factor, but a recent study indicates that the rate does vary on Pd by a factor of about 0.74 at 445K when the total pressure is varied by eight orders of magnitude (6). As we will see below, for a stoichiometric ratio but with the surface temperature at 573K the order of rates is Pd>Rh>Pt, just the reverse of that at 373K, and if maximum rates at a stoichiometric reactant ratio are compared (different surface temperatures) the metals are ordered Pd>Pt>Rh. Since the binding energy of CO is not a strong function of the metal, we surmise that what is most affecting this behavior is the ability of the metals to interact with oxygen and, in turn, how this affects the competition with CO as a function of temperature.

We will compare the activity of Pt, Pd and Rh around stroichiometric reactant ratios and optimum surface temperature and reactant fluxes in the range of 0.002 - 0.004 Torr total pressure. The reactants are directed at the foil surfaces with a free jet and the rates have been followed by mass spectrometry. While the combination of the free jet interception, foil surface and mass spectrometric detection do not allow us to calculate absolute turnover frequencies with a high degree of accuracy, the relative rates are good to within a few percent so that nothing is compromised in the kinetic comparison.

Experimental

A detailed description of the complete apparatus, the foil cleaning procedure, and Auger analysis can be found in ref. 3 and 4, but a brief description of the kinetic measurements is given here. A quadrupole residual gas analyzer that was equipped with a Faraday cup detector was used to measure the overall rate of the CO oxidation. The CO and O_2 were delivered to the surface through a free jet nozzle source, the axis of the nozzle intersecting the surface normal at a 30° angle and the 240 μm orifice lying 1 cm away from the surface. Typically, mass flow controllers were set to deliver 10 ccm = 0.16 cm^3 s^{-1} each of CO

and O_2 (in the case of Pt and Rh; a factor of two lower in the case of Pd); this corresponds to a total flux at the surface of 2.2×10^{18} cm^{-2} sec^{-1} and a density of 3.3×10^{13} cm^{-3}. Prior to each experiment, a measurement was made of the quadrupole's sensitivity to 5×10^{-6} Torr of argon.

The rate of reaction was assumed to be proportional to the CO_2^+ ion current measured by the mass spectrometer. Changes in the O_2^+ and CO^+ ion currents were not used because these signals did not provide the same degree of precision as the CO_2^+ signal. Of course, it was necessary to assume that the pumping speed for CO_2 provided by the cryogenic pumps remained constant throughout the measurement. In the case of CO_2, the dominant pumping mechanism would have been cryocondensation (as opposed to cyrosorption into the activated charcoal absorbent located in the bodies of the two cryopumps or cryotrapping by other pumped gases) because it was the most condensable gas in the system. Thus, the assumption that the pumping speed for CO_2 is independent of the CO_2 pressure in the chamber is very reasonable as long as the total pressure is well below 10^{-3} where the thermal load on the pumps would be too large. Typical background pressure for the kinetic experiments was 4×10^{-5} Torr.

Results

The conversion of CO to CO_2 was measured at three $CO:O_2$ ratios, 2:1, 1:1 and 1:2, on Pt, Pd and Rh foils. As can be seen in Figures 1, 2 and 3, the surface temperature range was about 400 -1100K for Pt, 300 - 900K for Pd and 300 - 750K for Rh, respectively. Below T_m, the surface temperature of the maximum rate, the kinetic form of the rate is

$$r = (k_1 P_{O_2})/(K P_{CO}) \qquad (1)$$

where k_1 is the rate constant for molecular O_2 adsorption and K is the equilibrium constant for CO adsorption. Since the adsorption of molecular oxygen is essentially non-activated, the apparent activation energy in this regime is approximately equal to the heat of adsorption of CO at the appropriate coverages and reaction conditions. The apparent activation energies in kcal/mol obtained from an Arrhenius plot below T_m and above T_m are collected in Table I.

Discussion

At surface temperatures above T_m, the reaction is proportional to CO coverage and some function of oxygen atom coverage, $f(\theta_O)$, i.e.

$$r = k_2 f(\theta_O)\theta_{CO} \qquad (2)$$
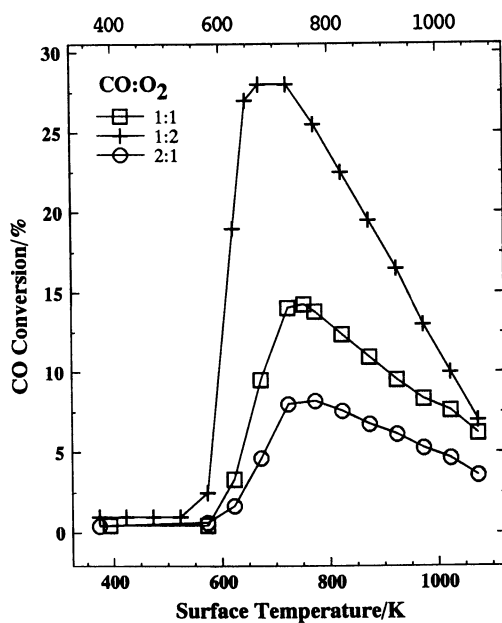
Figure 1.   Carbon monoxide conversion on Pt. The $CO:O_2$ ratios are provided in the legend, the total nozzle flow rate was (10ccm CO):(5ccm O_2), (10ccm CO):(10ccm O_2), (5ccm CO):(10ccm O_2), respectively, for 2:1, 1:1 and 1:2 CO/O_2 ratios.
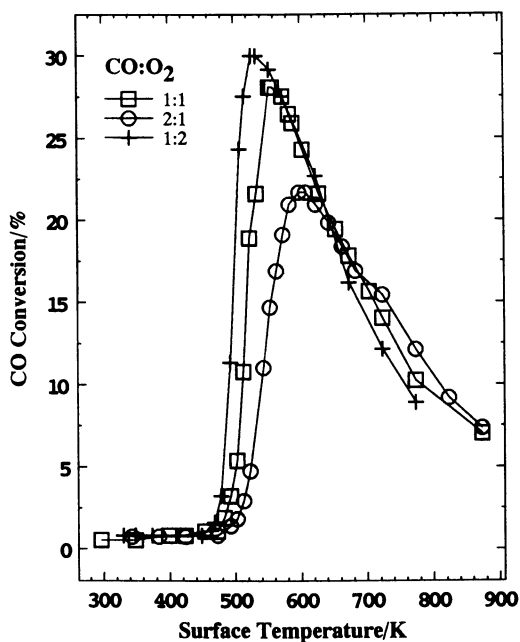
Figure 2.   Carbon monoxide conversions on Pd.   The $CO:O_2$ ratios are provided in the legend, the total nozzle flow rate was constant at 10 ccm.
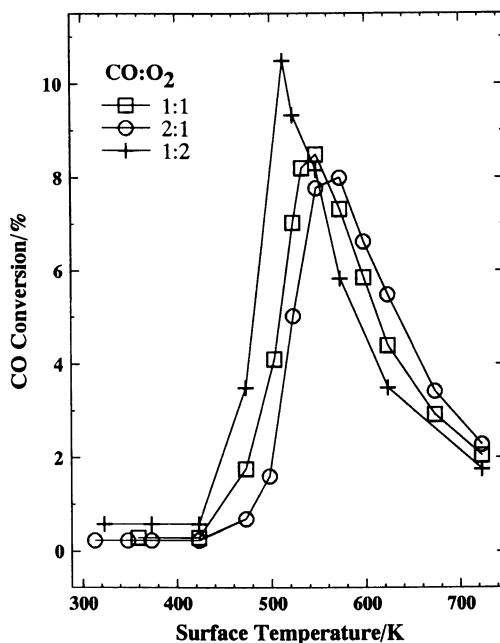
Figure 3. Carbon monoxide conversion on Rh. The $CO:O_2$ ratios are provided in the legend, the total nozzle flow rate was (10ccm CO):(5ccm O_2), (10ccm CO):(10ccm O_2), (5ccm CO):(10ccm O_2), respectively, for 2:1, 1:1 and 1:2 CO/O_2 ratios.

Table I. Apparent activation energies (kcal/mol) determined from the
rates of reaction with various $CO:O_2$ ratios on Pt, Pd and Rh

Metal	$CO:O_2$	E $(T<T_m)$ $= \Delta H_{CO}$	$E_{app} =$ E $(T>T_m)$	$\Delta E =$ E_{SR}
Pd	1:2	32.7	- 5.0	27.7
	1:1	28.1	- 4.5	23.6
	2:1	22.3	- 4.4	17.9
Pt[a]	1:2	24.0	- 8.6	15.4
	1:1	23.1	- 8.3	14.8
	2:1	14.0	- 10.1	3.9
Rh	1:2	13.8	- 6.4	7.4
	1:1	13.1	- 6.6	6.5
	2:1	19.5	- 6.9	12.6

[a]The activation energy on Pt for $T>T_m$ was corrected for changes in the
oxygen coverage with surface temperature.

The carbon monoxide will be essentially in equilibrium with the
surface. The oxygen coverage may be assumed to be high and the CO
coverage very low, as will be argued below. Thus, $f(\theta_O)$ is likely to be
only slightly temperature dependent (3) (and not much effected by the
oxygen coverage). In addition, we assume that the ΔH_{CO} determined
from $E(T<T_m) = \Delta H_{CO}$ is the appropriate heat of adsorption at $T>T_m$ as
well as at $T<T_m$. Therefore, we can calculate the surface reaction
activation energy, E_{SR}, from the equation (3), and these values are
given in Table I.

$$E_{app} = E(T>T_m) = E_{SR} - |\Delta H_{CO}| \qquad (3)$$

The activation energies and rate data may be used to estimate
the coverages of the reactants. The activation energies in Table 1, E
$(T<T_m) = \Delta H_{CO}$, were used to place an upper bound on the CO
coverage at T_m. To make this estimate, it was assumed that the CO
coverage was one monolayer (ML) at the temperature just below where
the rate becomes detectable. Assuming the CO was quasi equilibrated
with the surface, the measured heat of adsorption could then be used
to estimate θ_{CO} at T_m. These values are given in Table II.
The oxygen coverages were estimated for $T>T_m$ on each surface
by equating the rate of oxygen adsorption to twice the rate of CO_2
production and, since oxygen was expected to adsorb through a

Table II. Estimated carbon monoxide and oxygen coverages at T_m on Pd, Pt and Rh at various $CO:O_2$ ratios

Metal	$CO:O_2$	$\theta_{CO}{}^a$ at T_m	$\theta_O{}^b$ at T_m
Pd	1:2	3×10^{-3}	0.4
	1:1	4×10^{-3}	0.3
	2:1	5×10^{-3}	0.2
Pt	1:2	2×10^{-2}	0.1
	1:1	8×10^{-3}	0.15
	2:1	2×10^{-2}	0.1
Rh	1:2	1×10^{-2}	0.4
	1:1	1×10^{-2}	0.1
	2:1	1×10^{-2}	0.1

[a]Assuming $\theta_{CO}{}^{max} = 1.0$. [b]Assuming $\theta_O{}^{max} = 0.5$.

precursor state, (7,8) the rate of oxygen adsorption was assumed to be first order in the concentration of vacant sites.   Allowing for the possibility of oxygen desorption and recognizing that the CO coverage was already very low at T_m, we estimated the oxygen coverage using the relation

$$\frac{\theta}{\theta_m} = \frac{1 - \left(\frac{\chi_{CO}}{2S^o}\right)\left(\frac{P_{CO}}{P_{O_2}}\right)}{1 + \frac{k_d}{2F_{O_2}S^o}}$$

(4)

where χ_{CO} is the CO fractional conversion, F_{O_2} is the flux of oxygen to the surface, and P_{CO} and P_{O_2} are the pressures of CO and O_2, respectively, in the nozzle. The sticking coefficient S^o was taken as 0.4 for Pd (9), 0.1 for Pt (10), and 0.1 for Rh (11). The rate constant k_d in equation (4) was small enough to be neglected for the cases of Rh and Pd. However, taking the heat of adsorption of oxygen on Pt to be 55 kcal/mol and independent of coverage and assuming a normal first order desorption preexponential of 10^{13} s^{-1} indicated that oxygen desorption may have become appreciable at temperatures above 950K on the Pt foil. The coverage of oxygen on these surfaces for $T < T_m$ could not be determined. However, based on carbon monoxide's ability to prevent oxygen adsorption, the oxygen coverage should have remained

near zero until the temperature of incipient reaction, rising rapidly at that point to its coverage at the maximum rate. The estimated oxygen coverages on Pt, Pd, and Rh at T_m are given in Table II above.

The absolute magnitude of the coverages given in Table II are not to be taken too seriously, but the relative coverages and the order of magnitude of each are believed to be significant. First, it is to be noted that the coverage of CO is always very low at T_m and above. This is in accord with attempts to measure the CO by infrared spectroscopy at higher reaction temperatures where it was observed that the coverage was below 0.01 of a monolayer on Rh(111) at the surface temperature of maximun rate (12). Note also that the oxygen coverage at T_m is nearly independent of the gas mixture on each metal.

Carbon monoxide oxidation is known to be structure insensitive (5,13))so we can compare our rates with those reported for single crystals (14,15). Assuming a site density of 10^{15} per cm^2, our turnover frequencies (TOF, sec^{-1}) are about 155 and 83, respectively, for Pd (T_m = 600K) and Pt (T_m = 750K) using a 2:1 CO:O_2 ratio. These rates are significantly lower than those that would be estimated from the data of Berlowitz et al. (14) at the same CO:O_2 ratio, but their pressures were more than three orders of magnitude higher and this would cause the T_m to be moved to higher temperatures. Similarly, we estimate the TOF on Rh to be about 90 at T_m = 540 and a 1:1 CO:O_2 ratio. This value falls on the Arrhenius plot for Rh(111) for P_{CO} = P_{O_2} = 8 Torr (15), but Peden et al. do not observe a maximum in the rate up to the highest temperature investigated, 625K. Again, this can be rationalized by the three orders of magnitude higher pressures which would push the rate maximum to significantly higher reaction temperatures. Another factor that should not be overlooked is the relative surface and gas (reactant) temperatures. In the case of the single crystal work (14,15), the pressures were high enough that the gas tempertaure would have been essentially in equilibrium with the the surface while the reactants would have been rotationally and vibrationally cold for the nozzle fluxes we used in our experiments. Thus, we can only state that our TOF are probably in qualitative agreement with those measured on single crystals if corrections for pressure and gas phase temperatures could be made.

Perhaps the most interesting observation of this kinetic study is the Polanyi relation, the linear correlation of the surface reaction activation energy, E_{SR}, with the heat of adsorption of CO, ΔH_{CO}, shown in Figure 4. Obviously, each of the three reactant ratios for each metal would fit such a Polanyi relation also, but the fact that a single Polanyi relation correlates the data for all three metals at three CO:O_2 ratios is remarkable.

The usual interpretation of the Polany relation of Figure 4 would be that the formation of the activated complex involves the breaking of or concerted weakening of the metal-carbon bond of the adsorbed CO. Indeed, we have suggested that the barrier to formation of the activated complex is the barrier encountered when CO is moved on top of a chemisorbed oxygen atom and, while still partially bonded to the
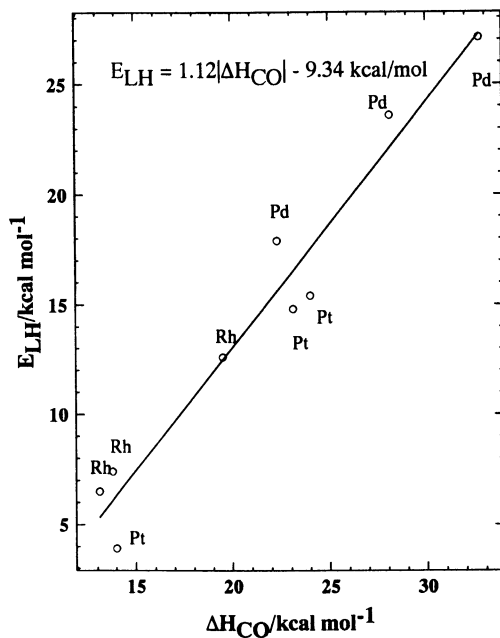
Figure 4.   Dependence of the surface reaction activation energy, E_{SR}, on ΔH_{CO}, a Polanyi relation.

metal, the new C-O bond to the chemisorbed oxygen atom is partially formed in the activated complex (*14*). This picture is consistent with the fact that CO is very mobile at the reaction temperature (while oxygen is not) and that our trajectory calculation modeling the activated complex suggests that it is nearly linear and normal to the surface (*16*).

At first glance, the above picture of the dynamics of the formation of the CO_2 activated complex does not appear to be in accord with three recent observations of the reactivity of "nascent" O atoms on Pt(111) formed by 1) thermal dissociation of chemisorbed O_2 at 150K (*17*), 2) photo-dissociation of chemisorbed O_2 at 100K (*18*) or partially accommodated O atoms arriving from the gas phase (*19*)(in all cases the CO was coadsorbed prior to the formation of the nascent O atoms). These experimental findings lead Mullins et al. (*19*) to conclude that the activation barrier to reaction at high temperature is largely associated with overcoming the strong binding energy to the surface of the available O atoms. If this is the correct conclusion it would suggest that the appropriate Polanyi relation should correlate the ΔH_O and E_{SR} instead of ΔH_{CO} and E_{SR}. However, we note that 1) the nascent O atom experiments were all performed at high CO and low O coverages while our experiments are at high O and low CO coverages, and 2) when Pt, Pd and Rh are compared, they have very different ΔH_O but about the same E_{SR} which suggests that the formation of the activation complex probably does not involve breaking of the M-O bond.

In the work of Mullins et al. (*19*), they determined the angular and velocity distributions of the CO_2 product of the interaction of gas-phase O atoms with CO adsorbed on Pt(111) at 90K. Because the angular distributions observed were nearly the same as seen by Matsushima (*18*) for temperature programed reaction at 150K (thermal dissociation of O_2 followed by reaction of the nascent O atom) and the steady state reaction of CO and O_2 on Pt(111) at 750K, Mullins et al. concluded that the same activated complex was formed in all three cases. Thus, we propose that the movement of CO onto a strongly bound O atom is yet another method of activating the chemisorbed O atom and that the ability of chemisorbed CO to perform this extraction of the O atom from the deep chemisorbed well is determined by ΔH_{CO} and this is the explanation for the observed Polanyi relation. We are in the progress of measuring the vibrational energy distribution of desorbed CO_2 formed by CO reaction with O atoms, i.e., an experiment parallel to that of Mullins et al. If the internal energy distribution is the same (on a given metal at a given T_m and coverage) independent of whether the oxygen is supplied as O_2 or O atoms, as would be predicted by the conclusion of Mullins et al., we believe that will also lend strong support for our interpretation of the Polanyi relation shown in Figure 4.

Acknowledgments

We are pleased to acknowledge partial support of this research by the National Science Foundation.

Literature Cited

1. Mantell, D. A.; Kunimori, K.; Ryali, S. B.; Haller, G. L.; Fenn, J. B.*Surf. Sci.* **1986**, *172*, 281.

2. Coulston, G. W.; Haller, G. L. *J. Chem. Phys.* **1990,** *92*, 5752.

3. Coulston, G. W., Ph. D. Thesis, Yale University, 1990.

4. Coulston, G. W.; Haller, G. L. *J. Chem. Phys.*, in press.

5. Böcker , D.; Gonzalez, R. D. In "Closed Cycle, Frequency-Stable CO_2 Laser Technology", Batten, C. E.; Miller, I. M.; Wood, G. M., Jr.; Willetts, D. V., Eds., NASA Conference Publication 2456, NASA Sci. & Tech. Inf. Branch, 1987, pp. 85-102.

6. Landry, S. M.; Dalla Betta, R. A.; Lü, J. P.; Boudart, M. *J. Phys. Chem.*, **1990**, *94*, 1203.

7. Fisher, G. B.; Sexton, B. A.; Gland, J. L. *J. Vac. Sci. Technol.*, **1980.** *17*, 144.

8. Imbihl, R.; Demuth, J. E. *Surf. Sci.* **1986**, *173*, 395.

9. Engel, T. *J. Chem. Phys.* **1978**, *69*, 373.

10. McClellan, M. R.; McFeely , R.; Gland, J. L. *Surf. Sci.* **1983**, *124*, 188.

11. Campbell, C. R.; White, J. M. *J. Catal.* **1978.** *54*, 289.

12. Goodman, D. W., Am. Chem. Soc. Abstracts, Atlanta National Meeting, 1991.

13. Engel, T.; Ertl, G. *Advan. in Catal.* **1979**, *28*, 1.

14 Berlowitz, P. J.; Peden, C. H. F.; Goodman, D. W. *J. Phys. Chem.*, **1988**, *92*, 5213.

15. Peden, C. H. F.; Goodman, D. W.; Blair, D. S.; Berlowitz, P. J.; Fisher, G. B.; Oh, S. H. *J. Phys. Chem.*, **1988**, *92*, 1563.

16. Kwong, D. W. J.; de Leon, D.; Haller, G. L. *Chem. Phys. Lett.*, **1988**, *144*, 533.

17. Matsushima, T. *Surf. Sci.*, **1982**, *123*, L663.

18. Mieher, W. D.; Ho, W. *J. Chem. Phys.*, **1989**, *91*, 2755.

19. Mullins, C. B.; Rettner, C. T.; Auerbach, D. J. *J. Chem. Phys.*, in press.

20. Becker, C. A., Ph. D. thesis, University of Chicago, 1979.

Chapter 5

Infrared Reflection–Absorption Spectroscopy
New Technique for In Situ Determination of Local Surface Structure

W. Kevin Kuhn, Jian-Wei He, and D. Wayne Goodman

Department of Chemistry, Texas A&M University,
College Station, TX 77843–3255

Ultra-thin films of Cu, Ni and Co on Rh(100) and Mo(110) substrates have been studied using carbon monoxide adsorption in conjunction with infrared reflection absorption spectroscopy (IRAS). The CO vibrational frequency on Cu/Rh(100) and Cu/Mo(110) at low Cu coverage (~0.1 ML) shows a blue-shift relative to its gas phase stretching frequency (2143 cm^{-1}). This blue-shift is explained as arising from CO adsorbed on well-dispersed Cu adatoms which are slightly positively charged due to polarization arising from the CO-Cu interaction. Three-dimensional Cu clusters, well-ordered pseudomorphic two dimensional Cu islands and single Cu atoms are distinctively characterized by their CO IR peaks. In addition, it is found that IR spectra of adsorbed CO show a remarkable sensitivity to surface structural phase transitions. Both order-order and disorder-order transitions are observed for Ni and Co overlayers on a Mo(110) substrate. It is further shown that localized segregation and ordering of C and O on Mo(110) and S on Co/Mo(110) are observable.

Considerable scientific attention has been directed toward the understanding of ultra-thin metal films supported on single crystal metal substrates (*1-11*). The interest in using these systems as well-characterized models for the more complex supported bimetallic systems relates to the importance of mixed metal catalysts. In a typical study, a metal is deposited onto a single crystal surface at ultrahigh vacuum conditions. The morphology and structural properties of the ultra-thin metal films are then characterized using Auger electron spectroscopy (AES), low energy electron diffraction (LEED), and temperature programmed desorption spectroscopy (TPD).

Recently, we have found that CO combined with infrared reflection absorption spectroscopy (IRAS) can be used as a molecular probe to study the

electronic properties, morphology and local surface structure of these ultra-thin metal films. The information obtained will be qualitative rather than quantitative in nature since the integrated peak areas obtained from IRAS spectra may not correlate directly with the CO surface concentration. An additional feature of IRAS is the inherent capability of being able to study surface structure at relatively high pressures. Thus, potentially the morphology of the bimetallic surface can be studied at reaction temperatures and pressures. Experimental data on Cu/Rh(100), Cu/Mo(110), Ni/Mo(110) and Co/Mo(110) will be presented and discussed in this paper.

Experimental

The experiments were carried out in an ultrahigh vacuum chamber equipped for IRAS, AES, and LEED. This apparatus has been discussed in detail elsewhere (12). The samples were spot-welded to two Ta wires which allowed resistive heating of the sample to 1500K and cooling to 80K. The Rh(100) and Mo(110) surfaces were cleaned using an oxidation and heating procedure described in reference 13. After this treatment, AES indicated a clean surface, with C, O and S impurities less than 1 atom %, and LEED exhibited sharp substrate patterns. The infrared spectra were obtained using a Mattson Fourier transform infrared spectrometer (Cygnus 100) in the single reflection mode at an 85° incident angle. The spectra in this work were obtained using 4 cm^{-1} resolution.

Cu, Co and Ni were evaporated from a copper, cobalt or nickel wire wrapped around a W filament. Prior to each deposition, the source was degassed extensively. AES showed that no impurities accumulated on the surface during the metal deposition. The copper, cobalt and nickel coverages were determined using the relationship of the AES ratio versus the corresponding TPD area from references 8, 9 and 11, respectively. One monolayer (ML) was defined to be one overlayer atom per substrate atom, i.e., the atomic densities of the Rh(100) and Mo(110) surfaces.

Results and Discussion

Ultra-Thin Metal Overlayers. Figure 1 shows the IR spectra of CO adsorbed on Cu/Rh(100) at the indicated Cu coverages (θ_{Cu}). The Rh(100) surface was dosed with Cu at 85K, flashed to ~900K, and exposed to 10 L of CO at 85K. It is noteworthy that the CO adsorbed on 0.1 ML of Cu on Rh(100) shows a peak at 2155 cm^{-1} which is higher than that of gas phase CO (2143 cm^{-1}). It is well known that the bonding of CO to metals is due to backdonation of electronic charge from the metal to the CO $2\pi^*$ orbital in conjunction with donation of electronic charge from the CO 5σ orbital to the metal (14). On metal surfaces, the $2\pi^*$ backdonation is usually the predominant contribution. Because of the antibonding nature of the $2\pi^*$ orbital, this predominant backdonation consequently results in a red-shift of the CO stretching frequency relative to its gas phase value (15). Figure 1, however, shows a blue-shifted frequency for CO adsorbed onto a low coverage of Cu supported on a Rh(100) surface. An unusually high CO stretching frequency (2138 cm^{-1}), although not
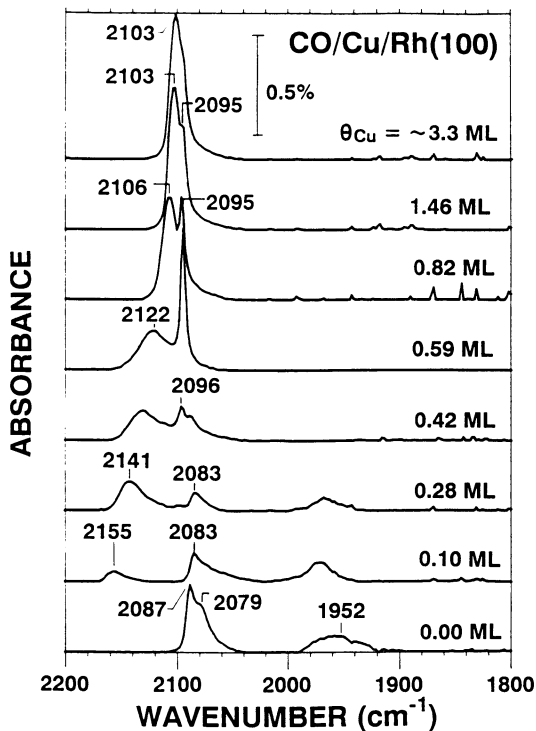
Figure 1. IR spectra of CO on Cu/Rh(100) surfaces. Cu was deposited onto the Rh(100) surface to the indicated coverage at 100K, annealed to ~900K, then dosed with 10 L of CO at 85K, followed by immediate spectral acquisition.

blue-shifted, has been observed for CO adsorbed onto 0.03 ML of Cu on a Ru(001) surface and was interpreted to correspond to CO adsorbed onto single Cu atoms (16). The blue-shifted CO frequency observed in this work suggests a considerable reduction in the $2\pi^*$ backdonation. In a recent XPS study of the Cu/Rh(100) system, it was observed that for low Cu coverages, the Cu $2p_{3/2}$ peak is shifted toward lower binding energy indicating an increase in electron density on the Cu (17). However, when CO is adsorbed, the $2p_{3/2}$ peak shifts to higher binding energy (17). Work on the Cu/Ru(0001) system indicates that there is a net charge transfer from the Cu overlayer to the Ru substrate upon CO adsorption (18). It is, therefore, likely that CO adsorption polarizes the CO/Cu/Rh(100) interface in such a way that charge flows from the Cu to the Rh substrate. Thus, for submonolayer Cu coverages on Rh(100), the bonding of CO to Cu, then, predominantly consists of a 5σ donation to the Cu. The slight antibonding properties of the 5σ orbital (16) and the inductive stabilization of the molecular electronic levels of CO both serve to strengthen the CO bond, to blue-shift the C-O stretching frequency, and to increase the CO desorption temperature compared to bulk Cu.

To further investigate the nature of this unusual blue-shift discussed above, CO adsorption was studied on 0.1 ML of Cu, Ni and Co on Mo(110). The results are shown on Figure 2, in which "u" and "a" indicate that the thin metal films were either unannealed or annealed to ~900K prior to the CO adsorption, respectively. In Figure 2, CO on the unannealed 0.1 ML Cu/Mo(110) surface shows a peak at 2166 cm^{-1} which is blue-shifted relative to the CO gas phase frequency. However, upon annealing, the blue-shifted peak disappears. No blue-shifted CO frequency is observed for 0.1 ML of either Ni or Co on Mo(110). The above results indicate that the blue-shift is associated specifically with Cu, a noble metal with a filled d band. It is generally believed that these d electrons are not significantly involved in the chemical bonding between CO and Cu (19). For Ni or Co on a Mo(110) surface, on the other hand, the $3d \rightarrow 2\pi^*$ backdonation serves as the primary bonding mechanism for CO.

The fact that the blue-shift is only observed at low Cu coverage and that it disappears upon annealing the Cu/Mo(110) surface indicates that the blue-shifted frequency corresponds to CO adsorbed onto well-dispersed Cu. As θ_{Cu} increases or the Cu film is annealed to increase the mobility of Cu atoms, the overlayer Cu forms large 2-D clusters. The Cu atoms in these 2-D clusters are expected to be less electronically perturbed compared to the well-dispersed Cu atoms because of the increase in the Cu-Cu coordination. Therefore, CO adsorbed onto the 2-D clusters exhibits only the expected red-shifted stretching frequency.

The peak at 2095 cm^{-1} in Figure 1 is very sharp, highly symmetric, and appears only after the Cu overlayer is annealed above room temperature. This peak is therefore interpreted to correspond to CO adsorbed onto the first monolayer of Cu that assumes the geometry of the Rh(100) surface, i.e., a pseudomorphic Cu overlayer (8). The peak at 2122 cm^{-1} corresponds to CO adsorbed onto relatively disordered 2-D Cu domains.
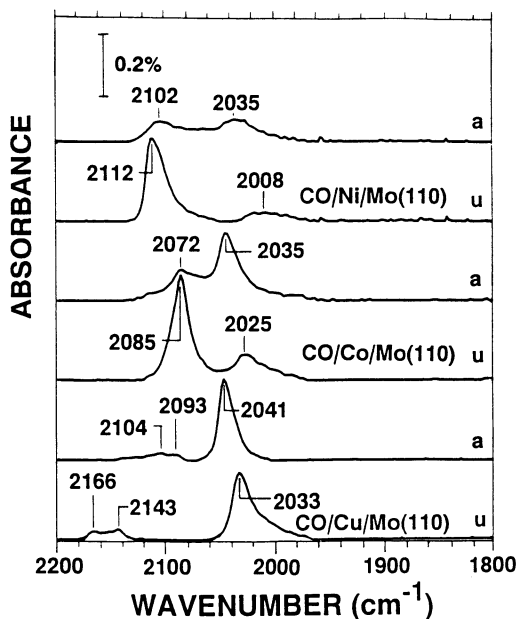
Figure 2. IR spectra of CO on 0.1 ML of Cu, Ni and Co on a Mo(110) surface. "u" and "a" indicate that prior to a 10 L CO exposure at 90K, the metal overlayers were either unannealed or annealed to ~900K after the metal deposition at 90K.

Multilayer Cu on Rh(100). In order to simulate the CO IR features of bulk Cu, the Rh(100) surface was dosed with ~7 ML Cu and then annealed to 871K. The morphology of Cu after this procedure is known to be two uniform layers covered with 3-D clusters (8). The CO IR spectrum from this Cu/Rh(100) surface is shown in Figure 3.

Figure 3 shows a peak at 2076 cm^{-1}, the approximate CO stretching frequency reported for CO on Cu(100) or Cu(111) (20-22). The 2076 cm^{-1} peak is, therefore, identified to correspond to CO adsorbed onto 3-D Cu clusters. The 2103 cm^{-1} peak corresponds to CO adsorbed onto uniform 2-D Cu overlayers (see also Figure 1a). Figure 3 also shows that as the CO/Cu/Rh(100) surface is heated to 215K, the CO on the 3-D clusters desorbs leaving considerable CO on the uniform films. This is consistent with the TPD results which show that CO adsorbed onto a uniform 2-D overlayer on Rh(100) has a higher bonding energy than CO adsorbed onto bulk Cu surfaces (8). From the above, CO adsorbed onto 3-D clusters, onto a pseudomorphic Cu monolayer and onto single Cu atoms are clearly distinguished by their characteristic frequencies.

Surface Phase Transitions. Recently, an (8x2) to (7x2) structural phase transition has been reported for Ni thin films on Mo(110) (10,11,23). The (8x2) and (7x2) Ni overlayers are best described as distorted Ni(111) structures with real space geometries that correspond to coverages of 1.25 and 1.29 ML, respectively. The density difference between the phases is therefore only 3%. The larger atomic density of Ni(111), compared to Mo(110), corresponds to a Ni coverage relative to Mo of 1.30 ML. As will be seen, the (8x2) and (7x2) structures of the Ni thin films can be unambiguously identified from their CO IR peaks.

Figure 4 shows the CO IR spectra for Ni on Mo(110). For Figure 4a, the Ni was deposited onto Mo(110) at 90K and annealed to ~900K. The CO exposure (saturation) and IR spectral acquisition were performed at 85K. From 0.3 to 0.95 ML, a peak at ~2087 cm^{-1} is evident, whereas, at 0.95 ML, a new peak at 2065 cm^{-1} appears. By 1.08 ML, the 2065 cm^{-1} peak becomes predominant, and the 2087 cm^{-1} peak is markedly attenuated. LEED results show that the abrupt spectral change at θ_{Ni} = 0.95-1.08 ML correlates with a surface structural phase transition from the (8x2) structure to the (7x2) structure. From 0.42 to 0.95 ML, the Ni/Mo(110) surface exhibits the (8x2) pattern, whereas, the (7x2) is observed at $\theta_{Ni} \geq$ 1.08 ML. In a recent paper, the structural change from (8x2) to (7x2) was also reported at θ_{Ni} = ~0.9 ML for Ni deposition onto Mo(110) at room temperature (10). The two IR peaks at 2065 and 2087 cm^{-1} in Figure 4a, therefore, originate from CO adsorbed onto Ni overlayers with the (7x2) and (8x2) structures, respectively. The fact that the transition occurs at $\theta_{Ni} \approx$ 1 ML instead of 1.25 ML indicates that the (7x2) structure is more stable than the (8x2) structure at coverages greater than ~1 ML.

The CO frequency shift appears to arise because of the difference in electronic properties of Ni in the two structures. It is noted that as the structure changes from (8x2) to (7x2), the Ni surface density, the work function (10), the
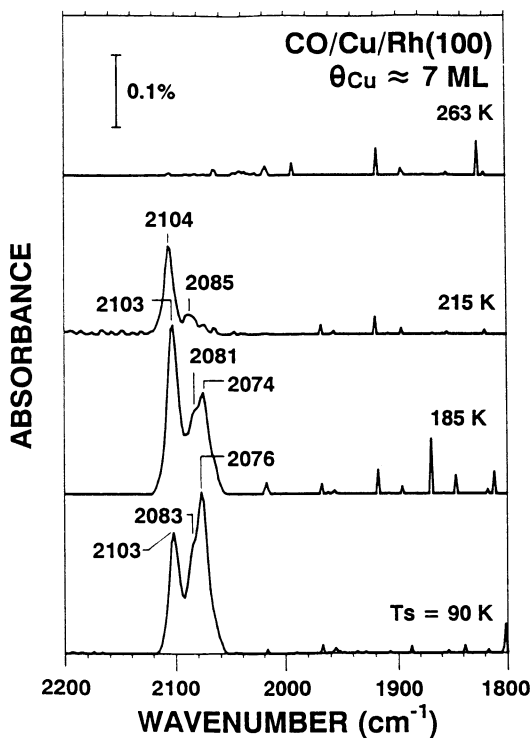
Figure 3. IR spectra of CO on ~7 ML of Cu on Rh(100). Cu was deposited at 100K, annealed to 870K, and dosed with 10 L of CO at 90K. The IR spectra were collected at 90K after the surface had been flashed to the indicated sample temperatures.
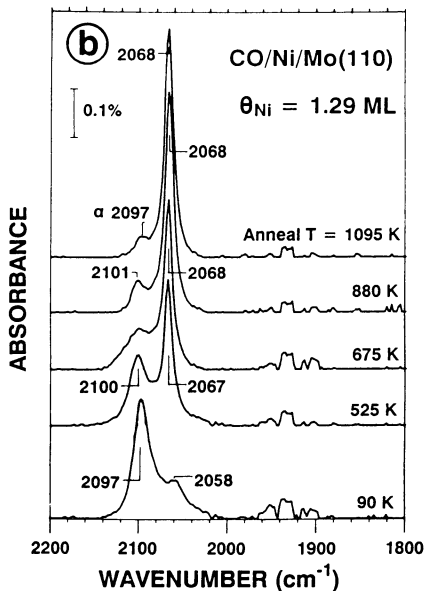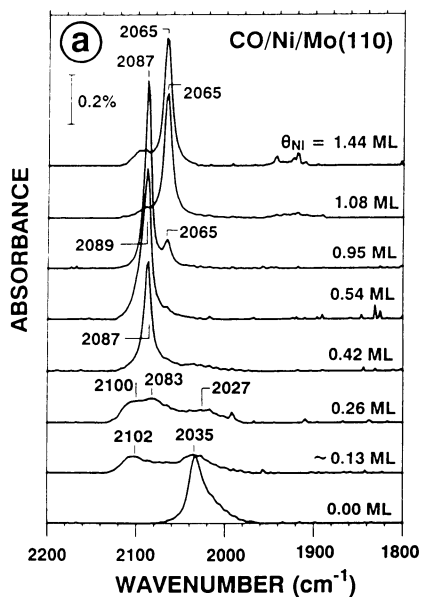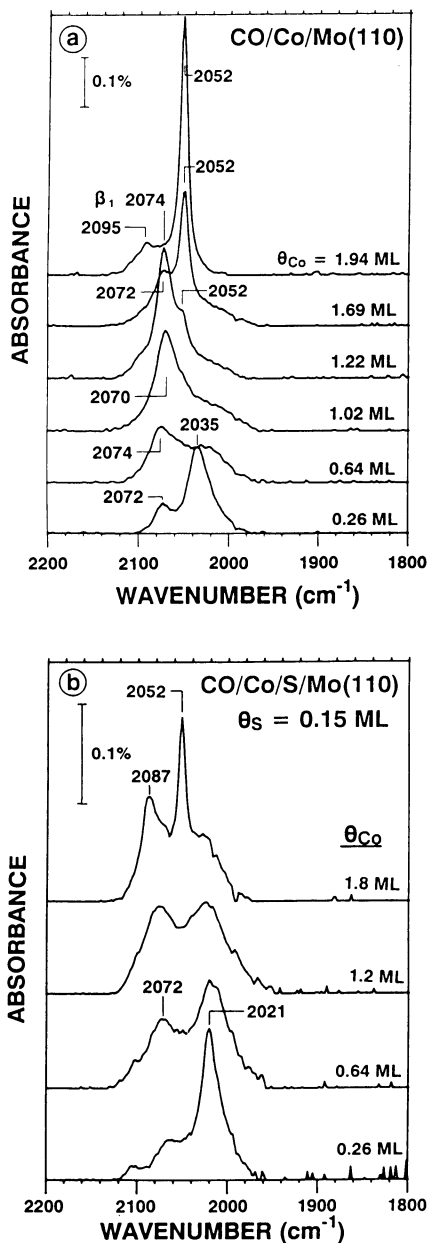
Figure 4. a, IR spectra of CO on Ni/Mo(110) at the indicated Ni coverages. Ni was deposited onto the Mo(110) surface at 100K, flashed to ~900K and then dosed with 10 L of CO at 90K. b, IR spectra of CO on 1.29 ML of Ni on Mo(110) after annealing to the indicated temperatures. The Ni was deposited at 100K and flashed to the indicated temperature prior to a 10 L CO exposure at 90K.

CO desorption temperature (*11*), and the CO stretching frequency all approach the corresponding values for the Ni(111) surface. The above suggest that the bonding between CO and Ni in the (8x2) phase is weaker than in the (7x2) phase, which, in turn is weaker than for bulk Ni. This is corroborated by CO TPD results for Ni/Mo(110) which show that CO is bound more weakly to mono- and submonolayer Ni films than to bulk Ni (*24*). It is the change in the electronic properties during the phase transition from (8x2) to (7x2) that leads to the abrupt frequency shift in Figure 4a.

For Figure 4b, the Mo(110) surface was covered with 1.29 ML of Ni at 90K, and then flashed to the indicated temperatures. Each annealed surface was exposed to 10 L of CO at 90K followed by IR spectral acquisition. Annealing the surface to higher temperatures reduced the intensity of the peak at ~2100 cm^{-1} with a concurrent increase in the intensity of the peak at ~2068 cm^{-1}. At annealing temperatures higher than 675K, the spectra are essentially identical to the spectrum at 1.44 ML in Figure 4a. LEED observations showed that the deposition of Ni at 90K attenuated the substrate spots and increased the background significantly, indicating a disordered Ni overlayer. Annealing above 500K decreased the background intensity considerably and yielded the (7X2) pattern. The IR spectral changes in Figure 4b correlate well with the LEED results and reflect the formation of the ordered (7X2) structure from a relatively disordered Ni overlayer. The broad peak at ~1932 cm^{-1} is interpreted as bridge-bound CO on the Ni overlayers (*25*).

It is also noteworthy that as the intensities of the 2087 and 2065 cm^{-1} peaks increase, the peak frequencies remain constant. This suggests that island growth occurs via two dimensional expansion with nucleation on the Ni adatoms at the island edges. CO adsorption at the interior of the islands is unaffected by island growth. A detailed discussion related to the use of CO IRAS to study surface phase transitions is given elsewhere (*23*).

Non-Metallic Adsorbate Interactions. Since non-metallic adsorbate structures are of considerable interest in the surface chemistry of catalysis, work has been carried out to explore the use of IRAS as a probe of the local structure of these adsorbates as well. For example, the effect that dissociated CO has on the IR spectra of subsequently adsorbed CO is shown in Figure 5. Spectrum 1 is of saturation CO on a clean Mo(110) surface and shows the characteristic peak at 2035 cm^{-1}.

To determine the effects of co-adsorbed oxygen, the Mo(110) surface was dosed with O$_2$ at 90K, flashed to 1100K and then dosed with 10 L of CO at 90K followed by spectral acquisition. The co-adsorbed O induces two new peaks at 2054 and 1977 cm^{-1}. The peak at 2038 cm^{-1} is due to CO adsorbed on clean Mo domains. To explain the two new features, two types of electronic interactions between CO and O must be considered: (a) an indirect electronic interaction mediated via the substrate, and (b) a direct electronic interaction between CO and O (*26*). In the indirect mechanism for the interaction between CO and O, the electronegative species O withdraws electronic charge from the metal substrate. This, in turn, causes a reduction in the backdonation from Mo to the CO in the immediate vicinity which stabilizes the C-O bond and thus shifts its
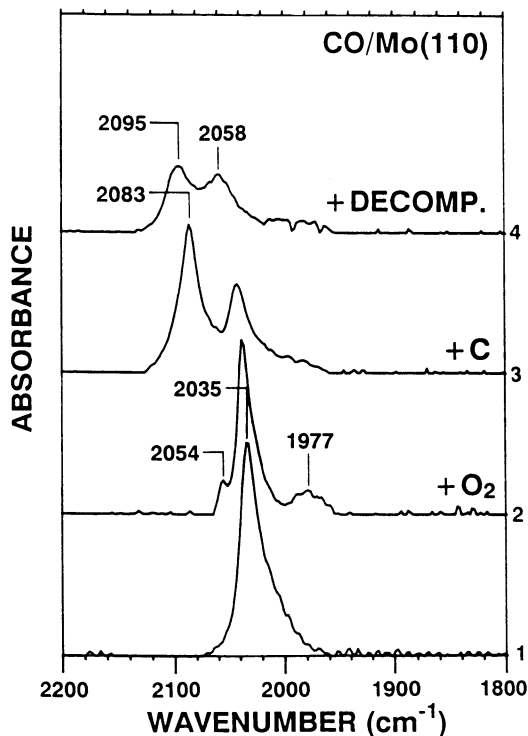
Figure 5. IR spectra of CO on Mo(110) with the indicated co-adsorbed species. The Mo surface was exposed to propylene and flashed to ~1200K, exposed to O_2 and flashed to ~1200K, or exposed to CO and flashed to ~500K; to give ~0.15 ML of C, O or C & O (0.3 ML total), respectively. The surface was then exposed to 10 L of CO at 90K.

stretching frequency toward the blue (2054 cm^{-1}). In the direct mechanism for a CO-O electronic interaction, a partial bond develops between the CO and the O. This interaction weakens the C-O bond, red-shifts the C-O stretching frequency, and leads to the IR feature at 1977 cm^{-1}.

The effects of co-adsorbed carbon are shown in spectrum 3 of Figure 5 where C was deposited by adsorption of propylene (C$_3$H$_6$) at 90K and subsequently heating the surface to 1200K to decompose the propylene and to desorb hydrogen. CO adsorption and IR spectral acquisition were then carried out at 90K. The preadsorption of C induces a new peak at 2083 cm^{-1}. This frequency is blue-shifted relative to that of CO on clean Mo(110), consistent with the C reducing the backdonation from Mo to the CO $2\pi^*$ orbital. The two peaks at 2043 and 2083 cm^{-1}, then, correspond to CO adsorbed onto clean Mo domains and onto C-covered domains of Mo, respectively.

Spectrum 4 in Figure 5 shows the effect of decomposed CO on subsequent CO adsorption. The Mo surface was exposed to 10 L CO at 90K, flashed to ~500K and dosed with an additional 10 L of CO at 90K, followed by spectral acquisition. Flashing the surface above 350K causes any remaining CO to decompose into atomic C and O with a total carbon and oxygen coverage of ~0.3 ML. CO adsorption onto this surface yields two main peaks at 2095 and 2058 cm^{-1} with a weak feature at ~1980 cm^{-1}, as shown in Figure 5. The peak at 2095 cm^{-1} is attributed to CO adsorbed in the vicinity of C, while the peaks at 2058 and ~1980 cm^{-1} are attributed to CO adsorbed in the vicinity of O, as discussed above.

It is noteworthy that the adsorption of C causes a larger blue shift (40 cm^{-1}) in the CO stretching frequency compared to the adsorption of O (19 cm^{-1}). However, previous TPD results have reported a significant reduction in the desorption activation energy for CO on O/Mo(110), while for CO on C/Mo(110), the desorption activation energy remains essentially unchanged from that of the clean surface (27). Clearly, there is little correlation between the desorption activation energy and the direction of the shift in the CO stretching frequency.

Figure 6 shows the IR spectra for CO adsorbed onto Co/Mo(110) and onto Co on S/Mo(110). For Figure 6a, the Co was deposited onto the Mo(110) surface at 90K and annealed to ~1100K prior to a saturation CO exposure at 90K. For Figure 6b, the Mo surface was exposed to 2L of H$_2$S at 90K, then flashed to ~1400K to decompose the H$_2$S and desorb the hydrogen. This procedure then leaves the Mo(110) surface with a sulfur coverage of ~0.15 ML. Co was deposited at 90K, the surface flashed to ~1100K, followed by a saturation CO exposure at 90K. In Figure 6a, the peaks at ~2072 and 2035 cm^{-1} for low Co coverages arise from CO adsorbed onto pseudomorphic Co and clean Mo, respectively. For Co on Mo(110), previous studies have shown that as the Co coverage is increased above 1 ML, a surface phase transition from a pseudomorphic (1X1) structure to an (8X2) structure occurs (9,10,23). This transition is apparent in the CO IR spectra of Figure 6a by the abrupt appearance of a peak at 2052 cm^{-1}.

The effects of preadsorbed S are shown in Figure 6b. For low S coverages, the two main peaks are at 2072 and 2021 cm^{-1}. The 2072 cm^{-1}

Figure 6. a, IR spectra of CO on Co/Mo(110) at the indicated Co coverages. Co was deposited onto the Mo(110) surface at 100K, flashed to ~1000K and then dosed with 10 L of CO at 90K. b, IR spectra of CO on Co/S/Mo(110) at the indicated Co coverages. The surface was exposed to H_2S and flashed to ~1400K to give a sulfur coverage of ~0.15 ML. Co was deposited onto the S/Mo(110) surface at 100K, flashed to ~1100K and then exposed to 10 L of CO at 90K.

feature corresponds to CO adsorbed onto pseudomorphic Co islands on the Mo(110) surface and is in agreement with an identical feature (2072 cm^{-1}) on the clean Co/Mo(110) surface (Figure 6a). The peak at 2021 cm^{-1} correlates with the frequency observed for CO adsorbed onto ~0.15 ML of S on Mo(110) (*28*). These features do not change substantially until the Co coverage increases above ~1.5 ML. For example, in the spectrum of 1.8 ML of Co on S/Mo(110) in Figure 6b, three features at ~1920, 2052 and 2087 cm^{-1} are apparent. These features correspond to CO adsorbed onto discrete domains of S/Mo(110), (8X2) Co/Mo(110) and Co-S/Mo(110).

It is noteworthy that in all the co-adsorption systems discussed in this section, multiple peaks have been observed. These features are due to CO adsorbed onto discrete domains of the clean and adatom-covered substrate. These results imply that there is a segregation of the adatoms into 2-D islands and that the different domains are distinguishable by the stretching frequency of adsorbed CO.

Summary and Conclusions

This paper has addressed the use of CO IRAS as an in-situ technique for the determination of surface structure. The results can be summarized as follows:

1. At a low coverage (<0.3 ML) of Cu on a Rh(100) surface, the CO vibrational frequency shows a blue-shift with respect to its gas phase frequency. This blue-shift is also observed for CO adsorbed on 0.1 ML of Cu on Mo(110), but not on Ni/Mo(110) or Co/Mo(110). The blue shift is believed to correspond to CO adsorbed on well-dispersed Cu that is polarized because of CO-Cu-substrate interactions.

2. 3-dimensional Cu clusters, 2-dimensional pseudomorphic Cu overlayers and single Cu atoms on a Rh(100) surface are characterized by their CO stretching frequencies at 2074, 2095, and 2162 cm^{-1}, respectively.

3. The '(8x2) to (7x2)' and 'disorder to (7X2)' structural phase transitions of Ni/Mo(110) lead to abrupt changes in the stretching frequency of adsorbed CO. The growth of the domains of these structures apparently follows a mechanism of two dimensional island expansion via nucleation of the adatoms at island edges.

4. C and O adsorbed onto Mo(110) form 2-dimensional islands which can be characterized by the stretching frequency of adsorbed CO (~2095 and ~2060 cm^{-1}, respectively).

5. CO IRAS spectra show that Co-S, pseudomorphic (1X1) Co, (8X2) Co, and S-Mo domains are observed when Co is deposited onto a S/Mo(110) surface (2087, 2072, 2052, and 2020 cm^{-1}, respectively).

Acknowledgments

Literature Cited

1. Christman, K.; Ertl, G.; Shimizu, H. *J. Catal.*, **1980**, *61*, 397.
2. Schlenk, W.; Bauer, E. *Surface Sci.*, **1980**, *93*, 9.
3. Kolacziewicz, J.; Bauer, E. *Surface Sci.*, **1984**, *144*, 495.
4. Berlowitz, P. J.; Goodman, D. W. *Surface Sci.*, **1987**, *187*, 463.
5. Berlowitz, P. J.; Goodman, D. W. *Langmuir*, **1988**, *4*, 1091.
6. Goodman, D. W.; Peden, C. H. F. *J. Chem. Soc., Faraday Trans. 1*, **1987**, *83*, 1967.
7. He, J.-W.; Goodman, D. W. *J. Phys. Chem.*, **1990**, *94*, 1496.
8. Jiang, X.; Goodman, D. W. *Surface Sci.*, submitted.
9. He, J.-W.; Goodman, D. W. *Surface Sci.*, **1991**, *245*, 29.
10. Tikov, M.; Bauer, E. *Surface Sci.*, **1990**, *232*, 73.
11. He, J.-W.; Kuhn, W. K.; Goodman, D. W., to be published.
12. Leung, L.-W. H.; He, J.-W.; Goodman, D. W. *J. Phys. Chem.*, **1990**, *93*, 8328.
13. Grunze, M.; Ruppender, H.; Elshalzly, D. *J. Vac. Sci. Technol. A6*, **1988**, 1266.
14. Cotton, F. A.; Wilkinson, G. *Advanced Inorganic Chemistry*; John Wiley & Sons: New York, 1988.
15. Hoffmann, F. M. *Surface Sci. Reports*, **1983**, *3*, 107.
16. Hoffmann, F. M.; Paul, J. *J. Chem. Phys.*, **1987**, *87*, 1857.
17. Rodriguez, J. A.; Campbell, R. A.; Goodman, D. W. *J. Phys. Chem.*, **1991**, *95*, 2477.
18. Houston, J. E.; Peden, C. H. F.; Feibelman, P. J.; Hamann, D. R. *Surface Sci.*, **1987**, *192*, 457.
19. Bagus, P. S.; Nelin, C. J.; Bauschlicher, C. W. *J. Chem. Phys.*, **1983**, *28*, 5423.
20. Ryberg, R. *Surface Sci.*, **1982**, *114*, 627.
21. P. Hollins; Pritchard, J. In *Vibrational Spectroscopies of Adsorbates*, Willis, R. F., Ed.; Springer: Berlin, 1980, Vol. 15.
22. Pritchard, J. *Surface Sci.*, **1979**, *79*, 231.
23. He, J.-W.; Kuhn, W. K.; Goodman, D. W. *J. Am. Chem. Soc.*, in press.
24. Surnev, L.; Xu, Z.; Yates, Jr., J. T. *Surface Sci.*, **1988**, *201*, 1.
25. Goodman, D. W.; Yates, Jr., J. T.; Madey, T. E. *Surface Sci.*, **1980**, *93*, L135.
26. Ryberg, R. In *Advances in Chemical Physics*, Lawley, R. P., Ed.; John Wiley & Sons: 1989; p.1.
27. Ko, E. I.; Madix, R. J. *Surface Sci.*, **1981**, *109*, 221.
28. Kuhn, W. K.; He, J.-W.; Goodman, D. W., to be published.

Chapter 6

Nickel Monoxide Surface Films on Ni(100)

High-Temperature Structure, Thermal Stability, and Reactivity Toward Hydrogen

R. B. Hall[1], C. A. Mims[2], J. H. Hardenbergh[1], and J. G. Chen[1]

[1]Exxon Research and Engineering Company, Annandale, NJ 08801
[2]Department of Chemical Engineering, University of Toronto, Toronto, Ontario M5S 1A4, Canada

The formation, thermal stability and reactivity of NiO surface films on Ni(100) have been studied in the temperature range of 300 to 900 K. The well known, 2-3 monolayer surface oxide film formed at 300 K undergoes a phase transformation at 525 K, disproportionating into small, crystalline clusters of NiO(100) and large regions of c(2x2)-O on Ni(100). Based on electron scattering model simulations of XPS data, the NiO(100) clusters are estimated to be roughly 50 Å thick, and to occupy approximately 6% of the surface. The method of fluorescence yield near-edge X-ray absorption spectroscopy (FYNES) was used to characterize the subsurface oxygen, before and after this phase transformation. The FYNES results show that there is no loss of oxygen due to bulk diffusion. The NiO(100) clusters are thermally stable to above 800 K.

Only the c(2x2)-O regions of the annealed surface are oxidized by subsequent exposure to oxygen at 300 K. No preference for oxidation at the NiO(100) island edges is observed. Upon annealing, the newly oxidized c(2x2) regions disproportionate in the same way as the original oxide film. By repeated cycles of oxidizing at 300 K and annealing to 800 K, a stable NiO(100) film, roughly 50 Å thick, can be produced. The reactivity of the surface toward hydrogen as a function of the number of oxidation/anneal cycles was investigated using time-resolved XPS and time-resolved FYNES. Both methods indicate that the rate of oxygen removal from these clusters is roughly zero order in oxygen content, and that subsurface oxygen is removed completely. This supports the conclusion that the clusters are solid or continuous and that no oxygen is lost to the bulk.

1. Introduction

The oxidation of Ni(100) surfaces has been the subject of many experimental and theoretical efforts [1-9]. One reason for this is that the O/Ni(100) system has been considered a "prototype" for the oxidation of metal surfaces in general. Additional interest originates from the technological importance of various Ni and NiO-related

compounds in catalysis, such as in steam reforming [10] and oxidative coupling of methane [11, 12]. At temperatures below 450 K, the oxygen-Ni(100) interaction can bedescribed within the framework of a 3-stage oxidation model proposed by Holloway [4]: (1) At low coverages, oxygen chemisorbs dissociatively, with the oxygen atoms bonded to four-fold hollow sites [13-20], sitting at ~ 0.9 Å above the Ni(100) plane [13, 15, 16, 18, 21-25]. Above 250 K, chemisorbed oxygen progresses through a p(2x2)-O, to a c(2x2)-O overlayer structure, at 0.25 and 0.5 monolayers (ML) respectively [1, 26-28]. (2) NiO islands start to grow on the Ni(100) surface at a local oxygen coverage above 0.5 ML and these NiO islands expand laterally at continued oxygen exposure until two to three layers of NiO are completed [3, 4, 24, 26, 29, 30, 31]. Significantly, the surface oxide does not exhibit the (100) orientation of the substrate. The NiO surface grown at or below 300 K has been shown to be NiO(111) [1, 26, 27], while the oxide grown between 300-400 K has a more complex (7x7) LEED pattern [1, 32]. (3) The NiO layers can be thickened (growth of NiO into the Ni bulk) at higher oxygen exposures, although this diffusion-controlled process [9] has been found to be extremely slow experimentally [4, 29].

    Although the initial oxygen chemisorption on and the subsequent oxidation of Ni(100) have been extensively investigated in the temperature range of 80-450 K, the thermal behavior and stability of the NiO species at higher temperatures have been rarely addressed in the literature. The few investigations that were carried out above 450 K have indicated that the NiO/Ni(100) layers prepared at 300 K are thermally unstable above roughly 500 K. The dissolution of oxygen into the bulk Ni(100) at 527 K was briefly mentioned by Holloway [4]. Thiel and coworkers [1] in their detailed video-LEED studies found that in the range 500-550 K part of the NiO(111) film converts back to metallic nickel, covered with a chemisorbed c(2x2)-O layer, and part converts to NiO(100) clusters. Using RHEED, Mitchell et al. [26] observed that the diffraction pattern from NiO(111) disappears around 600-625 K, with a concomitant intensification of a NiO(100) pattern. Using XPS, Norton et al. [3] found that by heating the NiO formed on a Ni(110) surface to 600 K in vacuum for 300 s, the XPS O 1s intensity decreased by a factor of 90%. The apparent decrease in oxygen surface coverage upon heating was attributed to diffusion of oxygen (and/or Ni) along the <110> direction.

    In this paper, we report a detailed investigation of the thermal stability of surface oxides on a Ni(100) substrate in the temperature range of 500-800 K. We observe at 525 K a disproportionation of the NiO(111) surface oxide into NiO(100) clusters and a c(2x2)-O covered Ni(100) surface. A simple electron-scattering calculation simulating the XPS results indicates that the NiO(100) clusters are roughly 50 Å thick. Subsurface oxygen is investigated by fluorescence-yield near-edge X-ray absorption spectroscopy (FYNES). We find, contrary to earlier reports based solely on XPS [3, 4], that there is little or no diffusion of oxygen into the bulk, but rather that all of the oxygen is contained in the NiO(100) clusters. We find that a finite thickness NiO(100) film can grown by repeated oxidation at 300 K of the c(2x2)-O regions produced upon annealing the surface. This film is stable to significantly higher temperatures than the original oxide, enabling us to investigate the reactivity of the composite surface in the temperature range of 600-800 K. This is a temperature range more characteristic of catalytic process involving NiO. We find the mechanism and kinetics of the reaction of these surfaces with hydrogen are different than that of the lower temperature, NiO(111) surface.

2. Experimental Methods

The results reported here were obtained in two separate ultrahigh vacuum (UHV) chambers. The near-edge X-ray absorption experiments were performed at the U1 beam line of the National Synchrotron Light Source, Brookhaven NationalLaboratory. Details concerning the optics on the beam line and the

fluorescence yield detector have been described previously [33, 34]. The fluorescence yield near-edge spectra in the present study were recorded near the oxygen K-edge with the incident photon energy in the range of 510-585 eV. The oxygen K-edge fluorescence yield was measured by using a differentially pumped, UHV-compatible proportional counter filled with 200 torr of P-10 (10% methane, 90% argon) as the counter gas, as described previously [34]. In brief, the oxygen K-edge photons from the sample were collected by the proportional counter at a fixed solid angle and were subsequently absorbed by the counter gas, which in turn created electron-ion pairs in the proportional counter. These electrons were accelerated by a high electric field of the proportional counter anode and the electron charge was multiplied as a consequence of impact ionization gas multiplication in the counter gas. The resulting pulse of electron charge was then collected at the anode and amplified by a charge-sensitive amplifier [34].

The XPS experiments were performed in a separate Leybold-Heraeus XPS system equipped with a model EA-10 hemispherical analyzer for XPS, UPS and ISS analysis, a mass spectrometer for thermal desorption measurements and a Varian LEED system. The UHV chamber was pumped by a combination of turbomolecular and liquid nitrogen cooled titanium sublimation pumps. The background pressure was typically below 2×10^{-10} torr. The XPS results reported here were obtained using a 360 watt Al Kα (1486.6 eV) X-ray source, and an analyzer pass energy of 100 eV. Analyzer operation and data acquisition was controlled by an IBM PC system using software developed by one of the authors (JHH).

In both chambers, the synthesis of the NiO films was carried out by exposing the Ni(100) substrate at 300 K to O_2. The synthesis procedures and information on the structure of the resulting oxide films have been reported previously [1-5, 29].

The rate of reaction of the films was measured by monitoring, in real-time, the decrease in the O(1s) XPS signal, or in the FYNES signal at 541.0 eV, during exposure of the film to hydrogen. The background pressure of reactant gas ranged from 1×10^{-8} to 5×10^{-5} torr in the XPS experiments, and from 1×10^{-8} to 1×10^{-2} torr in the FYNES experiments. The kinetics of reaction were investigated as a function of the surface temperature over the range from 600 to 800 K. The temperature of the reactant gas remained at ambient temperature for all of the experiments reported here.

The Ni(100) single crystals were cut and mechanically polished using standard methods. The crystals were initially cleaned by repeated cycles of sputtering with Ar+ ions at 300 K and annealing at 1000-1100 K. The residual carbon species was removed by oxygen treatment at 800 K. The cleanliness of the surface prior to experiments was checked by either XPS or AES. Thermal desorption of CO, which has been demonstrated to be a sensitive method for the detection of small amount of impurities on the Ni(100) surface [35], was also performed prior to the experiments to assure the cleanliness of the surface. Research-grade oxygen (99.99% purity) was introduced into the UHV chambers through leak-valves and the oxygen pressure was monitored by uncorrected ion gauges.

3. Results

3.1 XPS measurement of clean Ni(100) oxidation.

In figure 1, we illustrate the oxygen uptake by the surface at 300 K during exposure to gaseous O_2. The oxygen content in the surface region is monitored by the area under the O(1s) XPS feature, normalized to the area of the Ni(2p) feature. Our results are in good agreement with prior studies [1, 24, 27, 29]. In brief, the oxidation of Ni(100) at 300 K occurs via a chemisorption stage at oxygen coverages less than or equal to 0.5 ML (monolayer), followed by the formation of NiO at higher oxygen coverages. There is

rapid uptake of oxygen up to the point at which a p(2x2) ordered overlayer is observed in LEED. This corresponds to 0.25 monolayer of O atoms. The reactive sticking probability declines rapidly upon reaching this coverage, and addition of sufficient oxygen to form the c(2x2) ordered overlayer (0.5 ML) requires substantially higher doses. The slower growth of the c(2x2) overlayer is shown in the inset in figure 1. Finally, at coverages exceeding 0.5 ML, there is an increase in the rate of oxygen uptake as NiO islands begin to form. As shown in the inset of figure 1, this occurs at a dose of roughly 40 L. The film exhibits a diffuse LEED pattern, containing both NiO(111) and Ni(100) spot patterns, similar to that reported by others [1,26,27].

The oxygen content in the saturated (at ~ 300 L) NiO film is estimated to be equivalent to either 4 ML of NiO(100) or 3 ML of NiO(111). This estimate is based on an experimental calibration of our XPS system for several known overlayer structures, and a calculation of the inelastic electron scattering of the XPS signal from subsurface levels, for (100) or (111) oxide structures. The adsorbate overlayers used to calibrate the XPS system were: a saturated CO overlayer (0.67 ML), O/Ni=0.065, a c(2x2)-O overlayer (0.5 ML), O/Ni=0.044, and a p(2x2)-O overlayer (0.25 ML), O/Ni=0.024. (These ratios are corrected for the relative excitation cross sections of O and Ni as given by Scofield [36], but not for the dependence of the electron energy analyzer on kinetic energy.) A scattering model calculation of electron escape probability from subsurface layers was performed for specified compositions for each layer, using scattering cross sections for each component atom derived from electron mean free paths as obtained from Penn's coefficients [37]. The scattering cross sections used were: Ni = 0.99 $Å^2$ at 952 eV (the kinetic energy of O(1s) electrons) and 1.33 $Å^2$ at 630 eV (the kinetic energy of Ni($2p_{3/2}$) electrons), Oxygen = 0.66 $Å^2$ at 932 eV, and 0.89 $Å^2$ at 630 eV. These cross sections are equivalent to the following electron mean free paths: λ (Ni($2p_{3/2}$) through Ni) = 8.3 Å, λ (O(1s) through Ni) = 11.0 Å, λ(Ni($2p_{3/2}$) through NiO) = 9.4 Å, (O(1s) through NiO) = 12.4 Å. Using this scattering model, the oxygen and nickel XPS signals as a function of oxide layer thickness and composition could be simulated. The oxygen content in the saturated oxide film estimated above is 25% to 50% higher than estimated in some earlier works [3,29], and 30% lower than estimated in others [32]. The uncertainty in the absolute oxygen content in the oxide film is considered to be small; it does not significantly effect the conclusions drawn in this work.

3.2 Thermal stability of initial oxide film.

The thermal stability of the oxide film was investigated using XPS, FYNES, LEED, and HREELS. The temperature dependence of the XPS O (1s)/Ni ($2p_{3/2}$) ratio is shown in figure 2. Although the data in Figure 2 were obtained at the indicated temperature, similar results were obtained if the spectra were taken at 300 K. The thermally-induced changes in the XPS spectra can be divided into three temperature ranges: (1) in the range from 300-525 K, the O 1s/Ni $2p_{3/2}$ ratio remains fairly constant; (2) starting at 525 K, the ratio decrease rapidly to about 1/3 of its initial value; and (3) between 750 and 900 K, the O 1s/Ni $2p_{3/2}$ ratio is relatively stable. At 800 K, less than a 10% decrease in the O 1s/Ni $2p_{3/2}$ ratio was observed over a period of 60 minutes.

The effect of annealing on the individual oxygen and nickel XPS features is illustrated in figure 3. Curve a is the initial spectrum of the clean Ni(100) surface. Curve b is the spectrum at 300 K after a dose of 400 langmuirs (L) at the same temperature. There is a decrease in the shake-up peaks in the Ni region and a broadening to higher binding energies. A single oxygen feature is observed at the same binding energy of 529.3 eV as is observed for chemisorbed oxygen. Curve c is
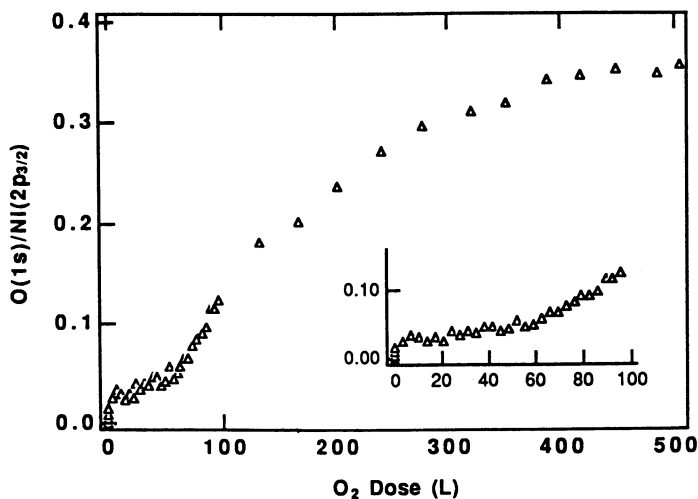
Figure 1: The intensity ratio of the O(1s) XPS signal to the intensity of the Ni(2p$_{3/2}$) signal from a Ni(100) surface, as a function of the exposure to O$_2$. The temperature of the surface is 300 K. The inset shows the same data at an expanded scale to provide more detail in the region approaching the critical oxygen coverage needed for the formation of the initial oxide.
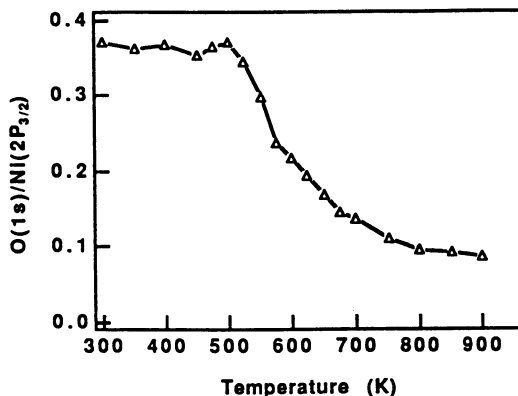
Figure 2: The ratio of the area of the O(1s) XPS signal to the area of the Ni(2p$_{3/2}$) signal from the oxidized surface from figure 1, as a function of annealing temperature. The surface was annealed at each temperature for 2 minutes, the spectra are taken at or below 400 K.

the spectrum observed after annealing to 800 K for less than 1 minute and recooling the surface to 300 K. There is an increase in the Ni intensity and in the metallic character of that line. In addition, there is a decrease of roughly a factor of 3 in the oxygen intensity, and a shift in the line center to 528.9 eV.

The thermally induced change in the oxide film was also investigated using LEED and high resolution electron energy loss spectroscopy (HREELS) [38]. Annealing the surface briefly to 800 K results in a transformation of the diffuse oxide NiO(111) and substrate Ni(100) LEED patterns into a c(2x2)-O pattern, and sharp NiO(100) and Ni(100) patterns. The NiO(100) pattern is easily distinguished from the substrate Ni(100) pattern because the lattice constant is about 15% smaller.   The c(2x2)-O LEED pattern suggests that a significant fraction of the surface is converted to regions resembling chemisorbed oxygen on Ni. This is consistent the increase in the intensity and metallic character of the Ni $(2p_{3/2})$ signal. The reduction in the O (1s) intensity is due to the formation of regions of NiO(100) that are sufficiently thick that the net escape probability of O (1s) electrons is reduced. This is described more quantitatively below.

A disproportionation of the initial oxide film is also suggested by results obtained using high-resolution electron energy loss spectroscopy (HREELS). These results are reported in more detail elsewhere [38], but can be summarized briefly as follows. After exposing a clean Ni(100) surface to 300 L of O_2 at 300 K, the HREELS spectrum is dominated by a broad feature at 515 cm^{-1}, with a shoulder at ~445 cm^{-1}. This broad feature has been previously assigned as the ν(Ni-O) mode of nickel oxide on Ni(100)[13]. (The structure of the oxide in the earlier study was not determined, but it was likely to have been same 2-3 layer NiO(111) film observed in the present work as the synthesis procedures are similar.) Upon heating to 800 K, we observe the following changes in the EELS spectra. The ν(Ni-O) feature narrows substantially and shifts upward in frequency to 565 cm^{-1}. This is accompanied by the appearance of an overtone and/or double loss of the ν(Ni-O) mode at 1135 cm^{-1}. Multiple loss features are characteristic of bulk oxide phonon modes [6,39], and these results suggest that the NiO(100) islands formed upon annealing are larger, more bulk-like than the initial surface oxide. This is consistent with the appearance of the sharp NiO(100) LEED pattern. A vibrational feature at 330 cm^{-1} is also observed after annealing.   This corresponds to the ν(Ni-O) vibrational frequencies for c(2x2)-O/Ni(100), observed by us [38] and others [13,14,40] at 325 cm^{-1}, in agreement with the observation of a c(2x2) pattern in LEED.

3.3   Oxygen uptake by the annealed surface

If regions of c(2x2) O on Ni(100) are created upon annealing, it should be possible to oxidize these regions to the same ~ 3 ML film produced on the clean surface. This is indeed the case. In figure 4, we plot the increase in the O(1s) XPS signal that results from a number of oxidation/anneal cycles. For each cycle, the surface at 300 K is oxidized to saturation, and then briefly annealed to 800 K. In each case, the oxygen dose is 350 L. The solid symbols indicate the XPS intensity before annealing, the open symbols after annealing. All spectra are taken at surface temperatures below 400 K.   It can be seen that a significant amount of additional oxygen is taken up by the annealed surface. For example, the incremental amount taken up in the second cycle is about 95% of that taken up by the clean surface. Upon annealing, the oxygen signal of the 2nd cycle surface decreases, but to a level that is higher than that of the annealed 1st cycle surface.   The incremental amount of oxygen taken up by the annealed surface decreases with each subsequent cycle.
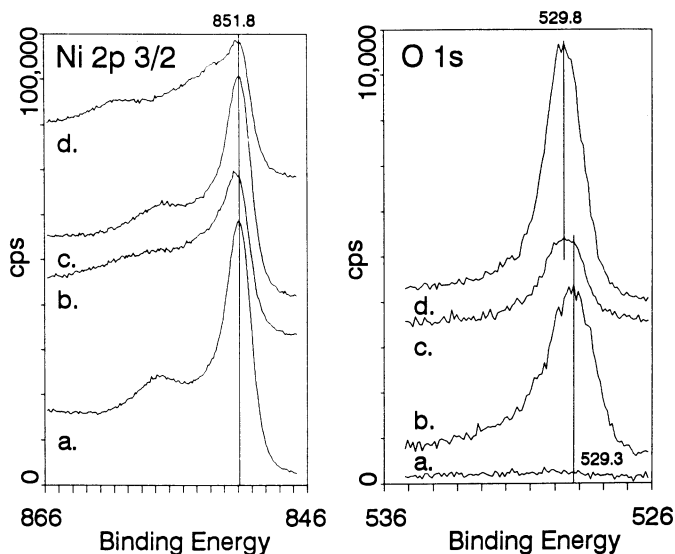
Figure 3.   XPS spectra of the O(1s) and Ni(2p$_{3/2}$) regions, from a Ni(100) surface at various stages during sequential oxidation and anneal cycles. Curve a), clean surface; curve b), after exposure to 400 L O$_2$; curve c), after annealing to 800 K for 1 minute; curve d), after 10 oxidation/anneal cycles equivalent to b) and c). All spectra are taken at or below 200 K.
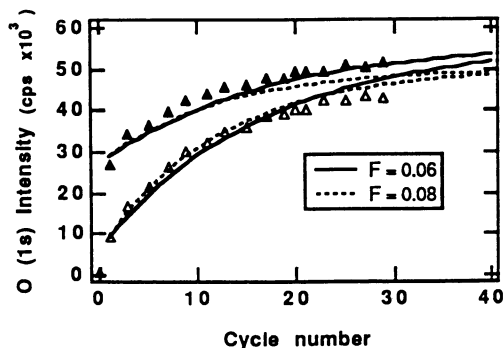
Figure 4.   Increase in the O(1s) XPS intensity from the Ni(100) surface, as a function of the number of oxidation/anneal cycles. Each cycle consisted of a 400 L exposure of the surface at 300 K, an XPS spectrum, an anneal to 800 K for 1 minute, and another XPS spectrum. All spectra were taken at or below 200 K. The solid symbols are for the unannealed surface, the open symbols for the annealed surface. The solid and dotted lines are fits to these data using a model described in the text. The solid line is for disproportionation in which 0.06 of the surface is occupied by NiO(100) clusters after each annealling, the dotted line is for 0.08 of the surface. (see text).

As will be discussed below, only the c(2x2) regions of the annealed surface are oxidized; the NiO(100) clusters once formed are not affected by subsequent exposure to oxygen. It is possible to derive from the data in figure 4 the average domain size of the c(2x2)-O regions and of the NiO(100) clusters at each cycle. This is done by calculating the XPS signals from each domain, including attenuation of subsurface layers, and fitting the data to a weighted sum of the contributions from each domain, making some assumptions about the shape of the domains. The solid lines in figure 4 are calculated for a disproportionation, on each cycle, of the NiO(111)-like regions of the composite oxide surface into NiO(100) domains that occupy a fraction F of the surface, with c(2x2)-O regions occupying 1-F. The diameter of the NiO(100) clusters for F=0.06 is roughly 50 Å. The calculation, and the assumptions that go into it, are described in more detail in the discussion section.

In figure 5, we show, for several oxidation/anneal cycles, the dependence of the surface O(1s) XPS intensity on exposure to O_2. It can be seen that the O(1s) intensity at the beginning of the second cycle is roughly 1/3 that of the asymptotic O(1s) intensity of the first cycle, and that the asymptotic intensity for the second cycle is slightly higher than that of the first cycle. Qualitatively, this behavior is repeated in subsequent cycles. It is interesting to note that each of the oxidation steps exhibits initially a period of relatively slow increase in oxygen content. This is a consequence of the slow approach to the critical oxygen content required for oxide formation over the c(2x2) portion of the surface. The existence of this induction for cycles beyond the first indicates that there is no preferential oxidation at the edges of the NiO(100) clusters in the surface. Note also that there is a decrease in the length of the induction period with cycle number. This reflects the decreasing fraction of the surface covered by chemisorbed oxygen and the increasing fraction covered by NiO(100).

3.4 Reduction of the annealed oxide surface by hydrogen.

The kinetics of reaction of the annealed oxide surfaces with hydrogen have been investigated with time-resolved XPS spectroscopy. In these experiments, the oxide surface at a high temperature is exposed to ambient temperature hydrogen gas. The O(1s) XPS intensity is used to monitor the removal of oxygen from the surface, presumably as water. The decrease in time of the O(1s) intensity at several surface temperatures and a background pressure of hydrogen of 5 x 10^{-7} torr is shown in figure 6. In the absence of hydrogen, the oxide surface is stable at 800 K for a time at least a factor of 10 longer than the reaction times investigated here (see figure 6). Upon exposure to hydrogen, the removal of oxygen from the annealed surface begins immediately, for reaction temperatures in the range of 650 to 850 K. We do not observe the induction period reported previously for unannealed surfaces at temperatures from 430 to 500 K [27, 28, 41]. To the contrary, we find that the rate of oxygen removal is independent of the amount of oxygen in the oxide film, until it drops below the c(2x2) level. In figure 6, the relative O(1s) intensity that corresponds to a c(2x2) coverage is 0.4. The curvature exhibited in figure 6 at relative intensities above 0.4 is a consequence of inelastic scattering of O(1s) electrons originating from subsurface layers. This is confirmed both by modeling and by the FYNES results discussed below.

The NiO(100) clusters appear to react preferentially. The NiO(100) LEED pattern and ν(Ni-O) HREELS vibrational band can be removed completely, leaving only the features characteristic of a c(2x2) chemisorbed overlayer [38]. With further exposure to hydrogen, the c(2x2) layer can be reacted away. As Ni metal sites become exposed at the surface, the rate of oxygen removal accelerates [27, 28]. We tested for the existence of Ni metal at the surface at various times during the reduction of the oxide using temperature programmed desorption (TPD) of H_2. Molecular hydrogen only
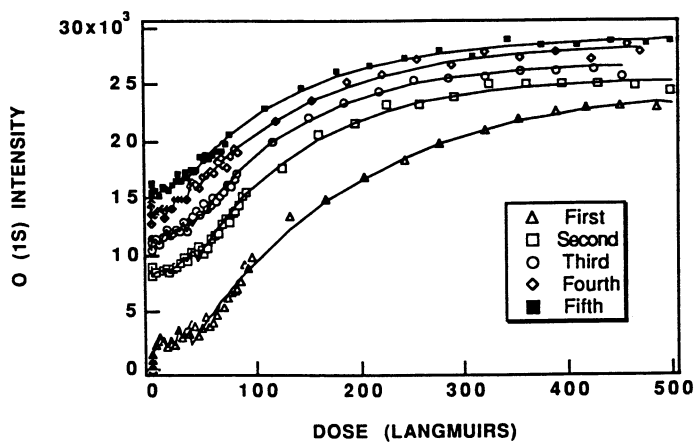
Figure 5.   The increase in the O(1s) XPS intensity from the Ni(100) surface, as a function of exposure to O_2, for several sequential oxidation/anneal cycles.
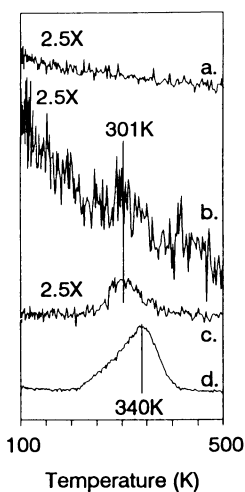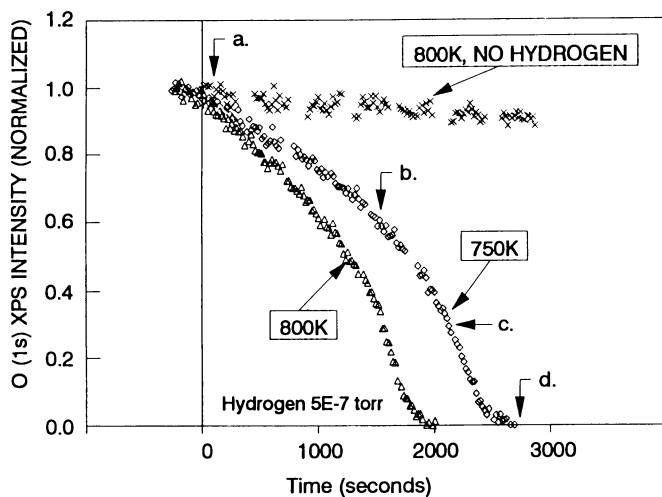
Figure 6. Top: O(1s) XPS intensity as a function of time during exposure to hydrogen of a composite oxide surface from a single oxidation/anneal cycle. The hydrogen pressure is 5×10^{-7} torr. The time dependence for reaction at surface temperatures of 800 K (triangles) and 750 K (diamonds) is shown. Also shown ($\times$) is the time dependence of the O(1s) intensity at 800 K in vacuum ($<2 \times 10^{-10}$ torr).

Bottom: H_2 TPD spectra from the composite oxide surface at various stages during the course of reaction. For each curve, the reaction was arrested by rapidly cooling the surface to 180 K while maintaining the background pressure of H_2 at 5×10^{-7} torr. The total exposure during cooling was roughly 500 L. The hydrogen pressure was then reduced to below 1×10^{-9} torr, and the surface heated back to reaction temperature (750 K) at 5 K/s. The desorption of molecular hydrogen was monitored at 2 AMU.

weakly adsorbs to the oxide surface, but if Ni metal is present on the surface, we expect to see a desorption feature between 300 and 340 K. Furthermore, the area of the H_2 TPD peak provides a measure of the total surface area of the metal. The results of these tests are shown in the right hand panel of figure 6. In these experiments, the reduction of the surface is arrested by cooling the surface to 200 K at various times indicated by (a) to (d) in the left hand panel of figure 6. The surface receives a several hundred L exposure of H_2 during the cool down. The surface is then heated at 5 K/s and the H_2 desorption is monitored by a quadrupole mass spectrometer. It can be seen in figure 6, that the annealed surface, prior to reduction (time (a)), exhibits no H_2 desorption peak. After more than half of the oxygen has been removed (time (b)), there is possibly a small peak at 300 K. The peak is questionable given the signal/noise ratio of the spectrum. Based on this spectrum, the limit on the fractional coverage of metal at the surface is 0.02±.02. This is not enough to significantly affect the rate of reduction. At time (c), the oxygen content of the surface is slightly below that required to maintain a c(2x2)-O coverage, and there is a significant H_2 desorption feature. The area under this feature indicates that the fractional coverage of metal at the surface is 0.15±.02. At this stage, the rate of removal of the remaining oxygen is increased; presumably because the probability for dissociative adsorption of H_2 on the metallic regions is increased dramatically relative to that on the oxygen covered regions. Finally, after complete reduction (time (d)), the TPD spectrum resembles that of a saturated hydrogen layer on a clean Ni(100) surface.

3.5 Characterization of subsurface oxygen by FYNES

The thermally induced disproportionation of the initial oxide film drives a significant fraction of the oxygen to subsurface layers where they cannot be detected using XPS. We have investigated the subsurface oxygen using FYNES. This technique is similar to other x-ray near edge structure spectroscopies except that it detects the fluorescence photon yield [34, 42] instead of the conventional electron yield [33]. The large escape depth of the energetic photons, which is at least 1000 Å near the oxygen K-edge, allows us to detect oxygen species up to several thousand angstroms below the surface.

In figure 7, we show the FYNES spectrum for the oxide film formed by exposing the clean Ni(100) surface at 300 K to 300 L O_2 (solid line). Also shown is the spectrum for the same surface annealed to 800 K (dotted-line). Several O K-edge features are observed in both spectra, including a fairly sharp feature at 533 eV and a relatively strong feature at 541 eV. The peak positions of these two features are very similar to those reported previously for thick nickel oxide (NiO) using either electron energy loss spectroscopy [43, 44] or near-edge X-ray absorption spectroscopy by means of measuring the low-energy electron yield [45].

The assignment of the O K-edge features of the 3d-transition metal oxides has been discussed previously by Grunes et al. [43]. By using a symmetry-determined molecular-orbital model, various O K-edge features can be related to the creation of oxygen core holes via electronic transitions to the partially-filled or unfilled molecular orbitals of metal oxides. The 533 and 541 eV O K-edge features can be related to the electronic transitions to the $3e_g$ (Ni 3d + O 2pσ) and $3a_{1g}$ (Ni 4s + O 2pσ) orbitals of NiO, respectively. The atomic orbitals given in parentheses are those contributing dominantly to the corresponding molecular orbitals. It should be pointed out that the above assignment involves an assumption that the NiO clusters formed on Ni(100) possesses an octahedral symmetry. This assumption is supported by previous results indicating the formation of face-centered cubic bulk NiO at oxygen exposures above 160 L [46], and by the similarity of the spectra in figure 7 to that observed for bulk NiO [45].
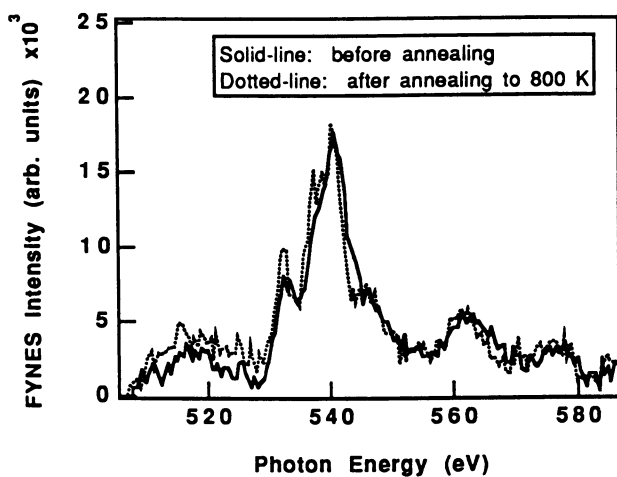
Figure 7.   FYNES intensity as a function of x-ray photon energy above the oxygen-edge. The solid line is from a Ni(100) surface exposed to 350 L of O_2 at 300 K.   The dotted line is from the same surface, after annealing to 800 K. Both spectra are taken with the surface at 300 K.

It is evident from figure 7 that there is no significant decrease in FYNES intensity on annealing. Furthermore, the spectrum is not changed appreciably, although there is a slight narrowing of the lines, suggesting that the (100) oxide clusters are more uniform or ordered than the initial film. These results indicate that all of the oxygen remains in the near surface region, and that it retains the spectrum characteristic of bulk oxide.

The FYNES spectra for a range of oxidation/anneal cycles is shown in figure 8a. With each cycle, there is a monotonic increase in the intensity of each of the spectral features. The increase in the area under the feature at 541 eV is plotted in figure 8b. The solid line in figure 8b is the increase in total oxide content predicted if the fraction of the surface that can take up additional oxygen is reduced by 6% on each cycle. This is the same percentage obtained from the XPS results. The agreement strongly supports the postulated morphology of the clusters and c(2x2) regions induced by annealing.

3.6   FYNES Measurement of Kinetics of Reaction with H_2

In figure 9, we show, as a function of time, the reduction in the FYNES intensity of the oxygen near-edge feature at 541 eV, resulting from the reaction of H_2 with an oxide surface produced by 6 oxidation/anneal cycles. Two features are immediately apparent. The first is that the time rate of change of the FYNES intensity is constant. This indicates that the reaction rate is independent of the oxygen content in the film. Note that the curvature observed in XPS measurement of the reaction is absent. This corroborates the electron-scattering model calculation that the curvature in the XPS signal at early times is associated with the signal contributed by O(1S) electrons from subsurface layers. Since the escape depth of the fluorescence photons exceeds the thickness of the oxide film, no correction of the FYNES data for escape probability is necessary. The second important feature is that the reaction proceeds to completion. All of the subsurface oxygen detected by FYNES is removed, and it is removed at a fixed rate. This is compelling evidence that the NiO(100) clusters produced by annealing are continuous particles. It argues strongly against the possibility that oxygen is distributed into the bulk by diffusion.

4.   Discussion

The structure and reactivity of the of the surface oxides formed by exposing Ni(100) at 300 K to O_2 have been well characterized in earlier studies [1-7]. In the present study, we have focussed on the structure and reactivity of higher temperature forms of the oxide. The low temperature form, whether it exhibits a NiO(111) or a 7x7 LEED pattern [1, 27, 32], is not the thermodynamically most stable form of surface oxide. At temperatures above 525 K, there is a phase separation of the low temperature surface oxide into clusters of NiO(100) and regions of c(2x2)-O on Ni(100). The phase separated surface is thermally stable to about 900 K, in vacuum. First, we will discuss implications of our results concerning the morphology of the NiO(100) clusters. We follow this with a discussion of the high temperature reaction of these clusters with hydrogen, which exhibits qualitatively different kinetics than that observed at lower temperatures .

As the temperature of the initial oxide film in increased above 525 K, there is a decrease in intensity of the O(1s) XPS signal, and an increase in intensity of Ni(2p3/2), as illustrated in figures 2 and 3. These changes are due to migration of near-surface oxygen to deeper layers. It is not, however, the result of simple diffusion of oxygen into the bulk, as suggested earlier [4, 9, 29]. Instead, stable NiO(100) clusters of a critical size are formed. Qualitatively, the most persuasive evidence for this comes
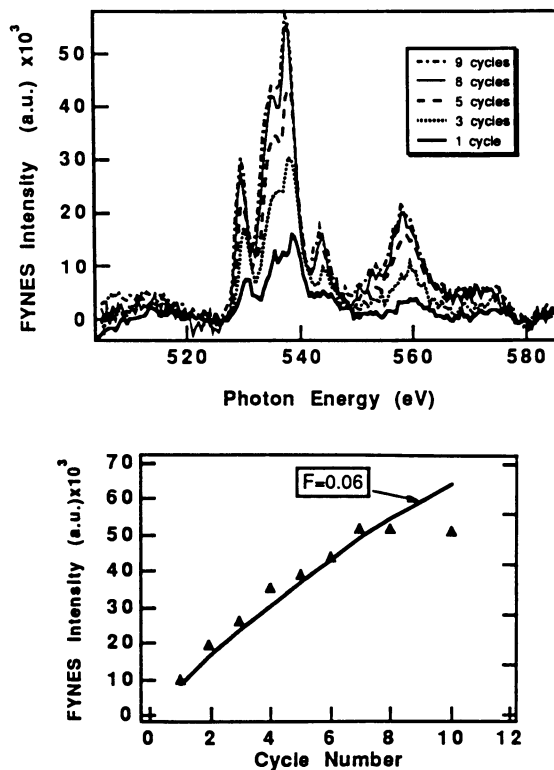
Figure 8. Top: FYNES intensity as a function of x-ray photon energy above the oxygen-edge for the indicated number of oxidation/anneal cycles. The procedure for each cycle is the same as that indicated for Figure 4. All spectra are taken at 300 K.

Bottom: Total FYNES intensity at 541 eV as a function of the number of oxidation/anneal cycles. The solid line is the increase expected in the total oxygen content of the surface oxide if 0.06 of the surface is converted to NiO(100) clusters for each annealing (*see* text).
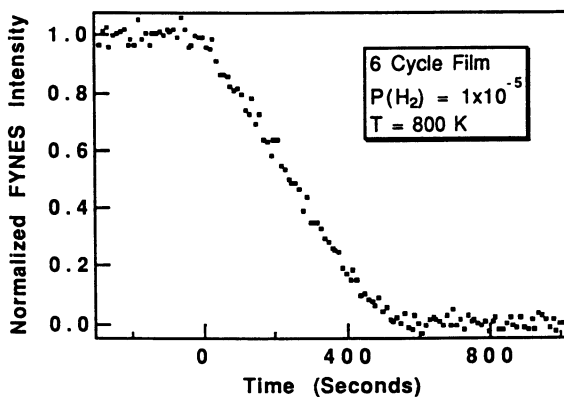
Figure 9.   FYNES intensity at 541 eV, as a function of time, during exposure to hydrogen of a composite oxide surface from 6 oxidation/anneal cycles. The hydrogen pressure is 1x10⁻⁵ torr. The surface temperature is 800 K.

from the FYNES results shown in figures 7 and 9. No decrease is observed in the intensity of the FYNES oxygen edge spectrum upon heating the surface above the phase separation temperature (figure 7), and in reaction with hydrogen, <u>all</u> of the oxygen reacts at a rate independent of the instantaneous oxygen content of the oxide. A more detailed analysis of the XPS and FYNES results provides more quantitative information on the morphology of these particles.

Because the escape depth of electrons measured in the XPS experiments is comparable to or smaller than the thickness of the surface oxide, it is necessary to model the scattering in order to interpret the XPS intensity quantitatively. A scattering calculation was performed of electron escape probability as a function of thickness for NiO(100) and NiO(111) overlayers on a Ni(100) substrate. In this calculation, the escape probability for electrons from each component in each layer is calculated, using scattering cross sections for O and Ni atoms in higher layers derived from electron mean free paths for the appropriate material (NiO or Ni) as obtained from Penn's coefficients [37]. The scattering cross sections used were: Ni = 0.99 $Å^2$ at 952 eV (the kinetic energy of O(1s) electrons) and 1.33 $Å^2$ at 630 eV (the kinetic energy of Ni(2p$_{3/2}$) electrons), Oxygen = 0.66 $Å^2$ at 932 eV, and 0.89 $Å^2$ at 630 eV. These cross sections are equivalent to the following electron mean free paths: λ (Ni(2p$_{3/2}$) through Ni) = 8.3 Å, λ (O(1s) through Ni) = 11. Å, λ (Ni(2p$_{3/2}$) through NiO) = 9.4 Å, (O(1s) through NiO) = 12.4 Å. From this, O and Ni XPS signals can be simulated by taking the product of the composition in each layer times its escape probability, and summing over a sufficient number of layers. We found that for the escape depths used here, summing over 50 layers gives results within 0.1% of those for an infinitely thick slab.

Consider initially two aspects of the XPS results, first, the decrease in O(1s) intensity upon heating, and second, the decreased amount of oxygen that can subsequently be taken up by the annealed surface. These are illustrated in figures 2 and 3, for the first oxidation/anneal cycle, and in figure 4, for 30 oxidation/anneal cycles. To first order, the decrease in the O(1s) intensity (or in the O/Ni ratio) provides information on the thickness of the oxide particles. The decrease in the amount of oxygen taken up by the annealed surface provides information on the average area of the particle at the surface. The latter is true only if the regions of the surface occupied by NiO(100) oxide particles do not take up additional oxygen. This can be seen qualitatively in the data in figure 5. Each of the oxidation cycles exhibits an initial period of relatively slow increase in oxygen content. This is a consequence of the slow approach to the critical oxygen content required for oxide formation over the c(2x2) portion of the surface. The existence of this induction for cycles beyond the first indicates that there is no preferential oxidation at the edges of the NiO(100) clusters in the surface. Note also that there is a decrease in the length of the induction period with the number of cycles. This reflects the decreasing fraction of the surface covered by chemisorbed oxygen and the increasing fraction covered by NiO(100). There is not sufficient accuracy in these data to analyze the decrease in the induction period quantitatively, but the roughly 20% decrease over the 5 cycles shown in figure 5 is consistent with the analysis discussed below.

The following assumptions are made in modelling the XPS results shown in figure 4. First, oxygen is conserved in the phase transformation, i.e. no oxygen is lost to the deep bulk by diffusion. This is supported by the FYNES results mentioned above. Second, only the c(2x2)-O regions of the annealed surface can be oxidized at 300 K, and the asymptotic thickness of the oxide formed in these regions is the same as that observed for the clean surface. Finally, we assume that the XPS signal for the composite surface, consisting of NiO(100) clusters separated by c(2x2)-O/Ni(100), is given by the area weighted sum of the individual component intensities from electron

escape probability calculations for uniform NiO(100)/Ni(100) and for c(2x2)-O/Ni(100). That is, for example:

$$O(1s, composite) = (F) * O_{NiO(100)/Ni(100)} + (1-F) * O_{c(2x2)-O/Ni(100)} \qquad (1)$$

where, F is the average fraction of the surface occupied by the NiO(100) particles, $O_{NiO(100)/Ni(100)}$ is the O(1s) XPS intensity calculated for z layers of NiO(100) on a Ni(100) substrate, and $O_{c(2x2)-O/Ni(100)}$ is the O(1s) XPS intensity calculated for a c(2x2)-O adlayer on Ni(100).

The decrease in the amount of oxygen taken up by the annealed surface as a function of the number of oxidation/anneal cycles is obtained from the data in figure 4 by subtracting the oxygen signal of the annealed surface following the nth oxidation cycle/anneal cycle from the oxygen signal from the unannealed film of the subsequent (n+1) oxidation cycle. That the oxygen uptake decreases with the number of cycles can be seen from the convergence of the data from the annealed and unannealed surfaces. The first differences between these data can be well fitted to a function of the form, $I_0 (1-F)^{n-1}$, where, I_0 is the O(1s) intensity from the first cycle (oxidation of the clean surface), and n is the cycle number. The value of F obtained from this fitting is 0.06 ± 0.02. A plot of these results is not shown because it is equivalent to the fit of the simulated results (solid line in figure 4) to the convergence between the two sets of data.

The thickness of the NiO(100) regions can be obtained from the decrease in the O(1s) intensity with the first annealing. The thickness calculated for the first cycle is the same value derived from a similar calculation for all subsequent cycles. Given a value of 0.06 for the fraction of the surface occupied by NiO(100) after the first annealing, and that the oxygen content of the initial unannealed film is contained in the sum of the NiO(100) particles and the 0.94 of the surface covered by c(2x2)-O, the electron escape depth calculations indicate that the thickness of the oxide particles is 50 (- 10, +25) Å. Using this same thickness for particles produced in subsequent cycles. the solid line illustrated in figure 4 are obtained. Also shown in figure 4, is the increase in oxygen content calculated for F=0.08. For this latter value, the calculated thickness of the oxide particles changes only slightly, but the calculated lines converge too rapidly. For F=0.10, the simulated curve (not shown) is an unambiguously poor fit to the data. The same is true for F=0.04.

Confirmation of this growth pattern is obtained from the FYNES results. For FYNES, no correction for the escape probability of photons from subsurface layers is necessary. Although no information on the thickness or diameter of the NiO particles can be obtained from the FYNES data because the escape depth is greater than the oxide thickness, the increase in FYNES intensity provides a direct measure of the increase in the total oxygen content of the surface oxide for each oxidation/anneal cycle. The FYNES spectra for a series of oxidation/anneal cycles is shown in figure 8a. The increase in intensity under the feature at 541 eV is shown in figure 8b.

For the proposed oxidation process, a sequential oxidation of residual c(2x2) regions, the FYNES intensity, I(n), should increase with the number of oxidation/anneal cycles, n, as:

$$I(n) = I_0 + \left[(I_0 - I_{c(2x2)}) \cdot \sum_{i=2}^{n} (1-F)^{n-1} \right] , \qquad (2)$$

where I_0 is the FYNES intensity measured for the initial oxidation of the clean surface, and $I_{c(2x2)}$ is the FYNES intensity for a c(2x2) O adlayer (negligible for 541 eV excitation). We find that the increase in FYNES intensity can be adequately

reproduced by equation 2 for F=0.06±0.02. The solid line illustrated in figure 8b is for F=0.06. This is in excellent agreement with the value obtained from the analysis of the XPS results.

The morphology of the NiO(100) particles is not uniquely determined by the XPS and FYNES data. The average fraction of the surface covered by the particles after the first annealing may be 0.06, but this does not provide information on the number of particles, on the diameter of the average particle, or on the distribution of diameters. It is likely that the particle morphology is determined both by some critical size necessary for thermodynamic stability, and by the kinetics of particle formation. In regard to the thermodynamic stability, it is interesting to note that for Ni(111) substrates, although oxidation at 300 K leads to a NiO(111) oxide film, this film converts to a NiO(100) structure when heated above 625 K [26]. Similarly, if the oxidation is carried out at temperatures in excess of 470 K, NiO(100) is formed[47]. This is consistent with the fact that for the bulk oxide, NiO(100) is the most stable structure [8, 48]. Apparently, for the Ni(100) substrate used here, the 3-4 layer oxide initially formed is not thick enough to derive the full thermodynamic benefit of the (100) structure. Considerable thickening, for a fraction of the surface, occurs on heating. The remainder of the oxygen (roughly 1/2) returns to the less thermodynamically favored c(2x2) chemisorbed adlayer. With respect to the kinetics of forming the (100) clusters, it seems unlikely that clusters with very large aspect ratios would be formed. We cannot imagine a mechanism for the formation and stabilization of oxide "needles" that are stable against continued migration of oxygen into the bulk. It is conceivable that small aspect ratio clusters are formed, i.e. clusters with a diameter much larger than the thickness. The averagefractional area for the oxide of 0.06 may be a simple consequence of the oxygen content of the initial film. The current results also do not distinguish between an increase in diameter of existing oxide clusters, or an increase in the number of clusters, with subsequent oxidation/anneal cycles. There is weak evidence from the development of the multiple-loss HREELS features for the oxide that there is an increase in the long range order of the particles as the number of oxidation/anneal cycles increases [38]. We suspect, however, that for the initial few cycles at least, that the most likely morphology of these clusters is one in which, on average, the diameter of the cluster is similar to the thickness derived from the XPS results, ~ 50 Å. We emphasize that although this morphology is plausible, it is not yet supported by any direct measurements.

The results on the reaction of the NiO(100) clusters with hydrogen in the temperature range from 600 to 800 K are interesting and revealing. The FYNES data shown in figure 9, indicate that all of the subsurface oxygen is removed, and is removed at a fixed rate. This is compelling evidence that the NiO(100) clusters produced by annealing are continuous particles. It argues strongly against the possibility that oxygen is distributed into the bulk by diffusion. In addition, both the XPS and FYNES measurements of the kinetics of reduction of the NiO(100) clusters indicate that the kinetics are qualitatively different than that observed for reduction of the initial, lower-temperature oxide film.

The reaction with hydrogen of the initial oxide film on Ni(100), at temperatures between 450 and 500 K, has been studied previously [27, 28, 41]. The kinetics are characterized by an induction period, followed by an increase and then a decrease in the reaction rate. Similar results have been obtained by us. These kinetics have been interpreted as reaction at the edges of oxide islands. The induction period is related to the formation of gaps in the oxide film, exposing regions of metal that have a higher rate for the dissociative adsorption of H_2 than does the oxide. The increase and then decrease of the reaction rate following the induction period are interpreted as indicating that reaction occurs preferentially at the oxide/metal perimeter edges. During the course

of reaction, the oxide/metal perimeter increases to a maximum dimension as the metal area grows, and then decreases as the oxide particle diameters are reduced by reaction. None of these characteristics is observed for the reaction of the NiO(100) clusters in the temperature regime investigated here.

For the composite surface of NiO(100) clusters and c(2x2)-O/Ni(100), we find that the NiO(100) clusters react preferentially. LEED and HREELS results indicate that the c(2x2)-O adlayer persists until there is insufficient oxygen to maintain a 0.5 ML coverage. The TPD results shown in figure 6 indicate that during the course of reaction of the composite surfaces, less than a few percent of a monolayer of metal is exposed on the partially reduced surface, until the total oxygen content is below about 0.5 ML. These results suggest that the reaction is occurring at the surface of the oxide particles, or, if the reaction occurs on the c(2x2)-O regions, that "chemisorbed" oxygen is replenished from the oxide clusters. The fact that we observe the same absolute rate for oxygen removal from films formed by from 1 to 10 oxidation/anneal cycles indicates that the former is the case; the reaction rate does not scale with the area of the c(2x2) region.

That reaction occurs at the surface of the oxide clusters is also supported by the fact that the reaction rate remains constant during the course of reaction. This is not at all characteristic of reaction at island edges. The same absolute rate and time dependence is obtained from the XPS data shown in figure 6 and the FYNES data of figure 9. As discussed above, the XPS results must be corrected for electron escape probability from subsurface layers. When this is done, the curvature in the XPS data is removed for relative intensities above 0.4, which is the intensity of a c(2x2) adlayer.

Both the FYNES and XPS results indicate that the rate of oxygen removal is first order in hydrogen pressure (data not shown here), and roughly zero order in oxygen content. At fixed temperature in the range from 600 to 800 K, the reaction rate is well described by the product of the collision frequency of hydrogen gas with the surface times the probability of removing an O atom per collision. That is:

$$R_{O\ atom\ removal} = P_{H_2} \cdot (2\pi mkT)^{-1/2} \cdot p_{rxn} \qquad (3)$$

where P_{H_2} is the pressure of hydrogen gas, m, is the mass of hydrogen, T, is gas temperature and, p_{rxn} is the reaction probability per collision. Both the FYNES and XPS results give a value for p_{rxn} of 8×10^{-4}.

We summarize the qualitative aspects of the reaction of the composite oxide surfaces as follows. The NiO(100) clusters react preferentially, at a single rate, until all of the subsurface oxygen is removed. No preference for reaction at cluster edges is observed. The time dependence of reaction is characteristic of reaction at the cluster surface, with fast repopulation by the subsurface oxygen. The curvature of the XPS data in figure 6 can only be rationalized with respect to the lack of curvature in the FYNES data of figure 9, if the signal equivalent to that from oxygen from the deepest layers of the oxide clusters is the first to be lost. This is consistent with fast repopulation of oxygen at the surface by diffusion of oxygen from subsurface oxide layers. We believe that this mechanism is more characteristic of NiO under catalytic reaction conditions above 600 K. More quantitative aspects of the reaction kinetics of the NiO surface clusters, with hydrogen and with light hydrocarbons, will be the subject of a separate paper, to be published elsewhere.

5. Summary:

The self-passivating, 2-3 monolayer surface oxide film formed on Ni(100) at 300 K is thermally unstable above 525 K. This film undergoes a phase transformation,

disproportionating into thicker, crystalline clusters of NiO(100) and large regions of c(2x2)-O on Ni(100). Based on electron scattering model simulations of XPS data, the NiO(100) clusters are estimated to be roughly 50 Å thick, and to occupy approximately 6% of the surface. FYNES results show that the total oxygen content in the near surface region remains constant during this phase transformation.

Only the c(2x2)-O regions of the annealed surface are oxidized by subsequent exposure to oxygen at 300 K, and the oxidation again stops at 2-3 monolayers. No preference for oxidation at the NiO(100) island edges is observed. Upon annealing, the newly oxidized c(2x2) regions disproportionate in the same way as the original oxide film, 6 ±1 % going to NiO(100), the remainder returning to c(2x2) O on Ni(100). By repeated cycles of oxidizing at 300 K and annealing to 800 K, a stable NiO(100) film, roughly 50 Å thick, can be produced. These NiO(100) clusters, formed by a single or by multiple oxidation/anneal cycles are thermally stable to 800 K.

The reactivity of the surface toward hydrogen as a function of the number of oxidation/anneal cycles was investigated using time-resolved XPS and time-resolved FYNES. The NiO(100) clusters react preferentially. The subsurface oxygen is removed completely, and the rate of oxygen removal is independent of the instantaneous oxygen content. This supports the conclusion that the clusters are solid or continuous and that no oxygen is lost to the bulk by diffusion. The time dependence of reaction is characteristic of reaction at the island surface, with fast repopulation by subsurface oxygen. No preference for reaction at cluster edges is observed. These characteristics are qualitatively different than is observed for the unannealed oxide film at lower temperatures.

Acknowledgements:

References:

(1)   Wang, W.-D.; Wu, N. J.; Thiele, P. A. *J. Chem. Phys.* **1990**, *92*, 2025.
(2)   Wandelt, K. *Surf. Sci. Reports* **1982**, *2*, 1.
(3)   Norton, P. R.; Tapping, R. L.; Goodall, J. W. *Surf. Sci.* **1977**, *65*, 13.
(4)   Holloway, P. H. *J. Vac. Sci. Technol.* **1981**, *18*, 653.
(5)   Brundle, C. R. *J.Vac.Sci.Technol.* **1985**, *A 3*, 1468; Brundle, C. R.; Broughton, J. Q., in *"The Chemical Physics of Solid Surfaces and Heterogeneous Catalysis"*, Eds., King, D. A.; Woodruff, D. P., (Elsevier, Amsterdam, to be published) Vol. 3.
(6)   Kuhlenbeck, H.; Ordorfer, G.; Jaeger, R.; Illing, g.; Menges, M.; Mull, T.; Freund, H.-J.; Pohlchen, M.; Staemmler, V.; Witzed, S.; Sharfschwerdt, C.; Wennemann, K.; Liedke, T.; Neumann, M. *Phys. Rev. B* **1991**, *In Press*,
(7)   Baumer, M.; Cappus, D.; Kuhlenbech, H.; Freund, H.-J.; Wilhelmi, G.; Brodde, A.; Neddermeyer, H. *Surf. Sci.* **1991**, *to be publ.*,
(8)   Chakraborty, B.; Holloway, S.; Norskov, J. K. *Surf. Sci.* **1985**, *152*, 660.
(9)   Reindl, S.; Pastor, G. M.; Bennemann, K. H. *Surf. Sci.* **1989**, *211/212*, 912.
(10)   Twigg, M. V. *Catalysis Handbook*; Wolfe Publishing Ltd.: Frome, England, 1989; .
(11)   Hatano, M.; Otsuka, K. *Inorganica Chemica Acta* **1988**, *146*, 243.
(12)   Ungar, R. K.; Zhang, X.; Lambert, R. M. *Appl. Catalysis* **1988**, *42*, L1.
(13)   Rahman, T. S.; Mills, D. L.; Black, J. E.; Szeftel, J. M.; Lehwald, S.; Ibach, H. *Phys. Rev.* **1984**, *B30*, 589.

(14) Szeftel, J. M.; Lehwald, S.; Ibach, H.; Rahman, T. S.; Black, J. E.; Mills, D. L. *Phys. Rev. Lett.* **1983**, *51*, 268.
(15) Richter, H.; Gerhardt, U. *Phys. Rev. Lett.* **1983**, *24*, 1570.
(16) Rieder, K. H. *Phys. Rev. B* **1983**, *27*, 6978.
(17) Demuth, J. E.; Jepsen, D. W.; Marcus, P. M. *Phys. Rev. Lett.31540.* **1973**, *31*, 540.
(18) Stohr, J.; Jaeger, R.; Kendelewicz, T. *Phys. Rev. Lett.* **1982**, *49*, 142.
(19) Tong, S. Y.; Lau, K. H. *Phys. Rev. B* **1982**, *25*, 7382.
(20) Bauschlicher, C. W.; Bagus, P. S. *Phys. Rev. Lett* **1984**, *52*, 200.
(21) Hove, M. A. V.; Tong, S. Y. *J. Vac. Sci. Technol.* **1975**, *12*, 230.
(22) Brongersma, H. H.; Theeten, J. B. *Surf. Sci.* **1976**, *54*, 519.
(23) Hanke, G.; Lang, E.; Heinz, K.; Muller, K. *Surf. Sci.* **1980**, *91*, 551.
(24) Brundle, C. R.; Hopster, H. *J. Vac. Sci. Technol.* **1981**, *18*, 663.
(25) Rosenblatt, D. H.; Tobin, J. G.; Mason, M. G.; Davis, R. F.; Kevan, S. D.; Shirley, D. A.; Li, C. H.; Tong, S. Y. *Phys. Rev. B* **1981**, *23*, 2838.
(26) Mitchell, D. F.; Sewell, P. B.; Cohen, M. *Surf. Sci.* **1976**, *61*, 355.
(27) Boreskov, G. K.; Savchenko, V. I.; Dadayan, K. A.; Ivanov, V.; Bulgakov, N. N. *Probl. Kinet. Katal.* **1978**, *17*, 115.
(28) Dadayan, K. A.; Boreskov, G. K.; Savchenko, V. I. *Dokl. Akad. Nauk SSSR* **1976**, *230*, 625.
(29) Holloway, P. H.; Hudson, J. B. *Surf. Sci.* **1974**, *43*, 123.
(30) Akimoto, K.; Sakisaka, Y.; Nishijima, M.; Onchi, M. *Surf. Sci.* **1979**, *82*, 349.
(31) Smeenk, R. G.; Tromp, R. M.; Frenken, J. W. M.; Saris, F. W. *Surf. Sci.* **1981**, *112*, 261.
(32) Saiki, R. S.; Kaduwela, A. P.; Osterwalder, J.; Fadley, C. S.; Brunle, C. R. *Phys. Rev. B* **1989**, *40*, 1586.
(33) Stohr, J.; Kollin, E. B.; Fischer, D. A.; Hastings, J. B.; Zaera, F.; Sette, F. *Phys. Rev. Lett.* **1985**, *30*, 1468.
(34) Zaera, F.; Fischer, D. A.; Shen, S.; Gland, J. L. *Surf. Sci.* **1988**, *194*, 205.
(35) Johnson, S.; Madix, R. J. *Surf. Sci.* **1981**, *108*, 77.
(36) Scofield, J. H. *J. Electr. Spect. Rel. Phenom.* **1976**, *8*, 129.
(37) Penn, D. R. *J. Electr. Spect. Rel. Phenom.* **1976**, *9*, 29.
(38) Chen, J.G; Weisel, M. A.; Hall, R. B. *Surf. Sci.* **1991**, *accepted for publiction,*
(39) Fuchs, R.; Kliewer, K. L. *Phys. Rev. A.* **1965**, *140*, 2076.
(40) Anderson, S. *Surf. Sci.* **1979**, *79*, 385.
(41) deBokx, P. K.; Labohm, F.; Gijzeman, O. L. J.; Bootsma, G. A.; Geus, J. W. *Applic. Surf. Sci.* **1980**, *5*, 321.
(42) Fischer, D. A.; Colbert, J.; Gland, J. L. *Rev. Sci. Instr.* **1989**, *60*, 1596.
(43) Grunes, L. A.; Leapman, R. D.; Wilker, C. N.; Hoffmann, R.; Kunz, A. B. *Phys. Rev. B* **1982**, *25*, 7157.
(44) Grunes, L. A. *Phys. Rev. B* **1983**, *27*, 2111.
(45) Davoli, I.; Marcelli, A.; Bianconi, A.; Tomellini, M.; Fanfoni, M. *Phys. Rev. B* **1986**, *33*, 2979.
(46) Norman, D.; Stohr, J.; Jaeger, R.; Durham, P. J.; Pendry, J. B. *Phys. Rev. Lett.* **1983**, *51*, 2052.
(47) Christensen, T. M.; Raoul, C.; Blakely, J. M. *Appl. Surf. Sci.* **1986**, *26*, 408.
(48) Tasker, P. W. *J. Phys. C.* **1979**, *12*, 4977.

Chapter 7

Building of Complex Catalysts on Single-Crystal Surfaces

G. A. Somorjai, C. M. Kim, and C. Knight

Department of Chemistry, University of California, Berkeley, CA 94720 and Materials Sciences Division, Lawrence Berkeley Laboratory, Berkeley, CA 94720

Combined catalytic reaction and surface science studies using small area metal single crystal surfaces have shown these systems to be excellent model catalysts. In order to investigate more complex, multicomponent catalysts, other metals, oxides, chlorine, and sulfur were deposited from the vapor phase in controlled concentrations on the metal single crystals or polycrystalline foils to investigate their functions as structure or bonding modifiers. From studies of several of the complex catalyst systems (Pt/Au, Pt/Al2O3, Pt/Al2O3/Cl, Fe/Al2O3, Fe/Al2O3/K, Pt/Re, Pt/Re/S, Mo/S, Mo/Co/S), the molecular ingredients of their catalytic performance have been identified. These are the a) need for surface roughness; b) structural stabilization of rough surfaces; c) the presence of a strongly chemisorbed overlayer that causes surface restructuring; d) bonding modifier cooadsorbates; 3) active oxide-metal interfaces and f) active bimetallic interfaces.

Early studies in our laboratory indicated that single crystal surfaces of transition metals of about 1cm^2 surface area have detectable turnover rates for several catalytic reactions to be considered as model catalyst systems [1]. A high pressure-low pressure apparatus was constructed [2] that permits surface characterization and preparation of single crystal surfaces in uhv and then their exposure to high pressure reaction conditions without contamination by ambient gases. Using this apparatus, catalytic reactions could be studied in batch or in flow modes in what amounts to a microreactor system as long as the turnover rates were greater than 10^{-4} molecule/surface site/second and the reactor walls remained inert to the reaction mixture. Studies of hydrocarbon conversion reactions on platinum single crystals revealed the importance of atomic steps and kinks at the surface to obtain higher rates and selectivity [3]. The ammonia synthesis was studied on iron crystal surfaces and orders of magnitude larger turnover rates were found for the (111) and (211) crystal faces (Fig. 1) than for the more close packed (110) and (100) surfaces [4]. Thus, the surface structure sensitivity of certain catalytic reactions was discovered or reproduced on these model single crystal catalyst surfaces.

However, catalysts that are used in the chemical technology are complex systems containing several additives. To explore the role of these "promoters", alumina was deposited on the iron crystal face from the vapor phase in well controlled concentrations and its role in ammonia synthesis has been explored [5].

Its structural promotion was due to its ability to facilitate the restructuring of iron to produce (111) crystal faces under ammonia synthesis conditions by forming an iron aluminate phase that acts as a substrate for the restructured iron (Fig. 2). Then the promoter role of potassium was explored by depositing known amounts of the metal on iron. Its major effect is to decrease the heat of adsorption of ammonia on the metal surface, thereby reducing its surface concentration during the reaction [6]. Since ammonia blocks some of the active sites for dinitrogen dissociation, the reduction of its surface concentration greatly increases the reaction rate of ammonia synthesis, especially close to equilibrium when there is a large concentration of ammonia present over the iron catalyst.

Potassium alters the pressure dependence of the reaction rate on ammonia and hydrogen and also aids the dissociation of dinitrogen on the less active iron surfaces. These investigations were extended to probe the combined effects of Al_2O_3 and K that were co-deposited in different sequences. It was discovered that the formation of KAl_2O_4 should be avoided, as it is unreactive and blocks the active iron surface [7].

Single Crystal or Small Area Surface Studies of Multicomponent Catalyst Systems

The studies mentioned above pointed the way to investigate other complex catalyst systems using model single crystal surfaces and then sequentially depositing on them the various promoters from the vapor phase in vacuum. This way the surface atomic structure of the transition metal catalyst, the concentration, and location of the various additives can all be controlled independently. This method of building complex catalyst systems is similar in concept to the method of building microelectronic circuitry on silicon single crystal or on other semiconductor single crystal surfaces. If the reaction is not so surface structure sensitive, transition metal foils or gold foils could be used as substrates as well.

Over the past ten years, we studied the following catalyst systems:

1)   Hydrocarbon conversion over platinum catalyst systems [8]. (n-heptane, n-hexane, methyl-cyclopentane, cyclohexane, ethylene, benzene) (Figs. 3 and 4)

Substrate	Promoters
Platinum crystal faces	Rhenium
	Rhenium, Sulfur
	Potassium
	Gold
	Copper
Platinum foil	Alumina
	Alumina, Chlorine
Rhenium crystal face	Platinum
	Platinum, Sulfur
Alumina film deposited on gold foil	Platinum
	Platinum, Chlorine
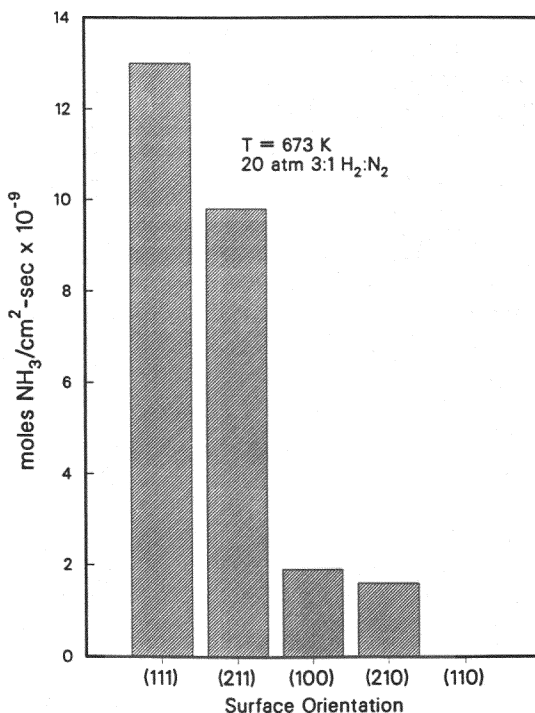
Figure 1. Rates of ammonia synthesis on various single crystal surfaces of iron.
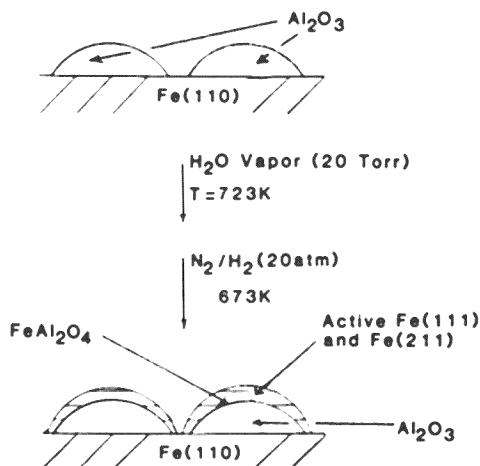
Figure 2. A schematic diagram indicating the formation of iron aluminate on iron surfaces by the interaction of alumina islands with iron and the growth of iron(111) and (211) surfaces of iron during ammonia synthesis on these surfaces.
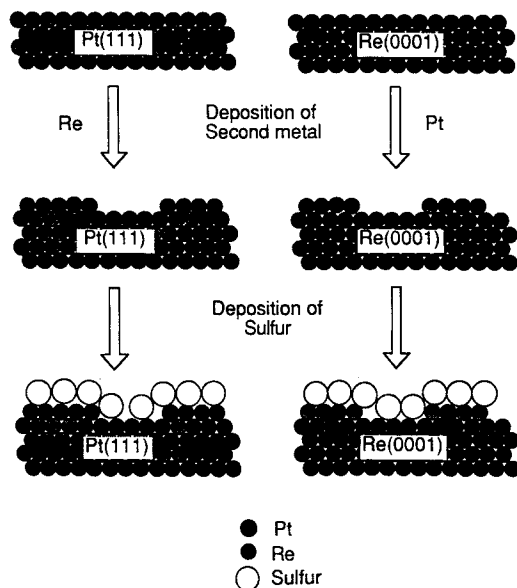
Figure 3. Preparation of Pt/Re/S model catalysts.
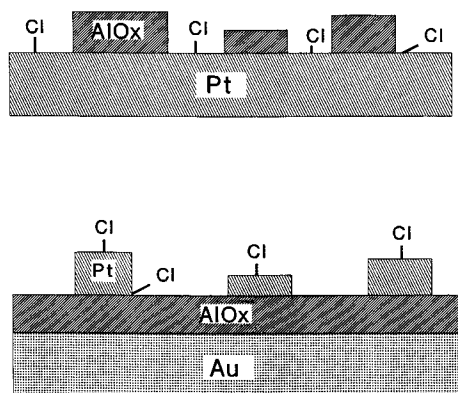
Figure 4. Preparation of model Pt-AlO$_x$-Cl catalysts.

2)   Ammonia synthesis over iron catalyst systems [9]
   Substrate   **Promoters**

   Iron crystal faces   Alumina
                 Potassium
                 Alumina, Potassium

3)   Hydrodesulfurization of tiophene over molybdenum catalyst systems [10]
 (Fig. 5)
   Substrate   **Promoters**

   Molybdenum crystal faces   Sulfur
                 Cobalt
                 Cobalt, Sulfur
                 Carbon
                 Cobalt, Carbon

4)   CO, CO_2, Acetone hydrogenation over rhodium catalyst systems [11]
   Substrate   **Promoters**

   Rhodium foil   Titanium Oxide
                 Vanadium Oxide

In addition, surface science studies have been completed on the Cu(110)/ ZnO [12] (Fig. 6), Pt(111)/ZrO2 [13], Pt(111/Fe2O3 [14] (Fig. 7) systems to lay the foundation for their future use in catalysis. Several reactions are also under study using small area single component model catalysts (NH3 + NO, hydrogenation of propylnitrile, CO + O2, H2 + O2) in preparation for their investigations on more complex catalyst systems.

What have we learned from the combined surface science and catalytic studies using these model catalyst systems? By investigating the roles of each component of the system, many of the molecular ingredients of heterogeneous catalysis could be identified. In the following, we will discuss these in some detail.

Ingredients of Complex Catalyst Systems

Rough surfaces are more active for catalysis. Stepped surfaces of platinum were more active for H2/D2 exchange (Table 1) and for most hydrocarbon conversion reactions than flat low Miller index close packed surfaces [15]. Stepped Ni surfaces dehydrogenate C2H4 at much lower temperatures (< 150 K) than the (111) face of Ni ($\approx$ 230 K) [16] (Fig. 8). The more open (111) and (211) crystal faces of Fe are orders of magnitude more active for NH3 synthesis than the close packed Fe(110) crystal face which showed no detectable reaction rate.

Surface science studies show that clean metal surfaces exhibit relaxation [17]; that is, the surface atoms move inward, closer to the second layer of atoms. The rougher, more open the surface is, the larger the relaxation [18]. Thus, surface atoms with less nearest neighbors relocate readily to optimize surface bonding depending on the changing chemical environment. If we assume that the magnitude of relaxation indicates flexible surface structural behavior, the more flexible is the surface to restructure according to the demands of the surface chemical

$$C_4H_4S + H_2 \xrightarrow{613\ K} C_4H_y + H_2S$$
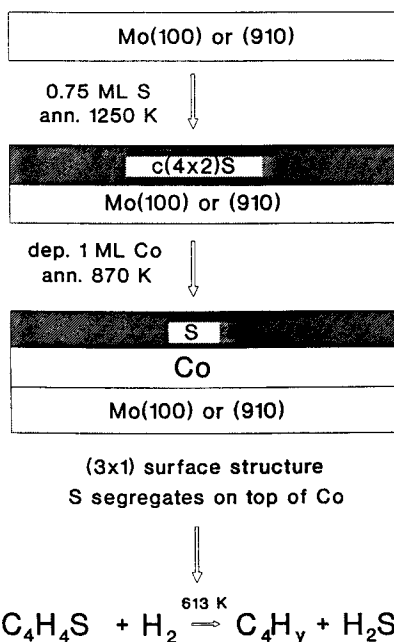
Figure 5. Model Co-Mo-S surfaces for hydrodesulfurization.
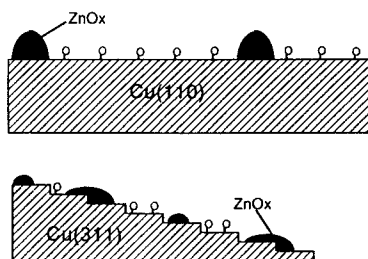
Figure 6. Model Cu-ZnO$_x$ surfaces for studies of methanol synthesis from carbon monoxide and hydrogen.
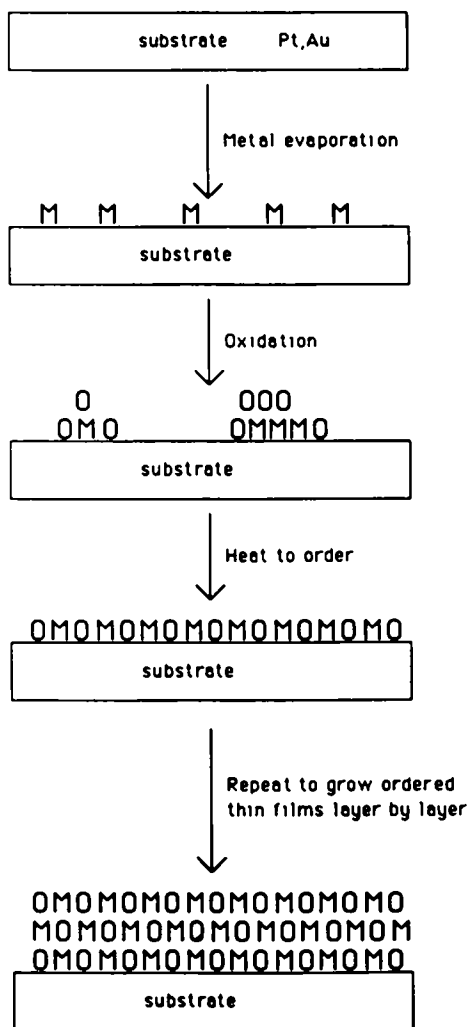
Figure 7. Preparation of ordered metal oxide thin films including iron oxide and zirconium oxide.

TABLE 1

Structure sensitivity of H_2/D_2 Exchange at Low Pressures ($\approx 10^{-6}$ torr)

	reaction probability
Stepped Pt(332)	0.9
Flat Pt(111)	$\approx 10^{-1}$
"Defect free" Pt(111)	$\leq 10^{-3}$

Ni(111) C_2H_4 $\approx 230K$ $\longrightarrow C_2H_4(g)$

$\longrightarrow C_2H_2 + 2H$ $\underline{400K}$ $C_2H + CH + H_2(g)$

Ni(110) C_2H_4 $\underline{220K}$ $\longrightarrow C_2H_4(g)$

$\longrightarrow C_2H + 3H$ $\underline{\approx 400K}$ $CH + C + H_2(g)$

Ni 5(111)x(110) C_2H_4 $\underline{\leq 150K}$ $\longrightarrow C_2H_2 + 2H$ $\underline{250K}$ $2C + 4H$

$\longrightarrow C_2 + 4H$ $\underline{180K}$ $2C + 4H$
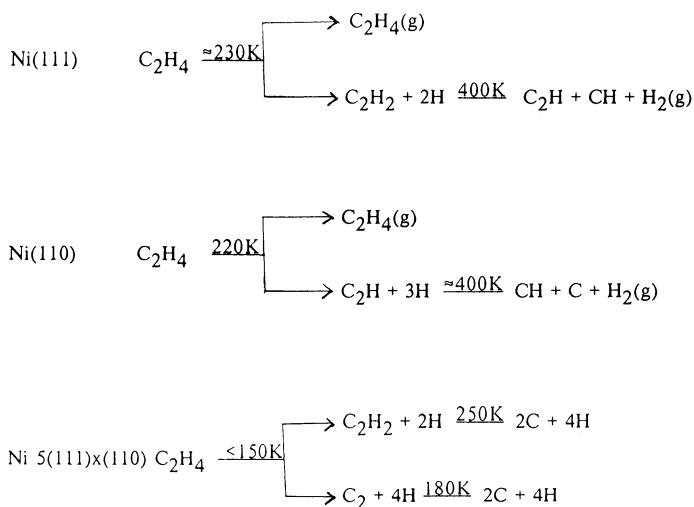
Figure 8. The composition of ethylene on the (111) (110) and the stepped single crystal surfaces of nickel.

environment, the more reactive it will be. This may be the reason for using small clusters as catalysts as these systems have many low coordination surface atoms and, therefore, should restructure readily as the chemical environment changes.

The catalytically active surface is covered with a strongly chemisorbed overlayer. During hydrocarbon conversion reactions, the platinum or other transition metal surfaces are covered with a carbonaceous overlayer of average composition of CH [19]. During ammonia synthesis, the iron crystal faces are covered by chemisorbed N. The Mo surface is covered with a mixture of S and C during hydrodesulfurization [20]. Nevertheless, the reactions proceed at a steady state rate in the presence of these overlayers. ^{14}C and ^{35}S labeling studies indicate that these overlayers are stagnant; they exchange with the gas phase reactants at rates that are orders of magnitude slower than the turnover rates of the catalytic reactions. Thus, they do not seem to impede the reaction turnover while they do not participate as reaction intermediates.

There are two ways of rationalizing the role of these strongly chemisorbed species in catalysis. Chemisorption leads to restructuring of the substrate metal surface. Adsorbate induced restructuring has been observed for every system that has been studied by surface crystallography including C/Ni [21], S/Fe [22], H/Rh [23], O/Cu [24], C_2H_3/Rh [25] (Figs. 9a,b,c,d,e). During chemisorption, the metal atom relocates to optimize bonding with the chemisorbed species at the expense of the strength of the metal-metal bond. The more open the surface, the more marked is the restructuring. I would like to propose that the chemisorption induced restructuring creates the catalytically active sites as the strongly chemisorbed overlayer is formed. Thus the strongly chemisorbed overlayer is an important part of the catalyst system.

The other possible explanation is that the strongly chemisorbed overlayer passivates the metal surface and the reaction occurs at a few uncovered sites of very high activity. Both of these proposals lack experimental verifications. One should monitor the structure of the surface and the bonding of the adsorbates in a time resolved mode that is shorter than the turnover time for the catalytic reaction. This way the catalytic site concentration and its dynamical restructuring behavior could be monitored. Hopefully these types of studies will be carried out in the future.

There is experimental evidence that the catalyst surface restructuring occurs not only on the timescale of chemisorption but also on the timescale of catalytic reactions [26]. This is observed during CO oxidation that exhibits oscillatory reaction rates in certain regimes of partial pressures of the reactants and in certain temperature ranges. The oscillation is due to two branches of this reaction, one for the oxygen rich surface, the other for the CO rich surface. Surface restructuring either induced by surface phase transformations or periodic partial oxidation and reduction of the metal surface has been detected.

High reactivity of oxide-metal interfaces. Depending on the oxide support, the high surface area transition metal catalyst can exhibit orders of magnitude variations of the reaction rates for the same reaction. This is shown for CH_4 formation [27] from CO and H_2 for Ni in Fig. 10. Recent studies indicate that TiO_2 is capable of increasing the activity of many transition metals for this reaction. Figure 11 shows the CH_4 formation rate from CO_2 and H_2 as a function of TiO_2 coverage [28]. The rate is at a maximum at about 50% oxide coverage and about 14 times greater than on the clean metal. TiO_x is unreactive and thus the oxide-metal interface must be responsible for the high reaction rates. There are several oxide-metal interfaces that exhibit similar large increases of activity as compared to the metal alone.
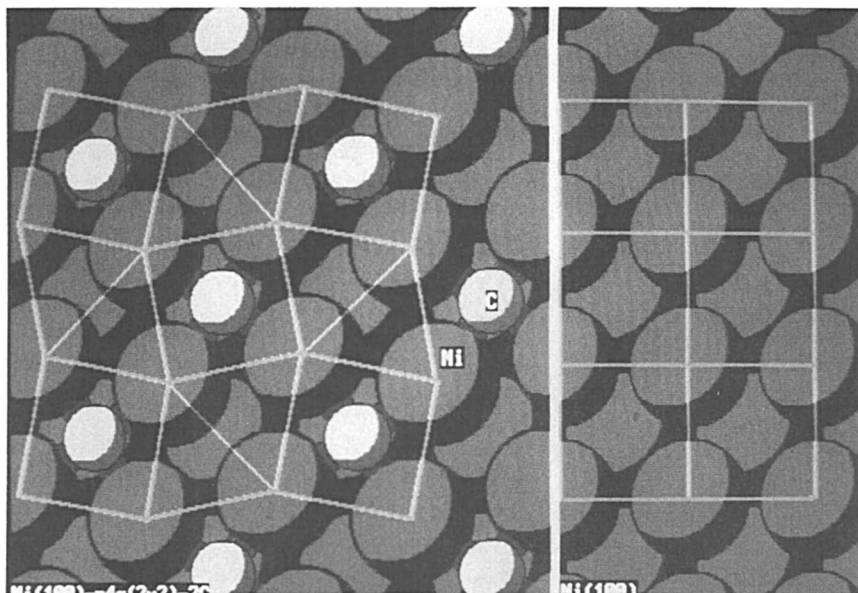
Figure 9a. The carbon adsorption induced restructuring of the Ni(100) crystal face.
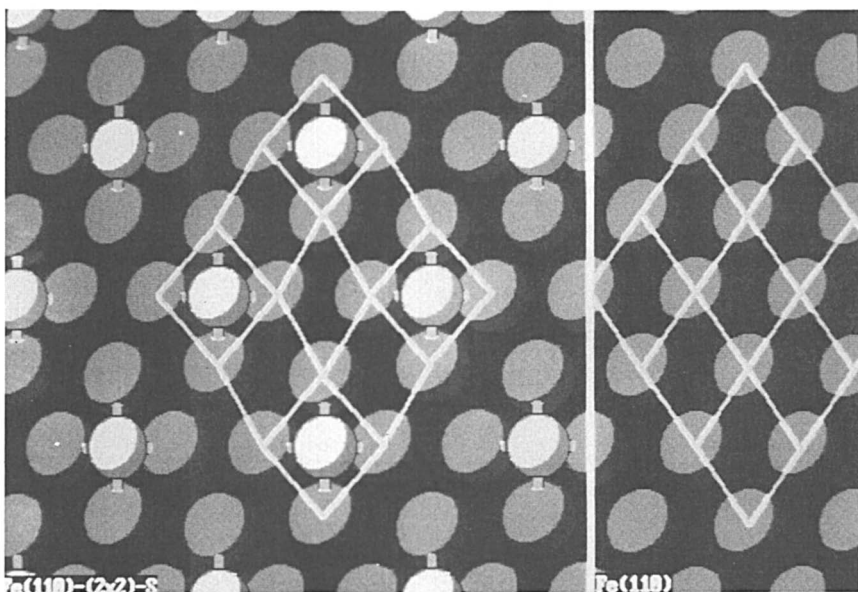
Figure 9b. The sulfur adsorption induced restructuring of the Fe(111) crystal face.
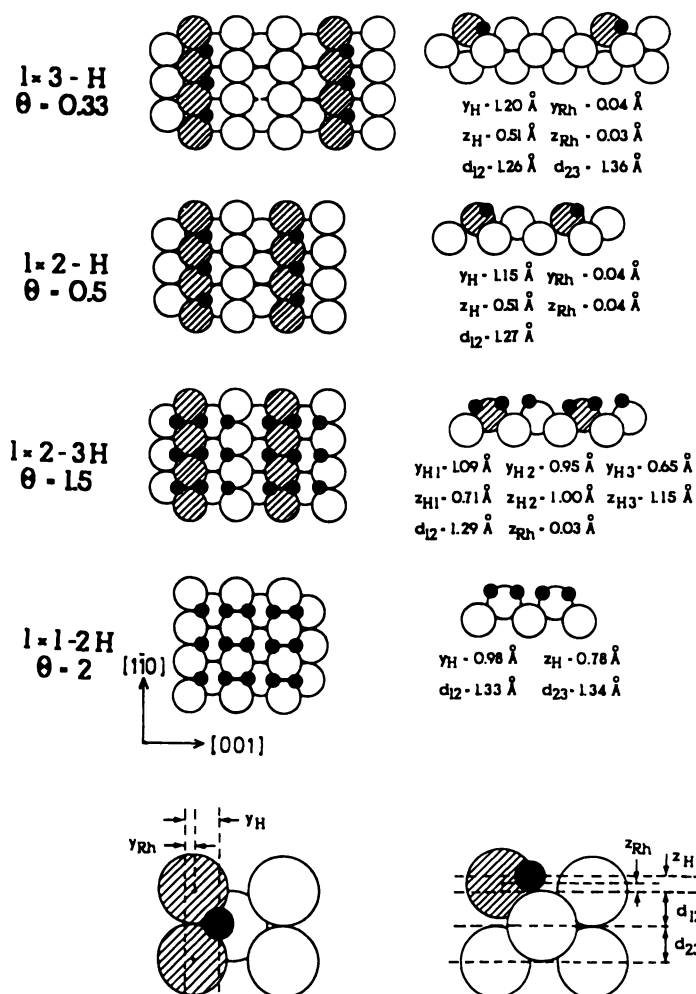
Figure 9c. The hydrogen adsorption induced restructuring of the Rh(110) crystal face. (Reproduced with permission from ref. 23. Copyright 1990 Pergamon.)
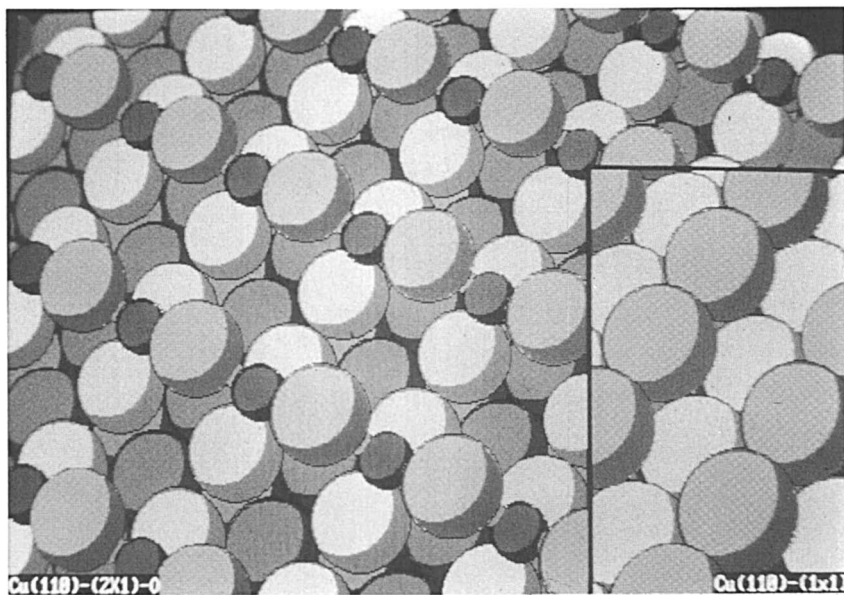
Figure 9d. The oxygen chemisorption induced restructuring of the Cu(110) crystal face.
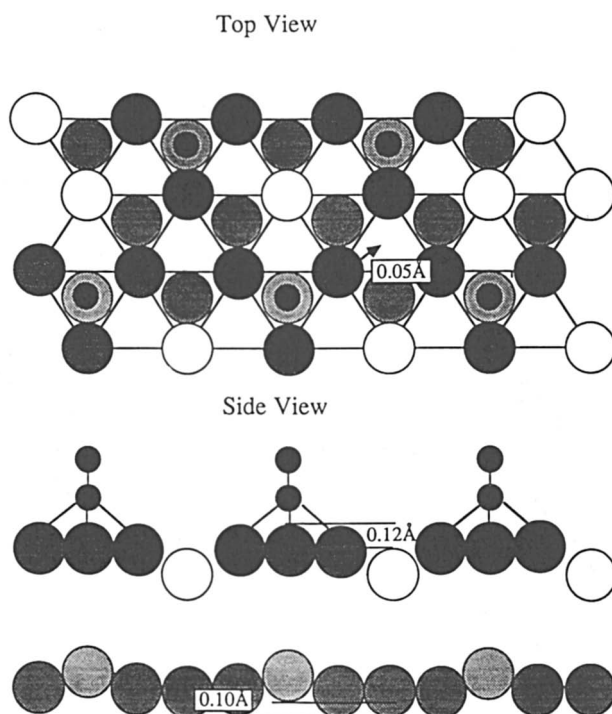
Figure 9e. The ethylene adsorption induced restructuring of the Rh(111) crystal face.
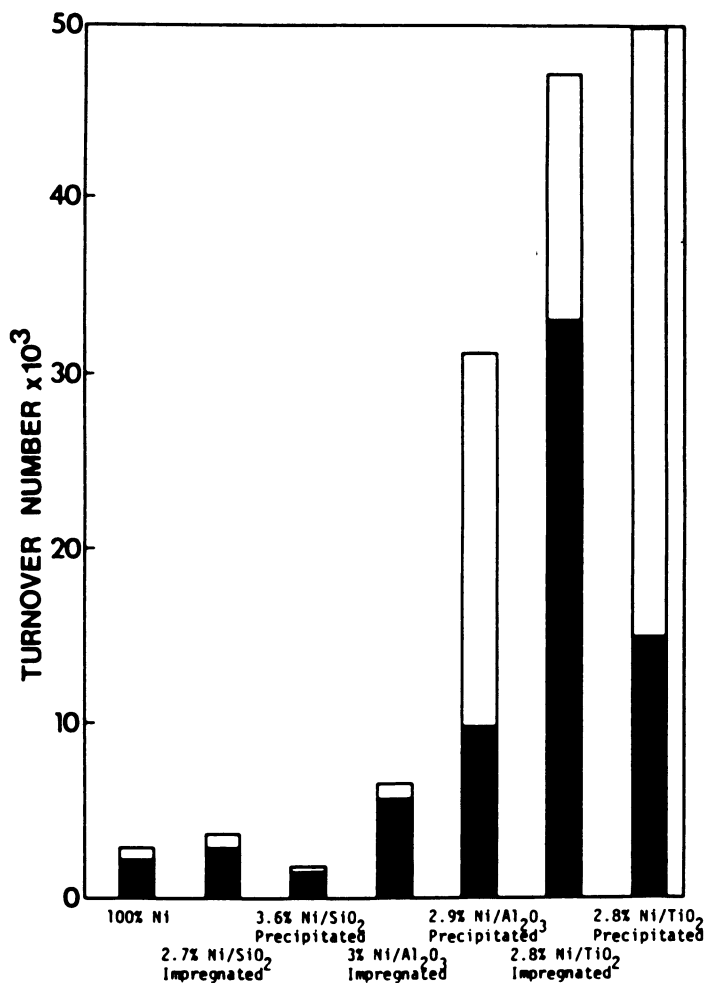
Figure 10. Effect of various supports on CO hydrogenation over Ni catalysts. (Reproduced with permission from ref. 27. Copyright 1980 Academic.)
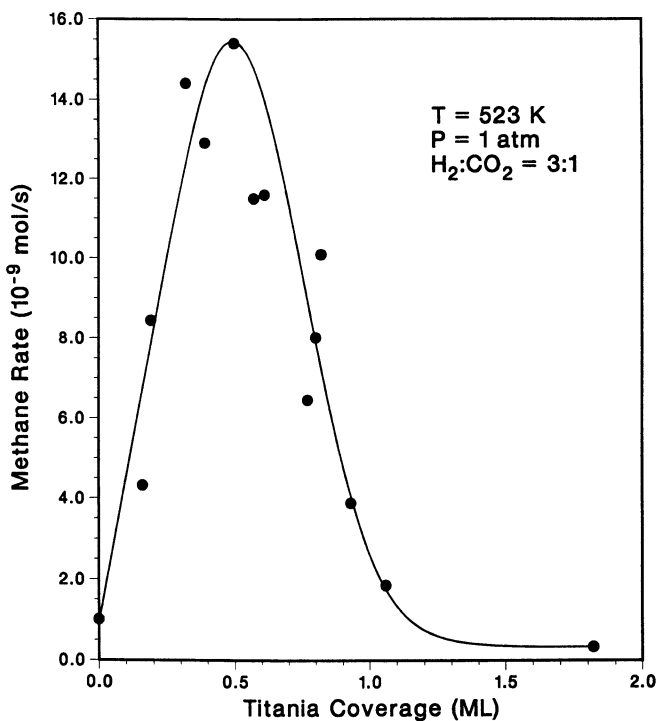
Figure 11. The rate of methane formation from carbon dioxide and hydrogen as a function of titania coverage over rhodium.

Recent surface science studies using scanning tunneling microscopy (STM) and x-ray photoelectron spectroscopy (XPS) reveal that the oxide is somewhat reduced at the oxide-metal interface and Ti^{3+} ions have been detected for the TiO_2-metal systems. One possible explanation of the increased activity is the roughening of the metal at the interface that permits more facile adsorbate induced restructuring and thereby increased turnover rates. Again, time resolved studies of the dynamical changes of surface structure at the oxide-metal interface should help to verify the reasons for their uniquely high catalytic activities.

High reactivity of bimetallic systems. When gold was added to a Pd catalyst used for the H_2/O_2 reaction to produce water, the reaction rate increased 50-fold (Fig. 12) at a certain gold concentration [29]. Gold itself is a poor catalyst for this reaction. Enhancement of hydrocarbon conversion rates of platinum by the addition of gold were also reported from our laboratory (Fig. 13) using model single crystal systems [30]. There are many bimetallic catalyst systems Pt/Re, Os/Cu, that show much enhanced reactivity by the addition of a second inactive metal as compared to the turnover rate of the active metal component.

Again, we suggest roughening of the active metal at the bimetalic interfaces due to decreased coordination. This way its restructuring rate can be increased giving rise to higher catalytic turnover rates.

Coadsorbed bonding modifiers and structure modifiers. Increasing the coverage of a given chemisorbed atom or molecule usually leads to a decrease in its heat of adsorption [31]. This is due to repulsive interactions among the adsorbates (Fig. 14). When two different species are coadsorbed, one an electron donor and the other an electron acceptor to the transition metal substrate, the molecules order to form structures in which the molecules alternate [32]. One of these is shown for C_2H_3 and CO on Rh(111) (Fig. 15). Such a packing indicates an attractive interaction between the coadsorbates. Donor acceptor interaction appears attractive on transition metal surfaces, while the coadsorption of two donors or two acceptors leads to surface phase separation and island formation indicating repulsive interactions.

Alkali metal atoms are electron donors to transition metal surfaces. When coadsorbed with reactants that are electron acceptors, they interact to increase the heat of adsorption of the reactant. This is the case when K is used as a promoter in CO hydrogenation. K increases the heat of adsorption of CO thereby increasing it dissociation probability [33]. CO dissociation is one of the elementary steps for this catalytic reaction.

When K is used as a promoter during NH_3 synthesis, it reduces the heat of adsorption of ammonia, another electron donor on the Fe surface. Thus, this donor-donor repulsive interaction reduces the NH_3 reaction product surface concentration thereby reducing product poisoning in this catalytic reaction.

Chlorine is an electron acceptor and its promoter action may be associated with this property. However, surface science studies have not been used to investigate the effect of chlorine on other coadsorbed molecules as yet.

In all these descriptions of coadsorption, we neglect the possibility of the restructuring effects due to alkali-metals or to other promoter additives. There is evidence that such restructuring does occur on Fe_2O_3 (Fig. 16) and possibly for other catalyst surfaces as well [34]. Of course, Al_2O_3 on Fe exerts its promoter influence by restructuring the transition metal. Structure modifier and bonding modifier promoters may not be readily separated into two distinct classes.

There are adsorbate promoters that block sites, thereby deactivating it for a given undesirable or desirable reaction. In the first case, such a blocking adsorbate
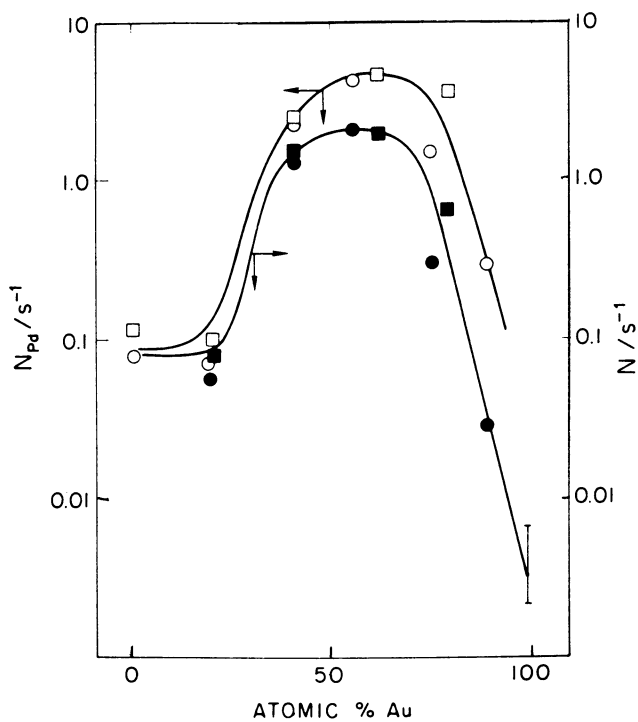
Figure 12. The rate of formation of water from hydrogen and oxygen over palladium as a function of addition of gold.

$\text{VV} + H_2 \quad 570\,K$

$H_2/HC = 10 \quad P_{TOT} = 220\,TORR$

Au–Pt
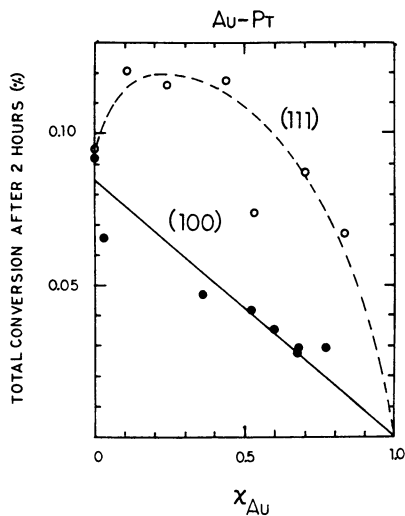
Figure 13a. The total conversion of n-hexane in the presence of hydrogen over platinum(111) and (100) single crystal surfaces as a function of the addition of gold coverage.
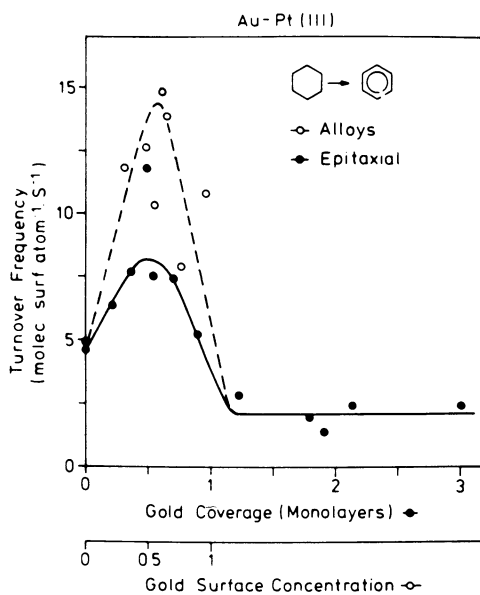
Figure 13b. The rate of cyclohexane dehydrogenation to benzene over platinum(111) crystal faces as a function of gold coverage.
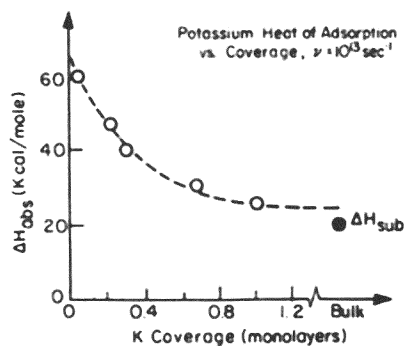
Figure 14. The heat of adsorption of potassium on rhodium as a function of potassium coverage.

Rh(111) + c(4×2) CO + Ethylidyne(CCH₃)
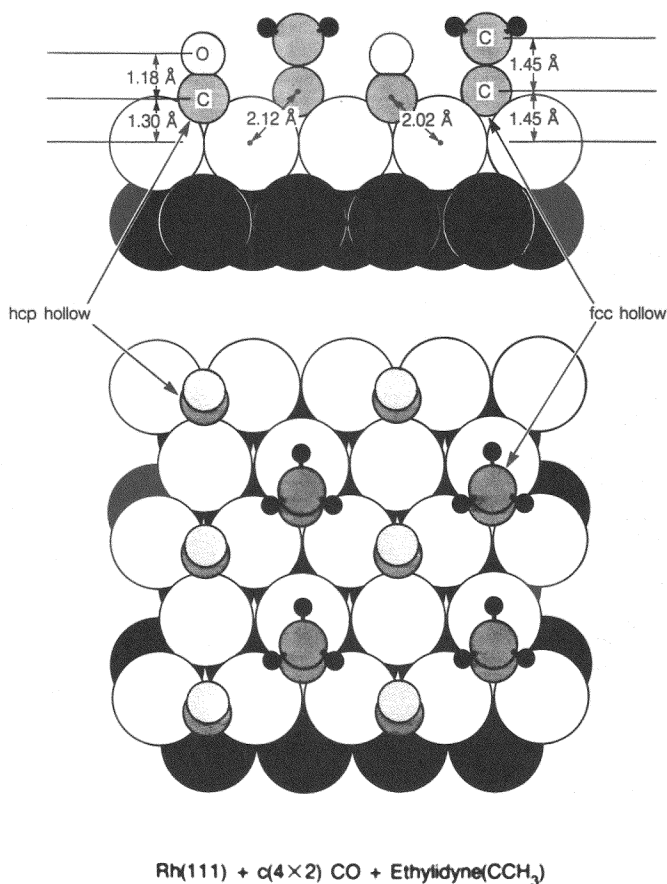
Figure 15. The coadsorbed surface structure of carbon monoxide and ethylidyne on the Rh(111) crystal face.
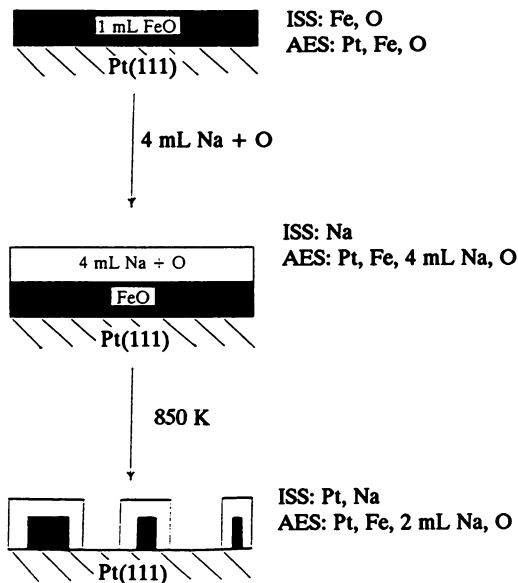
Figure 16. Model for alkali induced restructuring of one monolayer of FeO_x on Pt(111).

is a promoter; in the second it is a poison. Sulfur is often used as an inhibitor of hydrogenolysis but it can also readily poison transition metal surfaces both by blocking active sites and by restructuring the surface.

Future Directions of Research Using Model Catalyst Systems

We identified several molecular ingredients of heterogeneous catalysis using model low surface area single crystal based complex catalyst systems. There are instrumentation limitations to explore in a time resolved way the dynamical changes that occur in the surface chemical bonds on both sides of the interface, the adsorbate and the substrate sides. There is increasing evidence of dynamical restructuring of surfaces during chemisorption, catalytic reactions, or longer timescales. We need time resolved techniques that can monitor these changes on a timescale that is short compared to the catalytic turnover times and can be utilized at high pressures.

We should explore the molecular ingredients of reactions that occur at solid-liquid interfaces and near room temperatures so that we can develop correlations between heterogeneous and biological catalysis.

Finally, new methods should be explored to develop model complex catalyst systems. There is evidence that ion sputtering deposition can produce thin films of chemically active alumina silicates [35]. It is hoped that many innovative approaches will be used to explore the molecular ingredients of important catalysts of increasing complexity.

Acknowledgement

REFERENCES

1. G.A. Somorjai, Adv. Catal. <u>26</u>, 1 (1977).

    G.A. Somorjai, <u>Catalyst Design, Progress and Perspectives</u>, Chapter 2 by John Wiley & Sons, NY, 11-69 (1987).

2. D.W. Blakely, E. Kozak, B.A. Sexton, and G.A. Somorjai, J. Vac. Sci. & Techn. <u>13</u> (5), 1091 (1976).

    A.L. Cabrera, N.D. Spencer, E. Kozak P.W. Davies, and G.A. Somorjai, Rev. Sci. Instrum. <u>53</u> (12), 1893 (1982).

3. S.H. Davis, F. Zaera, and G.A. Somorjai, J. Am. Chem. Soc. <u>104</u>, 7453 (1982). 272

    S.M. Davis, F. Zaera, and G.A. Somorjai, J. Catal. <u>85</u>, 206 (1984)

4. D.R. Strongin, J. Carrazza, S.R. Bare, and G.A. Somorjai, J. of Catal. <u>103</u>, 213-215(1987).

5. D.R. Strongin, S.R. Bare, and G.A. Somorjai, J. of Catal. <u>103</u>, 289-301(1987).

6. D.R. Strongin and G.A. Somorjai, J. of Catal. <u>109</u>, 51-60 (1988).

7. D.R. Strongin and G.A. Somorjai, Catalysis Letters <u>1</u>, 61-66(1988)

8. F. Zaera and G.A. Somorjai, J. Am. Chem. Soc. <u>106</u> (8), 2288 (1984).

    G. A. Somorjai, ISISS Proceedings 1983, Springer Series in Chemical Physics, <u>35</u>, 1-22 (1984).

    J.W.A. Sachtler and G.A. Somorjai, J. Catal., <u>89</u> (1), 35-43,(1984).

    F. Zaera and G.A. Somorjai, J. of Phys. Chem. <u>89</u>, 3211-3216 (1985),.

    S.M. Davis and G.A. Somorjai, Platinum Metals Review <u>27</u> (2), 54 (1983).

9. G.A. Somorjai and D.R. Strongin, in "Catalytic Ammonia Synthesis: Fundamentals and Practice" Ed. J.R. Jennings, Plenum Pub. Co. (1991)

10. M.E. Bussell and G.A. Somorjai, J. of Phys. Chem. <u>93</u>, 2009 (1989).

    M.E. Bussell and G.A. Somorjai, Catalysis Letters <u>3</u>, 1 (1989).

    M.E. Bussell, A.J. Gellman, and G.A. Somorjai, Catalysis Letters <u>1</u>, 195 (1988).

    A.J. Gellman, D. Neiman, and G.A. Somorjai, J. of Catal. <u>107</u>, 92-102 (1987).

A.J. Gellman, M.E. Bussell,and G.A. Somorjai,   J. of Catal. 107, 103-113 (1987).

C.C. Knight and G.A. Somorjai, Surf. Sci., 240, 101 (1990).

11.   M.E. Levin, M. Salmeron, A.T. Bell, and G.A. Somorjai, J. of Catal. 106, 401 (1987).

M.E. Levin, K.J. Williams, M. Salmeron, A.T. Bell, and G.A. Somorjai, Surf. Sci. 195, 341 (1988).

K.J. Williams, M.E. Levin, M. Salmeron, A.T. Bell, and G.A. Somorjai, Cat. Letts. 1, 10, 331 (1988).

K.J. Williams, A.B. Boffa, M.E. Levin, M. Salmeron, A.T. Bell, and G.A. Somorjai,   Cat. Let., 5, 385 (1990).

12.   S. Fu and G.A. Somorjai, Surf. Sci., 237, 87 (1990).

S. Fu and G.A. Somorjai, Proceedings for the International Conference on Solid Films and Surfaces-5, Appl. Surf. Sci.,48/49, 93 (1991).

13.   V. Maurice, M. Salmeron, and G.A. Somorjai,   Surf. Sci., 237, 116 (1990).

14.   G.H. Vurens, M. Salmeron, and G.A. Somorjai,   Surf. Sci. 201, 129-144 (1988)

15.   T.-H. Lin and G.A. Somorjai,   J. Chem. Phys., 81 (2), 704-709 (1984).

N.D. Spencer and G.A. Somorjai,   Rep. Prog.Phys. 46, 1 (1983).

M. Salmeron, R.J. Gale, and G.A. Somorjai, J. Chem. Phys. 70 (6), 2807 (1979).

16.   G.A. Somorjai, J. of Phys. Chem., 94, 1013 (1990)

17.   G.A. Somorjai, Bonding Energies and the Thermodynamics of Organometallic Reactions, ACS Book,Chapter 15, 218- (1990).

G.A. Somorjai, Cat. Let., 2, 311 (1991).

18.   F. Jona and P.M. Marcus, The Structure of Surfaces, Springer Verlag, Berlin, 80 (1988).

19.   G.A. Somorjai, 8th International Congress on Catalysis, Volume l: Plenary Lectures, Berlin, ll3 (l984)

S.H. Davis, F. Zaera, and G.A. Somorjai, J. Catal. 77, 439 (1982).

20.   M.E. Bussell and G.A. Somorjai,   J. of Catal. 106, 93-104 (1987).

21.   J.H. Ouerferko, D.P. Woodruff and B.W. Holland, Surf. Sci., 87, 357 (1979).

22.   G.A. Somorjai and M.A. Van Hove, Prog. Surf. Sci., 30, 201 (1989).

23.   W. Nichtl-Pecher, W. Oed, H. Landskron, K. Heinz and K. Müller, Vacuum, 41, 297 (1990.

24.   C. Woell, R.J. Wilson, S. Chang, H.C. Zend and K.A.R. Mitchel, Phys. Rev. B, 42, 11926 (1990).

25.   A. Wander, M.A. Van Hove, and G.A. Somorjai,   accepted Phys. Rev. Lett. (1991).

26.   G. Ertl, Phys. Chem., 90, 284 (1986).

      R.C. Yeates, J.E. Turner, A.J. Gellman, and G.A. Somorjai,   Surf. Sci. 149 (l), 175 (1985).

27.   C.H. Bartholomew, R.B. Pannell, and J.L. Butler, J. Catal., 65, 335 (1980).

28.   K.J. Williams, A.B. Boffa, M. Salmeron, A.T. Bell, and G.A. Somorjai, submitted Cat. Ltrs. (1991).

29.   Y.L. Lam, J. Criado and M. Boudard, Nouv. J. Chim, 1, 461 (1977).

30.   J.W.A. Sachtler and G.A. Somorjai,   J. Catal. 81, 77 (1983).

31.   G.A. Somorjai and E.L. Garfunkel, Alkali Adsorption on Metals and Semiconductors, H.P. Bonzel, A.M. Bradshaw, and G. Ertl (eds), Elsevier, 319 (1989),

32.   G.S. Blackman, C.-T. Kao, B.E. Bent, C.M. Mate, M.A. Van Hove, and G.A. Somorjai,   Surf. Sci. 207, 66-88(1988).

      C.M. Mate, C.-T. Kao, and G.A. Somorjai,   Surf. Sci. 206, 145-168 (1988).

33.   F. Zaera and G.A. Somorjai,   J. Catal. 84 (2), 375 (1983).

34.   G.H. Vurens, D.R. Strongin, M. Salmeron, and G.A. Somorjai,   Surf. Sci. 199, L387 (1988).

35.   I. Boszormenyi, M. Nakayama and G.A. Somorjai, to be published, Cat. Ltrs. (1991).

Chapter 8

Forward and Reverse Water–Gas Shift Reactions on Model Copper Catalysts

Kinetics and Elementary Steps

Charles T. Campbell and Karl-Heinz Ernst

Chemistry Department, University of Washington, Seattle, WA 98195

The forward and reverse water-gas shift reactions have been studied in detail in our laboratory over clean Cu(111) and Cu(110) single-crystal surfaces, which serve as good kinetic models for high-area Cu/ZnO catalysts. We review here the results of those studies. The steady-state kinetics of these reactions have been measured in an apparatus which combines a medium-pressure (1-2000 torr) microreactor with an attached ultrahigh vacuum chamber for surface preparation and analysis. These kinetics are compared here to the rates of various elementary reaction steps potentially involved in the reaction mechanism, and it is concluded that a "surface redox" mechanism, involving the formation and removal of oxygen adatoms, is most consistent with the results. The kinetics and energetics of the various elementary steps involved in this mechanism are discussed in detail. Kinetic evidence for a hydrogen-induced surface reconstruction or phase transition which strongly affects the reaction rate is discussed as well.

The water-gas shift reaction ($CO + H_2O \rightarrow CO_2 + H_2$) is an industrially important route to H_2 as well as a potential player in many scenarios for future energy technologies. It is typically accomplished using the so-called "low-temperature" catalyst, consisting mostly of CuO and ZnO in the precursor state. In the working catalyst, most of the Cu has been reduced to tiny metallic Cu particles sitting on ZnO particles, although some Cu may still exist as ions in or on the ZnO lattice. In this review, we hope to show that very well-defined model catalysts based on clean Cu (111) and Cu(110) single-crystal surfaces give steady-state kinetics at medium pressures which are very similar to those obtained using high-area Cu/ZnO catalysts in both the forward water-gas shift (FWGS) and reverse water-gas shift (RWGS) reactions. We will argue that this proves that these reactions occur mainly at the surfaces of metallic Cu particles in real catalysts. We will then go on to investigate the kinetics of elementary steps on the Cu(110) "model catalyst", and use this to show that a "surface redox" or "oxygen adatom" mechanism explains the observed kinetics well. Finally, a potential energy diagram for the full sequence of elementary steps will be discussed.

It is hoped that this case study of one particular catalytic reaction will demonstrate somewhat more generally how a rich picture of the atomic-level details

of surface catalyzed reactions can be developed through a state-of-the-art approach combining (1) preparation and characterization of well-defined model catalysts using ultrahigh vacuum (UHV) surface science techniques, (2) medium-pressure (~10^{-2} to 2000 torr) kinetics of both the steady-state catalytic reaction and various of its elementary steps, and (3) ultrahigh vacuum studies of the kinetics of the other (more rapid) elementary steps.

Experimental Approach

The types of experiments described here can be accomplished in any apparatus which properly combines ultrahigh vacuum (UHV) surface preparation and analysis techniques with an attached medium-pressure microreactor for kinetic measurements. The design considerations for and drawings of such equipment as well as a general discussion of the experimental techniques for such experiments was presented already elsewhere [1]. More specific experimental details concerning the particular techniques used in obtaining the data reviewed here can be found in the source manuscripts where these data are originally found.

Results and Discussion
1. Steady-State Kinetics of the Forward Water-Gas Shift Reaction Over Cu(111) and Cu(110)

Figure 1 shows the rate of the FWGS reaction over Cu(111) and Cu(110) under steady-state, low conversion conditions at 10 torr H_2O and 26 torr CO as a function of temperature, plotted in Arrhenius form. More extensive studies of the kinetics on these surfaces were presented earlier [2-3]. From the slopes in Fig. 1, Cu(111) and Cu(110) show apparent activation energies of 17 and 10 kcal/mol, respectively, and Cu(110) is more active than Cu(111) by a factor of ~2.5 to 7.0. These differences have been attributed to the fact that Cu(110) has a lower activation energy for the rate-determining step, which is the dissociation of adsorbed H_2O [2-3]. Also shown in Fig. 1 is the rate expected for a high-area Cu/ZnO catalyst of the type studied by van Herivijnen et al. [4], based on a global kinetic equation they derived from rate data taken at somewhat higher pressures. In converting their rates to absolute rates per cm^2 of metallic Cu surface area, we have assumed that 20% of the BET surface area of their catalysts was metallic Cu area.

As can be seen, the Cu(111) surface closely approximates the extrapolated kinetics over high-area Cu/ZnO, which shows that the active part of Cu/ZnO are the metallic Cu islands. Because of the relatively small differences between the Cu(110) and (111) surfaces compared to the potential errors associated with such an extrapolation, we were at first reluctant to conclude that these Cu islands had surfaces more like Cu(111) than Cu(110). However, Ovesen et al. [5] have recently extrapolated these single-crystal data to the conditions of the Cu/ZnO data using a full mechanistic model, which is more trustworthy. They concluded that the Cu islands probably are indeed (111)-like, which is not surprising since the (111) plane is thermodynamically most stable.

The reaction orders with respect to the H_2O and CO partial pressures have also been measured over Cu(111) [2] and Cu(110) [3]. They were found to be
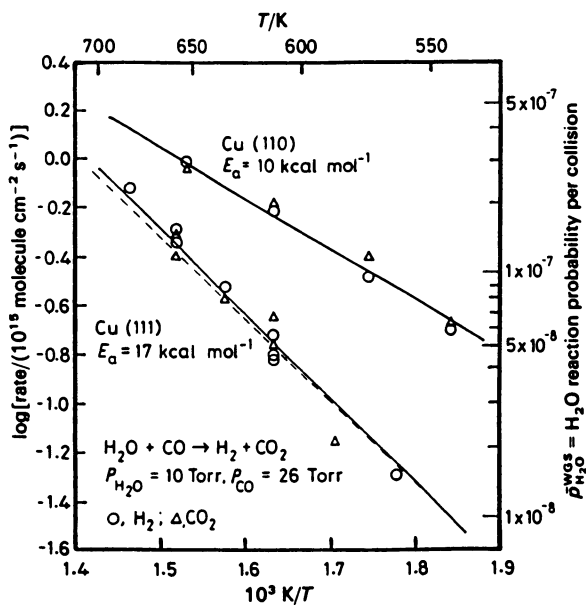
Fig. 1.   Comparison of the WGS reaction rates on Cu(110) (ref. [3]) and
            Cu(111) (ref. [1]), as a function of reaction temperature in
            Arrhenius form. The rate for a high-area Cu/ZnO catalyst is also
            shown as the dashed line (---), extrapolated to the present
            conditions from data presented in ref. [4] using a global kinetic
            expression from that reference. The reaction probability per
            collision of H_2O molecule with the surface is also shown on the
            right-hand axis.

nearly first-order in H_2O and zero-order in CO, consistent with a model where the surface coverages of all species is very low, where H_2O and CO are in rapid adsorption/desorption equilibrium, and where the dissociation of adsorbed H_2O is the rate determining step. Such a model has been presented in full mechanistic and quantitative detail elsewhere [3,5].

2. Elementary Step Analysis Over Cu(110)

A simplified, one-dimensional potential energy diagram which shows the entire sequence of elementary steps is presented in Fig. 2, for Cu(110). The energetics were derived from kinetic and equilibrium studies of most of the individual steps, as described in detail elsewhere [3].

An example of one such study is presented in Fig. 3, which shows the dissociative adsorption probability for H_2 ($H_{2,g} \rightarrow 2H_a$) as a function of temperature, in Arrhenius form, from data presented elsewhere [6]. From the slope, the activation energy for this process is 14.3 ± 1.4 kcal/mol, and the preexponential factor is approximately unity. It turns out that making this particular measurement was quite difficult since the activation energy is scaled largely by H_2 translational energy in a "direct" or "impact-type" adsorption process. This means that the H_2 gas molecules hitting the surface must have a temperature equal to the surface temperature in order to get a true activation energy. This in turn required a high pressure (~100 torr) of some bath gas such as N_2 in the reaction vessel. Since the activation energy for the desorption of hydrogen ($2H_a \rightarrow H_2$) is ~13 kcal/mol on Cu(110) [7], the adsorption of hydrogen is nearly thermoneutral.

Some of the energies presented in Fig. 2 were obtainable going in either direction, forward or reverse. For example, the barrier height between $CO_a + O_a$ and $CO_{2,g}$ was obtained both from the kinetics of the reaction $CO_g + O_a \rightarrow CO_{2,g}$, and from the kinetics of the dissociative adsorption of CO_2 on Cu(110). An average of the two values was used in Fig. 2. We recently proved that the former reaction occurs over Cu(110) via a Langmuir-Hinshelwood coupling between CO_a and O_a, with an activation energy of ~19 kcal/mol [8]. The adsorption probability for the reverse reaction, $CO_{2,g} \rightarrow CO_a + O_a$ over Cu(110) is presented in Fig. 4 as a function of temperature, in Arrhenius form from data of Nakamura et al. [9]. From the slope, the activation energy is ~16 kcal/mol, and the preexponential factor is ~$\underline{10}^{-3}$. At the temperatures where these rates were measured, the product CO_a desorbs immediately, and the rate was directly determined from the initial build-up of oxygen Auger signal ($\theta_0 \leq 0.1$). The similarities in these two activation energies (~19 vs. 16 kcal/mol) suggests that the reaction $CO_a + O_a \rightarrow CO_{2,g}$ is also nearly thermoneutral, which is indeed consistent with the known heats of adsorption of CO and O_2 on Cu as explained elsewhere [3].

The dissociative adsorption of H_2O to produce O_a and H_2 gas has been observed on Cu powder at 346K by Chinchen et al. [18], but no rate data were presented. The fact that the reaction $H_{2,g} + O_a \rightarrow H_2O_g$ is easily observed on Cu(110) also proves by microscopic reversibility that the reverse process, $H_2O_g \rightarrow H_{2,g} + O_a$, must also occur. Previously [3], we have estimated the Gibbs free energy and equilibrium constant for this process and, from the rate of the reaction $H_{2,g} + O_a \rightarrow H_2O_g$ reported in [6], shown that water must dissociatively adsorb at
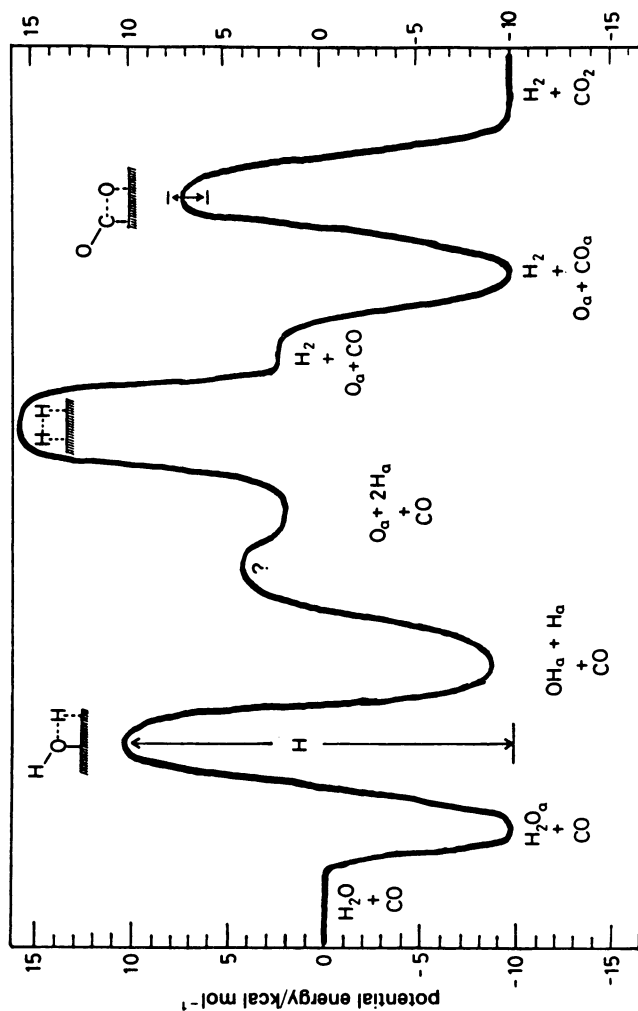
Fig. 2. Simple potential energy diagram of the WGS reaction on Cu(110) for the "surface redox" or "oxygen adatom" mechanism we propose. Each energy level has been determined from calorimetric data, equilibrium measurements, or kinetic data (see ref. 3). This figure was originally presented in ref. 3 but has been corrected slightly here to reflect a new and more accurate value for the activation energy for H_2 adsorption. Species that remain unchanged in various reaction steps shown here are not meant to participate in those steps but are included only to maintain a proper energy reference for subsequent steps.
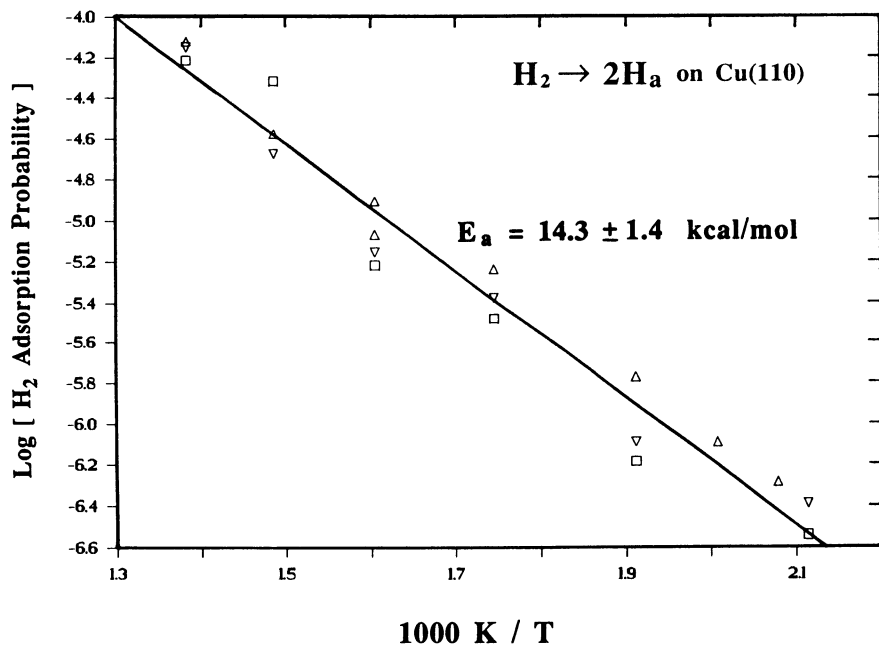
Fig. 3.   Arrhenius plot of the dissociative adsorption probability for H_2 on Cu(110) as a function of (surface + gas) temperature, from ref. [6].
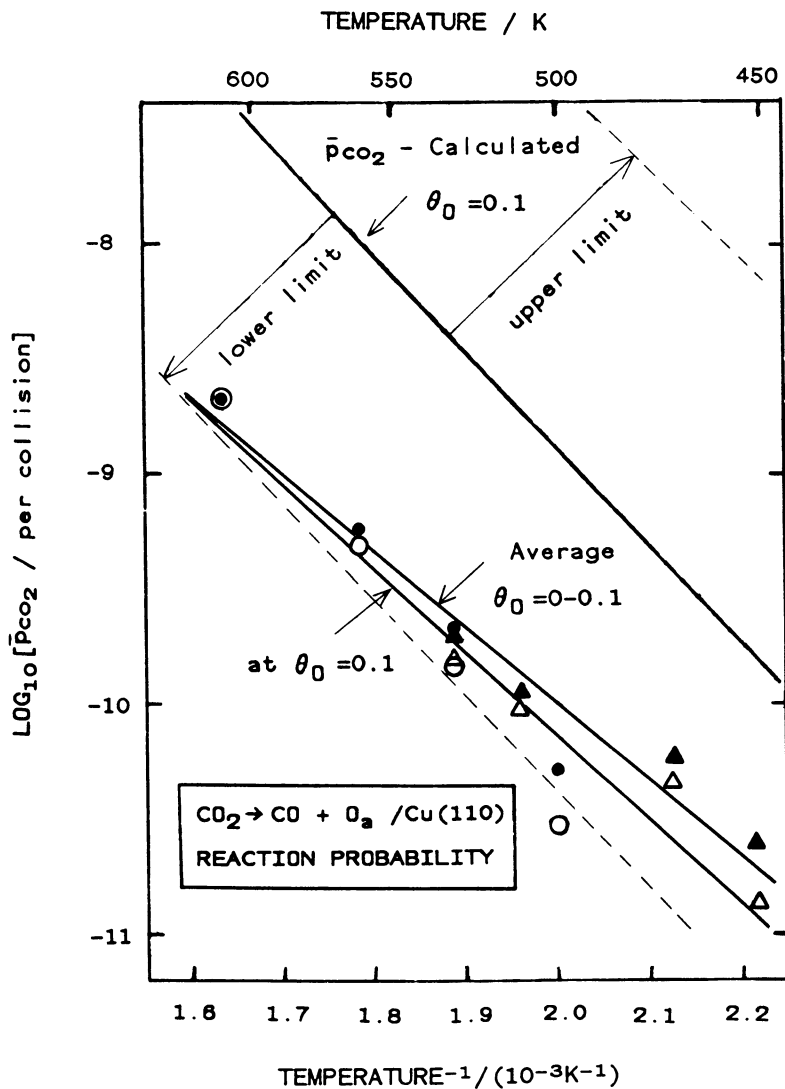
Fig. 4. Arrhenius plot of the dissociative adsorption probability for CO_2 ($\bar{p}_{CO_2}$) on Cu(110) versus temperature. The experimental data points were determined from the slopes of oxygen coverage versus time under high-pressure exposure to CO_2 (i.e., $CO_2 \rightarrow CO + O_a$). The dashed lines show the lower and upper limits for $\bar{p}_{CO_2}$ at $\theta_0 = 0.1$, calculated in ref. 9 using the known heat of oxygen adsorption, the known rate and activation energy of the reverse process, and equilibrium considerations. (Reproduced with permission from ref. 9. Copyright 1989 IOP Publishing.)

600K with a reaction probability of ~10^{-7} at 600K. To our knowledge, there have been no direct measurements of the activation energy for the dissociative adsorption of H_2O. We attempted such measurements but failed due to impurity problems   [3]. In any case, the dissociative adsorption probability is very tiny (<10^{-6}) below 700K [3]. The barrier between H_2O_g and $OH_a + H_a$ in Fig. 2 was taken from the activation energy for the FWGS reaction, which is rate-limited by this step [3].

An important point should be made concerning the equilibrium constant for the reaction $H_2O_g \rightleftarrows H_{2,g} + O_a$. We have estimated this in ref. [3] based upon a Born-Haber cycle using known gas-phase enthalpies and entropies, the measured heat of adsorption of oxygen on Cu and an estimated entropy of adsorption of oxygen. The method used for estimating this entropy should be very accurate [9]. The resulting equilibrium constant of 2×10^{-3} at 600K is drastically different than the value of ~60 estimated by Chinchen et al. [18] with another method which used the measured equilibrium coverage of oxygen on Cu catalysts under CO_2/CO mixtures. Their estimate relies entirely on the method they used to measure oxygen coverage, which is subject to some question. Their estimate also implies that the entropy for oxygen adsorption is positive, which is clearly impossible given the large amount of entropy associated with the rotational and translational degrees of freedom in O_2 which are lost upon adsorption [9]. Their equilibrium constant implies that a high oxygen coverage exists under reaction conditions when P_{H_2}/P_{H_2O} is less than ~60, whereas our value implies that the oxygen coverage is exceedingly low. A high oxygen coverage is inconsistent with the first-order dependence of the FWGS rate upon H_2O pressure mentioned above.

3. Kinetics of the Reverse Water-Gas Shift Reaction Over Cu(110)

We have recently studied the steady-state, low conversion kinetics of the RWGS reaction over Cu(110) at medium pressures [10]. Representative results are shown in Figs. 5 and 6. Figure 5 shows the specific rate per Cu surface atom (or turnover frequency) as a function of temperature in Arrhenius form for two different sets of partial pressures. The apparent activation energy is 16 ± 1.6 kcal/mol, at least for the partial pressures used here. Figure 6 shows the variation in the rate with CO_2 partial pressure at two different fixed H_2 pressures, and at two different fixed temperatures. For high H_2/CO_2 ratios (>10), the rate increases strongly with P_{CO_2} (order in $P_{CO_2} \cong 0.6$), but is nearly zero order in P_{H_2}. When the H_2/CO_2 ratio drops below about ten as P_{CO_2} is increased, the rate becomes at first independent of P_{CO_2}. Decreasing the H_2/CO_2 ratio further by adding even more CO_2 leads to a slight decrease in rate and then, very curiously, the rate begins to increase again with P_{CO_2} as the H_2/CO_2 ratio falls below ~0.6. In this latter regime, the order in P_{CO_2} is again quite high (~0.7). When the rate is at the curious minimum versus P_{CO_2} (i.e., at $P_{CO_2} = 150$ torr and $P_{H_2} = 110$ torr), the rate is nearly first order in H_2 partial pressure. This curious minimum in the rate versus P_{CO_2}, which leads to two separate regimes where the order of the rate is very high in P_{CO_2}, has been explained as due to a surface phase transition or reconstruction induced by high hydrogen coverages (see below and ref. [10]). It is argued in ref. [10] that the coverages of all other species besides H_a should be quite low under the RWGS conditions of Figs. 5 and 6.
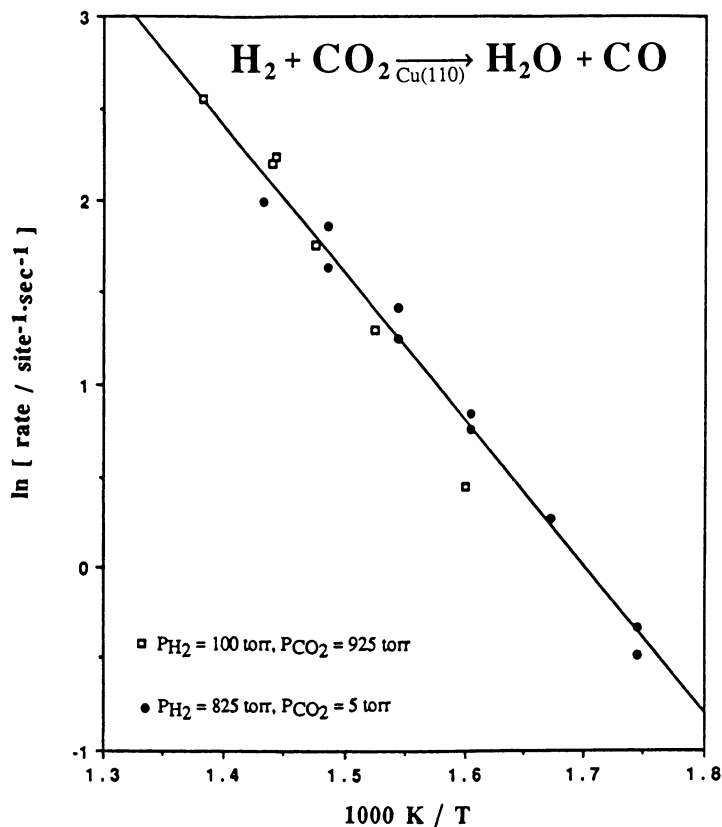
Fig. 5.   The rate of the reverse water-gas shift reaction over Cu(110) as a
           function of temperature, in Arrhenius form, for two different
           pressure conditions: one with low H_2/CO_2 ratio, and one with very
           high H_2/CO_2. The latter case should reflect the "active phase,"
           whereas the former should reflect the "less active" phase (see text).
           Data from ref. [10].

$$H_2 + CO_2 \xrightarrow[Cu(110)]{} H_2O + CO$$
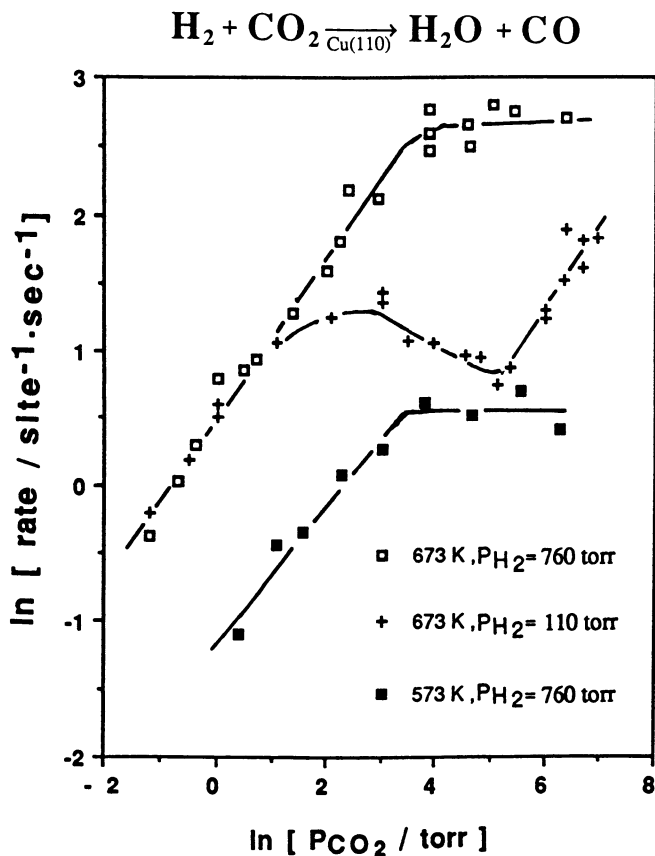
Fig. 6.   Dependence of the rate of the reverse water-gas shift reaction over Cu(110) upon CO_2 pressure at fixed H_2 pressure and temperature. Several different choices of H_2 pressure and temperature are shown. Data from ref. [10].

Discussion

Figure 2 really assumes that the mechanism is via a "surface redox" process involving O_a. Other authors have postulated a mechanism involving the decomposition of a surface formate ($HCOO_a$) intermediate [4,11-13]. We have attempted without success to produce formate via the reaction $OH_a + CO_a \rightarrow HCOO_a$ over CU(110), although our rate limits for this process were insufficiently low to rule out such a step in explaining the WGS rate [15]. Formate is readily produced by such a reaction on rhodium surfaces [16].

Let us now consider the "surface redox" or "oxygen adatom" mechanism (Fig. 2). By "surface redox" we simply mean that the surface sites are alternately "oxidized" and "reduced", wherein "oxidizing" a surface site simply means placing an oxygen adatom (O_a) on that site. Perhaps "oxygen adatom mechanism" would be a better name for this mechanism. In the forward WGS reaction, the "surface oxidation" reaction is simply $H_2O_g \rightarrow H_{2,g} + O_a$, whereas in RWGS, the "surface oxidation" occurs by the dissociative adsorption of CO_2 ($CO_{2,g} \rightarrow CO_g + O_a$). The dissociation of CO_2 to produce O_a occurs with a probability of ~10^{-9} (per collision) at 573K on the clean Cu(110) surface at $\theta_0 \cong 0.1$ (see Fig. 4). This probability is even higher in the absence of O_a [9]. The reverse WGS reaction proceeds at 573K, $P_{H_2} = 800$ torr, and $P_{CO_2} = 15$ torr with a turn-over frequency of ~1 per site per second (Fig. 6), which corresponds to a reaction probability of ~3×10^{-7} per CO_2 collision with the surface. Again, one may wish to conclude that CO_2 dissociation is far too slow to explain the observed rate. One must, however, realize that the CO_2 dissociation rate was measured in the complete absence of adsorbed hydrogen, whereas the RWGS rate was measured under 760 torr of H_2, which gives an estimate H_a coverage of nearly a full monolayer (based on known adsorption/desorption kinetics [6b]). This high hydrogen coverage may influence the rate of CO_2 dissociation favorably, perhaps via a known hydrogen-induced surface reconstruction to a (1 x 2) phase [17], or via some direct interaction with CO_2. Hydrogen is thought to directly assist in CO dissociation on iron surfaces [14].

Indeed, a very unusual minimum in the RWGS rate versus P_{CO_2} at lower H_2 pressures (Fig. 6) is suggestive of some sort of phase transition from an "active" phase at low CO_2 pressure (high H_2/CO_2 ratio) to a "less active" phase at high CO_2 pressure (low H_2/CO_2 ratios). Such a minimum is not seen in the curves of Fig. 6 for high H_2 pressure, where the H_2/CO_2 ratio is apparently always high enough to stabilize the "active phase." The "active phase" would be the high θ_H phase, and the "less active" phase would be more representative of clean Cu(110), or low θ_H. In fact, the RWGS rate in the "low hydrogen coverage" regime is characterized by a turnover frequency of ~5 site^{-1}s^{-1} at 673K, 900 torr CO_2 and 110 torr H_2, or a reaction probability of ~2×10^{-8} per CO_2 collision. This is much closer to the dissociative adsorption probability for CO_2 on clean Cu(110) of 1 x 10^{-8} obtained by extrapolating Fig. 4 to 673K. This difference is in fact so small, given the error bars in both measurements and particularly in their absolute units calibration, that one cannot really claim based on these numbers that CO_2 dissociation is too slow to explain the RWGS reaction on the basis of a "surface redox" mechanism alone. Indeed, one might even claim that the proximity of these

rates provides significant evidence that the RWGS proceeds by a "surface redox" mechanism of the type depicted in Fig. 2.

The activation energy for CO_2 dissociative adsorption (~16 kcal/mol, Fig. 4) is also very close to the measured activation energy for the RWGS reaction of ~16 kcal/mol (Fig. 5). One must, however, remember that the barrier for CO_2 dissociation shown in Fig. 2 is for clean Cu(110), which may be quite different than the barrier existing at high hydrogen pressures (coverages) where the "active phase" postulated above dominates. The lack of dependence of the RWGS activation energy upon the H_2/CO_2 ratio (Fig. 5) suggests, however, that both phases show a very similar activation barrier. Since the order in CO_2 is not really unity for either set of conditions in Fig. 5, interpretation of these apparent activation energies in terms of barriers for elementary steps is somewhat questionable.

Clearly the kinetics for the forward and reverse water-gas shift reactions are rich in detail and not simple to completely understand. While the data can be explained within a surface redox mechanism, very curious effects appear in the reverse WGS reaction at high H_2/CO_2 ratios which are as yet unclear. We postulate that the high hydrogen coverages present at these conditions cause a surface phase transition or reconstruction which yields a structure that is more reactive in CO_2 dissociation than in clean, unreconstructed Cu(110). This implies a hydrogen-assisted CO_2 dissociation. If this occurs with some H--CO_2 bonding in the transition state, this mechanism starts to resemble the formate mechanism, and the ambiguity concerning opposing mechanisms resurfaces. In any case, we have learned a great deal concerning the overall kinetics on Cu(110) and Cu(111), and also concerning the kinetics and energetics of the many elementary reaction steps involved in these processes. Fuller understanding will await further experiments. For example, it would be quite informative to make some in situ measurements under RWGS reaction conditions to probe directly the hydrogen coverage or the surface reconstruction. Similarly, it would be interesting to use very high energy CO_2 beams to probe the effect of hydrogen coverage on the dynamics of CO_2 dissociative adsorption. This could be done at temperatures below 300K where H_a, deposited using hot filaments, can be stabilized on the surface.

Acknowledgements

References

1.   C. T. Campbell, Adv. in Catal. <u>36</u> (1989) 1.
2.   C. T. Campbell and K. A. Daube, J. Catal. <u>104</u> (1987) 109.

3.   J. Nakamura, J. M. Campbell and C. T. Campbell, J. Chem. Soc. Faraday Trans. <u>86</u> (1990) 2725.
4.   T. van Herwijnen and W. A. deJong, J. Catal. <u>63</u> (1980) 83, 94.
5.   C. V. Ovesen, P. Stoltze, J. K. Norskov and C. T. Campbell, sub. to J. Catal.
6.   a) J. M. Campbell, M. E. Domagala and C. T. Campbell, J. Vac. Sci. Technol., <u>A9</u> (1991) 1693.
      b) J. M. Campbell and C. T. Campbell, Surface Sci. (submitted).
7.   a) I. E. Wachs and R. J. Madix, Surface Sci. <u>84</u> (1979) 375.
      b) G. Anger, A. Winkler and K. D. Rendulic, Surface Sci. <u>220</u> (1989) 1.
8.   M. E. Domagala and C. T. Campbell, Catal. Lett. (in press).
9.   J. Nakamura, J. A. Rodriguez and C. T. Campbell, J. Phys.: Condens. Matter <u>1</u> (1989) SB149.
10.   K. H. Ernst, G. Moretti and C. T. Campbell, submitted to J. Catal.
11.   D. C. Grenoble, M. M. Estadt and D. F. Ollis, J. Catal. <u>67</u> (1981) 90.
12.   T. Salmi and R. Hakkarainer, Appl. Catal. <u>49</u> (1989) 285.
13.   K. Klier, C. W. Young and J. G. Nunan, Ind. Eng. Chem. Fundam. <u>25</u> (1986) 36.
14.   G. Blyholder and M. Lawless, Langmuir <u>7</u> (1991) 140.

15.   J. A. Rodriguez, W. D. Clendening, J. M. Campbell, W. Min and C. T. Campbell, J. Vac. Sci. Technol. <u>A7</u> (1989) 2118.
16.   B. A. Gurney and W. Ho, J. Vac. Sci. Technol. <u>A5</u> (1987) 632.
17.   B. E. Hayden, D. Lackey and J. Schott, Surface Sci. <u>239</u> (1990) 119.
18.   G. C. Chinchen, M. S. Spencer, K. C. Waugh and D. A. Whan, J. Chem. Soc., Faraday Trans. I <u>83</u> (1987) 2193 (Faraday Symp. 21).

Chapter 9

Carbon Monoxide Oxidation on Model Single-Crystal Catalysts

Charles H. F. Peden

Inorganic Materials Chemistry Division, Sandia National Laboratories, Albuquerque, NM 87185−5800

The activity of a variety of model single crystal catalysts [*e.g.*, Rh(111), Rh(100), Ru(001), Ru(101), Pt(100), Pd(110), Ir(111), and Ir(110)] for CO oxidation has been studied. Kinetic measurements as a function of temperature and partial pressure of O_2 and CO in a high-pressure reactor - UHV surface analysis apparatus over the temperature range 425 to 725 K, and pressure range of 0.1 to 600 torr have been made. From the measured rate parameters, the reaction mechanisms for a variety of experimental conditions are proposed. In addition, a number of ex-situ probes of the surface composition and structure are used, including Auger electron, X-ray photoelectron, and high-resolution electron energy loss spectroscopies, temperature programmed desorption, and low-energy electron diffraction. Recently, we have also used fourier transform reflection-absorption infrared spectroscopy as an in-situ probe of reaction intermediates. The behavior of the various metals is exemplified by Rh and Ru whose reactivity patterns will be compared and contrasted in this paper. For all of the metal surfaces studied to date, the reaction kinetics (specific rates and their dependence on the reactant partial pressures) that are measured on the model single crystal catalysts are in excellent agreement with results obtained previously for high surface area supported catalysts, demonstrating the structure insensitivity of this reaction. For Rh, Pt, Pd and Ir, we observe simple Arrhenius behavior over most of the temperature range studied with activation energies ranging between 22 and 33 kcal/mol, close to the desorption energy of CO from these surfaces. These results (and the partial pressure dependencies of the reaction) are consistent with the generally accepted model in which the formation of CO_2 occurs by the Langmuir-Hinshelwood reaction between CO molecules and O atoms, both chemisorbed to the metal surface. In contrast, the reaction kinetics measured on Ru are not readily reconciled within such a model, and further suggest that the mechanism *may* involve the direct reaction between gas-phase or weakly bound (physisorbed) CO molecules and chemisorbed oxygen on Ru (Eley-Rideal mechanism).

The development of coupled high-pressure ($\approx$ 1 atm.) microcatalytic reactor/ultra-high vacuum (UHV) surface science apparatus has resulted in significant new insights into the mechanisms of a number of catalytic processes (for recent reviews, see references *1-3*). Notably, the chemical and physical state of the surface prior and subsequent to reaction can be analyzed without exposing the sample to an ambient other than the reactants. A number of ex-situ electron spectroscopic probes of the surface composition and structure can be used, including Auger electron (AES), X-ray photoelectron (XPS), and high-resolution electron energy loss (HREELS) spectroscopies, low-energy electron diffraction (LEED), and temperature programmed desorption (TPD). Recently, the utility of fourier transform infrared reflection-absorption spectroscopy (FT-IRAS) as an in-situ probe of reaction intermediates present at high-pressure reaction conditions in the microcatalytic reactor has been demonstrated (*4,5*). It is the purpose of this paper to describe the variety of useful information obtained in these type of coupled kinetic and spectroscopic studies. Specifically, the focus will be on the CO oxidation reaction on single crystal Rh and Ru in which we have used all of the above listed experimental probes to unravel the mechanistic details of this process for these two metals.

The catalytic oxidation of CO by O_2 over group VIII metals is important for the control of automotive exhaust emissions (*6,7*). As such, considerable attention has been focused on the kinetics and mechanisms of this reaction (*8*). Furthermore, the relative simplicity of the reaction on a metal surface makes it an ideal model system of a hetereogeneous catalytic process - a process involving molecular and dissociative (atomic) adsorption, surface reaction, and desorption of products. This additional motivation has led to numerous fundamental studies of the various elementary steps of the reaction; for example, the adsorption and desorption of CO and O_2, and the surface reaction between chemisorbed CO molecules and O atoms (= CO(ad) and O(ad), respectively) (*9*). In most cases, such studies have provided strong evidence that CO_2 formation on supported and unsupported transition metal surfaces, under steady-state conditions, is a result of this surface reaction, a process defined as the Langmuir-Hinshelwood (L-H) mechanism (*9*). An alternate mechanistic proposal, the Eley-Rideal (E-R) mechanism, involves the reaction between a gas-phase or physisorbed CO molecule and O(ad) (*9*). This mechanism, although often invoked to explain kinetic and spectroscopic data, has yet to be unambiguously established for the CO oxidation reaction. The results to be reviewed in this paper concern a direct comparison between the activity for the CO oxidation reaction, and in-situ and post-reaction spectroscopic characterization of model single crystal Rh and Ru surfaces. In this way, we demonstrate that while the L-H mechanism seems most appropriate for explaining the Rh data, the E-R mechanism may well best account for the results obtained on Ru. In addition, we describe kinetic and spectroscopic data obtained on Rh under highly oxidizing conditions in which the L-H reaction mechanism is altered due to the oxidation of the Rh surface.

Experimental

The experiments reported here involved the use of several small high-pressure ($\leq$ 1 atm.) reactors directly coupled to ultra-high vacuum (UHV) surface-science apparatus. Detailed descriptions of the procedures are contained in the original literature (*10-16*). Briefly, the single crystals are mounted on the sealed end of a reentrant tube connected to a retractable bellows allowing for

sample transfer in vacuum from the reactors to the UHV analysis chambers. The crystals were heated resistively and temperature monitored by thermocouples spot welded to the sample edges. Cooling was accomplished by partially filling the reentrant tube with liquid nitrogen.

The surface analysis apparatus used here typically contain a cylindrical mirror analyzer (CMA) for AES and a quadrupole mass spectrometer for TPD. In addition, one of the systems had capabilities for HREELS, LEED and XPS (*14*). Finally, a separate apparatus was used for in-situ FT-IRAS studies of the CO oxidation reaction over Ru(001) which also contained UHV surface analysis equipment for AES, TPD and LEED (*5*).

High-pressure reactions were performed by heating the crystals for several minutes after charging the reactor with the premixed gases (CO and O_2). CO and O_2 were both ultra-high purity grades and the CO was further purified prior to mixing by passing it through a liquid-nitrogen cooled trap to prevent the introduction of volatile metal carbonyls into the reactor. One of the systems used contained a gas chromatograph for the quantitative determination of product (CO_2) formation (*10*). Additional more qualitative probes of reaction rates included the appearance of gas-phase CO_2 in the FT-IRAS spectra (*15*), and a mass spectrometric measurement of the product gas mixtures leaked into the UHV chamber (*16*).

Results and Discussion

Steady-State Kinetics for Stoichiometric Reaction Conditions. As will be seen below, the CO oxidation reaction mechanism is very sensitive to the state of the surface. We begin the discussion with a measurement of the kinetics for reaction at or near stoichiometric conditions (*i.e.*, reactant partial pressure ratios, $CO/O_2 = 2$). Figure 1 is an Arrhenius plot comparing CO_2 formation rates obtained on several single crystal catalysts (*10,11,13*). These results can be directly compared to previously published rates obtained on high-surface area supported catalysts containing these same metals as shown in Figure 2 (*17-23*). Note that rates obtained on different single crystal faces of Ru, Ir and Rh (Figure 1) give identical results showing that at least for these metals there is no intrinsic sensitivity of the reaction to the surface structure. This conclusion is reinforced by the very good agreement of the results on the supported and unsupported catalysts (Figure 2). Furthermore, it demonstrates that the single crystal metal surfaces are, in fact, very good models for the practical materials. The implication here is that the post-reaction analysis we carry out will be relevant to understanding the operation of the actual catalysts. This agreement extends also to the measured pressure dependence of the reaction for these systems (*e.g.*, see reference *17a*). From these kinetics, models of the mechanism of the CO oxidation reaction have been developed.

Reaction Mechanism for stoichiometric conditions on Rh (and Pt, Pd and Ir). The dependence of the CO_2 formation rate on the partial pressures of both CO and O_2 for reaction over a Rh(111) single crystal catalyst and a supported Rh/Al_2O_3 catalyst were both found to be first order in O_2 pressure and negative first order in CO pressure (*11,17a*). This behavior was accounted for by a kinetic model developed by Oh, *et al.* (*17a*) which correctly predicts this observed behavior assuming a Langmuir-Hinshelwood (L-H) reaction mechanism between chemisorbed CO molecules and dissociatively adsorbed O atoms. It should be noted that these model calculations use only parameters, such as CO and O_2 adsorption energies, obtained from experimental UHV determinations. For the reaction conditions we used, the model predicts that
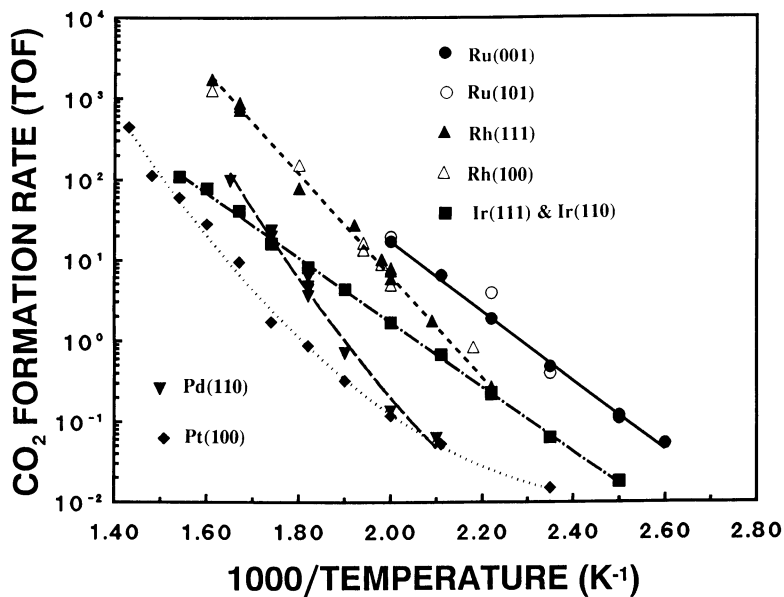
Figure 1. Specific rates of reaction (turn-over frequencies, TOF) as a function of inverse temperature for single crystal catalysts. (Adapted from refs. 10, 11 and 13. Ru(101) data have not been published previously.)
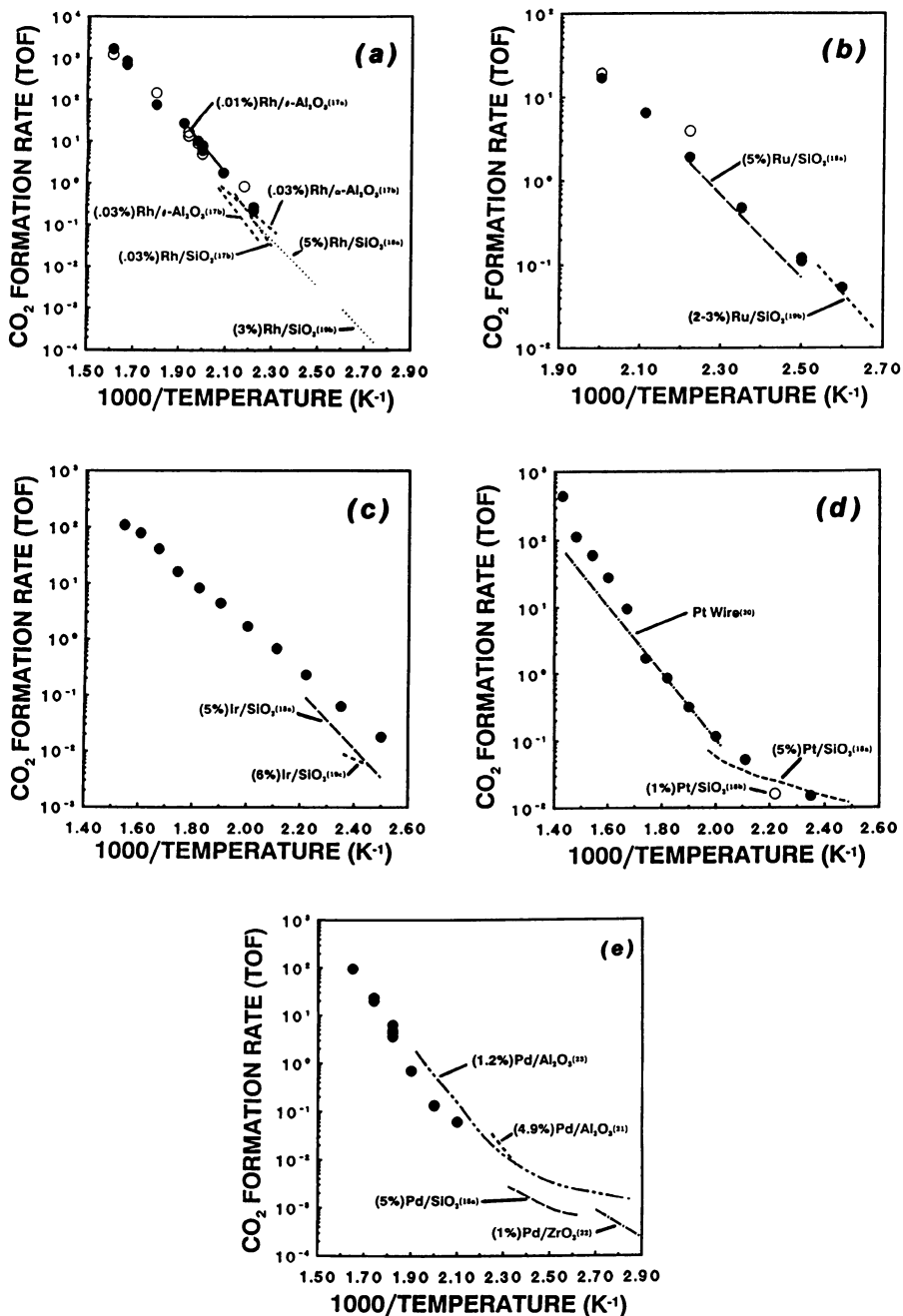
Figure 2. Arrhenius plots of CO oxidation reaction rates (TOF) showing a comparison between results on single crystal (a) Rh, (b) Ru, (c) Ir, (d) Pt, and (e) Pd (data points are from Figure 1) and supported (*17-23*) catalysts.

the surface is predominantly covered by CO, and that the reaction is rate-limited by the adsorption of oxygen, a process that is poisoned by the adsorbed CO. In this case, the equation for the CO_2 formation rate simplifies such that it correctly predicts the first order dependence on O_2 pressure and negative first order dependence on CO (17a). The model also predicts that the overall activation energy for reaction will be approximately the CO desorption energy, again in agreement with experiment (11). In fact, Oh, et al. show quantitative agreement between the reaction rates predicted by the model and those measured on single crystal and supported catalysts over a wide temperature and pressure range.

Post-reaction analyses of the Rh single crystal surface also demonstrate the applicability of the model. The prediction of high surface coverages of adsorbed CO under these conditions is verified in AES, TPD and HREELS data obtained subsequent to reaction on Rh(111). The Auger results indicated a coverage of adsorbed oxygen of less than a tenth of a ML. As such, little if any CO_2 desorption (Figure 3a) was observed in TPD obtained just prior to the AES measurement. Instead, a large CO TPD peak was seen (Figure 3a, inset) with a desorption profile essentially identical to that obtained for saturation CO coverages on clean Rh(111). Finally, the HREEL spectrum of the surface obtained just prior to TPD (Figure 3b) is also identical to that for saturation CO on Rh(111) including both linear and bridged CO species (24). These kinetics and post-reaction analyses are typical for reaction conditions ranging from highly reducing, that is at very CO rich conditions, to mildly oxidizing with a slight excess of O_2 beyond that needed for stoichiometric reaction.

Reaction Mechanism on Deactivated Rh(111). However, things change rather dramatically for still more oxidizing environments as illustrated in Figure 4. The top graph (Figure 4a) is the dependence of the reaction rate on O_2 pressure. At very high O_2 partial pressures, the reaction rate goes down and (not shown) eventually becomes zero-order with further increases in pressure (12). Corresponding to the change in kinetics is a large increase in the oxygen Auger signal observed in post-reaction analysis (11,12) as illustrated in Figure 4b. These results clearly indicate that the surface is being deactivated by this increase in oxygen levels likely corresponding to the onset of metal oxidation. Note that although this oxidized Rh surface is less active than the Rh catalyst surface present under more reducing conditions, it is not inactive.

Further insight into the changes in kinetics was obtained in post-reaction TPD, and in HREEL vibrational spectroscopy as shown in Figure 5 (14). In contrast to the TPD results obtained under reducing conditions, we now find little if any CO desorption (not shown). Instead, a significant quantity of CO_2 is observed (Figure 5a) with a desorption temperature even higher than that for CO from clean Rh. The nature of the species responsible for this CO_2 TPD was investigated by HREELS with the spectrum obtained after oxidizing reaction conditions, just prior to TPD, shown Figure 5b. Based on previous HREELS studies of CO_2 adsorption on other metal surfaces (25,26), we have identified the presence of a carbonate-like species which disappears from this spectrum in the same temperature range that CO_2 TPD is observed (14). There was another somewhat unexpected result in this study; namely, the presence of large quantities of hydroxyl groups on the oxidized Rh surface. In fact, from other data we obtained (14) it appears that these hydroxyl groups are involved somehow in stabilizing the carbonate intermediate.

What we believe to be occurring during reaction on Rh under highly oxidizing conditions is schematically illustrated in Figure 6. The carbonate species that we observe in the HREEL spectra (Figure 5b) is suggested to be an
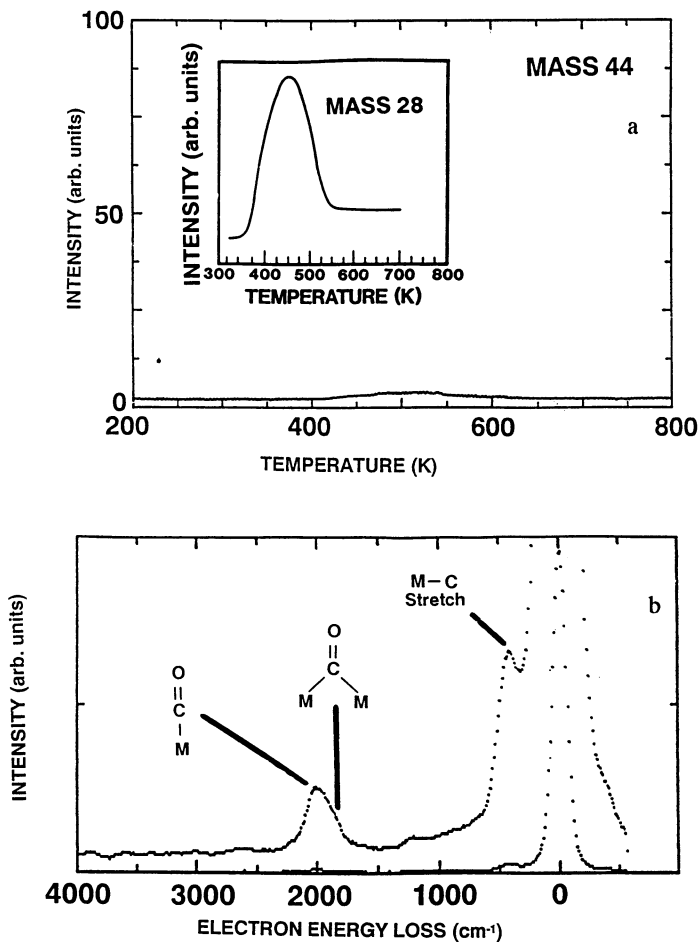
Figure 3. (a) CO_2 TPD and (b) HREELS data obtained subsequent to high-pressure reaction for 2 min in 0.5 Torr gas mixture (CO/O_2 = 11/1) at 500 K. The HREEL spectrum was measured at 100 K just prior to TPD. The inset in (a) shows the CO TPD data obtained subsequent to reaction under similar reducing conditions. (Adapted from ref. 14.)
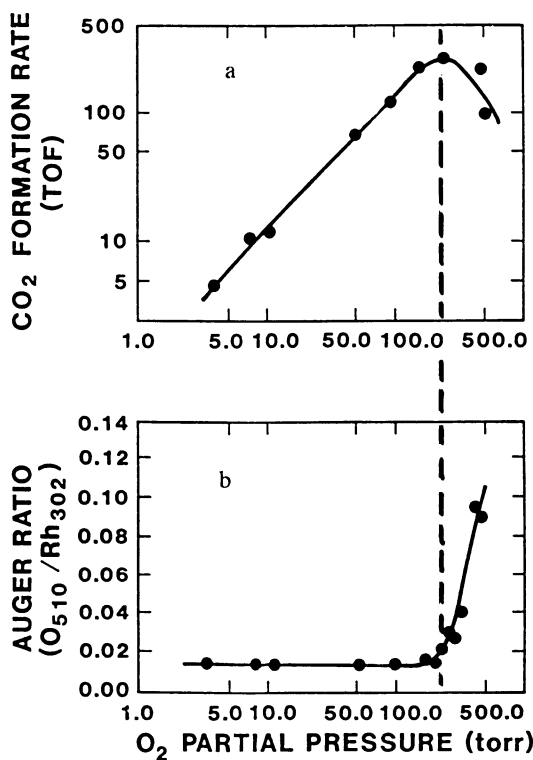
Figure 4. A comparison of the effect of O_2 partial pressure on (a) the rate of reaction, and (b) the level of surface oxygen detected by AES subsequent to reaction on Rh(111). P(CO) = 8 Torr, T = 500 K. (Adapted from ref. 11.)
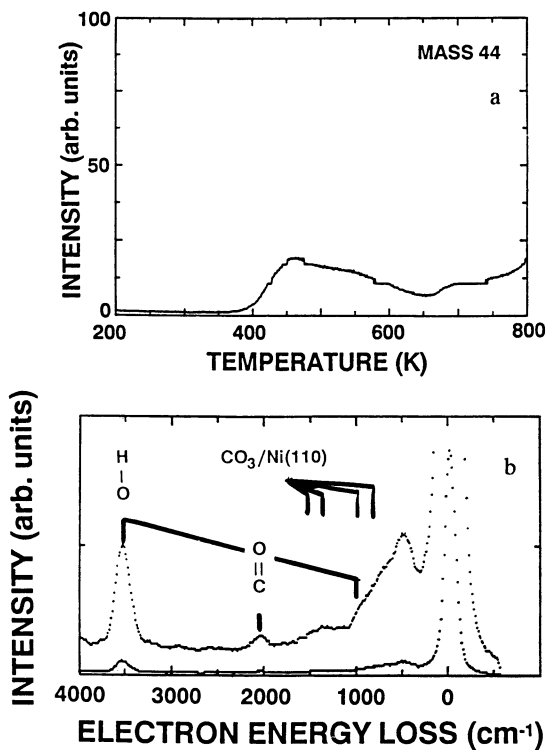
Figure 5. (a) CO_2 TPD and (b) HREELS data obtained subsequent to high-pressure reaction for 2 min in 0.5 Torr gas mixture (CO/O_2 = 1/32) at 600 K. The HREEL spectrum was measured at 100 K just prior to TPD. (Adapted from ref. 14.)
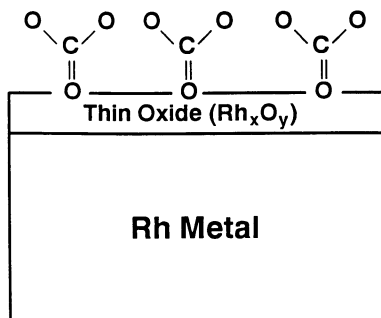
Figure 6. Model of the Rh surface under oxidizing conditions showing one of several possible bonding geometries for a proposed carbonate reaction intermediate. (Adapted from ref. 14.)

intermediate responsible for the CO_2 formation. This intermediate forms on an oxide that grows on the Rh surface due to the high O_2 partial pressures of the reactant mixture. Further evidence for this mechanism comes from the measured reaction kinetics (12). Notably, a change in mechanism is suggested by the significant change in the apparent activation energy for reaction under these highly oxidizing conditions. Furthermore, we find that the rate of reaction is now independent of the partial pressure of either reactant. Thus, we suggest that the overall rate of CO_2 formation is limited by the decomposition of this intermediate carbonate species. (It should be pointed out that Figure 6 is highly schematic and that the bonding geometry of the carbonate intermediate is just one of several possibilities that cannot be distinguished using our data.)

The results on Pt, Pd and Ir single crystal catalysts resemble in many ways the data just presented on Rh (13). In all cases, optimum reaction occurs on the reduced surfaces of these metals by a L-H reaction between CO molecules and O atoms, both chemisorbed on the metal surface. In the following, I discuss results for CO oxidation on Ru where we believe that the reaction mechanism may well be different from this.

The Nature of the Active Ru Surface. It is useful first to return to the Arrhenius data presented in Figures 1 and 2 in order to note that under similar reaction conditions, both the single crystal and supported Ru catalysts are considerably more active than any of the other metals. This result is in sharp contrast to the data obtained in low-pressure UHV measurements on single crystal metals (27) where Ru was found to be much less active, by as much as an order of magnitude than Pt, Pd, Rh and Ir. This apparent discrepancy can be rationalized by the kinetic and spectroscopic data to be discussed below.

In particular, Figure 7a (10) shows the CO_2 formation rate as a function of O_2 partial pressure. At low O_2 pressures, the rate increases dramatically with increasing pressure with kinetics much greater than first order. However, the rate saturates at moderate O_2 pressures and the kinetics become zero-order in O_2. As shown in Figure 7b, this saturation in the rate exactly corresponds to the highest oxygen levels recorded after reaction. Clearly, this behavior is in sharp contrast to the results on Rh (Figure 4) where an increase in oxygen levels correlated with a deactivation of the catalyst surface. In the case of Ru, there is now a one-to-one correspondence between the rate and the oxygen levels on the surface subsequent to high-pressure reaction. In fact based on calibration experiments (10,15), this Auger ratio indicates that the oxygen levels at saturation correspond to approximately 1 full monolayer, or 1 adsorbed oxygen atom for each Ru surface atom. Coverages of oxygen above 1/2 ML are not readily obtainable with typical UHV exposures. Furthermore, these results clearly demonstrate that lower coverages lead to significantly lower rates of reaction. As such, the low activity of Ru for CO oxidation in the UHV studies (27) are, in fact, compatible with the high-pressure results.

The nature and concentration of this surface oxygen species was further characterized by post-reaction LEED (15,16) and XPS (16). In the XPS studies, it was again found that the reaction rate directly correlates with the oxygen levels observed in these post-reaction analyses. LEED data were also obtained and either show (2x2) patterns for the lower oxygen coverages and reaction rates, or a (1x1) pattern for the highest coverages and rates. (Note that Ru(001) shows (2x2) LEED patterns at both 1/4 and 1/2 ML oxygen coverages (28). The pattern at 1/2 ML is composed of three independent domains of p(2x1) rotated by 120° with respect to each other.) The XPS and
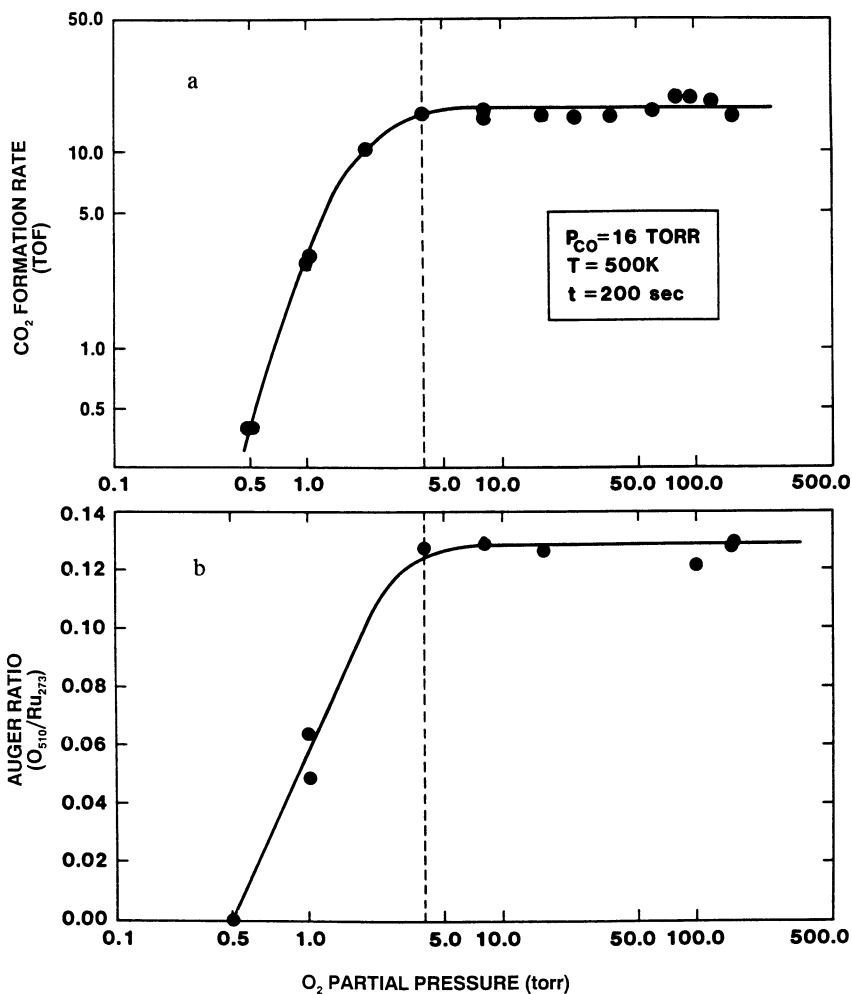
Figure 7. A comparison of the effect of O_2 partial pressure on (a) the rate of reaction, and (b) the level of surface oxygen detected by AES subsequent to reaction on Ru(001). P(CO) = 16 Torr, T = 500 K. (Reproduced from ref. 10. Copyright 1986 American Chemical Society.)

LEED results are essentially identical to those obtained by just dosing the Ru(001) surface to O_2 at room temperature in UHV. However, the results differ dramatically following a sample preparation procedure that likely led to more bulk-like oxidation. In this latter case, the LEED is much more complex, the oxygen content much higher, and the O(1s) binding energy is significantly lower. From the XPS data just described, the oxygen species observed after high-pressure reaction is clearly a chemisorbed oxygen and not an oxide-like oxygen, with a concentration equal to a monolayer in agreement with the previous Auger results. The (1x1) LEED pattern, possibly a result of a commensurate 1 ML oxygen overlayer, also supports this conclusion. On such a surface, there exist no readily available binding sites for CO except for those at possible defects in a commensurate overlayer. In fact, CO and CO_2 were not observed in post-reaction TPD. Before discussing this latter result in more detail, it is important to first demonstrate that the oxygen-covered surface is indeed the active surface for CO oxidation. This is important because although there is a good correlation between the reaction rates and oxygen levels (Figure 7), this does not guarantee the relevance of the correlation.

The Arrhenius data shown in Figure 8 (*10*) were obtained by first preparing a 1 ML oxygen-covered surface by carrying out a CO oxidation reaction under oxidizing conditions. After an Auger measurement to verify the oxygen coverage, the surface was exposed to pure CO in the reactor at various temperatures. The rates of CO_2 formation shown in Figure 8 were determined from an AES measurement of the drop in oxygen coverage assuming that the initial coverage was 1 ML. The solid line is an extrapolation of the steady-state rate of CO_2 formation (Figure 1) to the lower temperatures of these experiments. That these rates of reaction are identical demonstrates that the 1 ML oxygen-covered surface is the most active Ru surface for CO oxidation.

In-Situ FT-IRAS Studies of CO Oxidation on Ru. In the remaining, I would like to change the focus of this paper from a correlation of ex-situ surface analysis and kinetic data, to some recent work using in-situ fourier transform reflection absorption infrared (FT-IRAS) spectroscopy (*15*) to provide additional insight into the unique activity of oxygen-covered Ru. Specifically, we are looking at the carbon-oxygen stretch of adsorbed CO which is well known to be very sensitive to the strength of the bonding interaction of CO with the surface.

The FT-IRAS spectra illustrated in Figure 9 were obtained in-situ under the high-pressure reaction conditions shown. For reference the spectrum at the bottom (9f) was obtained in pure CO at 500 K. The feature with a C-O stretching frequency of 2048 cm^{-1} can be attributed to adsorbed CO on Ru(001) at near saturation coverages (*28*). As oxygen is added to the reactant mixture, this band disappears and a new peak grows in at somewhat higher frequency of about 2080 cm^{-1}. This latter feature can be readily assigned to CO coadsorbed with oxygen (*28*). The somewhat weaker bonding of CO to Ru in the presence of oxygen is the cause of the shift to higher wavenumbers. At still more oxidizing reaction conditions, the 2080 cm^{-1} feature begins to dissappear. Finally, at the highest O_2 partial pressures where, again, CO_2 formation rates are highest, no evidence for adsorbed CO in the spectra was observed (Figure 9a). If this reaction mixture is cooled from 500 K to room temperature, we see no change in the FT-IRAS spectrum. In fact, no evidence for adsorbed CO in either the FT-IRAS spectrum or in TPD was observed subsequent to pumping out the reactant mixture, cooling the crystal to 80 K and exposing the surface to CO. In terms of the results presented earlier on the characterization of this oxygen-covered surface, the lack of CO adsorption is not surprising since access
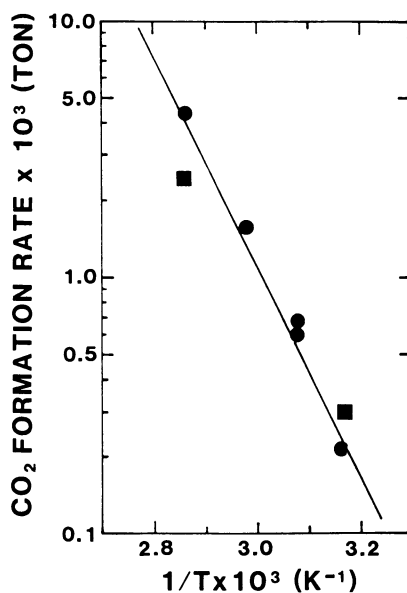
Figure 8. Rate of oxygen atom removal by high pressures of CO ($\blacksquare$, P(CO) = 16 Torr; $\bullet$, P(CO) = 8 Torr) from Ru(001). The surface was precovered with 1 ML of oxygen and the reaction rate followed by AES. The solid line is an extrapolation of the CO_2 formation rate from Figure 1. (Reproduced from ref. 10. Copyright 1986 American Chemical Society.)

of CO to the surface Ru atoms will be restricted by the 1 ML oxygen coverage. What is surprising and significant is that the CO oxidation reaction rates are highest on this surface where apparently no CO is directly interacting with the Ru surface atoms.

Reaction Mechanism on Ru(001). Let me quickly summarize the kinetic and spectroscopic results on Ru just presented. First of all, it was demonstrated that the Ru surface most active for CO oxidation is one that is covered with a full monolayer of chemisorbed oxygen atoms (Figure 7). In addition, kinetic data obtained in a titration of this oxygen-covered surface by CO (Figure 8) clearly show that this oxygen species is an active intermediate for the reaction. Thirdly, the reaction on the 1 monolayer oxygen-covered surface is zero-order in O_2 partial pressure (Figure 7), and first-order in CO pressure (*10*). Finally, I've just shown that although this is the most active surface, chemisorbed CO levels were below the detection limit of FT-IRAS and TPD, even at an adsorption temperature of 80 K.

The interpretation of these results is schematically illustrated in Figure 10. (A more detailed discussion is contained in the original literature (*15*).) Instead of the L-H mechanism that is now well established for reaction on the other transition metal surfaces that we've studied, we believe these data are strongly suggestive of an Eley-Rideal (E-R) process in which gas-phase CO reacts directly, or perhaps more likely through a very weakly-adsorbed precursor with the chemisorbed oxygen atoms. In either case, the data for reaction on the fully oxygen-covered surface where reaction rates are highest are not readily accounted for by the L-H mechanism in which CO *chemisorbed to the Ru surface* is an active intermediate. However, we recognize that these results do not constitute proof of an E-R mechanism. More direct evidence should come from, for example, a determination of the lifetime of the *reacting* CO molecules (*29*). From the fact that CO does not chemisorb even at 80 K, one can estimate that this residence time is less than 2×10^{-12} seconds for reaction at the temperature and pressure conditions we have used (*5c*). It would still be desirable to directly measure this lifetime in a molecular-beam experiment. This has not been done to date.

Summary and Conclusions

In this paper, the utility of a number of post-reaction UHV surface analysis probes for studying catalytic reactions has been demonstrated. The favorable comparison between the kinetic data on the single crystal and realistic supported catalysts demonstrates the relevance of the spectroscopic data obtained on the model systems. Specifically in the case of CO oxidation, the results on Rh, and on Pt, Pd and Ir, are clearly compatible with the now well accepted Langmuir-Hinshelwood model for the reaction mechanism on the reduced surfaces of these metals. However, important information about the deactivation of these surfaces under oxidizing conditions was also obtained. In this case, the spectroscopic and kinetic data suggest an altered mechanism on the oxidized surfaces of these metals which involves the rate-limited decomposition of a strongly bound carbonate-like intermediate. Finally, the possibility of the operation of the Eley-Rideal mechanism on Ru surfaces is suggested by the dramatically altered kinetics observed in this case. Spectroscopic data obtained in-situ by FT-IRAS supports this conclusion.

CO + O$_2$ / Ru(001)
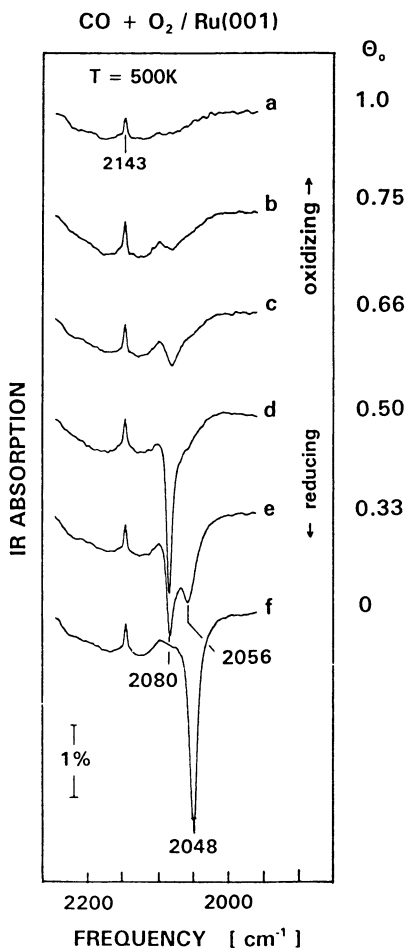
Figure 9. FT-IRAS vibrational spectra of the C–O stretching region during steady-state CO oxidation reaction at 500 K on Ru(001) for constant partial pressure of CO (2.5 Torr) and various oxygen partial pressures (in Torr): (a) 5.0; (b) 2.5; (c) 1.0; (d) 0.1; (e) 0.05; and (f) 0.0. Oxygen surface coverages, determined by AES, are shown at the right-hand side of the panel. (Adapted from ref. 5c.)
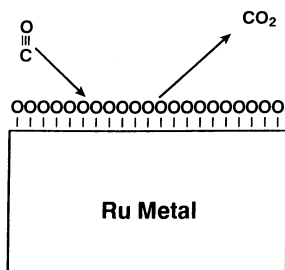
Figure 10. Schematic model of the proposed Eley-Rideal mechanism for CO oxidation on fully oxygen-covered Ru(001).

Literature Cited

1. Zaera, F.; Gellman, A. J.; Somorjai, G.A. *Acc. Chem. Res.* **1986**, *19*, 24.
2. (a) Goodman, D. W. *Ann. Rev. Phys. Chem.* **1986**, *37*, 425. (b) Goodman, D. W.; Houston, J. E. *Science* **1987**, *236*, 403. (c) Sault, A. G.; Goodman, D. W. *Adv. Chem. Phys.* **1989**, *76*, 153.
3. Campbell, C. T. *Adv. Catal.* **1989**, *36*, 1.
4. Chabal, Y.J.; Christman, S.B.; Burrows, V.A.; Collins, N.A.; Sundaresan, S. In *Kinetics of Interface Reactions*; Grunze, M.; Kreuzer, H.J., Eds.; Springer-Verlag: New York, 1987; pp 285-295, and references therein.
5. Hoffmann, F.M.; Robbins, J.L. (a) *J. Elect. Spectrosc. Rel. Phenom.* **1987**, *45*, 421. (b) In *Proceedings of the Ninth International Congress on Catalysis*; Phillips, M.J.; Ternan, M., Eds.; The Chemical Institute of Canada: Ottawa, 1988, Vol. 3; pp 1144-1151. (c) Hoffmann, F.M.; Weisel, M.D.; Peden, C.H.F. *J. Elect. Spectrosc. Rel. Phenom.* **1990**, *54/55*, 779.
6. Hegedus, L.L.; Gumbleton, J.J. *CHEMTECH* **1980**, *October*, 630.
7. Taylor, K.C. *CHEMTECH* **1990**, *September*, 551.
8. Kummar, J.T. *J. Phys. Chem.* **1986**, *90*, 4747.
9. Engel, T.; Ertl, G. *Adv. Catal.* **1979**, *28*, 1.
10. Peden, C.H.F.; Goodman, D.W. *J. Phys. Chem.* **1986**, *90*, 1360.
11. Peden, C.H.F.; Goodman, D.W.; Blair, D.S.; Berlowitz, P.J.; Fisher, G.B.; Oh, S.H. *J. Phys. Chem.* **1988**, *92*, 1563.
12. Peden, C.H.F.; Berlowitz, P.; Goodman, D.W. In *Proceedings of the Ninth International Congress on Catalysis*; Phillips, M.J.; Ternan, M., Eds.; The Chemical Institute of Canada: Ottawa, 1988, Vol. 3; pp 1214-1221.
13. Berlowitz, P.J.; Peden, C.H.F.; Goodman, D.W. *J. Phys. Chem.* **1988**, *92*, 5213.
14. Peden, C.H.F.; Houston, J.E. *J. Catal.* **1991**, *128*, 405.
15. Peden, C.H.F.; Goodman, D.W.; Weisel, M.D.; Hoffmann, F.M. *Surf. Sci.* **1991**, *253*, 44.
16. Peden, C.H.F.; Houston, J.E. in preparation.
17. (a) Oh, S.H.; Fisher, G.B.; Carpenter, J.E.; Goodman, D.W. *J. Catal.* **1986**, *100*, 360. (b) Oh, S.H.; Eickel, C.C. *J. Catal.* **1991**, *128*, 526.
18. (a) Cant, N.W.; Hicks, P.C.; Lennon, B.S. *J. Catal.* **1978**, *54*, 372. (b) Cant, N.W. *J. Catal.* **1980**, *62*, 173.
19. Kiss, J.T.; Gonzalez, R.D. *J. Phys. Chem.* **1984**, *88*, (a) 892; (b) 898. (c) Saymeh, R.A.; Gonzalez, R.D. *J. Phys. Chem.* **1986**, *90*, 622.
20. Harold, M.P.; Garske, M.E. *J. Catal.* **1991**, *127*, 553.
21. Landry, S.M.; Dalla Betta, R.A.; Lu, J.P.; Boudart, M. *J. Phys. Chem.* **1990**, *94*, 1203.
22. Baiker, A.; Gasser, D.; Lenzner, J.; Reller, A.; Schlogl, R. *J. Catal.* **1990**, *126*, 555.
23. Vorontsov, A.V.; Kasatkina, L.A. *Kinet. Catal.* **1981**, *21*, 932.
24. (a) Dubois, L.H.; Somorjai, G.A. *Surf. Sci.* **1980**, *91*, 514. (b) Crowell, J.E.; Somorjai, G.A. *Appl. Surf. Sci.* **1984**, *19*, 73.
25. Stuve, E.M.; Madix, R.J.; Sexton, B.A. *Chem. Phys. Lett.* **1982**, *89*, 48.

26. Lindner, H.; Rupprecht, D.; Hammer, L.; Muller, K. *J. Electron. Spectrosc. Relat. Phenom.* **1987**, *44*, 141.
27. Savchenko, V.I.; Boreskov, G.K.; Kalinkin, A.V.; Salanov, A.N. *Kinet. Catal.* **1984**, *24*, 983.
28. Hoffmann, F.M.; Weisel, M.D.; Peden, C.H.F. *Surf. Sci.* **1991**, *253*, 59.
29. Campbell, C.T.; Ertl, G.; Kuipers, H.; Segner, J. *J. Chem. Phys.* **1980**, *73*, 5862.

Chapter 10

Molecular Ingredients of Platinum–Tin Reforming Catalysts

Y. Zhou and S. M. Davis

Exxon Research and Development Laboratories, P.O. Box 2226, Baton Rouge, LA 70821

A series of model Pt/SnO_2, $PtSn/SiO_2$, and $PtSn/Al_2O_3$ reforming catalysts was investigated using X-ray photoemission, electron microscopy, oxygen chemisorption, and hexane reaction studies. Extensive reduction of tin to the metallic state (and/or intermetallic compounds) was detected with Pt/SnO_2 and $PtSn/SiO_2$, and the resulting catalysts were characterized by low catalytic activity. By contrast, reduced tin could not be detected in $PtSn/Al_2O_3$ catalysts with Sn/Pt atomic ratios less than two. The presence of unreduced tin in $PtSn/Al_2O_3$ lowered hexane conversion activity and changed the product distribution in favor of isomerization and C_5-cyclization relative to aromatization and hydrogenolysis. We propose that these changes result from a strong Pt-SnOx interaction which operates to provide a high density of isolated reforming sites which contain few contiguous platinum atoms.

Catalysts containing platinum and tin dispersed on alumina are employed extensively in petroleum reforming and have recently been the subject of many investigations (1-12). While it is now well established that the reducibility of tin is strongly dependent on catalyst preparation and the nature of the support, it remains unclear how tin modifies platinum on an atomic scale to improve reforming selectivity and/or activity maintenance. Recent EXAFS investigations by Meitzner et. al (1) together with photoemission studies by Sexton (2) and Schwank (3) and coworkers indicate convincingly that little if any tin is reducible to the metallic state under the activation conditions normally applied with commercial $PtSn/Al_2O_3$ catalysts. These findings complement the early investigations of PtSnx intermetallic compounds by Dautzenberg and Sachtler (4) which showed poor catalytic activities for skeletal rearrangement reactions, especially with tin rich compounds such as Pt_2Sn_3 and $PtSn_2$.

To further clarify the nature of the interactions between dispersed platinum and tin, we have combined surface characterization and hexane reaction studies

using a series of model, monofunctional Pt/SnO_2, $PtSn/SiO_2$, and $PtSn/Al_2O_3$ catalysts. Our results reveal substantial differences in catalytic behavior depending on whether or not tin is present in the metallic state. Reduced tin in Pt/SnO_2 and $PtSn/SiO_2$ acts as a potent posion for all skeletal rearrangement reactions, whereas non-metallic tin in $PtSn/Al_2O_3$ modifies the selectivity of platinum in favor of isomerization and C_5-cyclization relative to hydrogenolysis and aromatization. The latter changes appear to result from strong Pt-SnOx interactions which produce highly dispersed reforming sites with few contiguous platinum atoms.

Experimental

Combined photoemission and hexane reaction studies were carried out using a Leybold UHV apparatus equipped with a microreactor that has been described previously (13). In most experiments, a fresh (ca. 100 mg) catalyst sample mounted on a copper (or BN) holder was activated by heating in flowing H_2 at atmospheric pressure at 7K/min to 708K. After about 10 minutes, the sample was cooled and transferred to the analysis chamber for XPS measurements which were carried out with computer controlled data aquisition, Mg(Ka) and/or Al(Ka) excitation, and an analyzer pass energy of 50 eV. Binding energies were referenced to the Si(2p) and Al(2p) lines of the supports at 103.4 and 74.7 eV, respectively. When appropriate, tin chemical state distributions were estimated using XPS peak fitting software provided by Leybold. After the XPS measurements, the sample was returned to the microreactor where hexane reforming was investigated under differential flow conditions (maximum conversion <4%) at atmospheric pressure and 708K with a H_2/C_6 molar feed ratio of 6.0. The samples were heated under flowing H_2 to 708K prior to introducing hexane, and the products of the reforming reaction were monitored on-line using a gas chromatograph equipped with carbowax and chromosorb columns that was calibrated using certified CH_4/N_2 mixtures.

Dynamic, volumetric oxygen uptake studies were carried out using a separate chemisorption apparatus employing a 100-200 mg sample charge, a TCD detector, 2% O_2/He, and activation procedures similar to those noted above. Electron microscopy studies were carried out using a JOEL 200 CX instrument using samples derived from the XPS/reaction studies.

A summary of the catalysts investigated is provided in Table I. SnO_2 was produced by hydrolyzing aqueous $SnCl_2$ with NH_4OH, followed by filtration, drying, and air calcination at 923K for 4 hours. Supported tin materials were similarly produced by impregnating Cabosil or high purity (reforming-grade) Cyanamid gamma-Al_2O_3 60/150 mesh powders with aqueous $SnCl_2$ to the point of incipient wetness followed by drying and air calcination at 923K. Platinum was subsequently incorporated by impregnation of aqueous H2PtCl6, drying, and air calcination at 673K for four hours. Elemental compositions were determined by X-ray flourescence. It is notable that residual chloride in the alumina based catalysts was less than about 0.3 wt%. These low chloride loadings together with the modest 708K hexane reaction temperature were deliberately chosen to

emphasize metal site reactions with minimal interference from acid-site reactions associated with the alumina support that become significant at higher temperatures above 750K (14).

Results and Discussion

Tin Photoemission Studies. Tin(3d) binding energies and chemical state distributions measured after H_2-activation at 708K are summarized in Table I. Figure 1 shows representative Sn(3d) XPS data for several materials. Following the work of Wertheim (*15*) which indicated that the +2 and +4 oxidation states of tin are not distinguishable by XPS, we have simply grouped tin into "oxidized" (+2/+4 oxidation states) and "reduced" (metallic state) components. In partially reduced SnO_2, the Sn(3d5/2) peak maxima corresponding to oxidized and reduced tin are apparent at 486.4 and 484.5 eV with no indication for other features. While partial reduction of SnO2 (ca. 7%) was detected in the absence of platinum, the extent of tin reduction was increased substantially to to 30-40% with 5% Pt/SnO_2.

As a consequence of charge-induced broadening, the XPS resolution obtained with $PtSn/SiO_2$ and $PtSn/Al_2O_3$ catalysts was of lower quality than that recognized with Pt/SnO_2. Nevertheless, significant differences in tin reducibility were easily distinguished depending on the support and the presence or absence of platinum. In the absence of platinum, no reduction was detectable for tin dispersed on both silica and alumina. However, for 5%Pt-5%Sn/SnO_2, most (ca. 70%) of the tin was easily reduced following H_2-treatment at 708K. Using measured XPS intensities for the $PtSn/SiO_2$ catalyst simply corrected for photoionization cross sections, we estimate that the atomic ratio of reduced tin to platinum in this catalyst is about 1.1:1.

By contrast, reduced tin could not be detected (<10%) in any of the $PtSn/Al_2O_3$ catalysts with Pt and Sn loadings in the range of 0-5 wt%. NO INCREASE in tin reducibility was noted when a 0.3%Pt-0.4%Sn/Al_2O_3 catalyst was subjected to more severe activation at 793K for 2 hours. In all cases, the Sn(3d) XPS lineshapes for $PtSn/Al_2O_3$ catalysts after in situ H_2-treatment were essentially identical to those for unreduced catalysts.

Our findings for the states of tin present in $PtSn/SiO_2$ and $PtSn/Al_2O_3$ are in excellent agreement with earlier XPS studies by Sexton (*2*) and Schwank (*3*) and coworkers as well as the EXAFS results reported by Meitzner (*1*). Specifically, these workers previously noted that tin on silica was easily reducible in the presence of platinum, whereas tin oxides on alumina could not be reduced to the metallic states with or without platinum. While Davis and others (*9-11*) have reported evidence for partial tin reduction in $PtSn/Al_2O_3$ catalysts produced using different procedures, there appears to be overwhelming evidence that alumina has a special ability to stabilize oxidized tin in $PtSn/Al_2O_3$ catalysts prepared using conventional impregnation methods. A likely explanation for this behavior is based on the model proposed by Burch et al (*6,7*) which suggested the formation of surface stabilized "tin-aluminate" like species.

Table I. Properties of PtSn Catalysts Following H$_2$-Treatment at 708 K

Composition	Sn(3d5/2) XPS Binding Energies	Reduced Tin (%)	O$_2$-Uptake (O/Pt atom ratio)	
			1st Cycle	2nd Cycle
SnO$_2$	486.4/484.5	5-10	--	--
5%Pt/SnO$_2$	486.4/484.7	30-40	--	--
5%Sn/SiO$_2$	486.5	None	--	--
5%Pt/SiO$_2$	--	--	0.30	0.23
5%Pt-5%Sn/SiO$_2$	484.6	60-70	0.22	0.16
5%Sn/Al$_2$O$_3$	486.4	None	--	--
5%Pt/Al$_2$O$_3$	--	--	1.31	1.14
5%Pt-1.9%Sn/Al$_2$O$_3$	486.4	None	1.46	0.93
5%Pt-5%Sn/Al$_2$O$_3$	486.5	None	1.72	0.82
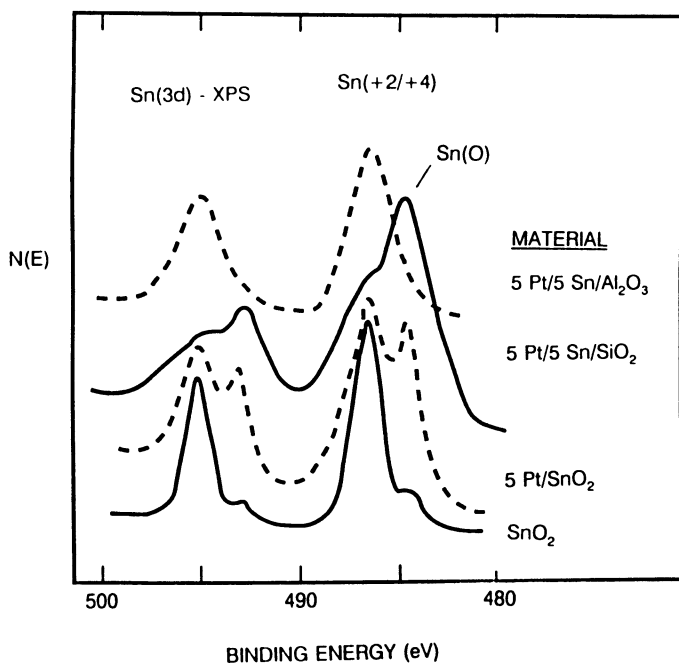
Figure 1. Tin(3d) XPS results for several materials following H2-reduction at 708 K.

Hexane Conversion Studies. Rates and product distributions for hexane conversion over Pt/SiO_2, $PtSn/SiO_2$, and $Pt/SnO2$ at 708K are compared in Figure 2. Platinum only on silica displayed significant rates for hexane conversion to benzene (Bz) via aromatization, C_1-C_5 alkanes via hydrogenolysis, and 2-methylpentane (2MP) and methylcyclopentane (MCP) via isomerization and C_5-cyclization. By contrast, $PtSn/SiO2$ displayed catalytic activity that was lowered by over an order of magnitude. The product distribution was also changed with only trace levels of 2MP and MCP. Platinum dispersed on tin oxide did not exhibit measurable activity (rate< 10^{-9} mole/gr sec).

These results provide striking evidence that REDUCED tin acts as a potent poison for hydrocarbon skeletal rearrangement reactions catalyzed by platinum. As discussed below, the magnitude of these changes is much too large to be simply explained by reduced platinum dispersion in $PtSn/SiO_2$. While these results were initially surprising, they appear to be in good agreement with the work reported by Dautzenberg and Sachtler (4) which showed that intermetallic $PtSnx$ compounds were significantly less active for hydrocarbon skeletal rearrangement as compared to bulk platinum. Catalytic activity decreased with increasing tin content in the sequence $Pt_3Sn > Pt_2Sn_3 > PtSn_2$.

Very different catalytic behavior was observed with $PtSn/Al_2O_3$ catalysts with variable composition as indicated by the rates and selectivities shown in Figure 3. In this case, the addition of tin selectively poisoned hydrogenolysis and aromatization, whereas rates of isomerization and C_5-cyclization showed only small variations. As a consequence, selectivity for the latter reactions was improved substantially in the tin containing catalysts. As discussed below, these changes appear to result with little or no change in overall platinum dispersion. In addition to the altered selectivities, the tin containing catalysts displayed reduced rates of deactivation. For example, while the hexane conversion activity of Pt/Al_2O_3 was reduced by about 50% after 100 minutes reaction time, the $PtSn/Al_2O_3$ catalysts showed less than a 20% decrease in activity under identical conditions. We have previously shown that this deactivation is associated with gradual build-up of carbonaceous deposit (16). Hydrogenolysis product distributions were roughly similar for all catalysts with roughly equimolar amounts of C_1-C_5 products.

These changes in catalytic behavior indicate that oxidized tin strongly alters the reforming chemsitry of platinum on alumina. This modification must occur through a mechanism other than intermetallic formation, as XPS data showed no evidence for reduced tin in $PtSn/Al_2O_3$ catalysts. A strong interaction between Pt and $SnOx$ ($x \approx 1$) is clearly implicated.

Oxygen Chemisorption and Electron Microscopy. To better establish platinum dispersion in the different catalysts, a "two-cycle" oxygen uptake test was developed which involved catalyst activation, first cycle oxygen uptake at 298K, hydrogen titration of chemisorbed oxygen on platinum at 298K, and second cycle oxygen uptake at 298K. Table I summarizes oxygen uptakes (expressed as oxygen atoms per platinum atom) in both adsorption cycles. In this test, the

REDUCED TIN POISONS PLATINUM
● 1 ATM, 708 K, H2/HC=6

C6 CONVERSION RATE (mole/gr sec x 10E7)
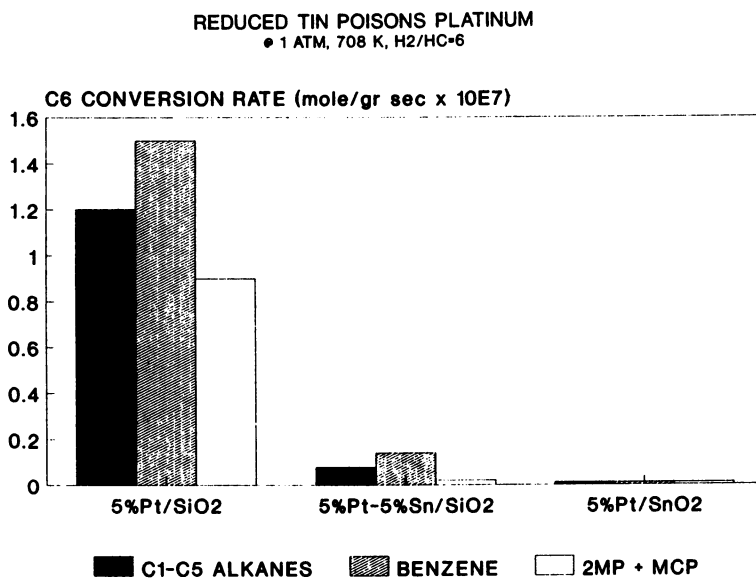
Figure 2. Rates and product distributions for hexane conversion over Pt/SiO2, PtSn/SiO2, and Pt/SnO2.

OXIDIZED TIN MODIFIES SELECTIVITY
● 1 ATM, 708 K, H2/C6=6

C6 CONVERSION RATE (mole/gr sec x 10E6)
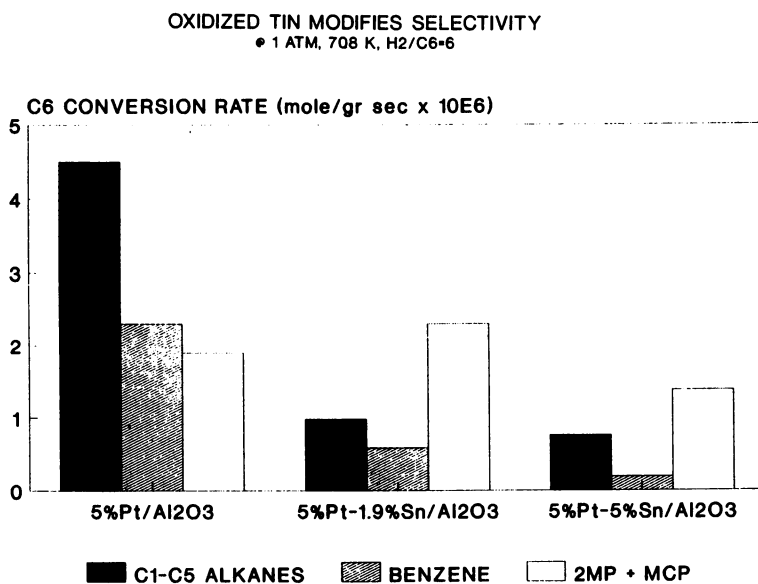
Figure 3. Rates and product distributions for hexane conversion over Pt/Al2O3 and PtSn/Al2O3.

first oxygen adsorption cycle was intended to measure BOTH tin and platinum adsorption sites produced during H_2-activation. This is confirmed by the large uptakes which greatly exceed the platinum content of the PtSn/Al_2O_3 catalysts. Since chemisorbed oxygen on platinum can be titrated with H_2 at 298K (17), the second adsorption cycle was designed to selectively count platinum surface sites. While it is conceivable that this measurement may be complicated by particle restructuring during successive adsorption measurements, we believe that this test represents a simple and convenient approach to gain semi-quantitative insight regarding the density of exposed platinum sites in the PtSn/Al_2O_3 catalysts. This possibility is supported by the data for Pt-only/Al_2O_3 where uptakes were similar in both the first and second adsorption cycles. The large uptakes detected in the first adsorption cycle with PtSn/Al_2O_3 may reflect conversion of Sn(II) to Sn(IV) or, more likely, replacement of Pt-Sn bonds with Sn-O bonds.

Comparison of the oxygen uptake data for PtSn/Al_2O_3 catalysts suggests platinum was highly dispersed in all cases (eg. O/Pt>0.8). By contast, the Pt/SiO_2 and PtSn/SiO_2 catalysts displayed lower apparent dispersions in the range of about 15-25%. The smaller platinum dispersion of the PtSn/SiO_2 material likely contributes to the reduced activity of this catalyst, although the O_2-uptake difference clearly appears inadequate to account for the 15-fold difference in hexane conversion rates.

Electron microscopy studies using prereduced Pt/Al_2O_3 catalysts with 0-1.9% tin loadings confirmed that platinum was very highly dispersed with an average particle size no greater than 10-12 A; eg. no larger particles were detectable. A small number of larger particles with sizes in the range of 15 to 25 A was detected with 5%Pt-5%Sn/Al_2O_3, although the average particle size appeared to remain quite small. These results are in excellent agreement with the high dispersions estimated from O_2-uptake and clearly confirm that the altered catalytic behavior of the tin containing catalysts is not associated with significant changes in apparent platinum dispersion.

Model for the Working PtSn/Al_2O_3 Reforming Catalyst. The PtSn/Al_2O_3 catalysts investigated here displayed high platinum dispersion, little or no reduced tin, and sharply altered hexane conversion selectivities as compared to Pt/Al_2O_3. The observed changes in selectivity are reminiscent of those reported previously for bimetallic PtAu alloy catalysts when investigated under similar reaction conditions (18-20). Specifically, PtAu catalysts exhibited reduced rates of hexane hydrogenolysis and aromatization combined with improved selectivities for isomerization and methylcyclopentane formation. In the PtAu case, it has been clearly established that the altered catalytic behavior results from an ensemble effect wherein the density of multiatomic platinum surface sites with several contiguous platinum atoms is reduced. Sites with several contiguous platinum atoms are required for aromatization and hydrogenolysis, whereas isomerization and MCP formation are catalyzed readily with smaller platinum ensembles (18).

We propose that a similar ensemble effect occurs in PtSn/Al_2O_3 catalysts that is characterized by a strong Pt-SnOx interaction which operates to provide

a high density of "isolated" platinum sites with fewer contiguous platinum surface atoms as compared to the sites found in Pt/Al_2O_3. Strong supporting evidence for this model is provided in the earlier EXAFS studies by Meitzner et al (*3*). Namely, comparison of the Pt-Pt coordination numbers for 1.1%Pt-0.6%Sn/Al_2O_3 and 1.1%Pt/Al_2O_3 (3.2 and 7.0, respectively) showed that the number of platinum nearest neighbors was reduced significantly in the PtSn catalyst. Both catalysts exhibited high overall platinum dispersion as measured by H_2-chemisorption similar to the O_2-uptake results obtained with our catalysts. While we cannot rule out a Pt-SnOx electronic interaction and/or more subtle effects associated with surface hydrogen availablity as possible contributors to the altered catalytic behavior of the tin containing materials, there appears to be good evidence for platinum site isolation, and...by analogy to PtAu...this site isolation appears adequate to simply explain the observed changes in hexane conversion selectivity.

Differences in deactivation behavior for $PtSn/Al_2O_3$ versus Pt/Al_2O_3 also appear consistent with this site isolation model. The tin-containing catalysts displayed reduced deactivation rates, and the magnitude of these changes was similar to that noted previously for PtAu and sulfided PtRe catalysts (*21*). Presumably site isolation tends to reduce the density of strongly bound carbonaceous deposits with high Pt-organic bond multiplicity (*16*).

The situation for $PtSn/SiO_2$ and Pt/SnO_2 is very different and appears to reflect formation of low activity intermetallic PtSnx compounds. The presence of these compounds in similarly prepared $PtSn/SiO_2$ catalysts was carefully demonstrated in earlier EXAFS (*3*) and powder X-ray diffraction (*10,22*) studies. Evidence for these compounds in our studies was provided by Pt(4f7/2) binding energies of 71.4 and 71.8 eV that were measured for $PtSn/SiO_2$ and Pt/SnO_2, respectively. These XPS binding energies were significantly larger than those (ca. 71.0 eV) obtained with Pt/SiO_2 and bulk platinum and compare favorably with the 71.7 eV Pt(4f) binding energy recently reported for Pt_3Sn by Hoflund et al (*23*).

In summary, the altered catalytic behavior of tin-modified Pt/Al_2O_3 appears to reflect the presence of isolated Pt-reforming sites that are stabilized by strong interactions with a non-reducible surface tin oxide phase. The isolated sites with few contiguous platinum atoms favor isomerization and C_5-cyclization reactions relative to aromatization and hydrogenolysis.

Acknowledgments

Literature Cited

1.   Meitzner, G.; Via, G.H.; Lytle, F.W.; Fung, S.C.; and Sinfelt, J.H., J. Phys. Chem., 92, 2925 (1988).
2.   Sexton, B.A.; Hughes, A.E.; and Foger, K., J. Catal., 88, 466 (1984).

3.   Balakrishan, K.; and Schwank; J., J. Catal., 127, 287 (1991).
4.   Dautzenberg, F.M.; Helle, J.N.; Biloen, P.; and Sachtler, W.M.H., J. Catal., 63, 119 (1980).
5.   U.S. Patent No. 3,577,474 (1971); U.S. Patent No. 3,692,501 (1972).
6.   Burch, R., J.Catal., 71, 348 (1981).
7.   Burch, R.; and Garla, L.C., J. Catal., 71, 360 (1981).
8.   Lieske, H.; and Volter, J., J. Catal., 90, 96 (1984).
9.   Adkins, S.R.; and Davis, B.H., J. Catal., 89, 371 (1984).
10. Srinivisan, R.; DeAngelis, R.J.; and Davis, B.H., J. Catal., 106, 449 (1987).
11. Stencel, J.M.; Goodman, J.; and Davis, B.H., Proc. 9th Int. Congr. Catal., Calgary, 1988, Vol. 3, pg 1291.
12. Muller, A.C.; Engelharrd, P.A.; and Weisang, J.E., J. Catal., 56, 65 (1979).
13. Davis, S.M.; and Somorjai, G.A., Bull. Soc. Chim. France, 1985, 271 (1985).
14. McVicker, G.B.; Kramer, G.M.; and Ziemak, J.J., J. Catal., 83, 286 (1983).
15. Lau, C.L.; and Wertheim, G.K., J. Vac. Soc. Technol., 15, 622 (1978).
16. Davis, S.M.; and Somorjai, G.A., J. Catal., 77, 439 (1982).
17. Benson, J.E.; and Boudart, M., J. Catal., 4, 704 (1965).
18. Sachtler, J.W.A.; and Somorjai, G.A., J. Catal., 81, 77 (1983).
19. Clarke, J.K.A.; Manninger, T.; and Baird, T., J. Catal., 54, 230 (1978).
20. van Schaik, J.R.H.; Dessing, R.P.; and Ponec, V., J. Catal., 38, 273 (1975).
21. Sinfelt, J.H., Bimetallic Catalysts, J. Wiley & Sons, New York, 1984.
22. Behal, S.K.; Disko, M.M.; Ayer, R.; Scanlon, J.; Meitzner, G.; Fung, S.C.; Sinflet, J.H.; and Via, G.H.; Proc. 46th Meet. Elect. Micr. Soc.; San Francisco, 1988, pg. 718.
23. Gardner, S.D.; Hoflund, G.B.; and Schryer, D.R., J. Catal., 119, 179 (1989).

Chapter 11

Controlled-Atmosphere Photoelectron Spectroscopy

M. Grunze[1], Daniel J. Dwyer[2], M. Nassir[2], and Y. Tsai[2]

[1]Angewandte Physikalische Chemie, Universität Heidelberg, INF 253, 6900 Heidelberg, Germany
[2]Department of Chemistry and Laboratory for Surface Science and Technology, University of Maine, Orono, ME 04469-0107

In this article we describe an x-ray photoelectron spectrometer capable of measuring surface compositions *in situ* under controlled gas atmospheres of pressures up to 1 mbar. The instrument is a UHV capable surface analysis apparatus, which allows the application of high pressures by inserting a movable aperture between the sample and the input lens system of the electrostatic hemispherical analyzer. We describe the basic design of the instrument, its capability to measure gas phase and surface spectra, and briefly review the methods to determine the pressure at the location of photoelectron ejection. The application of the instrument in catalytic model reactions is demonstrated by examples referring to the reduction of nickel oxide as a function of temperature and pressure. We will emphasize the unique aspect of the instrument compared to molecular beam methods, which is the capability to perform experiments in a steady state equilibrium between gas phase and adsorbate phase.

Pressures exceeding 10^{-5} mbar are not recommended in typical x-ray photoelectron spectrometers for surface science because of the sensitivity of the electron detector to higher pressures and the attenuation of the signal owing to inelastic scattering of electrons in the gas phase. However, gas phase photoelectron spectra and spectra of liquids are measured routinely in specially designed instruments (1-3). Crucial for these experiments is a pressure gradient of approximately five orders of magnitude between the location of photoelectron ejection and the input lens of the analyzer. This can be achieved either by applying molecular beam techniques or by differentially pumped high pressure cells in which the gases or liquids are contained. The incident photon flux passes through a defined volume of the gas or liquid from which photoelectrons are emitted through a small aperture into the detector system . However, these instruments are specifically designed for high pressure applications and are

therefore not suitable for experiments on reactive metal single crystal surfaces under ultra-high vacuum conditions.

Joyner et al. (4) designed a commercially available instrument where the sample is located within a high-pressure gas cell to obtain *in situ* XPS spectra from surfaces exposed to higher pressures. A similar approach, where the solid surface is contained in a small high pressure volume was pursued by Littrell et al. (6) to overcome the pressure limitations of typical surface science studies. In both instruments pressures in the 10^{-1} mbar range could be applied and the pressures were measured by a Pirani gauge in the gas cell (4,5) or by measuring the background pressure in the UHV chamber which is pumping the high pressure attachment (6). However, since the pressures at the surfaces were not determined directly, the true pressures at the location of photoelectron ejection are uncertain because of the differential pumping of the cells through the electron emission apertures. Further, contamination of the solid substrates in the high pressure ambients could not be ruled out due to the use of water-cooled oil diffusion pumps (4,5).

An instrument which allows application of high pressures at the same sample position where UHV data can be recorded and where the sample could be characterized by auxiliary methods was described by Ruppender et al. (7). Contrary to the design concepts of the other high pressure photoelectron spectrometers, this was achieved by inserting a differentially pumped aperture incorporated into a gate valve mechanism between sample surface and analyzer input lens. When this instrument is not used as a controlled atmosphere photoelectron spectrometer, it is a true UHV system allowing the application of standard surface analysis techniques to the sample.

In this article, we will review the performance and summarize the calibration procedures of the instrument described previously (7). Following the review of the design concepts and performance, we will discuss experiments relating to the reduction of oxide phases on nickel single crystal surfaces by hydrogen and methane which demonstrates the abilities of the instrument to follow in real time the kinetics of surface reactions.

Design Concepts, Pressure Calibration and Performance

The instrument is designed to allow the combination of several UHV surface analysis techniques to be applied and to perform XPS experiments at pressures up to 1 mbar. Figure 1 shows a schematic of the CAPES instrument. The sample is attached to a horizontally mounted movable sample rod with heating and cooling capabilities. As a sample rod either a commercial transfer rod (Leybold SRT 11) or alternatively a custom-built rod can be used. The mechanism by which the rod is moved and manipulated is a standard Leybold design. The chamber containing the surface analysis techniques (XPS, UPS, ISS, AES) is of cylindrical shape, where the hemispherical electron energy analyzer (Leybold EA11) is mounted on the top of the cylinder. The cylindrical chamber itself is pumped with a liquid nitrogen cooled titanium sublimation pump and a 300 l/s turbo molecular pump. At the top of the cylindrical chamber a second cryo pump (900 l/s) and on top of the analyzer a third cryo pump (1500 l/s) are attached. A movable aperture inserted into a drawer-type mechanism can be introduced between the sample surface and the input lens of the hemispherical analyzer. This aperture system is differentially pumped with a 1500 l/s

cryopump to absorb the high flux of gases (up to 1 mbar 1/s) when high pressures are applied to the sample surface. Differential pumping of the detector in the analyzer is thus achieved by the aperture itself, the 900 l/s cryo pump in the upper part of the chamber, and the 1500 l/s pumped on top of the hemispherical analyzer. As described in detail in reference 7, the pumping was optimized to establish five orders of magnitude pressure difference between the samples and the analyzer when the pressure above the sample is 1 mbar.

The x-ray source itself is pumped with an ion pump and is sealed against the high pressure ambient with a gas-tight 1.5 μm thick aluminum foil. Thus, by retracting the aperture system, the design of the instrument allows application of standard UHV techniques without compromises, but also enables the application of high pressure ambients to the sample surface while investigating the surface composition by x-ray photoelectron spectrometry.

Under high vacuum and ultra-high vacuum conditions, pressures were measured with a Bayard-Alpert type ionization gauge. When higher pressures are applied the pressure is measure with a spinning ball rotor gauge (VISCOVAC) and/or with a Pirani gauge mounted within the high pressure zone approximately 19 cm from the aperture. Of course, the pressures measured with these devices are not necessarily identical to the ambient pressure at the location of photoelectron ejection due to the high differential pumping of the aperture system.

Although pressures up to 2 mbar can be applied to the sample in the high pressure zone; due to gas phase absorption of the photoelectrons and charging effects due to gas phase ionization, the practical maximum pressure is between 0.5 and 1 mbar (7). Accordingly, the size of the apertures in the differential pumping arrangement have been optimized for this pressure and for maximum XPS sensitivity. The first aperture has the dimensions 5.48 x 0.89 mm, the second aperture in the drawer mechanism is of the size 8 x 2 mm. With this aperture system, the pressure ratio between the analyzer and the high pressure chamber is determined by Knudsen flow through the first aperture and at pressures greater than 10^{-1} mbar the formation of a molecular beam through the aperture system.

The system is baked by internal IR heaters and external flange heaters regulated by monitoring the temperature of every cooling stage of the cryo pumps. This is necessary because the temperature of the cooling stage must not exceed a temperature of 70°C during bake out. With this baking system, a bake out temperature of 150°C can be established in the vacuum chamber without overheating the cryo pumps.

When the aperture system is retracted, XPS spectra with maximum sensitivity can be recorded under ultra-high vacuum conditions. In Figure 2a we show the XPS spectrum of a sputter cleaned polycrystalline silver surface recorded at 3 x 10^{-10} mbar. Spectrum 2b was recorded after inserting the aperture and introducing a nitrogen pressure of 3 x 10^{-1} mbar into the sample chamber. The experimental conditions were such that the resolution on the silver 3d peaks is 0.9 eV, the x-ray power was 300 Watts Mg K_α radiation. In this spectrum we can see a gas phase N1s peak at a kinetic energy of 848 eV. We further note an increase in background signal and four distinct peaks (1,1',2,2') on the high binding energy side of the silver 3d doublet. The increase in secondary electron background is due to inelastic losses of silver photoelectrons in the gas phase; the distinct maxima in the background (1,2 and 1',2' located at 10.2 eV and 13.4 eV above the silver 3d 5/2 and silver 3d 3/2-emission) are losses due to excitations of gas phase nitrogen molecules. This can be seen in Figure 3 where we show
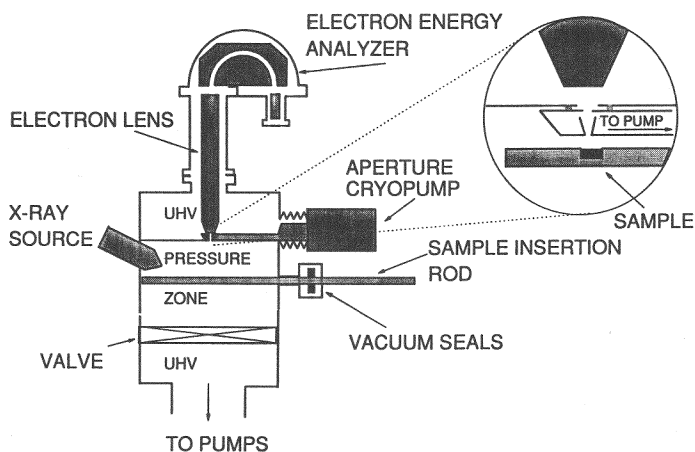
Figure 1. Schematic drawing of the controlled atmosphere photoelectron spectrometer.
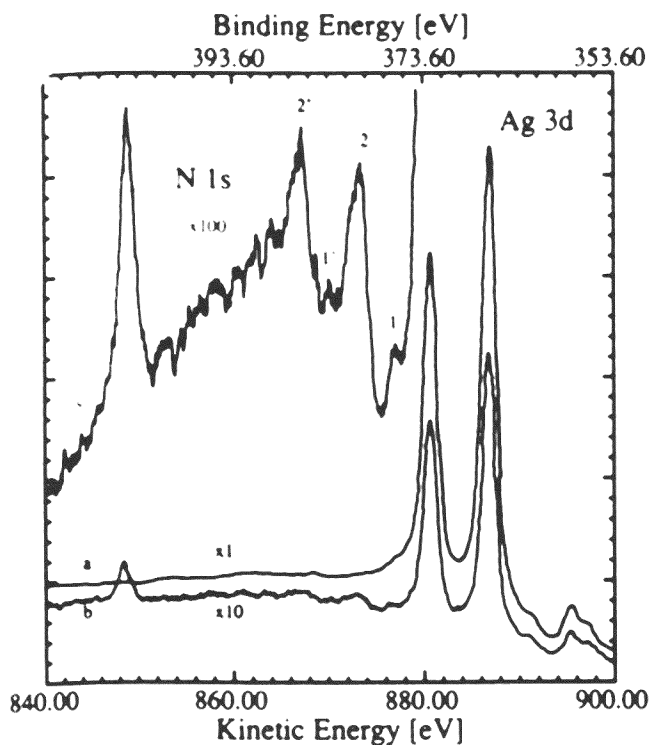
Figure 2. XPS spectrum of a clean silver sample (Ag 3d lines) recorded at a) 3 x 10^{-10} mbar and after the introduction of 3×10^{-1} mbar of N_2 b) 3 x 10^{-1} mbar of nitrogen. (Reproduced with permission from ref. 7. Copyright 1990 John Wiley & Sons.)

the gas phase nitrogen XPS spectrum recorded as a function of pressure without a sample in the sample position. We note that the N1s spectrum shifts slightly (by approximately 0.5 eV) to higher binding energies when the pressure is increased by 2 orders of magnitude. This decrease in kinetic energy or increase in binding energy is due to space charge effects in the gas phase due to the incident x-ray flux (7). The N1s shake-up spectrum at lower kinetic energies shows the typical shake-up transitions observed for gas phase nitrogen, albeit with a poorer instrumental resolution than those published by the Upsala group (1-3). In the shake-up spectrum we clearly identify the inelastic loss-peak at 13.2 eV lower kinetic energy than the N1s core-level emission. The loss peak denoted 1,1' in Figure 2 is hidden in the shake-up spectrum in the first shake-up transition at 9.1 eV assigned to a $1\pi \rightarrow 2\pi$ excitation. The relatively large width of this peak has been attributed to vibrational broadening of the peak (1). From a comparison of our gas phase spectra, however, it appears that at the low kinetic energy side of the $1\pi \rightarrow 2\pi$ transition an inelastic loss feature is included. This example demonstrates that the instrument, although without highest resolution, can be used to record a gas phase XPS spectra.

A shift of the primary N1s excitation peak with gas pressure was only noted when no sample was present in the sample position. With a surface present, the distance between sample surface and first aperture is approximately 1 mm, i.e. the gas phase volume from which the N1s photoelectrons originate and the electrostatic potential is reasonably well defined. In this case, the photoelectrons travel a relatively short distance through the gas and inelastic collosions at a given pressure are at a minimum and the N1s peak exhibits little broadening. The situation, however, is different when the sample is removed and spectra are recorded from a volume defined by the x-ray cone and acceptance angle of the analyzer, which gives a correspondingly longer average electron path through the gas phase. Thus, the width of the N1s peaks rise with increasing pressure due to the ill-defined electrostatic potential. These measurements have been described in detail in reference 7. Also, for x-ray powers exceeding 300 W even at a relatively low pressure (7 x 10^{-2} mbar) broadening effects are observed owing to charging of the gas phase by the photo-ions. This result indicates, that for this particular instrument, care has been taken when performing surface studies under high pressure conditions because of the potential effect of gas phase ions on the surface chemistry under investigation. The space charge effect in the gas phase has been determined to increase the binding energy by 1.5 eV, consistent with positive charging of the gas phase (7).

An important question relates to the actual pressure at the site of photoelectron ejection if steady state measurements are to be performed in a gas ambient. It is expected that the pressure measured in the volume of the chamber will be too high considering the small distance (typically 0.8 mm) between sample surface and the differentially pumped first aperture. Fortunately, the substrate signal itself can be used to determine the true pressure.

This can be done by two different approaches: a) adsorption-desorption isobars of a gas can be measured or b) the condensation of the gas (water) can be determined as a function of substrate temperature and the pressure measured in the chamber by the attenuation of the substrate signal. The measured condensation curve for ice is then correlated to tabulated values for the sublimation equilibrium of ice. As described in reference 7, a comparison between the tabulated values for the sublimation equilibrium pressures can be used to extract the pressure at the site of photoelec-

tron ejection. By this method we found approximately an order of magnitude difference between the measured pressure in the chamber and the real pressure at the site of photoelectron ejection. This large difference was attributed not only to the high pumping speed through the aperture, but also to cooling of the gas in the vicinity of the sample surface by the liquid nitrogen cooled sample rod, leading to a decrease in gas phase density because of the restricted gas flow conditions at the sample surface.

A more accurate method to determine the actual pressure at the site of photoelectron ejection is to measure indirectly the ionization cross sections for the gas phase by the emitted photoelectrons through the attenuation of the substrate peak and comparing these ionization cross sections with respective tabulated values. In Figure 4 we show a plot of the attenuation of the silver substrate signal (lnI/Io) as a function of pressure measured with the VISCOVAC gauge. These data were obtained with a first aperture size of 2.9 x 0.6 mm; the distance between sample surface and first aperture was measured by mechanical means to be 0.83 ± 0.1 mm. From the decreased inelastic intensity of the silver 3d photoelectrons with respect to the background intensity (a linear background subtraction was used for data evaluation) the electron mean free path through the gas can be determined. Furthermore, if a set of data is taken for other substrate peaks with different kinetic energies, the electron mean free path can be evaluated also as a function of electron kinetic energy. For these measurements we used the attenuation of the silver valence band, silver 3d 5/2, silver 3p 3/2 and silver M_5VV Auger transitions.

The attenuation of electrons passing through a gas atmosphere is given by

$$I = I_0 \exp(-p\, d/\lambda\,(E)) \tag{1}$$

where I_0 is the intensity of the electron flux in a vacuum, p is the pressure, d is the path length of the electrons through the gas, and $\lambda(e)$ is the electron mean free path as a function of kinetic energy. Hence, for a given kinetic energy, a plot of $\ln(I/I_0)$ versus pressure will give a value for λ if the path length (d) is known. The straight line in Figure 4 indicates that equation 1 can be used to describe the gas phase attenuation and that the slope of the lines can be used to calculate the electron mean free path for the electrons. For the three gases, hydrogen, water and nitrogen, we measured the electron mean free path, of the silver 3d electrons having a kinetic energy of 886 eV to be 2.08 x 10^{-3} m, 8.3 x 10^{-4} m and 4.19 x 10^{-4} m, respectively.

If we assume that the attenuation of the elastic photoelectron flux is solely due to ionization processes, we can calculate the ionization cross section σ (in m^2) from the equation

$$I = I_0 \cdot \exp(\sigma \cdot d \cdot N_g/V) \tag{2}$$

where d is the path length (in m) and N_g is the number of gas molecules in volume V. Rearranging gives

$$\sigma = -\ln(I/I_0) \cdot R \cdot T/d \cdot p \cdot N_L \tag{3}$$

where p is the pressure (in Pa), N_L is Avogadro's number, R is the gas constant (in
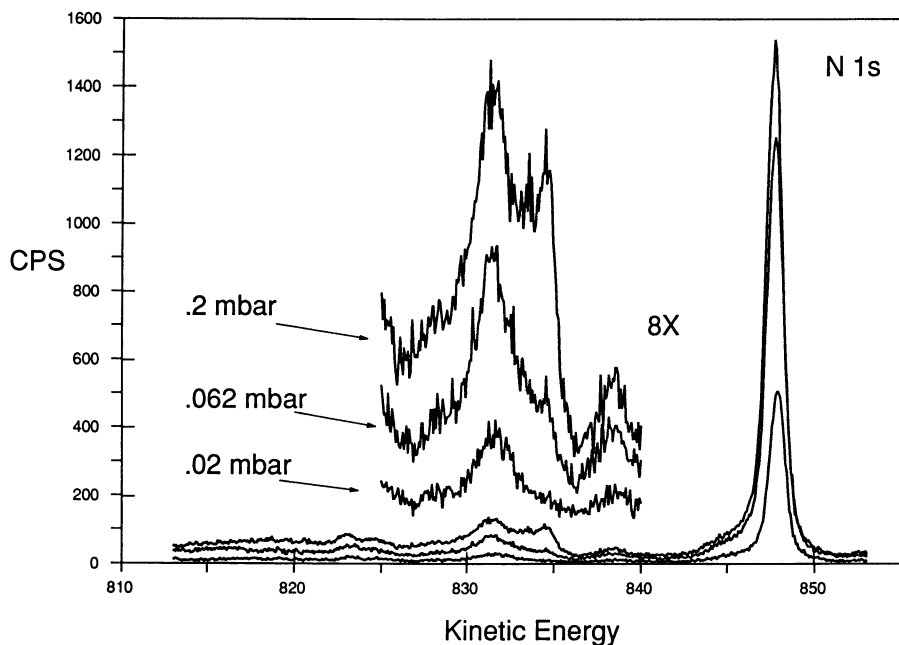
Figure 3. The nitrogen 1s XPS spectrum of nitrogen gas at various pressures.
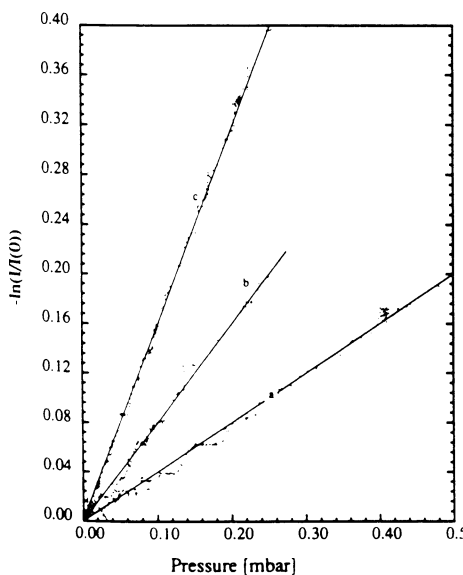
Figure 4. Attenuation of Ag substrate signals (lnI/Io) as a function of pressure for three gases. Pressures as recorded on the VISCOVAC spinning rotator gauge. (Reproduced with permission from ref. 7. Copyright 1990 John Wiley & Sons.)

J/mol K) and T is the temperature of the gas phase. Using this expression, the current experiments yield ionization cross sections for the 886eV electron of $2.x10^{-21}$, $5x10^{-21}$ and $9.9x10^{-21}$ M^2 for H_2, H_2O and N_2 respectively. The agreement between the measurements and literature values (8,9) for σ is excellent (identical for H_2, within 20% for H_2O and within 10% for N_2). This implies that the pressures at the site of photoelectron ejection is within 10 to 20% of the real pressure, depending on the quality of the pressure measurements in references 8 and 9.

In Figure 5, the attenuation of the silver signals of different kinetic energy are plotted versus kinetic energy. The attenuation is expressed by an attenuation coefficient $\alpha = d/\lambda(E)$ which contains the energy dependence of the electron mean free path. As expected, we see a decrease in attenuation coefficient (or increase in electron mean free path) with increasing kinetic energy of the electrons. The data points can be fitted by a single exponential giving $\alpha \sim E^{0.6\pm.2}$ which describes the energy dependence of the electron mean free path. This compares to a value $\alpha \sim E^{0.5-0.75}$ which typically is used for solids. Our value of α is also an excellent agreement with the energy dependence of the electron mean free path calculated from the ionization cross sections given in reference 8.

From these calibration measurements it follows that for the geometry and aperture size given above the pressure at the site of photoelectron ejection is within 20% of the pressure read by the VISCOVAC gauge in the high pressure volume. This approximate correlation between pressure above the sample and pressure in the volume is only true if the sample rod and the sample is at room temperature. As described in reference 8, heating the sample leads to heating of the gas phase and therefore a decrease in gas phase density around the sample surface. This effect was described using the example of the reduction and oxidation of molybdenum oxide surfaces (7).

Reduction of NiO

In this section we present one example of the type of experiment which can be done with the CAPES system which is impossible in most conventional XPS instruments. In this study, the kinetics of a simple surface reaction, the reduction of NiO, were followed *in-situ* and in real time by monitoring the surface oxygen concentration with the CAPES system. These experiments utilized an ultra-thin oxide film grown on a Ni(100) substrate as model for bulk NiO. The films were prepared by growing a self-passivating three layer NiO film which readily forms on an atomically clean Ni(100) surface upon exposure to gaseous oxygen at room temperature (10,11). The self-passivated film grown at room temperature is somewhat unstable but restructures into stable NiO crystallites upon heating to 600K in vacuum. (12). The kinetics of the NiO crystallite reduction were carried out by preparing an atomically clean Ni(100) surface, exposing this surface to oxygen at room temperature to grow the three layers of NiO, annealing the three layer NiO to form NiO crystallites and finally exposing the NiO crystallites to hydrogen or methane at various temperatures and pressures. Hydrogen and methane are of course both reducing gases which convert the NiO back to Ni metal by removing the oxygen as water and or CO. Typical experimental results are shown in Figure 6 where the surface oxygen concentration obtained from the oxygen 1s XPS signal are plotted as a function of time at various hydrogen pressures within the CAPES instrument. In these particular experiments the temperature of the
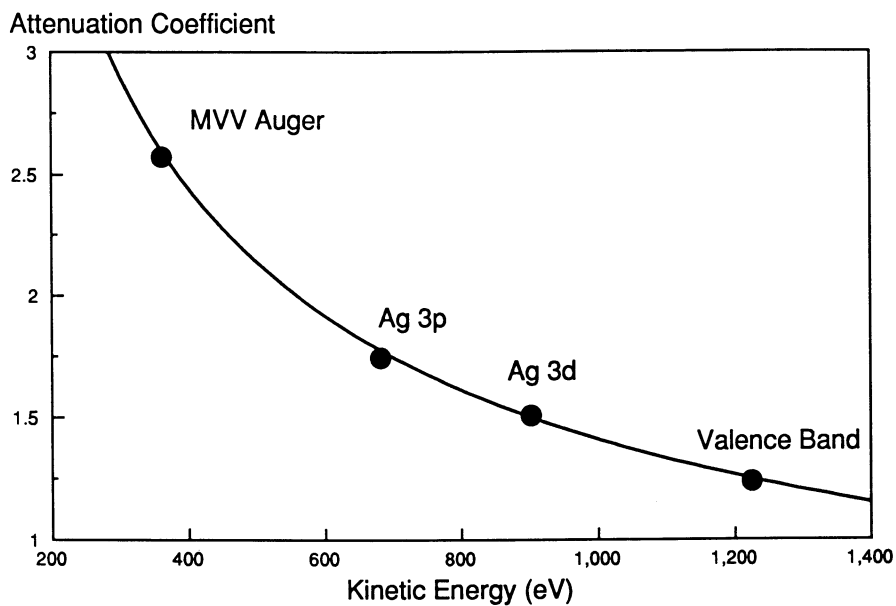
Figure 5. The attenuation of various silver signals of different kinetic energies plotted versus kinetic energy.

SURFACE OXYGEN
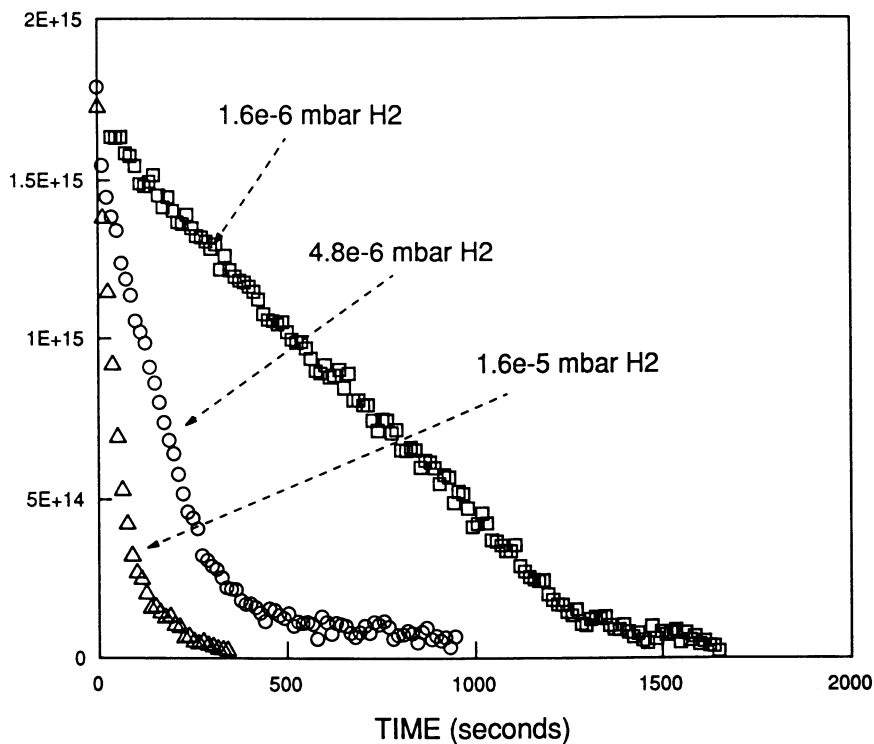
Figure 6. Typical experimental results for the reduction of NiO on Ni metal substrate. The oxygen surface concentration obtained from oxygen 1s signal intensity is plotted as a function of time for various hydrogen pressures at a fixed surface temperature of 623K.

surface was 623K and the hydrogen pressure was varied one order of magnitude (1.6 x 10^{-6} to 1.6 x 10^{-5} mbar). In can be seen in Figure 6 that, under these conditions, the removal of surface oxygen by hydrogen is relatively facile. It can also be seen that the reaction velocity (the derivative of these curves) is constant over the initial part of the reaction and that the reaction velocity is highly dependent on the hydrogen pressure. The capes system because of its ability to operate over an extensive temperature and pressure range (almost ten orders of magnitude in pressure and 100 to 1200K surface temperature) makes this instrument well suited to mapping out kinetics of surface reactions of this type. This point is demonstrated in Figure 7 where the reaction velocity of the oxide reduction reaction is presented in an Arrhenius format for three different hydrogen pressures and a single pressure of methane. The pressure dependence of NiO crystallite reduction is clearly seen in the data. Reaction rates increase by an order of magnitude when the hydrogen pressure increases an order of magnitude. The highest hydrogen pressure explored was 1.58 x 10^{-5} mbar because beyond this pressure the reaction was so rapid it became difficult to follow the kinetics due to inherent time constant of the XPS measurements. Reduction of the NiO with methane, on the other hand, required a pressure of at least 7 x 10^{-3} mbar for the reaction to proceed rapid enough to be monitored within a reasonable time frame. This pressure could only be reached in the differentially pumped CAPES system and demonstrates the unique ability to follow low probability surface reactions. The difference in reaction probability is demonstrated in Figure 8 where the rate data in Figure 7 has been scaled by the collision frequency of gas phase molecule with the surface to normalize out pressure effects. The normalized data thus represents the probability that a gas phase molecule will undergo a reactive collision with the surface. Notice in Figure 7 that the methane reaction is about four orders of magnitude lower in probability than hydrogen thus requiring the higher pressure to achieve rates comparable to the hydrogen reaction. In Figure 7 the hydrogen data is clustered around a single Arrhenius curve which has two linear sections indicating that the reaction rate is first order in hydrogen pressure within these experimental conditions. The origin of the two linear sections in the curve is not fully understood but may be associated with a change in the rate limiting step of the reaction. For example, at lower temperatures the reaction may be limited by desorption of the product (water) and therefore exhibits a strong temperature dependence. At higher temperatures, water desorption might no longer be rate limiting but may be determined by intrinsic energetics of the initial collision of the hydrogen molecule with the surface.

Summary

The CAPES instrument's unique ability to combine conventional UHV surface science capabilities with *in-situ* surface analysis in controlled atmospheres of up to 1 mbar allows for many novel experiments. Equilibrium measurements to evaluate surface thermodynamics and surface reaction kinetics are both possible in this instrument. The instrument could be improved by increasing the surface sensitivity of the technique. The detection limit of the current instrument for adsorbate phases on metal surfaces (O_2 on Ag, SO_2 on Cu) is estimated to be about 10^{14} atoms/cm^2 for data collection times $\geq$ 10 min. and an ambient pressure of 5 x 10^{-1} mbar. Under these conditions, the distance between x-ray source and sample, and sample surface and first differential pumping stage, have to be minimized to maximize the sensitivity, i.e. this
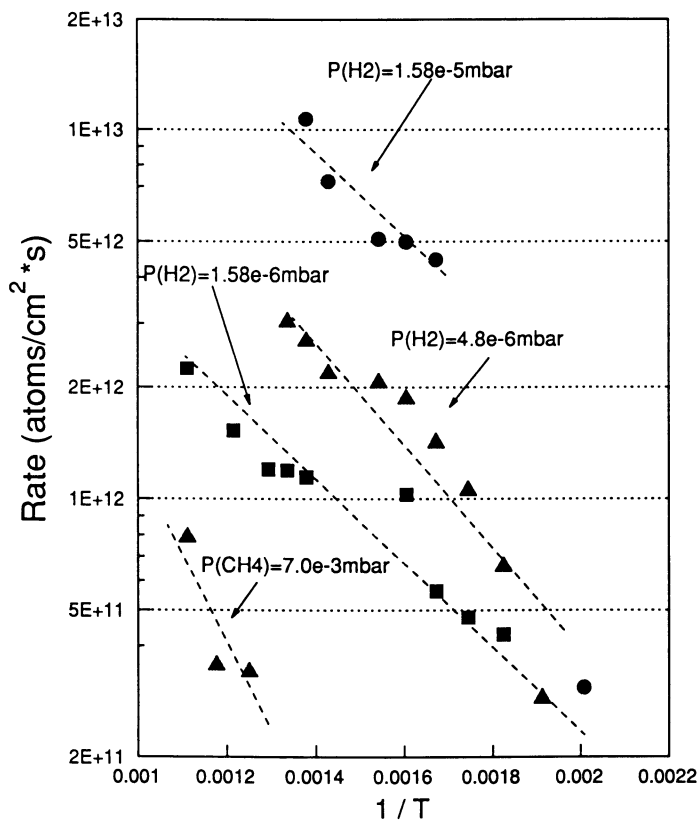
Figure 7. Arrhenius plot for the kinetics of NiO reduction with hydrogen at three pressures and methane at one pressure.
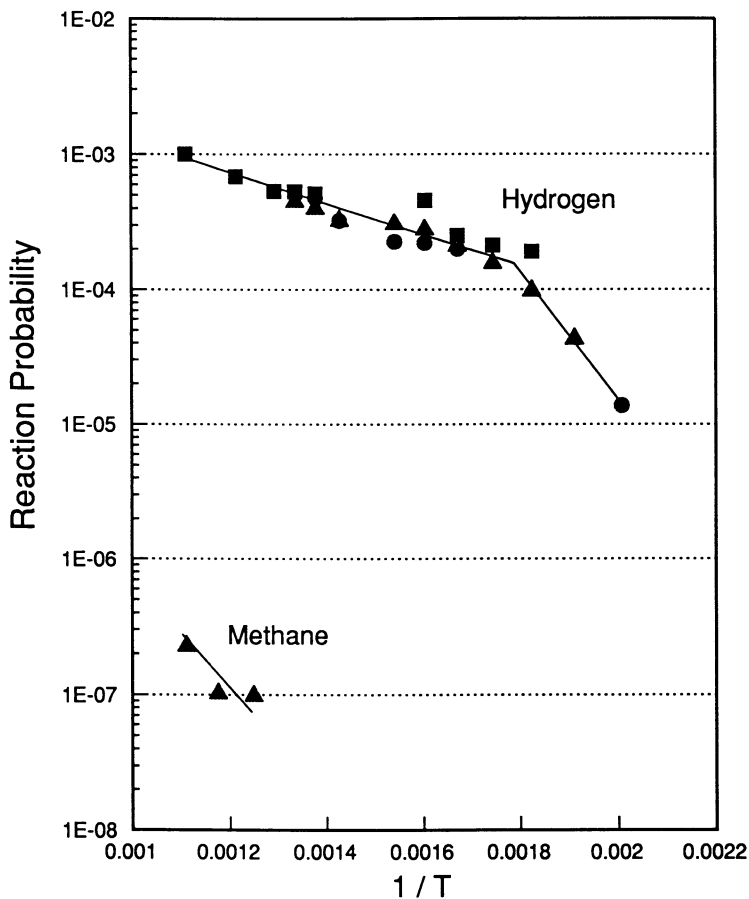
Figure 8. Rate data of Figure 7 after normalizing by the gas flux on the surface. The rate is now represented as a probability for reactive collision with the surface. Markers correspond to those used in Figure 7.

sensitivity limit is considered to be true in general for instruments with single channel detectors. Of course, a significant improvement in sensitivity and resolution would be obtained by using a focussed x-ray beam utilizing a monochromator or synchrotron radiation source and by employing a multi-channel detection system in the analyzer. However, despite these limitations with respect to maximum pressure and sensitivity, novel experiments can be done in a pressure range that is not accessible with conventional instruments.

Acknowledgments

Literature Cited

1.   Gelius, U. *J. Electr. Spectrosc.* **1974, 5,** 985.
2.   Siegbahn, H.; Lunholm, M.; Arbman, A.; Holmberg, S. *Physica Scripta* **1983** **27** 241.
3.   Siegbahn, H.; Lunholm, M.; Holmberg, S.; Arbman, A. *Physica Scripta* **1983** **27** 431.
4.   Joyner, R. W.; Roberts, M. W.; Yates, K. *Surf. Sci.* **1979 87** 501.
5.   Joyner, R. W.; Roberts, M. W. *Chem. Phys. Lett.* **1979 60** 3.
6.   Littrell, D. M.; Tararehuk, B. J. *J. Vac. Sci. Techn.* **1986** A4(3) 1608.
7.   Ruppender, H. J.; Grunze, M.; Kong, C. W.; Wilmers, M. *Surf. and Interf. Anal.* **1990 15** 245.
8.   Tawara, H.; Kato, T. *At. Data Nuc. Data Tables* **1987** 36(2) 168.
9.   Schutten, J.; de Heer, F. J.; Moustafa, H. R.; Boerboom, A. J. H.; Kistemacher, J. *J. Chem. Phys.* **1966 44** 3924.
10.   Holloway, P. H.; Hudson, J. B. *Surface Sci.* **1974 43** 123.
11.   Norton, P. R.; Trapping R. L.; Goodale, J. W. *Surface Sci.* **1977 65** 13.
12.   Wang, W. D.; Wu, N. J.; Thiel, P. A. *J. Chem. Phys.* **1990 92** 2025.

Chapter 12

Ultrasoft X-ray Absorption Detected by Fluorescence Yield

In Situ Method for Characterizing Adsorbates and Surface Reactions

John L. Gland[1], Tecle Rufael[1], and Daniel A. Fischer[2]

[1]Department of Chemistry, University of Michigan, Ann Arbor, MI 48109
[2]National Institute of Standards and Technology, Gaithersburg, MD 20899

The recent development of ultra soft X-Ray fluorescence detection methods have greatly enhanced our ability to characterize adsorbed species and surface reactions containing low-Z elements. Three examples of surface processes involving carbon containing species are summarized here to illustrate the interesting capabilities of Fluorescence Yield Near Edge Spectroscopy (FYNES). Transient in-situ studies have revealed that more strongly adsorbed carbon monoxide is displaced well below it's usual desorption temperature for hydrogen pressures above 0.01 torr on both the Pt(111) and Ni(100) surfaces. Transient in-situ kinetic studies of hydrogen induced C-S bond activation in adsorbed methylthiolate on the Pt(111) surface have also been performed for hydrogen pressures in the 10^{-4} to 10^{-2} torr range. Taken together these examples suggest that a broad range of adsorbed species and elementary surface reaction steps can be characterized by this new in-situ method.

The availability of high intensity synchrotron radiation in the ultra-soft X-ray energy range (200-1000 eV) makes it possible to characterize adsorbed species and materials containing the naturally abundant low-Z elements carbon, nitrogen, oxygen and fluorine. Fluorescence detection makes the ultra soft X-ray absorption spectroscopies photon-in, photon-out methods which can be performed in the presence of reactive atmospheres. The capabilities of Fluorescence Yield Near Edge Spectroscopy (FYNES) are illustrated by considering three examples of surface processes involving monolayer and submonolayer coverages of

adsorbed carbon containing species. Carbon monoxide displacement by more weakly adsorbed hydrogen has been observed for hydrogen pressures above 0.01 torr on both the Pt(111) and Ni(100) surfaces. Displacement occurs well below the usual thermal desorption temperatures. "Crowding" or repulsive interactions between large coverages of coadsorbed atomic hydrogen and carbon monoxide are consistent with the displacement energetics and kinetics observed. Recently, FYNES has been used to perform transient studies for hydrogenolysis of well characterized methylthiolate monolayers on the Pt(111) surface for hydrogen pressures up to 0.02 torr. These studies of an elementary surface reaction involving hydrogen induced C-S bond cleavage indicate that the reaction is first order in surface thiolate coverage with an activation energy of approximately 18 kcal/mole. Taken together these illustrations suggest that a wide range of surface reactions can be characterized by this new in-situ method.

Fluorescence Yield Near Edge Spectroscopy (FYNES)

Fluorescence detection in the ultra soft X-ray region makes it possible to obtain X-ray absorption spectra of carbon, nitrogen, oxygen and fluorine in the presence of reactive gaseous environments since Fluorescence yield (FY) makes ultra soft X-ray absorption a photon-in, photon-out method (1). FY measurements have been used extensively in the hard X-ray region to characterize both near edge structure and extended X-ray absorption fine structure (EXAFS) (2). The lack of high performance fluorescence detectors in the ultra-soft X-ray region has restricted the study of materials containing low-Z atoms until recently. Near edge spectra in the ultra-soft X-ray region can furnish important information concerning the structure and bonding of adsorbed species as indicated by several recent reviews (3-5). Since the resonant transitions observed between core levels and the lowest unoccupied molecular orbitals obey dipole selection rules, the linearly polarized soft X-rays from synchrotron sources can generally be used to establish the orientation of adsorbed molecules and intermediate species. In addition, the separation between the core levels and a number of low lying unoccupied molecular orbitals is a sensitive function of bond distances and molecular structure (6).

FYNES in the Ultra Soft X-ray Region. Because of a strong interest in characterizing surface species under reaction conditions, a program to establish FY as a viable detection method in the ultra-soft X-ray region has been undertaken. Initial vacuum experiments focused on thiophene adsorption on the Ni(100) surface were performed at the sulfur K-edge (2472 eV) (7,8). Recently, high performance, vacuum compatible ultra soft X-ray fluorescence detectors have been developed

as a method for detecting X-ray absorption above the carbon K-edge (285 eV) *(1,9,10)*. Our first fluorescence detector for use at the carbon K-edge was used initially to characterize ethylene chemisorption on the Cu(100) surface in vacuum *(9)*. A more sophisticated high resolution fluorescence detector system capable of performing FY measurements at the carbon K-edge in the presence of up to 100 torr of gas *(10)* is described in the experimental section

In the past, X-ray absorption studies for low-Z atoms have relied primarily on electron yield (EY) detection schemes *(2)*. Total electron yields (TY), partial electron yields (PY) and Auger electron yields (AY) have all been used to characterize ultra soft X-ray absorption*(11)*. Unfortunately, electron yield techniques are limited to ultra-high vacuum (UHV) environments due to the short mean free path of electrons in gasses. Detection of characteristic fluorescence yield (FY), on the other hand, eliminates this difficulty so that adsorbed species and surface reactions can be characterized in reactive atmospheres. This new method promises to substantially improve our ability to bridge the gap between surface science and high pressure catalytic systems. Fluorescence detection also offers spectroscopic advantages over the traditional electron detection methods because of improved signal to background levels.

However, until recently, FY has been considered to be poorly suited for detection of X-ray adsorption by low Z elements. since the FY decreases abruptly with decreasing atomic number *(12)*. In addition to small fluorescence cross sections for carbon, carbon contamination on the optical components of the beam line often decreases the incident flux available at the carbon K edge and may contribute to normalization problems. Nevertheless, with a good ultra soft fluorescence detection system the advantages far outweigh limitations and a broad new class of experiments become feasible.

Apparatus

Recently, we developed a system consisting of an entrance window system to isolate the experimental region from the UHV beam line, a sample/reaction chamber equipped with a high performance fluorescence detector for in-situ studies, and an attached surface science system for sample preparation. This system has been used for measuring ultra soft X-ray fluorescence over the 10^{-10} torr to atmospheric pressure range. Such a system allows the FY method to address a range of materials problems from monolayers to bulk materials even in the presence of a reactive gas atmosphere.

The end station consists of a multiple level vacuum chamber with a small high pressure reaction chamber on top where the FYNES experiments are performed *(1)*. The primary vacuum chamber is

equipped with standard surface science instrumentation including facilities for Auger electron spectroscopy, thermal desorption, low energy electron diffraction and ion sputtering. A long travel manipulator is used to transfer the sample to the reaction chamber on the upper level. The reaction chamber can be isolated from the main chamber by a gate valve and pumped independently using a turbomolecular pump as indicated in figure 1. The reaction chamber could also be isolated from the UHV soft X-ray beam line and synchrotron by two thin ultra soft X-ray windows and a ballast region. The window material can be boron, diamond, aluminum or tin, on a mesh substrate capable of withstanding **atmospheric pressures** in the case of diamond. The choice of window material clearly depends on the experiment, e.g. a diamond window is quite useful for the fluorine K edge but highly absorbing just above the carbon K edge. The windows used for these experiments were 1000 Å boron and tin films supported on a high transmission nickel grid mounted on the center of two 2-3/4" gate valves so that they could be inserted or removed independently. Each window could withstand a hydrogen pressure differential over 10 torr without any significant leakage. These windows transmit over 30% of the radiation in the 300 eV energy range. The tin window also has an absorption edge around 490 eV which absorbs second order radiation for primary energies above 245 eV in the carbon edge region.

X-ray adsorption by the sample was measured using a high performance fluorescence detector optimized for carbon radiation *(1,9)*. The detector is a differentially pumped ultra high vacuum compatible proportional counter whose position could be varied in order to maximize the fluorescence signal, as shown in figure 1. The radiation from the sample passes through two 1 μm thick polypropylene windows (each 85% transmitting for C-Kα radiation) with a differentially pumped region in between. The windows were mounted on 60% transmitting stainless steel grids of cylindrical symmetry for optimum energy resolution and improved physical strength. This also allowed us to set the detector away from the plane of incidence, thereby, minimizing the signal coming from scattered light. Several detection gases were tried for the proportional counter and the best results were obtained by flowing a gas mixture of 90% methane and 10% argon through the detector while maintaining a pressure of 200 torr in the inner section. Photons passing through the window system are absorbed by the counter gas mixture creating electron-ion pairs. These electrons are accelerated by high electric field of a gold plated tungsten anode wire and create impact ionization gas multiplication. The resulting pulse of electron charge is collected at the anode and amplified by a charge sensitive pre-amplifier mounted close to the anode to minimize noise. Under typical operation conditions the anode is kept at a potential of +1300 V, which results in a charge collection of about 0.1

pC per pulse at the carbon edge. These charge pulses are then energy analyzed using standard pulse-height techniques. Energy resolution of up to + 0.25 eV are normally attainable. Photons from scattered light result in some background counts on our FYNE spectra, but this did not greatly affect our results. Regarding the sensitivity of the technique, detailed study of three detection modes, namely, fluorescence yield(FY), Auger electron yield (AY) and partial electron yield (PY) of ethylene on Cu(100) has been reported by Fischer et al.*(9)*. The work shows that this technique is capable of detecting 0.02 monolayers ($3x10^{13}$ carbon atoms/cm^2), more sensitive by a factor of 17 than AY detection and by a factor of 60 than PY detection. However, the study also showed that the PY detection technique exhibits a better signal-to-noise ratio than the FY and AY methods, with the latter two being comparable.

The experiments were done on the U1 beam line at the National Synchrotron Light Source, Brookhaven National Laboratory. We estimated the total photon flux to be about 10^{11} photons per second at 300 eV photon energy for a ring current of 100 mA.

H$_2$ + CO on Pt(111) Surface

The adsorption and interactions of CO and H$_2$ on transition metal surfaces has received widespread attention due to the fundamental importance of these molecules as model adsorbates, the extensive use of these molecules to characterize catalytic surfaces, and due to the importance of these molecules in the Fischer-Tropsch synthesis of hydrocarbons. In this investigation, we independently verified that the CO π^* intensity on both the Pt(111) and Ni(100) surfaces is proportional to CO coverage*(1,13)*. A π^* intensity measurement for an exposure of 1L ($1L=10^{-6}$ torr.sec) of CO on the Pt(111) surface at 293K was made in the presence of 0.1 torr of hydrogen. The hydrogen was pumped and the experiment was repeated in vacuum and no intensity change was observed at this temperature. This rules out the possibility of π^* intensity changes with hydrogen coverage as a result of a change in the molecular orbital interactions due to the presence of coadsorbed hydrogen. The photon energies were calibrated using the strong carbon absorption feature at 291 eV in the incoming beam due to carbon deposited on the beam line optics. The CO π^* resonance occurred at 288.9 eV. Control experiments were performed to ensure that the energy position of the CO π^* resonance was invariant with coverage and temperature. FYNES spectra were recorded periodically to verify that the energy position of the π^* resonance had not drifted due to instrumental instabilities. Two adsorption configurations of carbon monoxide on the Pt(111) surface are known *(14,15)*: the strongly bonded terminal configuration and the bridge bonded configuration. CO chemisorbs in an upright geometry via the C 5σ lone

pair orbital stabilizing through backbonding of metal orbitals with the $2\pi^*$ antibonding orbitals of the molecule *(16)*. Thus the in-situ capability of FYNES to monitor the π^* resonance of chemisorbed CO as a function of time at various crystal temperatures and over a range of hydrogen pressures was used in order to obtain the surface CO concentration as a function of time in the presence of substantial hydrogen overpressures.

CO-Hydrogen Coadsorption on the Pt(111) Surface. Hydrogen adsorption alone on platinum surfaces has been investigated in detail by several groups *(17-19)*. Hydrogen adsorbs dissociatively on the Pt(111) surface and has a saturation coverage of 0.80 ML *(18)*. The activation energy for hydrogen desorption is 19 kcal/mol in the limit of zero coverage *(17)*. CO adsorption on Pt(111) has also been studied extensively *(20-24)*. CO is adsorbed molecularly on Pt(111) with a desorption activation energy of 31 kcal/mol at low coverage *(20-23)* which decreases sharply above $\theta_{CO} = 0.50$ ML where compression of the adlayer begins and repulsive interactions become important *(20)*. Coadsorption of CO and H_2 on the Pt(111) surface has also been studied particularly because of the repulsive nature of the interactions between these adsorbed species, and because of the tendency for these coadsorbed species to form islands *(25)*. Bernasek et al. *(26)* performed thermal energy atom scattering (TEAS) experiments on a Pt(111) surface precovered with $\theta_{CO} = 0.22$ ML which showed that CO forms islands having a local density of $\theta_{CO} = 0.50$ ML on the hydrogen saturated surface at 180 K. This CO islanding induced by coadsorbed hydrogen has also been studied by infrared reflection absorption spectroscopy (IRAS) *(14)* which confirms the results of Bernasek et al. *(26)* and suggests an optimum temperature of 150 K for the growth of large CO islands.

Isothermal FYNES. A series of in situ isothermal displacement experiments for both vacuum and 0.2 torr hydrogen in the 318 to 348 K temperature range are shown in figure 2. A typical transient isothermal FYNES desorption experiment involved dosing a clean Pt(111) crystal with a saturation exposure of CO at T<100 K in the main chamber and then positioning the sample in the reaction chamber where the FYNES spectrum was recorded at normal incidence and 288.9 eV (the CO π^* resonance energy). Initially the intensity of the CO π^* resonance was monitored for about 100 sec to calibrate the signal at saturation coverage. At this point, hydrogen flow at 0.2 torr was initiated while the crystal was at 100 K. In agreement with previous work *(27)* no CO displacement occurs at this temperature and H_2 pressure. After the hydrogen pressure was stabilized, the temperature was quickly ramped to the desired temperature. Reaction temperature was reached in about
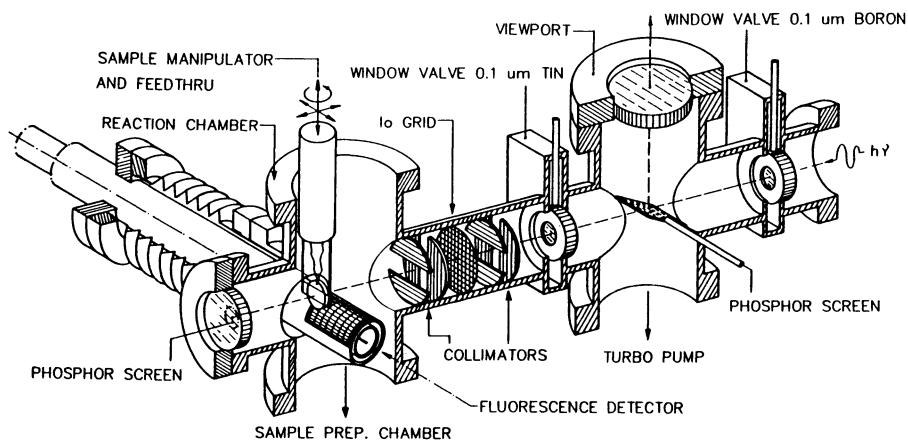
Figure 1. A schematic of the apparatus for fluorescence yield near edge spectroscopy (FYNES) under reactive gases at elevated pressures. The drawing shows a cross section of the fluorescence detector and the combination of thin windows used to isolate the reaction chamber from the photon source. (Reproduced with permission from ref. 1. Copyright 1988 Elsevier.)
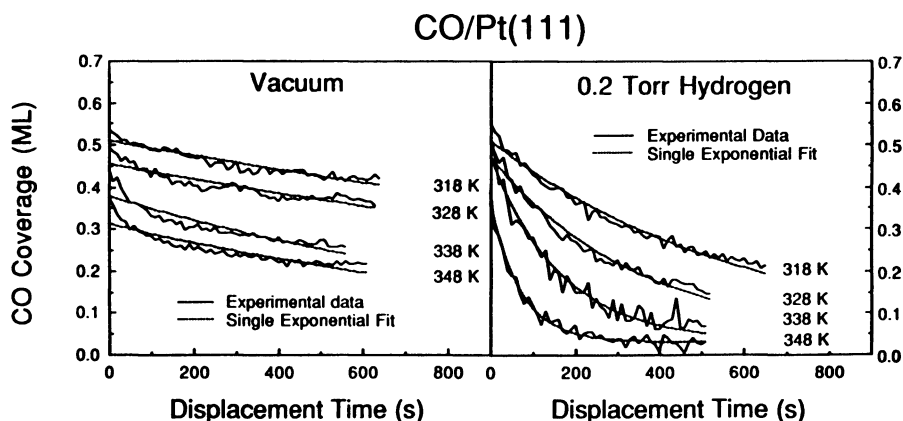
Figure 2. Transient isothermal experiments on Pt(111) at 318, 328, 338, and 348 K. The left panel shows isothermal desorption of CO performed in vacuum. The right panel shows isothermal desorption (displacement) of CO in the presence of 0.2 torr hydrogen. The dotted lines in both panels are single exponential fits of the form $\theta_t = \theta_\infty + \theta_o \exp(-kt)$. (Reproduced from ref. 55. Copyright 1990 American Chemical Society.)

40 to 60 seconds. The zero of the time axis is defined as the time when the reaction temperature was reached. Some of the CO is already displaced or desorbed by the time reaction temperature is reached; the amount becomes more significant with increasing reaction temperature and H_2 pressure, giving rise to different initial coverages in figure 2. Once the signal has decayed to a constant value, the temperature of the crystal was flashed to 650 K so that a calibration point for zero CO coverage could be established. The results illustrated in figure 2 clearly show that for all temperatures, the rate of CO removal is greater in the presence of hydrogen than in vacuum. In vacuum, at 308 K, the coverage decays to a constant value of 0.28 ML, while in the presence of 0.2 torr H_2, the CO coverage decays to 0.03 ML.

Norton, Davies and Jackman (28) have determined the absolute saturation coverage of CO on Pt(111) using nuclear microanalysis (NMA) to be 0.64 ±0.03 ML at 160 K. Thus, at ~100 K and for hydrogen pressures greater than 0.2 torr essentially all of the 0.64 ML of CO can be removed from the surface with a constant activation energy of about 11 kcal/mol (29). In the absence of hydrogen, CO desorption activation energies in the 15-26 kcal/mol range are expected for this range of coverages. The activation energy should increase rapidly as CO desorbs because of the well-established increase in the desorption activation energy with decreasing coverage. Thus, as illustrated in the left panel of figure 2, isothermal desorption into vacuum cannot be described accurately by a simple first order exponential process. These experimental results clearly indicate that substantial interactions between coadsorbed CO and hydrogen are modifying the energetics for the desorption process of adsorbed CO in the presence of hydrogen pressures.

Each displacement and desorption experiment in figure 2 has been fit to a single exponential function of the form $\theta_t = \theta_\infty + \theta_0 \exp(-kt)$ the integrated rate expression for a first order reaction. The hydrogen displacement data is fit nicely by this integrated rate equation. The fits for the vacuum desorption data in the right panel are quite poor, because the activation energy of desorption of CO from Pt(111) is a strong function of coverage (22). In fact isothermal desorption in vacuum at a particular temperature only removes a small amount of CO because of the increase in the activation energy as the coverage drops. Essentially all of the chemisorbed CO can be displaced in the presence of hydrogen because the activation energy remains constant until very small CO coverages are reached (~3% ML).

Figure 3 shows the Arrhenius plot for the rate constants determined from the exponential fits to the displacement data shown in figure 2. An activation energy of 10.9 kcal/mol is obtained for the isothermal displacement of CO by 0.2 torr hydrogen. A mechanistic proposal consistent with these kinetic results is presented following a

brief summary of the Temperature Programmed displacement experiments.

Temperature Programmed FYNES. Figure 4 shows in-situ TP FYNES data for CO on the Pt(111) surface in vacuum and for a series of increasing hydrogen pressures (0.001, 0.01, and 0.1 torr) *(27)*. The vacuum experiment shows a sharp drop in the CO coverage with the maximum desorption rate occurring at 399 K. This corresponds to the thermal desorption of CO from the clean Pt(111) surface *(17-20)*. When the hydrogen pressure is increased to 0.01 torr, a new low temperature CO displacement channel is observed with a maximum rate at 168 K. Under these experimental conditions (0.01 torr H_2, 0.5K/sec heating rate), almost one fourth of the saturated CO monolayer is lost through low temperature displacement, lowering the surface CO coverage from $\theta_{CO} = 0.64$ ML to 0.5 ML. As the temperature increases further the remaining CO is displaced from the surface with a maximum rate at 386 K, 13 K lower than for the vacuum desorption case. When the hydrogen pressure is increased to 0.1 torr, the thermal conductivity of the room temperature hydrogen gas causes the temperature of the sample to increase to 200 K. Thus, the displacement of 0.14 ML of CO occurs during H_2 introduction and the starting coverage is $\theta_{CO} = 0.5$ ML. The curve exhibits a major inflection point at 386 K, as in the 0.01 torr hydrogen case. However, a small drop (<0.05 ML) at ~250K is observed. This could be due to slight tilting of the CO molecules, or due to CO or to early desorption of over-compressed CO molecules or a combination of several effects.

The activation energy for this hydrogen induced CO displacement can be estimated using the method of Redhead *(30)*. Assuming a pre-exponential factor of 10^{13} s^{-1} and a reaction order of 1, we estimate that the activation energy for this process is 10.6 kcal/mol. The amount of CO displaced, from $\theta_{CO} = 0.64$ ML to 0.5 ML, corresponds to the amount present in the compressed layer. Thus, it appears that the low temperature displacement under the conditions of these TP FYNES experiments corresponds to the removal of the CO compression structure.

CO Displacement Mechanism on the Pt(111) Surface. Hydrogen induced displacement of carbon monoxide from the Pt(111) surface is consistent with simple energetic arguments. The heat of desorption of CO is strongly dependent on the surface coverage *(20)*. Hydrogen will displace more weakly bound CO under conditions where repulsive interactions in the adsorbed layer ($CO_{(a)}$–$CO_{(a)}$, $CO_{(a)}$–$H_{(a)}$) reduce the desorption energy for CO to a value smaller than the heat of adsorption for hydrogen. Based on the predominance of nearest neighbor interactions, and using the 6 - 8 kcal/mol value for the CO–H repulsion
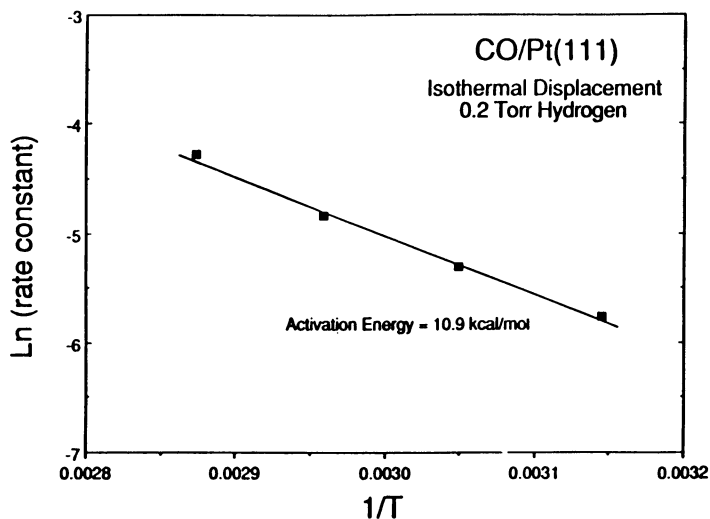
Figure 3. An Arrhenius plot for the rate constants determined from the exponential fits shown in Figure 2. The slope gives an activation energy of 10.9 kcal/mol. (Reproduced from ref. 55. Copyright 1990 American Chemical Society.)
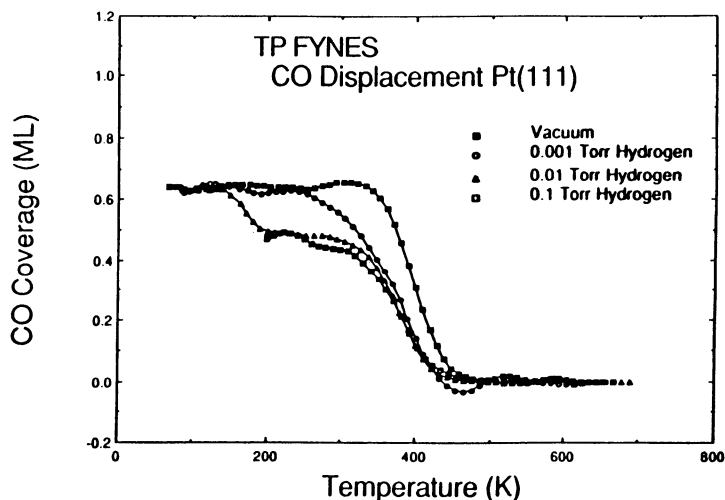
Figure 4. A series of temperature programmed fluorescence yield near edge spectroscopy (TP FYNES) experiments illustrating the effect of hydrogen pressure on CO removal from the Pt(111) surface. Note the new CO removal process which begins at 130 K for hydrogen pressure above 0.01 torr. (Reproduced from ref. 55. Copyright 1990 American Chemical Society.)

energy estimated by Bernasek et al. *(26)* in vacuum coadsorption studies, the lowering of the activation energy for desorption (displacement) from 26 kcal/mol to 11 kcal/mol suggests that two to three hydrogen atoms are involved in the displacement of each CO molecule. We propose that under isothermal conditions, hydrogen overpressures are inducing formation of CO islands with local coverages near the saturation value of 0.64 ML coverage because of repulsive interactions in the coadsorbed overlayer. Thus as displacement proceeds the coverage of hydrogen increases to maintain the densely packed CO islands which contain CO molecules with a heat of adsorption of about 11 kcal/mol. In the absence of hydrogen, desorption of a small amount of CO increases the heat of adsorption rapidly causing a rapid decrease in the desorption rate. Temperature programmed FYNES experiments on the Pt(111) surface indicate that at a temperature of 168K even for hydrogen pressures below 0.2 torr where CO displacement by hydrogen is not complete, hydrogen removes the $(3^{1/2} \times 3^{1/2})$ compression structure observed for the saturated monolayer (0.67ML) and induces the formation of the well known (2x2) structure (0.5ML) with reduced CO-CO repulsive interactions (figure 4). This also corresponds to the temperature for the hydrogen induced onset of CO mobility reported by Lenz et al. *(31)*. Based on several structural studies in agreement with the results presented here, a CO coverage of 0.5 ML seems to have special stability in the presence of hydrogen. Lower coverages coalesce to form 0.5 ML local coverages in the presence of hydrogen *(14)*, and higher coverages are removed at 130 K to form an overlayer containing 0.50 ML of CO. Taken together this data strongly supports our contention that the low temperature displacement process on Pt(111) is caused by destabilization of the compressed CO monolayer in the presence of hydrogen pressures above 0.01 torr.

H$_2$ + CO Coadsorption on the Ni(100) Surface

Carbon monoxide and hydrogen have also been studied extensively on the Ni(100) *(32-36)* surface. CO is adsorbed with a heat of adsorption of 30 kcal/mole *(36)* on the Ni(100) surface. Increasing repulsive interactions between adsorbed CO molecules results in decreasing heats of adsorption with increasing CO coverage. Hydrogen has a heat of adsorption of 23 kcal/mole on the Ni(100) surface *(37,38)* The interaction between coadsorbed hydrogen and CO is quite complex on the Ni(100) surface *(39-41)*. CO adsorbed on a hydrogen pre-saturated surface desorbs at about 210K, about 100K lower than CO desorption from the clean surfaces; this suggests that a weakened CO-Ni interaction can occur in the presence of large amount of coadsorbed hydrogen. Earlier *ex-situ* TPD and AES work on hydrogen displacement of CO

from the Ni(100) surface *(42)* indicates that hydrogen pressures in the 10^{-3} to 10^{-4} torr range cause displacement of chemisorbed CO in the 290 to 330K temperature range in a matter of minutes. However, the same study also shows no CO displacement in the 270 to 330K temperature range for pressures up to 10^{-3} torr of He, Ne, CH_4 or N_2. Moreover, the CO displacement rate is insensitive to deuterium substitution.

Isothermal FYNES. Hydrogen induced displacement of CO from the Ni(100) surface has been characterized using a series of isothermal transient FYNES experiments similar to those discussed in the previous section for the Pt(111) surface. As shown in Figure 5 chemisorbed CO is rapidly displaced in the presence of hydrogen in the 278 to 308K temperature range. On the Ni(100) surface, displacement begins well below the temperature where substantial desorption begins even for hydrogen pressures as low as 10^{-4} torr. The displacement kinetics are more complex on the Ni(100) surface than on the Pt(111) surface as indicated by the nonlinear behavior of the log coverage versus time plots (figure 5). The displacement rate can be modeled accurately by two sequential first order displacement processes which operate in the high and low CO coverage regimes. This model for the displacement rate seems physically reasonable since CO forms a compression structure at high CO coverage with substantial CO-CO repulsions leading to decreased desorption energies at high coverage. Displacement in the high coverage regime occurs with an activation energy of 7 kcal/mole, while displacement of CO for coverages below 0.4 ML results in an activation energy of 11 kcal/mol. Thermal desorption activation energies are in the 25 to 30 kcal/mol range for the Ni(100) surface. Displacement was found to be approximately half order in hydrogen pressure over the entire pressure range suggesting that adsorbed atomic hydrogen is involved in the rate limiting step.

Hydrogen Induced C-S Bond Activation in Adsorbed CH3S on the Pt(111) surface

Mechanistic studies of hydrogen induced C-S bond activation are interesting because of the important role C-S bond activation plays in a wide range of catalytic hydrodesulfurization (HDS) processes. This study represents an initial step in our effort to examine the role of hydrogen in bond activation on metal surfaces. In conventional reactivity studies separation of the elementary reaction steps involved in complex processes is often difficult. By studying the hydrogenolysis of the well characterized methylthiolate (CH3S) surface intermediate we have been able to isolate a single elementary reaction step so that detailed kinetic studies can be performed.

Adsorption and decomposition properties of thiols, particularly methanethiol (CH_3SH), have been investigated on a variety of metallic single crystals by several groups, namely, Pt(111) *(43)*, Ni(100) *(44,45)*, Ni(110) *(46)*, Fe(100) *(47)*, Cu(100) *(48)*, Cu(111) *(45,49)*, Au(111) *(50)*, W(211) *(51)*. It is generally believed that in most of these situations the parent thiol undergoes low temperature S-H bond cleavage and forms a S bound thiolate surface intermediate. Koestner et al *(43)* characterized adsorbed methanethiol using NEXAFS on the Pt(111) surface in vacuum via partial electron yield detection. Combined with high-resolution electron energy loss spectroscopy (HREELS) and temperature programmed desorption (TPD), they were able to investigate the structure, stability and orientation of adsorbed intermediates in the thermal decomposition of CH_3SH. They propose that the primary surface species are adsorbed methylthiolate (CH_3S, at 200K) and methylene sulfide (CH_2S, at 350K) on the Pt(111) surface. Gas phase ionization yield (IY) NEXAFS work on a series of thiols and thioethers was also reported by Dezarnaud, Tronc and Hitchcock *(52)*.

Isothermal FYNES. A series of in-situ isothermal methylthiolate hydrogenolysis experiments were performed over the temperature range 305 to 330 K for hydrogen pressures from 2×10^{-4} to 2×10^{-2} torr so that the kinetics of hydrogen induced C-S bond activation could be characterized. Unpublished TPD experiments of CH_3SH on Pt(111) surface indicate that methane production is promoted by the presence of 10^{-7} torr of hydrogen during the hydrogenolysis of methylthiolate in the 300 to 330 K temperature range *(53)*. A series of previous ex-situ Auger and TPD hydrogenolysis experiments also indicate that all surface carbon was removed after hydrogenolysis of adsorbed methylthiolate on the Pt(111) surface above 2×10^{-4} torr of hydrogen *(54)*. The total surface carbon concentration was measured using FY by monitoring continuum X-ray absorption at 315 eV energy (well above the molecular resonances of methylthiolate). This method insures us that kinetic measurements reflect the total removal rate of all carbon containing species.

A saturation dose of molecular methanethiol was initially adsorbed on the Pt(111) surface at 100 K. A saturated CH_3S monolayer was then formed by heating the molecular methanethiol overlayer to 200 K in vacuum. The sample was then isolated in the high pressure reaction chamber and the desired pressure (e.g. 0.02 torr) was obtained by flowing hydrogen through the chamber. The pressure was allowed to stabilize for about 6-8 minutes before the reaction was initiated by a temperature jump. FY measurements were taken during this period to calibrate the initial carbon surface concentration. The reaction was initiated by heating the sample to the indicated reaction temperatures at a heating rate of 10 K/sec (figure 6). Kinetic FY data
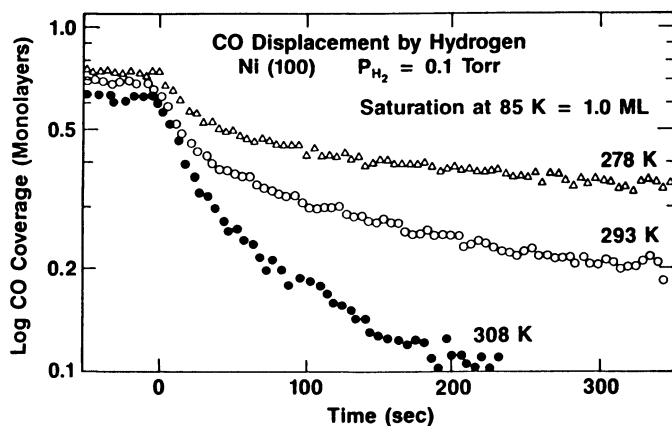
Figure 5. A set of in situ displacement experiments for the Ni(100) surface at 0.1 torr hydrogen pressure. These surface transients were determined with FYNES as a real-time monitor of the CO displacement. (Reproduced from ref. 55. Copyright 1990 American Chemical Society.)
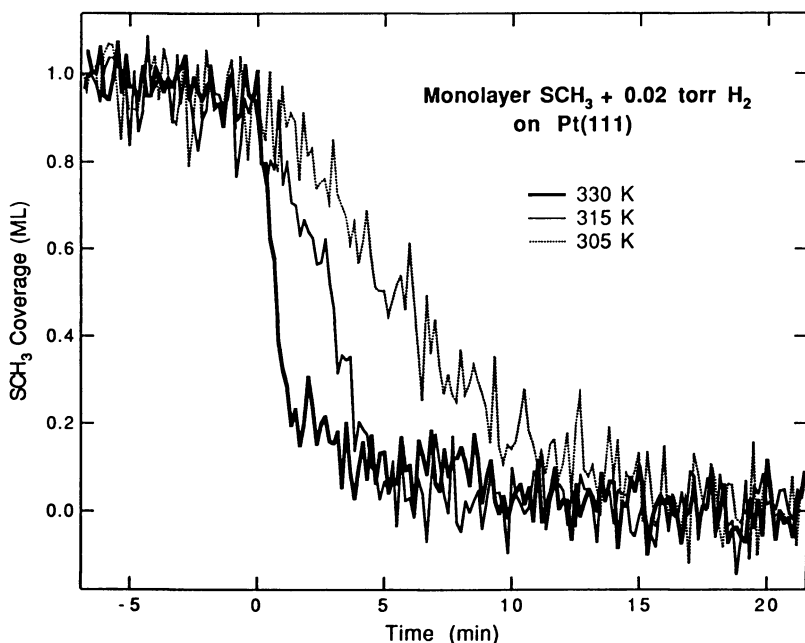
Figure 6. A set of transient isothermal experiments of the hydrogenolysis of methylthiolate on Pt(111) at 305, 315 and 330 K. Zero time corresponds to onset of the indicated temperatures.

were accumulated for about 15-20 minutes. After reaction had ceased the sample was heated to 750K at 2 K/sec so that an internal zero coverage calibration could be established. Auger spectra after each run indicate that the sample was free of carbon after this procedure. The amount of sulfur remaining on the surface is unchanged indicating that complete C-S bond activation is achieved in the presence of 0.02 torr hydrogen.

As in the case of CO displacement on Pt(111) the carbon loss vs real time curves were nicely fitted to first order single exponential equation ($\theta_t = \theta_\infty + \theta_0 \exp(-kt)$). The hydrogenolysis of methylthiolate (CH_3S) was found to be first order with respect to surface carbon coverage and roughly half order with respect to hydrogen pressures. Figure 7 illustrates the Arrhenius plot based on the rate constants determined from the exponential fits to the isothermal runs shown in figure 6. The C-S bond activation energy in presence of 0.02 torr hydrogen was found to be approximately 18.0 kcal/mol. In their recent paper Castro et al.*(44)* reported 8.81 kcal/mol C-S bond activation energy for CH_3S on Ni(100) in vacuum, showing that Ni surface to be more active towards C-S bond activation than platinum.

Future FYNES

Soft X-ray absorption has played an important role in characterizing adsorbed species and improving our understanding of bonding on surfaces. The additional flexibility provided by fluorescence detection promises to add substantially to our ability to characterize the structure and bonding of adsorbed species even in the presence of reactive environments. With current light sources and detector systems a wide range of important surface reactions can be characterized in detail using transient soft X-ray absorption methods. More intense light sources and more sophisticated monochromators promise to improve intensity by several orders of magnitude. The increased intensity will result in substantially improved time resolution and improved sensitivity. Improved intensities will be especially important for the development of FYNES since pressure isolation windows cause a substantial decrease in intensity available at the sample.

More sophisticated soft X-ray detector systems also promise to improve the sensitivity of the FYNES technique. Rapid advances in detectors and soft X-ray optics may result in detectors with higher sensitivity and energy resolution. Pressures in the 1 atmosphere range and temperatures in the 1000 K range can be achieved with extensions of current technology. A wide range of important surface reactions will become accessible with these improvements. The opportunities to characterize adsorbed surface species in detail under reaction conditions will be enhanced substantially by FYNES. This capability for

Hydrogenolysis of CH_3S on Pt(111), P_{H_2} = 0.02 torr
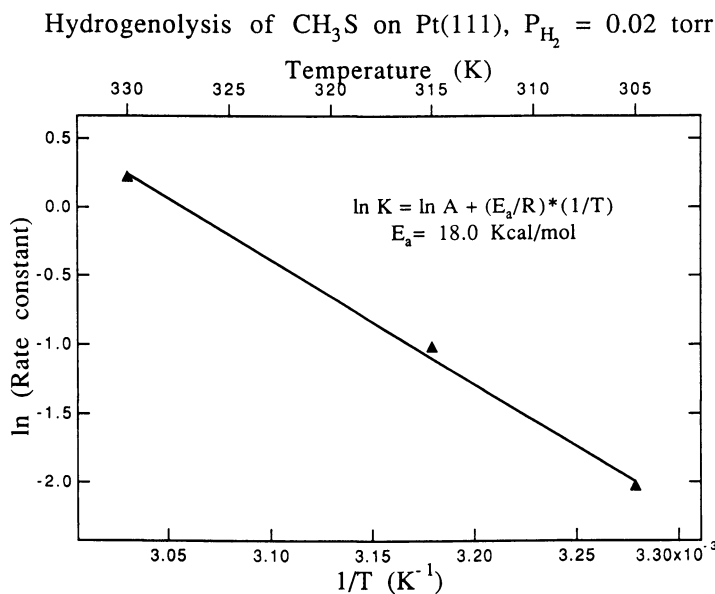
Figure 7. An Arrhenius plot for the rate constants determined from the exponential fits of the curves shown in figure 6. The slope gives an activation energy of about 18.0 kcal/mol.

characterizing adsorbed species and reaction rates may play an important role in increasing our understanding of the factors which control surface reactions.

Conclusions

On the Pt(111) surface in situ isothermal displacement experiments in the temperature range 318 to 348K clearly indicate that CO displacement is a first order process with an activation energy of 10.9 kcal/mol in the presence 0.2 torr of hydrogen. In the absence of hydrogen, isothermal desorption cannot be modeled by a simple first order exponential process, reflecting the increase in the desorption activation energy with decreasing coverage. Temperature programmed FYNES experiments on the Pt(111) surface indicate that even for hydrogen pressures below 0.2 torr where CO removal is not complete, hydrogen displaces the CO coverage from 0.67 ML for the saturated compressed monolayer to 0.50 ML the well known (2x2) structure with reduced CO-CO repulsive interactions. On the Ni(100) surface in situ isothermal displacement experiments in the 278 to 308 K temperature range indicate that CO is rapidly displaced by hydrogen pressures above 1.0×10^{-3} torr. These experimental results clearly indicate that there are

substantial interactions between coadsorbed CO and hydrogen which modify the removal mechanism for adsorbed CO in the presence of hydrogen. The application of FYNES as a transient method is further illustrated by hydrogenolysis studies of methylthiolate on the Pt(111) surface. The hydrogenolysis of methylthiolate is first order with respect to surface carbon coverage and roughly half order with respect to hydrogen pressure, having approximate C-S bond activation of 18.0 kcal/mol.

These results illustrate the importance of in situ methods capable of performing kinetic experiments on well characterized adsorbed monolayers in the presence of reactive atmospheres. High coverages of coadsorbed species resulting from high pressures of the coadsorbate may substantially modify surface coverages of chemisorbed species, may affect desorption activation energies, and may provide new kinetic pathways available for adsorbed species. These processes and others waiting to be discovered may play an important role in surface reactions which occur at high pressure.

Acknowledgements

Literature Cited

1.   Zaedra, F, Fischer, D.A., Shen, S., Gland, J.L. *Surf. Sci.* **1988**, *194*, 205

2.   Jaklevic, J, Kirby, J.A., Klein, M.P., Robertson, A.S., Brown, G.S., Eisenberger, P. *Solid State Commun.* **1977**, *23*, 680..

3.   Stohr, J., *Z. Physik*, **1985**, *B61*, 439.

4.   Outka, D.A., Stohr, J. In *Chemistry and Physics of Solid Surfaces VII*, edited by R. Vanselow and R. Howe, Springer-Verlag, New York, 1988, 201-220.

5.   Horsley, J.A. In *Chemistry and Physics of Solid Surfaces VII*, edited by R. Vanselow and R. Howe, Springer-Verlag, New York, 1988, 183-201.

6.   Stöhr, J, Sette, F., Johnson, A.L. *Phys. Rev. Lett.* **1984**, *53*, 1684.

7.   Stöhr, J, Kollin, E.B., Fischer, D.A., Hastings, J.B., Zaera, F., Sette F. *Phys. Rev. Lett.* **1985**, *55*, 1468.

8.   Fischer, D.A., Hastings, J.B., Zaera, F., Stöhr, J., Sette, F. *Nucl. Instrum. Methods Phys. Res.* **1986**, *561*

9.   Fischer, D.A., Döbler, U., Arvanitis, D., Wenzel, L, Baberschke, K., Stöhr, J. *Surf. Sci.* **1986**, *177*, 114.
10. Fischer, D.A., Gland, J.L. *Proc. Int'l. Conf. of Soft X-ray Optics and Technology,* **1986**, Berlin.
11. Stöhr, J., Denley, D., Prefetti, P., *Phys. Rev.* **1978**, *B18*, 4132.
12. Kraus, M.O., *J. Phys. Chem. Ref. Data* **1979**, 8, 307.
13. Gland, J.L., Fischer, D.A., Shen, S., Zaera F.*J. Am. Chem. Soc.* **1990**, *112*, 5695
14. Hoge, D., Tüshaus, Bradshaw, A.M. *Surf. Sci.* **1988**, *207*, L935.
15. Gland, J.L. and Kollin, E.B. *Surf. Sci.* **1984**, *151*, 260.
16. Sette, F., Stöhr, Kollin E.B., Dwyer, D.J., Gland, J.L., Robbins, J.L., Johnson, A.L. *Phys. Rev. Lett.* **1985**, *54*, 935.
17   Poelsema, B., Mechterscheimer, G., Comsa, G. *Surf. Sci.* **1981**, *111*, 519.
18. Christmann, K., Ertl, G., Pignet, T.*Surf. Sci.* **1976**, *54*, 365.
19. Norton, P.R., Richards, P.J., *Surf. Sci.* **1974**, *44*, 129..
20. Ertl, G., Neumann, M., Streit, K.M. *Surf. Sci.* **1977**, *64*, 393.
21. Krebs, H.J., Luth, H.*Appl. Phys.* **1977**, *13*, 147
22. McCabe, R.W., Schmidt L.D. *Surf. Sci.* **1977**, *66*, 101..
23. Poelsema, B., Palmer, R., Comsa *Surf. Sci.* **1984**, *136*, 1.
24. Norton, P.R., Goodale, J.W., Selkirk, E.B. *Surf. Sci.* **1979**, *83*, 189.
25. Thrush, K.A., White, J.M. *Appl. Surf. Sci.* **1985**, *24*, 157.
26. Bernasek, S.L., Lenz, K., Poelsema, B., Comsa, G. *Surf. Sci.* **1987**, *183*, L319.
27. Parker, D.H., Fischer, D.A., Colbert, J., Koel, B.E., and Gland, J.L. *Surf. Sci. Lett.* **1990**, *236*, L372.
28. Norton, P.R., Davis, J.A., and Jackman, T.E. *Surf. Sci.* **1982**, *122*, L593.
29. (Parker, D.H., Fischer, D. A., Colbert, J., Koel, B.E., and Gland, J.L. *Surf. Sci.* **1991**, in press).
30. Redhead, P.A. *Vacuum* **1962**, *12*, 203.
31. Lenz, K., Poelsema, B., Bernasek, S.L., Comsa, G. *Surf. Sci.* **1987**, *183*, L319.
32. Tracy, J.C*J. Chem. Phys.* **1971**, *56*, 2736.
33. Sanderson, S. *Solid State Commun.* **1977**, *21*, 75.
34. Mitchell, G.E., Gland, J.L., and White, J.M.*Surf. Sci.* **1983**, *131*, 167.
35. Christmann, K., Schober, O., Ertl, G., Neumann, M. *J. Chem. Phys.* **1974**, *60*, 4528.
36. Froitzheim, H., Hopster, H., Ibach, H., and Lehwald, S. *Appl. Phys.* **1977**, *13*, 147.
37. Lapujoulade, J., Neil, K.S. *Surf. Sci.* **1973**, *35*, 288.

38. Anderson, S.*Proc. Int. Vac.Congr., 7th Int. Conf. Solid Surfaces, 3rd Vienna,* **1977**, 1019.

39. Goodman, D.W., Yates, J.T., Jr., Madey, T.E. *Surf. Sci.* **1980**, *93*, L135.

40. Koel, B.E., Peebles, D.E., White, J.M. *Surf. Sci.* **1981**, *107*, L367.

41. Koel, B.E., Peebles, D.E., and White, J.M. *Surf. Sci.* **1983**, *127*, 709.

42. Shen, S., Zaera F., Fischer, D.A., and Gland, J.L. *J. Chem. Phys.* **1988**, *89*, 590.

43. Koestner, R.J., Stohr, J., Gland, J.L., Kollin, E.B., and Sette, F. *Chem. Phys. Lett.* **1985**, *120*, 285.

44. Castro, M.E., Ahkter, L., Golchet, A., White, J.M., Sahin, T. *Langmuir* **1991**, *7*, 126.

45. Bao, S., McConville, C.F., Woodruff, D.P. *Surf. Sci.* **1987**, *187*, 133.

46. Huntley, D.R. *J. Phys. Chem.* **1989**, *93*, 6156-6164.

47. Albert, M.R., Lu, J.P., Bernasek, S., Cameron, S.D., Gland, J.L. *Surf. Sci.* **1988**, *206*, 348.

48. Sexton, B.A., Nyberg, G.L. *Surf. Sci.* **1987**, *165*, 251.

49. Seymour, D.L., Bao, S., McConville, C.F., Crapper, M.D., Woodruff, D.P., Jones, R.G. *Surf. Sci.* **1987**, *529*, 189-190 .

50. Nuzzo, R.G., Zegarski, B.R., Dobois, L.H. *J. Am. Chem. Soc.* **1987**, *109*, 733..

51. Benziger, J. B.; Preston, R. E. J. Phys. Chem. **89** (1985), 5002.

52. Dezarnaud, C., Tronc M., Hitchcock, A.P. *Chem. Phys.* ***1990***, *142*, 455.

53. (Rufeal, T., Slaughter, E. and Gland, J.L., unpublished TPD work of CH3SH on Pt(111)).

54. (Rufael, T., Prasad, J., Fisher, D.A., and Gland, J.L., in preparation).

55. Gland, J.L., Fischer, D.A., Parker, D.H., and Shen, S., In *Fundumentals Aspects of Chemistry and Physics*, 1990, Special Edition of Langmuir, in press.

Chapter 13

In Situ Studies of Catalytic Reactions with Fourier Transform–Infrared Reflection–Absorption Spectroscopy

Island Formation and Stability of Ultrathin Layers at High Pressure

Friedrich M. Hoffmann and Mark D. Weisel

Exxon Research and Engineering Company, Annandale, NJ 08801

Time-resolved Fourier Transform-Infrared Reflection Absorption Spectroscopy (FT-IRAS) can be used to follow *in-situ* catalytic reactions on single crystal surfaces at high pressure. This is illustrated with studies of the CO dissociation and methanation reactions on Ru(001), where the formation of adsorbate islands is observed *in-situ* at high pressure. Vibrational frequencies, intensities and lineshapes allow us to determine *both local and total* coverage of surface adsorbates, and to estimate island domain sizes. In the case of Cu-Ru surfaces, we are able to estimate domain sizes of copper islands and investigate their stability at high pressure. Time-resolved measurements allow us to investigate the kinetic implications of island formation for the CO disproportionation and methanation reactions over Ru(001).

Lateral interactions and island formation of adsorbates on solid surfaces are important factors which determine the kinetics of surface reactions. The application of surface sensitive probes to well-defined surfaces has greatly contributed to the understanding of these interactions at low pressures. Island formation in catalytic reactions at higher pressures, on the other hand, remains largely unexplored due to the pressure limitation of most surface science probes (typically 10^{-5} Torr). Recently, Fourier Transform-Infrared Reflection Absorption Spectroscopy (FT-IRAS) has been applied to study catalytic reactions at higher pressures on polycrystalline foils (*1*) and single crystal surfaces (*2-4*) of bridging the pressure gap between surface science and catalysis at high pressures.

Here, we review some examples, which demonstrate the *in-situ observation of island formation during catalytic reactions*. IRAS has been utilized in the past to study intermolecular interactions between adsorbed molecules. Early infrared studies of CO adsorption on metal surfaces have revealed large frequency shifts as a function

of surface coverage as discussed in detail earlier (*5*). Two effects contribute to this shift. First, the sensitivity of the molecule with respect to its "chemical" or "electronic" environment, i.e. the adsorption site on the metal and/or the presence of a coadsorbed atom or molecule which electronically modifies the adsorption site. Second, the intermolecular interaction within the adsorbate layer. The latter causes coverage dependent frequency shifts both as a result of vibrational coupling and of electronic interaction among neighboring molecules. Therefore, *frequency shifts from intermolecular interaction are a sensitive probe of the intermolecular spacing in an adsorbate layer*. This fact has been exploited in several UHV studies of CO island formation (*6,7*) and CO compression phases (*8,9*).

Experimental Description

The experiments were performed in a multilevel UHV chamber (1×10^{-10} Torr), shown in Figure 1, which was equipped for Infrared Spectroscopy, LEED, Auger Spectroscopy, Thermal Desorption Mass Spectroscopy and workfunction measurements (Kelvin probe). Infrared Spectroscopy was performed at a high pressure level, which could be isolated from the UHV chamber with a gate valve. This permits *in-situ* FT-IRAS at gas pressures from 10^{-10} torr to 1000 torr. Reaction products can be measured either with a Gas Chromatograph or by IR gas-phase spectra.

Infrared spectra were obtained with a Perkin Elmer 1800 FTIR and a wide band MCT detector in single reflection with an angle of incidence of 80°. Typically, 100 scans at 4 cm^{-1} resolution were added in a total measurement time of 50 seconds and ratioed against the background from the clean surface. In the "fast" time-resolved mode, spectra were obtained at 300 msec per scan and a spectral resolution of 8 cm^{-1}.

A typical experiment proceeded in the following manner. The Ru crystal was cleaned and characterized for surface cleanliness according to procedures described elsewhere in detail (*7*). Subsequently, adlayer films (e.g. Cu) were prepared by in-situ evaporation and characterized for surface coverage and cleanliness. After the film preparation, the sample was translated to the high-pressure reactor level. After an IR background spectrum of the clean crystal was obtained, the surface was exposed to the reaction gases by increasing the pressure to the desired value. All the reactant gases were of high purity; however, CO was further purified by flowing the gas through a liquid nitrogen trap to remove residual carbonyl (particularly $Ni(CO)_4$). Following the high pressure IR experiments, the sample was cooled to room temperature. Then the high pressure cell was evacuated to $< 10^{-9}$ Torr (typically in < 2 minutes) and the crystal was reintroduced to the UHV chamber. There, post-reaction Multiple Mass Thermal Desorption Spectroscopy, LEED and Auger Spectroscopy spectroscopy were performed to characterize the state of the surface after reaction.

Island Formation and the Stability of Adlayers

The fact that lateral interactions within molecular adlayers result in vibrational frequency shifts can be used to determine the intermolecular spacing within an adsorbed CO layer (*5*). This allows us to determine surface coverages *in-situ* during reaction at high pressures. The case of CO/Ru(001) is in this respect ideal, since CO
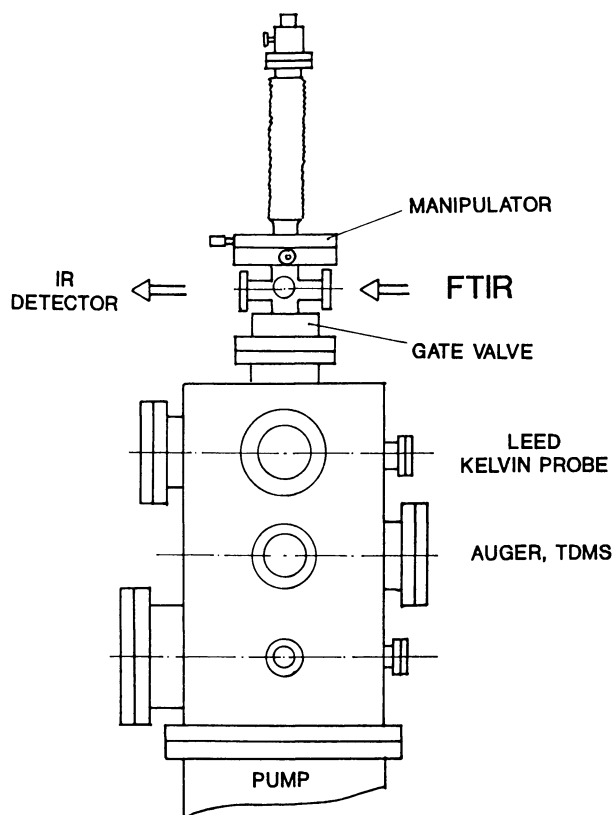
Figure 1.   Experimental System with multilevel UHV chamber and high pressure cell. FT-IRAS is performed at the top level which can be isolated from the UHV chamber with a gate-valve and pressurized up to 1 atm.

adsorbs in on-top sites over the entire coverage range and frequency shifts from adsorption site changes (e.g. linear to bridge sites) are absent in most cases.

Figure 2 presents vibrational spectra for CO adsorbed on Ru(001) at 325 K as a function of increasing coverage. Spectra (a) - (f) were obtained after CO exposures under UHV conditions while spectra g-j were taken at equilibrium pressures of CO from 10^{-7} to 2.5 Torr. Increasing the coverage in Figure 2 results in a shift of the C-O stretching frequency from 1990 cm^{-1} at low coverage to 2066 cm^{-1} at 2.5 Torr equilibrium pressure. The calibration of the CO stretching frequency as a function of surface coverage with thermal desorption and LEED (*7*) is shown in the inset of Figure 2. The latter allows us to determine the coverage of CO at high pressures of CO. From Figure 2 we estimate a coverage of $\theta_{CO} = 0.72$ at a pressure of 2.5 Torr. We note that this calibration is strictly valid only for the substrate temperature of 300 K. At higher substrate temperature the C-O stretch frequency is redshifted due to dephasing (*10*). Therefore we have to apply dephasing corrections for the appropriate substrate temperature in order to determine CO coverages at higher substrate temperature.

The fact that we can determine adsorbate coverages under high pressure conditions is less trivial than it sounds. At low pressure (UHV), surface coverages can be determined with a variety of surface sensitive probes. One such case is the combination of LEED with Thermal Desorption Mass Spectroscopy (TDMS) or X-Ray Photoemission Spectroscopy (XPS). However, most surface probes utilize electrons and hence are restricted to low pressure. In-situ measurements at high pressure have been restricted to-date to supported metals. There, transmission IR or NMR methods are frequently used for in-situ spectroscopy at high pressure. However, for supported metals the absolute calibration of surface coverage is often difficult since it requires the measurement of the total surface area, which depends on the dispersion of the catalyst. The use of single crystals with known surface area alleviates this problem and in combination with an optical probe allows us to obtain data at high pressure and calibrate them with low pressure measurements.

The formation of CO islands can be revealed both by characteristic C-O stretch frequency shifts and by the vibrational lineshape, as discussed earlier in detail (*7*). In the absence of island formation, the intermolecular C-O stretching frequency displays a steady shift with increasing coverage due to a steady decrease of the CO-CO distance. The inset of Figure 2 shows for low and high coverage of CO two almost linear regions. However, at an intermediate coverage of $\theta_{CO} \approx 0.30$, we recognize a characteristic plateau in the CO frequency vs. coverage plot. There, an increase in CO coverage occurs at constant frequency. This is due to the fact that the intermolecular CO-CO distance remains constant, while the total surface coverage increases, i.e. the increase in coverage occurs via the growth of islands. The sensitivity of the C-O stretch frequency to lateral interactions within the CO layer also leads to pronounced effects in the vibrational lineshape. For example, ordering of the adlayer in a $\sqrt{3} \times \sqrt{3}$-R30° structure, confirmed with LEED, results in a sharp decrease in IR linewidth, as is evident from spectrum (d) in Figure 2 (*7*). The observation of a homogeneous Lorentzian linewidth for a highly ordered adlayer of CO reflects the narrow homogeneous distribution of CO-CO intermolecular distances and a large average domain size, i.e. long-range ordering. Disordering of the adlayer, on the other hand, results in inhomogeneous line broadening due to a loss
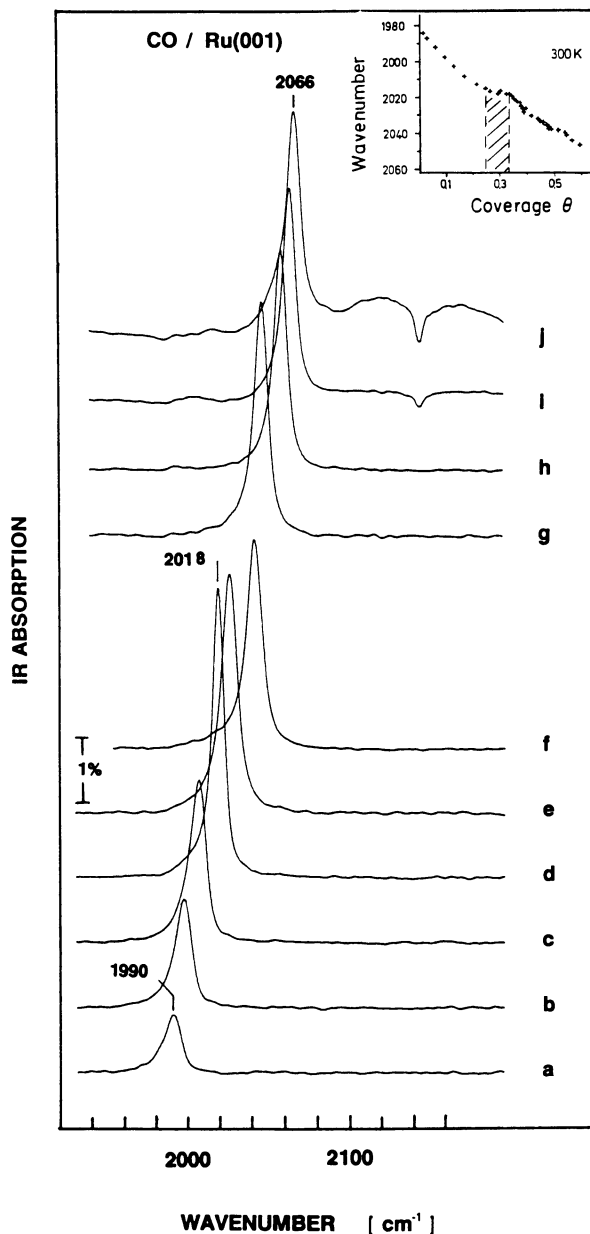
Figure 2. Infrared spectra of CO adsorbed at 325 K on Ru(001): (a) 0.1 L; (b) 0.2 L; (c) 0.4 L; (d) 0.8 L; (e) 1.5 L; (f) 5.0 L; (g) 10^{-7} Torr CO; (h) 2×10^{-2} Torr CO; (i) 0.2 Torr CO; (j) 2.5 Torr CO. Inset: C–O stretch frequency vs. coverage for CO adsorption at 300 K. Hatched areas indicate ordered structures observed with LEED. (Reproduced with permission from ref. 7. Copyright 1980 Elsevier.

of homogeneity in the intermolecular spacing. Inhomogeneous broadening can also be caused by finite domain sizes of an adlayer both for the ordered and disordered case, as discussed elsewhere in detail (*5,11*). This is due to the fact that for finite domain sizes the molecules at the domain edge feel less intermolecular interaction due to the smaller number of neighbors than molecules in the domain center. This can result in asymmetric IR lineshapes as will be shown later in the case of copper islands on Ru(001).

In the following sections we will utilize the sensitivity of the C-O stretching frequency to the CO-CO intermolecular distance for in-situ spectroscopy of catalytic reactions of CO at high pressure. These examples illustrate the formation of carbon islands under disproportionation conditions (pure   CO) as well as under hydrogenation conditions (CO/H), and the formation and stability of copper islands on Ru(001) under CO/H reaction conditions.

Carbon Island Formation from the Dissociation of CO on Ru(001)

The adsorption and dissociation of carbon monoxide on metal surfaces has been of continuing great interest both in surface science and in catalysis. The dissociation of CO is the first step in the methanation reaction which in simplified form contains the following reaction steps:

$$CO(ad) \quad \rightarrow \quad C(ad) + O(ad) \tag{1}$$
$$C(ad) + 4H \quad \rightarrow \quad CH_4(g) \tag{2}$$
$$O(ad) + 2H \quad \rightarrow \quad H_2O(g) \tag{3}$$
$$O(ad) + CO \quad \rightarrow \quad CO_2(g) \tag{4}$$
$$C(ad) \quad \rightarrow \quad C \text{ (graphite)} \tag{5}$$
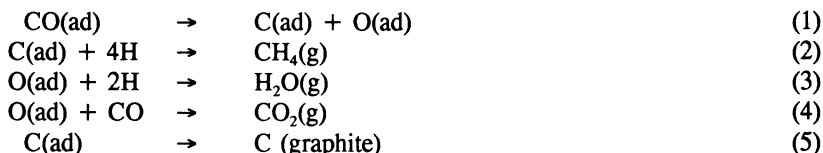
The nature of the carbon species which is formed as a result of the dissociation step (1) is of crucial importance as an intermediate in this reaction. The carbon species formed can either be reactive and further hydrogenated (*12,13*) or form graphite, which poisons the reaction and prevents further CO adsorption. The pressure of hydrogen is critical in determining the product distribution in the Fischer-Tropsch process. Higher pressures of hydrogen result primarily in the production of methane, while lower hydrogen pressure results in a Fischer-Tropsch product distribution, which is dominated by longer hydrocarbon chains (*12*). Finally, at very low pressures or in the absence of hydrogen, the carbon species produced from step (1) is no longer removed via hydrogenation leading to graphite formation (5) and deactivation of the surface. The effects of hydrogen both with respect to the dissociation of CO and to the formation of carbon species are still not well understood to date and are subject of continued interest in surface science and catalysis.

CO dissociation in the absence of hydrogen constitutes an extreme of low hydrogen pressure. In this case steps (2) and (3) are absent, leading to the disproportionation of CO (Boudouard reaction). CO dissociates to form carbon and oxygen on the surface. The latter reacts with undissociated CO on the surface to form CO_2 which desorbs into the gas phase (4). The carbon left on the surface accumulates and blocks further CO adsorption. On a Ru(001) single crystal surface, which is a good model for a supported ruthenium catalyst (*13,14*), CO dissociation is not observed under UHV conditions. At elevated temperatures and CO pressures,

however, this reaction can be followed by time-resolved vibrational spectroscopy (*4*). Experimental results are shown in Figure 3 (A) (left panel), where the reaction of CO (2.5 Torr) with a Ru(001) surface at 662 K is followed as a function of reaction time. The spectra depicting the reaction at time intervals of 108 seconds exhibit a single absorption band, which decreases in intensity as a function of reaction time. The frequency of 2026 cm^{-1} is characteristic of CO adsorbed in the on-top adsorption site. With the coverage calibration in Figure 2 and appropriate correction for the substrate temperature of 662 K (as discussed earlier) we can use the C-O frequency to determine the total surface coverage of CO *at the start of the reaction* to $\theta = 0.42$. As the reaction proceeds the intensity of the CO band decreases steadily, indicating the build-up of carbon which suppresses CO adsorption. We note, however that this intensity decrease occurs at constant frequency. From the previous discussion, we can infer that the *local* CO coverage must remain constant even though the *total* coverage is reduced. This means that the decrease in total CO coverage proceeds through the formation of islands, which maintain a *constant local* CO coverage, but decrease in domain size as the reaction proceeds. This implies also that *the build-up of carbon from CO dissociation occurs in the form of islands*, which block further CO adsorption. The formation of carbon islands is also evident from post-reaction spectroscopy performed after quenching the reaction and evacuating the high pressure chamber. Figure 4 shows thermal desorption mass spectra obtained after the CO dissociation reaction (b) - (d) in comparison to CO desorption from the clean Ru(001) surface (a). The post-reaction spectra (b-d) exhibit strongly reduced total intensities as the build-up of surface carbon increases. However, the lineshapes of the thermal desorption traces exhibit two desorption peaks at 450 K and 400 K characteristic of a locally high CO coverage similar to that of the clean surface in spectrum (a). This suggests desorption of CO from patches of bare (clean) ruthenium. Similar post-reaction thermal desorption spectra have previously led Tamaru and collaborators to conclude on carbon island formation resulting from CO dissociation on ruthenium (*15*).

The amount of carbon produced in the reaction can be determined by post-reaction oxygen titration, i.e. by adsorbing oxygen on the carbon covered surface and observing the amount of CO from the recombination of C + O → CO (*4*). The inset in Figure 4 depicts a plot of the amount of carbon left after reaction versus the amount of remaining surface sites available to CO adsorption. We can see that the increase in carbon relates linearly to the decrease in CO coverage at a 1:1 ratio indicative of the formation of *2-dimensional* carbon islands. From the observed C + O reaction temperature peak at 780 K (not shown here), we can conclude on the reactivity of this carbon layer, at least with respect to oxidation. As discussed elsewhere in detail (*4*), we find the reactivity of this 2-dimensional form of "graphite" to fall between that of unreactive 3-dimensional graphite and that of highly reactive amorphous carbon.

CO dissociation in the presence of hydrogen exhibits an entirely different behavior. Kinetic studies of the CO/H reaction on Ru(001) indicate that the dissociation of CO is accelerated by about two orders of magnitude in the presence of hydrogen (*3*). Figure 3 (B) (right panel) shows time-resolved vibrational spectra obtained during the reaction of a mixture of 2.5 Torr CO + 1.0 Torr H$_2$ with the Ru(001) surface at 475 K. The hydrogen pressure has been chosen lower than for

CO / Ru(001)   **CO/H Ru(001)**
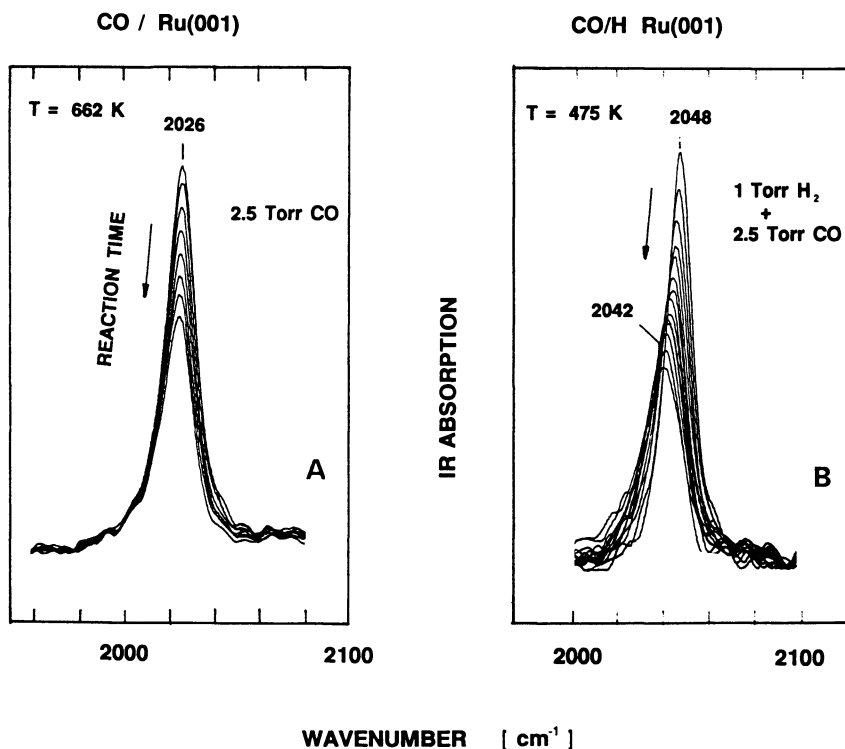
Figure 3.   A) In-situ vibrational spectroscopy following the dissociation of CO on Ru(001) as a function of increasing reaction time at 2.5 Torr pressure and 662 K temperature. The time interval between the spectra is 108 seconds (100 scans each, 4 cm^{-1} resolution) (*4*).
B) Dissociation of CO on Ru(001) in the presence of hydrogen (2.5 Torr CO + 1 Torr H$_2$) and at a reaction temperature of 475 K. The time interval between the spectra is 44 seconds (16 scans each, 4 cm^{-1} resolution).
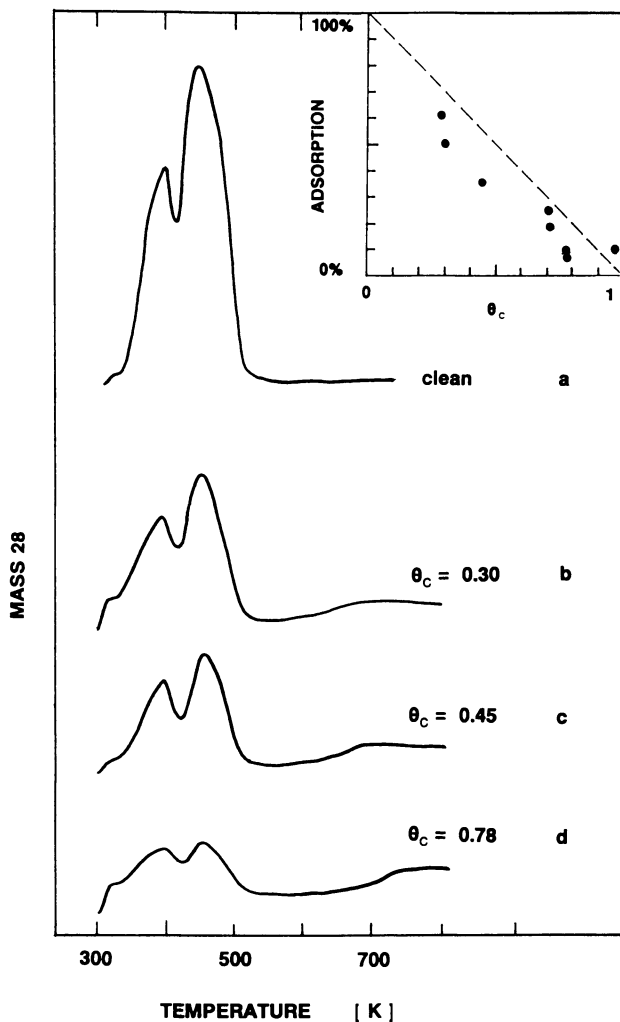
Figure 4.   Post-reaction thermal desorption spectra of CO after the reaction of 2.5 Torr of CO with Ru(001) at temperatures of 600 to 700 K and various reaction times. The fact that the lineshape of the CO thermal desorption feature remains unchanged in spite of the strongly reduced band intensity indicates the formation of islands.

Inset: The plot of carbon coverage vs. the number of surface   sites available for CO adsorption reveals a 1:1 correspondence characteristic of the formation of 2D-carbon islands.

typical methanation conditions. This reduces the hydrogenation of carbon and emphasizes the build-up of carbon. From Figure 3 (B), we see that in the presence of hydrogen CO dissociation requires a drastically lower reaction temperature of 475 K compared to the reaction temperature of 662 K in pure CO. It is also evident from the vibrational spectra that the decrease in intensity due to the build-up of carbon now is accompanied by a substantial broadening of the IR band as well as by a frequency shift to lower values. The line broadening, as well as the frequency shift, indicates the build-up of amorphous carbon on the surface. The latter acts as a "dilutant" to the CO layer thus causing the inhomogeneous line broadening and the shift to lower frequencies. Post-reaction spectroscopy further supports the existence of amorphous carbon during reaction. Oxygen titration thermal desorption spectra show a reduced C+O recombination temperature of 550 K (*16*). The latter is characteristic of amorphous or carbidic carbon as discussed by Lauderback and Delgas (*17*). The observation of this carbon species is significant since it is considered a reactive intermediate in the methanation of CO as suggested by Kelley and Goodmann (*13*). Based on studies over nickel and ruthenium single crystal surfaces, these authors find a direct correspondence between the methanation reaction rate and the steady state coverage of carbidic carbon on the surface.

The effect of carbon island formation on the kinetics of CO dissociation is shown in Figure 5, where the decrease in IR intensity observed in Figure 3 is plotted on a logarithmic scale versus reaction time. For the case of *pure CO* the reaction follows pseudo-first-order kinetics, i.e $\ln(\theta/\theta_0) = -k_1 t$, where k_1 is the rate constant, t the reaction time and θ_0 the initial coverage at t=0. Similar behavior is observed for a range of reaction temperatures and allows us to determine the activation energy of this reaction via an Arrhenius plot. For dissociation of CO on Ru(001) in the absence of hydrogen we thus determine an activation energy of ≈ 21 kcal/mole (*4*). The fact that this reaction follows pseudo-first-order kinetics is a direct consequence of the island formation of CO. As discussed elsewhere in detail (*4*), the reaction rate constant for CO dissociation is pressure dependent and depends on the *local* surface coverage of CO. Therefore the observation of pseudo-first-order behavior is expected only if the *local* surface coverage of CO remains constant. The kinetic behavior observed here, therefore supports a reaction model where carbon and CO segregate to forms islands. *In the presence of hydrogen*, the reaction does not obey pseudo-first-order behavior as shown in Figure 5. The build-up of dispersed carbon obviously seems to be mainly responsible for this effect. Details of the effect of hydrogen on CO dissociation and carbon formation, however, remain to be investigated further.

The Formation and Stability of Copper Islands on Ru(001)

The Cu/Ru system is regarded as a classical model to study catalytic reactions on bimetallic surfaces (*18*) and has received much attention in both catalysis and surface science. The characterization of metal dispersion in these bimetallic catalysts, however, is still considered a controversial subject. This is partly due to a lack of surface sensitive probes which perform both on single crystal surfaces in UHV and under catalytic pressure conditions. The adsorption behavior of Cu/Ru(001) single crystal surfaces has been investigated by Christmann and collaborators in a series of
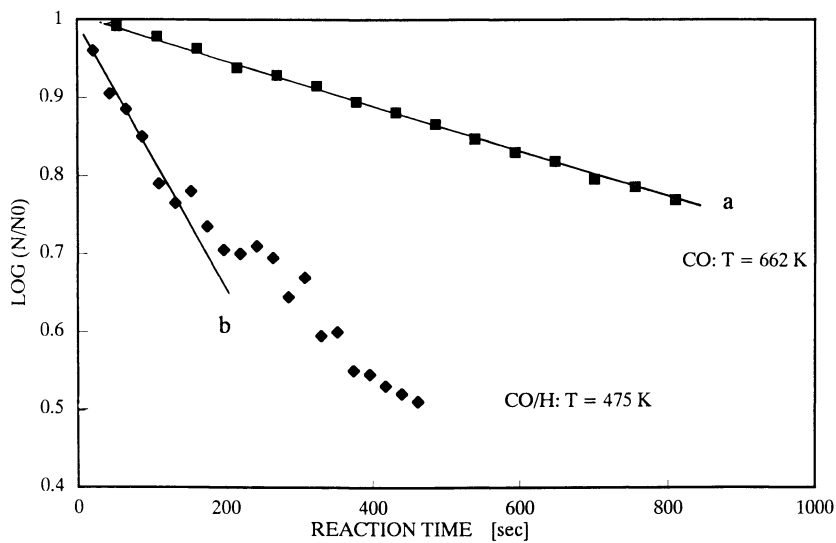
Figure 5.   Change in the IR intensity of the C-O stretching vibration (logarithmic scale) as a function of reaction time: (a) 2.5 Torr CO at 662 K; (b) 2.5 Torr CO + 1 Torr H_2 at 475 K.

detailed surface science studies (19-22). The formation of 2D-copper islands pseudomorphic to the Ru(001) substrate has been suggested by Houston et.al. (23) based on LEED observations. Utilizing CO as a probe molecule and high resolution FT-IRAS the dispersion of copper on Ru(001) has been studied in detail under UHV conditions (24-26). The knowledge gained from these UHV studies can now be applied to characterize the formation, domain sizes and stability of copper islands under reaction conditions at high pressure and temperature.

Experimental results demonstrating the formation of 2D-copper islands at submonolayer copper coverage are shown in Figure 6. There, the equivalent of about half of a monolayer of copper ($\theta_{Cu}=0.45$) has been evaporated under UHV conditions on a Ru(001) surface held at 85 K and subsequently annealed to higher temperatures. Adsorption of CO after each annealing produces vibrational spectra characterizing the dispersion of copper as a function of annealing temperature. Spectrum (a), which was obtained after evaporation at 85 K and saturation with CO, shows two broad bands centered at 2120 cm^{-1} and 2050 cm^{-1}. These bands can be assigned to CO adsorbed on copper and ruthenium sites respectively. The large inhomogeneous line broadening of both bands indicates a randomly dispersed copper overlayer. The high frequency of the CO-Cu band of 2120 cm^{-1} is typical of highly dispersed small 2D- and 3D-copper clusters, as discussed previously (26). Annealing to 250 K produces a sharper CO-Ru band at 2056 cm^{-1}. As discussed further below, this is indicative of larger domain sizes of CO adsorbed on the ruthenium substrate. The splitting of the broad CO-Cu band into two bands at 2130 cm^{-1} and 2105 cm^{-1} signals ordering into apparently well-defined 2D- and 3D- copper aggregates, whose nature, however, is at present not well understood. Annealing to 350 K produces two major bands at 2056 cm^{-1} and 2083 cm^{-1}. The linewidth of the 2056 cm^{-1} band indicates the formation of large domains of bare ruthenium surface. The frequency of the CO-Cu band at 2083 cm^{-1} is characteristic of a pseudomorphic monatomic copper layer and its lineshape indicates a large domain size of the copper layer (25).

The lineshape of the CO-Ru band allows us to estimate domain sizes of bare ruthenium patches from which we can infer the average domain size of the copper islands. Earlier studies of the formation of islands of CO adsorbed in an ordered $\sqrt{3}x\sqrt{3}$-R30° structure on Ru(001) have shown that a reduction of the domain size leads to a characteristic inhomogeneous line broadening with a pronounced asymmetry at the low frequency side of the absorption band (7). This effect on the lineshape is also observed for the formation of copper islands on Ru(001). In Figure 7, we compare vibrational spectra of a $\sqrt{3}x\sqrt{3}$-R30°-CO structure of different domain sizes on Cu-Ru(001) surfaces with increasing copper coverage (a-c). The choice of a CO adsorption temperature of 250 K ensures sufficient surface mobility for ordering of the CO molecules in the $\sqrt{3}x\sqrt{3}$-R30° structure, which is observed also in LEED. At the same time adsorption of CO on copper sites is suppressed at this temperature. This prevents distortion of the vibrational lineshape due vibrational coupling between CO-Cu and CO-Ru molecules. The vibrational spectra in Figure 7 exhibit increasing line broadening as the copper coverage is increased. Based on theoretical calculations described in Ref. (7) and (11), we estimate for $\theta_{Cu}=0.38$ (b) an average Ru-CO island size of about 100 Å and for $\theta_{Cu}=0.60$ (c) an average island size of 20 Å (25).

It is obviously of interest to study the stability of these Cu-Ru surfaces under
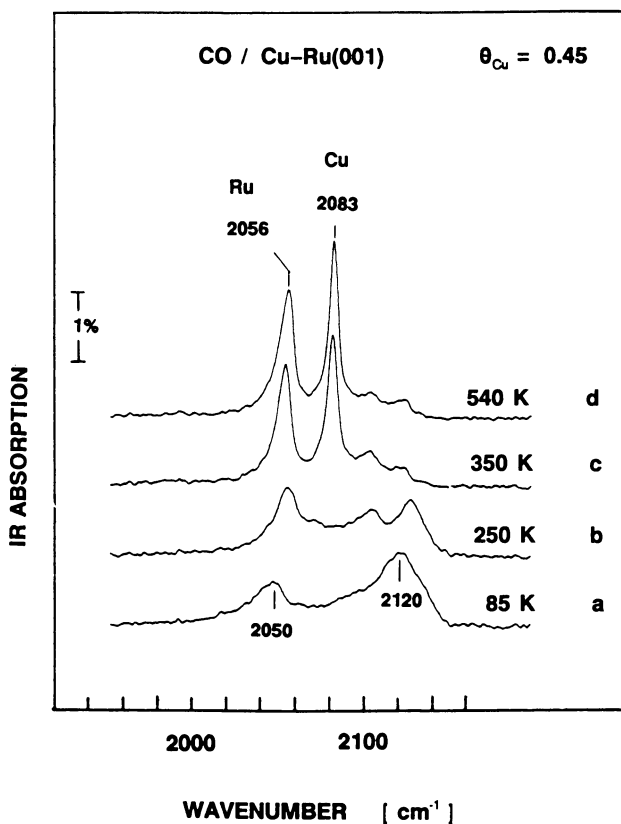
Figure 6.   The formation of copper islands demonstrated with vibrational spectra of CO adsorbed on a Cu-Ru(001) surface (θ_{Cu} = 0.45) which has been annealed successively to higher temperature (15): (a) Randomly dispersed copper after evaporation at 85 K; (b) Formation of 3D- and 2D- copper aggregates after annealing to 250 K; (c-d) Annealing above room temperature produces pseudomorphic 2D-copper islands exposing large domains of bare ruthenium substrate.
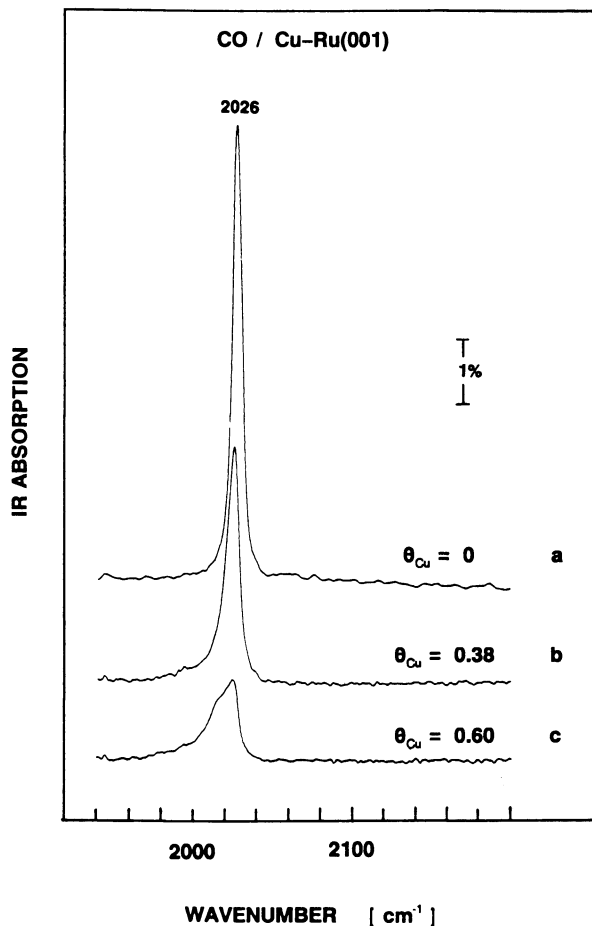
Figure 7.   Vibrational lineshape for CO adsorbed in the $\sqrt{3}x\sqrt{3}$-R30° structure on Ru(001) with different domain sizes resulting from island formation of copper on Ru(001) (*15*): (a) clean Ru(001); (b) θ_{Cu} = 0.38; θ_{Cu} = 0.60. In all cases CO was adsorbed at 250 K and spectra were taken after cooling to 85 K. The copper layers in (b) and (c) have been annealed to 540 K after evaporation and prior to CO adsorption.

CO / Cu–Ru(001)

P_{co} = 2.5 Torr
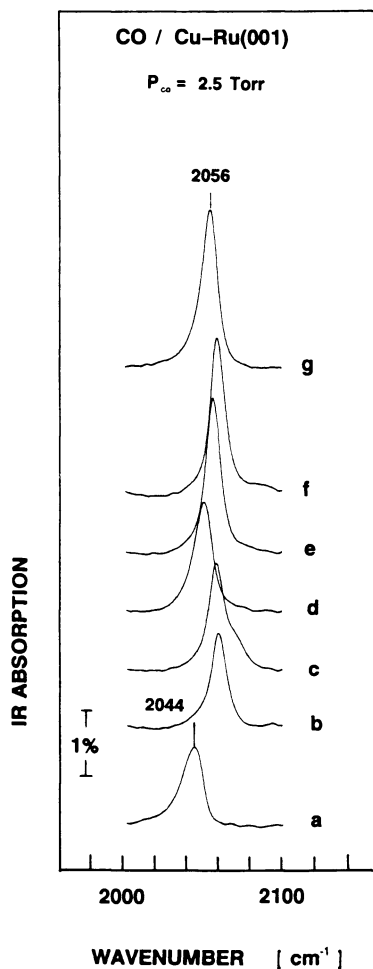
Figure 8.   Stability of Cu-Ru(001) surface (θ_{Cu} = 0.50) under reaction conditions of high pressure (2.50 Torr) and temperature.
(a) CO saturation (6 L) at 300 K in UHV; (b-d) 2.5 Torr CO and increasing the reaction temperature from 300 K to 500 K; (d-f) Recooling from 500 K to 300 K; (g) evacuation to 10^{-9} Torr at 300 K.

conditions of catalytic reactions, i.e. at high pressure and temperature. To this end we have prepared and annealed under UHV conditions a Cu-Ru(001) surface with θ_{Cu}=0.50. This produces a surface similar to that shown earlier in Figure 6(d). Saturation with CO at 300 K results in the vibrational spectrum of Figure 8(a) with a CO-Ru band at 2044 cm^{-1}. We note that the adsorption temperature of 300 K prevents the occupation of CO-Cu sites due to the lower adsorption energy of CO on copper (*24*). Increasing the CO pressure to 2.5 Torr Figure 8(b) and the surface temperature from 300 K to 500 K Figure 8(b-d) simulates conditions under which CO hydrogenates in the presence of hydrogen. The change in pressure and reaction temperature results in a frequency shift of the CO-Ru band which is similar to that observed on the clean Ru(001) surface and which reflect a change in the local CO coverage due to the increase in substrate temperature (*14*). Upon recooling to 300 K Figure 8(f) we observe a marked increase in the IR band intensity compared to Figure 8(b)(prior to heating) . As discussed earlier, the intensity of the IR band yields information on the *total* surface area accessible to CO adsorption. However, it is *not* a measure of the *local* CO coverage because of the non-linearity of the IR extinction coefficient at higher CO coverage (hence we use the C-O stretch frequency to determine the local coverage). The comparison between spectrum (b) and (d) shows an increase in the IR band intensity, but the C-O stretch frequency remains essentially unchanged. This indicates an increase in the *total* surface area of bare ruthenium accessible to CO adsorption due to a loss of "site-blocking" copper atoms. Post-reaction spectroscopy indicates no loss of copper atoms. Thus we must conclude on a change in copper dispersion from 2D islands to 3D aggregates as a result of the pressure/temperature conditions to which the surface was subjected. It remains to be seen from further studies, whether these results are characteristic of the stability of other bimetallic systems under conditions of catalytic reactions. Although these results are preliminary in character they demonstrate, however, the potential of FT-IRAS to the in-situ characterization of bimetallic surfaces during catalytic reactions at high pressure.

Acknowledgments

Literature Cited

1. Burrows, V.A.; Sundaresan, S.; Chabal, Y.J.; Christman, S.B. *Surface Sci.* **1985**, *160*, 122.
2. Hoffmann, F.M.; Robbins, J.L. *J. Vac. Sci. Technol.* **1987**, *A 5*, 724.
3. Hoffmann, F.M.; Robbins, J.L. *J. Electron Spectr. Rel. Phen.* **1987**, *45*, 421.
4. Hoffmann, F.M. *J. Chem. Phys.* **1989**, *90*, 2816.
5. Hoffmann, F.M. *Surface Sci. Reports* **1983**, *3*, 107.
6. Crossley, A.; King D.A. *Surface Sci.* **1980**, *95*, 131.
7. Pfnür, H.; Menzel, D.; Hoffmann, F.M.; Ortega, A.; Bradshaw, A.M. *Surface Sci.* **1980**, *93*, 431.
8. Bradshaw, A.M.; Hoffmann, F.M. *Surface Sci.* **1978**, *72,* 513.

9. Persson, B.N.J.; Tüshaus, M.; Bradshaw, A.M. *J. Chem. Phys.* **1990**, *92*, 5034.
10. Hoffmann, F.M.; Persson, B.N.J. *Phys. Rev. B* **1986**, *34*, 4354.
11. Hollins, P. *Surface Sci.* **1981**, *107*, 75.
12. Biloen, P.; Sachtler, W.H.M. *Adv. Catalysis* **1981**, *30*, 165.
13. Kelley, R.D.; Goodman, D.W. in *The Chemical Physics of Solid Surfaces*, D.A. King; D.P. Woodruff, Eds.; Elsevier, Amsterdam,1982; *Vol. 4.*
14. Hoffmann, F.M.; Robbins, J.L. in *Proceedings of the 9th International Congress in Catalysis*, M.J. Phillips; M. Ternan, Eds.; 1988; Vol.3, 1144.
15. Shincho, E.; Egawa, C.; Naito, S.; Tamaru, K. *Surface Sci.* **1985**, *149*, 1.
16. Hoffmann, F.M.; Weisel, M.D.; unpublished.
17. Lauderback L.L.; Delgas, W.N. *J. Catalysis* **1987**, *105*, 55.
18. Sinfelt, J.H. in *Bimetallic Discoveries and Concepts and Applications*; Wiley, New York, 1983.
19. Christmann, K.; Ertl, G.; Shimizu, H. *J. Catal.* **1980**, *61*, 397.
20. Shimizu H.; Christmann, K.; Ertl, G. *J. Catal.* **1980**, *61*, 412.
21. Vickerman, J.C.; Christmann, K.; Ertl, G. *J. Catal.* **1981**, *71*, 175.
22. Vickerman, J.C.; Christmann, K. *Surface Sci.* **1982**, *120*, 1.
23. Houston, J.E.; Peden, C.H.F.; Blair, D.S.; Goodman D.W. *Surface Sci.* **1986**, *167*, 427.
24. Paul, J.; Hoffmann, F.M. *Surface Sci.* **1986**, *172*, 151.
25. Hoffmann, F.M.; Paul, J. *J. Chem. Phys.* **1986**, *86*, 2990.
26. Hoffmann, F.M.; Paul, J. *J. Chem. Phys.* **1987**, *87*, 1857.

Chapter 14

NMR Studies of the Structures and Reactions of Simple Molecules Adsorbed on Metal Clusters

C. A. Klug[1], C. P. Slichter[1-3], and J. H. Sinfelt[4]

Departments of [1]Physics and [2]Chemistry and [3]Materials Research Laboratory, University of Illinois at Urbana–Champaign, 1110 West Green Street, Urbana, IL 61801
[4]Exxon Research and Engineering Company, Annandale, NJ 08801

Our group has used NMR to study the simple hydrocarbons acetylene and ethylene adsorbed on the surfaces of small supported Group VIII metal clusters typical of industrial catalysts. This article will introduce the NMR techniques employed and review some of our results, focussing on recent work studying surface reactions. The reactions studied include: the conversion of the low temperature species of ethylene to ethylidyne, hydrogen-deuterium exchange in ethylidyne, the reaction of vinylidene with hydrogen to form ethylidyne, and the dehydrogenation of vinylidene.

Surface science, in particular the study of molecules adsorbed on metal surfaces, has been a very active field of research for many years and it has drawn to it many excellent workers who have applied a rich variety of experimental techniques to study both the metal surfaces themselves and the molecules adsorbed on the surfaces. Much of the early work was motivated by a desire to understand catalysis and was done using thin metal films and reactor vessels which allowed the experimenter to monitor the products of reactions catalyzed by these metals. With the advent of highly disperse catalysts on the one hand and the availability of single crystals and the necessary ultra high vacuum techniques to study them on the other hand, surface science has broken off into two main groups-those working with ultra high vacuum techniques to study single crystals and the molecules adsorbed on them and those studying disperse catalyst systems. For reasons that will be outlined below, our group falls in the latter category. NMR is a powerful technique that has been successfully used in the field of surface science by a number of researchers.

We shall not attempt to review all of the NMR results of our group, especially since several review articles have already been published.(1) Instead we shall focus our attention on the more recent results where we have been able to study the reactions of small hydrocarbon molecules adsorbed on metal clusters. This article shall begin with a brief discussion of the samples used in our work. Next, as a means of introducing some of the experimental techniques involved in these studies, we will present some of the results of Po-Kang Wang et al. from our group where they determined the structure of the stable room temperature species formed from acetylene

and ethylene adsorbed on several group VIII metal catalysts. Next, we shall discuss some of the recent results of our group where we have begun to exploit our ability to detect the structure of the hydrocarbon species on metal surfaces and have studied various reactions. Finally, we shall conclude with a brief summary and a discussion of some of the remaining questions we hope to answer using NMR to study surface reactions.

Samples

A typical (111) surface contains roughly 10^{15} surface sites per cm^2. However, NMR usually requires at least 10^{19} nuclei for adequate signal detection. Hence, it is impractical for us to use single crystals in NMR experiments. However, a disperse supported metal catalyst contains roughly 10^{20} metal surface sites per gram where one gram corresponds to roughly 1 cm^3, a convenient NMR volume. Hence disperse metal catalysts are suitable for NMR studies. Of course, the very nature of these samples introduces some complications. The surface of an ideal single crystal has a well-defined orientation. However, supported metal clusters will offer surfaces with many different orientations. Furthermore, one would prefer a sample where all the metal clusters were the same size and shape thereby giving a well understood distribution of surface sites but, instead, the size distribution for these clusters is log-normal. In each sample there will be a large variety of cluster sizes and shapes. In addition, one expects small clusters such as the ones used in this study to have irregular faces and edges and hence a variety of surface sites (e.g. edge and planar). The chemisorption and catalyst properties may vary from site to site. The variety of surface sites for our samples is a disadvantage compared to single crystals since we observe an average behavior. However, recent work has shown that single crystals are by no means the idealized regular surfaces once imagined. Furthermore, since these supported metal clusters are more typical of industrial catalysts, studies with these samples may be more easily related to industrial work.

The samples are prepared by impregnating a support, typically η-alumina, with a solution of a metal precursor such as chloroplatinic acid in the case of Pt catalysts. The material is then dried, calcined and exposed to hydrogen at an elevated temperature. The metal clusters are formed in the latter step as a result of the reduction of the metal precursors. The samples used in the work typically contained 5 or 10% metal by weight. The dispersion of the metal clusters, defined as the fraction of metal atoms occupying surface sites and determined from hydrogen chemisorption measurements, varied from 83% for the Ir samples to about 50% for the Pt samples.

The cleaning procedure involves a series of steps outlined below:

a) evacuate the sample to 10^{-6} Torr at 300°C
b) apply alternating flows (0.1 L/min) of ultra high purity hydrogen and oxygen
c) re-evacuate the sample to 10 Torr

The entire procedure was carried out in a glass manifold system of known volume connected directly to cylinders of oxygen and hydrogen as well as a mechanical and diffusion pump system.

The hydrocarbon gas was usually adsorbed at room temperature, the exception being for samples where we adsorbed the gas at lower temperatures. The coverages were calculated from the change in gas overpressure. Prior to sealing, the samples were re-evacuated to 10^{-6} Torr. Most of the samples were sealed at 77 K to reduce heating by the hydrogen torch. We have shown that re-evacuation removes the species adsorbed on the alumina support (2). It is important to note that coverages calculated in the above manner are overestimates since they include some weakly adsorbed species. We conclude that saturation coverage is roughly 25% for both acetylene and ethylene

adsorbed on Pt. This is in agreement with the results of Bertolini et al. and Koel et al.(*3*)

One important feature of these samples needs to be highlighted. Due to the large surface area confined in a small volume the surface species remain chemisorbed on the metal clusters-i.e. the desorption of even a small fraction of a surface layer would correspond to a very large gas overpressure. Thus desorption is effectively eliminated. Therefore, the coverages for our samples which are usually high remain constant throughout our experiments. Since gas phase species are a negligible part of the total, we can ignore them in our studies of the surface reactions. This is in sharp contrast to many experiments where conditions of very low pressure are maintained, thus allowing species such as hydrogen to desorb readily from the surface.

Room Temperature Structure of Adsorbed Species

The first goal of an experimental study of hydrocarbons on surfaces is to determine the structure of the adsorbed species. Indeed, one must develop a set of techniques which can be used to determine the structure of surface species adsorbed on the catalyst surfaces if one is to be able to monitor surface reactions. Our group has employed techniques which allow one to observe and measure the dipolar couplings between nuclei e.g. ^{13}C- C, ^{13}C- H. In addition, we have recently used ^2H NMR to detect the presence of rotating methyl groups in ethylidyne (CCD_3), a common surface species formed from either ethylene or, in the presence of excess hydrogen, acetylene.

^{13}C- ^{13}C **Dipolar Couplings.** The dipolar coupling between two nuclei is proportional to the inverse cube of the internuclear distance r. This sharp dependence on r allows one to extract carbon-carbon bond lengths from a measurement of the dipolar coupling. Unlike high resolution NMR, where one often obtains a spectrum with sharp features from which one can directly determine the dipolar coupling in units of Hz, the spectra for our samples are broad and essentially structureless. The lack of visible structure results from inhomogeneous broadening due to the metal particle susceptibility and chemical shift anisotropy effects. Fortunately, spin echos are designed to eliminate such broadening effects and by using a so-called "slow beat" technique we are able to observe the carbon-carbon dipolar coupling. We observe a series of ^{13}C spin echos with a variety of spacings T_{delay} between the ^{13}C $\pi/2$ and ^{13}C π rf pulses. One observes decaying oscillations in the data, the frequency of which corresponds to the dipolar coupling. (Indeed a Fourier transform of the slow beat data should give a lineshape with two peaks whose separation is the dipolar coupling in units of Hz.) We have found that it is generally very difficult to prepare a sample with all carbon-carbon bonds initially intact and the data are generally described as a sum of two terms, an exponentially decaying oscillating term corresponding to ^{13}C nuclei in ^{13}C-^{13}C pairs, and a simple exponentially decaying term corresponding to isolated ^{13}C nuclei. Fitting such slow beat data, Wang et al. were able to show that the ^{13}C-^{13}C bond length of the stable room temperature species formed from acetylene adsorbed on Pt is 1.44 ± 0.02Å (*4*). This is intermediate between the length of a single bond (1.54Å) and the length of a double bond (1.34Å). Wang used this technique to determine the ^{13}C-^{13}C bond length for a number of samples and the results are summarized below(*5*):

$$C_2D_2 \text{ on Os, Ir, Pt: } 1.44 \pm 0.02\text{Å}$$
$$C_2H_4 \text{ on Os, Ir, Pt: } 1.49 \pm 0.02\text{Å}$$

A secondary result from these fits is a determination of the fraction of ^{13}C nuclei in ^{13}C-^{13}C pairs. This information was used when Wang studied the scission of the ^{13}C-^{13}C bond.

^{13}C-^{1}H Dipolar Couplings. To measure the ^{13}C-^{1}H dipolar couplings we employ a technique known as spin echo double resonance-SEDOR. As for the ^{13}C slow beat experiment, one observes ^{13}C spin echos, but this time one compares a regular spin echo with one where we have applied a ^{1}H π pulse at a time τ (usually less than T_{delay}) after the ^{13}C π/2 pulse. The ^{1}H π pulse affects the refocusing of the ^{13}C nuclei due to ^{13}C-^{1}H dipolar couplings. One then plots the relative change in the echo amplitude, known as the SEDOR fraction, versus τ, the position of the ^{1}H π pulse. In general, if a ^{13}C nucleus has a carbon-hydrogen bond, one observes complete destruction of its spin echo signal due to the application of the ^{1}H π pulse for times τ of the order of 50 μsec. Hence for a surface covered only with CCH$_2$, one expects to observe a plateau in the SEDOR fraction data corresponding to 50% destruction for τ around 50 μsec followed by another plateau at 100% destruction at longer τ when next nearest neighbor couplings contribute to the SEDOR destruction. Wang applied this technique to help determine the room temperature structure for acetylene (4) and ethylene (6) adsorbed on Pt. Wang et al. were able to show that the room temperature species formed from ethylene could not be CH-CH$_3$ which would give 100% destruction for τ of the order of 50 μsec, but was ethylidyne (CCH$_3$) with a rotating methyl group.

D Spectra. Recently, one of the most useful techniques for monitoring the structure of surface species has been ^{2}H NMR. ^{2}H has spin 1 and therefore possesses a quadrupolar moment. The spectra for D nuclei is described as a Pake doublet (7) with two large peaks or discontinuities, the separation of which corresponds to the quadrupolar coupling of the D nuclei. D nuclei in fixed carbon-deuterium bonds have Pake lineshapes with roughly 120 kHz between singularities. However, the rotation of the methyl group in ethylidyne (CCD$_3$) reduces this width due to averaging by a factor of about 3 to roughly 40 kHz. Therefore, a 40 kHz Pake pattern in the D spectra is a feature unique to D nuclei in a rotating methyl group. We used this technique to verify the presence of rotating methyl groups for C$_2$D$_4$ adsorbed on Pt, confirming the identification of the surface species as CCD$_3$ with a rotating methyl group. In addition, this unique signature spectrum has been used extensively to monitor the progress of surface reactions whose products include deuterium-containing ethylidyne: CCH$_2$D, CCHD$_2$, CCD$_3$.

Surface Reactions

Carbon-carbon Bond Scission. Once the stable room temperature species had been determined, the first reaction studied was the decomposition of the surface species. As remarked earlier, the ^{13}C slow beat measurements which allow us to determine ^{13}C-^{13}C dipolar couplings and hence ^{13}C-^{13}C bond lengths also give us information concerning the fraction of ^{13}C nuclei in ^{13}C-^{13}C pairs. Therefore, we have an ideal method for monitoring the scission of carbon-carbon bonds as a function of the heat treatment of the samples. Wang et al. used an annealing technique combined with slow beat measurements to follow the fraction of broken carbon-carbon bonds as a function of annealing temperature. Wang used the following procedure:

    a) measure the data at 77 K- in this case the ^{13}C slow beat was measured from which was determined the fraction of unbroken carbon-carbon bonds.

    b) anneal the sample to an elevated temperature for 3 hours where this time is long enough to ensure thorough heating of the sample while short enough so as to prevent too much decomposition.

    c) repeat steps a) and b) for a series of increasing annealing temperatures.

       Figure 1 shows the data resulting from this type of experiment where the fraction of broken carbon-carbon bonds is plotted as a function of annealing temperature for two samples: C$_2$H$_4$ on Pt and C$_2$D$_2$ on Pt (both saturation coverage). Wang had previously determined that the room temperature species formed from acetylene and

ethylene adsorbed on Pt are primarily vinylidene (CCH$_2$) and ethylidyne (CCH$_3$) respectively. In the case of C$_2$H$_4$ on Pt, Wang et al. observed a sharp increase in the fraction of broken carbon-carbon bonds for annealing temperatures of around 450 K. In contrast, the carbon-carbon bonds appear much more stable for acetylene on Pt. Wang observed a region of gradual carbon-carbon bond scission for temperatures between 450 and 650 K followed by a sharp jump in the data at 670 K where most of the remaining carbon-carbon bonds broke. From these two sets of data one can calculate activation energies for carbon-carbon bond scission assuming a simple unimolecular reaction with a preexponential factor of 10^{13} s^{-1}. One obtains 36 and 53 kcal/mol for carbon-carbon bond scission in the surface species formed in room temperature adsorption of ethylene on Pt (at 450 K) and acetylene on Pt (at 670 K) respectively.

This method of observing carbon-carbon bond scission via changes in the ^{13}C slow beat has been used extensively in our group to study both acetylene and ethylene adsorbed on a variety of metal surfaces(5).

Dehydrogenation of Surface Species. ^{13}C-H SEDOR measurements have proven to complement the slow beat measurements. Just as the ^{13}C slow beat measurements allow us to monitor the fraction of ^{13}C nuclei in ^{13}C-^{13}C pairs, ^{13}C-^{1}H SEDOR measurements allow us to monitor the fraction of ^{13}C nuclei with ^{13}C-^{1}H bonds. Hence we are able to monitor the dehydrogenation of the surface species as a function of the heat treatment of the samples. Wang et al. were able to show that for the case of acetylene and ethylene on Pt, after the carbon-carbon bond scission was complete, the carbon atoms were completely dehydrogenated (5,6). Combining SEDOR measurements with an annealing technique for acetylene on Pt, Wang observed a marked decrease in the fraction of ^{13}C nuclei with carbon-hydrogen bonds for temperatures well below 670 K, the temperature of carbon-carbon bond scission. Therefore Wang proposed that dehydrogenation preceded carbon-carbon bond scission for acetylene on Pt and ascribed the sharp jump at 670 K in the data of Figure 1 as due to the decomposition of C$_2$ surface species.

We have recently performed SEDOR measurements at <u>high</u> temperatures, in contrast with Wang's annealing experiments where the data were measured at 77 K, in order to verify Wang's proposed mechanism for decomposition (8). Figure 2 shows an example of two ^{13}C lineshapes obtained from Fourier transforms of spin echos measured at 300 K for a Pt catalyst sample on which ^{13}C$_2$H$_2$ was adsorbed at room temperature. Figure 2(a) was obtained from a Fourier transform of a ^{13}C spin echo and represents the signal for all the ^{13}C nuclei in the sample. Figure 2(b) was obtained from a Fourier transform of a SEDOR echo and represents the signal for ^{13}C nuclei without strong carbon-hydrogen dipolar couplings. Clearly, the low frequency line at 100 ppm is greatly affected by the SEDOR ^{1}H pulse while the high frequency line at 300 ppm is left virtually unchanged. Therefore, we conclude that the low frequency line corresponds to surface species containing hydrogen, namely CCH$_x$, (x>0), while the high frequency line corresponds to dehydrogenated surface species i.e. C$_2$ and C atoms. We obtained data for a series of increasing temperatures remaining at each temperature for 3 hours and obtained the spectra shown in Figure 3. From these data one clearly sees a conversion of intensity from the low frequency line to the high frequency line corresponding to the dehydrogenation of CCH$_x$ (x>0) species to form C$_2$ species and C atoms. Although we have shown that the high frequency line corresponds to dehydrogenated surface species, we still need to prove that C$_2$ species are indeed contributing to the intensity of this line. This is an area of current work. Recently, by using slow beat measurements of this high frequency line and utilizing the fact that the relaxation times for C$_2$ species and C atoms are different, we have obtained preliminary evidence confirming the presence of species other than C atoms contributing to the intensity of the high frequency line-i.e. C$_2$ species. Nevertheless,
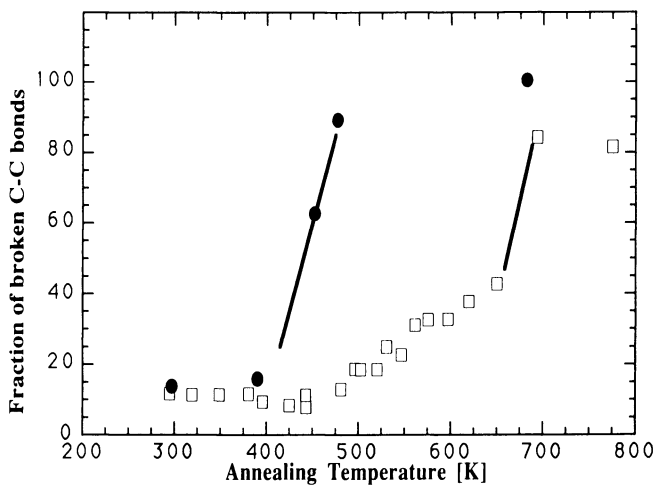
Figure 1: A plot of the fraction of broken carbon-carbon bonds, as determined from slow beat measurements, versus annealing temperature for two samples. The solid discs are for a sample of ethylene adsorbed on a Pt catalyst at room temperature and the open squares are for a sample of acetylene adsorbed on Pt at room temperature.
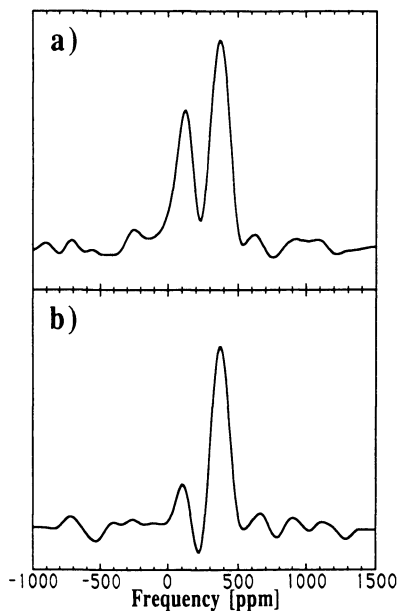
Figure 2: Two ^{13}C lineshapes obtained by Fourier transforming spin echos: (a) was obtained from the Fourier transform of a ^{13}C spin echo and (b) was obtained from the Fourier transform of a ^{13}C spin echo with the addition of a ^1H 180° pulse (a SEDOR spin echo).
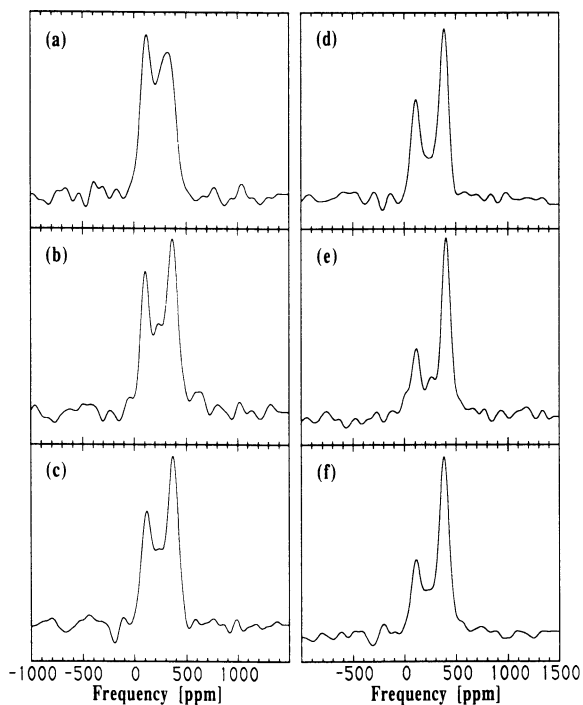
Figure 3: A series of ^{13}C lineshapes obtained by Fourier transforming spin echos measured at different temperatures, where the sample was held at each temperature for 3 hours: a) 473 K, b) 500 K, c) 533 K, d) 563 K, e) 593 K, f) returned to 473 K.

we have demonstrated that gradual dehydrogenation does indeed occur over a broad temperature range from 473 to 593 K.

Finally, after measuring the spectrum at 593 K (Figure 3(e)), we re-cooled the sample to 473 K (Figure 3(f)) and observed no significant changes. Hence, we can conclude that there is no reversibility of the dehydrogenation process at these temperatures.

D NMR. The third technique described earlier, namely D NMR, has proved invaluable for studying a group of reactions involving ethylidyne, in particular reactions whose products include deuterium-containing ethylidyne. In these experiments we used an annealing technique combined with D NMR to monitor the reaction progress.

The Conversion of Ethylene to Ethylidyne. Ethylene and acetylene adsorb molecularly at low temperatures. As already mentioned it has been determined that near room temperature the ethylene converts to form ethylidyne (CCH_3) whose carbon-carbon axis is perpendicular to the metal surface. We have studied this reaction using ^2H NMR (9). We prepared samples with deuterated ethylene adsorbed at low temperatures (194 K) and measured the D spectra as a function of annealing temperature. Due to significant differences in the NMR relaxation times of the D nuclei in the ethylene and ethylidyne, we were able to suppress the signal due to D nuclei in molecular ethylene and observe only the D in the rotating methyl groups of the product ethylidyne. One observes a series of spectra for increasing annealing temperatures where the methyl intensity increases as the reaction progresses. Assuming simple kinetics we can obtain the activation energy for this conversion reaction. We conclude that the activation energy is 15.2 ± 2.0 kcal/mol and the preexponential factor is 9 x $10^{7\pm1.7}$ s^{-1} for the conversion of ethylene to ethylidyne.

H-D Exchange. As has been demonstrated above in the case of acetylene decomposition on Pt, the strength and stability of the carbon-hydrogen bond is of great importance in understanding surface reactions on catalysts. We were able to study hydrogen-deuterium exchange in ethylidyne by preparing a sample with CCH_3 and D co-adsorbed (ethylene was adsorbed at room temperature, the sample was then evacuated to remove the hydrogen atoms leaving only CCH_3, and then the sample was cooled to 77 K when the D atoms were coadsorbed) and then monitoring the incorporation of D nuclei into the ethylidyne species (9). Again we obtained a plot of integrated methyl intensity as a function of annealing temperature. The kinetics of this reaction are slightly more complicated since one now has a set of three coupled reactions to consider.

$$CCH_3 + D \quad <---> \quad CCH_2D + H$$
$$CCH_2D + D \quad <---> \quad CCHD_2 + H$$
$$CCHD_2 + D \quad <---> \quad CCD_3 + H$$
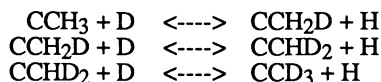
Fortunately, there is a simple analytical solution to the kinetic equations for exchange which allow one to fit the data (10). We obtained an activation energy of 14.3 ± 2.5 kcal/mol and a preexponential factor of 4 x $10^{7\pm2}$ s^{-1} for hydrogen-deuterium exchange. It is instructive to compare this result with that of Ogle and White (11) who also studied hydrogen-deuterium exchange in ethylidyne. In their work, Ogle and White had a constant hydrogen overpressure of 1.1 x 10^{-7} Torr which is insufficient to keep the hydrogen atoms on the surface for the temperatures of this reaction. Hence, as the temperature increased, the surface coverage of the key reactant hydrogen varied. Taking this effect into account, we have re-analyzed Ogle and White's data using Christmann et al.'s results for hydrogen chemisorption on Pt (111)(12) and obtained an activation energy of 11.8 kcal/mol and a preexponential

factor of 7 x 10^6 s^{-1}(Ogle and White's initial numbers were 7.2 kcal/mol and 4 x 10^2 s^{-1}). These numbers are in better agreement with our NMR results.

Conversion of Vinylidene to Ethylidyne. Some of the early work to study surface species suggested that the stable species formed from acetylene and ethylene adsorbed on Pt (111) surfaces were the same, namely ethylidyne (*13*). Later, it was determined that the presence of excess hydrogen in the experimental apparatus had allowed the conversion of the vinylidene (CCH$_2$) to ethylidyne and it became generally accepted that vinylidene was the stable room temperature species formed from acetylene adsorbed on Pt (111) (*14*). We set out to study this reaction and prepared a sample with C$_2$D$_2$ and H atoms coadsorbed (*15*). We monitored the formation of ethylidyne via the observation of D in the product ethylidyne species. This work was partially motivated by our work to study the decomposition of acetylene on Pt and a desire to understand Wang's results for carbon-carbon bond scission for temperatures between 450 and 650 K (see Figure 1). It was proposed that the dehydrogenation of some CCH$_2$ may provide hydrogen for other CCH$_2$ to form ethylidyne which was found to break at the relatively low temperature of 450 K. Indeed the temperature region of gradual carbon-carbon bond scission Wang observed begins at 450 K. Hence, this alternate decomposition mechanism was proposed as the explanation for Wang's carbon-carbon bond scission data for temperatures between 450 and 650 K.

Again, we monitored the progress of the reaction from vinylidene to ethylidyne by following the methyl intensity as a function of annealing temperature. In this case there are a number of reactions to consider: hydrogen-deuterium exchange in the reactant vinylidene and hydrogen-deuterium exchange in the product ethylidyne as well as the conversion from vinylidene to ethylidyne. Figure 4 shows plots of integrated methyl intensities versus annealing temperature for three samples. In Figure 4(a) the data were taken for a sample where the number of hydrogen atoms adsorbed was much greater than the number in vinylidene species. We ascribe the sharp drop in methyl intensity above 300 K as due to hydrogen-deuterium exchange between the ethylidyne and the excess hydrogen. Figure 4(b) shows data for a sample where the initial number of hydrogen atoms was roughly equal to the number of vinylidene species. As expected, there is a plateau in the data near 325 K. However, upon annealing to 375 K, one again observes a sharp drop in the data. This drop cannot be easily explained without the introduction of a new source of hydrogen atoms available for hydrogen-deuterium exchange. We postulated that this may be a support effect. Figure 4(c) shows the data for a sample where the number of hydrogen atoms was again roughly equal to the number of vinylidene surface species and for which the hydrogen atoms of the alumina support have been replaced with deuterium. (To deuterate the support, we exposed the cleaned catalyst to deuterium gas at 300°C) Clearly, we have removed the sharp drop in the methyl intensity at 350 K and indeed the data continues to rise as the ethylidyne becomes completely deuterated. This proves that the support provides hydrogen atoms for exchange with hydrogen atoms of the surface species and is a very clear demonstration of such support effects. Solving the set of kinetic equations numerically and assuming the hydrogen deuterium exchange in vinylidene is comparable to that for ethylidyne, we obtained the curves shown in Figure 5 which fit the data reasonably well for temperatures below 325 K where the support does not have much effect. We conclude that the activation energy for the conversion of vinylidene to ethylidyne is 9.3 ± 2.5 kcal/mol with a corresponding preexponential factor of 3.8 x $10^{3\pm2}$ s^{-1}. In view of the temperature at which this reaction occurs, this reaction is a reasonable candidate for providing an alternate mechanism for carbon-carbon bond scission for acetylene on Pt.

Summary and Conclusions

NMR has proven to be a useful tool for the study of a number of surface reactions. Many important questions remain regarding further details of the reaction mechanisms. For example, there is some evidence that the data shown in Figure 1 for the carbon-
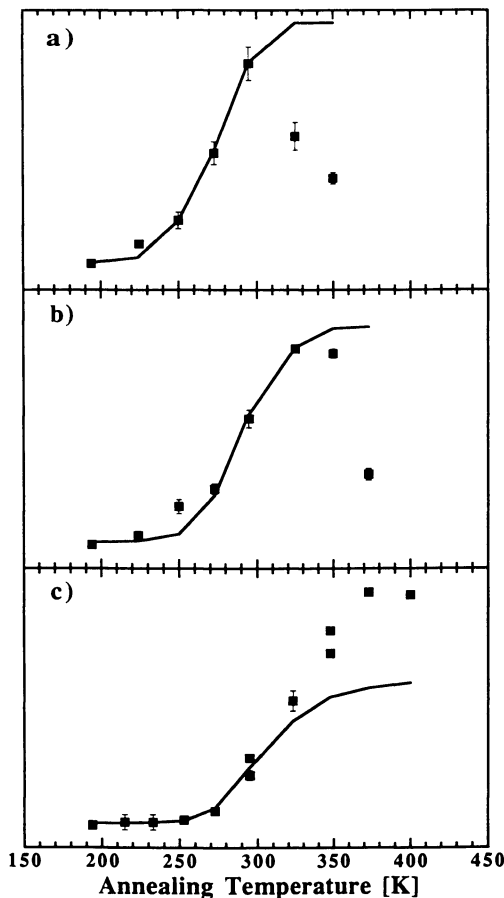
Figure 4: Plots of integrated methyl intensity versus annealing temperature for 3 samples used to study the conversion of vinylidene to ethylidyne: a) the number of H atoms adsorbed was much greater than the number of vinylidene species, b) the number of H atoms adsorbed was roughly equal to the number of vinylidene species c) same as b) except the alumina support was deuterated. The curves shown were calculated for an activation energy of 9.3 kcal/mol and a preexponential factor of 3.8×10^3 s^{-1} where we did not include a support effect in this calculation.

carbon bond scission of acetylene on Pt may not represent a "universal" curve for all acetylene coverages and metal cluster dispersions. Indeed, as remarked earlier, different cluster sizes and their different sets of surface sites may have different average kinetic properties for certain reactions. Furthermore, the availability of empty surface sites may affect decomposition rates. Clearly a systematic study of coverage and dispersion effects is in order.

The somewhat low preexponential factors observed lead one to suspect reaction mechanisms are more complicated than first assumed. Inter-cluster migration may play a role, especially since one expects reactant coverages to vary from metal cluster to metal cluster. This brings one back to coverage effects. The assumption of simple rate laws based on a uniform surface may also need testing. Clearly there are a number of interesting issues which remain to be studied, all of which are feasible using NMR techniques outlined above. Further reactions involving other simple hydrocarbons of interest are also feasible for study. It is hoped that the work of our NMR group, combined with the work of the many other researchers in this field, will unravel some of the mysteries of surface reactions.

Acknowledgement

Literature Cited

1. Slichter, C. P. *NMR and Surface Structure*, In <u>The Structure of Surfaces</u>, eds. M. A. Van Hove and S. Y. Tong (Springer-Verlag, Heidelber, 1985), pp.84-89
   Wang, P.-K.; Ansermet, J.-Ph.; Rudaz, S. L.; Wang, Z; Shore, S.; Slichter, C. P.; Sinfelt, J. H. *Science* **1986**, *234*, 35.
   Ansermet, J.-Ph.; Slichter, C. P.; Sinfelt, J. H. *Prog. NMR Spect.* **1990**, *22*, 401.
2. Klug, C. A.; Slichter, C. P.; Sinfelt, J. H., accepted, *J. Phys. Chem.*
3. Abon, M.; Billy, J.; Bertolini, J. C. *Surf. Sci .***1986**, *171*, L387.
   Windham, R. G.; Bartram, M. E.; Koel, B. E. *J. Phys. Chem.* **1988**, *92*, 2862.
4. Wang, P.-K.; Slichter, C. P.; Sinfelt, J. H. J. Phys. *Phys. Rev. Lett.* **1984**, *53*, 82.
5. Wang, P.-K.; Slichter, C. P.; Sinfelt, J. H. *J. Phys. Chem.* **1990**, *94*, 1154.
6. Wang, P.-K.; Slichter, C. P.; Sinfelt, J. H. *J. Phys. Chem.* **1985**, *89*, 3606.
7. Pake, G.E.; *J. Phys. Chem.* **1948**, *16*, 327.
8. Klug, C. A. PhD thesis, University of Illinois, Urbana, IL 1990.
9. Zax, D. B.; Klug, C. A.; Slichter, C. P.; Sinfelt, J. H. *J. Phys. Chem.* **1989**, *93*, 5009.
10. Bolder, H.; Dallinga, G.; Kloosterzeil, H. *J. Catal.* **1964**, *3*, 312.
11. Ogle, K. M.; White, J. M. *Surf. Sci.* **1986**, *165*, 234.
12. Christmann, K.; Ertl, G.; Pignet, T. *Surf. Sci.* **1986**, *165*, 234.
13. Kesmodel, L. L.; Dubois, L. H.; Somorjai, G. A. *Chem. Phys. Lett.* **1978**, *56*, 267.
    Ibach, H.; Hopster, H.; Sexton, B. *Applications of Surface Science* **1977**, *1*,1.
14. Salmeron, M.; Somorjai, G. A. *J. Phys. Chem.* **1982**, *86*, 341.
15. Klug, C. A.; Slichter, C. P.; Sinfelt, J. H. *J. Phys. Chem.* **1991**, *95*, 2119.

Chapter 15

In Situ Surface Kinetics by Dynamic Isotopic Tracing

Application to Methane Oxidative Coupling

C. A. Mims[1], R. B. Hall[2], A. J. Jacobson[2,3], J. T. Lewandowski[2], and G. Myers[2]

[1]Department of Chemical Engineering and Applied Chemistry, University of Toronto, Toronto, Ontario M5S 1A4, Canada
[2]Corporate Research Laboratories, Exxon Research and Engineering Company, Annandale, NJ 08801

By providing an in-situ measure of the concentrations and lifetimes of surface intermediates, transient isotope tracing provides a strong link between surface science, other spectroscopic investigations and catalytic reaction mechanisms. A brief discussion of the method is followed by recent results on methane oxidation catalysis to demonstrate its use. Mixed metal (Bi/Sn,Pb/Ta) oxide catalysts with the pyrochlore structure as well as lithium-magnesia were studied. The catalysts show an immeasurably small (<0.01) surface coverages by carbon-containing intermediates. These catalysts, like others, rapidly exchange their surface oxygen with the bulk, as well with the gas phase, particularly with CO_2. These exchange reactions obscure much of the variation in surface oxygen species reactivity.

A catalytic reaction can be said to be understood when the reaction intermediates have been identified and all the factors governing their reactivities discovered. For heterogeneous catalytic reactions, this is generally beyond current experimental capabilities and we must settle for a more primitive picture. The course and speed of the reaction is often governed by a complex set of interrelated factors operating at many scales. For example, the presence of co-adsorbates (reactive or not) can modify the reaction kinetics by site-blocking, can influence the encounter rate for bi-"molecular" events by island formation, and can strongly affect the bonding of other species, even to the point of restructuring the catalyst. Many elegant examples of these and other aspects of surface reaction kinetics are contained in other contributions to this volume.

As a result of these effects, the surface reaction chemistry can be almost ecological in its complexity. The kinetic behavior often results from a delicate balance of factors: a balance which is easily upset by *ex-situ* examination and

[3]Current address: Department of Chemistry, University of Houston, Houston, TX 77204

is difficult to simulate in low-pressure or vacuum experiments, or even in the transient kinetic behavior following concentration perturbations, which are often accompanied by profound changes in reactivity. Surface science investigations have greatly enriched our understanding of surface species, putting a **structural**, chemical face to many proposed species and discovering new ones. Many of the effects listed above were first demonstrated by UHV surface investigations. However, relating this information to catalytic kinetics is still difficult even for simple reactions, and many surface species are still merely candidates (albeit well characterized) for the intermediates in "real" catalytic reactions.

Against this complexity, the paucity of information contained in the steady state kinetic behavior offers little help (although its study is the first order of business in the study of a reaction). From the study of the steady state kinetic behavior, it is not possible to discern whether a reaction results from a few active centers or many less reactive ones, or how these parameters change with conditions. The same issue confronts *in-situ* spectroscopic studies of operating catalysts. The surface is often populated by robust species which are not part of the main reaction sequence, and the catalysis literature contains many arguments about the role of such "intermediates". Without **dynamic** information, the answers are inaccessible.

As many of the papers in this volume illustrate, there has been considerable progress made towards closing the "pressure gap" through the development of analytical techniques capable of following the details of surface reactions at modest pressures and with better time resolution. Progress has also been made on the "high pressure" side by more detailed kinetic and spectroscopic investigations of operating catalysts. Transient kinetic experiments have been extremely useful for resolving mechanistic steps which are inaccessible from steady state kinetic studies (1,2), as has the use of isotopes to trace reaction pathways (3). Combination of these two tools in "stop action" tracer experiments contain valuable information relevant to the steady state, provided the reactivities are relatively insensitive to the changing conditions imposed (2,4,5). However, transient isotope tracing at reaction steady state uniquely provides the time resolution of pulsed experiments while maintaining reaction steady state and has become an important tool in catalysis research (6,7). A brief discussion of the method and its role in mechanistic research will be followed by some of our recent results on methane oxidation catalysis which serve to point out the advantages and limitations of this valuable tool.

Isotopic transients

Isotopic perturbations provide "timing marks" which allow the experimenter to follow atoms (and in favorable cases, molecular groups) as they move through the manifold of reactive intermediates and ultimately appear in the products. Except for kinetic isotope effects, these isotopic transients occur without disturbing the steady state reaction. This gives the experimenter the opportunity to: 1) directly measure the steady state surface concentrations and

lifetime distributions of the pool of reaction intermediates, 2) determine further details of the sequence of reaction steps by the shapes of the transients, 3) observe the reaction flow through the intermediates themselves with isotope sensitive spectroscopies such as IR and possibly NMR. This is precisely the type of information required to tie high pressure and low pressure experiments together.

It is not surprising that dynamic isotope tracing found extensive development in the study of complex biological and ecological systems (8,9). It has seen increasing use in the investigation of catalytic mechanisms, beginning with work by Happel (6,10), with significant contributions by Biloen and co-workers (7,11) and is now used by many research groups around the world. The reader is referred to recent reviews (12), books on the method (6) and the associated mathematics (6,8,9,13) as well as the references quoted herein for a more complete picture than is possible here.

Any type of perturbation can be applied but two are most common. Figure 1 illustrates the application of these to the model reaction network schematically represented in Figure 1a. Figure 1b illustrates a sudden switch from one isotope to another. The shaded curves represents the fraction of the old isotope in the intermediates and product as a function of time. After the switch, the only source of products (and intermediates) containing the old isotope is the inventory (steady state) of surface intermediates at t=0. The fraction of "old" isotope in the product (or intermediate) at time, t, directly measures the fraction which arises from surface intermediates with surface ages greater than t. The total integrated amount of the old isotope evolved is a direct measure of the steady-state surface concentration of atoms in active surface intermediates. The derivative (negative) is the surface residence time distribution of the reactive atoms.

In the other common experiment, a pulse of isotope is applied (Figure 1c). The shaded curves here represent the fraction of the pulsed isotope. If the pulse is short compared to the lifetime(s) of the initial intermediates(s), the resulting transient directly measures the residence time distribution, equivalent to the derivative of the previous experiment. Pathways with large pools of relatively unreactive intermediates are less obvious in the pulsed experiment, since they are sparsely populated during the pulse. Nevertheless, identical information is contained in the two experiments, given sufficient signal/noise. This is also true for pulses which are long enough to saturate some of the species with the new isotope, although the interpretation in this case is more complicated.

The shape of a transient response contains information about the structure of the reaction network. A simple reaction which proceeds irreversibly with rate f, through a single kinetically homogeneous intermediate, present in amount N_B

$$A \xrightarrow{f} \boxed{B} \xrightarrow{f} C \qquad (1)$$
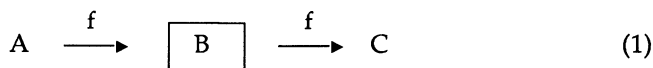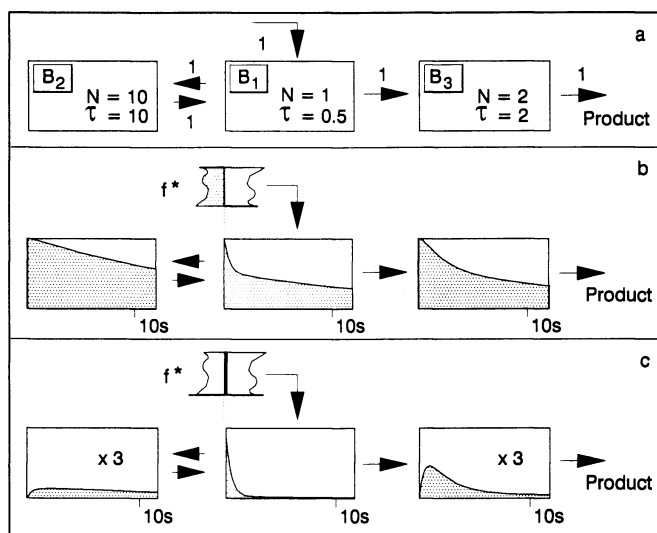
Figure 1. Illustration of the isotope transient experiment (see text): a. model reaction network with the rates, abundances, and resultant lifetimes indicated; b. results of a step isotope transient, shaded curves indicate the washout of the old isotope in each intermediate; c. results of a pulsed isotope transient, shaded curves show the evolution of pulsed isotope.

will exhibit a simple exponential decay in the old isotope after a switch:

$$q_B = \exp\{-t/\tau_B\} \tag{2}$$

where τ_B is the species lifetime:

$$\tau_B = N_B/f = k_B^{-1} = \Theta_B/\nu \tag{3}$$

The pseudo first order rate constant, k_B, is the turnover rate **of the intermediate**, related to the site turnover frequency, ν, by the site coverage, Θ_B.

More complex transients reflect more complex mechanisms and/or kinetic heterogeneity. These situations can generally be described by a network of kinetically homogeneous intermediates such as that above. With sufficient number of these intermediates, even complex situations such as island formation can be represented, although Monte Carlo methods are often better suited to these problems. The reaction kinetics is then equivalent to the flow of material through a series of well-mixed compartments with population N_i. As above, each compartment (or species) is continuously "turned over" at steady state with its characteristic rate, κ_i

$$\kappa_i = (\tau_i)^{-1} = \Sigma_j f_{ij}/N_i = \Sigma_j f_{ji}/N_i \tag{4}$$

where the f_{ij} are the rates of conversion of species j to species i; the second equality holds at steady state. The kinetic equations for the individual turnover frequencies can form a non-linear set of coupled differential equations. However, because the flows are constant at steady state, the isotopic transient is represented by a linear set of differential equations (*6,8,9,13*). In the cases described above, the solution of the isotopic composition $q_i(t)$ of each of the compartments, i (and the product) is a series of exponentials.

$$q_i(t) = \Sigma_n C_{in} \exp\{\lambda_n t\} \tag{5}$$

The real parts of the system eigenvalues, λ_n, are always negative and are **combinations** of (not generally equal to) the individual species rate constants, κ. The coefficients, C_{in}, can be of either sign. Negative coefficients generally appear for series reactions and produce "induction" times such as those seen in the example above. The eigenvalues can also be complex (unobserved to our knowledge in catalytic situations) showing damped oscillatory behavior (*9*). In light of these considerations, the representation of a deconvolved eigenvalue spectrum as a rate constant spectrum (*14*) can be somewhat misleading.

Several of the features mentioned above are illustrated by the results for the model mechanism in Figure 1. It has two intermediates on the main pathway and one "dead-end" intermediate, B_2, which can reinter the main pathway. For the flows and residence times indicated in Figure 1a, the

transient behaviors in 1b and 1c are those predicted for a step change and pulsed isotope transient respectively. The "dead end" species B_2 is responsible for the long decay in all compartments - much less obvious in the pulsed experiment. For species B_2 and B_3, the zero initial slopes in Figure 1b and delays in the appearance of label in 1c result from the series nature of the pathway. Soong, et. al. (15) give an excellent discussion of these features with respect to the methanation of carbon monoxide on nickel. The long decays in Figure 1 reflect a time constant longer than the lifetime of B_2 because of the reversible character of this path.

Although the form of the isotope transient can be predicted if the reaction network is known, the inverse problem is usually not unique (6,9). However, gathering additional information in the experiment such as conditional isotope probabilities and dynamic surface (IR) information provides more constraints on the mechanism. The experimenter can be comforted by the fact that the knowledge gained, even if incomplete, is unequivocally relevant to the steady state reaction mechanism. Changes in catalytic activity (with materials properties, for example) can be easily assigned to either 1) an increase in reactivity of the surface intermediates or 2) to a change in their surface coverages. The measured coverages tell the spectroscopist what the concentration of active intermediates are (or whether they are measurable at all). Finally, the reactivities can be related to those measured in UHV experiments for well characterized surface species. All such insights are of direct significance to bridging the pressure gap in catalytic research.

A brief word about techniques is appropriate. Because of desirability of good time resolution (and sensitivity) and real time analysis, mass spectroscopy is the most popular analytical technique. Other less sensitive isotope selective techniques (IR, NMR) require off-line analysis of trapped samples or larger sample volumes. More detailed analysis (e.g. GCMS) of time-resolved samples has proven necessary for complex reaction products such as in Fischer-Tropsch synthesis where conflicting fragmentation patterns makes the interpretation of MS data very difficult (16). IR has been used profitably in steady state tracing (17-19) as well as in at least one isotope transient (20). The contribution by Slichter and co-workers to this volume demonstrates the promise of NMR for following the surface species in such experiments (21). In addition to avoiding interferences, the more detailed isotope distribution measurements gained by off-line analysis by techniques such as NMR and GCMS provide additional mechanistic detail such as position sensitive information in products (or reactants) with more than one tagged atom. Some examples of these are mentioned below. As mentioned by Mirodatos (12), the most popular reactor configuration has been the fixed bed flow reactor for reasons of time resolution and simplicity. Sometimes integral effects complicate the analysis (6,11,12). Since the method is general to all reacting systems, experimental ingenuity will undoubtedly expand its utility in the future.

Applications of Isotope Transients. Of the catalytic systems which have been investigated by this technique, the most heavily studied has been CO hydrogenation. On nickel, methane formation has been studied by Biloen (15) and Happel (22,23). While most of the work involves carbon tracing via ^{12}CO-^{13}CO transients, hydrogen pathways have been investigated by H_2-D_2 transients (22). The carbon transients reveal an amount of active surface carbon in relatively good agreement with transient kinetics and *ex-situ* studies of Goodman et. al. (24) which showed a correlation between post-reaction surface carbon and reaction rate. Some unresolved issues still remain regarding this reaction; a more complete discussion is contained in reference (2).

More subtle effects operate in higher hydrocarbon formation in the Fischer-Tropsch synthesis and isotopic transients were essential for the understanding of the surface usage in this reaction. The surfaces of Fe, Co and Ru catalysts have a large amount of hydrocarbonaceous material at steady state (25-27) and concentration transient experiments indicated that this material was active, slowly growing hydrocarbon chains (28). Isotopic transients at steady state, however, showed that this carbonaceous surface material does not participate greatly in the reactive pathway (25,11), that the hydrocarbon chains grow rapidly, and that the growing oligomers occupy a very small portion of the surface (11,16,27). The factor most responsible for the disparate interpretation is the drastic change in the reactivity of the hydrocarbon fragments upon desorption of CO. These studies of the isotopic transients in the products have been nicely enhanced by IR measurements of the adsorbed material (20). The value of detailed analytical measurements of the isotope distribution in the higher hydrocarbon products has been demonstrated on several occasions. A distinct C_2 intermediate was shown to be involved in higher hydrocarbon growth on ruthenium catalysts (30,31) by observing the simultaneous flow of ^{13}C into two neighboring positions in the hydrocarbons. Similarly, a long tail in the carbon transient on iron showed that a large reservoir of carbon reinters the main pathway rather than forming an parallel reaction channel (32). The statistics of multiple ^{13}C labels in the hydrocarbons during the transient were necessary to reach this conclusion. There are many issues still unresolved in Fischer-Tropsch synthesis, including the degree of reversibility of chain growth (5,33,34), and, of course, the identity of the active intermediates. Other workers have used IR to examine the importance of support bound intermediates on the mechanism of CO hydrogenation, particularly on relatively inactive metals such as Pt, where large support effects are seen (35).

Other catalytic systems which have received attention include carbon oxidation (36), ammonia synthesis (37), CO oxidation (38) benzene hydrogenation (39,40) and selective oxidation (41-45), which we discuss further below. Variations of the technique in which the isotope replacement is accompanied by an interruption of the reaction has also produced valuable results (5,46) in cases where the surface reactivity is not disturbed during the experiment. The next few years will undoubtedly see a rapid increase in the number of applications of this technique.

Isotopic Transients of Methane Oxidative Coupling

Below we present some of our data on methane oxidative coupling (47). Recent reviews of this fast-developing field have been published (48,49). It is almost universally agreed that the reaction proceeds on a large number of oxides by initial H abstraction to form gas-phase methyl radicals. Higher hydrocarbons are formed by gas phase radical chemistry led by methyl recombination, although some workers have proposed C-C bond formation on the catalyst surface. The deep oxidation products arise from an as yet undetermined (and probably catalyst-dependent) mixture of gas-phase and surface reactions. Evidence has been gathered to support surface O^-(50), O_2^{2-} (51), and other oxygen forms as both the initiating oxygen species as well as the species responsible for deep oxidation. One of the issues which we could hope to resolve in isotope transients is the amount of the various types of reactive oxygen species. Other work on oxides, however, shows that rapid interconversion between active surface species (52,53) and the bulk of the catalyst is a likely complicating factor. Another issue which has been investigated is the nature of methane activation. Heterolytic,"sticky" activation has been proposed by some (54) and some evidence has been gained using isotopic transients to support an appreciable surface coverage by carbon-containing precursors. Others see no evidence for any such species. We extend these investigations to another class of catalysts while comparing the results to (Li)MgO and previous reports.

Experimental. Two types of catalyst were used: (1) lithium-magnesia, first reported by Lunsford (50) and now arguably the standard, and (2) two catalysts based on pyrochlore oxides, which perform well at higher temperatures (>800C). The lithium-magnesia catalyst was prepared according to the method described by Lunsford. The fresh catalyst had a Li/Mg ratio of 0.29. Exposure to reaction conditions (650-700C) resulted in gradual (tens of hours) loss of selectivity, lithium, and surface area (to less than 1 m^2/g). A bismuth-tin oxide catalyst was prepared by base precipitation from solution (55). The catalyst contained Bi in excess of the $Bi_2Sn_2O_7$ stoichiometry and initially consisted of a single phase with an expanded pyrochlore structure. Exposure to reaction conditions resulted in exsolution of excess bismuth oxide phases and reduction in surface area. The activity and selectivity were relatively stable over a two week period at 850C. A Pb-Ta pyrochlore was prepared similarly.

     The reactions were carried out at one atmosphere in a tubular quartz reactor with 4mm inside diameter. The catalyst temperature was monitored by a thermocouple in a 1mm quartz sheath embedded in the catalyst charge. The reactor narrowed to 2mm i.d. below the catalyst bed to minimize gas phase reactions in the post-bed region. Two complete reactant gas mixtures, one for each isotopic reactant were synthesized by mass flow controllers. A switch between the streams was accomplished with a computer controlled 4-port valve. A standard gas mixture of CH_4/O_2/Inert(Ar,He) = 2/1/5 was used for these studies. $^{13}CH_4$ (99.5%^{13}C), and CD_4 (99%D) were obtained from

Icon and $^{18}O_2$ (98.7%) from MSD Isotopes. Differences between the compositions of the inert components in the two isotopic streams provided an instrumental time mark. The operating conditions and conversion/selectivity data for the isotopic transients are given in Table I.

Table I. Operating parameters for the isotope transient experiments

	T(C)	SA m²/g	CH₄ conversion	C₂ selectivity	C₂H₄/C₂	CO/COₓ
Pb₂Ta₂O₇	810	2.4	0.16	0.54	0.34	0.15
Bi₂Sn₂O₇	840	2.8	0.14	0.65	0.28	0.17
(Li)MgO	705	0.3	0.11	0.56	0.19	0.09

Carbon transients. A rapid switch from $^{12}CH_4$ to $^{13}CH_4$ produced the data in Figures 2-4 and the derived surface abundances summarised in Table II.

CH_4. The replacement of the old isotope in the methane was identical to the apparatus function revealed by the inert, thus indicating that the amounts of reversibly adsorbed methane on these catalysts is immeasurably small.

C_2H_6. To within the apparatus resolution, the isotopic responses in the ethane product on all three catalysts are identical to the apparatus response and to the methane curve. Thus only small upper limits to the surface inventory of carbon-containing intermediates are obtained (see Table II). These findings are consistent with the currently accepted mechanism in which methane activation is prompt and the C_2 products are formed in the gas phase. The transient in ethylene appears to be similar, according to the mass spectral data, but is more uncertain due to mass spectrometric interferences and smaller concentrations. A GCMS analysis would provide a better resolution of this issue.

CO_2. Figures 2-4 also show the carbon transients in the CO_2 product. Two types of behavior are seen. For the pyrochlore catalysts, the isotopic transient in the CO_2 is as prompt as the ethane transient, again indicating an undetectably small concentration of surface intermediates in this reaction channel. On the lithium-magnesia catalyst, however, a substantial amount of carbon is held on the catalyst which ultimately appears as CO_2. The total amount of material is uncertain since the decay is not a pure exponential and was not pursued to completion, but an estimate based on an exponential extrapolation of the last portion of the decay produces the lower limit shown in Table II. This represents several layers (at 10 Å²/CO_2 and assuming 0.3 m²/g under reaction conditions) and undoubtedly corresponds to a carbonate pool on this alkali catalyst. However, this amount corresponds to only 1% of
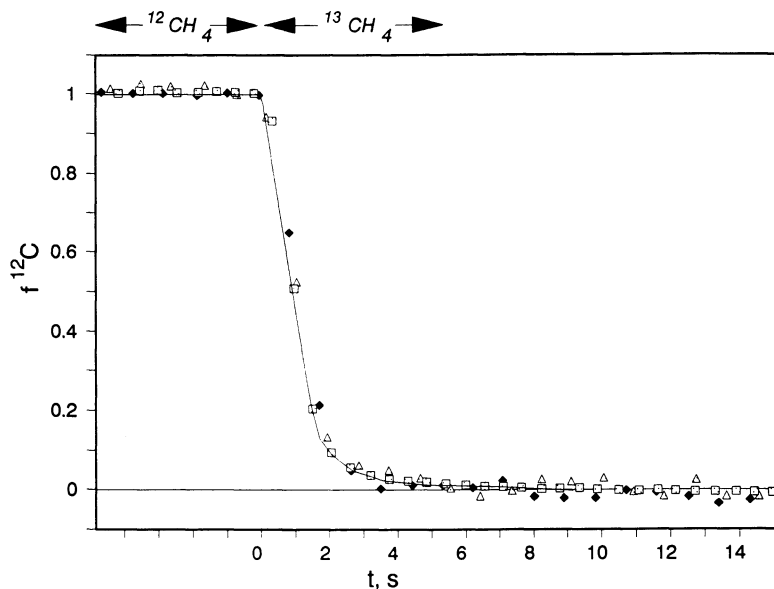
$\blacktriangleleft$ $^{12}CH_4$ $\blacktriangleright$ $\blacktriangleleft$ $^{13}CH_4$ $\blacktriangleright$

Figure 2. Results of a $^{12}CH_4$ - $^{13}CH_4$ isotopic transient on a lead tantalum oxide catalyst. Solid line is the inert marker, squares are methane, triangles are ethane, and diamonds are CO_2.
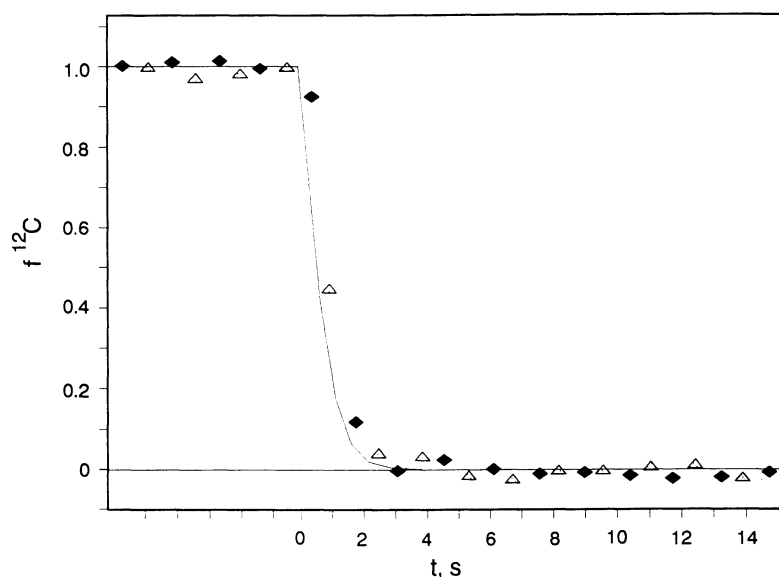
Figure 3. Results of a $^{12}CH_4$ - $^{13}CH_4$ isotopic transient on a bismuth-tin oxide catalyst. Solid line is the inert marker, triangles are ethane, and diamonds are CO_2.

that required to convert all the lithium in the catalyst to Li_2CO_3. This agrees well with results obtained by Mirodatos et. al. (42) and Peil, et. al. (44). A portion of this exchangeable carbonate pool is reversibly adsorbed (56).

Table II. Carbon Transients - Surface Concentrations of Intermediates Leading to the Indicated Products

	C_2H_6		CO_2	
	μmol/g	coverage[a]	μmol/g	coverage[a]
$Pb_2Ta_2O_7$	<0.12	<0.007	<0.10	<0.0025
$Bi_2Sn_2O_7$	<0.13	<0.007	<0.07	<0.0015
(Li)MgO	<0.13	<0.025	0.33	6.5

[a] Assumes 10Å^2/site and the surface areas in Table I.

It is interesting to compare these results with similar published studies of methane coupling. There are several reports of measurable amounts of adsorbed methane on some catalysts. In a pulsed isotopic study of methane coupling on Sm_2O_3, Ekstrom et. al. (43) reported a similarly small number of intermediates for the ethane product, but obtained evidence of a substantial amount of methane adsorbed in (on) the catalyst which shows up as a long tail on the methane transient. Mirodatos and coworkers (42) saw appreciable amounts of adsorbed methane which is rapidly displaced on an unpromoted lanthana catalyst but, in agreement with our results, observed none on (Li)MgO and lithiated lanthana. These authors explained their results on unpromoted lanthana by a "sticky" heterolytic activation process which is poisoned by CO_2 or carbonate. As we show later, our pyrochlore surfaces contain little or no carbonate or adsorbed CO_2 at these conditions. Peil (44) and Miro (45) saw no adsorbed methane on (Li)MgO and lithiated nickel titanates, respectively.

Differences in the dynamics of C_2 production are also reported in other studies. On lithiated magnesia, Mirodatos reports a small number of ethane precursors (42), while Miro (45) sees none on the lithium nickel titanates, in agreement with our results and with those of Ekstrom (43) on Sm_2O_3. These results apparently reflect activation kinetics which are catalyst-dependent and are certainly worthy of further study. Better time resolution is needed since most of the amounts are near the apparatus resolution, although this is difficult to achieve while maintaining the high-pressure steady state conditions.

Hydrogen transient. The result of a switch from CH_4 to CD_4 on the Pb/Ta catalyst is shown in Figure 5. While similar to the carbon transient, a kinetic isotope effect of approximately 1.9 for ethane production is obvious. The isotope effect in this reaction is complex (57) and arises from changes in 1) activation rate, 2) radical chain length in the gas phase (58,59) as well as 3)
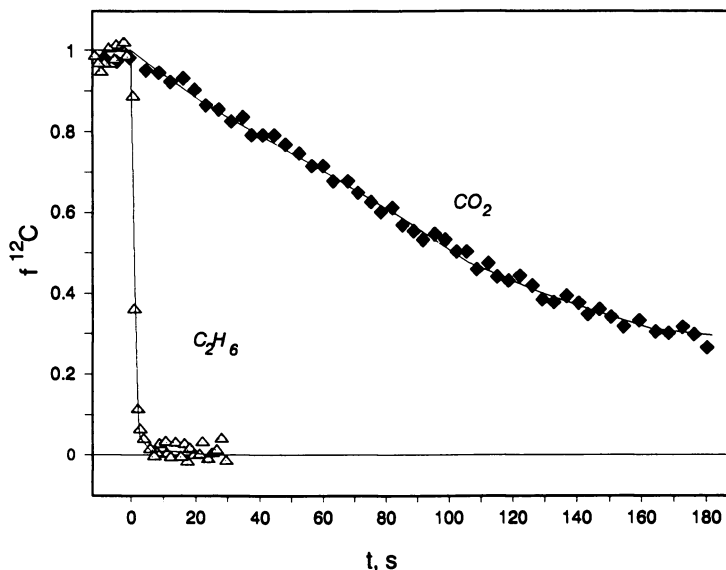
Figure 4. Results of a $^{12}CH_4$ - $^{13}CH_4$ isotopic transient on lithiated magnesia catalyst. Solid line is the inert marker, triangles are ethane, and diamonds are CO_2.
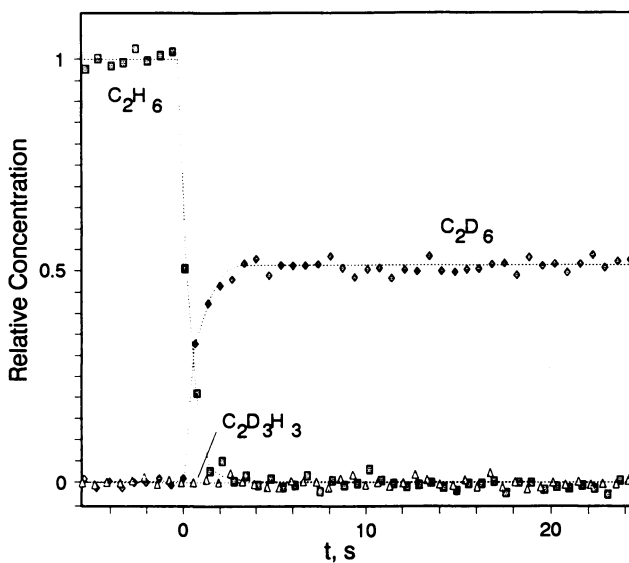
Figure 5. CH_4 - CD_4 transient on lead-tantalum oxide.

conversion rate and isotope-dependent selectivity changes. Nelson, et. al. (57) and we (60) have shown that the methyl groups generally remain intact during methane coupling as shown by the formation of only $(CH_3)_n(CD_3)_{2-n}$ products from CH_4-CD_4 mixtures - a fact which holds for this pyrochlore catalyst (56). We see no evidence of CH_3CD_3 production during the transient, again indicating no concurrent production of the two isotopomeric methyl groups, either from adsorbed methyl precursors and/or gas mixing.

Oxygen transients. The results of $^{16}O_2$ - $^{18}O_2$ transients are shown for (Li)MgO and the Pb/Ta oxide in Figures 6 and 7 (the Bi/Sn oxide catalyst results were similar). These reveal the flow of oxygen on and in these catalysts during the oxidation reaction. Carbon oxides are the only oxygenated products of any significance on these catalysts (with the exception of water). The results are summarized in Table III.

O_2. After a $^{16}O_2$ - $^{18}O_2$ switch, the oxygen leaving the reactor contains ^{16}O as a result of exchange with the catalyst. Multilayer amounts are evolved by the end of the experiment, indicating facile exchange of the surface layer with the bulk of the catalyst. The shape of this transient is governed by a complex convolution over particle characteristics (sizes, surface exchange and bulk diffusion rates) and integration along the catalyst bed. In addition to this lengthy exchange process, there is an indication of a smaller amount of more labile oxygen in the transient on the Pb/Ta catalyst to which we return later. A detailed analysis of the exchange reactions cannot be adequately covered here, but some qualitative observations will be made in the discussion of exchange rates below.

CO_2. The oxygen isotope transient in the CO_2 product shows a very large amount of oxygen available for the CO_2 product as well. As with molecular oxygen, the ^{16}O evolved corresponds to multilayers in both cases. Extrapolation of the CO_2 transient with the time constant at the termination of the experiment (see Table III) indicates involvement of a significant fraction of the bulk oxygen. The details of the transient shape reflect all the factors mentioned above. The relative amounts of CO_2 with molecular weights 44,46 and 48 are binomially distributed, signalling full statistical accommodation with the surface. Although it is possible that the CO_2 initially is formed with this complement of isotopes, a very rapid exchange process completely masks this original distribution (see below). It is interesting to note that the 44/46 ratio in CO_2 is different from the 32/34 ratio in O_2, signifying that the desorbing oxygen is not equilibrated with the same bath of oxygen atoms. The amount of exchangeable oxygen is much larger than the carbonate reservoir on (Li)MgO, signifying oxygen exchange between the carbonate and other species.

CO. Mass spectroscopic complications precluded measuring the CO transients. Peil, et. al. (44) reported a complex transient in the CO product
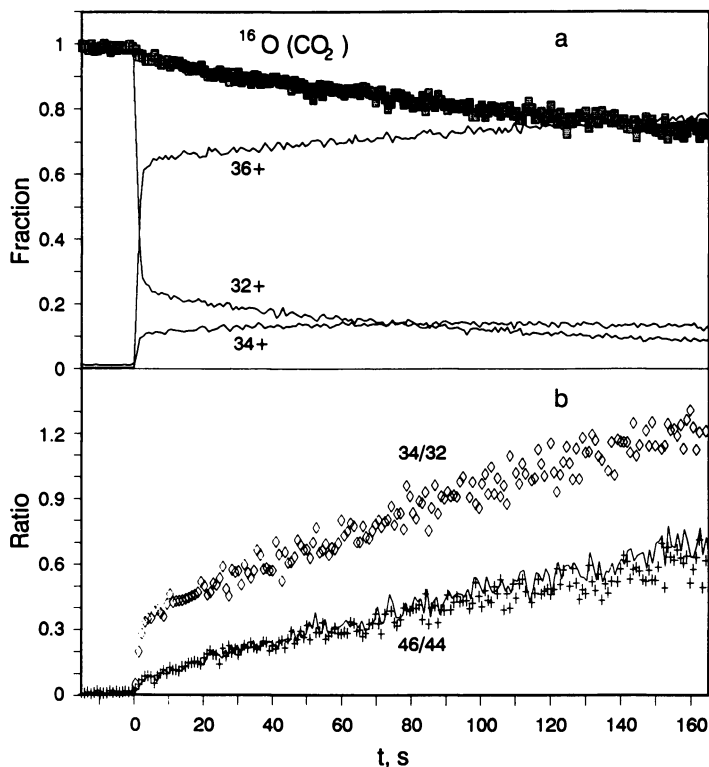
Figure 6. $^{16}O_2$ - $^{18}O_2$ transient on lithiated magnesia. Panel a: Solid lines are oxygen with the indicated molecular weights, rectangles are carbon dioxide. Panel b: Ratios of isotopomers, solid line is statistical 44/46 ratio for the $^{16}O(CO_2)$ content in the upper panel.
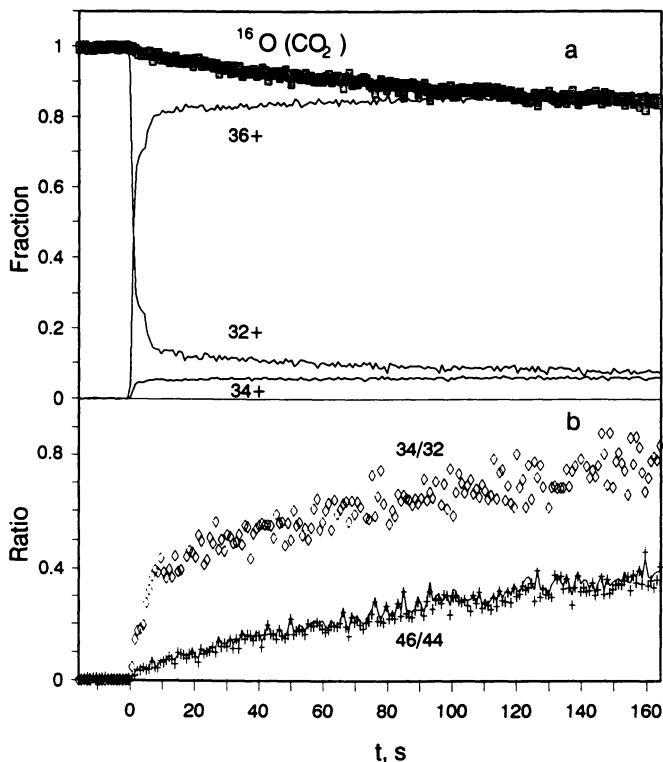
Figure 7. $^{16}O_2$ - $^{18}O_2$ transient on lead-tantalum oxide. Panel a: Solid lines are oxygen with the indicated molecular weights, rectangles are the ^{16}O content of carbon dioxide. Panel b: Ratios of isotopomers, solid line is statistically expected 44/46 ratio.

which contained a rapid drop accompanied by a more lengthy component with a characteristic lifetime similar to the CO_2 transient.

Table III. Oxygen transients - concentrations of catalyst oxygen appearing in the indicated molecules

	$\underline{CO_2}$		$\underline{O_2}$		total
	µmol/g	coverage[a]	µmol/g	coverage[a]	%bulk
$Pb_2Ta_2O_7$	>1900	>45	>500(1.1)[b]	>13(0.03)[b]	29
$Bi_2Sn_2O_7$	>700	>15	>210	>4	10
(Li)MgO	>720	>140	>300	>60	4

[a] Assumes 10Å^2/site and the surface areas in Table I.
[b] Number in parentheses is fast component.

Oxygen exchange reactions. Isotope exchange is a significant factor in these reactions. We have investigated the rates of some of the exchange reactions and present some relevant, qualitative observations here. Most of the exchange rates were evaluated during isotope transients which left the steady state reaction as unperturbed as possible.

O_2 - surface. The rate of exchange between gas phase oxygen and the catalyst surface can be evaluated from the data in Figures 6 and 7 by extrapolating to t=0. The short-lived component on the Pb/Ta catalyst complicates this analysis. Once the shortlived intermediate is replaced with ^{18}O, the exchange process takes place at a rate very similar to the methane activation rate. Cant, et. al. (*18*) and Peil et. al. (*44*) have observed changes in the O_2-surface exchange rate accompanying changes in the gas composition over (Li)MgO. Particularly noted is the reduction of the exchange rate in the presence of CO_2. We observe similar effects on (Li)MgO. These effects are not significant on the pyrochlore catalysts, however.

O_2-O_2 exchange. The possibility of additional exchange processes involving surface species which are kinetically isolated from the bulk was examined by switching from $^{16}O_2$ to a <u>mixture</u> of $^{16}O_2$ and $^{18}O_2$. Comparing these results to those involving a switch to $^{18}O2$ (where only bulk-gas exchange produces changes in the isotopic constitution) reveals the extent of additional O_2-O_2 exchange. On the pyrochlore catalyst this exchange is faster by almost an order of magnitude than the O_2-surface exchange rates thus providing an explanations for the differences between the $32/34(O_2)$ and the $44/46(CO_2)$ ratios in Figures 6 and 7. The excess 34 could arise from further exchange of desorbed oxygen, or it could reflect equilibration with the rapidly exchanged pool evident in Figure 7. It is tempting to associate this intermediate with excess oxygen such as surface peroxides, but much more

work is needed for such an assignment. The amounts in Table III serve as a guide to the spectroscopist in this search.

CO_2 - **catalyst exchange.** These were performed in a similar manner (isotope switches $C^{16}O_2$ - $C^{18}O_2$ in various atmospheres) except for evaluation of the exchange rate during the methane coupling reaction, where CO_2 is a product. In this case, the reactants were spiked with a pulse of $C^{18}O_2$ during otherwise steady state reaction with $^{16}O_2$. The result of this experiment on Pb/Ta is revealing and is shown in Figure 8. In agreement with Cant's (18) results on (Li)MgO, CO_2 exchanges its oxygen with the catalyst several hundred times faster than does O_2 and leaves the reactor equilibrated with the catalyst in this experiment. The ^{18}O deposited reappears in CO_2 and O_2 after the pulse (Figure 8b). Minor variations are seen in the CO_2-surface exchange rate with gas phase composition. It is clear from these exchange rates that even if the CO_2 product had resulted from a kinetically distinct form of oxygen on the surface, post-reaction exchange with the surface erases any memory of this before leaving the reactor. The likely intermediate for this exchange is a surface carbonate:

$$O=C=O \; + \; {}^*O^= \; \longrightarrow \; \overset{O \;\; O}{\underset{\underset{O^*}{|}}{C}} \, [=] \; \longrightarrow \; {}^*O=C=O \; + \; O^= \qquad (6)$$
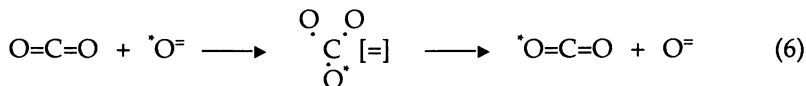
even though the carbon transient does not reveal a surface carbonate reservoir at steady state. Pulsed uptake studies on one Bi/Sn catalyst have revealed a measurable amount of reversible CO_2 adsorption at lower temperatures. Fits of these data to a Langmuir adsorption model provide estimates of surface coverages of order 10^{-4} at reaction conditions (56) - much too small to be seen in these experiments.

In oxidation reactions, the facile interchange of the many oxygen forms often prohibits their kinetic isolation in tracer experiments. Nevertheless, this feature is thought to be important in many selective oxidation reactions by healing reaction-created defects.

Concluding Remarks

As illustrated by the data above, reaction complexity often contrives to deprive the experimenter of some of the desired insight, often by readsorption (post reaction scrambling) and other information destroying processes. Nevertheless dynamic isotope tracing at steady state allows UHV information and post reaction characterization to be put in proper context. The study of isotope flow is well established in UHV experiments, and will undoubtedly be used more in the future on well-characterized "flat" surfaces with tools such as IRAS and SIMS as well as product gas analysis.
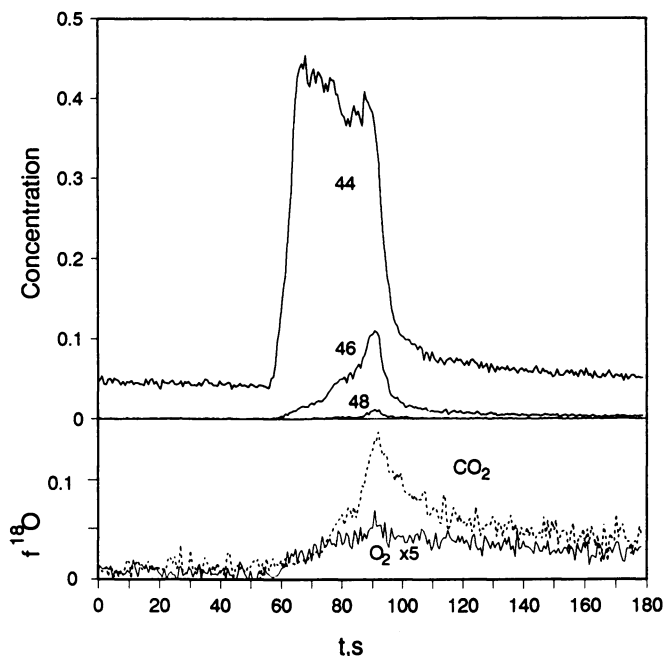
Figure 8. Results of an injection of $^{18}CO_2$ into the reactant stream of an operating lead tantalum oxide catalyst. Upper panel, concentrations of the various CO_2 isotopomers. Lower panel, fraction of ^{16}O in CO_2 (dashed) and O_2 (solid).

Literature Cited

(1)   Tamaru, K., *Dynamic Heterogeneous Catalysis*, Academic Press, New York NY, 1978.

(2)   Schwarz, J. A. and Falconer, J. L., *Catal. Today*, **1990**, 7.

(3)   Ozaki, A. *Isotopic Studies of Heterogeneous Catalysis*, Kondasha, Ltd., Tokyo and Academic Press, NY, 1977.

(4)   Monnier, J.R. and Keulks, G.W., *J. Catal.* **1981**, *68*, 51.

(5)   Kobori, Y., Yamasaki, H., Naito, S., Onishi, T. and Tamaru, K., *J. Chem. Soc., Faraday Trans. 1*, **1981**, *77*, 2913.

(6)   J. Happel, *Isotopic Assessment of Heterogeneous Catalysts*, Academic Press, New York NY, 1987.

(7)   Biloen, P., *J. Mol. Cat.*, **1983**, 2117.

(8)   Jacquez, J. A., *Compartmental Analysis in Biology and Medicine: Kinetics of Distribution of Tracer-labeled Materials*, Elsevier, Amsterdam, 1972.

(9)   Anderson, D. H., *Compartmental Modeling and Tracer Kinetics*, Lecture Notes in Biomathematics Series, no. 50, Springer-Verlag, Berlin, 1983.

(10) Happel, J., *Chem. Eng. Sci.* **1978**, *33*, 1567. contains a short history.

(11) Biloen, P., Helle, J.N., Van den Berg, F.G.A. and Sachtler, W.M.H., *J. Catal.* **1983**, *81*, 450.

(12) Mirodatos, C., *Catal. Today*, **1991**, *9*, 83.

(13) LeCardinal, G., Walter, E., Bertrand, P., Zoulaliam, A., and Gelus, M., *Chem. Eng. Sci.*, **1977**, *32*, 733.

(14) de Pontes, M., Yokomizo, G. H. and Bell, A. T., *J. Catal.*, **1987**, *104*, 147.

(15) Soong, Y., Krishna, K. and Biloen, P., *J. Catal.*, **1986**, *98*, 330.

(16) Mims, C.A. and McCandlish, L.E., *J. Chem. Phys.*, **1987**, *91*, 929.

(17) Li, C., Domen, K., Maruya, K.-I., and Onishi, T., *J. Catal.*, **1990**, *123*,436.

(18) Nelson, P.F., *Appl. Spectr.*, **1990**, 44, 876; Cant, N.W., et. al., *J. Catal.*, **1990**, *124*, 336.

(19) Nelson, P. F., Lukey, C. A., and Cant, N. W., *J. Phys. Chem.*, **1988**, *92*, 6176.

(20) Zhou, X. and Gulari, E., *Langmuir*, **1988**, *4*, 1332.

(21) Duncan, T. M., et. al. *J. Catal.*, **1985**, *93*, 1 also report *ex-situ* NMR studies of transiently labelled surface species.

(22) Otarod, M., et. al., *J. Catal.*, **1983**, *84*, 156.

(23) Happel, J., et. al., *J. Catal.*, **1982**, *75*, 314.

(24) Goodman, D.W., et. al., *Surf Sci.*, **1978**,.

(25) Winslow, P. and Bell, A. T., *J. Catal.*, **1984**, *86*, 158.

(26) Cant, N.W. and Bell, A.T., *J.Catal.*, **1982**, *73*, 257.

(27) Anderson, R. B., *The Fischer-Tropsch Synthesis*, Academic Press, New York NY, 1984.

(28) Dautzenberg, F.M., Helle, J.N., van Santen, R.A. and Verbeek, J., *J.Catal.*, **1977**, *50*, 8.

(29) Mims, C.A. and McCandlish, L. E., *J. Amer. Chem. Soc.*, **1985**, *107*, 696.

(30) Mims, C.A., McCandlish, L.E. and Melchior, M.T., *Cat. Lett.* **1988**, *1*,121.

(31) Mims, C.A., McCandlish, L.E. and Melchior, M.T., *Proc. Int. Conf. Catal. (9th)*, Calgary, 1988, CIC Press, Ottawa, p. 1992.

(32) McCandlish, L.E. and Mims, C. A., *Proc. A.I.Ch.E. Nat'l Meeting*, Seattle, Washington, 1985.

(33) Mims, C.A., Krajewski, J.J., Rose, K.D. and Melchior, M.T., *Catal. Lett.*, **1990,** *7*,119.

(34) Norval, G.W. and Phillips, M.J., *J. Catal.*, **1990.**

(35) Robbins, J., and Marucchi-Soos, E., *J. Phys. Chem.*, **1989,** *93*, 2885.

(36) Mims, C. A., Du, Z.Y., Longwell, J. and Sarofim, A. F., to be published.

(37) Nwalor, J. U., Goodwin, J. G.,Jr. and Biloen, *J. Catal.*, **1989,** *117*, 121.

(38) Happel, J., et. al. *J. Catal.*, **1977,** *50*, 429.

(39) Mirodatos, C., *J. Phys. Chem.*, **1987,** *90*, 481.

(40) Mirodatos, C., Dalmon, J.A. and Martin, G. A., *J. Catal.*, **1987,** *105*, 405.

(41) Ekstrom, A. and Lapszewicz, J.A., *J. Amer. Chem. Soc.*, **1988,** 110, 5226.

(42) Mirodatos, C., Holmen, A., Mariscal, R. and Martin, G. A., *Catal. Today*, **1990,** *6*, 601-610.

(43) Ekstrom, A. and Lapszewicz, J.A., *J. Phys. Chem.*, **1989,** *93*, 5230.

(44) Peil, K.P., Goodwin, J.G., and Marcelin, G., *J. Phys. Chem.*, **1989,** *93*, 5977.

(45) Miro, E., Santamaria, J. and Wolf, E. E., *J. Catal.*, **1990,** *124*, 451.

(46) Keulks, G., *J. Catal.*, **1970,** *19*, 232.

(47) Keller, G.E. and Bhasin, M.M.; *J. Catal.*, **1982,** *73*, 9.

(48) Amenomiya, Y., et. al. *Cat. Rev. - Sci. Eng.*, **1990,** *32*, 163.

(49) Hutchings, G., Scurrell, M.S. and Woodhouse, J.R., *Chem. Soc. Rev.*, **1989,** *18*, 251.

(50) Ito, T., Wang, J.X., Lin, C.H., and Lunsford, J.H., *J. Amer. Chem. Soc.*, **1985,** *107*, 5062.

(51) Otsuka, K., et. al., *J. Catal.*, **1990,** *121*, 122.

(52) Machida, K. and Enyo, M., *J. Chem. Soc., Chem. Commun.*, **1987,** 1639.

(53) Kalenik, Z. and Wolf, E. E., *Catal. Lett.*, **1991,** *9*, 441.

(54) Grzybek, T. and Baerns, M., *J. Catal.*, **1991,** *129* 107.

(55) Jacobson, A.J., Lewandowski, J.T., Mims, C.A., Hall and Myers, G.R., NIST Spec. Publ. 804, *Proc.Intl. Conf. on Elect. Cer. Matls.* 1991. p.151.

(56) Mims, C.A., et. al. to be published.

(57) Nelson, P. F., Lukey, C.A. and Cant, N. W., *J. Catal.*, **1989,** *120*, 216.

(58) Lunsford, J., et. al. unpublished calculations.

(59) Mims, C. A. and Dean, A. M., modelling calculations to be published.

(60) Mims, C. A., Hall, R.B., Rose, K.D., and Myers, G., *Catal. Lett.* **1989,** 2,316.

Chapter 16

Infrared Study of Surface Species Under High-Pressure Conditions

S. D. Worley, J. P. Wey, and W. C. Neely

Department of Chemistry, Auburn University, Auburn, AL 36849

The design, construction, and operation of a novel high-pressure infrared-cell reactor is discussed. The reactor functions in the temperature and pressure ranges of 100-600 K and 10^{-8} - 10^4 Torr, respectively. The use of FTIR to monitor surface species during the interactions of N_2, H_2, D_2, O_2, and CO with supported Rh catalyst films at ambient temperature and high pressure is discussed.

One of the most important means of spectroscopically studying reactive intermediates on the surfaces of supported catalysts is by use of transmission FTIR. Most of the work reported from these laboratories and elsewhere concerning this topic has referred to reactive systems at subatmospheric pressures. However, industrially important chemical processes are often performed at pressures well above one atmosphere, so it should be desirable to monitor surface species under high-pressure conditions to insure that the mechanistic processes do not change in passing from the low-pressure to high-pressure regimes.

The two primary limitations which occur in infrared sutdies of catalytic surfaces at high pressure are: (1) interference from small amounts of impurity surface species which have high infrared extinction coefficients and (2) interference from gas-phase reactants or products which have infrared-active vibrational modes. In this work our efforts in addressing these problems for surface species of interest for supported catalyst films will be discussed.

Experimental

The high-pressure-infrared-cell reactor designed and constructed in these laboratories and used in the work to be described is shown in Figure 1. This cell-reactor has recently been discussed in detail (1), but briefly it has been fabricated from three 4.62 in stainless steel flanges. The outer two flanges contain water-cooled 13 mm diameter, 2 mm thick CaF_2 infrared windows mounted by means of 0.375 in ultra-torr adaptor fittings capable of operation in the 10^{-8} - 10^4 Torr pressure regime. The inner flange contains a stainless steel block in which a third 25 mm CaF_2 window containing the supported catalyst film is mounted. The sample block also contains a U-shaped tunnel drilled about the window for use in sample heating or cooling by means of circulation of
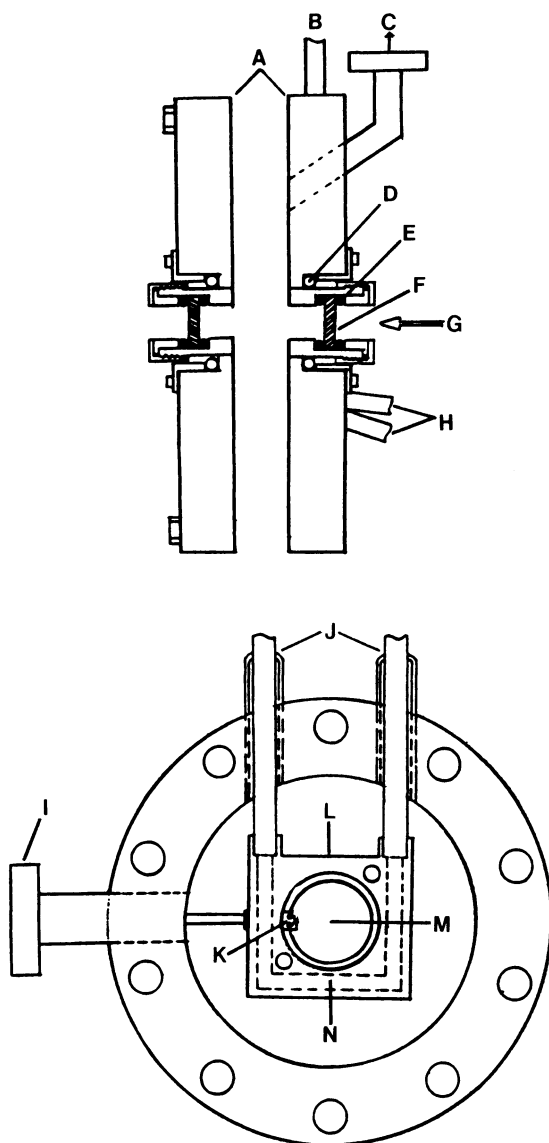
Figure 1. The high-pressure infrared-cell reactor. A: Outer 4.62 in stainless steel flanges, B: To GC, C: To vacuum/high-pressure manifold. D: Water cooling copper tubing, E: 13 mm Viton O-ring, F: 13 mm CaF_2 window, G: IR beam, H: Sample gas inlet and outlet, I: 1.3 in thermocouple feed-through in center flange, J: Heating/cooling gas inlet and outlet, K: Cr-Al thermocouple, L: Stainless steel sample holder block, M: 25 mm sample window, N: U-shaped tunnel for heating and cooling gas.

heated or cooled N_2 and a chromel-alumel thermocouple for measuring sample temperatures. The cell-reactor is attached to a stainless steel manifold capable of operation in the 10^{-10} to 10^4 Torr pressure regime utilizing a cryopump and 60 Ls^{-1} ion pump. Pressure measurements are made using a 10^4 Torr MKS Baratron capacitance manometer which establishes the upper pressure limit of the cell reactor. The reactor could be safely operated at least up to a pressure of 16 atm using the current CaF_2 windows.

The supported catalyst films were prepared by spraying suspensions of $RhCl_3.3H_2O$, Al_2O_3, acetone, and distilled water on to the 25 mm sample window held at 80°C so as to achieve a final loading of 2.2% by weight Rh. The solvents rapidly evaporated leaving infrared-transparent films (_ca_. 4.4 mg cm^{-2}) which could then be prereduced in the cell-reactor. It has been shown in these laboratories (2) and elsewhere (3) that this technique produces excellent supported catalyst samples for use in transmission-infrared analyses. Sample gases were purchased from Air Products (H_2, 99.999%; N_2, 99.999%; O_2, 99.993%) and Matheson (D_2, 99.5%; CO, 99.99%). Further purification was generally necessary with high-pressure H_2, D_2, N_2, and O_2 being passed through a 5% Rh/Al_2O_3 a catalytic converter heated to 373 K, and then trapped at 77 or 158 K, as appropriate. The CO was trapped at 77 K only. All of the sample films were pretreated by evacuation to 10^{-6} Torr at 373 K for 1 h, followed by several reduction/evacuation cycles in 100 Torr H_2 at 473 K, and further evacuation at 298 K for 1 h, before exposure to the gases of interest. In some cases preoxidation was effected by exposure to 100 Torr O_2 at 298 K for 10 min immediately following reduction treatment.

All infrared spectra were obtained with an IBM 32 FT spectrometer operated at 2 cm^{-1} resolution. Generally 500 scans were generated for each spectrum over a period of 7.5 min. All IR data displayed in this work represent difference spectra relative to appropriate reference spectra.

Results and Discussion

Dinitrogen. Wang and Yates (4) have presented a detailed infrared analysis of the $N_2/Rh/Al_2O_3$ system for low pressures (<218 Torr) and subambient temperatures (90-189 K). These conditions were necessary in their study because the interaction of N_2 with Rh/Al_2O_3 is very weak and not observable by infrared at 298 K and low pressure. For a prereduced surface they observed bands at 2331 and 2257 cm^{-1} which they assigned to physisorbed N_2 on Al_2O_3 and a N_2/Rh species, respectively (4). In Figure 2 are presented infrared spectra obtained using our cell-reactor corresponding to the interaction of 8000 Torr N_2 with 2.2% Rh/Al_2O_3 at 298 K, first for 99.999% N_2 with no further purification (Figure 2a), and second for 99.999% N_2 subjected to a catalytic converter and trapping at 158 K (Figure 2b).

The band near 2250 cm^{-1} corresponding to N_2/Rh actually begins to develop upon exposure of the surface to _ca_. 250 Torr even at ambient temperature, but the bands at 2330 (due to physisorbed N_2 on Al_2O_3) and 2301 cm^{-1} (Figure 2a) are not observed until the pressure rises above 4000 Torr. The 2301 cm^{-1} band was _not_ observed for purified high-pressure N_2 (Figure 2b). Wang and Yates detected this band at 2303 cm^{-1} in their low-pressure, low-temperature work only after preoxidation of the Rh/Al_2O_3 surface. Thus it is evident that the surface causing the 2301 cm^{-1} band at high pressure is related to oxidized Rh^{d+}, attributable to the presence of impurity CO, the cause of the bands in the 2000-2100 cm^{-1} region. The assignments of the CO/Rh species (gem dicarbonyl, linear, bridged) are well established (5,6). It has been demonstrated that CO disrupts Rh metallic sites (7,8), causing partial oxidation of Rh to create highly dispersed Rh^+ sites (9) which are produced as isolated OH groups on Al_2O_3 are
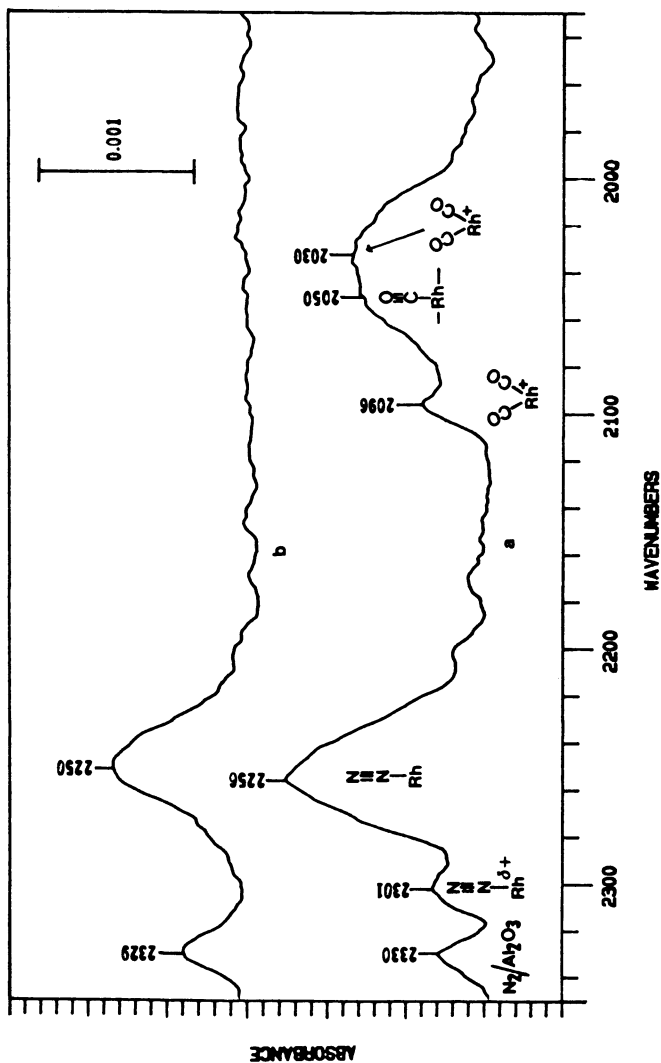
Figure 2. Infrared spectra for the interaction with prereduced 2.2% Rh/Al₂O₃ at 298 K with: (a) 8000 Torr N₂ containing impurity CO and (b) 8000 Torr ultrapure N₂.

consumed (*10*). The 2301 cm^{-1} band was observed clearly as the prominent feature in the spectrum for 8000 Torr N_2 exposed to a preoxidized Rh/Al_2O_3 sample (not shown in Figure 2) thus confirming our assignment of it to a $N_2/Rh^{\delta+}$ species. It should be noted that all of the adsorbed N_2 species disappear rapidly upon evacuation indicating their reversibility. Thus surface species involving weak interactions can be detected using our high-pressure-cell-reactor. A significant observation in this work is that the catalytic converter described in the Experimental section does an excellent job of removing all CO from the high pressure N_2 gas stream (Figure 2b).

Dihydrogen. When H_2 is reacted with CO or CO_2 over a supported Rh film to produce methane, an infrared band in the 2020-2040 cm^{-1} region is generally detected (*2,11*). Solymosi and coworkers (*12,13*) first suggested that the surface species causing this band was a rhodium carbonyl hydride Rh(CO)H. This was later confirmed in these laboratories by an isotopic labeling experiment; the substitution of D_2 caused a red shift of *ca.* 10 cm^{-1} as might be expected for the C-O stretch given substitution two bonds removed (*14,15*). However, the infrared band for the Rh-H vibrational mode for the carbonyl hydride or any other Rh-H species on supported Rh catalysts has thus far escaped detection. The frequency for the Rh-H stretch in inorganic and organometallic complexes has been reported to be typically in the range 2000-2150 cm^{-1} (*16-20*), *i.e.* in the same spectral region as C-O stretching modes for RhCO species. An early report (*21*) of the Rh-H band in the 1890-1930 cm^{-1} region upon exposure of low pressure (<1 Torr) H_2 to Rh/Al_2O_3 probably was erroneous due to impurity CO which gives the well-known bridged Rh_2CO species band in this region. Several computational studies (*15,22-26*) utilizing ab initio methods at various levels of sophistication have predicted that the Rh-H stretching frequency should appear in the range 1008-2028 cm^{-1}, emphasizing the need for an accurate experimental determination.

Figure 3 shows the infrared spectra obtained at 298 K following exposure of 2.2% Rh/Al_2O_3 films to 8000 Torr H_2 (Figure 3a) and 9382 Torr D_2 (Figure 3b) both of which were ultra pure following treatment in the catalytic converter discussed in the Experimental section. The broad band centered at 2013 cm^{-1} which begins to develop at pressures between 100 and 1000 Torr in Figure 3a may be tentatively assigned to the Rh-H stretching mode. Evacuation causes the immediate removal of this band, indicating that the Rh-H species is weakly bound in a reversible fashion. The band centered at 1441 cm^{-1} in Figure 3b then can be assigned to the Rh-D stretching mode. The 572 cm^{-1} isotopic shift to lower frequency is <u>exactly</u> that predicted from an average of the isotopic shifts for several organometallic Rh complexes which have been reported (*16-20*), thus confirming our Rh-H band assignment. The band at 1618 cm^{-1}, which is not removed upon evacuation, in Figure 3a corresponds to H_2O on the Al_2O_3 support. The fact that neither the 2013 or 1618 cm^{-1} bands were observed for high-pressure H_2 over Al_2O_3 alone indicates that H_2 dissociates on Rh to form the Rh-H species, and the remaining H reacts with OH on the Al_2O_3 support to produce adsorbed H_2O. We have also observed rapid isotopic exchange when high-pressure H_2 is interacted with the surface previously exposed to high-pressure D_2. Thus our high-pressure-infrared-cell reactor has proven useful in detecting the infrared band for Rh-H for the first time; it clearly occurs above 2000 cm^{-1} in the CO stretching region.

Carbon Monoxide/Dioxygen. When preoxidized Rh/Al_2O_3 films are exposed to CO, several infrared bands corresponding to $Rh^{\delta+}CO$ species generally occur. Bands due to the well-known gem dicarbonyl species at 2030 and 2100 cm^{-1} which contains Rh in a +1 oxidation state (*5,6*) are always present, and those which have been assigned to Rh^{+2} (probably for a Rh(O)CO species) at *ca.* 2120 cm^{-1} and Rh^{+3} at 2135 cm^{-1} (*6*) have been reported for highly oxidized surfaces. The assignment of the 2120 cm^{-1} band
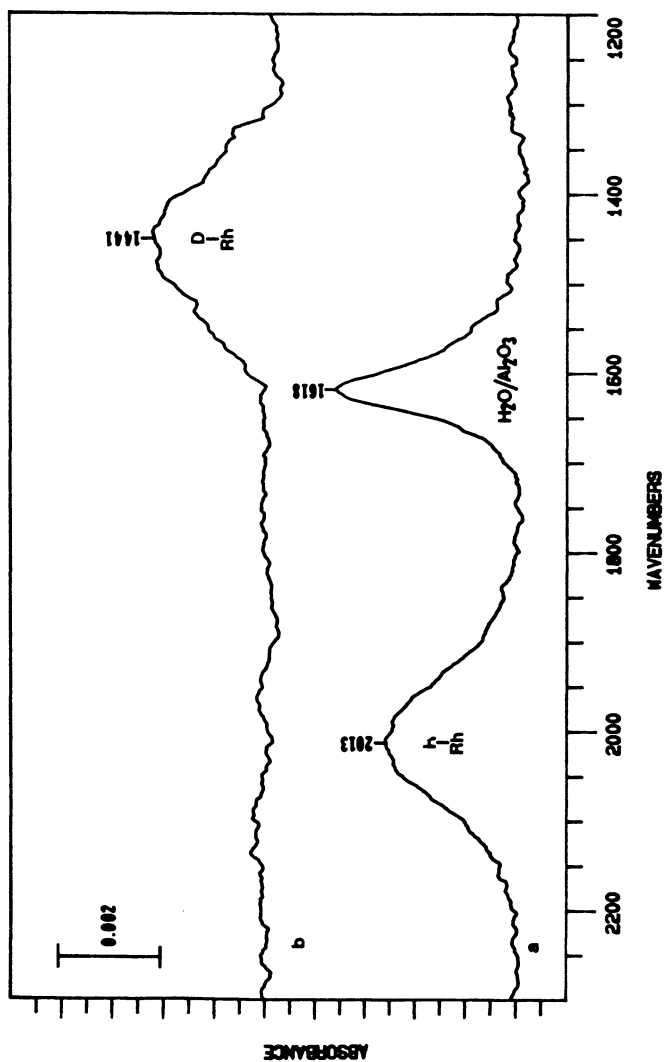
Figure 3. Infrared spectra for the interaction with prereduced 2.2% Rh/Al₂O₃ at 298 K with: (a) 8003 Torr H₂ and (b) 9382 Torr D₂.

to a Rh^{+2} CO species is somewhat controversial. In fact, it has been suggested that the 2120 cm^{-1} band corresponds to one stretching component for a Rh^+ tricarbonyl species (27). High-pressure infrared spectroscopy could help resolve the controversy.

Spectrum a in Figure 4 represents a 2.2% Rh/Al_2O_3 surface which was prereduced in the usual way, evacuated, exposed to 0.5 Torr of CO for 5 min at 298 K, and then evacuated to 10^{-6} Torr. As can be seen, the usual bands representing the "gem dicarbonyl" species (2031 and 2101 cm^{-1}), the "linear" CO species (2065 cm^{-1}), and the "bridged" CO species (1850 cm^{-1}) are present. Then the sample was exposed to 8040 Torr O_2 for 13 h at 298 K which altered the spectrum to that shown in Figure 4b. The high-pressure O_2 caused the disappearance of the bands associated with the linear and bridged CO states and declination of intensity of the two gem dicarbonyl bands. At the same time new bands at 2350 cm^{-1} corresponding to the production of CO_2 gas and 2125 cm^{-1} result. It is extremely unlikely that exposure of the surface to high-pressure O_2 could cause a conversion of the two types of metallic Rh sites and/or the Rh^+ site to a Rh site housing a tricarbonyl species. It is much more probable that the high-pressure O_2 partially oxidizes the Rh/Al_2O_3 surface, causing loss of Rh metal sites, and production of Rh^{+2} sites which then give rise to the band at 2125 cm^{-1}. Recent work here has also shown that the 2125 cm^{-1} band declines in intensity as the pressure of CO in the cell is increased, an observation which also must ague against a Rh tricarbonyl species. Increasing the pressure of CO undoubtedly causes reduction of the Rh^{+2} species to Rh^+ and $Rh^•$, and hence loss of the 2125 cm^{-1} band for Rh(O)CO. One might expect the intensities of the three bands at 2125, 2101, and 2031 cm^{-1} to increase concomitantly with increasing CO pressure if a tricarbonyl species were being formed.

Dioxygen. Attempts have been made to study the interaction of high-pressure O_2 with 2.2% Rh/Al_2O_3 at 298 K using the cell reactor also. Figure 5 shows the infrared spectra obtained as a function of increasing pressure. Several spectral band components were resolved at high pressure in the 1400-1750 cm^{-1} range. Of these, only the sharp band at 1552 cm^{-1} disappears upon evacuation. The spectra obtained for an Al_2O_3 sample containing no Rh were very similar, with the sharp band corresponding to a reversible species appearing at 1555 cm^{-1}. The Raman band corresponding to the O-O stretching mode for gas phase O_2 occurs at 1555 cm^{-1} (28). This it can be concluded that the 1555 cm^{-1} band for O_2/Al_2O_3 corresponds to physisorbed O_2. The samll shift to 1552 cm^{-1} observed in spectrum 5c for $O_2/Rh/Al_2O_3$ probably is indicative of a weak interaction of physisorbed O_2 on Al_2O_3 with the $Rh^{\delta+}$ sites. The remaining spectral features in the 1400-1750 cm^{-1} range which do not disappear upon evacuation can be attributed to H_2O produced upon reaction of O_2 with the support and possible carbonate species resulting from impurities introduced during the sample spraying procedure.

Conclusions

The high-pressure-infrared-cell reactor discussed in this work was employed successfully in detecting several chemisorbed N_2 species on Rh/Al_2O_3 at 298 K as well as Rh-H and Rh-D species for the first time. The interaction of high-pressure O_2 with adsorbed CO species showed that a 2125 cm^{-1} band could be attributed to a $Rh^{+2}CO$ species rather than to the CO stretching component of a Rh^+ tricarbonyl species. Infrared bands corresponding to the physisorbed N_2 and O_2 on Al_2O_3 at 298 K and high-pressure were also detected.
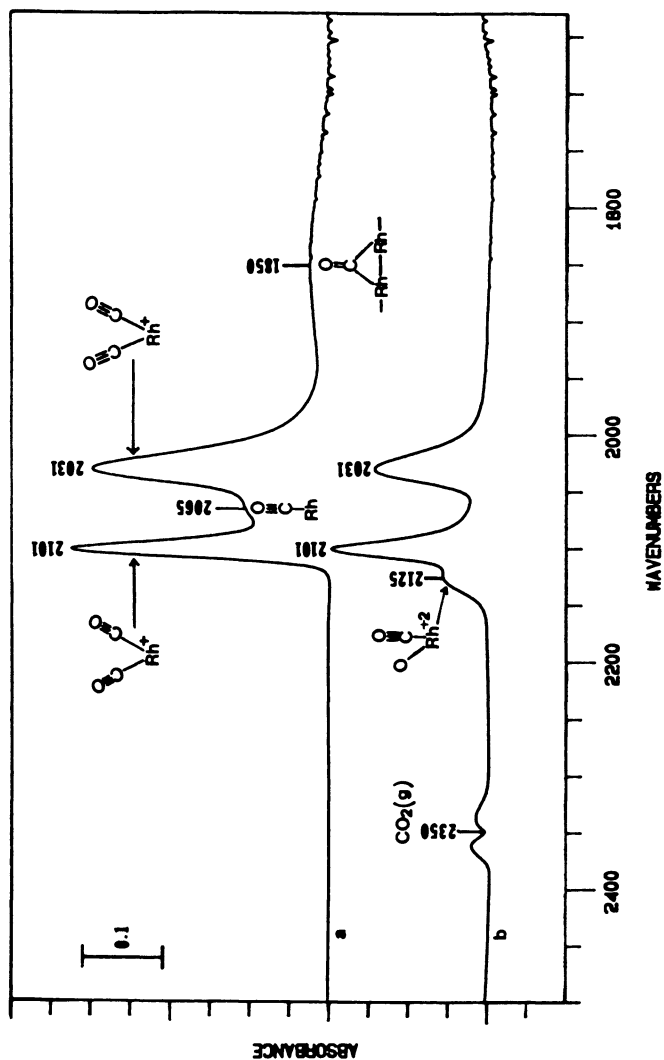
Figure 4. Infrared spectra for the interaction with prereduced 2.2% Rh/Al_2O_3 at 298 K with: (a) 0.5 Torr CO for 5 min followed by evacuation and (b) subsequent exposure to 8040 Torr O_2 for 13 h at 298 K.
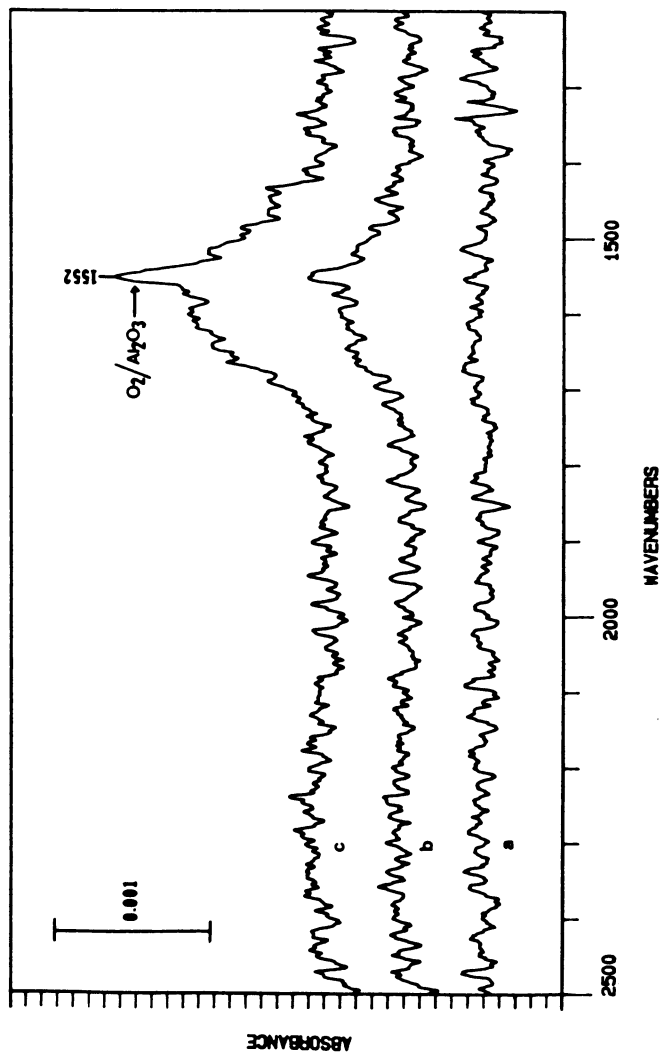
Figure 5. Infrared spectra for the interaction with prereduced 2.2% Rh/Al_2O_3 at 298 K with: (a) 2950 Torr O_2, (b) 6012 Torr O_2, and (c) 8610 Torr O_2.

Acknowledgments

Literature Cited

1. Wey, J. P.; Burkett, H. D.; Neely, W. C.; Worley, S. D. *J. Am. Chem. Soc.* **1991**, *113*, 2919.
2. Henderson, M. A.; Worley, S. D. *J. Phys. Chem.* **1985**, *89*, 1417.
3. Yates, J. T.; Duncan, T. M.; Worley, S. D. Vaughan, R. W. *J. Chem. Phys.* **1979**, *70*, 1219.
4. Wang, H. P.; Yates, J. T. *J. Phys. Chem.* **1984**, *88*, 852.
5. Yang, A. C.; Garland, C. W. *J. Phys. Chem.* **1957**, *61*, 1504.
6. Rice, C. A.; Worley, S. D.; Curtis, C. W.; Guin, J. A.; Tarrer, A. R. *J. Chem. Phys.* **1981**, *74*, 6487.
7. Van't Bilk, H. F. J.; Van Zon, J. B. A. D.; Huizinga, T.; Vis, J. C.; Koningsberger, D. C.; Prins, R. *J. Phys. Chem.* **1983**, *87*, 2264.
8. Solymosi, F.; Pasztor, M. *J. Phys. Chem.* **1985**, *89*, 4789.
9. Solymosi, F.; Knözinger, H. *J. Chem. Soc. Faraday Trans.* **1990**, *86*,   389.
10. Basu, P.; Panaytov, D.; Yates, J. T. *J. Am. Chem. Soc.* **1988**, *110*, 2074.
11. Worley, S. D.; Mattson, G. A.; Caudill, R. *J. Phys. Chem..* **1983**, *87*, 1671.
12. Solymosi, F.; Erdohelyi, A.; Kocsis, M. *J. Catal.* **1980**, *65*, 428.
13. Solymosi, F.; Erdohelyi, A.; Bensagi, T. *J. Catal.* **1981**, *68*, 371.
14. Henderson, M. A.; Worley, S. D. *J. Phys. Chem.* **1985**, *89*, 392.
15. McKee, M. L.; Dai, C. H.; Worley, S. D. *J. Phys. Chem.* **1988**, *92*, 1056.
16. Takesada, M.; Yamazaki, H.; Hagihara, N. *Bull. Chem. Soc. Japan,* **1968**, *41*, 270.
17. Ito, T.; Kitazume, S.; Yamamoto, A.; Ikeda, S. *J. Am. Chem. Soc.* **1970**, *92*, 3011.
18. Dewhirst, K. C.; Keim, W.; Reilly, C. A. *Inorg. Chem.* **1968**, *7*, 546.
19. Saceo, A.; Ugo, R.; Moles, A. *J. Chem. Soc. A,* **1966**, 1670.
20. Osborn, J. A.; Jardine, F. H.; Young, J. F.; Wilkinson, G. *J. Chem. Soc. A.,* **1966**, 1711.
21. Kavtaradze, N. N.; Sokolova, N. P. *Russ. J. Phys. Chem.* **1970**, *44*, 1485.
22. Langhoff, S. R.; Pettersson, L. G. M.; Bauschlicher, C. W.; Partridge, H. *J. Chem. Phys.* **1987**, *86*, 268.
23. Balasubramanian, K.; Liao, D. W. *J. Chem. Phys.* **1988**, *88*, 317.
24. Paniagua, J. C.; Illas, F. *Chem. Phys. Lett.* **1990**, *170*, 561.
25. Rochefort, A.; Andzelm, J.; Russo, N.; Salahub, D. R. *J. Am. Chem. Soc.* **1990**, *112*, 8239.
26. Mains, G. J.; White, J. M. *J. Phys. Chem.* **1991**, *95*, 112.
27. Wang, H. P.; Yates, J. T. *J. Catal.* **1984**, *89*, 79.
28. Herzberg, G. *Spectra of Diatomic Molecules*; Van Nostrand Inc.: New York, NY, pp. 62.

Chapter 17

Effect of Structure in Propylene Oxidation on Molybdenum Trioxide

Anantha N. Desikan[1] and S. Ted Oyama[1,2]

Departments of [1]Chemical Engineering and [2]Chemistry, Clarkson University, Potsdam, NY 13699

Samples of unsupported and silica-supported molybdenum oxide were used to study the oxidation of propylene. The samples were characterized by laser Raman spectroscopy, x-ray diffraction, and high temperature oxygen chemisorption. Raman spectroscopy revealed that the structure of the molybdenum oxide varied from small crystallites (MoO_3) at high loadings, to monomeric molybdate units (MoO_4^{2-}) at low loadings. Oxygen chemisorption, calibrated using unsupported standards, allowed titration of surface metal centers and gave good correlation with the Raman results. Turnover rates based on sites counted by oxygen chemisorption were measured for propylene oxidation to acrolein. The reaction was found to be structure-sensitive, acrolein formation was favored on sites of low molybdenum coordination.

The effect of structure on the catalytic activity of oxides has been attracting increasing attention in recent years (1,2). In this investigation the propylene oxidation reaction is compared on unsupported MoO_3 and a series of MoO_3/SiO_2 samples, where the molybdenum concentration is systematically changed. Oxygen chemisorption and laser Raman spectroscopy reveal that the samples have different dispersion and are thus well-suited for examining the effect of structure in the reaction. Support effects are minimized because the interaction between molybdenum oxide and silica are small.

The results in this study are contrasted to those of others using a different approach to determine the effect of structure. These other studies relate the relative amounts of different crystal planes in macrocrystalline samples to the selectivity to different reaction products (3,4). In this manner, they make pos-

sible the assignment of the formation of various products to specific crystal faces. Thus, for example, it has been concluded that the (100) side face of MoO_3 is responsible for acrolein production in propylene oxidation and that the (010) basal face results in CO_x formation (5,6). This method has been criticized for overanalyzing scant data (7), however, the results appear to be reproducible. In a refinement of the earlier studies, it has been concluded that stepped (1k0) faces of the {100} family are involved in acrolein formation (8).

These conclusions are contested in another study involving allyl halides and allyl oxalate (9) in which the basal (010) plane is suggested to be responsible for acrolein production. But these studies were carried out with uncontrolled water vapor partial pressure in a pulse mode, and the conclusions were based on a model involving sequential activation and reaction of propylene on different planes. Such behavior of propylene has not been observed on molybdenum oxide.

EXPERIMENTAL

The supported MoO_3 catalysts were prepared by impregnating SiO_2 (Cab-O-Sil L90) to incipient wetness with ammonium molybdate (Aldrich, 99%) solutions, drying at 393 K, and calcining at 773 K. Pure unsupported MoO_3 (Aldrich, Puratronic, 99.999%) and $Bi_2Mo_3O_{12}$ (Alfa 99%) in the form of powders were used after calcination in air at 773 K. Surface areas (BET) and oxygen uptakes were measured with a flow apparatus equipped with a mass spectrometer detector. Oxygen uptakes were measured at 623 K on samples reduced in H_2 at the same temperature by adsorbing calibrated pulses of O_2. For $Bi_2Mo_3O_{12}$, a reduction temperature of 573 K was used because TPR analysis indicated that its reduction took place 50 K lower than MoO_3.

Catalytic activity was obtained in a 15 mm OD/13 mm ID quartz packed bed flow reactor at a total flow rate of 70-71 μmol s^{-1} and a total pressure of 101 kPa. (Flow rates in μmol s^{-1} may be converted to cm^3(NTP)min^{-1} by multiplying by 1.5). In the reactivity experiments the partial pressure of reactants were P_{C3H6} = 10 kPa, P_{O2} = 10 kPa, P_{H2O} = 5 kPa and P_{He} = 75.1 kPa. In all the experiments amounts of catalyst corresponding to 20.4 μmol of O_2 uptake were loaded in the reactor, except for the case of $Bi_2Mo_3O_{12}$, where an amount corresponding to 22.7 μmol of O_2 uptake was loaded. For analysis of reaction products a mass spectrometer (Dycor Ametek MA100) was used.

Particular care was used to ensure that the catalysts were stable at the reaction conditions employed. Before every run the catalysts were pretreated in the O_2-He-H_2O mixture for 1 h at the maximum temperature of reaction.

After the highest temperature was attained, a lower temperature measurement was always repeated to verify catalyst stability and lack of deactivation. Carbon balances closed to $100\pm10\%$.

Rates are reported as turnover rates based on the surface molybdenum atoms counted by oxygen chemisorption:

$$v_t = \frac{Qyx}{Vw2S}$$

In the equation above v_t is the total propylene turnover rate, Q is the total volumetric flow rate, y is the mole fraction of propylene, V is the molar volume at the condition of flow measurement, w is the weight of the catalyst, and 2S is the oxygen uptake value. The other turnover rates are defined as

$$v_i = v_t S_i$$

where S_i, the selectivity of the products i, represents the fraction of propylene that gets converted to i and takes into account the number of carbon atoms in the product. (Thus CO and CO_2 production is divided by 3). The turnover rates are given in units of s^{-1}.

RESULTS AND DISCUSSION

Dispersion of the Catalysts. A complete study of oxygen chemisorption on unsupported standards and the supported samples was carried out and is reported elsewhere (*10*). Complementary XRD and laser Raman spectroscopy measurements indicate that the technique titrates surface metal centers on the catalysts. Raman spectroscopy further reveals that the structure of the dispersed phase is that of isolated, distorted tetrahedral units (MoO_4^{2-}). At intermediate loadings, this surface phase coexists with small (< 5nm) crystallites with the bulk MoO_3 structure. At high loadings, the MoO_3 crystallites are the predominant form (Fig. 1). Comparative studies with MoO_3 supported on Al_2O_3 and TiO_2 show that the degree of interaction of MoO_3 with the support is minimal. This agrees with reports in the literature (*11*).

The oxygen uptake values of the fresh catalysts are reported in Table 1. It was found that the catalysts had the same uptakes after reaction. Table 1 also reports the dispersions, defined as the fraction of molybdenum atoms on the surface as measured by oxygen chemisorption. Dispersions range from 0.16 to 0.96 for the catalysts used.

The Raman spectroscopy results and the oxygen chemisorption values indicate that the structure of the catalyst is varying substantially over the range of molybdenum oxide loading employed here (Fig. 1). Thus, these samples are suitable for examining the effect of structure on the reaction.

Table 1. Oxygen Uptake on Catalyst Samples

Catalyst	SA[a]/ m^2g^{-1}	O_2Up[b]/ $\mu mol\ g^{-1}$	D[c]
SiO_2	89	8	
0.3% MoO_3/SiO_2	61	18	0.96
1.0% MoO_3/SiO_2	83	29	0.60
3.0% MoO_3/SiO_2	71	38	0.29
5.0% MoO_3/SiO_2	66	43	0.20
9.0% MoO_3/SiO_2	73	59	0.16
MoO_3	5.5	46	0.013
$Bi_2Mo_3O_{12}$[d]	2.4	9.08	

[a] Surface Area.
[b] Oxygen molecule uptake ($T_{red} = T_{ads} = 623$ K).
[c] Dispersion = fraction of Mo atoms at the surface.
[d] $T_{red} = T_{ads} = 573$ K

Propylene Oxidation. Propylene oxidation on the silica supported catalysts was studied between 600 and 800 K. The results are presented as turnover rates, based on metal centers titrated by oxygen chemisorption (Fig. 2). All samples regardless of dispersion showed similar behavior. CO and CO_2 were produced at all temperatures of operation and increased in amount at higher temperatures. At the lowest temperature the predominant selective oxidation product was acrolein. At higher temperatures propionaldehyde and acetaldehyde were also produced with acrolein. The conversions varied from 10% at 623 K to 50% at 773 K. The oxygen conversions approached 90% at the highest temperature.

Silica was inert at lower temperatures but at higher temperatures produced selective and total oxidation products. Unsupported MoO_3 was completely inactive at low temperatures (623 - 723 K) and was moderately active at 773 K. The only selective oxidation product observed in the case of unsupported MoO_3 and unsupported bismuth molybdate was acrolein.

Examination of the data (Fig. 2) reveals that bulk MoO_3 behaves differently from the supported samples. It has about 30 times lower activity than
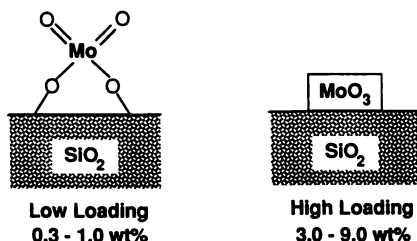
Figure 1. Structure of supported molybdenum oxide catalysts.
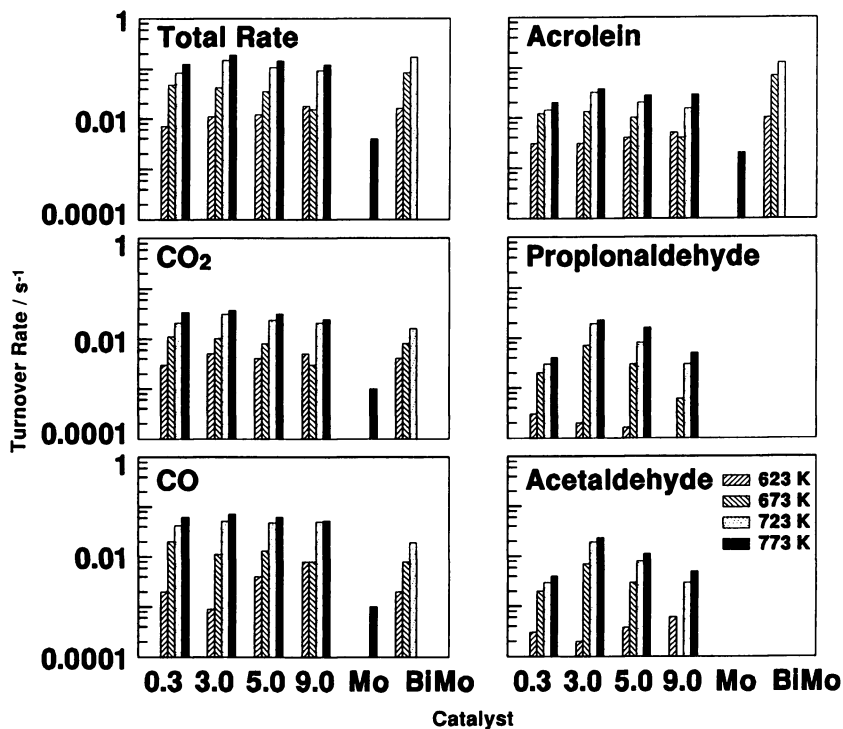
Figure 2. Effect of molybdenum concentration on propylene oxidation.

the supported samples with lower selectivity to selective oxidation products, and does not produce saturated aldehydes. This suggests that the propylene oxidation reaction is structure-sensitive. The bismuth molybdate sample shows superior activity and selectivity to the plain molybdenum oxide catalysts, as expected, because of the presence of the bismuth component. The results are presented for comparison and will not be discussed further.

The data also reveals (Fig 2) that for the supported samples the total turnover rates and selective turnover rates do not vary considerably for the whole range of dispersions used. This seems to contradict the conclusion that propylene oxidation is structure-sensitive. A possible explanation could be that despite considerable differences in dispersion, 0.16-0.96, a structural feature critical in propylene activation remains unchanged with molybdenum loading. We suggest that this structural feature is low coordination, defined here as a molybdenum coordination less than six. Thus, low coordination results in higher activity and selectivity.

The molybdenum species on the silica support vary from isolated MoO_4 monomers of a distorted tetrahedral structure to very small crystallites of nm dimensions. It is likely that these small crystallites expose a substantial amount of (1k0) edge planes, rather than (010) basal planes, which are prevalent in larger crystallites. This has been found recently (*12*). The steps on the (1k0) edge planes cause the molybdenum centers to have lower coordination than on the basal planes. Thus, the finding that the activity of the small supported crystallites resembles that of the monomers could be due to the low Mo coordination found on the surface species for both samples.

The differences between the bulk and the supported samples could alternatively be ascribed to a MoO_3-SiO_2 support effect, but this is unlikely. Raman spectroscopy indicates that there is little support interaction and that the structure of the MoO_3 crystallites is identical to that of bulk MoO_3. Moreover, such a support effect should be manifested more strongly in going from the monomeric MoO_4^{2-} monomers to the MoO_3 crystallites on the supported samples. This is not observed.

The greatest difference between the supported MoO_3 crystallites and the unsupported powder is the crystallite size. In the supported system, the size is of the order of nm, whereas in the powder it is of the order of μm. The large powder grains expose larger proportions of (010) basal planes and selectivity drops. This agrees with earlier findings (*5,8*). The lower coordination species found on the supported samples are expected to result in higher activity because the molybdenum ions are more accessible to the reacting propylene molecules.

The main difference between our conclusions and the earlier work on macroscopic MoO_3 crystals (*6,5,8*) is that we do not claim that the side plane (1k0) is <u>exclusively</u> the face for acrolein formation.

CONCLUSION

Considerable differences in activity and selectivity between unsupported MoO_3 and a series of MoO_3/SiO_2 samples indicate that the reaction is structure-sensitive. Similar differences are not found within the MoO_3/SiO_2 series even though the molybdenum species changes from a dispersed surface molybdate to small supported crystallites. The lack of variation among the supported samples may arise because surface molybdenum atoms are structurally similar on both the highly dispersed surface phase and the small supported crystallites. In the surface phase the molybdenum atoms have low coordination because of their isolated monomeric form, while on the small crystallites the molybdenum centers also have low coordination because of their location on steps on the edge planes.

ACKNOWLEDGEMENT

LITERATURE CITED

1. Y. Murakami, M. Inomata, A. Miyamoto and K. Mori, *Proc. 7th Int. Cong. Catal.*, Tokyo, 1980, Part B, p. 1344, Elsevier, 1981.
2. J. C. Volta and J. L. Portefaix, *Appl. Catal.* **1985**, *18*, 1.
3. J. C. Volta, W. Desquesnes, B. Moraweck and G. Coudurier, *React. Kin. Catal. Lett.* **1979**, *12*, 241.
4. J. C. Volta, W. Desquesnes, B. Moraweck and J. M. Tatibouët, *Proc. 7th Int. Cong. Catal.*, Tokyo, 1980, Part B, p. 1398, Elsevier, 1981.
5. J. C. Volta, J. M. Tatibouët, C. Phichitkul and J. E. Germain, *Proc. 8th Int. Cong. Catal.*, Berlin, 1984, Vol. 4, p. 451, Verlag Chemie, 1984.
6. J. C. Volta and B. Moraweck, *J.Chem.Soc., Chem. Commun.* **1980** 330.
7. S. T. Oyama, *Bull. Chem. Soc. Japan* **1988**, *61*, 2585.
8. M. Abon, B. Mingot, J. Massardier and J. C. Volta, *Preprints*, Division of Petroleum Chemistry, American Chemical Society Boston Meeting, April 22-27, 1990, Vol. 35, p. 44.
9. K. Brückman, R. Grabowski, J. Haber, A. Mazurkiewicz, J. Sloczynski and T. Wiltowski, *J. Catal.* **1987**, *104*, 71.
10. A. N. Desikan, L. Huang and S. T. Oyama, *J. Phys. Chem.* **1991**, In press.
11. H. C. Liu, L. Yuan and S. W. Weller, *J. Catal.* **1977**, *47*, 100.
12. B. Mingot, N. Floquet, O. Bertrand, M. Treilleux, J. J. Heizmann, J. Massardier and M. Abon, *J. Catal.* **1989**, *118*, 424.

Chapter 18

Chemical Reactions in High Electric Fields

H. J. Kreuzer

Department of Physics, Dalhousie University, Halifax, Nova Scotia B3H 3J5, Canada and Fritz-Haber-Institut der Max-Planck-Gesellschaft, Faradayweg 4–6, D–1000 Berlin 33, Germany

In external electrostatic fields of the order of volts per angstrom, comparable to those experienced by valence electrons in atoms and molecules, a redistribution of the valence electrons takes place affecting both internal molecular bonds as well as surface bonds in adsorbed molecules. Whether this leads to stabilisation or de-stabilisation of molecular structures depends on whether bonding or anti-bonding orbitals are more strongly affected. New pathways in chemical reactions may be established, e.g. in heterogeneous catalysis. The microscopic theory of electrostatic fields at metal surfaces is reviewed. We next survey the selfconsistent theory of field evaporation of metals. As examples of field-induced chemistry we study the formation of Ru subcarbonyls and the reaction $2NO \rightarrow N_2O + O$ on $Pt(111)$.

The term "high electric fields" in the title of this article refers to field strengths of the order of volts per angstroms. To put this into perspective, we note that the maximum field strength that can be maintained between two conductors in air is limited to less than about $10^4 V/cm$ above which dielectric break-through leads to the formation of an ionized plasma. In semi-conductors, fields of the order of $10^6 V/cm$ can be maintained, whereas fields within the double layer at the electrolyte-electrode interface can reach $10^7 V/cm$. Around localized charges in zeolite cavities electric fields of the order of $10^8 V/cm = 1 V/\overset{o}{A}$ have been estimated on the basis of Coulomb's law. Fields of this order can also be established within $10^3 \overset{o}{A}$ of a metal tip with a tip radius of less than $10^3 \overset{o}{A}$, provided dielectric break-through is avoided by working in ultrahigh vacuum. The upper

limit of electric field strength that can be maintained over macroscopic distances is dictated by the onset of field emission and field evaporation, and is of the order of $6V/Å$.

Electric fields of the order of volts per angstrom are comparable to those experienced by valence electrons in atoms and molecules. One should therefore expect that in external fields of that magnitude a redistribution of the valence electrons in molecules and in particular in molecules adsorbed on surfaces takes place affecting both internal bonds as well as the surface bond. Whether this redistribution leads to enhanced or reduced binding depends on whether bonding or antibonding orbitals are more strongly affected. We will refer to this phenomenon as field-induced chemistry; the physics and chemistry in high electrostatic fields has been reviewed recently (*1*). To estimate the field strength needed to affect the chemistry of a reaction, we note that the equilibrium constant, K, of a reactive system depends on the field strength, F, via a van't Hoff equation (*2*)

$$\frac{\partial \ell n K}{\partial F} = \frac{\Delta M}{RT} \tag{1}$$

where ΔM is a partial molar energy related to the change in electric moment in the reaction, i.e.

$$\Delta M = \Delta p F + \tfrac{1}{2}\Delta \alpha F^2 + \ldots \tag{2}$$

Here Δp is the difference in the permanent dipole moments of the products and the reactants, and $\Delta \alpha$ is the change in their polarizability. In order to achieve values for ΔM comparable with typical reaction enthalpies or volumes, one needs fields in excess of $0.1V/Å$.

Block and coworkers, following earlier work by Inghram and Gomer (*3*) have developed a field pulse technique in the field ion microscope that allows the investigation of the field effect on chemical reactions; a detailed account has been given by Block (*4*). Systems that have been studied by this technique are the formation of metal subcarbonyls, the polymerization of acetone, the reaction of sulphur on metal surfaces, the decomposition of methanol on metal surfaces, hydride formation on semiconductors, NO reactions on metals and many more.

Electric field effects on matter can be classified, rather arbitrarily, into two categories: (*i*) in low fields, i.e. below roughly $10^{-1}V/Å$, atoms, molecules and condensed matter only get polarized; we will call such effects physical. (*ii*) In fields larger than typically $10^{-1}V/Å$ chemical effects come into play in addition in that the electronic orbitals get distorted to such a degree as to effect the chemical characteristics of an atom or molecule e.g. by establishing new bonding orbitals. In this way, molecules, unstable in field free situations, may be stabilized by a strong electric field. Also, new pathways in chemical reactions, and in particular in heterogeneous catalysis, may be established.

A microscopic theory can elucidate the changes in the stability of molecules and in reaction pathways induced by high electric fields. To discuss field effects qualitatively, we look, in Figure 1, at a molecule AB adsorbing on a metal. Far from the surface and in the absence of a field, the atomic orbitals of A and B hybridize into molecular orbitals which we take to be a lower-lying bonding orbital and an empty antibonding orbital. As the molecule approaches the surface, additional hybridization with the conduction electrons occurs leading to shifts and broadening of these orbitals. As illustrated in Figure 1, the antibonding orbital would also get partially occupied resulting in (*i*) bonding to the surface and (*ii*) weakening of the A-B bond and stretch vibration. Molecules such as CO and N_2 are examples. Applying an electric field, F_0, pointing away the surface, adds the potential energy, $eF_0 z$, for the electrons outside the metal. For simplicity, we assume total expulsion of the field from the metal. This raises the atomic levels of the atoms A and B by amounts of the order $eF_0 z_a$ and $eF_0 z_b$, respectively, resulting in a substantial *re*-arrangement of the molecular orbitals. For the situation depicted in Figure 1, the anti-bonding orbital would empty out again, leading to restabilization of the molecule and probably a weakening of the surface bond. If we increase the field strength to the point where the bonding orbital is lifted above the Fermi energy of the metal, it will drain as well, leading to field-induced dissociation. The effect of electric fields on the vibrational frequency of a molecule adsorbed on a metal has been demonstrated for N_2 on Fe(111) (5). In concluding this qualitative discussion we note that in the absence of the field the bonding orbital of the AB molecule is more B-like whereas the anti-bonding orbital has more A character. As the electric field is increased, these characteristics are changed in a continuous manner into a situation where the bonding orbital is more A-like and the anti-bonding orbital has B character. This possibility of changing the relative position of orbitals of the constituent atoms in a molecule with respect to each other, leads to new, field-induced chemistry.

In this review, we will demonstrate field-induced chemistry in a number of different systems. In the next section we will look at field evaporation of metals as an example of bond weakening and breaking. We will then summarize the formation of metal-subcarbonyls in a field, followed in by a description of the formation of N_2O from NO on a Pt(111) surface in a field as examples of new, field-induced reaction pathways. We conclude the paper with an outlook to future work.

Field Evaporation

Field evaporation is the removal of lattice atoms as singly or multiply charged positive ions from a metal in a strong electric field of the order of several volts per angstroms, as it occurs at field ion tips. Like desorption, it can be viewed as a chemical reaction in which the surface bond is ruptured leading to the dissociation of the initial atom-surface "molecule" into a free atom (or ion) and the solid. Field evaporation is a thermally activated process; its rate constant can be parametrized

according to Frenkel-Arrhenius as

$$r_d = \nu(T,F) \exp[-Q(F)/k_B T] \tag{3}$$

where $Q(F)$ is the field dependent activation barrier to be overcome by the evaporating particle. The prefactor $\nu(F,T)$ can also be field-dependent and is usually weakly temperature-dependent as well. The minimal field strength beyond which at low temperature the metal evaporates instantaneously, is termed the evaporation field strength; it varies from $2.5V/Å$ for *Ti* to $5.6V/Å$ for *W*.

Two phenomenological models have been used in the past to calculate the activation energy $Q(F)$, the "image-force" model (6) and the "charge-exchange" model (7). A recent assessment has been given by Kellogg (8). Field evaporation is a dramatic demonstration of the limitation of classical concepts in solid state physics. Maxwell's theory says that the electric field drops to zero at the image plane, i.e. just outside the metal. Thus the electric field has, classically, no effect on the ion cores of the metal, and thus, classically field evaporation is not possible. On the other hand, selfconsistent calculations of the electron and field distribution on a flat jellium metal have demonstrated that field expulsion from the metal is not complete and that the field strength at the topmost ion cores in a metal can be substantial, and in particular strong enough to cause field evaporation.

Experiment suggests that field evaporation of metal atoms occurs most likely at steps, kinks and edges or for small clusters of atoms on larger planes. Theory should calculate the electric field, the electron density, and the geometry of the ion cores for such configurations selfconsistently. Early work (9) on field evaporation lacked this selfconsistency, employing the ASED-MO cluster model with electric fields taken from jellium calculations (10). Recently, this deficiency has been overcome with the first selfconsistent calculation of atomic adsorption on metals in high electric fields (11).

To understand field effects at metal surfaces, one would like to calculate the local field at kink sites or around single atoms on densely packed planes of transition metals. As a model of the latter, self-consistent calculations of the electric field around a metal atom adsorbed on a structureless jellium surface have been performed using the local density functional theory (11). As examples, a light and a medium heavy metal atom, *Ti* and *Nb*, respectively, on a jellium metal with a Wigner-Seitz radius $r_s=3.0$ bohr have been considered in a field pointing away from the surface, appropriate for the field ion microscope. Although this model describes the chemisorption of metal atoms on a free electron metal in the presence of a field, it turns out that the results have quite general features that allow a discussion of field effects in chemisorption on transition metals.

Classical electromagnetic theory assumes that the surface of a metal is a mathematical plane with excess charges and a dipole layer at which the normal component of the electric field drops discontinuously to zero, at least for a perfect conductor. On

real surfaces, however, the electron distribution and electric
fields vary smoothly over distances of a few angstroms. A
simple model (12,13) that exhibits these features is the jellium
model of a metal, in which it is assumed that the ionic lattice
can be smoothed into a uniform positive charge density, n_+, that
drops to zero abruptly half a lattice constant above the top-
most layer of ion cores. In front of this jellium metal one adds
a metal atom (14) around which we will study the local electron
and field distribution within the framework of density func-
tional theory. The latter determines the exact ground-state
electron density from which the electric field is calculate via
Poisson's equation.

In Figure 2, we show the adiabatic energy curves for niobium
on jellium for several field strengths. In zero field the depth
of the surface potential is 5.2eV, which is, not surprisingly,
somewhat less than the cohesive energy of Nb, 7.47eV, because
the jellium lacks p- and d-orbitals. This deficiency is also the
cause of the rather weak repulsion at short distances. As we
apply a field, we note a shift of the potential minimum by about
0.2 Å away from the surface. We will trace this shift to a
transfer of electronic charge from outside the adatom to the
region between the adatom and the surface. With a field appl-
ied, the ground state energy curves must assume an asymptotic
form $-eF_0z$ for large z, appropriate for a singly charged positive
ion. Ionization of the adatom can occur when its highest occup-
ied level is lifted by the field energy term, eF_0z, above the
Fermi level of the jellium. If the ionization level were not
shifted and broadened by the interaction with the metal, the
changeover to the asymptotic form would happen abruptly at the
apex of the potential energy curve, i.e. at the point where the
diabatic energy curves for the neutral and ionic species cross.
For the fields chosen for Figure 2, the apex is so close to the
metal surface that considerable interaction between the adatom
and the metal is still in effect. This results in a considerable
broadening of the ionization level of the adatom so that only
partial charge draining occurs in the apex region.

We will call the energy difference between the minimum of the
surface potential and the local maximum at its apex the activa-
tion energy, $Q(F_0)$, for ionization. In zero field, the activa-
tion energy is equal to the binding energy of the adatom. We
note that the activation energy becomes zero for the evapora-
tion field strength which we estimate for Nb on jellium to be
3.6V/Å, which compares very favorably with the experimental
value for Nb, F_{ev}=3.5V/Å. Similar results are obtained for Ti.

It has been suggested (9) that the field dependence of the
activation energy for different metals obeys a universal scal-
ing law if one plots $Q(F_0)/Q(F_0=0)$ as a function of $f=F_0/F_{ev}$. In a
simple model, this scaling law is given by

$$Q(F_0)/Q(F_0=0) = \sqrt{1-f} + \tfrac{1}{2}f \, \ell n[(1-\sqrt{1-f})/(1+\sqrt{1-f})] \qquad (4)$$
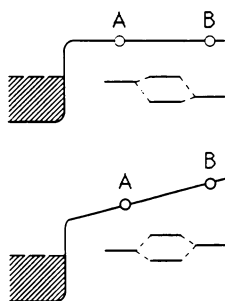
Figure 1. Schematic view of the electronic level structure of an AB molecule adsorbed on a metal without and with an external electric field.
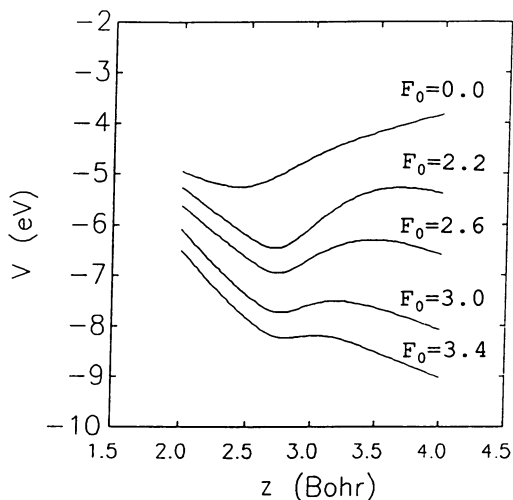
Figure 2. Potential energy for *Nb* on jellium with r_s=3.0 bohr as a function of nuclear distance, z, from the jellium edge. F_0 in $V/\mathring{A}$.

Experimental data on tungsten (8) and theoretical results obtained in the jellium model and by the ASED-MO method (9) have confirmed this conjecture.

In Figure 3 we plot the external field along a line through the center of the adatom. Compared with the field in the absence of the adatom, we note the expulsion of the field from the adatom region which results in an enhancement of the field just outside the adatom. This field enhancement is, however, not as much as classical theory predicts, i.e. a factor 3 at the apex of a hemispherical boss on a flat metal surface. Rather, the partial field penetration into the adatom results in a smearing out of the field as a reflection of the adjustability of the electronic distribution at the surface, reducing the enhancement effect. Note that for the heavier adatom, Nb, one is closer to the classical result. It is also noteworthy that the Friedel oscillations inside the bulk jellium are quite similar with and without the adatom. In closing, we note that the dipole moment and polarisability of the adatom has also been calculated with the results in good agreement with experimental data (15).

Formation of Ru-Subcarbonyls

The interaction of CO with a Ru field emitter surface was experimentally studied using field electron emission (16,17) and field desorption (18). In a recent investigation using pulse field desorption mass spectrometry (PFDMS) (19,20) the ionic species $Ru(CO)_n{}^{2+}$ ($n=1-4$) were observed. It was found that the influence of the electric field was to increase the intensities of the lower index $Ru(CO)_n{}^{2+}$ species, which is clearly shown in Figure 4. For small values of field strength, F, considerable ion intensities of $Ru(CO)_n{}^{2+}$ ($n=2-4$) were found, the $Ru(CO)^{2+}$, however, was missing in the mass spectra. With increasing F the $Ru(CO)_4{}^{2+}$ species intensity decreases and for $F>0.7$ $V/Å$ this species cannot be detected any longer. In contrast to this behaviour increasing amounts of $Ru(CO)^{2+}$ were found. The $Ru(CO)_2{}^{2+}$ ions also become slightly more abundant within the measured range of F values, whereas no change of the amount of $Ru(CO)_3{}^{2+}$ was observed in strong electric fields. In this section we will review theoretical work to explain the formation of Ru-subcarbonyls.

Most of the work on field-induced chemistry has used a semiempirical tight-binding type approach, called the atom-superposition and electron-delocalization molecular orbital, or ASED-MO, method (21) to calculate adsorption energies, equilibrium geometries and charge transfers of molecules adsorbed on metal surfaces in strong electric fields, e.g. (1). On the basis of a charge-partitioning model one writes the total energy E as a sum of a repulsive term, R_r, that accounts for the Coulomb interaction of isolated atoms with each other, and a remainder E_{npf}, that entails the rearrangement within the atoms in the presence of each other. The latter is calculated from a hamiltonian
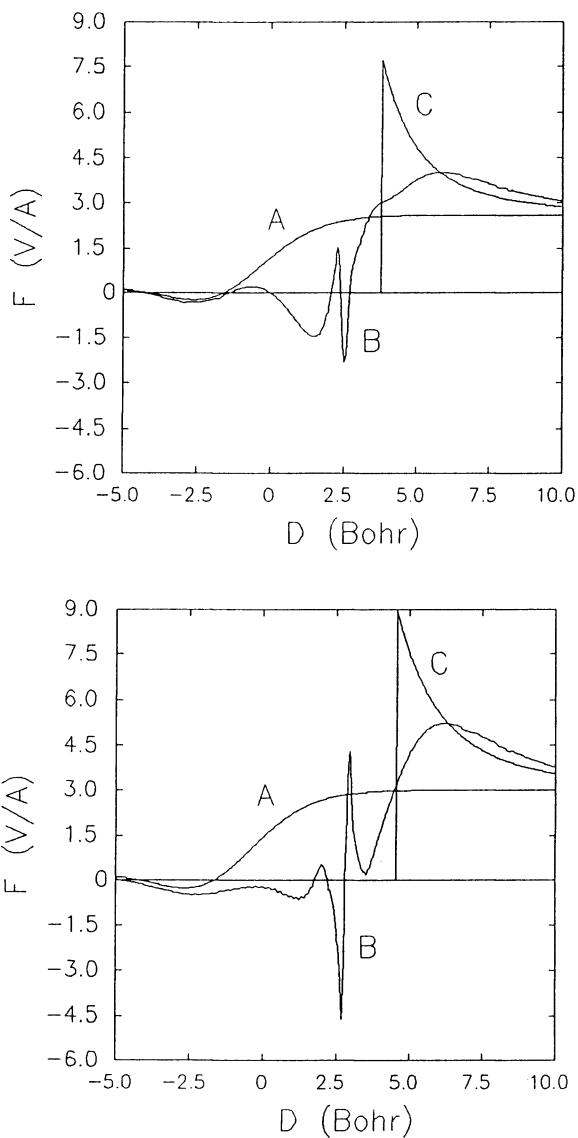
Figure 3. Electrostatic field strength along line through the center of the adatom for *Ti* (top) and *Nb* (bottom) on a metal as in Figure 2. Curves *A* and *B*: without and with the adatom; curve *C*: classical result.

$$H = \sum_{i\alpha} H_{ii}{}^{\alpha\alpha} \; |\phi_i{}^{\alpha}><\phi_i{}^{\alpha}| + \sum_{ij,\alpha\neq\beta} H_{ij}{}^{\alpha\beta} \; |\phi_i{}^{\alpha}><\phi_j{}^{\beta}| \tag{5}$$

where, in the spirit of an extended Hückel scheme, one puts the diagonal elements

$$H_{ii}{}^{\alpha\alpha} = -E_i{}^{\alpha} \tag{6}$$

equal to the negative of the ionization energy of level i on atom α, taken from experiment. The remaining off-diagonal elements are a modification of the extended Hückel formula

$$H_{ij}{}^{\alpha\beta} = \kappa \; (H_{ii}{}^{\alpha\alpha} + H_{jj}{}^{\beta\beta}) S_{ij}{}^{\alpha\beta} \; \exp(-\alpha R_{\alpha\beta}) \tag{7}$$

with

$$S_{ij}{}^{\alpha\beta} = \langle\phi_i{}^{\alpha}|\phi_j{}^{\beta}\rangle \tag{8}$$

being the overlap integral between the i-th atomic orbital on atom α and the j-th orbital on atom β, the latter being a distance $R_{\alpha\beta}$ away. Fitting bond strengths and lengths to first row diatomics, one determines the parameters in (7) to be $\kappa = 1.125$ and $\alpha = 0.13 \; \mathring{A}^{-1}$.

To include electric field effects (9,22) within the framework of the ASED-MO cluster calculations, we note that in the notation of (5) we have to add terms

$$H_{ij}{}^{\alpha\beta}(F) = \int \phi_i{}^{\alpha}(\mathbf{r})^* V_F(\mathbf{r}) \phi_j{}^{\beta}(\mathbf{r}) d\mathbf{r} \tag{9}$$

where the field potential is given by

$$V_F(\mathbf{r}) = e \int_{-\infty}^{\mathbf{r}} \mathbf{F}(\mathbf{r}') \cdot d\mathbf{r}' \tag{10}$$

In these calculations, the electric field is taken from density functional calculations on a flat metal surface (10). Additionally one must, of course, also add the field energy of the nuclei

$$- \sum_{\alpha} Z_{\alpha} V_F(\mathbf{R}_{\alpha}) \tag{11}$$

where Z_{α} is the charge of the α-th nucleus.
  In (10) we write

$$V_F(\mathbf{r}) = V_F(\mathbf{R}_{\alpha}) + V_F(\mathbf{r}) - V_F(\mathbf{R}_{\alpha}) \tag{12}$$

and get

$$H_{ij}{}^{\alpha\beta}(F) = V_F(\mathbf{R}_\alpha)\, S_{ij}{}^{\alpha\beta} + \int \phi_i{}^\alpha(\mathbf{r})^*[V_F(\mathbf{r}) - V_F(\mathbf{R}_\alpha)]\phi_j{}^\beta(\mathbf{r})d\mathbf{r} \qquad (13)$$

which we approximate, for an electric field in the z direction depending on z only, by

$$H_{ij}{}^{\alpha\beta}(F) \simeq$$
$$\tfrac{1}{2}[V_F(\mathbf{R}_\alpha)+V_F(\mathbf{R}_\beta)+\langle\psi_i{}^\alpha|\,(V_F(z)-V_F(z_\alpha))\,|\psi_i{}^\alpha\rangle+\langle\psi_j{}^\beta|\,(V_F(z)-V_F(z_\beta))\,|\psi_j{}^\beta\rangle]S_{ij}{}^{\alpha\beta}$$
$$(14)$$

The diagonal parts of the first two terms in (14) lead to the raising of the energy levels in (6) by the field energy, i.e.,

$$H_{ii}{}^{\alpha\alpha} = (E_i{}^\alpha + V_F(\mathbf{R}_\alpha)) \qquad (15)$$

The off-diagonal parts of the first two term in (14) are obviously proportional to the overlap integrals between atomic orbitals on different atoms and are accounted for by modifying the Hückel-type hopping matrix elements (7) by again raising the energy levels by the field energy. This approximation seems to be the most natural in the context of an extended Hückel model. Note that the second term in (13) for $\alpha\neq\beta$ is expressed in (14) in terms of matrix elements on the same atom. This model basically substantiates the qualitative picture that we developed in the introduction.

Adsorption energies of carbon monoxide adsorbed on a top Ru atom above a cluster of 3 Ru atoms, simulating the (100) surface, have been calculated as a function of the number of adsorbed carbon monoxides n and the field strength F (23). As shown in Figure 5, all $Ru(CO)_n$ (n=1-4) species are stable within the calculated range of F values from 0 to 0.8 $V/\mathring{A}$. With increasing F, the adsorption energy of $Ru(100)Ru(CO)$ increases rapidly. In contrast, the adsorption energy of $Ru(100)Ru(CO)_4$ decreases. One also gets a slight increase of the adsorption energy of $Ru(100)Ru(CO)_2$, whereas the adsorption energy of $Ru(100)Ru(CO)_3$ remains constant within the same range of F values.

The formation of Ru subcarbonyls is envisaged to be a sequential process that starts with a CO molecule attaching itself to a Ru atom at a kink step site. After diffusion into the (100) terrace regions, formation of high index $Ru(CO)_n$ species then occurs by successive addition of CO to the respective species. Looking at the incremental adsorption energy, $E_{ad,nth}$, associated with adding the nth CO to $Ru(CO)_{n-1}$ species to form $Ru(CO)_n$ species, it is found that with increasing field strength, $E_{ad,1st}$ increases and, in contrast, $E_{ad,2nd}$ and $E_{ad,3rd}$ decrease, whereas $E_{ad,4th}$ decreases and, when $F>0.4$ $V/\mathring{A}$, $E_{ad,4th}<0$, that is, the formation of $Ru(CO)_4$ by adding a CO to $Ru(CO)_3$ becomes endothermic.

With increasing field strength, more electronic charge is transferred from the CO to the metal and the net charge on the oxygen atom, Q_0, changes from negative to positive, which leads to a slight decrease of the angles ϕ_{CO} between the C-O bond and the surface normal. The net charges Q_c, Q_0, ϕ_{RuC} and ϕ_{CO} for the optimized geometries of the $Ru(CO)_2$ are shown in Figure 6.
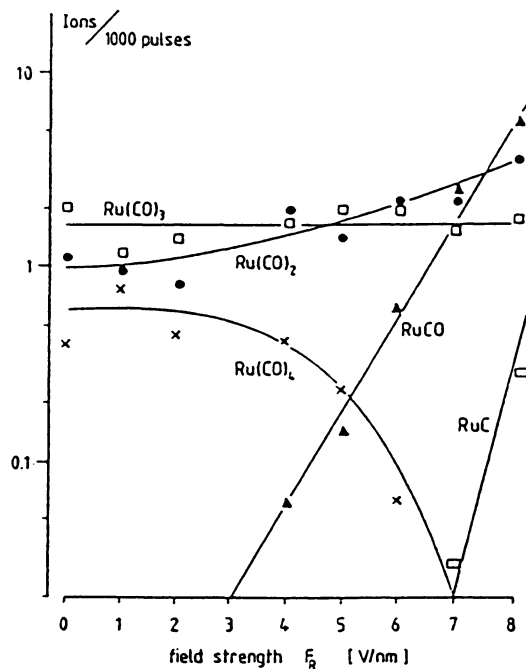
Figure 4. Experimental intensities of $Ru(CO)_n$ as a function of steady field strength. (Reproduced with permission from ref. 23. Copyright 1989 Les Editions de Physique.)
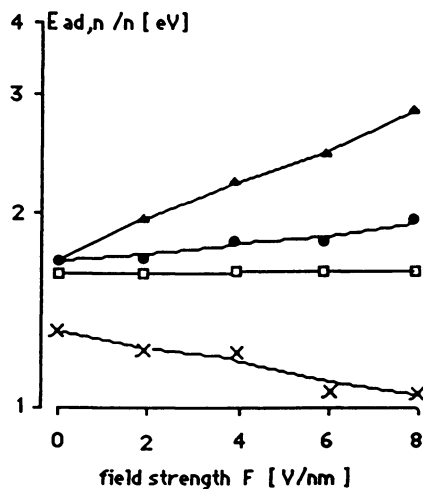
Figure 5. Adsorption energies of $n(CO)$ to form $Ru(CO)_n$ on a Ru cluster. Triangles: RuCO; full dots: $Ru(CO)_2$; open squares: $Ru(CO)_3$; crosses: $Ru(CO)_4$. (Reproduced with permission from ref. 23. Copyright 1989 Les Editions de Physique.)
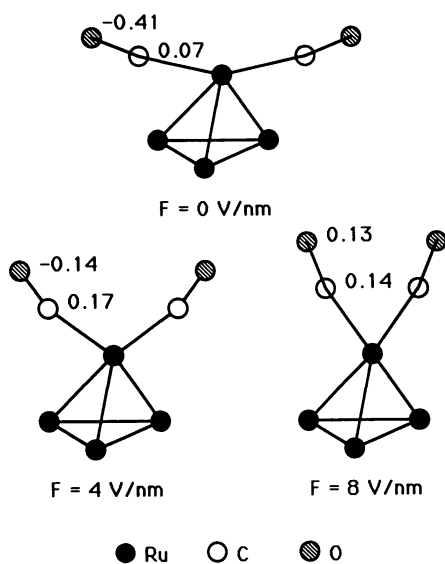
Figure 6. Net charges on the *C* and *O* atoms and adsorption configuration of *Ru*(CO)$_2$. (Reproduced with permission from ref. 23. Copyright 1989 Les Editions de Physique.)

In the absence of an electric field, adsorption of CO on a transition metal is caused predominantly by charge transfer from the CO 5σ orbital to the metal and the mixing of the CO antibonding π^* orbitals with the metal d-s band. Moreover, there is a little mixing of the CO 5σ orbital to the metal d-s band. In high electric fields, raising the energies of the atomic orbitals on the C and O atoms, the effect of the first term in (14) results in increasing the charge transfer from the CO 5σ orbital to the metal and decreasing the mixing of the CO π^* and 5σ orbitals with the metal d-s band. In addition, for the Ru(CO) species, the interaction between the z component of the dipole moments and the external field in the direction z, the effect of the second term of (14), leads to an increase in the transfer of the CO 5σ orbital to the metal and increasing the mixing of the CO 5σ orbital to the metal d-s band. For the higher n Ru(CO)$_n$ species, owing to the repulsion between the carbon monoxides adsorbed on the same top Ru atoms, the Ru-C bonds and the C-O bonds rotate more apart from the surface normal, which, in high electric field, leads to a decrease in the difference of the potential between different atoms in the electric field and the z component of the dipole moment of the Ru-C bonds and the C-O bonds, implying weakening of the interaction between the Ru(CO)$_n$ species and the external electric field. The corresponding data for Ru(CO)$_4$ show a small, monotonic increase of charge transfer from the CO 5σ orbital to the metal and a slight, monotonic decrease of the mixing of both the CO π^* and 5σ orbitals into the metal d-s band.

Summarizing, we can say that due to the repulsion between carbon monoxides adsorbed on the same top Ru atom, they displace as far as possible from each other, leading to a weakening of the interaction between the Ru(CO)$_n$ species and the external electric field with rising index n. In strong electric fields, the net charge on the oxygen atoms changes from negative to positive, so that the Ru-C bonds and, especially, the C-O bonds tend to rotate towards the direction of the electric field, which results in an increase of the repulsion between the carbon monoxides, especially for the higher Ru-subcarbonyls. Consequently, the adsorption energy in the process of adding the nth carbon monoxide decreases with rising n and, when $F > 0.4$ $V/Å$, $E_{ad,4th}$ becomes negative. In conclusion, increasing the field strength is disadvantageous for the formation of the higher Ru-subcarbonyls Ru(CO)$_n$, in good agreement with experiment.

The Reaction $2NO \rightarrow N_2O + O$ on $Pt(111)$

In this section, we will look at the adsorption, dissociation and reaction of NO on a Pt surface in high electric fields. We briefly describe the experimental findings: although NO adsorbed on various planes of platinum does not dissociate at room temperature, applying electric fields in excess of $0.4 V/Å$ causes rapid decomposition. Employing pulsed field desorption mass spectrometry, Kruse et al (24) observed N_2O^+, N_2^+ and, to a lesser extend, O^+ ions from the stepped $Pt(111)$ regions of a field emitter tip as the field is increased, with decreasing amounts of NO^+ being recorded. Beyond $1.2 V/Å$ no NO^+ could be desorbed.

XPS, EELS and IRS experiments have provided evidence that NO adsorbs on $Pt(111)$ *(25)* (and on $Ni(111)$ *(26)* and on $Ru(001)$ *(27)* in bridge sites at low coverage and in on-top sites at higher coverages with about the same binding energies. In particular on $Pt(111)$ the bridge-bonded NO has a dipole moment of 0.42D with the negative O end outward in accordance with multiply-coordinated NO groups in large molecules, whereas the linearly bonded on-top species has a positive dipole moment with the O end positively charged as it happens with terminal NO groups. This flexibility is due to the lone electron in the 2π antibonding level, consisting mainly of the $2p_x$ levels of O and N. This picture has been confirmed by ASED-MO calculations which are also used to study the field effects *(28)*.

As an electric field is applied *(28)*, the levels on the O atom, being further away from the surface, are raised up relatively higher than those on the N atom. This in particular effects the $2p_x$ levels on O and N resulting in a shift of the electronic charge of the 2π level to the O atom. As a result the overlap between the 2π level of NO and the levels of the metal decreases with a subsequent decrease in the electron transfer from the metal to the 2π level stabilizing the adsorbed NO molecule. Also note that the dipole moment of adsorbed NO, i.e. O^-N^+, is opposite to the field direction, thus the total energy increases as the field is increased.

Looking next at the bending mode of adsorbed NO, we note that as the molecular axis of NO bends away from the surface normal, the O atom moves into regions where the electric field energy is less, e.g. in the extreme case where the NO axis is parallel to the surface, N and O would experience the same field. Thus bending away from the surface normal reduces the electric field effect, i.e. the electronic distribution of the 2π level moves closer to the metal leading to an increase in the charge transfer from the metal. With the electron distribution of the 2π level shifting back from the O atom to the N atom as bending takes place away from the surface normal, the additional charge in the 2π level leads eventually to the decomposition of the adsorbed NO molecule. Energies and geometries are depicted in Figure 7 as a function of the reaction coordinate, indicating the dramatic decrease in the activation barrier for dissociation as a function of field strength due to the dipole moment of adsorbed NO being along the vibrational direction. We should point out that the ASED-MO method is not very reliable in its predictions of absolute energies; however, the trends as a function of reaction coordinates and field strength should be trustworthy.

We next look at a situation where, in a field larger than about $0.4V/Å$ a NO molecule is adsorbed next to a N atom, the latter the result of dissociation. As depicted in Figure 8 the bending vibrations of the two species towards each other can result in such close approaches that a strong N-N bond can establish itself. For fields larger than $1.2V/Å$ the reduction of the activation barrier becomes so significant that the NO molecule will snap on top of the adsorbed N atom leading to the formation of adsorbed N_2O. A detailed analysis of the participat-
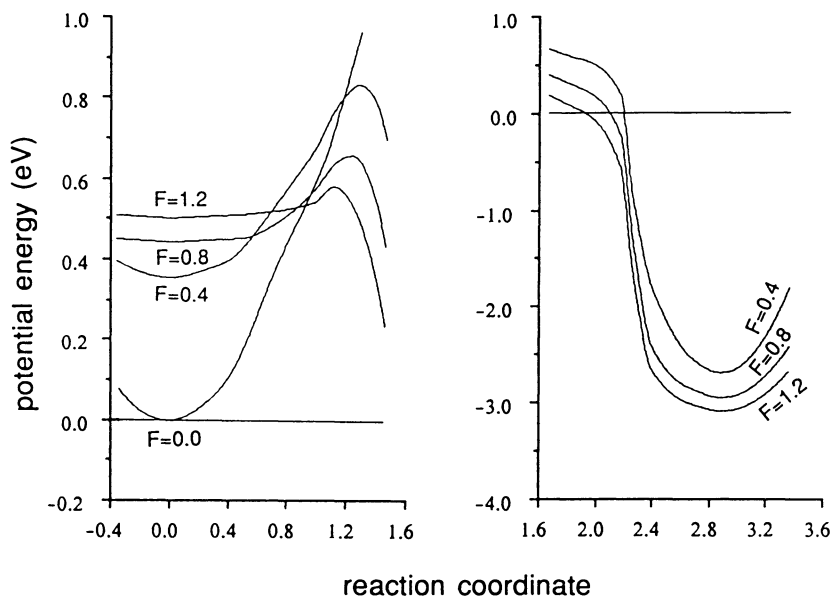
Figure 7. Potential energy curves and adsorption geometries of NO on *Pt*(111) as a function of reaction coordinate. (Reproduced with permission from ref. 28. Copyright 1990 AIP.)
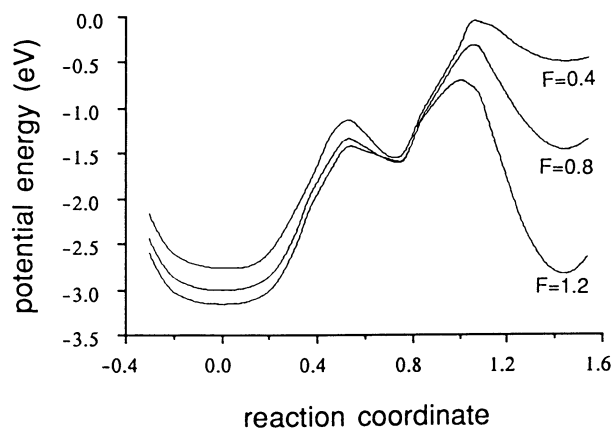
Figure 8. Potential energy curves and adsorption geometries of *NO+N* on *Pt*(111) as a function of reaction coordinate. (Reproduced with permission from ref. 28. Copyright 1990 AIP.)

ing molecular orbitals reveals that the electron transfer between the adsorbed N_2O and the metal mainly involves the 6σ, 7σ abd 2π orbitals of N_2O. The 6σ level is antibonding consisting mainly of $O\ 2p_z$, mixed with $O\ 2s$, and the antibonding level of N_2 originating from the $2s$ levels. In zero field the charge in the 6σ level is mainly on the O atom. Next, the 7σ level is bonding, resulting from the combination of the $O\ 2p_z$ level and the bonding level of N_2, namely 5σ originating from the combination of the $2p_z$ levels of the two N atoms. In zero field the charge is centered on the N atom closest to the metal. Lastly, the 2π level is nonbonding. In our calculation we found that in zero field the N_2O molecule will decompose upon adsorption into an adsorbed N_2 and most likely a free O.

As we increase the electric field, the electronic configuration of adsorbed N_2O changes drastically, because the $O\ 2p_z$ level is raised relative to the the $2s$ levels on the N atoms resulting in the center of gravity of the charge distribution in the 6σ level to shift to the N atom closest to the metal thus strengthening the bond to the metal and increasing the electron charge transferred from the antibonding 6σ level of N_2O to the metal, leading to the stabilization of the adsorbed N_2O. As for the 7σ level, the decreased energy difference between the $O\ 2p_z$ and the $2p_z$ level on the N farthest from the metal and the increased energy difference between the $2p_z$ levels on the two N atoms, results in a shift of the electronic charge to the O atom thus decreasing the overall charge transfer from the 7σ level to the metal. In terms of dipole moments, the situation in low field is metal-$N^-N^+O^-$ whereas in fields in excess of $0.8V/\text{Å}$ we have metal-$N^-N^+O^+$. Thus the chemical structure of adsorbed N_2O is stabilized in fields of this magnitude.

Outlook

Electric fields of the order of volts per angstrom affect the valence electrons on atoms shifting their energies by electron volts with respect to each other. In recent years a microscopic theory has emerged that looks at the new physics and chemistry from a microscopic point of view. We now understand field adsorption as field-induced chemisorption, a mechanism that affects even the lightest rare gases (29). In this field a lot of work still remains to be done to understand local field enhancements and also image formation in the field ion microscope. We also now have a microscopic theory to describe kinetic effects in high electric fields at surfaces such as thermal field desorption and field evaporation (30,31). The electronic structure calculations have been based so far on two vastly different approaches, namely the semi-empirical tigh binding (ASED-MO) method and density functional theory. Where comparisons are possible, an astonishing degree of agreement in the predictions is found. The reason for this lies in the fact that fields of the order of volts per angstrom shift electronic levels in atoms and molecules by several eV relative to each other. Such large shifts can obviously be handled quite reliably by semi-empirical methods.

Chemistry in high electric fields is an even more exciting field. Because fields of the order of $V/Å$ affect the valence electrons of atoms, new molecular species are stabilized in high fields thus opening up new reaction pathways in heterogeneous catalysis. Most work so far has been concentrating on static electric fields; however, many new phenomena are to be expected in alternating fields as well, as the work on photon-induced field desorption suggests.

Acknowledgment

Literature Cited

(1) Kreuzer, H.J., in *Physics and Chemistry at Solid Surfaces VIII*; Vanselow, R., Ed.; Springer-Verlag: Berlin, Germany, 1990; *pp* 133-158.
(2) Bergmann, K.; Eigen, M.; de Maeyer, L. *Ber. Bunsenges. Phys. Chem.* **1963**, *67*, 819.
(3) Inghram, M.G.; Gomer, R. *Z. Naturforsch. Teil A* **1955**, *10*, 864.
(4) Block, J.H. in *Physics and Chemistry at Solid Surfaces IV*; Vanselow, R. and Howe, R., Eds.; Springer-Verlag: Berlin, Germany, 1982.
(5) Tomanek, D.; Kreuzer, H.J.; Block, J.H. *Surface Sci.* **1984**, *157*, L315.
(6) Mueller, E.W. *Phys. Rev.* **1956**, *102*, 618.
(7) Gomer, R., *J. Chem. Phys.* **1959**, *31*, 341; see also Gomer, R., ;*Field Emission and Field Ionization*; Harvard University Press: Cambridge, Mass., 1961.
(8) Kellogg, G.L. *Phys. Rev. B* **1984**, *29*, 4304.
(9) Kreuzer, H.J.; Nath, K. *Surface Sci.* **1987**, *183*, 591.
(10) Gies, P.; Gerhardts, R.R. *Phys. Rev. B* **1985**, *31*, 6843; **1986**, *33*, 982.
(11) Kreuzer, H.J.; Wang, L.C.; Lang, N.D. *Phys. Rev. B* (in press).
(12) Lang, N.D. in *Solid State Physics*; Seitz, F.; Turnbull,D.; Ehrenreich, H., Eds.; Academic Press: New York, 1973, Vol. 28, p.225.
(13) Lang, N.D.; Kohn, W. *Phys. Rev.B* **1970**, *1*, 4555; **1971** *3*, 1215; **1973**, *7*, 3541.
(14) Lang, N.D.; Williams, A.R. *Phys. Rev. B* **1978**, *18*, 616.
(15) Kellogg, G.L.; Tsong, T.T. *Surface Sci.* **1977**, *62*, 343.
(16) Klein, R. *Surface Sci.* **1970**, *20*, 1.
(17) Kraemer, K.; Menzel, D. *B. der Bunsenges., Phys. Chem.* **1974** *78*, 591.
(18) Charkabortty, S.; Grenga, H.E. *J. Appl. Phys.* **1978**, *44*, 500.
(19) Kruse, N. *Surface Sci.* **1986**, *178*, 820.
(20) Kruse, N.; Abend, G.; Block, J.H.; Gillet, E.; Gillet, M. *J. Physique* **1986**, *33*, C7-87.
(21) Anderson, A.B.; Parr, R.G. *J. Chem. Phys.* **1969**, *53*, 3375; Anderson, A.B. *J. Chem. Phys.* **1973**, *60*, 2477; **1974**, *62*, 1187; **1974**, *63*, 4430.
(22) Nath, K.; Kreuzer, H.J.; Anderson, A.B. *Surface Sci.* **1986**, *176*, 261.

(23) Wang, L.C.; Kreuzer, H.J. *J. Physique* **1989**, *50*, C8-53.
(24) Kruse, N.; Abend, G.; Block, J.H. *J. Chem. Phys.* **1988**, *88*, 1307.
(25) Kiskinova, M.; Pirug, G.; Bonzel, H.P. *Surface Sci.* **1984**, *136*, 285.
(26) Breitschafter, M.J.; Umbach, E.; Menzel, D. *Surface Sci.* **1981**, *109*, 493.
(27) Feulner, P.; Kulkarni, S.; Umbach, E.; Menzel, D. *Surface Sci.* **1980**, *99*, 489.
(28) Kreuzer, H.J.; Wang, L.C. *J. Chem. Phys.* **1990**, *93*, 6065.
(29) Ernst, N.; Drachsel, W.; Lin, Y., Block, J.H.; Kreuzer, H.J. *Phys. Rev. Lett.* **1986**, *57*, 2686.
(30) Kreuzer, H.J.; Watanabe, K.; Wang, L.C. *Surface Sci.* **1990**, *232*, 379.
(31) Wang, L.C.; Kreuzer, H.J. *Surface Sci.* **1990**, *237*, 337.

Chapter 19

Surface Reactions on an Atomic Scale
Field Desorption with Field and Photon Pulses

J. H. Block[1], G.-K. Chuah-Jaenicke[2], and N. Kruse[3]

[1]Fritz-Haber-Institut der Max-Planck-Gesellschaft, Faradayweg 4–6, W–1000 Berlin 33, Germany
[2]Department of Chemistry, National University of Singapore, Kentridge, Singapore, Republic of Singapore
[3]Technisch-Chemisches Labor, ETH Zentrum, CH–8092 Zurich, Switzerland

Field Pulse Desorption Mass-Spectrometry is applied to investigate intermediates of surface reactions. The formation of metal-subcarbonyl compounds is studied at rhodium- and ruthenium field emitters. Electrostatic field effects, field-induced reactions and field fragmentation are measured. The decomposition of methanol on rhodium and ruthenium shows two temperature regimes. At lower temperatures chemisorbed CO hinders the catalytic decomposition. Above the CO-desorption temperatures the C-H-bond cleavage of surface methoxy groups is rate determining. With photon-pulses the field-induced polymerization of ethylene is studied. Adsorbed water-layers form cluster ions $(H_2O)_z \cdot H^+$ with $3 < z < 16$. A photon energy of > 7 eV is needed for the formation of these cluster ions.

A special version of the atom probe can be used to study dynamic processes on an atomic scale (1). In the field ion microscope section, a particular area of a tip emitter (=catalyst-)surface is selected. Depending on the tip radius, the tip to screen distance and the probe hole diameter, either single surface atoms or up to several hundred surface sites can be analyzed in the time-of-flight mass spectrometer. With its high detection sensitivity, this technique is able to identifying individual chemisorbed species at characterized crystallographic sites on low- or high-index single crystal surfaces.

To investigate dynamic processes, pulse techniques are applied. From a steady flow of reacting gas ($p \leq 10^{-1}$ Pa), molecules are first chemisorbed, they then form intermediate surface compounds and are finally converted into products. Pulses for field desorption are applied such that all adsorbed material is completely removed and a clean surface is exposed to the reacting gas after each pulse. The desorbed material is mass-analyzed by time-of-flight measurements. In a series of experiments, the reaction time t_R, i. e. the time between two subsequent desorption pulses, can be altered stepwise. From these experiments mean residence times of surface species are determined and relaxation times of surface processes are derived within a time scale of $t_R \approx 10^{-5}$ s to $t_R \approx 10$ s. These experiments can provide detailed information on reaction steps in catalytic surface reactions.

Investigations with Field Pulses

The scheme of field pulses is given in Figure 1. A counter electrode in front of the emitter tip is provided with a time dependent potential, which creates positive fields, F, at the emitter surface. A pulse amplitude of up to 20 kV can produce, depending on tip radius, fields up to ≈ 50 V/nm. The pulse repetition time is ≤ 100 kHz with reaction times of $t_R \geq 10^{-5}$ s. The reaction field, F_R, is an intensive reaction variable.

The Formation of Metal-Carbonyls

Several metals (Me) such as Ni, Co, Pd, Rh and Ru form surface carbonyl compounds $Me(CO)_x^{n+}$ n= 1,2 and x=1...$\leq$ 4 when CO is chemisorbed. Metal subcarbonyl species (x=1, 2, 3) are frequently observed at, or even below, room temperature and some of these species display high surface mobilities (2-7). The mass spectrometric identification of the surface compounds $Me(CO)_x$, as the ionic species $Me(CO)_x^{n+}$, causes problems since the molecular species may undergo structural changes during the field desorption process. We have to consider three different phenomena: (i) the reaction field, F_R, (the field between desorption pulses) may influence the reactivities of neutral molecules (8), (ii) during the field desorption pulse, fragmentation (or association) processes may occur forming ions and, (iii) surface diffusion and surface population of molecular species in the analyzed area of the probe hole may be field dependent and influence the detected ion intensities. Some of these problems will be discussed with experimental results on Rh- and Ru-field emitter surfaces (9), with reference to questions such as: a) how surface species are disturbed by ion fragmentation and, b) how reaction fields influence surface chemistry.

Rhodium

The interaction of CO (P_{CO}=1.3·10^{-4} Pa) at T=298 K with Rh yields CO^+, and $Rh(CO)_x^{n+}$ ions (x=1-3, n=1,2) as products of a consecutive reaction towards neutral Rh-subcarbonyl species. Figure 2 displays the results of a desorption field, F_D, variation. At low fields (18-19.5 V/nm) a sharp increase of $Rh(CO)_x^{n+}$ with x = 2 and x = 3 is registered (with mainly n = 2), reaching a maximum before disappearing completely at higher desorption fields (F≤26 V/nm). At these high fields CO^+, and $RhCO^{2+}$ ions dominate the mass spectrum. The decrease in $Rh(CO)_2^{2+}$ and $Rh(CO)_3^{2+}$ intensities may either be due to the field fragmentation of ionic species or, to a suppression of carbonyl formation by depletion of the CO surface layer as a result of diffusion or desorption processes.

Kellogg (10) has recently investigated the intermediate formation of rhodium-carbonyls. From his measurements he concluded that $Rh(CO)_3$- molecules are formed and that $Rh(CO)_2$ species are true intermediates in this reaction. He also observed the species CO^+, Rh^{++}, $Rh(CO)^{++}$ which he considered as field fragments of the simultaneously detected $Rh(CO)_3^{++}$ parent molecular ion. Arguments for this fragmentation mechanism are, a constant CO/Rh ratio of 3 for all mass scans, and the fact that the activation energies are the same for all ions (except $Rh(CO)_2^{++}$), when the temperature dependence of the ion intensities is studied.

On the other hand, Kruse has suggested, that at $18 \leq F_D \leq 25$ V/nm the desorption pulses are not high enough to remove CO_{ad} from the apex and its surroundings so subcarbonyls can form. With increasing field strength the Rh surface is successively cleaned of all adsorbed species and the number of impinging gas molecules of CO (impingement rate about 10 particles/s into the monitored area) is not sufficient to form higher index carbonyls of rhodium. If, for instance, the reaction time, t_R, is increased at critical field strength values, the $Rh(CO)_2$ and $Rh(CO)_3$ intensities also increase (11). They should, however, be independent of t_R when field fragmentation applies.

For those data in Figure 2 which were taken at high field strength, we can estimate a surface concentration of less than 10^{-3} monolayers. Most of the CO is then bound to step sites and $Rh(CO)_x$ likely originates from kink sites of the (100)- or (111)-oriented Rh specimen. During reaction time variation (11) both CO^+ and $Rh(CO)^{2+}$ increase linearly with t_R, however, the $Rh(CO)_2^{2+}$ and $Rh(CO)_2^{2+}$ species, after their appearance with a delay time, increase considerably steeper. This suggests a consecution face reaction to take place involving neutral species. Furthermore, the dominant amount of CO^+ and $Rh(CO)^{2+}$ ions cannot be formed in a simple fragmentation process.
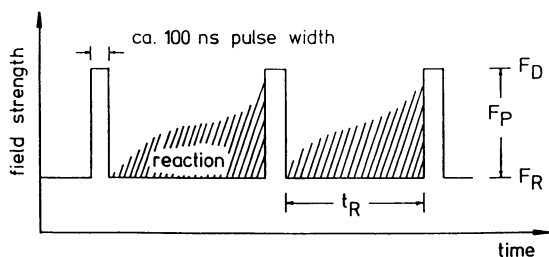
Figure 1. Time scheme of the field pulses leading to desorption at a field strength which is the sum of F_D (steady field, also called "reaction" field) and F_P (pulsed field). (Reproduced with permission from ref. 36. Copyright 1989 Les Editions de Physique.)
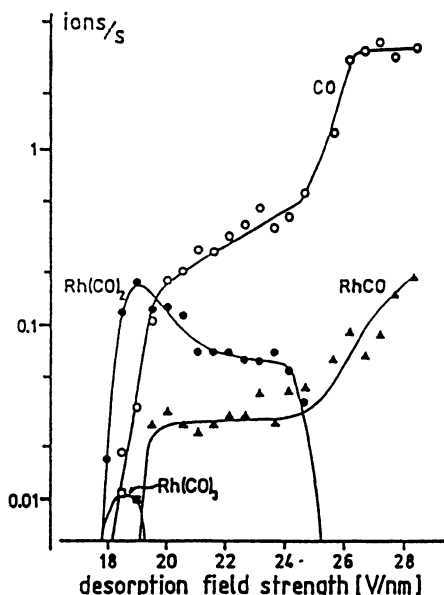
Figure 2. Variation of the desorption field strength (field pulses only, $F_R = 0$) for CO on Rh, $t_R = 1$ ms, $T = 298$ K, $P_{CO} = 1.3 \times 10^{-4}$ Pa. The intensities of evaporating Rh^+ and Rh^{2+} ions are not shown. (Reproduced with permission from ref. 9. Copyright 1988 Les Editions de Physique.)

Ruthenium

For ruthenium more detailed experimental data have been obtained which support the importance of field induced instabilities of certain sub-carbonyl compounds.

The variation of desorption fields for Ru (vicinity of the (0001)-pole) yields similar ionic species as Rh with the exception that $Ru(CO)_x$ shows a maximum of x= 4 (Figure 3). Again the decrease in the intensity of high index carbonyls at higher F_D-values is due to a depletion of the adsorbed layer. This is obvious if we consider the reaction time variation (Figure 4) between $t_R = 10^{-4}$ s and $t_R=1$ s. According to the impingement rate, the CO-signal displays a nearly first order time dependence. At short reaction times RuCO also represents chemisorbed CO, which field desorbs together with a lattice atom. When the CO-surface coverage is sufficient to form higher index subcarbonyls, the RuCO-signal vanishes. The formation of higher index carbonyls is a successive reaction, where $Ru(CO)_2$ and $Ru(CO)_3$ appear simultaneously after $t_R \approx 2$ ms. $Ru(CO)_4$ is found after a further time delay. In addition, it has been found that $Ru(CO)_4$ intensities decreased with increasing reaction fields (F_R) (12). This result has been obtained in a quantitative manner as displayed in Figure 5. The measurements have been performed by varying F_R and adjusting the pulsed field F_P, such that the desorption field strength, F_D, has remained constant. As $F_D = 29$ V/nm, complete desorption of the adsorbed species from the apex occurred. Different trends for the ion intensities of the various species with increasing F_R are found. For small F_R values considerable ion intensities of $Ru(CO)_x^{2+}$ (x=2-4) are measured, however, the $RuCO^{2+}$ is missing from the mass spectrum. With increasing F_R the $Ru(CO)_4^{2+}$ intensity decreases and for $F_R>7$ V/nm this species is no longer detected. In contrast to this behaviour there are increasing amounts of $RuCO^{2+}$, with an onset at a field strength $F_R \approx 3$ V/nm. The $Ru(CO)_2^{2+}$ ions also become slightly more abundant within the measured range of F_R values, whereas no change of the amount of $Ru(CO)_3^{2+}$ is observed. It is noted that the total CO content in $Ru(CO)_x^{2+}$ (x>2) remains nearly constant during F_R variation.

$RuCO^{2+}$ ions are thought to be formed by field desorption of CO_{ad} with simultaneous removal of the underlaying lattice atom. The occurrence of the $Ru(CO)_x^{2+}$ ions can be understood in terms of a consecutive surface reaction involving their neutral molecules as demonstrated in Figure 4.

The intensities of carbidic and oxidic species is small at low values. However, a sharp onset is found at $F_R = 7$ V/nm as evidenced by the appearance of RuC^{2+} species. This finding suggests that dissociation of adsorbed CO takes place and is promoted by the presence of steady (positive) electrical fields.
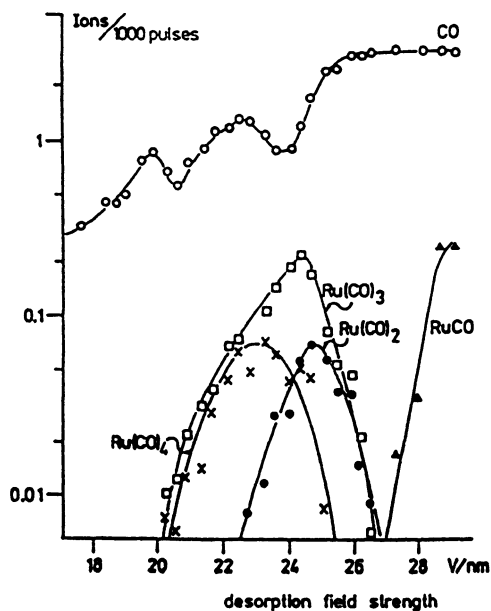
Figure 3. Experimental intensities as a function of the desorption field strength (pulses only, no steady field). Ru(0001)-pole, t_R = 1 ms, T = 328 K, P_{CO} = 1.3 × 10^{-4} Pa. (Reproduced with permission from ref. 35. Copyright 1988 Les Editions de Physique.)
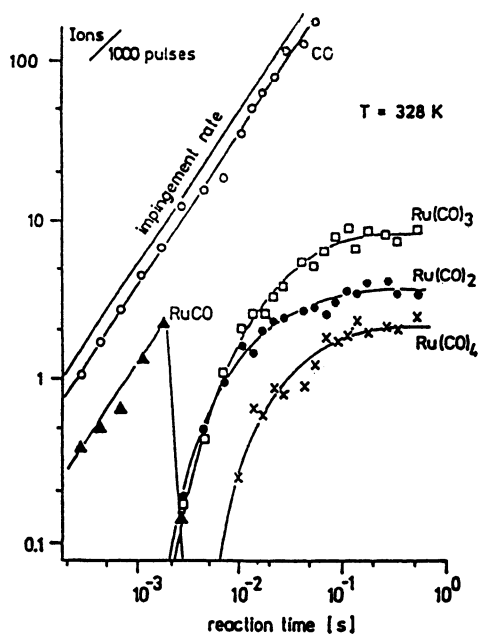
Figure 4. Experimental intensities as a function of the reaction time t_R, monitored at an area of about 140 surface sites. $F_P = 29$ V/nm, $F_R = 0$, $T = 328$ K, $P_{CO} = 1.3 \times 10^{-4}$ Pa. (Reproduced with permission from ref. 35. Copyright 1988 Les Editions de Physique.)

Shincho et al., (13), report the dissociative adsorption of CO at step sites on a macroscopic Ru{1,1,10} surface. Our measurements confirm this result, however, the concentration of carbidic and oxidic species is small here because the high frequency pulses (f=100 Hz, i.e. t_R =10 ms) leads to continuous field desorption.

The CO^+ intensity also decreases slowly during F_R variation (not shown in Figure 5). The reason for this observation is still unknown. However, we have previously stated that under pure pulsed field conditions, i.e. $F_D=F_P$= 29 V/nm, the measured CO^+ ionic rate equals the adsorption rate of CO from the gas phase. For details see ref. (7).

In their microscopic theory of field adsorption based on the atomic-superposition and electron-delocalization (ASED-MO-)method, Wang and Kreuzer (14) investigated the stability of Ru-subcarbonyls in the presence of high electrostatic fields. The result (Figure 6) was that the CO-molecules are displaced as far as possible from each other, due to the repulsion between CO-molecules bound to the same Ru atom, thereby weakening the interaction between the $Ru(CO)_x$ species and the external electric field with rising index x. In strong external electric fields, the net charge on the O atoms changes from negative to positive, so that the Ru-C bonds and, in particular, the C-O bonds tend to rotate towards the direction of the electric field. This results in an increase of the repulsion between the CO's, and the effect is most pronounced for the Ru-subcarbonyls with high index. In summary, increasing the field strength is disadvantageous to the formation of Ru-subcarbonyls with high index, a conclusion which is in good agreement with experiment shown graphically in Figure 6.

A comparison of experimental data for the formation of Rh- and Ru- surface-carbonyl compounds shows the general trend for the successive formation of higher index x, $Me(CO)_x$ compounds. There are, however, differences in the details concerning the measured intensities of intermediates.

The Decomposition of Methanol

Methanol decomposition has been extensively studied on different metal surfaces (15-17). In general, below the desorption temperature of CO on a metal, e.g. Rh (16,17) the catalytic CH_3OH-decomposition is hindered by CO-chemisorption. On the clean metal surface CH_3OH molecules decompose but the decomposition stops at intermediate stages when catalytically active surface sites are occupied by CO. Only above the CO desorption temperature can a catalytic reaction mechanism of the steady CH_3OH-decomposition be studied. For metals with strong CO-chemisorption the field desorption mass spectra display two different regimes below and above the CO-desorption temperature.

Figure 7 shows a typical mass spectrum for ruthenium, obtained at temperatures below 460 K and a CH_3OH gas pressure of 1.3 x 10^{-5} Pa. A high repetition frequency of 4000 Hz was applied during the
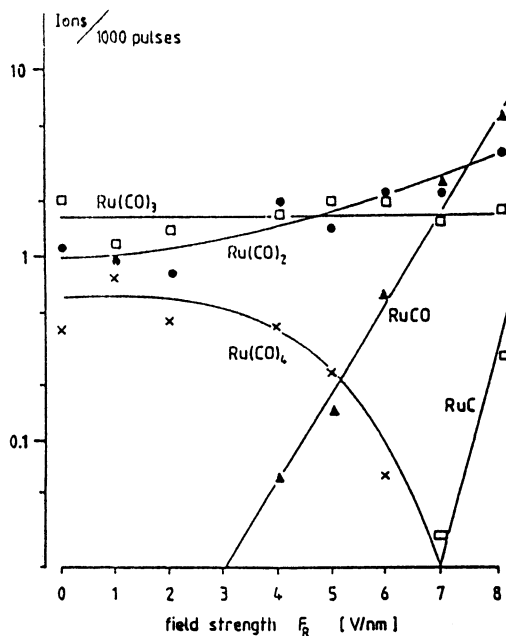
Figure 5. Experimental intensities as a function of the steady field strength, F_R. Parameters: F_D = 29 V/nm, constant during F_R variation, t_R = 10 ms, T = 328 K, P_{CO} = 1.3 × 10^{-4} Pa. (Reproduced with permission from ref. 12. Copyright 1986 Les Editions de Physique.)
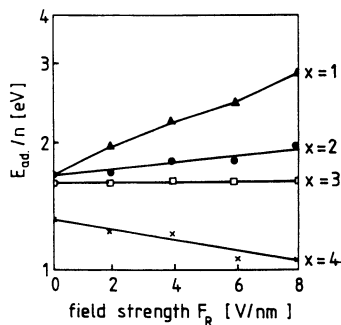
Figure 6. The dependence of adsorption energies E_{ad} for the nth CO on Ru(CO)$_{n-1}$ to form Ru(CO)$_{n'}$ according to ref. 14. (Reproduced with permission from ref. 14. Copyright 1989 Les Editions de Physique.)

measurements in order to detect short-lived intermediates. The desorption field strength, F_D, was relatively low, about 24 V/nm. A steady field of F_R = 9 V/nm, was applied during the measurements in order to stabilize intermediates, as discussed below.

Various ionic species are detected: the parent molecular ion, CH_3OH^+; the protonated molecule, $CH_3OH_2^+$; several dehydrogenated species, CH_xO^+ (x = 0-3); as well as H^+ and H_2^+. In addition, high intensities of CH_3^+ and RuO_y^{n+} (y=1-3, n = 1,2) were obtained.

Above 460 K, $RuCO^{2+}$ ions were seen and for reaction times, t_R, longer than 2 ms, higher subcarbonyls - $Ru(CO)_z^{n+}$ (z=1-3, n = 1,2) - were formed (Figure 8). This indicates that secondary reactions of adsorbed carbon monoxide, which is the final product of methanol decomposition, occur. The formation of subcarbonyls up to $Ru(CO)_4$ has been observed during the reaction of gaseous carbon monoxide with a ruthenium field emitter surface as previously discussed. It has been shown that this reaction involves ruthenium atoms at kink sites of the monitored area. At still higher temperatures (above 580 K), carbon ions, C^{n+} and RuC^{2+} were observed.

In order to gain an insight into the reaction kinetics of methanol decomposition on ruthenium surfaces, a series of measurements at different temperatures were performed under otherwise identical conditions, i. e. a relatively low desorption field strength where the carbon monoxide formed is not quantitatively desorbed with each field pulse.

For temperatures below 460 K, CH_3^+, RuO^{2+}, RuO_2^{2+}, RuO_2^+ and CH_2O^+ are the main species found in the mass spectra (Figure 9a). The count rates are high and almost independent of temperature. Within the temperature range 300-460 K, there are equal ion intensities of CH_3^+ and $\Sigma y\ RuO_y^{n+}$. This indicates that these species are formed from adsorbed methoxy species, $CH_3O_{(ad)}$. The desorption pulse may cleave both the CH_3O-Ru surface bond to form CH_3O^+ and the CH_3-O bond, resulting in CH_3^+. Indeed, both species were detected. CH_3^+ is approximately 100-times more abundant than CH_3O^+ and this ratio is independent of temperature, which proves that they are formed from the same surface species.

Above 460 K, the intensity of CH_3^+ is no longer equal to the sum of oxygen atoms contained in the ruthenium oxides (Figure 9b). The RuO_y^{n+} species rapidly disappears from the mass spectra whilst the CH_3^+ ion rate slowly decreases. Within a narrow temperature range, 460 < T < 520 K, the intensities of CHO^+ and CO^+ increase, reach maxima at about 490 K and decrease thereafter. On the other hand, the CH_2O^+ intensity starts to diminish at T ≥460 K. The increase in the intensities of CO^+ and CHO^+ reflects an enhanced rate of methanol decomposition.

The temperature of the maxima of CHO^+ and CO^+ coincides with the pressure peak of carbon monoxide during temperature programmed desorption of neutral methanol on Ru{001} as measured by Hrbek et al. (18) (Figure 9c). Thus, the increase in reaction rate can be attributed to the thermal desorption of adsorbed carbon monoxide.
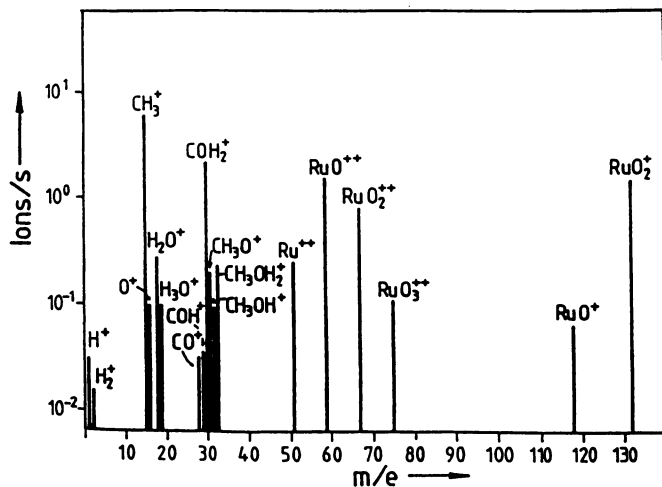
Figure 7. Mass spectrum of CH_3OH during decomposition over Ru at 305 K. The plotted intensities refer to the summed isotope distribution of the ruthenium. F_D = 24 V/nm (F_R = 9 V/nm, F_P = 15 V/nm), t_R = 250 μs, p = 1.3 × 10^{-5} Pa. (Reproduced with permission from *J. de Phys.* Vol. 47 (C7), p 437. Copyright 1986 Les Editions de Physique.)
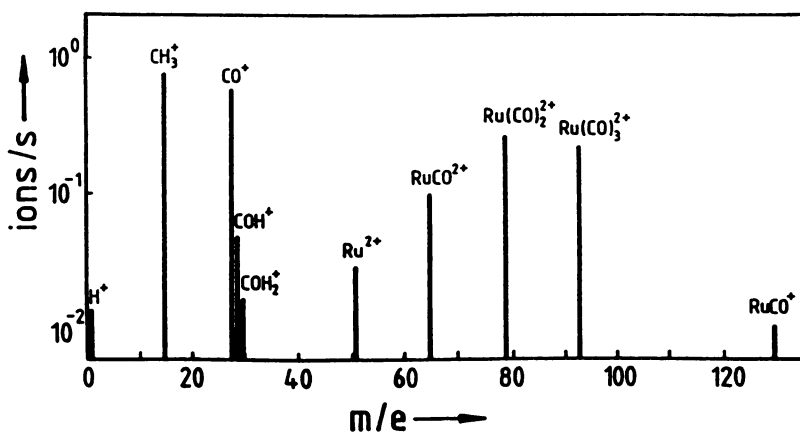
Figure 8. Mass spectrum of CH_3OH during decomposition over Ru at 46 K. t_R = 1000 μs, p = 2.5 × 10^{-5} Pa, F_D = 24 V/nm (F_R = 9 V/nm, F_P = 15 V/nm), the plotted intensities refer to the summed isotope distribution of the ruthenium.
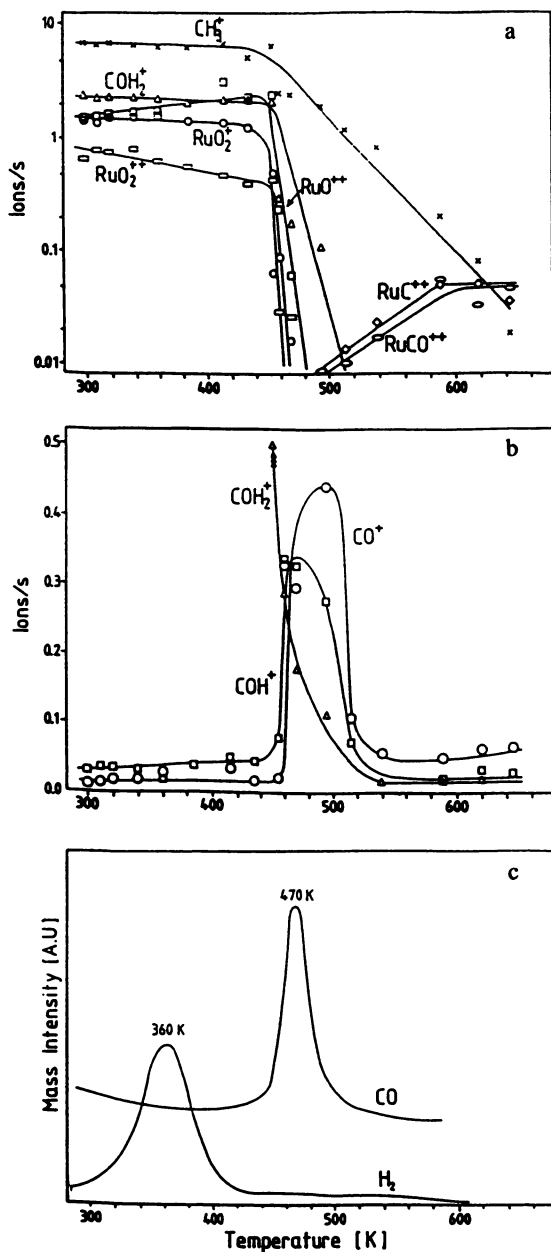
Figure 9. (a, b) Ion intensities of the various species as a function of the surface temperature with same experimental parameters as in Figure 7. CO^+, COH^+, COH_2^+ displayed separately for better visibility: note the linear intensity scale. (c) Thermal desorption spectrum of CO and H_2 after CH_3OH decomposition as measured by Hrbek et al. (18). (Reproduced with permission from J. de Phys. Vol. 47 (C7), p 437. Copyright 1986 Les Editions de Physique.)

At high temperatures, T>520 K, the lifetime, τ, of adsorbed carbon monoxide with respect to thermal desorption becomes shorter than the reaction time of methanol, t_R= 250 μs. The surface coverage and therefore the CO^+ intensity, drops to a small value. At temperatures below 460 K, τ is sufficiently long to allow for CO^+ detection but the desorption field strength is insufficient to yield complete CO^+ desorption. Therefore, the maximum in the CO^+ intensity reflects the optimum balance between field desorption and thermal desorption. Being a thermally activated process, field desorption is greatly enhanced at these high temperatures where carbon monoxide thermally desorbs. The measured CO^+ beyond the peak maximum is proportional to the thermal equilibrium concentration of carbon monoxide molecules at the surface. From this a value of 160 kJ/mol was estimated for the desorption energy of carbon monoxide, in excellent agreement with the results of Pfnür et al. *(19)* where for low carbon monoxide coverages, O<Θ<0.2, the desorption energy of desorption was also found to be 160 kJ/mol.

The results obtained give detailed insight into the mechanism of methanol decomposition on ruthenium. The only intermediates previously identified for this system were CH_3O and small amounts of formaldehyde, H_2CO. The use of PFDMS allows the detection of various intermediates from CH_3O to CHO, the final products, carbon monoxide and hydrogen, as well as secondary reaction products like $Ru(CO)_z^{n+}$(z=1-3, n= 1,2). However, it still remains the task to correlate the detected ions with the original surface species.

It is unlikely, but not impossible, that the CH_2O^+ is formed by field dissociation of adsorbed methoxy as this process would require the simultaneous breaking of a Ru-O- and a C-H- bond. The field-induced formation of CHO^+ or CH_2O^+ from the products, adsorbed hydrogen and carbon monoxide, can also be excluded since above 420 K, the concentration of adsorbed hydrogen is small due to thermal desorption (Figure 9c). A proton transfer reaction of the water formed, or of reacting CH_3OH with adsorbed carbon monoxide cannot explain the temperature dependence of the CHO^+ species. From these arguments it can be concluded that CHO^+ and CH_2O^+ are indeed formed from corresponding intermediate states during methanol decomposition.

For the field desorption of ions formed from a surface methoxy-group, only a qualitative picture can be drawn. The surface methoxy binds through the oxygen atom to the Ru-metal (Figure 10). The decrease in work function suggests a charge transfer to the metal, which leads to a stabilized surface dipole in the positive field. Thus, charge from the lone pair of electrons on O will be transferred to the metal. In this picture, the O-Me bond would be strengthened and accordingly the CH_3-O bond weakened. A preferential field desorption of CH_3^+ would be the consequence (Figure 10 a). The remaining oxygen leads to several oxide species (H_2O^+, RuO_y^+, etc.) as observed in the mass spectra of Figure 7 and Figure 8. Another rather unusual field-induced dissociation of the methoxy group leads to H_3^+ and CO_{chem} (Figure 10 b). This reaction is

observed in a narrow range of reaction fields $6.3 < F_R < 7.8$ V/nm and rather low desorption fields. Under such conditions the decomposition of CH_3O-species is blocked by chemisorbed carbon monoxide, which is not quantitatively removed by low pulses. Therefore CH_3O-concentrations accumulate and probabilities for H_3^+-formation are increased. The trimer-ion of hydrogen is confirmed as HD_2^+-ion from CHD_2OH, which excludes isotope mixing. One aspect for this reaction step may be found in energetic arguments: H_3^+ and CO_{chem} are energetically favoured products.

A quantitative evaluation of the CH_3-O-Me field interaction and field desorption within an atomistic model is still lacking.

Interaction of Methanol and Copper

After supply of methanol to copper field emitters, field evaporation of Cu^+ ions started at very low fields. It is unusual to observe field evaporation for applied voltages of less than 1 kV when voltages in the range of 4-6 kV are normally required. Furthermore, no blunting of the emitters was observed despite removal of some ten thousands of Cu^+ ions. The applied voltage could be increased without any danger of the tip breaking.

On introducing methanol to copper field emitter tips, only Cu^+ ions were observed in the PFD mass spectra. There was no indication of any CH_3OH or CH_3OH-containing species at zero reaction field. Only on applying a steady electric field, F_R, was it possible to detect some $Cu(CH_3OH)_nH^+$ (n=2,3) which appeared as the electric field was further increased and the Cu^+ ion rate was correspondingly lowered. In addition, under high steady electric fields, CH_2O^+, CH_3O^+ (and CH_3^+), CH_3OH^+, as well as protonated methanol, $CH_3OH_2^+$ were detected (Figure 11). Since it is known that the presence of oxygen can increase methanol adsorption and promote formaldehyde production, a 1:1 mixture of oxygen and CH_3OH (total pressure $=2.6 \times 10^{-4}$ Pa) was introduced. Again, only Cu^+-ions were observed under field-free conditions. In the presence of an electric field, however, the same species as in Figure 11 were observed. Heating the tip to 365 K (the temperature at which the methoxy is known to decompose on copper) led to high rates of Cu^+ ions. The copper single crystal planes Cu{111} and {100} are known to be rather inert towards methanol-decomposition and pre-adsorbed oxygen enhances the interaction (20, 21). A methoxy intermediate is then observed for T ≤ 365 K.

At T=298 K the surface population of CH_3OH on the Cu-field emitter may not be sufficient for mass detection. Only when a reaction field, $F_R \approx 0.65 F_D$, is applied are surface compounds, mainly protonated copper methanol ions, Cu^+-ions and molecular ions desorbed. This is a consequence of field adsorption of methanol.
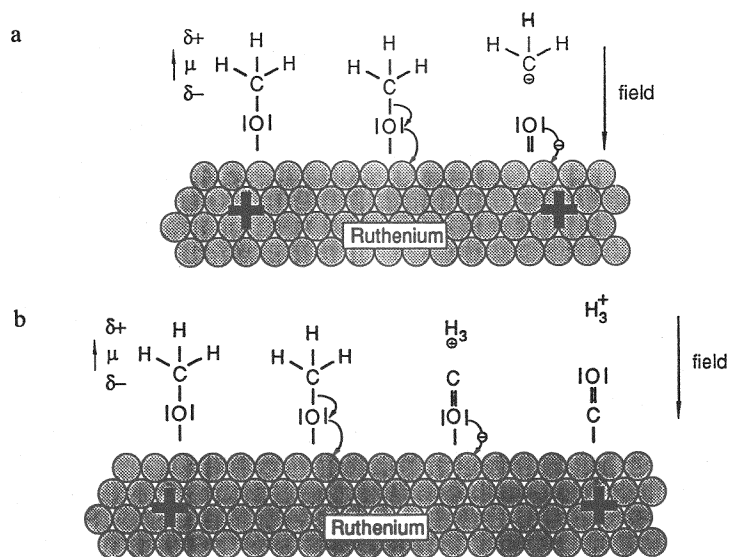
Figure 10. Methanol-decomposition. field dissociation of the methoxy-group: (a) formation of CH_3^+ (b) formation of H_3^+.
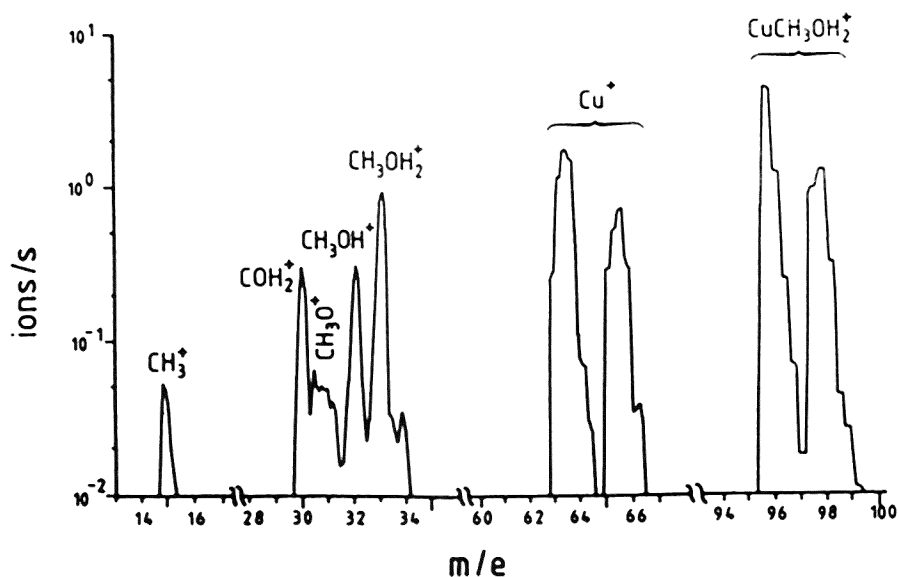
Figure 11. Mass spectrum of CH_3OH adsorbed on copper in the presence of a reaction field. Pulse height = 2.85 kV, reaction field = 1.88 kV, p = 1.3 × 10^{-4} Pa, T = 298 K, f = 1000 Hz.

The high intensity of Cu^+-ions at unusually low electric fields may be connected with a particular ion formation process, which has been observed earlier (22, 23). If an ionic surface compound (Ag_2S or Cu_2O) is present as a dielectric layer on top of the metal emitter, ion transport can be achieved by the field, and field evaporation can be observed at unusually low fields. Such a mechanism would also explain why many layers of Cu can migrate through the oxide layer as Cu^+ ions without blunting the emitter tip.

Investigation of the methanol/copper system by PFDMS is hampered by the following:

(i)   cleaning of the surface by field evaporation is not possible because of field-promoted Cu^+ migration from the bulk. The Cu_2O layer remains and the nature of any adsorbates on this surface is unknown,

(ii)   the desorption of adsorbates normally requires a higher field strength than for Cu^+ removal since this species is already in an ionic state. However, applying a higher field only leads to more Cu^+ which obscures the lower count rates from the adlayer,

(iii)   the adsorption of methanol on a clean surface is very small and the presence of oxygen is required to promote the reaction. This, in turn, will lead to the formation of a Cu_2O film even if it is possible to start with a clean copper surface.

Experiments with Photon-Pulses

Photon-pulse Induced Field Desorption (PIFD) combined with time-of-flight measurements and the atom probe technique provides another powerful method to analyze specific surface areas under high field conditions. Many of the experimental aspects concerning the field ion source, time-of-flight analyzing system and ion detector are similar to PFDMS. Photon-pulses may be much shorter than field pulses, their repetition rates are, however, much lower. Thus, reaction times of $t_R \approx 10^{-2}$ s are available at best.

Photon-pulses have been produced with laser sources (24) or with synchrotron radiation (25).

The molecular excitation and ionization process due to photon-pulses differs in principle from the corresponding processes with field pulses. Thus different ionic species may be obtained from the same system. With field pulses, field desorption is initiated by a sudden charge transfer caused by the field pulse at the surface bond. This leads to heterolytic bond cleavage with simultaneous ion desorption. With photon pulses molecular surface bonds are energetically excited while the field strength is kept constant. These excited states possess an increased ionization probability in the constant applied electrostatic field. The excitation processes may be either:

a)   thermal activation: the observed photons cause a temperature jump of the emitter tip and the thermally activated field desorption process is initiated, or

b)   photons of characteristic energy may excite particular electronic states in the adsorbed molecular layer, or in surface layers of the emitter material.

Experimental methods, such as varying the photon-energy and photon-density, the temperature and field strength, have been applied to prove the validity of one or other of the mechanisms (*26-30*).

Field-induced Polymerization of Ethylene

Ethylene shows a field-induced polymerization reaction which is independent of the emitter for Ag-, Cu- and Ni-surfaces (*30-32*) even at temperatures as low as T=80 K. In the mass spectrum shown in Figure 12 high molecular weight compounds are detected, which are formed in a condensed multilayers of C_2H_4. If the tip voltage and accordingly the reaction field F_R is increased at a constant photon pulse repetition rate of (60 Hz, λ=300 nm) the ions $(C_2H_4)_2^+$ and $C_2H_4^+$ are detected at $U_t \geq 2.0$ kV. These ions are initiated by photons. However, the photon-induced field desorption is only observed if the photon energy exceeds a certain level (wavelength $\lambda \leq 300$ nm, photon energy ≥ 4.2 eV). At lower photon energy (λ=435 nm) photon-induced field desorption is not detected, PIFD-ions display a maximum (at U_t=3 kV) because there are two competing processes. At low reaction fields (U_t <3 kV), the ionization probability increases with increasing field. With further increasing fields (U_t > 3 kV) normal field desorption begins, which has no correlation with photons any more. For the PIFD-process different mechanisms have been discussed (*30*), with the 4d-valence band transition as the most probable (Figure 13).

PIFD can only be obtained if multilayers of C_2H_4 are present (T< 100 K). In multilayers the re-neutralization of electronically excited molecules seems to be suppressed. If the photon-pulse repetition rate is changed (5 Hz to 100 Hz) no changes in ion intensities are observed. This shows that kinetic processes (adsorption, diffusion, ionization) are much faster than the experimental limit of t_R=10^{-2} s.

Using a potential energy diagram, the thermal field desorption at U_t > 3.5 kV can be explained as a thermally activated process, the activation energy being field dependent. Thus, the activation energy decreases and the desorption rate increases with increasing $F_R(U_t)$. At U_t > 4.5 kV steady state intensities are obtained since a mass flow balance is reached between impinging and ionized molecules.
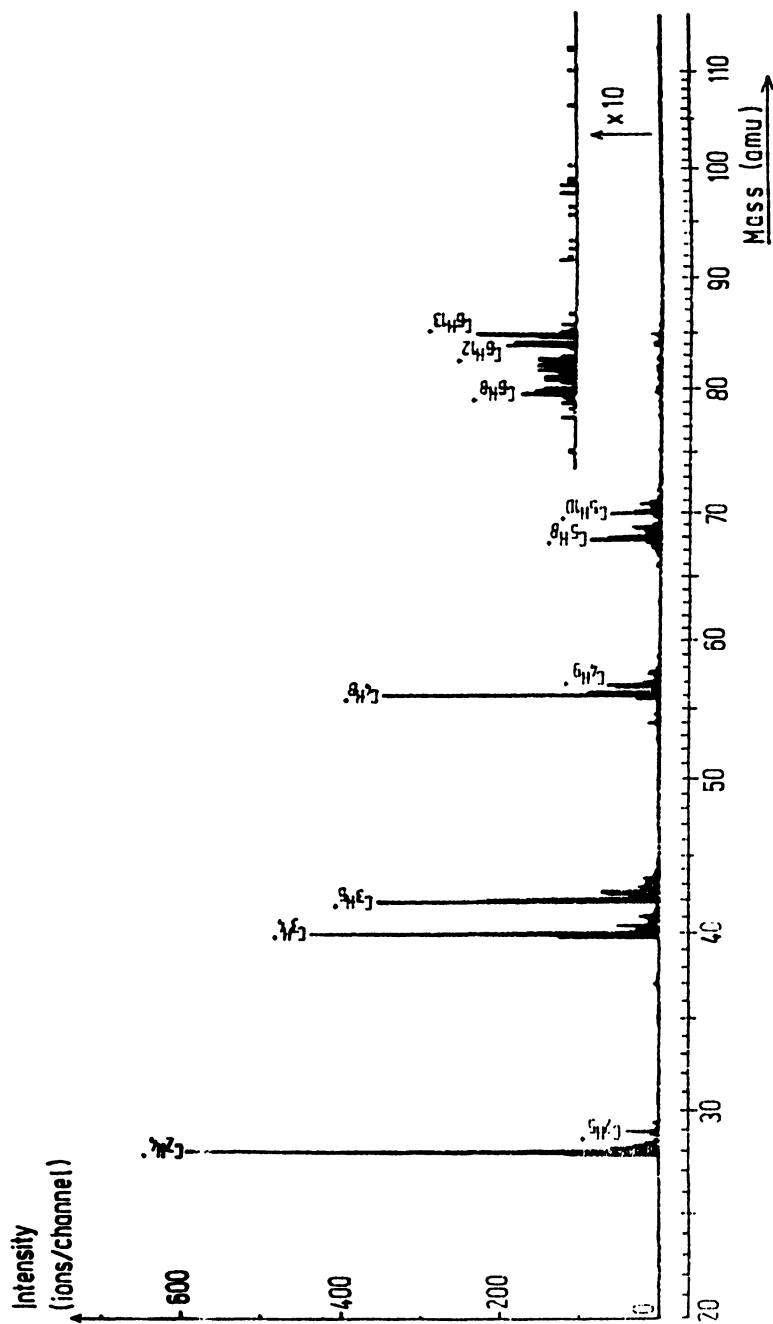
Figure 12. PIFD spectrum of C_2H_4 on Ag emitter, U_{tip} = 3 kV, T = 80 K, laser repetition rate of 45 Hz, photons: λ = 300 nm, energy density 7 × 10^4 J pulse^{-1} cm^{-2} max. power density 0.3 × 10^6 W cm^{-2}. (Reproduced with permission from ref. 30. Copyright 1979 Elsevier.)
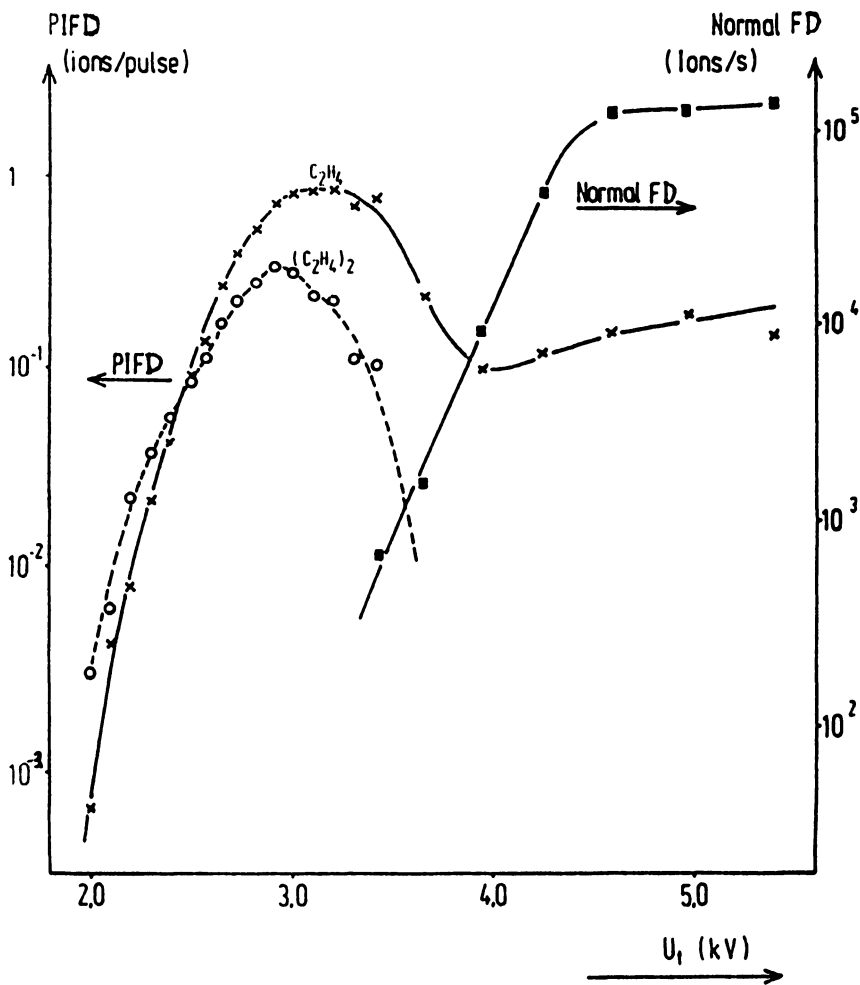
Figure 13. PIFD spectrum of C_2H_4 and $(C_2H_4)_2$ as function of $U_t(\alpha F_R)$, left, thermal field desorption F_D, right T_{tip} = 80 K, λ = 300 nm, photon energy density 7×10^{-4} J pulse^{-1} cm^2 max. power density 0.3×10^6 W cm^{-2}, $p_{C_2H_4}$ ~ 10^{-2} Pa. (Reproduced with permission from ref. 30. Copyright 1979 Elsevier.)
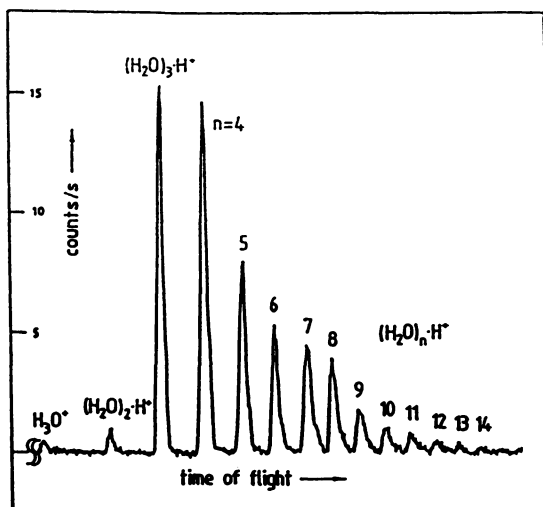
Figure 14. Time-of-flight mass spectrum of water clusters field-desorbed with photon pulses form a synchrotron-source (HASYLAB), photon energy: 24.8 eV, emitter: silver tip, tip temperature: 54 K, water pressure 2×10^{-8} mbar, tip potential ΔU:10 kV. (Reproduced with permission from ref. 36. Copyright 1989 Les Editions de Physique.)

The Photon-induced Field Desorption of Water Clusters

The formation of protonated water ion clusters were detected in the early years of field ion microscopy (33) and studied in detail by Beckey (34). Under steady field conditions multi-layers of water (or even ice-whiskers) are formed which field desorb in the form of $(H_2O)_x \cdot H^+$; x shows a maximum at x=4 (34).

Photon-induced field desorption of these species was first studied by Jaenicke et al. (35) and then extensively investigated by Dirks et al. (36). Synchrotron radiation with photon energies between 6 eV and 30 eV and low photon densities (temperature rise, T< 12m K) was used in these studies. The repetition frequency of light pulses (single bunch) was 1 MHz.

Only above a threshold photon energy of 7.1 eV is the desorption of a variety of water clusters, $(H_2O)_n \cdot H^+$, n=1,m ...., 15, observed. The cluster distribution (Figure 14) shows only very small traces of H_3O^+- and $(H_2O)_2 H^+$-ions, with a maximum at $(H_2O)_3H^+$ and decreasing intensity towards $(H_2O)_{15} \cdot H^+$, which is the largest detectable species. The low intensities of H_3O^+ and $(H_2O)_2H^+$ can be explained by energetic reasons. The threshold energy, which corresponds to the optical absorption maximum of liquid water, is found to be independent of cluster size and substrate material. The abundance of clusters decreases roughly exponentially with increasing cluster size and also depends on the substrate temperature and photon energy. The analysis of the cluster distribution reveals an energy increment of 9 meV per water molecule which seems to be correlated to the frustrated translational energy of water molecules on metals.

The threshold energy of 7.1 eV is connected with a heterolytic cleavage of an O-H-bond. The charge separation in the electrostatic field and a competition between charge and mass transfer lead to a certain cluster size distribution. In conjunction with such a model, the photon threshold energy of 7.1 eV decreases with increasing field strength as expected if a Stark-effect is involved in the photon-stimulated field desorption mechanism.

Acknowledgment

Literature Cited

(1) Block, J. H. In *Methods and Phenoma*; Czanderna, A. W., Ed.; Elsevier Scientific Publ. Corp.: Amsterdam, Netherlands, 1975, Vol. 1; pp 379-446.

(2) Liang, D. B.; Abend, G.; Block, J. H.; Kruse, N. *Surf. Sci.* **1983**, *126* , 392.

(3) Kruse, N; Abend, G.; Drachsel, W.; Block, J. H. In *Proc. 8th International Congress on Catalysis, Berlin(West)*; DECHEMA; Verlag Chemie: Weinheim, F.R.G., 1984, Vol. 3, pp 105-116.

(4) Block, J. H. In *Proc. IXth European Chemistry of Interfaces Conf., Zakopane/ Poland 1986;* Mater. Sci. Forum **1988**, *25/26,* 43.

(5) Block, J. H. ; Kruse, N. *React. Kinet. Catal. Lett.* **1987**, *35 (1-2),* 11.

(6) Kruse, N.; Abend, G.; Block, J. H. *J. Chem. Phys.* **1998**, *91 (1)* , 577.

(7) Kruse, N. *Surf. Sci.* **1986**, *178* , 820.

(8) Block, J. H.; Kreuzer, H. J.; Wang, L. C. In *Proc. 37th Int. Field Emission Symp., Albuquerque/USA 1990;* Surface Sci. **1991**, *246,* 125.

(9) Kruse, N.; Block, J. H.; Abend, G. *J. de Phys.* **1988**, *49(C6),* 249.

(10) Kellogg, G. L. *J. Phys.* **1987**, *48(C6),* 233.

(11) Kruse, N. *J. Val. Sci. Technol.* **1990**, *A8,* 3432.

(12)Kruse, N.; Abend, G.; Block, J. H.; Gillet, E.; Gillet, M. *J. de Phys.* **1986**, *47(C7)* , 87.

(13) Shincho, E.; Egawa, C.; Naito, S.; Tamaru, K. *Surf. Sci.* **1985**, *149,* 1.

(14) Wang, L. C.; Kreuzer, H. J. *J. Phys.* **1989**, *50(C8)* , 53.

(15) Chuah, G.-K.; Kruse, N.; Abend, G.; Block, J.H. *J. de Phys.* **1986**, *47(C7),* 59.

(16) Kruse, N.; Chuah, G.-K.; Abend, G.; Cocke, D.L.; Block, J.H. *Surf. Sci.* **1987**, *189/190* , 832.

(17) Chuah, G.-K.; Kruse, N.; Schmidt, W.A.; Block, J.H.; Abend, G. *J. of Catal.* **1989**, *119* , 342.

(18) Hrbek, J.; de Paola, R.A.; Hoffmann, F.M. *J. Chem. Phys.* **1984**, *81,* 2818.

(19)Pfnür, H.; Feulner, P.; Menzel, D. *J. Chem. Phys.* **1983**, *79,* 4613.

(20) Sexton, B.A.; Hughes, A.E.; Avery, N.R. *Surf. Sci.* **1985**, *155* , 366.

(21) Russell, J.N.; Gates, S.M.; Yates, Jr., J.T. *Surf. Sci.* **1985**, *163* , 516.

(22) Hayek, K.; Block, J.H. *Ber. Bunsenges. Phys. Chem.* **1977**, *81,* 256.

(23) Hayek, K.; Frank, O.; Schmidt, W.A.; Block, J.H. *Ber. Bunsenges. Phys. Chem.* **1977**, *81,* 262.

(24) Drachsel, W.; Nishigaki, S.; Block, J.H. *Int. J. Mass Spectrom. Ion Phys.* **1980**, *32* , 333.

(25) Weigmann, U.; Drachsel, W.; Jaenicke, S.; Block, J. H. *J. de Phys.,* **1984**, *45(C9),* 231.

(26) Block, J.H. In *Chemistry and Physics of Solid Surfaces;* Vanselow, R.; Howe,R., Eds.; Springer Ser. Chem. Phys. 20, Springer-Verlag: Berlin-Heidelberg-New York, 1982; Vol. IV; pp 407-434.

(27) Drachsel, W.; Weigmann, U.; Jaenicke, S.; Block, J. H. In *Proc. 2nd Int. Workshop Desorption Induced by Electronic Transitions, DIET II;* Brenig, W.; Menzel, D., Eds.; Springer Ser. Surf. Sci.: 1984; Vol. 4; pp 245-250.

(28) Jaenicke, S.; Weigmann, U.; Pitts, J. R.; Drachsel, W.; Block, J.H.; Menzel, D. *Chem. Phys.* **1987**, *115;* 381.

(29) Jaenicke, S.; Ciszewski, A.; Dösselmann, J.; Drachsel, W.; Block, J.H.; Menzel, D. In *Desorption Induced by Electronic Transitions, DIET III*, Stulen, R.H.; Knotek, M.L., Eds.; Springer Ser. in Surf. Sci., Springer-Verlag: Berlin-Heidelberg 1988, Vol. 13; pp 236-241.

(30) Nishigaki, S.; Drachsel, W.; Block, J. H. *Surf. Sci.* **1979,** *87,* 389.

(31) Drachsel, W.; Jentsch, Th.; Block, J.H. In *Proc. 28th Int. Field Emission Symp., Portland, Oregon/USA*; Swanson, L.; Bell, A., Eds.; The Oregon Graduate Center, Beaverton, USA, **1981,** pp 123-125.

(32) Jentsch, Th.; Drachsel, W.; Block, J.H. In *Proc. 30th Int. Field Emission Symp., Philadelphia, Pennsylvania/USA 1983*; Graham, W.R.; Melmed, A.J. ; Eds.; The University of Pennsylvania, **1981,** pp 43-45.

(33) Inghram,M.G.; Gomer, R. *Z. Naturforsch.* **1955,** *109,* 863.

(34) Beckey, H.D. In *Principles of Field Ionization and Field Desorption Mass Spectrometry*; Pergamon Press, Oxford/U.K.; **1977,** pp 153.

(35) Jaenicke, S.; Ciszewski, A.; Dösselmann, J.; Drachsel, W.; Block, J.H.; Menzel, D. *J. de Phys.* **1988,** *49(C6)* 185.

(36) Dirks, J.; Drachsel, W.; Block, J. H. *Coll. de Phys.* **1989,** *50(C8),* 153.

Chapter 20

Mass Effects in Photodissociation of Chloromethane

Quenching by Substrate Metal

S. K. Jo[1,2], J. Kiss[1,3], M. E. Castro[1], and J. M. White[1]

[1]Center for Materials Chemistry and Department of Chemistry, University of Texas, Austin, TX 78712-1167

The rates of photolysis of CH_3Cl and CD_3Cl on Pt(111) at 100 K were measured using a conventional mercury arc lamp. The rate is significantly faster for the lighter halide and, quantitatively, the rate ratio is $CH_3Cl:CD_3Cl::1.27:1$. This difference is explained by the Menzel-Gomer-Redhead (MGR) model, which predicts a mass-dependent variation of the competition between substrate quenching and dissociation. The rate ratio corresponds to the successful dissociation of 2.4~8% of the excited molecules.

This study extends our earlier work on CH_3Cl surface photochemistry (1) and investigates how mass influences the probability of photon-driven dissociation of the C-Cl bond, thereby quantifying the extent of substrate quenching. In the earlier work (1), we confirmed and extended the pioneering investigations of Cowin and co-workers (2, 3) who showed that the C-Cl photodissociation can be accounted for by dissociative attachment of substrate-excited photoelectrons. That work employed multilayer CH_3Cl on Ni(111) (2) and monolayer CH_3Cl on H_2O-precovered Ni(111) (3) to elucidate the underlying mechanism. After 248 nm (5 eV) laser pulses, they monitored time-of-flight (TOF) CH_3 signals and post-irradiation temperature-programmed desorption (TPD) areas of CH_3Cl as measures of photolysis for various initial CH_3Cl and H_2O spacer-layer coverages. As a function of layer thickness, they observed an initial increase and subsequent decay of both the photolysis cross section (s) and the CH_3 TOF signal, and concluded the importance of both a metal-to-adsorbate charge-transfer (dissociative electron attachment, DEA) mechanism and a strong perturbation (resonance quenching) of the CH_3Cl photolysis by the substratemetal. The decay at high coverages was ascribed to the attenuation of electrons coming from the substrate through several layers.

[2]Current address: Microelectronics Sciences Laboratories, Columbia University, New York, NY 10027
[3]Visiting scholar from Reaction Kinetics Research Group, Hungarian Academy of Sciences, University of Szeged, P.O. Box 105, Szeged H–6701, Hungary

Recently, we studied the same multilayer *(1a)* and D_2O-precovered monolayer CH_3Cl systems *(1b)*, but on $Pt(111)$ and with a CW Hg-arc light source. We directly measured the yield of ejected photoelectrons during irradiation, and successfully correlated it with the photolysis rate, confirming that DEA alone is sufficient to account for all the dissociation chemistry. Only those photons with energies greater than 4.3 eV were effective, indicating that hot electrons with energies in the range between the Fermi level and ~0.2 eV below the vacuum level are ineffective.

One remaining issue is the extent to which the substrate metal quenches the photolysis *(1b)*. The measured photolysis rate coefficient (**k'** in **d[CH_3Cl]/dt = -k'·[CH_3Cl]**), although approximately constant over small coverage ranges, generally drops with increasing CH_3Cl coverage *(1)*. We have, however, pointed out that the coverage-dependent variation of either the cross section or the (pseudo-) rate coefficient (**k'**) is not an appropriate parameter for an assessment of quenching because, as the coverage increases, the exponentially decaying electron flux contributes to their variation *(1a, 4)*. Taking account of the exponentially decreasing photoelectron yield gave a rate coefficient (**k**), which was *higher* for low coverages than for high coverages *(1a)*. This was attributed to the overwhelming effect, for molecules at the metal surface, of promotion over quenching. The possible origins for the net enhancement of the low-coverage photolysis, as discussed earlier *(1)*, are: **(i)** an additional contribution from direct photon excitation of the "metal-adsorbate complex" consisting of the surface metal layer and first adsorbate layer *(5)*; and, more likely, **(ii)** enhanced tunnelling attachment of "hot" electrons excited to levels between the vacuum level and ~0.2 eV below it.

Our earlier results *(1)*, however, still could not provide a quantitative estimate of the probabilities of quenching and dissociation. This very important branching ratio issue is addressed in this paper. Excitation and quenching both involve coupling between the adsorbed molecule and the metal *(6)*. This coupling takes the form of induced-dipole/induced-dipole coupling, electron-hole pair formation in the metal, and charge transfer mediated processes. Direct dissociation times along repulsive potential energy curves can be as short as 10^{-13} to 10^{-14} s *(7, 8)*; thus, quenching must operate on an equal or faster time scale to inhibit bond cleavage. Depending upon the resonant or non-resonant character of the relaxation process, theory predicts characteristic quenching times relatively close to this, lying between 10^{-15} and 10^{-13} s *(9, 10)*.

From an experimental point of view, one way to gain insight into the branching ratio is to compare photon-driven rates for hydrogenated molecules with those for deuterated ones. Within the MGR model *(11, 12)*, more quenching, and therefore a smaller dissociation cross section, is expected for heavier isotopes. As applied to surface photochemistry, this method was used by Wolf et al. *(13)* with the $H_2O/Pd(111)$ system. Here we report results for CH_3Cl and CD_3Cl on $Pt(111)$. The measured dissociation rate coefficient is a factor of 1.27 larger for CH_3Cl than for CD_3Cl. Depending on the effective reduced mass chosen, we estimate that, of the excited CH_3Cl molecules, between 2.4 and 8 % dissociate. The implications are discussed in relation to previous results *(1-3)*.

Experimental.

A UHV (2.5×10^{-10} torr) chamber equipped with X-ray photoelectron spectroscopy (XPS), ultra-violet photoemission spectroscopy (UPS), quadrupole mass spectroscopy (QMS), and an ion gun were used. The substrate, a $Pt(111)$ single crystal (8 mm diam. and 1 mm thick), could be resistively heated to 1500 K with a linear ramp (0.1 - 50 K/sec) and subsequently cooled to 50 K within 5 min by a

closed-cycle He cryostat. A collimated doser containing an inner pin-hole conductance (2 mm), mounted on a linear motion device, provided reproducible, uniform and localized (to the crystal surface) exposures of the adsorbate molecules. The crystal temperature was kept at 60 K during dosing and irradiation. The full emission ($\leq$5.4 eV) of a high-pressure Hg-arc lamp was used to irradiate the adsorbate-covered surface. At these wavelengths, both CH_3Cl and its deuterated counterpart are transparent. The ultraviolet (UV) light was incident (from outside the chamber through a UV-grade sapphire window) at 45° off the surface normal. Post-irradiation temperature-programmed desorption (TPD) of molecular CH_3Cl and CD_3Cl was used to quantify the photolysis. Line-of-sight TPD was performed with a 6 K/sec ramp rate. CH_3Cl (Linde; 99.9%) and CD_3Cl (MSD-Isotope; 99.9 atom % D) were dosed without further purification. Gas purities were confirmed using the QMS.

Results and Discussion.

Assuming the photolysis is first order with respect to the surface concentration of CH_3Cl (CD_3Cl), the rate equation can be written as $dI/dt = -k' \cdot I$ or $Ln\{I/I_0\} = -k' \cdot t$, where I_0 and I are the parent molecular TPD areas after 0 and t min irradiation, respectively, and k' is the rate coefficient. Thus, the rate coefficient (k') can be obtained from a semilogarithmic plot of the TPD area ratio (post- and pre-irradiation) as a function of irradiation time (t).

Figure 1 summarizes the results in first-order kinetic form. The nicely linear fits demonstrate the adequacy of our first order analysis for the C-Cl dissociation reaction. To obtain each data point, the clean (as judged by XPS) surface was covered with a full chemisorbed layer ($\pm$3%) and irradiated at 60 K for the time indicated. As described earlier, one monolayer coverage was taken as that of maximum TPD area without multilayer desorption. After irradiation, the residual parent TPD signal was measured and integrated to give, after division by the initial TPD area, the ordinate of Fig. 1. Clearly, with increasing irradiation time, the number of remaining parent molecules goes down, reflecting the photodissociation (other work shows the formation of Cl and CH_3 bound to Pt(111) (1)). The slopes of the two curves give the relative cross sections; that for CH_3Cl is 1.27 times larger than that for CD_3Cl. This is the new, key observation reported here.

We now turn to an interpretation and analysis of this isotope effect. We employ a model that is often used to describe electron stimulated desorption (ESD) (15-17). In 1964, Menzel, Gomer (11) and Redhead (12) proposed a model (MGR) for these kinds of processes that is analogous to direct photodissociation of a gas phase diatomic molecule. An adsorbate is assumed to be electronically excited to a repulsive excited state potential energy curve. After excitation, bond elongation (i.e. nuclear motion) occurs and can lead to dissociation. The presence of the metal surface opens up efficient quenching channels that are not available in the gas phase, and these operate to bring the adsorbate back to its ground state. The probability of successful dissociation is then proportional to a product of two parameters: the initial excitation probability, times the probability of survival on the excited state potential energy surface (PES) long enough to gain the required kinetic energy (bond elongation).

There is a mass dependence in these considerations. First, it is assumed that the dissociative, repulsive potential energy surfaces of negative ion states are the same for both isotopes. Then, the mass dependence occurs because of timing; that is, it takes longer to move the heavier (deuterated) methyl group through the distance required for dissociation. Since the electronic couplings are assumed to be the same and since these are responsible for the quenching, we expect the effective average quenching times to be identical and, thus, the average distance travelled by CD_3 to
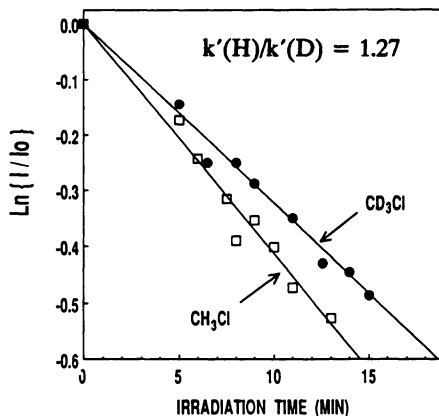
Figure 1: Ln (I/I_0) as a function of irradiation time for 1 ML initial coverage of CH3Cl and CD3Cl on Pt(111). I_0 and I are the CH3Cl (or CD3Cl) TPD areas before and after irradiation, respectively. The ratio of the slopes (rate coefficients, **k'**) is also shown. See the text for details.

be smaller. On the average then, the dissociation probability is higher, as observed, for the H-labelled, compared to the D-labelled, chloride.

This can be described in mathematical form. Following the formulation by Wolf et al. (*13*) and Madey et al. (*15*), the probability, P_d, of C-Cl bond dissociation from the adiabatically excited negative ion (CH3Cl^{-*}) is given by

$$P_d = exp\left(-\int_{x_0}^{x_c} \frac{dx}{\tau v}\right) \qquad (1)$$

where x is the coordinate of the bond being broken, x_0 is the starting value (equilibrium C-Cl distance) and x_c the critical value beyond which dissociation occurs, t is the quenching lifetime, and v is the velocity of the methyl fragment. The mass dependence appears when P_d is rewritten in terms of the potential energy change that occurs between x_0 and x_c.

$$P_d = exp\left(-\sqrt{\frac{\mu}{2}} \int_{x_0}^{x_c} \frac{dx}{\tau\sqrt{V(x_0)-V(x)}}\right) \qquad (2)$$

where m is the reduced mass of the dissociating *quasi* two-particle system, and $V(x_0)$ and $V(x)$ are the potential energies at x_0 and x_c. The Cl ends of CH3Cl and CD3Cl are known to be oriented toward the Pt(111) substrate (*1, 14*). Thus, it is reasonable to take the Pt into account in the reduced mass calculation ($\mu = m_1 \cdot m_2/[m_1 + m_2]$; $m_1 = Pt_n + Cl$ (n→∞) and $m_2 = CH_3$ or CD_3). Since, then, m_1 is so large compared to m_2, the μ value can be approximated as m_2 (15 amu for CH3Cl and 18 amu for CD3Cl). At the other extreme, ignoring the Pt mass will give a reduced mass of 10.5 amu for CH3Cl and 11.9 for CD3Cl. These can be used to establish limiting dissociation probabilities within the MGR formulation.

As noted above, the observable total cross section for dissociation, σ_d, is a product:

$$\sigma_d = P_d \cdot \sigma_{ex} \qquad (3)$$

where σ_{ex} is the excitation cross section. The repulsive negative ion states of CH_3Cl and CD_3Cl are assumed to be the same; thus, the σ_{ex} are the same for the two isotopes. Taking the σ_d ratio for two isotopes, after inserting the mass dependent formula from Eq. (2) and cancelling mass independent terms, leads to:

$$\sigma_d(H)/\sigma_d(D) = P_d(H)^{1-M}, \qquad (4)$$

where $M = \{\mu_D/\mu_H\}^{1/2}$. Using the $\sigma_d(H)/\sigma_d(D)$ of 1.27 obtained from the rate coefficient ratio in Figure 1 and $M = (18/15)^{1/2}$ or 1.095, we obtain $P_d(H) = 0.08$. Using $M = (10.5/11.9)^{1/2}$ gives $P_d(H) = 0.024$. The values for $P_d(D)$ are 0.06 and 0.02, respectively. These calculations, as noted above, set bounds on the dissociation probability within the framework of the MGR model and indicate that dissociation and quenching are competitive.

This range of P_d, 2.4~8%, is comparable to that (14%) obtained by Wolf et al. (13) for H_2O on Pd(111). The results of this work provide an important quantitative assessment of substrate quenching (>90%) and confirm the operation of strong quenching of the excited negative molecular ion by the substrate metal, in agreement with the suggestion of Cowin et al. (2, 3). Nonetheless, the photolysis rate coefficient in the submonolayer is higher than in the multilayer regime, and we have suggested the importance of enhanced tunneling attachment of hot electrons within 0.2 eV of the vacuum level (1-3).

Summary.

Based on measurements of photon-driven (<5.4 eV photons) dissociation for CH_3Cl and CD_3Cl on Pt(111), we have established that the dissociation cross section for CH_3Cl is 1.27 times that for CD_3Cl. Within the framework of the Menzel-Gomer-Redhead model, and assuming limiting values for the reduced mass of the Pt-methyl chloride system, we conclude that between 2.4 and 8% of those molecules excited actually dissociate. The remaining 92 to 98 % are quenched on a timescale that precludes dissociation.

Acknowledgments.

Literature Cited:

[1] (a) Jo, S. K.; White, J.M. *J. Phys. Chem.* **1990,** *94,* 6852; Jo, S. K.; Zhu, X.-Y.; Lennon, D.; White, J. M. *Surf. Sci.* **1991,** *241,* 231.
     (b) Jo, S. K.; White, J. M. *Surf. Sci.* submitted.
[2] Marsh, E. P.; Gilton, T. L.; Meier, W.; Schneider, M. R.; Cowin, J. P. *Phys. Rev. Lett.* **1988,** *61,* 2725.
[3] Marsh, E. P.; Tabares, F. L.; Schneider, M. R.; Gilton, T. L.; Meider, W.; Cowin, J.P. *J. Chem. Phys.* **1990,** *92,* 2004.
[4] Jo, S. K.; White, J. M. *J. Chem. Phys.,* in press.

[5]   White, J. M., in *Chemistry and Physics of Solid Surfaces VIII*; Betz, G.; Varga, P., Editors.; Springer Verlag; Berlin, 1990, p. 48.

[6]   Avouris, Ph.; Walkup, R. E. *Ann. Rev. Phys. Chem.* **1989**, *40*, 173.

[7]   (a) Marsh, E. P.; Tabares, F. L.; Schneider, M. R.; Cowin, J. P. *J. Vac. Sci. Technol.* **1987**, *A5* , 519.
      (b) Marsh, E. P.; Schneider, M. R.; Gilton, T. L.; Tabares, F. L.; Meier, W.; Cowin, J.P. *J. Chem. Phys.* **1990**, *92*, 2004.

[8]   Bersohn, R.; Zewail, A. H. *Ber. Bunsenges. Physik. Chem.* **1988**, *92*, 373.

[9]   Jennison, D. R.; Stechel, E. B.; Burns, A. R. In *Desorption Induced by Electronic Transitions (DIET) III*; Stulen, R. H.; Knotek, M. L., Eds. Springer-Verlag; Berlin, 1988, p. 167.

[10] (a) Stechel, E. B.; Jennison, D. R.; Burns, A. R. *ibid.*, p. 136.
      (b) Burns, A. R.; Stechel, E. B.; Jennison, D. R. *Phys. Rev. Lett.* **1987**, *58,* 250.

[11] Menzel, D.; Gomer, R. *J. Chem. Phys.* **1964**, *41,* 3311.

[12] Redhead, P. A. *Can. J. Phys.* **1964**, *42,* 886.

[13] Wolf, M.; Nettesheim, S.; White, J. M.; Hasselbrink, E.; Ertl, G. *J. Chem. Phys.* **1991**, *94*, 4609.

[14] (a) Henderson, M. A.; Mitchell, G. E.; White, J. M. *Surf. Sci.* **1987**, *184* L325.
      (b) Roop, B.; Lloyd, K. G.; Costello, S. A.; Campion, A.; White, J. M., *J. Chem. Phys.* **1989**, *91*, 5103.

[15] Madey, T. E.; Yates, Jr., J. T.; King, D. A.; Uhlaner, C. J. *J. Chem. Phys.* **1970**, *52*, 5215.

[16] Leung, C.; Vass, M.; Gomer, R. *Appl. Phys.* **1977**, *14, 79.*

[17] Madey, T. E. *Surface Sci.* **1973**, *36*, 281.

Chapter 21

Photoinduced Pathways to Dissociation and Desorption of Dioxygen on Ag(110) and Pt(111)

S. R. Hatch[1] and Alan Campion

Department of Chemistry, University of Texas, Austin, TX 78701

The rates for photodissociation and photodesorption of dioxygen on Ag(110) under UV irradiaton have been measured with TPD and HREELS. The bonding of O_2 to Ag(110) permits polarization measurements at normal incidence. The rates are found to be independent of the azimuthal orientation of the electric field of the light. Dependences on angle of incidence are consistent with the angle dependence of metal absorption predicted by Fresnel's equations. These observations rule out direct intra-adsorbate excitation and suggest a substrate mediated mechanism. Similar photoexcitation thresholds suggest that both channels are activated by a common process. A model is proposed whereby substrate charge transfer induces dissociation. Dissociating adatoms, in competition with molecular oxygen for adsorption sites, force the molecular desorption. This model reproduces the dependences on initial O_2 coverage and extent of irradiation for both channels and allows calculation of the photodissociation cross-section. In contrast, angle and wavelength dependences for O_2 on Pt(111) suggest the participation of direct excitation in the photochemistry.

The study of the photochemistry of surface adsorbates has enjoyed tremendous growth in recent years (*1-4*) Surface mediated photochemistry is interesting, both practically and fundamentally. From a catalytic standpoint, surface photochemistry provides an effective means of synthesizing at low temperatures, molecular fragments which may be important reaction intermediates normally found at higher temperatures. The adsorption of oxygen on Ag(110) and Pt(111) comprise two systems which have been extensively studied, due in part to their importance as models of silver catalyzed selective ethylene epoxidation and platinum catalyzed oxidation of NH_3, CO, and NO. We report here the results of mechanistic investigations of the photoinduced dissociation and desorption of dioxygen on Ag(110) and Pt(111).

---

[1]Current address: Exxon Research and Engineering Company, Annandale, NJ 08801

    With regard to the mechanisms responsible for photochemistry on metallic substrates, two limiting case models have been proposed. In the first, dissociation is induced by direct absorption of a photon by a bond within the adsorbate-substrate complex(*4-6*). In the second, dissociation results from adsorbate capture of a photogenerated hot carrier (substrate electron or hole) (*7-11*). Substrate-mediated photochemistry may involve photoelectrons, excited above the vacuum level, and/or hot electrons, excited above the Fermi energy but below the vacuum level.

    Polarization measurements would allow determination of the photochemical mechanisms in a system with aligned transition dipoles. For direct absorption, the photochemical rate will be determined by Fermi's Golden Rule, with the rate being sensitive to the angle between the relevant transition dipole and the electric vector of the exciting light. For substrate mediated photochemistry, the rate will be relatively insensitive to the orientation of the electric field vector and should follow light absorption by the metal. We have performed such a polarization experiment on Ag(110), a surface on which oxygen molecules adsorb with their internuclear axes aligned along the [110] azimuth (*12-17*). This orientation of the molecules permits alignment of the transition dipoles, a situation highly unlikely on surfaces of threefold or higher symmetry where the existence of domains scrambles the orientations. The results of the polarization measurements for Ag(110) provide strong evidence for substrate mediated oxygen photodissociation and desorption. In contrast, the importance of direct intra-adsorbate excitation is suggested in the oxygen photochemistry we observe on Pt(111).

Experimental

The experiments were performed in a multipurpose ultrahigh vacuum system equipped with temperature programmed desorption (TPD), low energy electron diffraction (LEED), Auger electron spectroscopy (AES), and high resolution electron energy loss spectroscopy (HREELS). The apparatus has been described in detail previously (*18*). Irradiation was provided by a PTI 100 W high pressure Hg arc lamp mounted outside the vacuum chamber. The light was directed through a polarizing prism, followed by a variable diameter aperature, before being refocussed through a fused silica biconvex lens and transmitted to the sample through a quartz window. By measuring the depth of the null in cross polarization, we determined the degree of polarization to be 0.98. For the wavelength, coverage, and time dependence studies, the polarizing prism was replaced by a narrow band interference filter centered at the indicated wavelength with a full width at half maximum of 10 ± 2 nm. The Pt(111) work was done before that on Ag(110) and used a simpler configuration. The unfiltered lamp output was directed through a circulating water quartz cell to reduce infrared heating, before being directed into the vacuum chamber. In all the experiments, photoelectrons should not contribute to the photochemistry since excitation energies are well below the relevant work function.

    The samples were prepared by sputter and anneal cycles until clean and well ordered as judged by AES, HREELS, and LEED. Gases were reproducibly dosed through a calibrated pinhole doser. We report molecular oxygen coverages in ML [O_2] and atomic coverages in ML [O], unless otherwise indicated, where one monolayer [ML] coverage is defined as the density of surface silver atoms (8.4×10^{14} cm^{-2}).

    Detailed error analyses have not been performed. On the basis of selected repeated measurements, we estimate our data reproduciblity to be ± 10 %.

Results

O_2/Ag(110). Figure 1(a) shows the HREELS spectrum following a 350 L dose of O_2 at 100 K. Two losses are seen: v (Ag-O_2) at 241 cm^{-1} and the peroxo v (O-O) at

638 cm^{-1}, in excellent agreement with literature values (*12,17*). Figure 1(b) is the HREELS spectrum of 0.33 ML of atomic oxygen (where the coverage was determined by the appearance of a 3 x 1 LEED pattern) adsorbed on Ag(110). The spectrum is characterized by a single loss, v (Ag-O) at 320 cm^{-1}. Figure 1(c) shows a typical HREEL spectrum of 0.25 ML O_2 at 100 K following 30 seconds of normal incidence UV irradiation with a 315 nm cutoff filter. The frequency of the 638 cm^{-1} loss remains unchanged but the intensity decreases with increasing photon fluence. Another loss is evident at approximately 275 cm^{-1}. This peak shifts to higher frequency with increasing fluence. We attribute this shift to an increase in the 320 cm^{-1} Ag-O stretch associated with photo-induced dissociation of oxygen overlapping with the Ag-O_2 stretch. The peak height of the 638 cm^{-1} loss was taken as the measure of the molecular oxygen coverage and the height of the 320 cm^{-1} peak was used for the atomic oxygen coverage after the molecular contribution at 241 cm^{-1} was spectrally subtracted. Previous work has shown that this loss is proportional to O coverage up to 0.25 ML (*19*). Atomic oxygen coverages were well below 0.25 ML. TPD measurements provided an independent check of the coverages.

Figure 2(a) shows the thermal desorption spectrum following a 350 L dose of O_2 at 100 K. In agreement with previous studies of oxygen on Ag(110),we see two peaks: a low temperature peak at 214 K arising from molecular O_2 desorption and a high temperature peak at 550 K arising from recombinative desorption of atomic oxygen. The low temperature state is reported to have a desorption temperature of 190 K while the high temperature state desorbs at 590 K (*12,20,21*). We attribute the discrepency between our desorption temperatures and those in the literature to poor thermocouple contact and have therefore plotted our TPD spectra versus time. Since we are using TPD only to measure coverage, this procedure is entirely satisfactory. In accord with previous work, we take the observation that both TPD and HREELS peaks saturate at 350 L to indicate a total oxygen coverage (θ) of 0.25 ML O_2.

Figure 2(b) is a thermal desorption spectrum following 30 seconds of normal incidence UV irradiation through a 315 nm cutoff filter. The area of the low temperature peak decreases, as observed on both Pt(111) (*18*) and Pd(111) (*6*), due to photo-induced desorption and dissociation. Interestingly, the area of the high temperature peak does not increase as observed for Pt and Pd. On Pt and Pd the increase in the area of the high temperature peak is attributed to thermal dissociation during the temperature ramp, followed by recombinative desorption at higher temperatures. Apparently, thermal dissociation during TPD is suppressed on Ag compared to Pt and Pd. A possible explanation for this observation is displacement by oxygen adatoms. On Ag(110) oxygen adsorbs in the troughs oriented in the [110] direction whereas it may adsorb in a number of different orientations Pt(111) and Pd(111). Since oxygen molecules and adatoms compete for the same sites on the silver surface and since dissociation and adsorption are confined to one dimension, it is easy to see how site blocking could be more effective than on Pt(111) or Pd(111) where the dissociating adatoms could take other directions in search of adsorption sites. This possibility makes determination of the relative amounts of photodissociated and thermally dissociated oxygen from TPD areas difficult. We have chosen, instead, to measure only the difference in total peak areas for both desorption states before and after photolysis to determine the number of photodesorbed molecules and desorption rates.

Angle Dependences. The alignment of the oxygen molecules on Ag(110) permits polarization measurements at normal incidence by rotation of the incident plane of polarization. For a direct absorption mechanism, a transition moment aligned along the surface normal would result in no photochemistry. A transition moment lying in
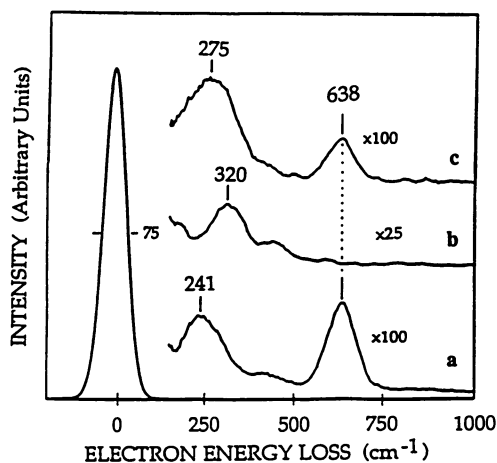
Figure 1. On Ag(110), HREELS spectra of (a) 0.25 mL [O₂] at 100 K; (b) 0.33 mL [O] calibrated using LEED; (c) 0.25 mL [O₂] following 30-s irradiation through a 315-nm cutoff filter at normal incidence to the 0.25 mL [O₂] saturated surface. (Reproduced from ref. 11. Copyright 1991 American Chemical Society.)
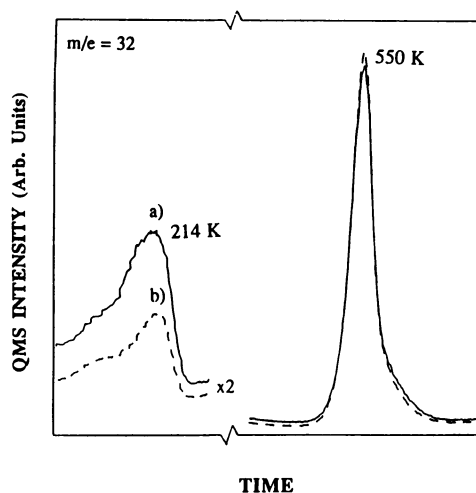
Figure 2. The TPD spectra (a) of 0.25 mL [O₂] dosed at 100 K on Ag(110); (b) following 30-s irradiation through a 315-nm cutoff filter. (Reproduced from ref. 11. Copyright 1991 American Chemical Society.)

the plane of the surface, on the other hand, would dictate that the photochemical rate should follow a $\cos^2 \phi$ dependence where ϕ is the angle between the transition moment and the electric vector. If the photochemistry is substrate-mediated then no ϕ dependence is expected. Figure 3 shows the average rates (30 sec.) derived for photoinduced desorption and dissociation as a function of the azimuthal angle ϕ, for polarized light at normal incidence with $\lambda > 315$ nm. The relevant angles are shown in Figure 12. For this experiment, the Ag(110) crystal was oriented using LEED so that the angle between the O-O bond axis and the incident electric vector could be accurately measured($\pm 2°$). The power density was 0.09 ± 0.01 W cm^{-2}. Since, at normal incidence the perpendicular component of the electric field is zero and since significant photochemistry is observed for both channels we conclude that electric field strength along the surface normal is not required. Neither the average photodissociation rate, derived from the atomic HREELS peak intensity, nor the photodesorption rate, derived from HREELS and TPD, show any dependence on the azimuthal angle of the incident electric vector, ruling out a direct intra-adsorbate excitation mechanism. These results are consistent with a substrate excitation mechanism.

To ensure that there was no azimuthal anisotropy in the surface fields we measured the azimuthal dependence of the Ag(110) reflectance for s-polarized light incident at 30° off-normal and found less than a 5% deviation for all angles at wavelengths of 289, 313, and 365 nm. That the reflectance is independent of azimuthal orientation of the surface indicates that the metal absorption and tangential electric field strengths are azimuthally invariant.

Average rates (1 min.) of photo-induced dissociation and desorption of O$_2$ are given in Figure 4 as a function of the angle of incidence (θ) of p-polarized light. Wavelengths shorter than 315 nm were eliminated during irradiation with a cutoff filter. The photodissociation and photodesorption rates are normalized to the corresponding rate for normal incidence photolysis and are compared with the Ag metal absorbance calculated from Fresnel's equations and the optical constants of Ag, indicated by the solid line (and the right hand ordinate). The rates in Figure 4 are in reasonable agreement with the metal absorbance curve. Thus, both the azimuthal angle dependence and the angle of incidence dependence are consistent with substrate excitation.

Wavelength Dependence. Figure 5 shows the wavelength dependences of the photoyields for both reaction channels deduced from HREELS intensity measurements. Unpolarized irradiation (bandpass filters) at normal incidence was used. A constant photon fluence of 1.25×10^{18} photons/cm^2 was maintained by changing the irradiation time to compensate for variations in throughput and wavelength of the bandpass filters. Figure 5 makes the important point that the cross sections for *both* photodesorption and photodissociation have similar wavelength dependences, extending to approximately 440 nm before dropping below our detection limits. The photolysis yields for both channels increase by a factor of 4 for decreasing wavelengths between 400 and 300 nm. For comparison, the silver absorbance increases by a factor of 7 with excitation energy from 400 nm to 320 nm (22). Also evident from Figure 5 and as noted in the inset, the ratio of desorption to dissociation remains constant at approximately 2 from 250 to 360 nm. The similarities in the optical responses suggest that a common mechanism describes both processes. These results contrast with the wavelength dependences of oxygen photochemisry on Pt(111) and Pd(111). For Pt(111), the threshold for oxygen dissociation is observed to be approximately 315 nm while that for desorption is approximately 460 nm. (Figure 11).
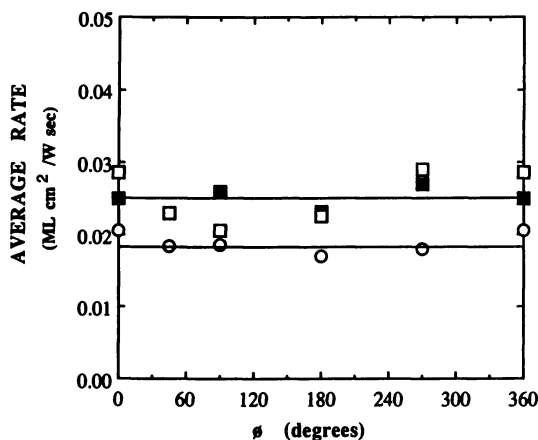
Figure 3. For O_2 on Ag(110), average rates (30 s irradiation of 0.25 mL $[O_2]$) for photoinduced desorption by HREELS (open squares) and TPD (solid squares); and dissociation, by HREELS (open circles) as a function of azimuthal angle (ϕ). $0°$ is parallel to the O_2 bond axis. (Reproduced from ref. 11. Copyright 1991 American Chemical Society.)
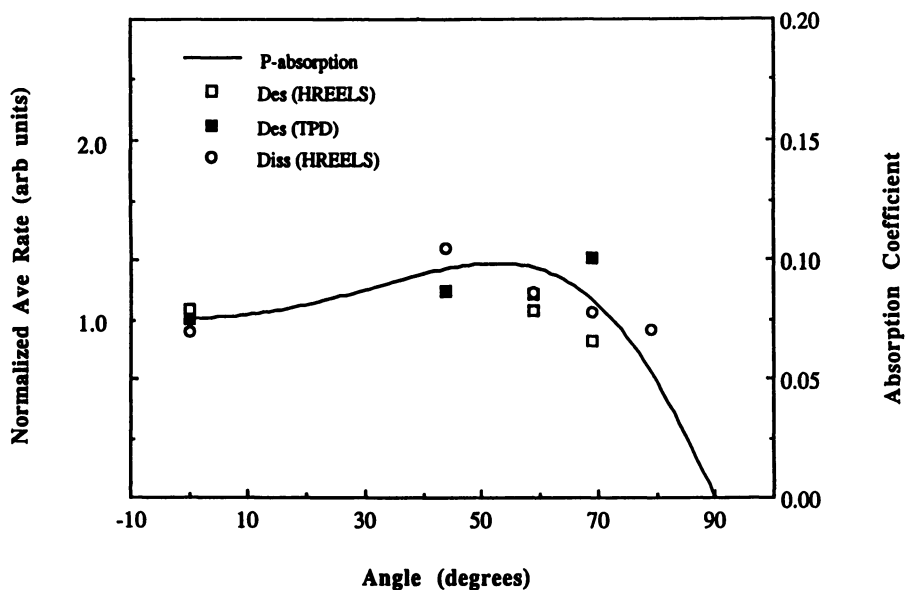
Figure 4. For O_2-saturated Ag(110), average rates for photoinduced desorption by HREELS (open squares) and TPD (solid squares); and dissociation (open circles) as a function of angle of incidence (θ) for p-polarized light. The solid curve is the calculated p-polarized metal absorption angle dependence. (Reproduced from ref. 11. Copyright 1991 American Chemical Society.)
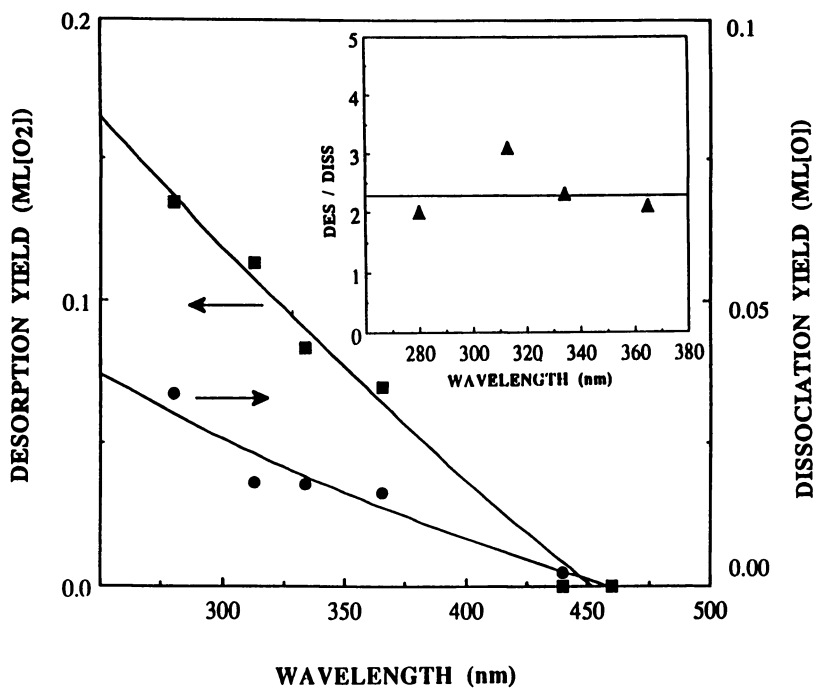
Figure 5. The wavelength dependences of the photoinduced desorption (squares) and dissociation (circles) yields of 0.25 mL [O_2] determined from HREELS. The inset shows the ratio of photodesorption to photodissociation yields. The lines are guides to the eye. (Reproduced from ref. 11. Copyright 1991 American Chemical Society.)

On Pd(111), photodissociation and photodesorption long wavelength cross sections are reported at 334 and 437 nm, respectively (6).

Also consistent with there being no direct excitation, we find that the threshold for photodissociation is significantly red-shifted (1.32 eV) from that for gas phase hydrogen peroxide. The hydrogen peroxide O-O bond dissociates upon photoexcitation below 300 nm via excitation from the non-bonding O electrons into a repulsive σ* orbital, antibonding with respect to the O-O bond (23).

Time and Coverage Dependence. The dependences of the photodissociation yield and adsorbed dioxygen coverage on irradiation time are shown in Figure 6. The O_2-saturated surface was irradiated at normal incidence with unpolarized light through a 313 nm bandpass filter. Also shown in Figure 6 are the results, represented by the solid lines, of a numerical simulation based upon a reaction mechanism described below.

Figure 7 shows how the yield depends on initial O_2 coverage under the same conditions as in Figure 6. Unpolarized light was directed through a 313 nm bandpass filter to the crystal at normal incidence for 1 min. giving a constant fluence of 0.91 x 10^{18} photons cm^{-2} for each coverage. Oxygen coverages were determined from the HREELS loss intensities. The solid line shown in Figure 7 is the initial coverage dependence of the photoyields extracted from a numerical simulation of the proposed reaction model (see below).

O_2/Pt (111). Figure 8(a) shows TPD spectra for 0.45 ML of O_2 adsorbed on Pt(111) before and after photolysis. As in previous reports, two desorption peaks are observed: a sharp peak at 150 K and a broad peak between 600 and 1000 K (24-26). Isotope mixing, hydrogen titration, and HREELS results have shown that dissociation occurs significantly only above 150 K where molecular desorption is also rapid. In previous work with oxygen on Pt(111) we have shown that an increase in the high temperature peak area correlates with an increase in surface atomic oxygen coverage (18). This is shown in Figure 8(c) where, after full-arc irradiation of oxygen on a Pt(111) crystal at 97 K with unpolarized light incident at 57° off-normal and having a power density of 0.07 ± 0.01 W/cm^2, the area of the high temperature peak increases. Also shown, Figure 8(c), is a decrease in the low temperature peak area and a shift of this peak to lower temperature following irradiation. Both effects increase with increasing fluence. These observations have been attributed to depletion of the molecular species from photoinduced dissociation and desorption of molecular oxygen and rearrangement of the molecular species to another surface site, respectively. Figure 8(b) shows that resistively heating the crystal with the same time/temperature profile as during irradiation results in some thermal dioxygen desorption. Thermal desorption varied between 5% and 15% with irradiation conditions, although the crystal temperature increase was typically less than 2 K. This effect was not observed on Ag(110), because the desorption temperature was higher, nor was it observed during polarized experiments because the intensity of the radiation was lower.

Both the photodesorption and photodissociation rates reported here for the O_2/Pt(111) system are derived from TPD. To do so requires a knowledge of the relative contributions from photoinduced and thermally induced dissociation in the high temperature peak. As was noted for Ag(110), one can envision photodissociated O adatoms sterically hindering dioxygen from thermally dissociating during TPD. Thus, the increase in the high temperature peak area would not be a true indication of the contribution of photoinduced dissociation. To calibrate the increase in area of the high temperature peak, we thermally dissociated a known coverage of atomic oxygen on the surface. To this, we co-dosed a known quantity of molecular oxygen following which a TPD was performed. This procedure was repeated, varying the initial coverages of atomic oxygen and codosed dioxygen in the ranges we expected to see following
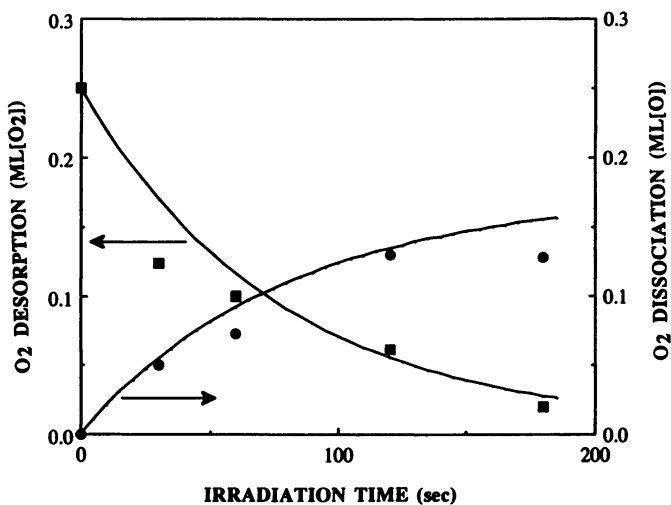
Figure 6. For O_2-saturated Ag(110), the dependence of the O_2 (squares) and O (circles) coverages on irradiation time. Unpolarized light was passed through a 313-nm bandpass filter and impinged at normal incidence. The lines are fits based on the mechanism described in the text. (Reproduced from ref. 11. Copyright 1991 American Chemical Society.)
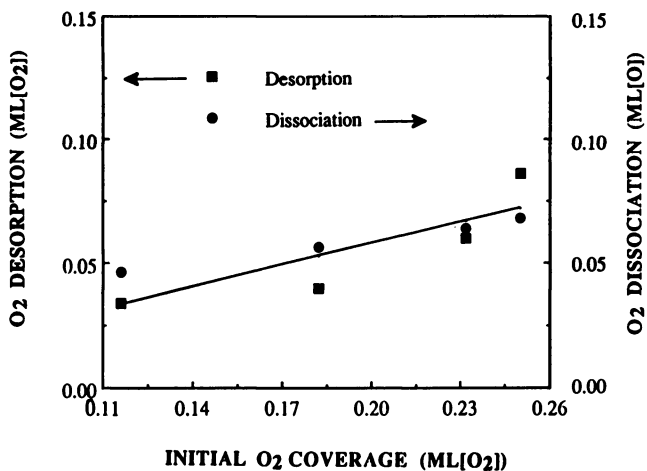
Figure 7. The dependence of the photodissociation (circles) and photodesorption (squares) yield as a function of initial coverage. The solid line is the fit based on the mechanism described in the text. (Reproduced from ref. 11. Copyright 1991 American Chemical Society.)
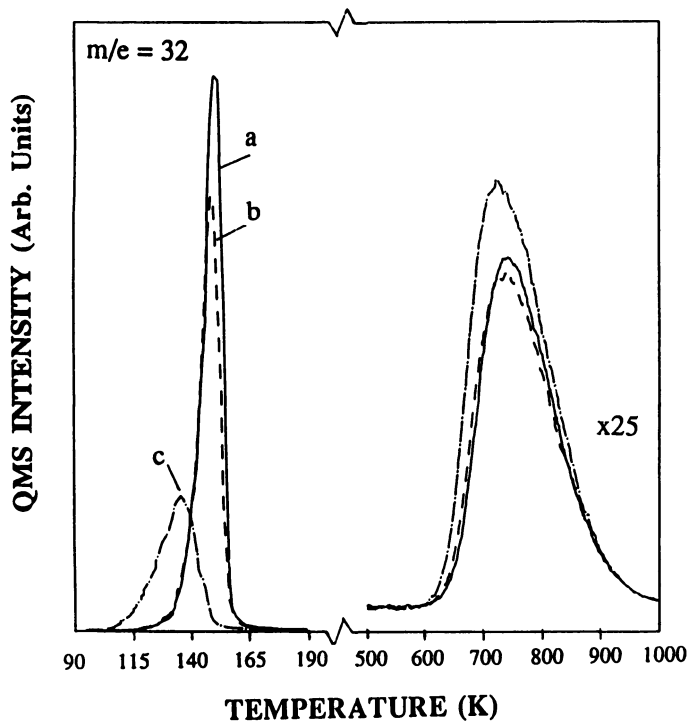
Figure 8. On Pt(111), the TPD spectra of (a) 0.45 mL [O_2] adsorbed at 95 K, (b) following resistive annealing at 97 K for 9 min, (c) following 6-min irradiation with no UV filtering. (Reproduced from ref. 11. Copyright 1991 American Chemical Society.)

photolysis. By varying the coverages of atomic and molecular oxygen, we correlate the sensitivity of thermal dissociation to the coverage of predissociated oxygen and obtain a sensitivity factor that gives the ratio of the measured to actual coverage of pre-TPD atomic oxygen. Typical values for this factor were between 0.2 and 0.3. The TPD determined rates we report are derived from the corrected coverages.

HREELS, used to monitor surface species before and after photolysis, showed increases and decreases following photolysis in the 480 and 860 cm^{-1} losses, respectively. Figure 9 contains typical spectra for: (a) 0.45 ML O_2; (b) 0.25 ML O; (c) 0.45 ML O_2 following 6 min of full arc irradiation (0.05 ± 0.01 W/cm^2). These spectra have been been previously examined in detail and will not be further discussed except to note that the increasing intensity of the 480 cm^{-1} peak corresponds to an increase in atomic oxygen coverage while the diminution of the 860 cm^{-1} peak is indicative of dioxygen depletion (*18*).

Unpolarized Angle-of-Incidence Dependence. Figure 10 shows, for Pt (111), the dependence of the average rates of photodesorption and photodissociation on angle of incidence for unpolarized light. The full-arc output, measured in a separate experiment outside the chamber, was 0.07 ± 0.01 W/cm^2. Shown in Figure 10 are the average of the rates following irradiation times of 2 and 5 minutes. For this measurement, irradiation time, not fluence, was constant. Unlike Ag(110), the dependences of the photoinduced desorption and dissociation rates on angle of incidence are strikingly different. Whereas photodesorption is observed to increase with angle, the photodissociation rate decreases. That the photodesorption rate does not appear to go to zero at 90° is probably a consequence of a nonuniform transverse intensity profile of the lamp. These data clearly demonstrate, however, that the two processes have different physical origins and suggest that at least one of the channels involves direct excitation of the adsorbate-substrate complex.

Also shown in Figure 10 are results obtained by measuring the initial O_2 pressure rise upon irradiation. These results are obtained by measuring the background pressure, insensitive to crystal angle, of m/e = 32 in the vacuum chamber. Mass spectrometry showed that O_2 was the only species desorbing from the surface during irradiation. We observed and subtracted significant backgrounds arising from excitation of oxygen adsorbed on a molybdenum heat sink near the crystal. The averages of 3 measurements are shown and are in reasonable agreement with the TPD and HREELS derived rates. The pressure rise determined rates are normalized to the value at 0° angle of incidence .

Wavelength Dependence. Figure 11 shows the cut-off wavelength dependence for photodissociation and photodesorption. The rates are averaged over a 6 min. photolysis interval. The initial coverage at each wavelength was 0.45 ML and the angle of incidence was 57° off normal. At the highest energies, the desorption rate is approximately twice the dissociation rate. As the average photon energy is lowered with successively higher cut-off filters, both rates rapidly decrease. Furthermore, the ratio of desorption to dissociation does not remain constant as on Ag(110). The ratio shows a dramatic increase at lower energy. The dissociation rate displays a threshold near 315 nm while the desorption rate threshold is above 480 nm. The desorption rate dependence may qualitatively be described by two components, one which controls the desorption above 350 nm and one which dominates at shorter wavelengths.

DISCUSSION

O_2/Ag(110). The photochemistry we observe could result from a number of excitations; thermal, plasmon, photoelectron, substrate hot carrier, or direct excitation.
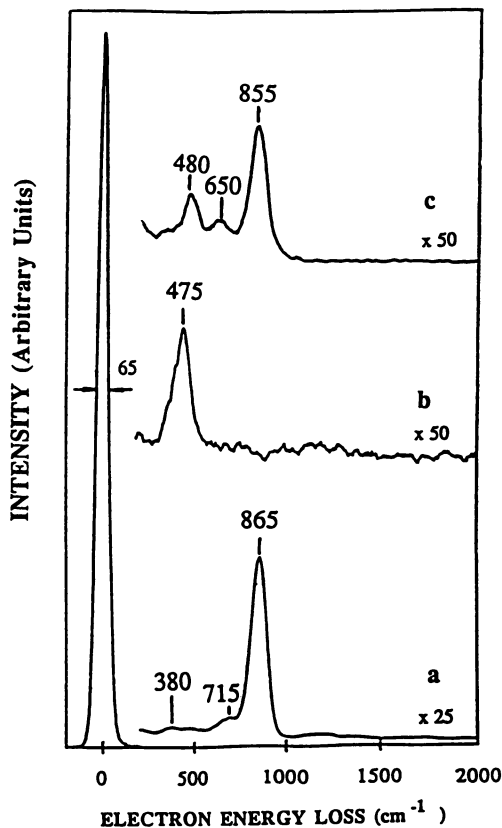
Figure 9. On Pt(111) at 95 K, HREELS of (a) 0.45 mL [O_2], (b) 0.25 mL [O], (c) 0.45 mL [O_2] following 6-min irradiation with the unpolarized full arc. (Reproduced from ref. 11. Copyright 1991 American Chemical Society.)
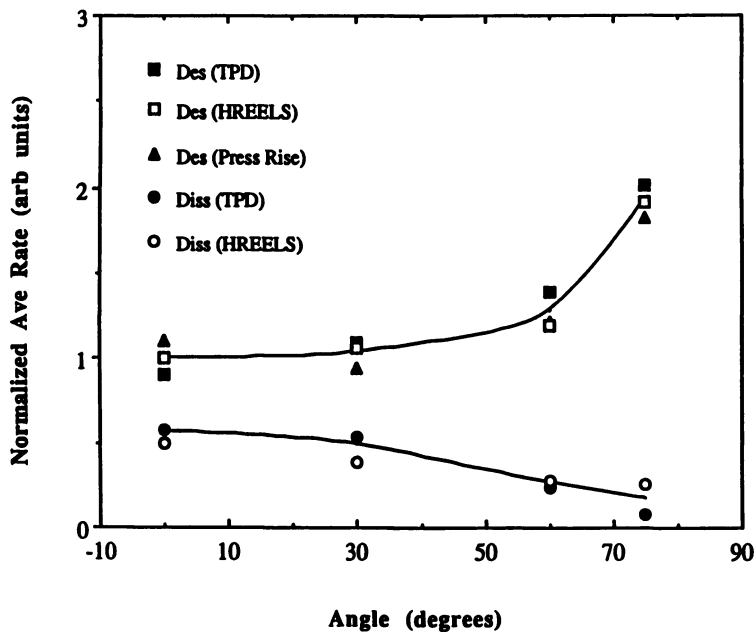
Figure 10. As a function of angle of incidence on O_2-saturated Pt(111), the average rates for photodesorption by TPD (solid squares), HREELS (open squares), and initial pressure rises (triangles); and photodissociation by TPD (solid circles), and HREELS (open circles). The lines are intended as a guide to the eye.
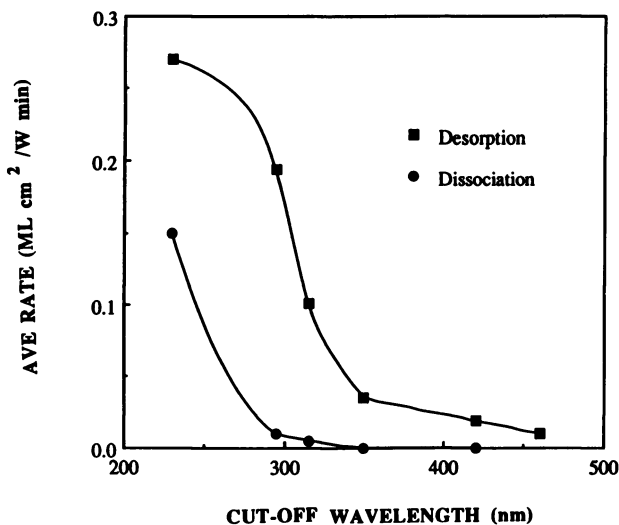
Figure 11. The wavelength dependences averaged over 6 min for photodesorption and photodissociation of O_2 from Pt(111). Each data point corresponds to the wavelength of the cutoff filter used. Therefore, the given rate is actually an integrated rate at wavelengths $\geq$ the indicated number. (Reproduced from ref. 11. Copyright 1991 American Chemical Society.)

Thermally induced dissociation and desorption were not observed during irradiation of the Ag(110) surface. The temperature rise was always less than 1 K (which is also consistent with thermal modelling from the base temperature of 100 K) and irradiation times were short, typically less than one minute. Since silver has both surface (3.75 eV) (27) and bulk (3.9 eV) (28) plasmons in the wavelength range of these experiments, their possible role in the photochemistry should be considered. The Ag(110) surface is flat so that excitation of the surface plasmon by light is forbidden by momentum conservation. The bulk plasmon could be excited, however, under the conditions of this experiment and one might therefore expect some signature in the excitation spectrum. We observe no features in the photochemical excitation spectrum that could be attributed to plasmon excitation and thus conclude that it is not important for this system. Photoelectrons should not be a contributing factor in the present study since we worked at energies well below the relevant work function. The Ag (110) work function is 4.52 eV (29) and it *increases* by 0.8 eV when 0.5 ML of atomic oxygen is adsorbed (30). The highest energy photon used in this study was 4.43 eV (280 nm) and the power densities used were so low (0.1 W cm^{-2}) that multiphoton processes were not important. Thus we conclude that the photochemistry we observe is not driven by the generation of photoelectrons. We consider the possibilities of direct and hot carrier excitation in the following section.

Polarization Probe of the Excitation Mechanism. The interaction of polarized light with an adsorbate covered surface will be governed by the energy and angle of incidence of the light and the optical properties of the surface. For monolayer coverages, the adsorbate layer may be considered optically thin, that is, we can neglect reflection and refraction of light in the thin layer. This approximation is valid for wavelengths (λ) much larger than the thickness of the adsorbate layer (d), so that the contribution d/λ to the phase shift upon reflection is negligible (31). A propagating light wave, shown schematically in Figure 12, incident on a surface may be described by two mutually orthogonal polarizations: p-polarization, where the electric vector lies in the plane of incidence, and s-polarization, where the electric vector is perpendicular to the plane of incidence. For p-polarization, there are two components of the electric field vector, one parallel (E_x) and one perpendicular (E_z) to the surface plane. The s-polarized electric field component (E_y) lies in the plane of the surface. The angle of incidence (θ), is defined with respect to the surface normal.

From Maxwell's equations and the appropriate boundary conditions, the Fresnel coefficients (r) correlating the electric field amplitudes (E) of incident and reflected light can be derived (31):

$$r_p = \frac{E_p^r}{E_p^i} = \frac{-n_t^2 \cos\theta + n_i (n_t^2 - n_i^2 \sin^2\theta)^{1/2}}{n_t^2 \cos\theta + n_i (n_t^2 - n_i^2 \sin^2\theta)^{1/2}} \qquad (1)$$

$$r_s = \frac{E_s^r}{E_s^i} = \frac{n_i \cos\theta - (n_t^2 - n_i^2 \sin^2\theta)^{1/2}}{n_i \cos\theta + (n_t^2 - n_i^2 \sin^2\theta)^{1/2}}, \qquad (2)$$

where the subscripts p and s refer to the incident polarization, and the superscripts i and r denote the incident and reflected fields. n_i ($n_i = 1$) and n_t ($n_t = n_t - ik_t$) are the respective complex indices of refraction of vacuum and the metal.

The reflection coefficients, r, may be expressed in the polar form,

$$r_p = R_p^{1/2} \exp(i\delta_{r_p}) \quad \text{and} \quad r_s = R_s^{1/2} \exp(i\delta_{r_s}). \qquad (3)$$

R is referred to as the reflectivity. δ is the phase shift between the two waves found by

$$\delta = \tan^{-1}[Im(r)/Re(r)]. \tag{4}$$

The total electric field at the surface is found by summing the incident and reflected fields. Considering the coordinate system of Fig. 12,

$$E_x = (E_p^i - E_p^r)\cos\theta \tag{5}$$

$$E_y = (E_s^i + E_s^r) \tag{6}$$

$$E_z = (E_p^i + E_p^r)\sin\theta \tag{7}$$

The mean square fields at the surface, given by $<E^2>$, for each orientation, are

$$<E_x^2> = <(E_p^i)^2>(1 + R_p - 2R_p^{1/2}\cos\delta_p)(\cos^2\theta) \tag{8}$$

$$<E_y^2> = <(E_s^i)^2>(1 + R_s + 2R_s^{1/2}\cos\delta_s) \tag{9}$$

$$<E_z^2> = <(E_p^i)^2>(1 + R_p + 2R_p^{1/2}\cos\delta_p)(\sin^2\theta) \tag{10}$$

The mean square electric fields and substrate absorbances have been calculated from these equations and the optical constants for Ag. Figure 13 shows the angle of incidence dependent results for p and s polarized radiation at 365 nm. At normal incidence ($0°$) the perpendicular field intensity is zero; only the parallel electric fields exist. With increasing angle the perpendicular field maximizes at $53°$ before returning to zero at grazing incidence. The parallel fields decrease monotonically to zero.

The transition rate ($w_{\nu\nu'}$) following direct local excitation of either intra-adsorbate or adsorbate-substrate bonds, assuming plane waves and low power, is described by Fermi's Golden Rule:

$$w_{\nu\nu'} = (2\pi c/ih\nu)|<\nu'|h_1|\nu>|^2\delta(\varepsilon_{\nu'} - \varepsilon_\nu - h\nu) \tag{11}$$

where,

$$h_1 = eE \cdot p/2mc. \tag{12}$$

Here, p is the linear momentum operator and E, the bulk electric field. The perturbation h_1 can lead to a transition between levels ν and ν', whose energies are given by ε_ν and $\varepsilon_{\nu'}$. $h\nu$ is the optical excitation energy. e and m are the electric charge and mass of an electron. Thus, for a given photon flux, the photolysis rate will be proportional to $<\mu\cdot E>^2$, where μ is the transition dipole moment vector and E is the electric field vector. At normal incidence, only electric field components in the plane of the surface exist. Transition moments oriented along the surface normal will not be excited. For transition moments lying in the plane of the surface, the photolysis rate should follow a $\cos^2\phi$ dependence, where ϕ is the angle between the transition dipole moment and the electric vector.
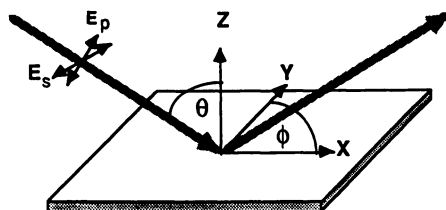
Figure 12. A schematic of the relevant angles and directions relative to the surface for the electromagnetic field vectors of the incident light. θ represents angle of incidence with respect to the surface normal . ∅ is the angle between the O_2 bond axis and the electric vector of the light in the plane of the surface.

ANGLE (degrees)
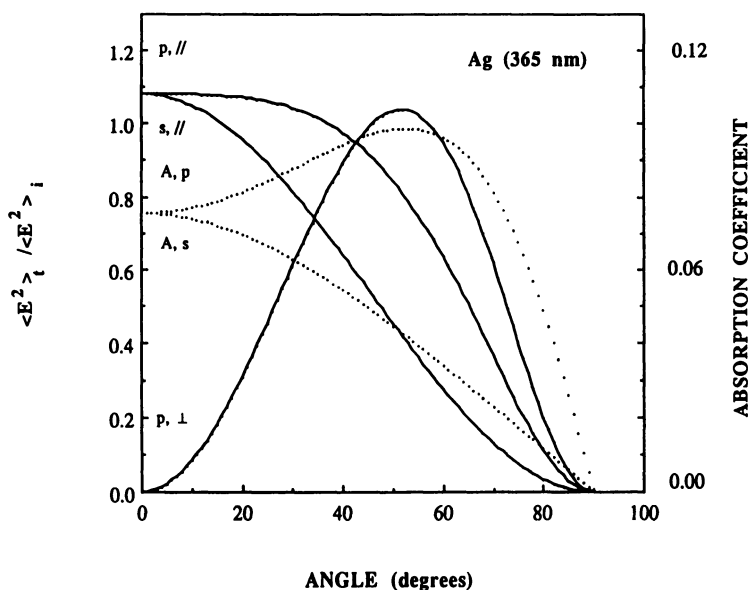
Figure 13. Mean square electromagnetic field strengths, $<E^2>$, and metal absorption coefficients, A, for 365 nm light impinging on a Ag surface as a function of the angle of incidence. The curves are derived from the complex index of refraction of silver and Fresnel's equations. The subscripts p and s are the incident polarizations, and // and ⊥, the orientation of the vector component with respect to the surface plane.

This dependence is illustrated for oxygen bound to the surface in a likely site of C_{2v} symmetry. The possible direct intra-adsorbate transitions favoring dissociation which are symmetry allowed are: (1) $\pi_{//}*$ $(\pi_{g//})$ ---> $3\sigma*$, (2) $\pi_{\perp}*$ $(\pi_{g\perp})$ ---> $3\sigma*$, (3) $\pi_{//}$ $(\pi_{u//})$ ---> $\pi_{//}*$ $(\pi_{g//})$, or (4) $\pi_{\perp}*$ $(\pi_{g\perp})$---> $\pi_{//}*$ $(\pi_{g//})$. These states are shown in Scheme I and their relevance to surface bonding is discussed in detail below. From symmetry considerations, the orientations of the transition dipole moments for each transition may be deduced. For direct excitations (1) and (4) the transition dipoles are oriented perpendicular to the O-O bond axis in the surface plane, for (2) the transition dipole is oriented normal to the surface, and in (3) it is oriented along the bond axis. Thus, for normally incident light, we expect in a direct excitation process to see photodissociation maxima for excitations (1) and (4) when ϕ is ±90° from the bond axis, for transition (3) when ϕ is oriented along the bond axis, and for (2) we expect no photodissociation.

If substrate-mediated charge transfer is the primary excitation mechanism, the photolysis rates will show the same wavelength, angular, and polarization dependences as the metal absorbance. The absorption coefficients (A) are given by

$$A_p = 1 - R_p \quad \text{and} \quad A_s = 1 - R_s . \tag{13}$$

Figure 13 shows the dependence of the the metal absorption coefficients calculated from these equations for s-polarized (A_s) and p-polarized (A_p) light as a function of angle of incidence. For both polarizations there is significant absorption at 0° with s-polarization decreasing monotonically to zero and p-polarization passing through a maximum at 53°. For normally incident light, the photochemical rates should not depend on polarization, the absorption coefficents being equal.

The different dependences on angle of incidence, each reflecting the source of the initial excitation, provide an effective means of distinguishing the surface photochemistry mechanisms. As shown in Figure 3, we find no dependence in the photodissociation or photodesorption rates on the angle between the molecular axis and the electric vector of the incident light. The observation of significant photochemistry at normal incidence further indicates that a normal component of the electric field is not required. These results provide strong evidence that substrate excitation is the dominant mechanism for this system.

The complimentary angle of incidence dependences in Figure 4 are also clearly consistent with substrate excitation. If direct absorption of p-polarized light were responsible for the photochemistry, then a combination of normal and parallel electric fields would be required to explain the observed angular dependences. This, in turn, would imply a transition dipole moment oriented somewhere between parallel and normal to the surface, but predominantly parallel. If this were the case, and we have already suggested that parallel dipoles should be highly oriented azimuthally due to the ordering of the oxygen molecules on this surface, then a strong azimuthal dependence for the photochemistry should be observed. Since this is contrary to our experimental results we take this observation as additional evidence in favor of a substrate-mediated mechanism. Thus, we conclude that hot-carrier driven photochemistry provides the most satisfactory explanation for both photodissociation and photodesorption of dioxygen on Ag(110).

Reaction Mechanisms. The bulk of the experimental and theoretical evidence shows that O_2 binds molecularly to Ag(110) with the O-O bond parallel to the surface and oriented along the [$1\bar{1}0$] azimuth. The low HREELS vibrational frequency of the ν (O-O) at 638 cm^{-1} (gas phase = 1580 cm^{-1}) (32) is generally attributed to the weakening of the O-O bond associated with substantial metal charge donation to the O_2
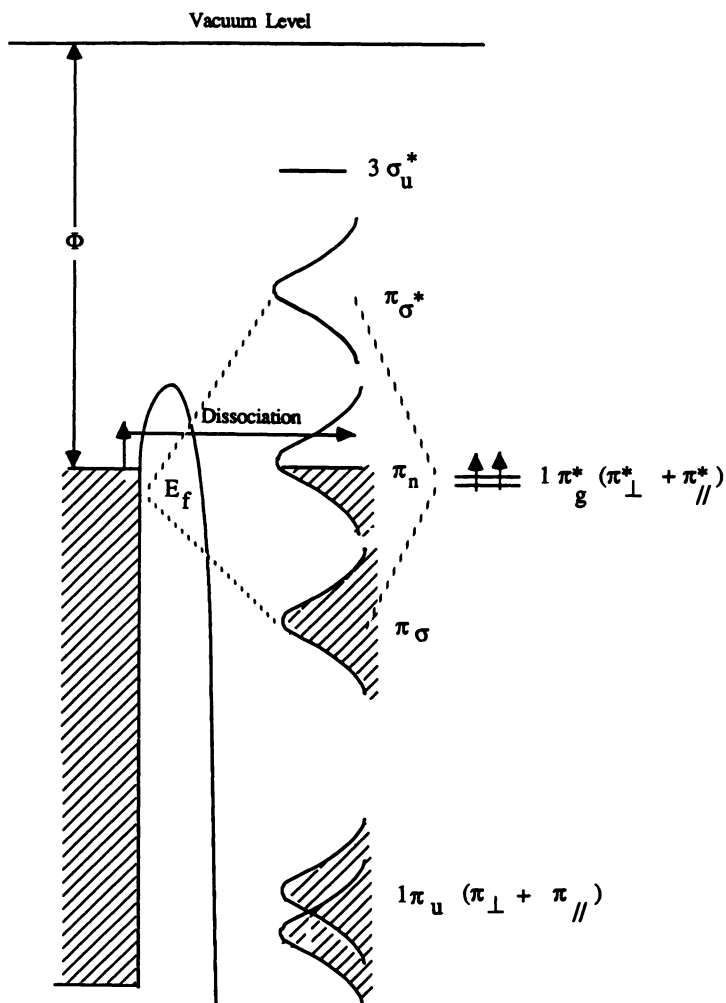
O_2 /Ag(110)   Scheme I

(π^*) orbitals. HREELS, UPS, NEXAFS, and calculations by Upton et al. suggest transfer of between one and two electrons to the O_2 (π^*) orbitals (12-17).

Van den Hoek and Baerands calculated the potential energy surface for O_2 chemisorbing and dissociating on Ag(110) (16). They found a backdonation from silver sp- and d- orbitals to the O_2 π^* (π_g) orbital of 1.40 electrons (Scheme I). However, strong overlap of the metal sp- and d- bands with the O_2 π (π_u) orbital results in a donation to silver of 0.46 electrons. They report negligible back donation to the σ^* orbital. The combined filling of the π^* state and depletion of the π bonding orbital lowers the O-O stretch frequency. Furthermore, the relative occupations of the orbitals are sensitive to the O-O internuclear separation. For increasing separation, the π^* population increases while the π population decreases. As a result of the increased bonding and backbonding, the O_2 chemisorption energy increases with O-O separation. The calculated barrier to dissociation is 0.20 eV. Campbell has reported a barrier of 0.34 eV (21).

Considering the bonding of O_2 to Ag(110), we suggest the model depicted in Scheme I for photo-induced O_2 dissociation. Upon adsorption, the degeneracy of the oxygen frontier $1\pi^*_g$ orbital is lifted: the orbital parallel to the surface (π_n) is primarily nonbonding with respect to the metal, while the perpendicular orbital mixes with Ag sp- and d- bands. The strong interaction results in a surface bonding state (π_σ) localized on O_2 and an antibonding state localized mainly on the metal (π_σ^*). Absorption of radiation initiates production of electrons. These hot electrons propagate through the silver lattice and tunnel to the affinity levels of the adsorbate; in the case of O_2/Ag(110) these include the π_n orbital and possibly the $3\sigma^*$, at higher energy. By analogy to the dynamic charge transfer process described above, transfer to the partially empty π_n level is likely sufficient to overcome the small barrier (0.2 to 0.34 eV) to dissociation (it is antibonding with respect to the O-O bond). Associated with charge transport to the π_n level and elongation of the O-O bond, is transfer in the reverse direction to empty metal bands from the O_2 π level. The increased π^* (π_n) orbital population together with the decreased π orbital population leads to dissociation. Molecular desorption is not promoted by these charge transfers.

The suggestion that metal-to-adsorbate charge transfer does not directly initiate desorption seems contrary to the experimental results. The experimental evidence suggests that substrate absorption is responsible for desorption as well as dissociation (Figures 3 and 4). For O_2/Ag(110), metal charge transfer to other orbitals, ie. π_σ^*, the antibonding component of the O_2 π^* surface interaction is a possibility, but the similarity in photolysis energy thresholds and the similar ratios of desorption to dissociation suggest that both channels are activated by the same excitation (Figure 5).

The results of Figures 3, 4, and 5 suggest a common photoexcitation mechanism for both dissociation and desorption. Following substrate absorption and charge transfer to π_n, O_2 dissociates, forming atoms which could chemisorb with bond energies in the range of 3.47 to 4.12 eV ($16,21$). Since dioxygen is much more weakly bound (0.1 to 0.4 eV) ($16,21$), atomic oxygen produced by photodissociation could force the desorption of molecular oxygen as both compete for available sites. At low coverage, little or no desorption is observed as vacant sites are readily available. At high coverages, however, each dissociating adatom will force desorption of a dioxygen molecule. This accounts for the 2:1 ratio observed for the relative rates of photodesoption and photodissociation shown in Figure 5. Backx et al. (12) proposed a similar mechanism for thermally induced desorption. Heating the surface to 190 K results in both dissociation and desorption as measured by HREELS and TPD.

Our mechanism may be described by the following reaction sequence:
a) creation of two nascent oxygen atoms,

$$O_2(a) + e^- \xrightarrow{ k_{diss} } 2\,O^*;$$
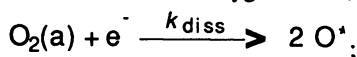
b) the nascent atom can either induce molecular desorption,

$$O^* + O_2(a) \xrightarrow{\ k_{des}\ } O(a) + O_2(g),$$
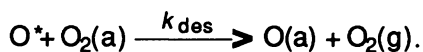
c) or it may bind to an available site without inducing desorption,

$$O^* \xrightarrow{\ k_{term}\ } O(a).$$
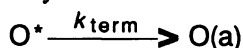
(Since the oxidation state of the nascent atom is unknown, we have supressed charge balance in the equations.) Steps b) and c) introduce a coverage dependence to the desorption rate. Combining these reaction steps and assuming a steady state concentration for nascent O^*, we derive the following rate laws for depletion of O_2, formation of O, and desorption of O_2:

$$\frac{d[O_2(a)]}{dt} = -k_{diss}[O_2(a)] - \frac{2k_{diss}\,k_{des}}{k_{term}[O_2(a)]^{-1} + k_{des}}[O_2(a)] \qquad (14)$$

$$\frac{d[O(a)]}{dt} = 2k_{diss}[O_2(a)] \qquad (15)$$

$$\frac{d[O_2(g)]}{dt} = \frac{2k_{diss}\,k_{des}}{k_{term}[O_2(a)]^{-1} + k_{des}}[O_2(a)]. \qquad (16)$$

The first term on the right hand side of eq.(1) is dioxygen loss from first order dissociation. The second term describes dioxygen loss arising from desorption. In the limit of high coverage the second term reduces to a first order rate that is twice the dissociation rate. As O_2 coverage decreases, the increasing influence of the termination step c), drives the rate down.

From the best fit to both the time dependences and intial coverages shown in Figures 6 and 7, we obtain the rate constant for dissociation, k_{diss}. The rate constant, converted to a cross section, σ, according to

$$\sigma = k/f \qquad (17)$$

where f is the photon flux, yields a photodissociation cross section, $\sigma_{diss} = 2 \times 10^{-19}$ cm^2 at 313 nm. Desorption is considered within this mechanism to be much faster than the initiating dissociation. The best fit is obtained when k_{des} is significantly larger than $k_{term}[O_2]^{-1}$, suggesting that the rate law for depletion of O_2 reduces to

$$\frac{d[O_2(a)]}{dt} = -k_{eff}[O_2(a)], \qquad (18)$$

where the effective rate constant for the process, $k_{eff} = 3k_{diss}$. The linear dependence of $\ln[O_2]$ shown in Figure 14 gives a k_{eff}, which, when converted to a cross section, yields $\sigma_{eff} = 6.0 \times 10^{-19}$ cm^2, or 3 times the σ_{diss} calculated above.

Further evidence for the validity of this model is found by comparing the ratio of the photolysis rates for a fixed coverage at different excitation energies. According to the proposed mechanism, if desorption is activated by dissociation, the ratio of the photolysis rates at saturation coverage should be independent of the excitation energy and should be approximately 2. From Figure 5 it is evident that the ratios of the photodesorption to photodissociation yields are nearly constant at approximately 2 for the wavelengths examined in this study.

O_2/Pt(111). Having discussed O_2/Ag(110) in terms of a simple substrate excitation model we now turn to O_2/Pt(111). The adsorption and photoactivity of O_2 on Pt(111) have been discussed at length previously (18). At 100 K, molecular oxygen adsorbs
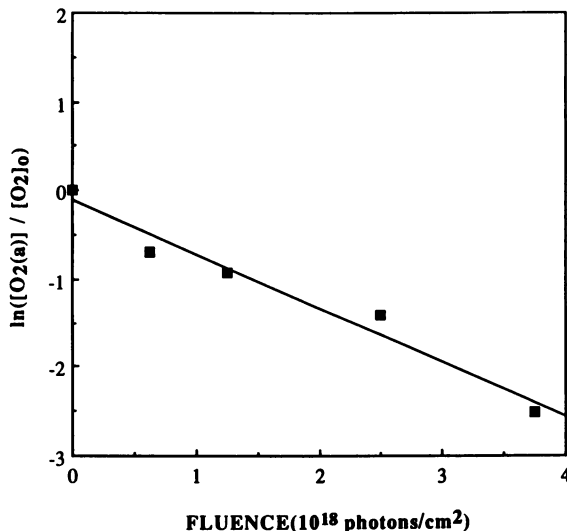
Figure 14. For O_2-saturated Ag(110), a semilog plot of O_2 concentration vs. photon fluence. Concentrations are determined from HREELS following exposure through a 313-nm bandpass to unpolarized radiation. (Reproduced from ref. 11. Copyright 1991 American Chemical Society.)

parallel to the surface as a peroxo (O_2^{2-}) or, possibly, a superoxo (O_2^{1-}) species. A saturation coverage of dioxygen increases the Pt work function from 5.8 eV to 6.6 eV, ruling out participation of photoelectrons for the energies reported here (< 5.3 eV). As the crystal temperature never exceeded 97 K during irradiation, thermally induced desorption and dissociation comprise only a very small fraction of the observed photochemistry and are accounted for in the rate calculations.

Opposing variations in the photolysis rates of dissociation and desorption with the incident angle of an unpolarized beam are clearly evident in Figure 10. Whereas the dissociation rate drops monotonically with increasing angle to 75°, the desorption rate increases. As the angle of incidence changes from normal to grazing incidence, the orientation of the plane of polarization changes from parallel to almost normal to the surface. The opposite trends in the angular rate dependence imply that two different mechanisms are at work here and we suggest that at least one channel is controlled by direct excitation. Assuming that hot electrons alone initiated the photochemistry, one would expect similar angular dependences in the photolysis rates.

The wavelength response given in Figure 11 provides some insight into the mechanisms responsible for the strikingly different angle dependences. The photodissociation energy dependence is very nearly the same as for gas phase hydrogen peroxide (discussed above), suggesting the influence of direct intra-adsorbate excitation. The angle dependence of dissociation is consistent with a direct excitation pathway if the transition dipole moment is in, or very close to, the plane of the surface. Dioxygen binds to Pt(111) in much the same way as on Ag(110): the π^* orbital perpendicular to the surface interacts strongly with the metal d band producing bonding (π_σ) and antibonding (π_σ^*) orbitals with respect to the surface while the parallel π^* orbital is primarily non-bonding (π_n). Direct excitation from π_n to the 3 σ^* level, as in hydrogen peroxide, can account for dissociation. The orbital symmetries for this transition suggest the relevant dipole is in the surface plane and perpendicular to the O-O bond axis, consistent with the observed angle dependence. Hot electron

tunneling to orbitals antibonding with respect to the O-O bond, the 3 σ^* or the π^* derived levels, as for Ag(110), might also lead to dissociation. The larger energy threshold for O_2 dissociation on Pt(111), suggests however, that transfer to the π^* levels may not be sufficient to induce dissociation. The shorter O-O bond distance on Pt(111), ~1.4 Å versus ~1.5 Å (*14,15*) on Ag(110), suggests a higher activation energy for dissociation.

The wavelength dependence for photodesorption shown in Figure 12, is consistent with the wavelength dependence for singlet O_2 elimination from the organometallic compound, $[P(C_6H_5)_3]_2PtO_2$, which has a threshold at 450 nm. (*33*). Based on this similarity, Zhu, et al. (*18*) have proposed an O_2 desorption mechanism similar to the photoinitiated ligand to metal charge transfer mechanism of $[P(C_6H_5)_3]_2PtO_2$. In this model, desorption is induced from a π_n to π^*_σ intra-adsorbate transition. Metal absorption alone cannot account for the large increase in desorption seen at high angles in Figure 10. Although we do not rule out a contibution from a hot electron mechanism, the angle dependence suggests that a direct excitation mechanism dominates the photodesorption of dioxygen on Pt(111).

Conclusions

The findings of this study may be summarized as follows. We have shown that UV irradiation of aligned dioxygen chemisorbed on Ag(110) induces dissociation and desorption at wavelengths shorter than 440 nm. In this study, the incident photon energy is not sufficient to excite photoelectrons above vacuum. The observations that (1), photolysis rates are independent of the orientation of the incident electric field vector and (2), that the rate dependence on angle of incidence is consistent with metal absorption, suggest a substrate-mediated process. The wavelength dependence of the cross-sections for both photo-induced dissociation and desorption have a long wavelength threshold near 440 nm and the ratio of dissociation to desorption rates remains constant at 1:2 for the wavelengths studied. These results suggest a common initiation step for both processes. Analysis of a proposed reaction model in which dissociating atoms displace molecular oxygen from the surface, reproduces the initial coverage and irradiation time dependences for both channels. The photolysis cross sections are estimated using this model.

We have also examined the angular dependence of photodissociation and photodesorption of O_2 on Pt(111). In contrast to Ag(110), we find a striking difference in the angular dependences of the rates of photodissociation and photodesorption: whereas photodissociation decreases with increasing angle, photodesorption increases. This difference demonstrates the channels cannot have a common origin; based upon this and other cited evidence we suggest that at least one channel is dominated by intra-adsorbate bond excitation. Although we are not able to determine the relative contributions of substrate or direct excitation to photoinduced dissociation, the angular dependence suggests that direct excitation contributes significantly to photodesorption.

Acknowledgements

Literature Cited

(1) Domen, K.; Chuang, T. J. *J. Chem Phys.* **1989,**90, 3318.
(2) Avouris, P.; Walkup, R. E. *Annu. Rev. Phys. Chem.* **1989,**40, 173.
(3) Ho, W. In *Desorption Induced by Electronic Transitions, DIET IV,* Springer Series in Surface Science, Springer: Berlin, in press.

(4) White, J. M. Presented at the 9th International Summer Institute in Surface Science at Milwaukee, WI 1989.
(5) Liu, Z.-M.; Costello, S. A.; Roop, B.; Coon, S. R.; Akhter, S.; White, J.M. *J. Phys. Chem.* **1989**,*93,* 7681.
(6) Hanley, L.; Guo, X.; Yates, Jr. J. T. *J. Chem. Phys.* **1989**, *91*, 7720.
(7) Marsh, E.P.; Schneider, M.R.; Gilton, T. L.; Tabares, F. L.; Meier, W.; Cowin, J. P. *Phys. Rev. Lett.* **1988**,*60*, 2251.
(8) Cho, C.-C.; Collings, B. A.; Hammer, R. E.; Polanyi, J. C.; Stanners, C. D.; Wang, J.H.; Xu, G.-Q. *J. Phys. Chem.* **1989**, *93*, 7761.
(9) Buntin, S. A.; Richter, L.J.; King,D. S.; Cavanagh, R. R.; *J.Chem. Phys.* **1989**, *91*, 6429.
(10) Hasselbrink, E.; Jakubith, S.; Nettesheim, S.; Wolf, M.; Cassuto, M.; Ertl, G. *J. Chem. Phys.* **1990**, *92,* 3154.
(11) Hatch, S. R.; Zhu, X.-Y.; White, J.M.; Campion, A. *J. Phys. Chem.* **1991**,*95*, 1759.
(12) Backx, C.; M. De Groot, C. P.; Biloen, P. *Surf. Sci.* **1981**, *104*, 300.
(13) Prince, K.C.; Paolucci, G.; Bradshaw, A. M.; *Surf. Sci.* **1986**, *175*, 101.
(14) Outka, D. A.; Stohr, J.; Jark, W.; Stevens, P.; Solomon, J.; Madix, R. J. *Phys. Rev. B.* **1987**, *35*, 4119 .
(15) Upton, T. H.; Stevens, P.; Madix, R. J. *J. Chem. Phys.* **1988**, *88*, 3988.
(16) Van Den Hoek, P. J.; Baerends, E. J. *Surf. Sci.* **1989**,*221*, L791.
(17) Sexton, B. A.; Madix, R. J.; *Chem. Phys. Lett.* **1980**,*76*, 294 .
(18) Zhu, X.-Y.; Hatch, S. R.; Campion, A.; White, J.M. *J. Chem. Phys.* **1989**,*91*, 5011 .
(19) Backx, C.; De Groot, C. P. M.; Biloen, P.; Sachtler, W.H.M. *Surf. Sci.* **1983**,*128*, 81.
(20) Barteau, M. A.; Madix,R. J. *Surf. Sci.* **1980**, *97*, 101.
(21) Campbell, C. T. *Surf. Sci.* **1985**, *157*, 43.
(22) *American Institute of Physics Handbook*, 3rd Ed.; Gray, D.E., Ed.; McGraw-Hill: New York, 1972.
(23) Okabe, H. *Photochemistry of Small Molecules*; Wiley: New York, 1978; p 282.
(24) Steininger, H.; Lehwald, S.; Ibach, H. *Surf. Sci.* **1982**, *123,* 1.
(25) Avery, N. R. *Chem. Phys. Lett.* **1983**, *96*, 371 .
(26) Gland, J. L. *Surf. Sci.* **1980**, *93*, 487 .
(27) Kempa, K.; Forstman, F.; Kötz, R.; Hayden, B. E.; *Surf. Sci.* **1982**, *118*, 649.
(28) *Handbook of Optical Constants of Solids*; Palik, E. D., Ed.; Academic Press: Orlando, 1985.
(29) Dweydari, A. W.; Mee, S. H. B.; *Phys. Stat. Solidi. A* **1975**, *27*, 233.
(30) Englehart, H. A.; Menzel, D.; *Surf. Sci.* **1976**, *57*, 591.
(31) McIntyre, J. D. E. *Advances in Electrochemistry and Electrochemical Engineering*, Vol. 9, Delahay, P.; Tobias, C.W., Eds.; John Wiley and Sons: New York, 1973; p 61.
(32) Huber, K. P.; Herzberg, G. *Constants of Diatomic Molecules*; Van Nostrand Reinhold: New York, 1979.
(33) Volger, A.; Kunkely, H. *J. Am. Chem.* Soc. **1981**, *103*, 6222.

Chapter 22

Time-Resolved Study of Laser-Induced Thermal Desorption

Z. Rosenzweig and M. Asscher

Department of Physical Chemistry and the Fritz Haber Center for Molecular Dynamics, The Hebrew University, Jerusalem 91904, Israel

A pump-probe experiment was performed to study the desorption of ammonia from a Re(0001),at nsec time scale,following a pulsed laser induced thermal desorption.Optical second harmonic generation (SHG) was utilized to monitor the decreasing ammonia coverage as a function of delay time between the pump and the probe laser pulses.It was found that coverage dependent desorption kinetic parameters,determined under equilibrium conditions,could reproduce very well the nsec time scale desorption event.Thermal heat diffusion model,was found to predict correctly the surface temperature,therefore also the directly monitored desorption rates.Desorption is thus employed for the first time as an indirect probe of transient surface temperature changes at nsec time scale.

In an attempt to find new ways to understand better and to control chemical processes at surfaces, several pulsed laser based techniques have been developed (1).Among them,laser induced thermal desorption (LITD) have emerged as a useful tool for the study of chemical kinetics (2-6) and diffusion (7-10) on surfaces.Analysis of the molecules leaving the surface is done at the gas phase ,typically by means of a quadrupole mass spectrometer or optical methods (e.g. laser induced fluorescence (5) or REMPI (6),after the desorption event has been completed.Traditional methods to directly follow the surface coverage in real time,such as work function change,Auger spectroscopy or SIMS are far too slow for the nsec time regime.

The purpose of this study was to address two main questions:The possible use of coverage

dependent desorption kinetic parameters of
ammonia,determined at equilibrium-thermal
conditions,to a transient temperature change at
the nsec time scale.The second goal was to check
if the thermal heat diffusion equations (11-13)
which are frequently used in LITD studies,correctly
describe the temporal profile of the surface
temperature,as a result of pulsed laser heating.
This question was experimentaly addressed for the
first time by Hicks et.al.(14).These authors
directly monitored the temperature change of
a Ag(110) surface, following the irradiation by
a 8nsec wide (FWHM) heating laser pulse.In their
study they have used the unique surface temperature
dependence of the optical second harmonic generation
(SHG) from this silver sample at 628nm fundamental
laser wavelength.Their conclusion was that thermal
heat diffusion equations correctly describe their
results (14).
         In the present study,a pump-probe experiment was
performed to directly monitor the decreasing surface
coverage of ammonia molecules,during their desorption
from Re(0001) surface,following a 10 nsec (FWHM)
pulsed laser heating.Optical second harmonic
generation technique was employed as a real time
probe of the decreasing ammonia surface coverage.
Here we took advantage of the high sensitivity
(exponential dependence) of the desorption rate to
the surface temperature in order to indirectly
monitor it.SHG was previously used for time
resolved studies of processes at surfaces (15-16)
and interfaces (17),employing its inherent high
temporal resolution and sensitivity to the surface
and interface environment (18).Previous attempts to
directly monitor the removal of molecules from
surfaces,were performed at psec time scale,however
they were limited to ill defined surfaces in
solution (19) or under atmospheric pressure
conditions (20).Attempts to monitor the removal of
adsorbates in real time following photoinduced
processes are in progress in the subpicosecond
regime (21),however,these are nonthermal processes,
thus generated via a different mechanism than the
pulsed laser induced thermal desorption studied
here.

EXPERIMENTAL

         Two separate Nd:YAG lasers (Quantel YG-585)
were used,one as the heating laser and the other
as the probe,providing the SHG signals.The heating
laser beam at 1064nm,was collimated to a spot of
$0.5cm^2$ at the center of the sample.It was directed
along the normal to the surface,with absorbed power
densities of up to 6.1 MW/cm^2.The p polarized probe

laser beam,at fundamental wavelength of 1064nm, incident angle of 47 degrees from the normal to the surface and power densities of less than 3.0 MW/cm^2,spatially overlapped the heating laser at the center of the sample,having an elliptical spot of 0.05 cm^2.

The two laser pulses could be delayed in time with the probe pulse arriving at the time range of 20nsec before the heating pulse to 500nsec after the heating pulse,with a jitter of less than 2nsec. The UHV chamber,sample preparation and the optical SHG measurements,applied to the NH$_3$/Re(0001) system were described in detail in previous publications (22,23).The equilibrium measurements,from which the coverage dependent activation energy for desorption,Ed(θ),and the preexponent A(θ),of ammonia from Re(0001),will be briefly described below.

The heating laser was operated at 0.25Hz at an ambient ammonia pressure of 5*10^{-7} mbar,with the surface kept at temperature of 120K.This way, a constant surface coverage of approximately one monolayer is kept, before each of the pump laser pulses is hitting the surface,regardless of the fraction of molecules desorbed from the surface as a result of the LITD process (22).At lower surface temperatures,a second layer of ammonia molecules is built up at this ambient pressure.At 10 nsec and longer before the pump laser strikes the surface,the SHG signal reflects the intensity obtained from a monolayer ammonia covered surface,which is 58 times the signal obtained from the clean Re(0001) surface (22).

The SHG signal intensity was measured to be proportional to the surface coverage squared,indicating linearity of the second order susceptibility with adsorbate coverage(18).The relative surface coverage was determined by temperature programmed desorption (TPD) uptake measurements of NH$_3$ from Re(0001) (22) and then calibrated against the SHG signal intensity.

Surface temperature effect on the SHG signal from the clean rhenium metal was measured.Small increase (of 50%) in the SHG intensity was found as crystal temperature was raised from 300 to 700K (opposite to the observation reported for silver(14]).At crystal temperatures in the range of interest for this study, namely 80-450K,the change was about 10% of the clean surfa signal, therefore was neglected.

In order to avoid any effect of dissociation of ammonia on defects (no dissociation was detected on the (0001) terraces),each of the data points taken was the result of 32 laser shots in a single run.Then the surface temperature was raised to 1100K and cooled back to 120K,before readsorption and recording the next data point. For each of the four pump laser power densities,there were 5 separate runs,therefore each of

the data points presented in figure 1,is the
average of 160 laser pulses.

RESULTS AND DISCUSSION

Real time monitoring of the decreasing ammonia
coverage as a result of the pulsed LITD is shown in
figure 1,for four different heating laser power
densities.The experimental data points represent delay
times in which the probe laser is 10nsec before the
heating laser pulse,to delays of 20nsec after the pump
pulse.The rate of desorption of the ammonia molecules
is observed to be independent of pump laser power,as
indicated by the decreasing SHG signal intensity as a
function of the delay time.At higher pump laser power
densities,lower ammonia coverage is left on the
surface at delay times of 15 nsec and longer.
In order to analyze the decay curves shown in
figure 1,one must know these important parameters:
a. The time profile of the surface temperature as a
result of the pulsed laser heating and **b.** The
desorption kinetic parameters as a function of ammonia
surface coverage. **c.** Absorbed laser power density.
For obtaining the first parameter, we have used
the one dimensional heat diffusion expressions for
calculating the surface temperature change as a
function of time following a pulsed laser heating
(11-12).The equations given by Burgess et.al.(13)
were adopted,using a symmetric triangular laser pulse
shape of 10nsec FWHM,as was done in previous studies
(5,6,14).The actual shape of the pump laser pulse is
shown in figure 2 as an insert.
The temporal profile of the surface temperature
$T(0,t)$,as given by the heat diffusion equations is
(11-13):

$$T(0,t)=T_0+(F_0*B/K_c)(K_d/\pi)^{-1/2}\int_0^\tau A(t-\tau)*\tau^{-1/2}\,d\tau \quad [1]$$

where T_0 is the initial crystal temperature,F_0 is the
maximum absorbed laser power density (in MW/cm^2),K_c is
the heat conductivity (the temperature dependence of
which for rhenium is negligible),K_d is the heat
diffusivity (the temperature dependence of which is
non negligible and was taken into account) and
$B=exp(-\alpha*z)$ is the decreasing laser intensity inside
the bulk (z direction,with z=0 at the surface) due to
light absorption by the rhenium atoms.For rhenium these
parameters are: K_c=0.48 Watts/cm^2*K,K_d=0.159 cm^2/sec at
350K,decreasing to 0.145 cm^2/sec at 600K (24).The
absorption coefficient α=6.8*10^5 cm^{-1} at 1100nm.$A(t-\tau)$
is the temporal profile of the heating laser pulse.As
was indicated by Burgess et.al.(13),the overall shape of
$T(0,t)$,is only slightly modified if $A(t-\tau)$ has a
triangle or a Gaussian shape.The resulting $T(0,t)$ is
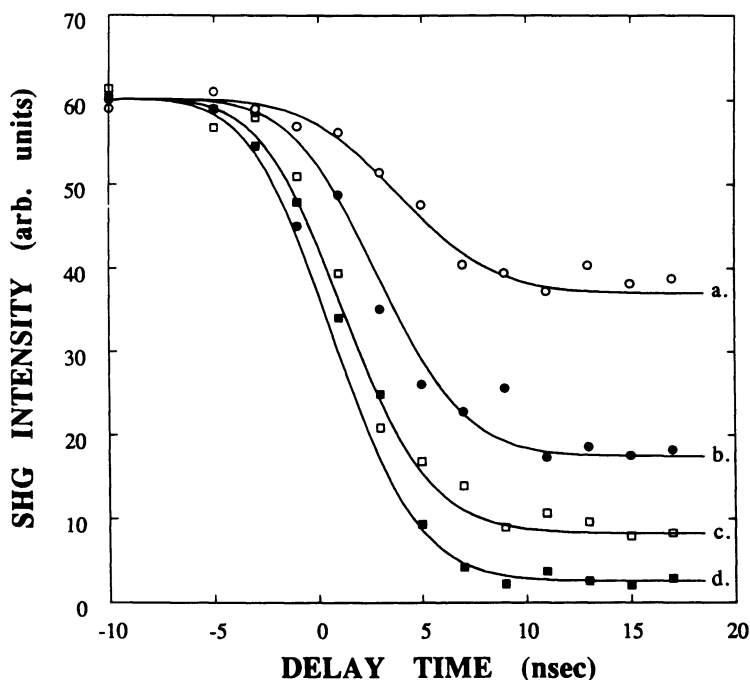
Figure 1 Relative SHG signal intensity as a function of delay time between the pump (LITD) laser and the probe (SHG) laser pulses for 4 heating laser power densities:**a.**4.3MW/cm^2 ;final coverage=θ/θ_s=0.74,θ_s is the saturation (1ML) ammonia coverage. **b.**5.0MW/cm^2 ; θ/θ_s=0.5 **c.**5.5MW/cm^2;θ/θ_s=0.33   **d.**6.1MW/cm^2;θ/θ_s=0.16. The initial ammonia coverage is 1ML on a Re(0001) surface at 120K.The solid lines through the data points are simulated signals,see text.
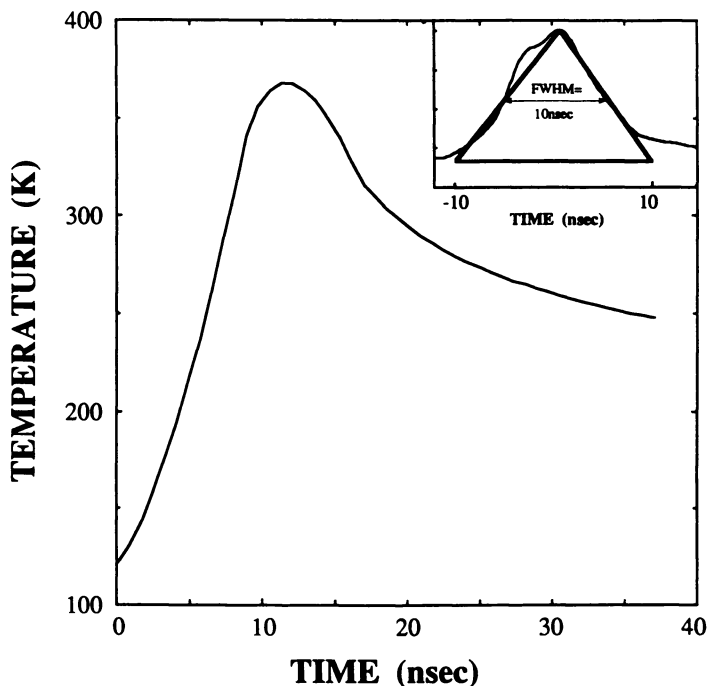
Figure 2   Calculated surface temperature following
a pulsed laser heating for absorbed laser power
density of 4.96MW/cm^2.In the inset the actual
temporal profile of the pump laser pulse is shown
(thin solid line) together with the approximate
triangular shape used in the simulations with
a width of 10nsec FWHM.

shown in figure 2 for an absorbed laser power density of 4.96 MW/cm^2.

The next parameter which we need to know, namely the coverage dependence of both activation energy for desorption and the preexponential factor, should be available over the entire coverage range spanned by the laser induced thermal desorption experiment. Since there is no indication for the dissociation of NH_3, the desorption was considered to be first order. The rate of desorption therefore is given by:

$$R_d = -d\theta/dt = \theta^n A_d(\theta) \exp(-E_d(\theta)/kT)$$, n=1 for a first order process, $A_d(\theta)$ is the preexponential factor and $E_d(\theta)$ is the activation energy for desorption.

By utilizing the SHG as an in situ surface coverage probe, we were able to measure the equilibrium surface coverage of ammonia at various ambient pressures and surface temperatures (22). The equilibrium coverage obtained this way is analyzed in terms of the Clausius-Clapeyron equation to provide the coverage dependent heat of adsorption. Assuming no barrier for adsorption (due to near unity sticking probability in the case of ammonia on rhenium), the heat of adsorption equals the activation energy for desorption $E_d(\theta)$. By equating the rate of adsorption with the rate of desorption under the equilibrium conditions, one may extract an expression for the (coverage dependent) preexponential factor for the rate of desorption (22). This can be done after adjusting for the fact that the adsorbing molecules are at different temperature than the surface (25,26). In figure 3, the resulting activation energy for desorption and the corresponding preexponent ,$A_d(\theta)$, are shown as a function of the SHG determined ammonia coverage. The solid lines through the experimental data points are polynomial fits (27).

The third parameter we need to control for accomplishing the full simulation is the absorbed laser power density. The actual laser power was measured in front of the UHV chamber at its collimated 8mm diameter size with a standard calorimetric power meter. Then the transmission of the specific entrance window of the UHV system was measured and so is the reflectance of our Re(0001) sample at normal incident (28). In the experiment reported here, 4 absorbed power densities of the heating laser were used: 4.3, 5.0, 5.5 and 6.1 MW/cm^2· Next, the actual lateral power density distribution at the sample was measured by utilizing a pinhole-photodiode system on a translation stage at a resolution of 0.12 mm. A relatively flat power distribution was measured at the center of the pump laser beam which enclosed 70% of the total power. Within this area, power fluctuations of 15% were found with a constant lateral distribution. The probe laser power distribution was also measured and found to have only 8% variations across its 2 mm diameter beam.
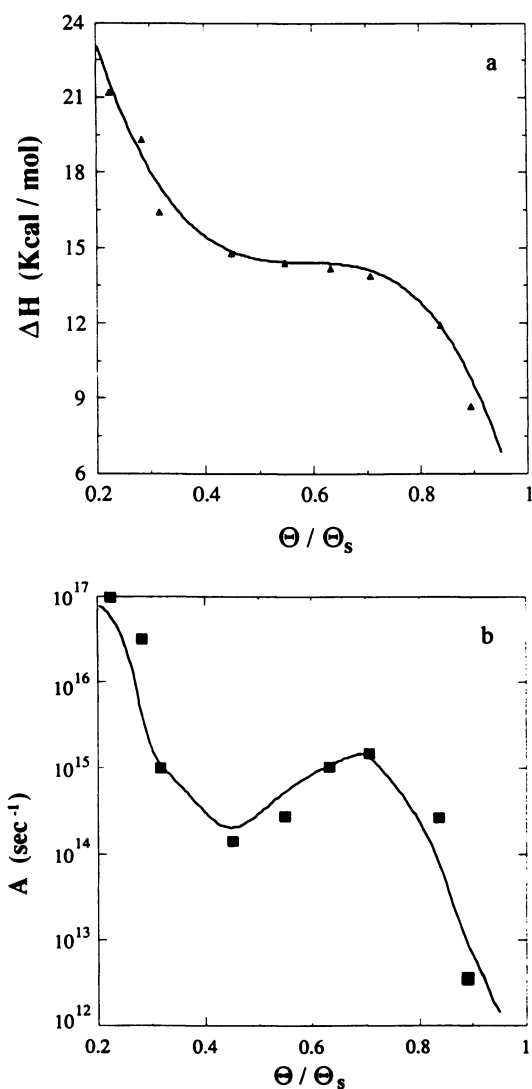
Figure 3   a. Activation energy for desorption E_d
of ammonia from Re(0001) as a function of surface
coverage. b.Preexponent for the rate of ammonia
desorption Ad as a function of coverage.The solid
lines are polynomial fits to the data (26).

Finally,in order to complete the simulation the probe laser temporal pulse shape has to be taken into account.It was calculated to have a Gaussian time profile (10nsec FWHM) in all the simulations presented in figure 1.

The simulated SHG signals as a function of the delay between the pump and the probe lasers are shown in figure 1 as solid lines through the experimental data points.The SHG signal variation with the delay time and its pump laser power independence,are reproduced very well by employing the heat diffusion model for calculating the surface temperature and thus also the temporal profile of the surface ammonia coverage.This temporal shape is totally independent of the desorption kinetic parameters used in the simulation.Only the final coverage left on the surface after the pump laser has terminated,depends on these parameters,as discussed below.

Due to the power variations within the pump laser beam at the area where the probe laser hits the surface,the surface temperature varies across this spot. As a result,the ammonia coverage,as detected by the SHG probe,is necessarily the average over coverages that may vary as much as 25%.Therefore,we do not consider an absolute agreement between the simulated power density which fits the data and the experimental value as a convincing evidence for the applicability of the equilibrium desorption parameters for the fast desorption discussed here.Instead,using the experimental power densities as an input for the simulations we arbitrarily changed the desorption kinetic parameters, so that a comparison can be made, between the equilibrium and the alternative parameters.The resulting surface coverage at delay times of 20nsec and longer are compared with the experimental values determined by the SHG probe. The parameters chosen for this comparison were a frequently used (29),coverage dependent activation energy for desorption: $E_d=20.4-10*\theta$, where the low and the high coverage limits are taken from the equilibrium measurements.With this activation energy,three different coverage independent preexponential factors were used: 10^{14}, 10^{15} and 10^{16} sec^{-1}. Lower preexponential factors, such as the "normal" $A_d=10^{13}$ sec^{-1} (29) or coverage independent activation energy for desorption ,were found to produce the wrong results at any input laser power.The results are displayed in table 1 as ratios of the surface coverage obtained from the simulations and that from the experiment at the same absorbed laser power densities (the experimental values), at delay time of 20nsec.From table 1 we may conclude that the equilibrium desorption kinetic parameters simulate the experimental values to within 15% at all 4 input powers.The other parameters may fit better a single power,but then will deviate much more

at the others.An interesting case is C in table 1 ($A_d=10^{16}$ sec^{-1}).Here,a constant deviation of about 30% is observed for all powers.It seems as if this particular set of parameters compensates well for the coverage dependence of E_d and A_d but predicts always too high desorption rates.

The better agreement of the parameters obtained from the equilibrium measurements may be explained only by their adequate coverage dependence formula for E_d and A_d over the entire coverage range.Although other combinations of desorption kinetic parameters may be tailored to fit the experimental data,we conclude that the equilibrium parameters describe accurately the desorption event which takes place at the nsec time scale.

This statement leads to the conclusion that the desorption of ammonia molecules originates from surface structures that are very similar to those found at equilibrium conditions.During the few nsec at which the surface temperature is at the maximum, the molecules are expected to be able to move away from their equilibrium position only a very short distance (probably less than 0.5Å,assuming a barrier for diffusion that is 1/3 of the activation energy for desorption).
This short diffusion distance together with the strong repulsive interactions among neighbor ammonia molecules, suggest that the desorption event proceeds gradually from the weaker to the more strongly bound molecule-surface complexes,with only minor surface rearrangements prior to desorption.

These desorption conditions, are necessarily similar to those obtained at the lower temperature and slower desorption, characteristic of the equilibrium conditions. We conclude therefore,that the same parameters describe well coverage dependent desorption rates that differ by more than 10 order of magnitude in their absolute values.

SUMMARY

A time resolved laser induced thermal desorption study was performed,utilizing two separate lasers in a pump-probe experiment for the first time in the nsec time range,under well defined UHV conditions.Optical SHG was used as a real time surface coverage probe. The coverage dependent desorption kinetic parameters of NH_3 from Re(0001),determined under equilibrium conditions,were found to describe well the fast desorption as a result of the LITD process.

It was found that the desorption proceeded at rates that were precisely predicted by the transient surface temperatures calculated by the thermal heat diffusion equations.This study,therefore,is the second

TABLE 1: Ratios of simulated to experimental coverages

Abs. power densities exptl. (MW/cm^2)	Exptl.[a] Coverage (E)	Equil.[b] Param./E	A/E[c]	B/E[d]	C/E[e]
4.3	0.74	0.85	1.12	0.90	0.70
4.9	0.5	0.85	1.39	1.03	0.73
5.5	0.33	0.94	1.79	1.21	0.70
6.1	0.16	1.13	3.02	1.76	0.69

(a) The experimental coverages determined by the SHG probe at delay time of 20nsec.
(b) The values for E_d and A_d are shown in figure 3.

(c,d,e) $E_d = 20.4 - 10*\theta$ (kcal/mole);

(c,d,e) $A_d = 10^{14}, 10^{15}, 10^{16}$ sec^{-1}, respectively.

real time experimental proof of the validity of the heat diffusion model for the description of the surface temperature as a function of time following a pulsed laser heating.In the present study,however,it was shown for a relatively poor heat conducting metal,which has ten times smaller heat conductivity and 4 times shorter heat diffusion length compared with silver,for which the first direct experimental proof was demonstrated (14).

LITERATURE CITED
1. Lin,M.C. and G.Ertl,Annu.Rev.Phys.Chem.,**1986**,37,587 ;Zacharias,H.,Appl.Phys.,**1988**,A47,37;King,D.S.and Cavanagh,R.,Adv.Chem.Phys.**1989**,76,45
2.a.Ertl,G. and Newmann,N.,Z.Naturforsch,**1972**,27a,1607 b.Cowin,J.P.,Auerbach,D.J.,Becker,C. and Wharton,L.; Surf.Sci.,**1978**,78,545
3. a.Viswanathan,Burgess,Jr.,R.D.R.,Stair,P.C. and Weitz,E.,J.Vac.Sci.and,Technol.**1982**,20,60
b.Burgess,Jr.,R.D.R.,Viswanathan,R.,Hussla,I. Stair,P.C. and Weitz,E.;J.Chem.Phys.,**1983**,79(10),5200
4.Hall,R.B.,J.Phys.Chem.,**1987**,91,1007
5.Burgess,Jr.,R.D.R.,Cavanagh,R.R. and King,D.S.,J.Chem.Phys.,**1988**,88,6556
6.Prybyla,J.A.,Heinz,T.F.,Misewich,J.A., and Loy,M.M.T.,Surf.Sci.,**1990**,230,L173 .

7. Viswanathan,R.,Burgess,Jr.,R.D.R.,Stair,P.C. and Weitz,E.,J.Electron Spectrosc.Relat.Phenom. **1983**,29,111

8. George,S.M.,DeSantolo,A.M. and Hall,R.B.;Surf.Sci.,**1985**,159,L425

9. Seebauer,E.G.,Kong,A.C.F. and Schmidt,L.D.;Surf.Sci.,**1986**,176,134

10. Mak,C.H.,Brand,J.L.,Koehler,B.G. and S.M.George,Surf.Sci.,**1987**,191,108

11. Ready,J.F.,"Effect of High Power Laser Radiation" (1971,Academic Press,New-York)

12. Bechtel,J.H.;J.Apl.Phys.,**1975**,46,1585

13. Burgess,Jr.,R.D.R.,Stair,P.C. and Weitz,E.,J.Vac.Sci.Technol.,1986,A4(3),1362

14. Hicks,J.M.,Urbach,L.E.,Plummer,E.W. and Dai,H.-L.,Phys.Rev.Lett.,1988,61,2588

15. Zhu,X.D.,Rasing,Th. and Shen,Y.R.,Phys.Rev.Lett.,**1988**,25,2883

16. Tom,H.W.K.,Aumiler,G.D. and Brito-Cruz,C.H.,Phys.Rev.Lett.,**1988**,60,1438

17. Sitzmann,E.V. and Eisenthal,K.B.,J.Chem.Phys.,**1989**,90,2831

18. Shen,Y.R.,Ann.Rev.Phys.Chem.,**1989**,40,327

19. Arjavalingam,G.,Heinz,T.F. and Glownis,J.H. in Ultrafast Phenomena V, Fleming,G.A. and Siegman,A.E. eds.,Springer Verlag,Berlin,**1986**.

20. Meech,S.R. and Yoshihara,K.,J.Phys.Chem.,**1990**,94,4913

21. Prybyla,J.A. and Heinz,T.F., Private communication.

22. Rosenzweig,Z. and Asscher,M.,Surf.Sci.,**1990**,225,249

23. Rosenzweig,Z.,Wittenzelner,C. and Asscher,M.,Surf.Sci.,**1990**,240,L583

24. Toulukian,Y.S.,Powell,R.W.,Ho,C.Y. and Nicolaou,M.C.,"Thermal properties of matter",Vols. 1,4,10,(IFI/Plenum,New-York,**1970**)

25. Chelvayohan,M. and Gomer,R.,Surf.Sci.,**1987**,186,412

26. Seebauer,E.G.,Kong,A.C.F. and Schmidt,L.D.,Surf.Sci.,**1986**,176,134

27. For the simulations presented in this manuscript ,the $E_d(\theta)$ and $A_d(\theta)$ curves in figure 2 were expressed as polynomials in θ as follows:$E_d(\theta)=38.67-123.31*\theta+210.31*\theta^2-119.83*\theta^3$. For $A_d(\theta)$ 4 different 3rd order polynomials were used in order to cover the entire coverage range.

28. The reflectance of Re(0001) at 1064nm is 0.78 as measured near normal incident at the experimental setup described in the text.The literature value is 0.72 at 1000nm (American Institute of Physics Handbook,McGraw Hill,New-York,1972)

29. Benndorf,C. and Madey,T.E., Surf.Sci.,**1983**,135,164

Author Index

Affiliation Index

353

Subject Index